Interpretation and Prediction of the Hydromechanical Behavior of Unsaturated Soils from Tropical Regions

By

Roberto Alves

Thesis proposal submitted to the University of Ottawa and Universidade Federal de Goiás in partial Fulfillment of the requirements for the

Doctorate in Philosophy degree in Civil Engineering

Department of Civil Engineering
Faculty of Engineering
University of Ottawa
Supervisor: Sai K. Vanapalli

Programa de Pós-Graduação em
Geotecnia, Estruturas e Construção Civil
Escola de Engenharia Civil e Ambiental
Universidade Federal de Goiás
Supervisor: Gilson de F. N. Gitirana Jr.

Dedicated to my daughter, Ana, my wife, Fran,
and my parents.

"Se a educação sozinha não transforma a sociedade, sem ela tampouco a sociedade muda."

"If education alone cannot transform society, without it society cannot change either."

Paulo Freire

ABSTRACT

Tropical soils are widespread in many countries and regions of the world, including Brazil, large portions of the African continent, and Asia. These soils are often found in an unsaturated state and their hydromechanical behavior is predominantly influenced by their structure which is often characterized by intra and inter-aggregate pores.

The intense weathering associated with high temperatures and relatively high annual rainfall results in the formation of aggregations associated with the cementation of clay particles. The top few meters of soil depth profile in tropical regions constitute a highly weathered layer (typically, lateritic soil) sitting on top of a less weathered layer with traces of the parent rock (normally, saprolitic soil). These lateritic soils attain aggregations that impart a dual-porosity resulting in a different pore size characteristics that contribute to bimodal soil-water characteristic curve (SWCC) behavior. Also, they attain different characteristics over their long formation period in comparison to conventional soils; due to this reason, traditional classification systems are not suitable.

Despite advances in recent decades, there are limited studies with respect to interpretation and prediction of the hydro-mechanical behavior of bimodal lateritic soils. For this reason, there is a need for rational tools for use in conventional geotechnical engineering practice for the design of various geo-infrastructures extending the principles of unsaturated soil mechanics that are simple, especially in the context of climate change in which unprecedent changes in suction arise.

Most existing constitutive models describing the behavior of unsaturated soils were developed for soils with a single pore-size family. As a result, these models have limitations

or are inadequate for lateritic soils that are typically bimodal in nature. Therefore, the two major objectives of this thesis are: (i) to model the bimodal SWCC, and (ii) to model the shear strength with respect to suction for these dual porosity soils. In this context, the modeling effort includes both advances in the understanding of soil behavior and the development of prediction models.

The SWCC behavior of bimodal lateritic soils was investigated by considering physicochemical aspects and their relation to the soil structure. The analyses were performed relying on a database of 27 soils divided into 25 and 15 datasets corresponding to undisturbed and remolded conditions, respectively. A new framework was proposed to estimate the bimodal SWCC for these soils based on a function describing the relation between particle and pore-size. The framework uses basic soil information and relates the macro and microstructure to the aggregated and disaggregated grain-size distribution (GSD) curves, respectively. Adsorption was indirectly considered by incorporating simple soil properties such as the liquid limit in the calibration of the function parameters. The coefficient of uniformity and the degree of aggregation were found to be associated with the desaturation zones of the macro and micropores.

A simplified prediction model for the SWCC based on correlations and nonlinear regression approaches was also proposed. The regression analyses indicated that the level of aggregation and the liquid limit are the most relevant factors affecting microstructure whereas the macrostructure is strongly governed by parameters from the aggregated GSD curve. The performance of both models evaluated through R^2 is reasonably good, with values consistently exceeding 0.80.

The shear strength model involved the analysis of the evolution of soil structure during shearing and its impact on the relationship between matric suction, net normal stress, and shear strength. Such analyses included the interpretation of the unusual behavior of some bimodal lateritic soils, where the contribution of suction to shear strength is greater than that of net normal stress (i.e., $\phi^b > \phi'$). The model assumes that only suctions within the micropores zone cause relevant structural changes during shearing that can decrease ϕ^b whereas ϕ' varies in all suction ranges. At high suctions, the contribution of suction to the shear strength becomes constant. These assumptions constitute the basis for a new shear strength prediction model that is easy to implement, requires only GSD and SWCC information, and offering superior results ($R^2 > 0.95$) in comparison to 14 unimodal and 2 bimodal models available in the literature. The increase in the effective friction angle, ϕ' with respect to matric suction during shearing seems to be a function of the level of aggregation; however, the values of the friction angle associated with matric suction, ϕ^b, greater than ϕ' are believed to occur due to the emergence of a contractive shear band in specimens with suctions higher than the first air-entry value in drained conditions. The relationship between apparent cohesion and matric suction appears to exhibit a linear relationship extending from saturation to the end of the macropores region, and a non-linear relationship starting from the preceding limit to the midpoint of the micropores transition region.

Although the purpose of the models presented in this thesis is not to replace direct determinations using laboratory tests, they can be considered a step forward in the implementation of unsaturated soil mechanics for lateritic soils because they offer reasonable estimates of the SWCC and the unsaturated shear strength. This information is

essential in developing preliminary geotechnical designs, such as those related to slope stability, retaining walls, bearing capacity of formation layers of roads and railroads, bearing capacity in foundations, cover and capillary barrier systems, and mining waste disposal systems.

ACKNOWLEDGEMENTS

Firstly, to my wife for her incentive and support. I am very grateful for all the effort and the things you gave up so that we could make this achievement possible. This journey presented difficult times, but you always were on my side.

To my mentors and supervisors, professors Gilson Gitirana Jr. and Sai Vanapalli, for their guidance, support, comprehension, dedication and constant knowledge sharing. Without their encouragement, I would not complete this work.

The financial support provided by Coordenação de Aperfeiçoamento de Pessoal de Nível Superior (CAPES).

To the support provided by Tribunal de Contas do Estado de Goiás (TCE-GO), for allowing me to work remotely while studying abroad.

To my friends Ricardo Vilhena, Larro e Renato for their constant incentive.

To the professors of the Program of Postgraduate Studies in Geotechnics, Structures and Civil Construction at Universidade Federal de Goiás, Maurício, Márcia, Lilian, Renato, and Marcus, for knowledge sharing along my journey.

To the professors of the Department Civil Engineering at University of Ottawa, Infante Sedano, Rennie Colin, and Imad Alainachi, for knowledge sharing along my journey.

Special thanks to the professor of the Department Civil and Environmental Engineering at Carleton University, Elena Zabolotnii, for knowledge sharing along my journey.

To all that contributed directly or indirectly for the accomplishment of this research.

TABLE OF CONTENTS

LIST OF FIGURES

LIST OF TABLES

LIST OF ABBREVIATIONS

AEV:	Air-Entry Value
AI:	Artificial Intelligence
ANN:	Artificial Neural Network
CD:	Consolidated Drained
CEC:	Cation Exchange Capacity
CW:	Constant-Water-Content
DEM:	Discrete Element Method
EGME:	Ethylene Glycol Monoethyl Ether
GSD:	Grain-Size Distribution
IPCC:	Intergovernmental Panel on Climate Change
LDF:	London Dispersion Forces
MIP:	Mercury Intrusion Porosimetry
PDF:	Probability Density Function
PI:	Plasticity Index
PSD:	Pore-Size Distribution
RA:	Relative Aggregation
RMSE:	Root-Mean-Square-Error
SEM:	Scanning Electron Microscopic
SSA:	Specific Surface Area
SWCC:	Soil-Water Characteristic Curve
THMC:	Thermo-Hydro-Mechanical-Chemical
TRB:	Transportation Research Board
USCS:	Unified Soil Classification System
μCT:	Computed Microtomography

CHAPTER 1

Introduction

1.1 Background

The focus of research in unsaturated soil mechanics during the last few decades was predominantly directed towards understanding the behavior of mostly stable soils. Soils from these regions usually have a structure characterized by a pore-size distribution (PSD) leading to a unimodal soil-water characteristic curve (SWCC) exhibiting three different desaturation zones, namely, the boundary effect, transition and residual zone. The hydromechanical (i.e., hydraulic conductivity and shear strength) behavior is significantly different in each of these zones due to the variations in the interphase contact area and the tortuosity associated with the water and air phase. Structural changes resulting from suction changes are minor for most of these soils, making these soils often referred to as "stable-structured" soils.

The potential application of unsaturated soil mechanics in practice is quite vast. The literature contains many examples of the use of this discipline in the design of geotechnical structures such as tailings (Satyanaga et al., 2021; Simms, 2021), pavements (Ceratti et al., 2004; Freitas et al., 2023), railroads (Castro et al., 2021; Menezes et al., 2023), dams (Pereira, 1996; Alonso and Cardoso, 2010), slopes (Gerscovich et al., 2006; Rahardjo et al., 2012; Zhang et al., 2014), shallow and deep foundations (Vanapalli and Mohamed, 2007; Vianna et el., 2007; Bernardes et al., 2023; Zacarin et al., 2023), and cover systems (Rahardjo et al., 2016; Perotti et al., 2022).

Even though substantial research has been developed in the field of unsaturated soils, its implementation remains challenging. The main difficulties are related to the cost of site investigations, soil testing and engineering analysis (Fredlund, 1999; Fredlund, 2018; Fredlund 2021). Information about the variations in the pore-water pressures along the lifespan of a geotechnical structure can be expensive and complex to obtain. For most projects, geotechnical investigations are performed only once and fluctuations in the groundwater table are considered based on previous experiences and engineering judgment. A common misconception is that *in-situ* suctions are temporary and disappear following rainfalls (Fredlund, 2021). For this reason, the assumption of saturated soil conditions is still attractive; however, it may lead to designs that are neither rational nor economical.

To gain the confidence of geotechnical engineers, research studies should focus on developing straightforward and simple techniques that clearly explain outcomes, while discussing their strengths, limitations, and suitability. Despite the reluctance of most geotechnical and geo-environmental engineers, the use of unsaturated soil mechanics into practice is necessary for dealing with the effects of climate change that are becoming more prevalent due to global warming.

In the recent years, the awareness towards climate change and extreme weather events has increased among scientists, as well as geotechnical and environmental engineers (Mendes, 2011; Clarke and Smethurst, 2010; Toll et al., 2012; Rahardjo et al., 2012; Strauch et al., 2015; Vardon, 2015; Satyanaga et al., 2021), leading to a growing demand for designs addressing these issues (Siemens, 2017). The Intergovernmental Panel on Climate Change (IPCC) indicates that, in 2100, the sea level rise will be between 0.29 to

0.59 m in most conservative predictions. In the worst scenario, this range is estimated to be 0.61 to 1.1 m (Oppenheimer et al., 2019). In other words, there is a greater likelihood of coastal areas to be flooded, affecting many urban areas and changing the soil conditions.

Extreme wetting and drying cycles resulting in winters and summers will become more frequent (IPCC, 2007; Tubiello et al., 2008; US EPA 2023). For example, erosion processes will be pronounced and many natural slopes that are currently stable may fail as consequence of severe droughts, rainfalls, and glacial retreat (Li and Fang, 2016; Gariano and Guzzetti, 2016; Coe, 2017). An example of the effects caused by climate change is the heatwave lasting more than 50 consecutive days resulting in record-breaking temperatures exceeding 40º in many cities in Brazil (Kew et al., 2023). In this context, the understanding of unsaturated soil mechanics associated with thermo-hydro-mechanic-chemical (THMC) processes are fundamental to assess future designs, identify and mitigate hazards (Vahedifard, 2018; Camapum and Gitirana Jr., 2021; Kandalai et al., 2023).

Recently, research attention has been directed towards understanding the behavior of tropical soils, considering their physicochemical properties and extending traditional soil mechanics (Villibor and Nogami, 2009; Camapum de Carvalho et al., 2023). However, tropical soils that are found in many regions of the world, including Brazil, Ghana, Malaysia, Nigeria, Philippines, Southern India, Singapore, Sri Lanka, and others (Huat et al., 2013), are predominantly in an unsaturated state. Most importantly, the behavior of these soils is not well understood.

Tropical soils are often found in an unsaturated condition either because the annual evaporation rate is higher than the annual precipitation or because drainage conditions are favorable (Huat et al., 2013; Carvalho Junior et al., 2022). In Brazil, these materials cover

approximately 80% of its territory (Carvalho Junior et al., 2022). These highly weathered materials frequently exhibit a structure with double porosity resulting in a SWCC which is bimodal in nature. Some of these materials even display collapsible behavior. Experimental evidence indicates that macro and micropores of bimodal soils are influenced by suction changes associated with structural changes. In the case of collapsible soils, significant structural changes during suction reduction led researchers to refer to these soils as "meta-stable" structured soils.

The lixiviation process suffered by these soils increases the concentration of iron and aluminum oxides and hydroxides, leading to the formation of aggregates (Fookes, 1994; Camapum de Carvalho et al., 2023). These aggregates comprise of cemented clay particles that form a pore network known as intra-aggregate porosity whereas the soil voids outside the aggregates are called inter-aggregate porosity, as illustrated in Fig. 1.1.

There are numerous models to estimate unsaturated soil properties such as the SWCC, shear strength envelope, and hydraulic conductivity function (Fredlund and Rahardjo, 1993). However, these models were developed in most cases for soils with a different pore-structure (i.e., unimodal). The current research focuses to model bimodal soils, which is still emerging, are based on soils originated from discontinuities in the grain-size distribution (GSD) curve (Satyanaga et al., 2013; Hassan et al., 2022) and not weathering processes typical of tropical soils. It is worth mentioning that estimation models do not replace experimental data, but they can be a helpful tool able to aid engineers in preliminary designs, estimates and feasibility studies.

A better understanding of the behavior of tropical soils can be valuable for developing simple tools for not only estimating the bimodal SWCC of tropical soils but

also can be useful for predicting their hydro-mechanical behavior. Such studies can alleviate unfeasible soil testing costs and investigation times.

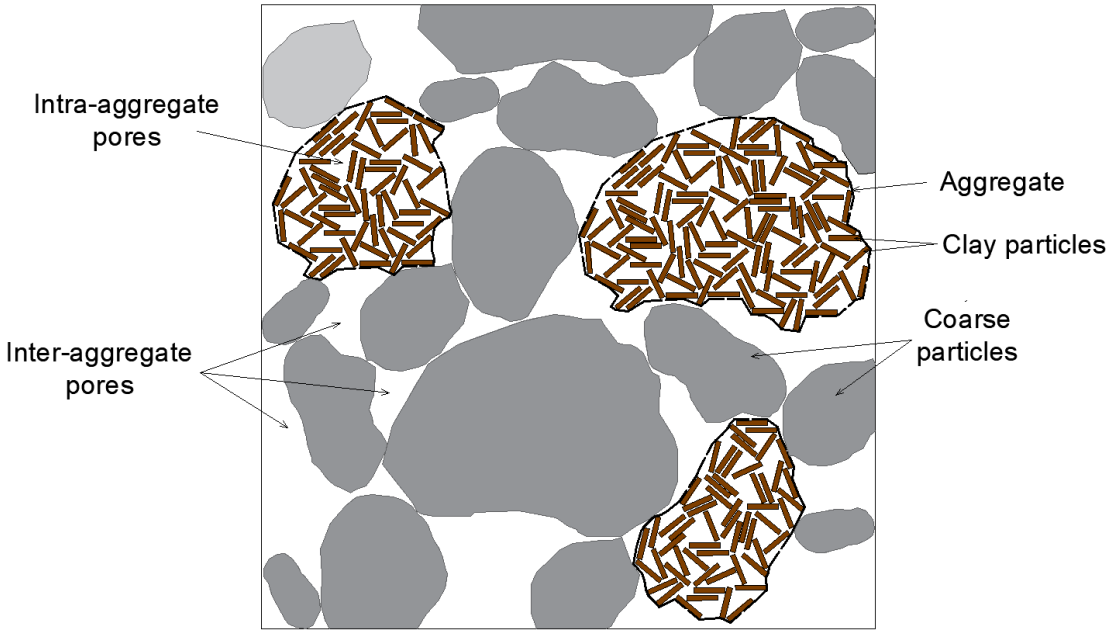

Figure 1.1 Representation of the intra-aggregate and inter-aggregate pores of bimodal tropical soils

Although more attention has been directed towards understanding the hydromechanical behavior of unsaturated bimodal lateritic over the last two decades, only few studies focus on modeling approaches. The small number of existing models focus on using an equation to fit the experimental data measured on one or a few soils. Consequently, more research is needed in the development of new models to estimate unsaturated properties for these soils. Moreover, there are some questions related to the behavior of bimodal lateritic soils that remain unanswered or unclear. First, results from experimental studies found in the literature on tropical soils suggest the contribution of the matric suction towards the shear strength (ϕ^b) is higher than that of the net normal stress (ϕ') (Abramento, 1988; Rohm, 1992; Rohm and Vilar, 1995; Teixeira and Vilar, 1997; Soares and Campos,

2005; Feuerharmel et al., 2006; Lopes et al., 2007; Kühn, 2014). Also, the relevance in quantitative terms of the adsorption for the water retention remains unaddressed. Finally, the relationship between the micro and macrostructure and the soil properties such as the SWCC and the volume change behavior needs a deeper understanding. The investigation of these soils from both a macro and micro scale can likely provide answers to some of these complex questions that can provide the basis for a theoretical framework describing their behavior.

The focus of the studies summarized in this PhD thesis is directed towards understanding the complex behavior of tropical soils; these soils are also referred herein as bimodal lateritic soils. Unlike unimodal SWCC, bimodal SWCCs have two air-entry values and two residual suctions due to the influence of their soil structure. Therefore, this thesis aims to build confidence among engineers in using the proposed simple tools for implementing the unsaturated soil mechanics in geotechnical practice, especially for tropical soils.

1.2 Research objectives and scope

The main objective of this thesis is to analyze and model the hydromechanical behavior of bimodal tropical soils in unsaturated conditions considering the influence of soil structure (i.e., encompassing both the macro and microstructure). Several tropical soils are investigated to analyze how the soil structure affects various behavioral aspects in terms of SWCC and shear strength and to support the development of models that are consistent with the principles of continuum mechanics. Such models aim to be useful tools that can used in geotechnical engineering practice. More details of the specific objectives are summarized below:

(1) *Structural behavior*

The investigation of the structural behavior of bimodal tropical soils is of paramount importance for the understanding of hydromechanical properties. Consequently, this study aims to examine the relation between the micro and the macrostructure under different conditions, including drying and wetting cycles, compaction energy, disturbance, effective stress, and matric suction. The state-of-the-art of previous studies from the literature is summarized in Chapter 2; they form the basis for developing relationships between soil structure and the SWCC. This understanding guided the modeling presented in Chapters 2 to 5 and led to the decision to analyze undisturbed specimens separately from remolded ones. In Chapter 5, the changes associated with volume, shear strength, micro and macropores are detailed as function matric suction, and disturbance revisiting published data from the literature from modified direct shear, modified triaxial, and diametral compression. These studies provide a rational basis for answering the several key issues addressed in the previous section, especially the reasons behind the first question (i.e., $\phi^b > \phi'$).

(2) *Models for predicting the bimodal SWCC from GSD and other simple properties*

Two novel models are proposed to estimate the drying SWCC of soils with dual structure relying on the GSD and the index properties. The first one (Chapter 3) is referred to as the general model and uses the GSD measured after it is treated with deflocculant to relate it to the microstructure whereas the GSD without deflocculant provides information about the macrostructure. Also, other physical and chemical aspects affecting the SWCC

are considered using information of the porosity, the degree of aggregation and the liquid limit. The second method (Chapter 4) is referred to as simplified model; it is based on similar hypothesis of the general model, but it requires less steps to be implemented.

(3) ***Investigation of the unsaturated shear strength behavior***

The objective of this part of the thesis is to analyze the unsaturated shear strength behavior of lateritic bimodal soils (Chapter 5). The investigations provided insights that led the formulation of a theory describing how the changes of soil structure during shear affects the unsaturated shear strength, as well resulting in ϕ^b greater than ϕ'. Additionally, a new prediction model is proposed is straightforward and requires only routinely geotechnical information for implementation in practice applications.

The scope of this thesis proposal is focused on using the data from Brazilian tropical soils with double structure. However, it is anticipated that this work can also be extended for other tropical soils from various other regions of the world. In other words, this thesis work can lay a foundation for providing a rational basis for explaining the hydromechanical behavior of tropical soils in general.

1.3 Thesis proposal outline

This thesis proposal is organized in five chapters as follows:

(1) Chapter 1 introduces the thesis proposal and presents some basic concepts related to unsaturated soil mechanics with reference to bimodal nature of tropical soils. In addition, it presents an overview of the challenges involving the implementation of unsaturated soil mechanics for tropical soils. The urgency of this discipline in the forthcoming geotechnical engineering practice from the context of addressing

climate changes associated with global warming is succinctly addressed. The justification for undertaking this research is outlined followed by its objectives.

(2) Chapter 2 introduces the fundamentals concepts and principles related to the hydromechanical behavior of unsaturated and bimodal lateritic soils. A background about mechanisms of water retention, SWCC, soil mineralogy, shear strength, soil structure are presented.

(3) Chapter 3 is presented in the form of a manuscript, which is under review with an international journal. The first model proposed to predict the SWCC of bimodal lateritic soils are detailed and evaluated using a database of 45 materials gathered from the literature, considering separately the undisturbed and remolded conditions.

(4) Chapter 4 is presented in the form of a manuscript, which is under review with an international journal. It presents the second model to predict the SWCC of bimodal lateritic soils using a simplified approach that are developed and evaluated using the same database of 45 materials gathered from the literature and used in Chapter 3.

(4) Chapter 5 is presented in the form of a manuscript, which is also under review with an international journal. It describes a sound basis modelling of the unsaturated shear strength employing data of 14 soils collected from the literature containing different type of tests and conditions.

(5) Chapter 6 summarizes the findings of the previous chapters and presents suggestions for future studies.

Appendix A presents the principal fitting and predicting models for bimodal SWCCs.

Appendix B presents all the predicted SWCCs obtained from the models developed in Chapter 3 and 4.

Appendix C presents a detailed information about the soils used in Chapter 5, including GSD, index properties, SWCC, saturated and unsaturated shear strength laboratory data, analyses and assumptions, and extended failure envelopes.

1.4 Publications

Journal

Li, Y., **Alves, R., D.**, Vanapalli, S., K., Gitirana Jr., G., F., N. 2024. Models for considering the THMC effects on soil-water characteristics curves. *Geosciences*, 14(2), 1-20. https://doi.org/10.3390/geosciences14020038

Alves, R. D., Gitirana Jr., G. F. N., Vanapalli, S. K. Modeling the bimodal SWCC of highly weathered tropical soils using grain-size information. Under peer review with a Journal.

Alves, R. D., Gitirana Jr., G. F. N., Vanapalli, S. K. A simple model for the estimation of the bimodal SWCC of highly weathered tropical soils. Under peer review with a Journal.

Alves, R. D., Gitirana Jr., G. F. N., Vanapalli, S. K. Modeling the unsaturated shear strength of bimodal lateritic soils. Under peer review with a Journal.

References

Alonso, E. E., Cardoso, R. 2010. Behavior of materials for earth and rockfill dams: perspective from unsaturated soil mechanics. *Frontiers of Architecture and Civil Engineering in China*, 4(1): 1-39. https://doi.org/10.1007/s11709-010-0013-6

Bernardes, H. C., Cruz Junior, A. J., Sales, M. M., Cunha, R. P., Rebolledo, J. F. R. 2023. Suction and reloading effects on pile behaviour in tropical soil. *International Journal of Geotechnical Engineering*, 17(2): 177-189. https://doi.org/10.1080/19386362.2023.2208919

Camapum de Carvalho, J., Gitirana Jr., G. F. N. 2021. Unsaturated soils in the context of tropical soils. *Soils and Rocks*, 44(3). https://doi.org/10.28927/SR.2021.068121

Camapum de Carvalho, J., Gitirana Jr., G. F. N., Machado, S. L., Mascarenha, M. M. A., Silva Filho, F. C., Rodrigues, R. A. 2023. Solos não saturados no contexto geotécnico. Associação Brasileira de Mecânica dos Solos e Engenharia Geotécnica, São Paulo, 2nd

ed.

Castro, G., Pires, J., Motta, R., Bernucci, L., Marinho, F., Merheb, A. 2021. Unsaturated numerical analysis of a railroad track substructure considering climate data. *Transportation Geotechnics*, 31. https://doi.org/10.1016/j.trgeo.2021.100662

Carvalho Junior, W., Calderano Filho, B., Bhering, S. B., Pereira, N. R., Chagas, C. S., de Macedo, J. R. 2022. Os solos tropicais e sua distribuição: uma visão segundo dados de livre acesso. *Brazilian Journal of Development*, 8(8): 54835-54848. https://doi.org/10.34117/bjdv8n8-009

Ceratti, J. A., Gehling, W. Y. Y., Núñez, W. P. 2004. Seasonal variations of a subgrade soil resilient modulus in southern Brazil. Journal of the Transportation Research Board, 1874: 165-173. https://doi.org/10.3141/1874-18

Clarke, D., Smethurst, J. 2010. Effects of climate change on cycles of wetting and drying in engineered clay slopes in England. *Quarterly Journal of Engineering Geology and Hydrogeology*, 43 (4): 473-486. https://doi.org/10.1144/1470-9236/08-106

Coe, J. A. 2017. Landslide hazards and climate change: A perspective from the United States. Slope Safety Preparedness for Impact of Climate Change, Edited by Ho, K., Lacasse, S., Picarelli, L. Tayler & Francis Group, London, UK.

Feuerharmel, C., Pereira, A., Gehing, W. Y. Y., Bica, A. V. D. 2006. Determination of the shear strength parameters of two unsaturated colluvium soils using the direct shear test. *In:* Fourth International Conference on Unsaturated Soils, Arizona, USA. https://doi.org/10.1061/40802(189)9

Fookes, P., G., 1994. A review: Genesis and classification of tropical soils for engineers. Proceedings of the Geotechnics in the African Environment, Balkema, Rotterdam, Netherlands, 423-442.

Fredlund, D. G. 1999. The 1999 R.M. Hardy Lecture: The implementation of unsaturated soil mechanics into geotechnical engineering. *Canadian Geotechnical Journal*, 37: 963-986. https://doi.org/10.1139/t00-026

Fredlund, D. G. 2018. State of practice for use of the soil-water characteristic curve (SWCC) in geotechnical engineering. *Canadian Geotechnical Journal*, 56, 1059-1069. https://doi.org/10.1139/cgj-2018-0434

Fredlund, D. G. 2019. Determination of unsaturated soil property functions for engineering practice. *In:* 17th African Regional Conference on Soil Mechanics and Geotechnical Engineering, Cape Town, South Africa.

Fredlund, D. G. 2021. Myths and misconceptions related to unsaturated soil mechanics. *Soils and Rocks*, 44(3). https://doi.org/10.28927/SR.2021.062521

Freitas, J. B., Rezende, L. R., Gitirana Jr., G. F. N. 2020. Prediction of the resilient modulus of two tropical subgrade soils considering unsaturated conditions. *Engineering Geology*, 270. https://doi.org/10.1016/j.enggeo.2020.105580

Gariano, S. L., Guzzetti, F. 2016. Landslides in a changing climate. *Earth-Science Reviews*, 162: 227-252. https://doi.org/10.1016/j.earscirev.2016.08.011

Gerscovich, D. M. S., Vargas, E. A., de Campos, T. M. P. 2006. On the evaluation of unsaturated flow in a natural slope in Rio de Janeiro, Brazil. *Engineering Geology*, 88: 23-40. https://doi.org/10.1016/j.enggeo.2006.07.008

Hassan, S. B. M., Dragonetti, G., Comegna, A., Sengouga, A., Lamaddalena, N., Coppola, A. 2022. A bimodal extension of the ARYA&PARIS approach for predicting hydraulic properties of structured soils. *Journal of Hydrology*, 610. https://doi.org/10.1016/j.jhydrol.2022.127980

Kandalai, S., John, N. C., Patel, A. 2023. Effects of climate change on geotechnical infrastructures — state of the art. *Environmental Science and Pollution Research*, 30:16878–16904. https://doi.org/10.1007/s11356-022-24788-7

Kühn, V. O. 2014. Resistência ao cisalhamento de um solo tropical não saturado considerando altas sucções. Master thesis, Universidade Federal de Goiás, Goiânia, Goiás, Brazil.

Kew, S., Pinto, I., Alves, L., Santos, D., Libonati, R., Philip, S., Zachariah, M., Barnes, C., Kimutai, J., Vahlberg, M., Arrighi, J., Otto, F., 2023. Strong influence of climate change in uncharacteristic early spring heat in South America. Report: Imperial College London. https://doi.org/10.25561/106753

Li, Z., Fang, H. 2016. Impacts of climate change on water erosion: a review. *Earth-Science Reviews*, 163: 94-117. https://doi.org/10.1016/j.earscirev.2016.10.004

Lopes, M. B. L., Campos, T. M. P., Antunes, F. S., Villar, L. F. S. 2007. Influência da sucção na resistência ao cisalhamento de um solo residual de filito da Região Metropolitana de Belo Horizonte (MG). *In:* VI Simpósio Brasileiro de Solos Não Saturados.

Mendes, J. P. D. C. 2011. Assessment of the impact of climate change on an instrumented embankment: an unsaturated soil mechanics approach. Doctor thesis, Durham University, Durham, United Kingdom.

Menezes, L. C. A., Guimarães, A. C. R., Marques, M. E. S., Ribeiro, T. S., Nascimento, F. A. C. 2023. Analysis of the influence of moisture variation on the behavior of tropical soils of Carajás railway. *Applied Sciences*, 13. https://doi.org/10.3390/app13137909

Oppenheimer, M., Glavovic, B.C., Hinkel, J., van de Wal, R., Magnan, A.K., Abd-Elgawad, A., Cai, R., Cifuentes-Jara, M., DeConto, R.M., Ghosh, T., Hay, J., Isla, F., Marzeion, B., Meyssignac, B., Sebesvari, Z. 2019. Sea Level Rise and Implications

for Low-Lying Islands, Coasts and Communities. *IPCC Special Report on the Ocean and Cryosphere in a Changing Climate*. Cambridge University Press, Cambridge, UK and New York, NY, USA, 321-445. https://doi.org/10.1017/9781009157964.006

Pereira, J. H. F., 1996. Numerical analysis of the mechanical behavior of collapsing earth dams during first reservoir filling. Doctor thesis, University of Saskatchewan, Saskatoon, Canada.

Perotti, D. A., Gitirana Jr. G. F. N., Mendes, T. A., Fredlund, M. D. 2022. Numerical analysis of cover systems for mining waste in tropical regions. *International Journal of Mining, Reclamation and Environment*, 36(7): 492-511. https://doi.org/10.1080/17480930.2022.2069915

Rahardjo, H., Satyanaga, A., Leong, E. C. 2012. Unsaturated soil mechanics for slope stabilization. *Geotechnical Engineering Journal of the SEAGS & AGSSEA*, 43(1): 48-58.

Rahardjo, H., Satyanaga, A., Leong, E-C., Noh, O. 2016. Performance of residual soil as cover system for a sanitary landfill in Singapore. *Journal of Performance of Constructed Facilities*, 31(1). https://doi.org/10.1061/(ASCE)CF.1943-5509.00009

Satyanaga, A., Wijaya, M., Zhai, Q., Moon, S-W., Pu, J., Kim, J. R. 2021. Stability and consolidation of sediment tailings incorporating unsaturated soil mechanics. *Fluids*, 6: 423. https://doi.org/10.3390/fluids6120423

Satyanaga, A., Rahardjo, H., Leong, E. C., Wang, J. Y. 2013. Water characteristic curve of soil with bimodal grain-size distribution. *Computers and Geotechnics*, 48: 51-61. https://doi.org/10.1016/j.compgeo.2012.09.008

Siemens, G. A. 2017. Thirty-Ninth Canadian Geotechnical Colloquium: Unsaturated soil mechanics — bridging the gap between research and practice. *Canadian Geotechnical Journal*, 55: 909-927. https://doi.org/10.1139/cgj-2016-0709

Simms, P. 2021. The role of unsaturated soil mechanics in unconventional tailings deposition. *Soils and Rocks*, 44(3). https://doi.org/10.28927/SR.2021.066721

Soares, R. M., Campos, T. M. P. 2005. Resistência ao cisalhamento de um solo coluvionar não saturado da cidade do Rio de Janeiro. *In:* IV Conferência Brasileira sobre Estabilidade de Encostas, Salvador, Bahia, Brazil.

Strauch, R.L., Raymond, C.L., Rochefort, R.M., Hamlet, A. F., Lauver, C. 2015. Adapting transportation to climate change on federal lands in Washington State, U.S.A. *Climatic Change*, 130: 185–199. https://doi.org/10.1007/s10584-015-1357-7

Toll, D. G., Mendes, J., Hughes, P. N., Gledinning, S., Gallipoli, D. Climate change and the role of unsaturated soil mechanics. *Geotechnical Engineering Journal of the SEAGS & AGSSEA*, 43(1): 76-82.

Vahedifard, F., Williams, J. M., AghaKouchak, A. 2018. Geotechnical engineering in the face of climate change: role of multi-physics processes in partially saturated soils. *In:* International Foundation Congress and Equipment Expo 2018, 353-364. https://doi.org/10.1061/9780784481585

Vanapalli, S. K., Mohamed, F. M. O. 2007. Bearing capacity of model footings in unsaturated soils. Proceedings of the Experimental Unsaturated Soils Mechanics, Ed. Schanz, T. Springer Proceedings in Physics, 112: 483-494. https://doi.org/10.1007/3-540-69873-6_48

Vardon, P. J. 2015. Climatic influence on geotechnical infrastructure: a review. *Environmental Geotechnics*, 2: 166-174. https://doi.org/10.1680/envgeo.13.00055

Vianna, A. P. F., Cintra, J. C. A., Aoki, N. 2007. Influence of footing size and matric suction on the behavior of shallow foundations in collapsible soil. *Soils and Rocks*, 30(3): 127-137. https://doi.org/10.28927/SR.303127

Villibor, D. F., Nogami, J. S. 2009. Pavimentos econômicos: tecnologia do uso dos solos finos lateríticos. Arte & Ciência, São Paulo, São Paulo, Brazil.

Zacarin, J. G. M. X., Silva, B. O., Tsuha, C. H. C., Vilar, O. M. 2023. Seasonal variation of the shaft resistance of CFA piles in unsaturated soil: a case study. *Canadian Geotechnical Journal*. https://doi.org/10.1139/cgj-2022-0102

Zhang, L. L., Fredlund, D. G., Fredlund, M. D., Wilson, G. W. 2014. Modeling the unsaturated soil zone in slope stability analysis. *Canadian Geotechnical Journal*, 51: 1384-1398. https://doi.org/10.1139/cgj-2013-0394

CHAPTER 2

Literature Review

2.1 Introduction

In this chapter, the building blocks of unsaturated soil mechanics that provide a background for the investigation of the hydromechanical behavior of bimodal tropical soils are summarized. Some of the topics include the basic concepts about the SWCC, the shear strength and the structure of bimodal tropical soils are succinctly discussed. Also, this chapter presents a brief review of measurement and estimation techniques for both SWCC and shear strength of unsaturated soils.

Unlike conventional soil mechanics, which only focuses on the behavior of soil considering the influence of solid (i.e., soil) and liquid (i.e., water) phase, unsaturated soil mechanics requires a comprehensive understanding of an additional phase of gas (i.e., water).

Fig. 2.1 illustrates the typical pore-water pressure distribution in a soil profile that has groundwater table at a certain depth. The soil above the groundwater table has a capillary fringe and a vadose zone in which the soil is in a state of unsaturated condition. In the saturated region the pore-water pressures are positive, and they present a linear distribution with depth under static equilibrium conditions. Above the groundwater table, the pore-water pressures are negative. The capillary fringe is related to the rise of water within the soil pores due to capillary stresses. Although in this zone the degree of saturation is very close to or at 100%, the soil is in an unsaturated condition because the water phase is under suction stress (i.e., negative pore-water pressure). The active zone corresponds to

the soil layer close to the surface that is susceptible to variation in the degree of saturation caused by environmental changes such as evaporation, transpiration and precipitation.

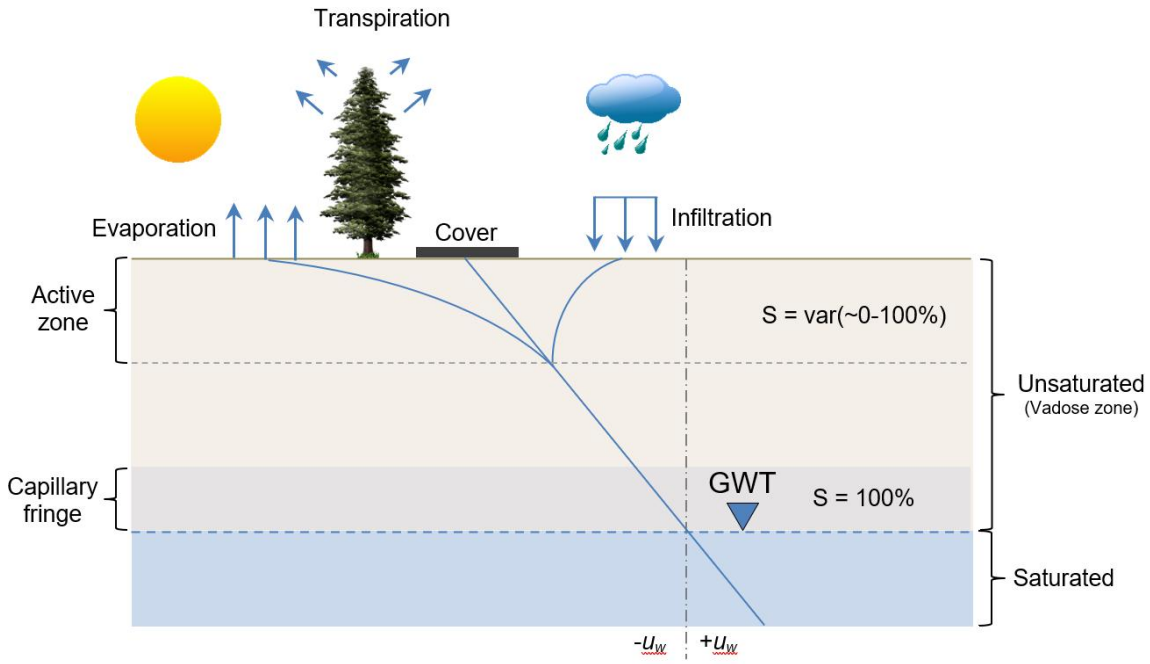

Figure 2.1 Pore-water pressure distribution of the saturated and unsaturated conditions (modified from Fredlund et al., 2012)

The negative pore-water pressures with respect to atmospheric pressure conditions in unsaturated soils are commonly referred to as soil suction. For saturated soils, the concept of effective stress (σ') proposed by Terzaghi (1936) has been extensively used in conventional geotechnical engineering practice. Nonetheless, it is not suitable to represent the stress tensors when negative pore-water pressures are present. To overcome this problem, Fredlund and Morgenstern (1977) proposed the use of the net normal stress (σ - u_a) and the matric suction (u_a - u_w) as stress state variables for unsaturated soils. This arrangement of the state variables makes the saturated condition (i.e., u_a = 0) a particular case of the unsaturated soil mechanics. These two stress state variables (i.e., net normal

stress and matric suction) have been widely accepted by geotechnical scientists as demonstrated by the significant number of constitutive models which they are based on.

2.2 SWCC

Using the definition given by Edlefsen and Anderson (1943), soil suction (ψ) can be defined as the free-energy state of soil-water. In other words, it consists of the amount of energy necessary to remove an infinitesimal mass of water inside the soil pores. The partial pressure of the pore-water vapor and the soil suction can be written in thermodynamic terms as:

$$\psi = -\frac{RT_K}{v_{w0}\omega_v}\ln\left(\frac{\bar{u}_v}{\bar{u}_{v0}}\right) \tag{2.1}$$

where: R is the universal gas constant [i.e., 8.31432 J/(mol K)]; T_K is the absolute temperature in K; v_{w0} is specific volume of water in m³/kg; ω_v is the molecular mass of water vapor (i.e., 18.016 kg/kmol); $\bar{u}_v$ is the partial pressure of pore-water vapor in kPa; $\bar{u}_{v0}$ is the saturation pressure of water vapor over a flat surface of pure water at the same temperature in kPa.

The soil suction has two components, namely, matric (u_a - u_w) and osmotic (π) related by the following equation:

$$\psi = (u_a - u_w) + \pi \tag{2.2}$$

According to Aitchison (1964, as cited in Fredlund et al., 2012), matric or capillary suction is the equivalent suction derive from the measurement of the partial pressure of the water vapor in equilibrium with the soil-water relative to the partial pressure of the water vapor in equilibrium with a solution identical in composition with the soil-water. Osmotic

suction is the equivalent suction derived from the measurement of the partial pressure of the water vapor in equilibrium with a solution identical in composition with the soil-water relative to the partial pressure of water vapor in equilibrium with free pure water.

The relationship between the amount of water in the soil and soil suction is defined as the soil-water characteristic curve (SWCC) (Fredlund et al., 2012). The amount of water can be represented in terms of degree of saturation (S), volumetric water content (θ), or gravimetric water content (w). If no volume change occurs during the measurement of the SWCC, these variables can be easily exchangeable using simple volume-mass relationships:

$$Se = wG_s \tag{2.3}$$

$$\theta = nS = \frac{Se}{1+e} \tag{2.4}$$

The SWCC has a strong relationship with the grain size distribution (GSD). The usual representation of the SWCC is through a semi-logarithmic graphical relationship. The soil suction values are conventionally displayed in the log scale ranging from 0.1 to 10^6 kPa. Fig. 2.2 shows some SWCCs for different types of soils.

The matric suction in an unsaturated soil is a function of water content which significantly influences the soil structure. Mitchell and Soga (2005) define structure as the combination of fabric and interparticle forces that reflect the soil composition, present state, history, and environment. Moreover, fabric refers to the arrangement of particles, aggregates, and pores in the soil. The matric suction has two constituents: capillary and adsorption. The former is related to the soil fabric whereas the latter is consequence of the interparticle forces.

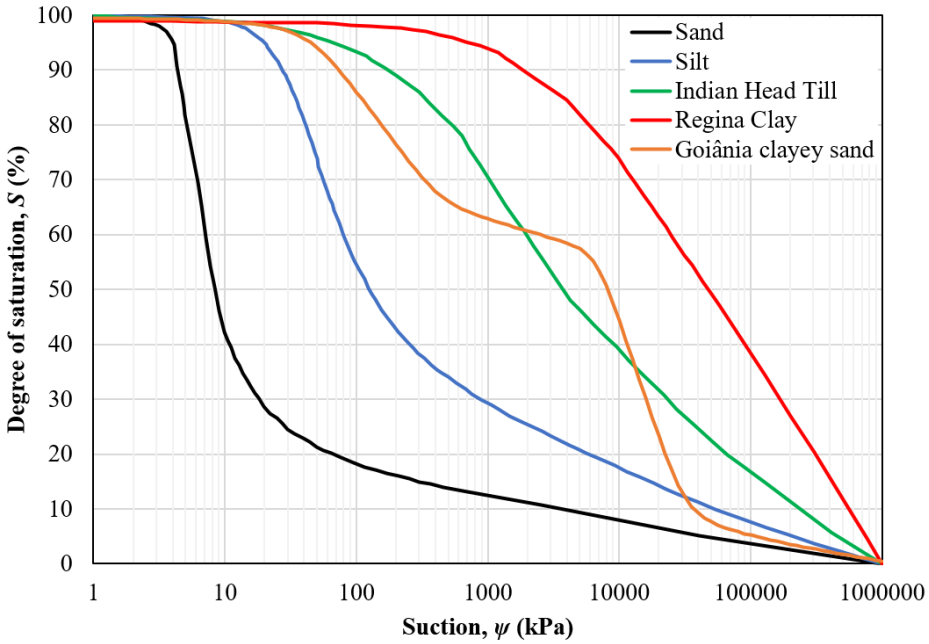

Figure 2.2 Some typical soil-water characteristic curves (data from Vanapalli et al., 1999; and Araújo, 2019)

2.2.1 Capillarity

The capillary forces emerge from the surface tension present at the water-air interface and are responsible for most of the water stored within the soil pores. Because of the complexity of the arrangement of particles and pores (i.e., soil fabric), the capillary phenomenon is illustrated using the capillary tube analogy described as follows.

Consider water in a glass tube under atmospheric conditions as illustrated in Fig. 2.3a. At the water-air interface, the intermolecular forces assume a different orientation to maintain equilibrium, creating something known as contractile skin. The force acting on the contractile skin is called surface tension (T_s) and holds the weight of the water inside the tube. As the matric suction is equivalent to the difference of pore-air (u_a) and pore-water (u_w) pressures, the equilibrium of forces acting on the contractile skin in the vertical direction gives:

$$(u_a - u_w) = \frac{T_s}{R_s} \tag{2.5}$$

where: R_s is the radius of the contractile skin.

The Young-Laplace equation is obtained by expanding this concept to the three-dimensional representation showed in Fig. 2.3b:

$$(u_a - u_w) = T_s\left(\frac{1}{R_1} + \frac{1}{R_2}\right) \tag{2.6}$$

where: R_1 and R_2 are the radius of contractile skin in each direction (i.e., x and y).

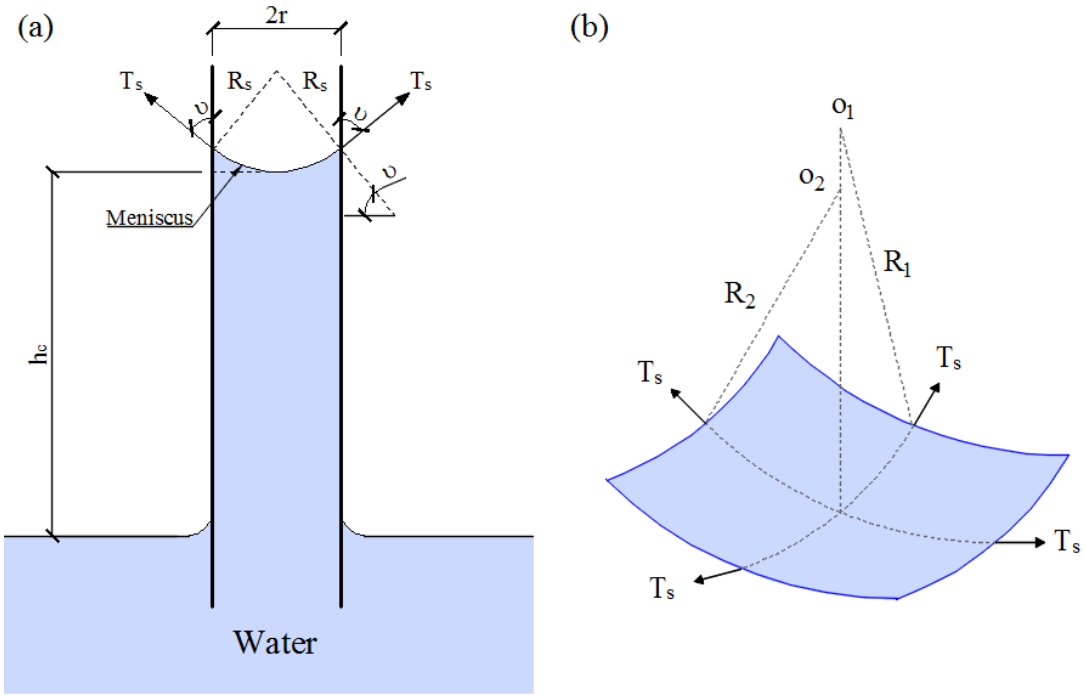

Figure 2.3 (a) Capillary tube model and (b) a three-dimensional representation of a menisci (modified from Fredlund et al, 2012)

The rise of water inside the tube is more significant when the radius of the tube is small enough for the effects of gravity be relatively small. The capillary length (l_c) corresponds to minimum radius for which the effects of gravity are small enough to be neglected.

$$l_c = \sqrt{\frac{T_s}{\rho_w g}} \tag{2.7}$$

where: ρ_w is the density of water; and g is the gravity acceleration (i.e., 9.807 m/s).

For temperature of 20º C, the density of water is 998 kg/m³ and the surface tension is 72.75 mN/m. Applying these values to Eq. 2.11, the capillary length in this condition is about 2.73 mm. In addition, the capillary height (h_c) can be calculated by:

$$h_c = \frac{2T_s \cos \upsilon}{\rho_w g r} \tag{2.8}$$

where: υ is the contact angle between the contractile skin and the tube wall; and r is tube radius.

In the soil profile, the capillary phenomenon results in the capillary fringe, a zone above the groundwater table nearly saturation, as defined in Section 2.2. The height of the capillary fringe depends on the pore sizes, and it is higher for finer soils. The thickness of the capillary fringe varies from a few millimeters for sand to many meters in the case of clays.

It is important to point out that the capillary tube model is unrealistic and an imperfect representation of capillarity in the soil, which has particles with a great range of sizes organized randomly and forming series of irregular pore networks with the menisci having shapes other than a simple spherical caps.

Two distinct water storage mechanisms arise from the capillary phenomenon: pendular and funicular water. The pendular regime is characterized by water held between two neighboring particles in pendular rings (Alves et al., 2020). The amount of water stored in the pendular regime corresponds to up to approximately 20% of the soil voids. Increasing the volume of water in the pores, the pendular rings merge forming water bridges that can

encompass several particles (Yuan and Chareyre, 2022). Funicular water, or the water that is not stored in form of pendular rings, varies from about 20 to 90% of the degree of saturation (Likos and Jaafar, 2013).

2.2.2 Adsorption

Due to the size of clay particles, water adsorption is particularly important and plays an essential role in the comprehension of soil properties such as plasticity, shear strength, hydraulic conductivity, swelling, consolidation and suction (Tuller and Or, 1999; Tuller and Or, 2005; Tokunaga, 2009; Khorshidi et al., 2016; Morrow et al., 2017). Adsorbed water refers to the thin liquid film of layers of water molecules attached to the particles surface as result of molecular interactions, such as hydrogen bonding, hydration of exchangeable cations, attraction by osmosis, charged surface-dipole attraction, van der Waals forces and capillary condensation (Mitchell and Soga, 2005).

Hydrogen bonding is an interaction mechanism that emerges from the oxygens (O^+) and hydroxyls (OH^-) on the surface of soil minerals that forms bonds with water molecules. Fig. 2.4a illustrate this interaction. Although the figure shows only one layer of water, more layers can form bonds due to the change in the electron distribution. The process known as hydration is presented in Fig. 2.4b. In this mechanism, the negatively charged clay surface attracts cations, which in turn attract water molecules.

Again, the cations on the clay surfaces increase the cationic concentration in this region. Thus, in order to equalize concentrations, water molecules tend to diffuse towards the surface as in Fig. 2.4c. This inward diffusion of water molecules is called attraction by osmosis.

Two clays particles in parallel act as condenser plates. The presence of aluminum makes the water molecules strongly bond to the clay surfaces. Consequently, the cations move toward the midplane of the plates as illustrated in Fig. 2.4d. The dipole attraction results in the surrounding of the cations by water molecules (hydration).

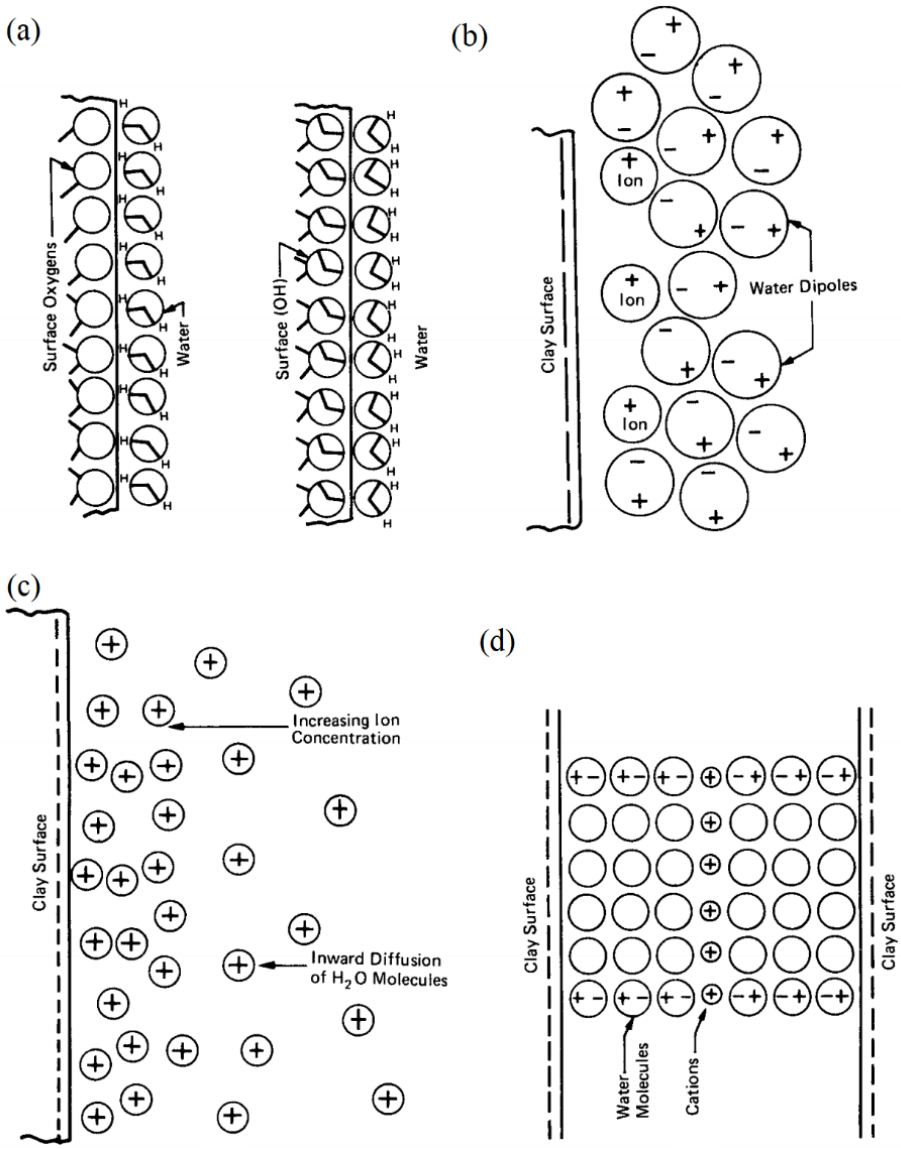

Figure 2.4 Clay particles and water molecules interactions: (a) hydrogen bonding; (b) hydration of exchangeable cations; (c) attraction by osmosis; and (d) dipole attraction (Mitchell and Soga, 2005)

Temporary dipoles induce water molecules to bond with clay surfaces because the presence of counterions different from hydrogen bonding. This interaction is weaker than hydrogen bonding and it is known as London Dispersion Forces (LDF).

The combined effects of surface tension and attraction to particle surfaces result in capillary condensation when the degree of saturation is less than 100%. In the capillary condensation, water is retained in the soil pores.

These mechanisms are complex, and they can be present simultaneously in the soil. As a result, modeling water adsorption is difficult. Despite of the existence of many physicochemical variables controlling the water adsorption, such as the cation exchange capacity, basal spacing, diffuse double layer, mineral dimensions, and cleavage, the drawings in Fig. 2.4 depicts the relevance of the specific surface area, SSA (Tuller et al., 1999; Mitchell and Soga, 2005; Woodruff and Revil, 2011; Dolinar, 2014).

Tuller and Or (2005) proposed an equation to calculate the thickness of the adsorbed water. The method is based on the van der Walls forces, the authors used a dataset of seven soils with a wide range of values of specific surface area. Ethylene glycol monoethyl ether (EGME) tests were carried out to measure the SSA for the dataset and to calibrate the Hamaker constant, A ($-6\text{x}10^{-20}$). The minimum and maximum measured SSA were 25 and 760 m²/g, respectively. The dry end of SWCC were calculated in terms of gravimetric water content (w) using the following expression:

$$w = \sqrt[3]{\frac{A}{6\pi\rho_w g\psi}} SSA \cdot \rho_w \qquad (2.9)$$

Fig. 2.5 shows the results for the seven tested materials. The Tuller and Or (2005) model is often used to incorporate the adsorbed water in SWCC estimation models

(Frydman and Baker, 2009; Tokunaga, 2011; Dolinar, 2014). A common approach to model the hydration mechanism is through adsorption isotherms (Woodruff and Revil, 2011; Revil and Lu, 2013; Dolinar, 2014; Khorshidi et al., 2016).

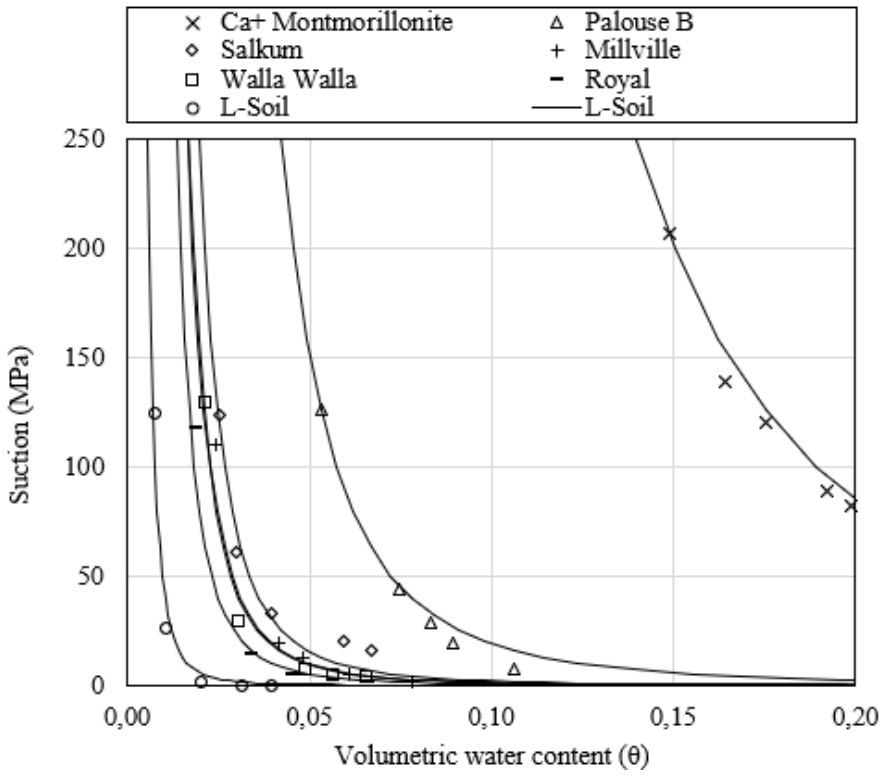

Figure 2.5 Measured and predicted dry ends of the dataset from Tuller and Or (2005)

2.2.3 Estimation techniques

As discussed in Chapter 1, the measurement of the unsaturated soil functions is cumbersome, expensive and time consuming. For these reasons, numerous methods have been proposed to estimate the SWCC as an alternative to performing field and/or laboratory tests. There are many different approaches that estimation techniques lay hand, and the fundamental idea of most of these models is to predict the SWCC using simple geotechnical information, such as GSD, pore-size distribution (PSD), and index properties.

The main approaches adopted by estimation techniques include the following models or representations: capillary tube, pore-scale, fractal, discrete element method (DEM), regression analysis, and artificial intelligence (AI). These approaches use a combination of techniques and different levels of empiricism. Table 2.1 shows some important predicting models with their respective equations and principles. Listing all models present in the literature to estimate the SWCC would be tedious as the goal here is to provide a general perspective in a succinct way of the existing methods.

2.2.3.1 Capillary tube models

This approach assumes that the water within the soil pores can be represented by a bundle of capillary tubes. The capillary tube model is shown in Fig. 2.3. The method relies on the GSD to obtain a PSD from which the matric suctions are calculated using the Young-Laplace equation (2.6). This process is done by splitting the GSD curve into several fractions, and each fraction is related to a pore-size calculated from the considered assumptions. These assumptions are the main characteristic that differs from the studies based on this approach. For example, the most notorious model proposed by Arya and Paris (1981) assumes that the soil particles are spheres with a cubic arrangement. Once the pore-size information is obtained, the volume-mass properties can be calculated to build the SWCC.

Some of the hypotheses and simplifications used in the capillary tube model includes:

i. For a given matric suction, it is considered that all pore-sizes equal or smaller than that corresponding to the matric suction is fully saturated while the remaining pore-sizes are completely empty;

ii. Each pore-size is calculated from a single fraction of particle-size. Therefore, the interactions between particles from different fractions are neglected; and

iii. The geometry of the soil particles can be approximated by circles or spheres.

The pore-network exhibits a complex geometry caused by the arrangement of particles with different sizes and shapes. Moreover, the drying and wetting process are continuous mechanisms in which the water slowly fills or empties the pores. Finally, other forces than capillary act on the soil particles resulting in water storage that cannot be described by the Young-Laplace equation, especially for fine grained soils. For these reasons, the performance of the capillary tube models is strongly related to how suitable are the hypothesis and simplifications made for the materials under study.

Some examples of studies using the capillary tube model are presented by Haverkamp and Parlange (1986), Arya and Dierolf (1989), Arya et al. (1999), Antinoro et al. (2014), Campos-Guereta et al. (2021), and You et al. (2022).

2.2.3.2 Pore-scale models

While the previous model relies on a PSD comprised of a bundle of capillary tubes, pore-scale models attempt to provide a better geometrical representation of the particles and pores. This is usually done by assuming a two or three-dimensional geometries, called unit cells, that are representative of a single particle-size (Fig. 2.6). The water is stored forming pendular rings whose geometry defines its volume and are described accordingly to the Young-Laplace equation. In this case, the pores can assume different saturations within the geometry limits imposed by the pendular shape (snap-off). Also, the unit cell model can incorporate the effect of the porosity by changing the arrangement of the particles.

The main distinguishing feature in this approach is how a single particle-size is upscaled to represent the entire GSD. This is a complex process because the unit cells have different matric suctions for a given water content. Because the soil structure of sands is simpler, the pore-scale model has demonstrated better results for granular soils. Some studies developed based on these concepts are Likos and Jaafar (2013), Cao et al. (2017), Chen et al. (2019), and Alves et al. (2020).

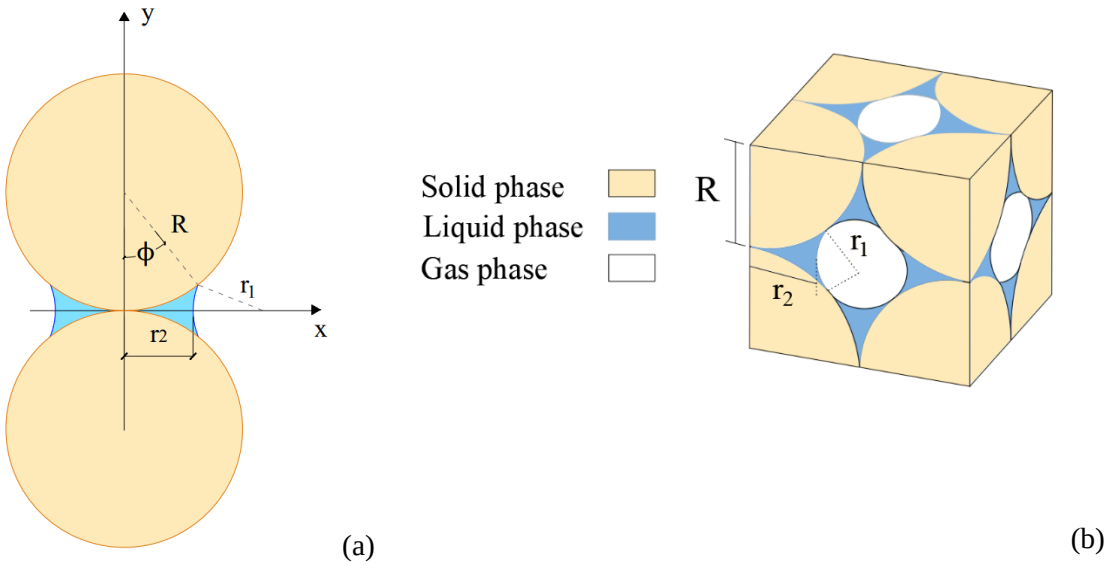

Figure 2.6 Unit cell model represented in: (a) 2D and (b) 3D

Table 2.1 Equations and principles of some predicting models

#	Author	Equation		Principle
1	Arya and Paris (1981)	$r_i = R_i\sqrt{\frac{4en_i^{1-\alpha}}{6}}$	(2.10)	Capillary tube
2	Haverkamp and Parlange (1986)	$\theta = \begin{cases} n\left[\frac{(u_a-u_w)_b}{(u_a-u_w)}\right]^{\lambda}\left[1-\frac{(u_a-u_w)_b}{(u_a-u_w)}\left(1-\frac{\theta_s}{n}\right)\right] & for\ (u_a-u_w) > (u_a-u_w)_b \\ \theta_n \quad for \quad (u_a-u_w) \le (u_a-u_w)_b \end{cases}$	(2.11)	Capillary tube
3	Arya and Dierolf (1989)	$r_i = \sqrt{\frac{4eR_i^3}{3\alpha^*}}$	(2.12)	Capillary tube
4	Fredlund et al. (2002)	$w = w_s\left[1-\frac{\ln\left(1+\frac{(u_a-u_w)}{h_r}\right)}{\ln\left(1+\frac{10^6}{h_r}\right)}\right]\left[\frac{1}{\ln\left[\exp(1)+\left(\frac{(u_a-u_w)}{a_f}\right)^{n_f}\right]^{m_f}}\right]$	(2.13)	Regression analysis
5	Aubertin et al. (2003)	$S_c = 1-\left[\left(\frac{h_c}{u_a-u_w}\right)^2+1\right]^m \exp\left[-m\left(\frac{h_c}{u_a-u_w}\right)^2\right]$	(2.14)	Adhesive, capillary forces and regression analysis
		$S_a = a_c C\frac{(h_c/\psi_n)^{2/3}}{e^{1/3}((u_a-u_w)/\psi_n)^{1/6}}$	(2.15)	
		$S = S_c + S_a^*(1-S_c)$	(2.16)	
6	Likos and Jaafar (2013)	$S = \int_{R_{min}}^{R_{fill}} f(R)dR + \int_{R_{fill}}^{R_{max}} S_{a/w} f(R)dR$	(2.17)	Pore-scale
7	Alves et al. (2020)	$V_p = 2\pi R^3\left\{(1-\cos\varphi)^2\left[\left[\sin\varphi+\cot\omega\left(1-\cos\varphi-\left(\frac{\sin\varphi}{\cos\omega}+\frac{1-\cos\varphi}{\sin\varphi}\right)\frac{\omega}{\cos\omega}\right)\right]\right]\right\}$	(2.18)	Pore-scale
		$R_{aev} = R\left[\sqrt{4\sin^2(\sigma/2)+1}-1\right]$	(2.19)	

Notes: Arya and Paris (1981) - r_i: radius of the cylindrical capillary tube of fraction i; R_i: particle radius of fraction i; e: void ratio; n_i: number of particles of fraction i; α: empirical parameter related to particle shape dependent of n_i; Haverkamp and Parlange (1986) – θ: volumetric water content; n: porosity; (u_a-u_w): matric suction; subscript b: air-entry value; λ: soil index value related to GSD; θ_n: volumetric water content at natural saturation; θ_s: volumetric water content at saturation; Arya and Dierolf (1989) – α^*: empirical parameter related to particle shape independent of n_i; Fredlund et al. (2002) – w: gravimetric water content; w_s: gravimetric water content at saturation; h_r: constant parameter used to adjust the lower portion of the curve; a_f: fitting parameter related to the air-entry value; n_f: fitting parameter related to the maximum slope of the curve; m_f: fitting parameter related to the curvature of the slope; Aubertin et al. (2003) - S_c: degree of saturation caused by capillary forces; h_c: equivalent capillary rise in the porous media; m: distribution parameter of the influence of pore-size distribution curve; S_a: degree of saturation caused by adhesive forces; a_c: adhesion coefficient; C: correction factor; ψ_n: normalization parameter; S^*_a: truncated adhesion component of the degree of saturation; Likos and Jaafar (2013) – R_{fill}: pore radius corresponding to snap off for cylindrical capillary; R_{min}: minimum bundled radius; R_{max}: maximum bundled radius; $f(R)$: probability distribution function; $S_{a/w}$: degree of saturation of a partially saturated unit pore; Alves et al. (2020) – V_p: volume of pendular water of a unit cell; φ: filling angle; ω: variable relating the filling angle and the contact angle; R: particle radius; R_{aev}: air-entry value pore radius; σ: packing angle.

2.2.3.3 Fractal models

Another possible description of the soil structure is using fractals. These mathematical shapes are comprised of patterns that can repeat infinitely. The shape pattern and the number of repetitions is chosen in such a way that soil porosity is represented. The most important concept in these models is the fractal dimension, which can be defined as the ratio of change in detail to the change in scale (Benoit, 1983). Because the fractal dimension is the key parameter in fractal models, the studies based on this approach are focused on extracting the fractal dimension from known soil properties, such as the PSD (Tyler and Wheatcraft, 1990; Tao et al., 2019; Zhao et al., 2023), GSD (Rieu and Sposito, 1991), clay content (Huang and Zhang, 2005), and the SWCC (Jin et al., 2019). Usually, fractal models also use the capillary tube representation to approximate the pores into a geometry that allows calculating the matric suction using the Young-Laplace equation.

2.2.3.4 Discrete element method models

The discrete element method is a set of numerical methods to represent for computing geometrically the structure of granular materials as well the interactions between the particles. This approach is computationally demanding but facilitates considering both capillary and adsorption mechanisms. The performance of these models is usually associated with the way the water storage mechanism is modeled and how similar is the material in terms of shape, size, amount, and arrangement of the particles.

The geometry can be represented in two (Gras et al., 2011; Guo et al., 2021) or three dimensions (Wang and Li, 2015; Wang et al., 2015; Mufti and Das, 2022) with single (Gras et al., 2011; Wang and Li, 2015) or multi-sized particles (Wang et al., 2015; Guo et al., 2021; Mufti and Das, 2022). Fig. 2.7 illustrates the representation of a single particle and

the soil structure using DEM. Usually, particles are depicted as spheres, but rounded shapes with edges is also possible (Guo et al., 2021; Góis et al., 2023). For these reasons, the applications using the DEM have been limited to granular materials such as sands and glass beads. However, with the increasingly processing power, the DEM can be extended for more complex soils.

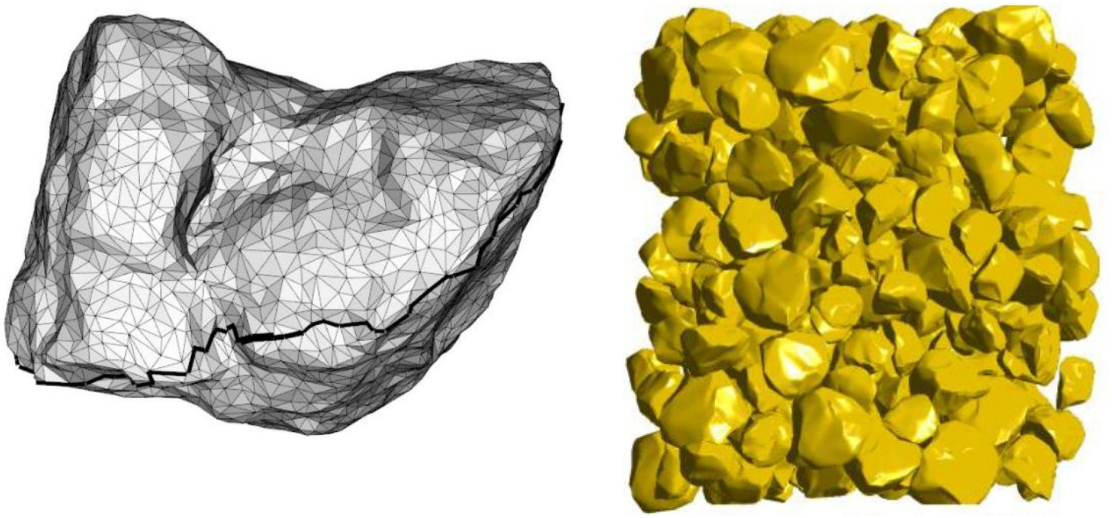

(a) (b)

Figure 2.7 (a) single particle; and (b) soil structure represented in a 3D DEM (Góis et al., 2023)

2.2.3.5 Regression models

So far, the approaches presented here were based on different representations of the soil structure. This is not the case in regression models where the main objective is to capture the most important properties and characteristics affecting the SWCC. The regression models commonly take advantage of existing equations to fit the SWCC or probability density functions (PDF). These are closed-form equations that have the advantage of allowing differentiation and integration, which are useful in constitutive models.

The van Genuchten (1980) equation is the most used fitting equation because its simplicity and ability to fit well a great part of the SWCC using only two parameters. The Fredlund and Xing (1994) is also another relevant fitting equation used in this context, it relies on three parameters and is adequate especially when is necessary to fit the entire range of the SWCC. Some examples of studies based on fitting equations are Fredlund et al. (2002), Zhou et al. (2014), Wang et al. (2017), Li and Vanapalli (2021), Wang et al. (2021), and Zhang et al. (2022).

The similarity between the PSD and some PDFs is the reason for their use in regression models. The SWCC is obtained using the cumulative PDF. The log-normal distribution is the common PDF adopted in the literature (Khlosi et al., 2006; Phoon et al., 2010; Satyanaga et al., 2013; Prakash et al., 2021). Earlier studies performed univariate (Gupta and Larson, 1979) and multivariate (Saxton et al., 1986) regressions to provide predictions of specific pre-established suctions.

Due its nature of incorporating the soil behavior by calibrating the parameters based on measured data without a geometrical representation of the soil structure, regression models can depict better performance for fine grained soils in comparison to models that tries to simulate the soil structure. It is important to mention that these prediction models have similarities to that of a regression approach, but their fundamental concepts are related to the representation of water storage mechanisms. Regression analysis in such cases is only a tool used to fulfill the theoretical basis.

2.2.3.6 Artificial intelligence models

The fundamental idea behind artificial intelligence models is to use an algorithm developed to “learn” the soil behavior from a collection of soil data called as training

dataset. Another group of soil data known as validation dataset is used to measure the performance of the algorithm. The application of machine learning for predicting the SWCC is commonly developed through artificial neural networks (ANN).

The results in these approaches are dependent on the network configuration in terms of number of layers, number of input and output neurons, type of activation function, and number of epochs. Also, the training and validation datasets as well the choice of adequate input and output parameters are crucial for a good performance. Parametric analyses are often performed to optimize the network configuration.

Basically, an ANN algorithm uses the data from the training dataset to calibrate the weight in each neuron to minimize the errors between predicted and measure data. This process is consistent to a regression analysis that is performed multiple times. Some studies proposing estimation models using artificial intelligence techniques include Pachepsky et al. (1996), Schaap and Bouten (1996), Minasny and McBratney (2002), Lamorski et al. (2017), Saha et al. (2018), Li and Vanapalli (2022), Bakhshi et al., (2023), Totola et al. (2023), and Pereira et al. (2023).

2.2.3.7 Other models and approaches

Chan and Govindaraju (2003) developed a stochastic method to represent the soil structure in three dimensions using spheres of different sizes. The spheres are allowed to overlap with each other to provide a more realistic representation of particles and aggregates.

A model using the concept of unit cell was proposed by Or and Tuller (1999). In this case, the authors used a unit cell representing only the pores instead of the particle-pores system described in Section 2.2.3.2. Differences in pore-sizes are considered by assuming

a log-normal distribution function. The model considered both capillary and adsorption mechanisms for pores with triangular, square, and circular shapes.

Dolinar (2014) introduced a model based on physical relationships of capillary and adsorption. The equation is dependent on the clay content and the specific surface area. Also, this model is valid only for fine-grained soils free of organic matter and at water contents between the liquid and plastic limits.

Revil and Lu (2013) combined the van Genuchten (1980) equation to incorporate both capillary and adsorption. The latter relied on the Freundlich isotherm using the cation exchange capacity (CEC).

2.3 Shear strength of unsaturated soils

This section presents a brief description of the main concepts related to shear strength of unsaturated soils. Also, measurement techniques are summarized. The estimation techniques are comprehensively discussed in Chapter 4, which will be focused on proposing a new model to predict the unsaturated shear strength of Brazilian tropical soils.

The most common representation of the shear strength of unsaturated soils is in terms of two stress state variables: net normal stress and matric suction. Assuming a linear relationship between these stress state variables and the shear strength, Fredlund et al. (1978) presented the following equation:

$$\tau_{ff} = c' + (\sigma - u_a)_f \tan\phi' + (u_a - u_w)_f \tan\phi^b \quad (2.20)$$

where: c' is the effective cohesion; $(\sigma - u_a)_f$ is the net normal stress on the failure plane at failure; ϕ' is the angle of internal friction; $(u_a - u_w)_f$ is the matric suction on the failure plane

at failure; and ϕ^b is the angle indicating the rate of increase in shear strength with respect to a change in matric suction.

The Mohr-Coulomb failure envelope can be extended for unsaturated soils plotting the matric suction in the third dimension forming a surface that can be planar or curved. The surface forming the failure envelope is tangent to the Mohr circles, as illustrated in Fig. 2.8.

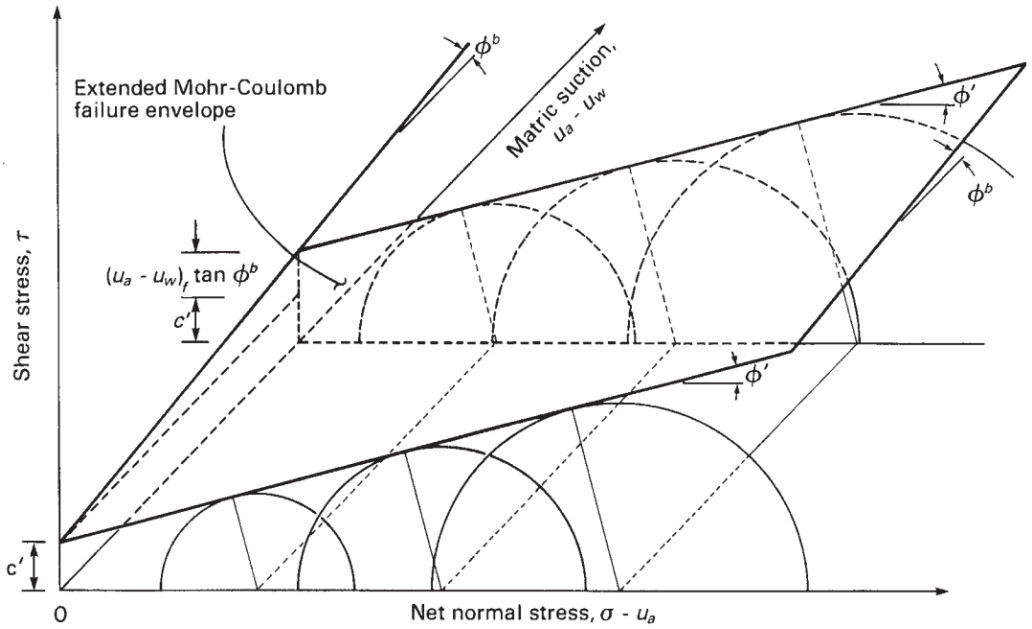

Figure 2.8 Extended Mohr-Coulomb failure envelope (Fredlund et al., 2012)

This envelope can also be represented using stress points at failure with coordinates (s_f, t_f, r_f) from the top of the Mohr circles, as described by the following equations:

$$s_f = \left[\left(\sigma_1 + \sigma_3 \right) / 2 - u_a \right]_f \tag{2.21}$$

$$t_f = \left(\sigma_1 - \sigma_3 \right)_f / 2 \tag{2.22}$$

$$r_f = \left(u_a - u_w \right)_f \tag{2.23}$$

As a result, the stress points form a different failure envelope, as shown in Fig. 2.9. The value of t_f at the intercept ($s_f = 0$ and $r_f = 0$) is referred to as d'. The angles indicating the slopes of the failure envelope in the s_f and r_f axes are, respectively, ψ' and ψ^b. Thus, to describe the failure envelope in this form, Eq. 2.20 becomes:

$$t_f = d' + s_f \tan\psi' + r_f \tan\psi^b \tag{2.24}$$

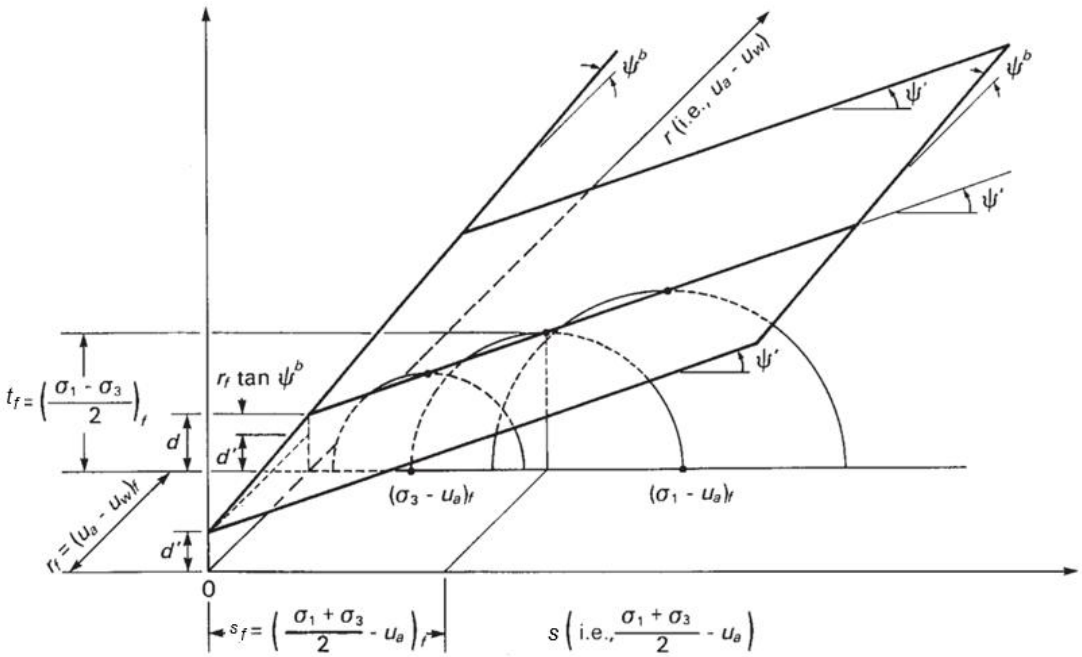

Figure 2.9 Extended stress point failure envelope (Fredlund et al., 2012)

The relationships between the parameters that characterize both failure envelopes are obtained using basic geometry resulting in the following equations:

$$\tan\psi' = \sin\phi' \tag{2.25}$$

$$\tan\psi^b = \tan\phi^b \cos\phi' \tag{2.26}$$

$$d = c\cos\phi' \tag{2.27}$$

$$d' = c'\cos\phi' \tag{2.28}$$

Despite the usual representation of the contribution of the matric suction to the shear strength be in the linear form as described by Eq. 2.20, the real behavior of the soil presents at least two regimes: linear and non-linear (Fig. 2.10). The linear regime is attributed for matric suctions less than the air-entry value where their contribution to the shear strength is equivalent to the contribution of the net normal stress (i.e., $\phi^b = \phi'$). In this stage, the soil is saturated or close to saturated conditions, and the water phase is under tension, compressing the particles against themselves. A good analogy for this situation is pulling out a syringe filled with water whereby its tip is closed, the water is being pulled equally from all directions. As the soil particles becomes completed surrounded by water, any matric suction will have the same effect as the application of a net normal stress with the same magnitude, resulting in ϕ^b equal to ϕ'. After the air-entry value is surpassed, some of the soil pores are drained reducing the wetted area in which the matric suction stresses are transmitted. Consequently, the effectiveness of the matric suction in increasing the shear strength is reduced entailing values of ϕ^b lower than ϕ'.

The literature contains limited information about the unsaturated shear strength suctions in the residual stage. The existing experimental data indicate distinct trends in terms of ϕ^b depending on the type of soil. Tests on sands performed by Donald (1956, as cited in Fredlund et al., 2012) point out a decrease in shear strength after the residual suction (i.e., $\phi^b < 0$). For the Botkin silt studied by Vanapalli et al. (2000), the shear strength kept increasing for residual suctions up to 100,000 kPa. After this value, the authors noticed no defined pattern. A similar behavior was observed by Nishimura and Fredlund (2000) studying a cohesionless fine-grained silt. The shear strength increases for low range values of residual suction (100 to 450 kPa) whereas it seems to be unaffected by suction values

over 38,600 kPa. Investigation of a kaolin performed by Nishimura and Fredlund (2002) over suctions of 30,000 kPa pointed out a very little increment in the shear strength (i.e., ϕ^b = 0.3º) and indicated hysteresis with respect to the shear strength.

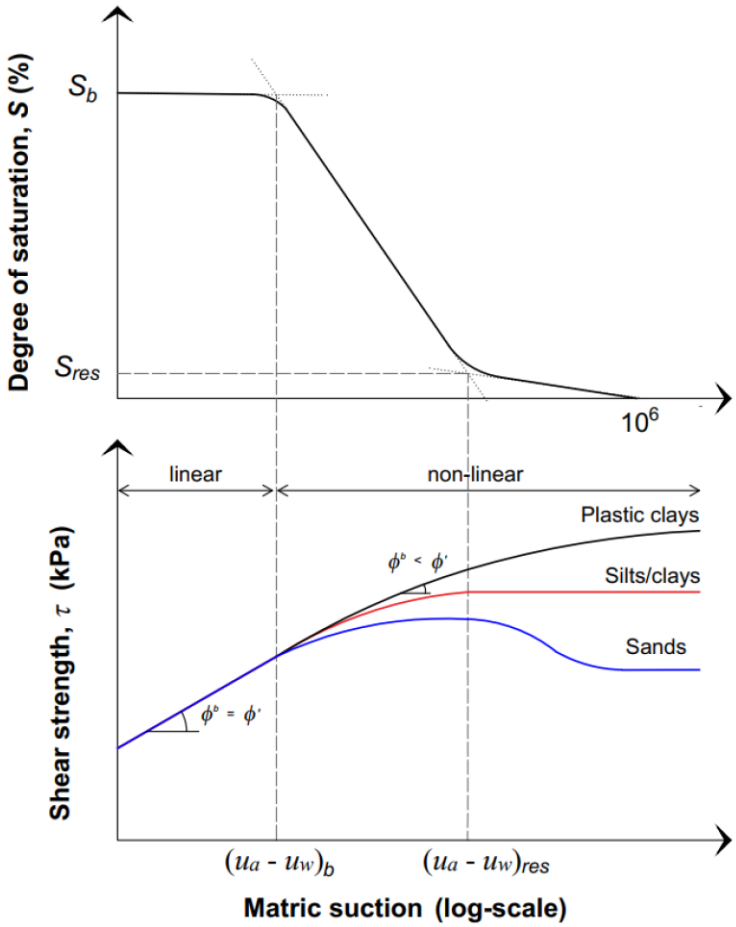

Figure 2.10 Relationship between the SWCC and the shear strength (Modified from Fredlund et al., 2012)

In summary, the relationship between the shear strength and the SWCC is illustrated in Fig. 2.10. According to Fredlund et al. (2012), it is reasonable to assume null ϕ^b for conditions beyond the residual suction for silts and clays. For sands, values of ϕ^b may be negative.

2.4 Tropical soils

The tropical soils exhibit different physicochemical properties and their hydromechanical behavior cannot be reliably interpreted using traditional soil mechanics. These soils possess a porous structure often marked by cementation induced by iron and aluminum oxides and hydroxides. This cementation is responsible for the formation of aggregates. In cases of robust cementation, lateritic concretions, known as petroplintites, may form.

The primary challenge associated with these soils lies in their classification. Brazilian tropical soils do not neatly align with commonly employed classification systems in road, dam, and building construction. The Unified Soil Classification System (USCS) and the Transportation Research Board (TRB) classification systems, which heavily rely on granulometry and Atterberg limits, were originally formulated based on soils from temperate climates. Consequently, when applied to Brazilian tropical soils, these systems often yield unsatisfactory or ambiguous results, particularly for lateritic soils. The necessity for a classification system for tropical soils emerged when it became evident that the traditional criteria for selecting paving materials, based on particle size ranges of maximum density, were insufficient. Despite the granulometry of tropical soils differing from the criteria in traditional guidelines, these soils performed well when utilized in sub-base and base-coarse layers.

Several researchers, particularly Nogami and Villibor (1995, as cited in Camapum de Carvalho et al., 2023), have noted instances where soils with identical liquid limits and plasticity indices exhibited vastly different expansibilities. Concurrently, materials with a high liquid limit (exceeding 50%) may either not expand or exhibit minimal expansion.

This phenomenon is particularly prominent in soils pedologically classified as latosols and argosols, prevalent in Brazil. Conversely, some soils, despite having a low liquid limit and plasticity index, demonstrate expansion; such a behavior is common in saprolitic soils that are rich in micaceous and/or kaolinitic silt.

Unless explicitly mentioned, most of the information in this section is a compilation of information presented in two books essential for the understanding of the hydromechanical behavior of Brazilian tropical soils. The first book, Mitchell and Soga (2005), contains the fundamental theory for the overall comprehension of soil behavior whereas the second one, Camapum de Carvalho et al. (2023), is focused on the unsaturated behavior of Brazilian tropical soils.

2.4.1 Weathering and pedogenesis

Water and temperature play pivotal roles in the weathering process. The level of water availability directly correlates with the extent of changes that can occur, making arid or semi-arid climates less prone to rock alterations. Abundant water facilitates intense percolation, enabling reactions, forming solutions that enhance base exchange, and transporting silica deeper into the rock.

Temperature is closely linked to physical alteration mechanisms. Exposure to climates with wide thermal variations subjects these soils to numerous and intense cycles of volumetric expansion and contraction, heightening susceptibility to weathering. Moreover, temperature acts as a catalyst for chemical reactions involving water in these regions. Heat broadens the range of chemical reactions, resulting in a significantly thicker mantle of rock alteration compared to temperate climates.

These conditions are compounded in Brazil's tropical climate, where temperature fluctuations often exceed 20ºC within a single day. The high incidence of sunlight adds energy for surface rock heating and endothermic reactions. The substantial annual rainfall supplies ample water for hydration, hydrolysis reactions, and solution percolation through rock cavities.

The climates in these regions can be divided into dry and rainy seasons, soils undergo leaching during the rainy season and drying out in the dry season. Abundant water in the rainy season transports silica from surface soil particles, while in the dry season, rising water by capillarity fixes iron and aluminum ions.

This climatic cycle is vital to the formation of lateritic soils, defined by a silica/sesquioxide ratio greater than or equal to 2 (i.e., highly weathered soils). The typical lateritic soil profile comprises a porous soil layer rich in iron and aluminum, often several meters thick, overlying a concretionary saprolite layer.

Saprolites are recent soils that are formed resulting from rock alteration, presenting as a powdery, unconsolidated material retaining the rock's structure but with low cohesion. These soils become exposed in regions with intense rainfall where erosion occurs faster than alteration. Pedology categorizes saprolitic or young residual soils as neosols, while lateritic soils encompass latosols, plinthosols, and argisols. Fig. 2.11 illustrates the distribution of these tropical soils from Brazil.

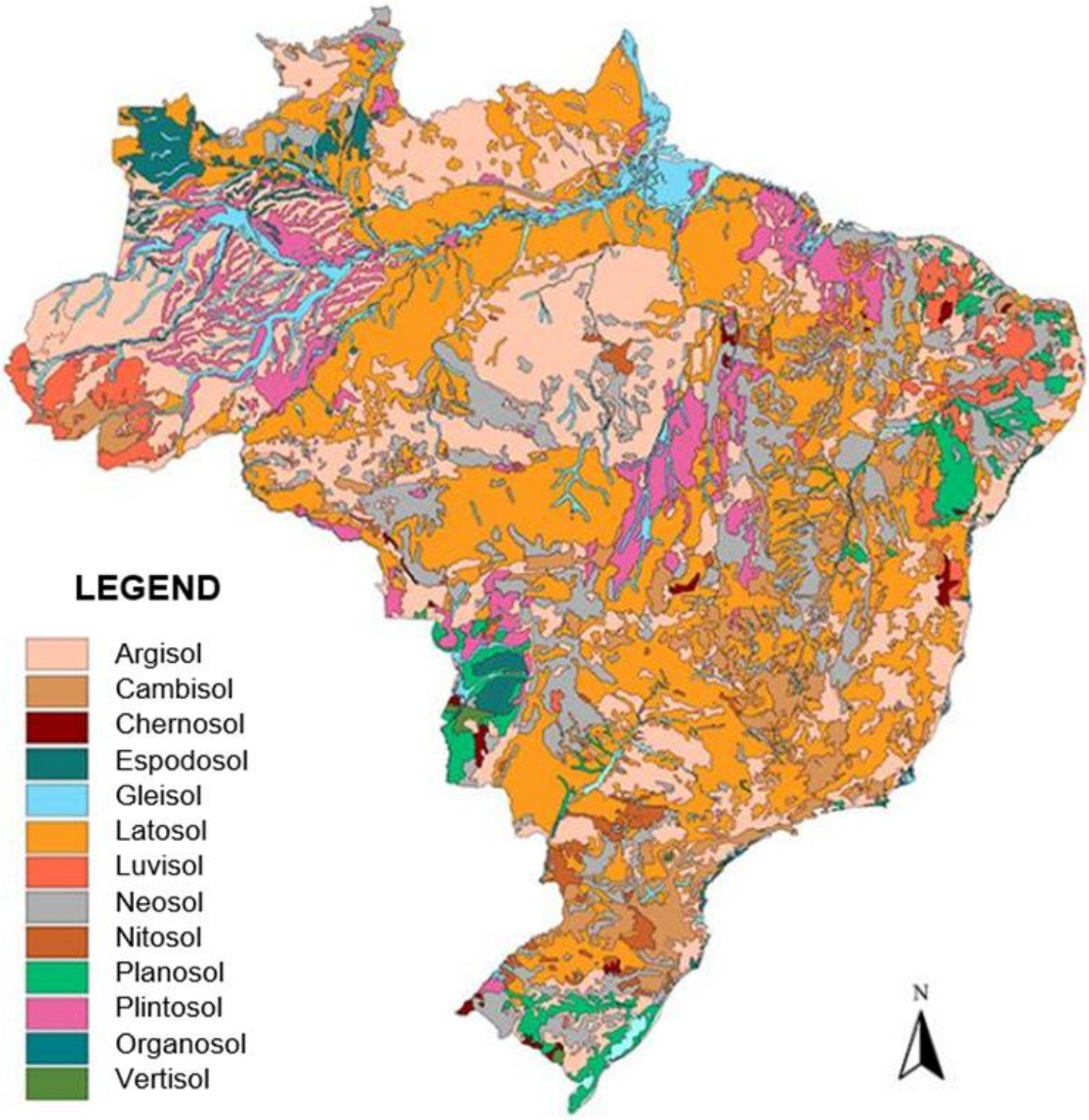

Figure 2.11 Map of Brazilian soils (Embrapa, 2014)

2.4.2 Minerology

Mineralogy plays a crucial role in determining the size, shape, and physical and chemical properties of soil particles, which directly impact their properties and behavior. While certain minerals may not be the predominant ones in soil composition, they can significantly influence the behavior of saturated and unsaturated soils. This is particularly important in tropical regions like Brazil, where soil profiles exhibit a diverse range of

minerals that directly affect the soil's physical-chemical properties and behavior. Primary minerals such as quartz, feldspars, and micas are important constituents, with quartz and feldspars being the most abundant. Special climatic conditions can lead to the presence of other primary minerals like pyroxenes, amphiboles, olivines, and rutile; with rutile being the one that is widely found. These minerals serve as indicators of soil profile evolution. In tropical regions with high precipitation and temperature, the weathering of rocks can result in the rapid decomposition of feldspars and ferromagnesian minerals, leading to the enrichment of iron and aluminum oxides and hydroxides. Iron and aluminum oxides and hydroxides are prevalent in Brazilian soils, and despite not being dominant in composition, they have a significant influence on the structure and behavior of these soils.

2.4.2.1 Primary minerals

2.4.2.1.1 Quartz

Quartz is the most common primary mineral found in intermediate acid igneous, metamorphic and sedimentary rocks. Quartz has little isomorphic substitution in its structure and a low proportion of bond breaks on its surface. As a result, it generally has low surface charge, specific surface area and cation exchange capacity (CEC).

These particularities result in matric suction due to the capillary effect, which is more physical than electrochemical. Being physical in nature, capillarity will depend on the particle size distribution and porosity and, consequently, on the pore distribution. For this reason, methods for estimating the characteristic water retention curve based on texture offer better results for soils with a low clay-mineral content.

In natural soils, quartz is mainly associated with granular particles, also occurring in the silt range and integrating aggregates and microaggregates. This aspect associated with

its low physical-chemical activity which means that it plays a minor role in moisture retention; due to this reason, there is a great variation in suction because of soil-atmosphere interaction.

2.4.2.1.2 Feldspars

Feldspars are silicate minerals commonly found in igneous and metamorphic rocks, and occasionally in sedimentary rocks. They have tabular or granular crystal structures. In soils, feldspars are present in the sand and silt fractions of poorly weathered soils. Feldspars exhibit higher physical-chemical activity than quartz due to the presence of ionic substitution between potassium, sodium, and calcium. This activity enables feldspars to contribute to moisture retention capacity through adsorption energy. As a result, this mineral can affect the capillarity and suction of unsaturated soils.

2.4.2.2 Clay minerals

2.4.2.2.1 Kaolinite group

The structural formula of the kaolinite unit cell is $Si_4Al_4O_{10}(OH)_8$, with a percentage composition of 46.54% SiO_2, 39.5% Al_2O_3, and 13.96% H_2O. This group is characterized by non-expansiveness, with a basal interplanar distance of approximately 7.2 Å, particles ranging from 0.1 to 0.4 μm with thickness from 0.05 to 2 μm, and a relative density of 2.63 for kaolinite. Halloysite, on the other hand, is less stable than kaolinite and is less frequently weathered in Brazil, although it is present in many soils. It can be found in less or more hydrated forms.

Although the kaolinite group is made up of minerals that are stable in the presence of water (i.e., they are not mineralogically expansive), hydrated halloysites dehydrate irreversibly when subjected to drying. The kaolinite clay mineral is plate-shaped, while

halloysite can be tubular or spherical, directly affecting the degree of anisotropy that the soil may exhibit. The kaolinite group has low surface charge density, CEC, and plasticity. Measurements of kaolinite indicates its SSA varies between 10 and 20 m^2/g and 35 to 70 m^2/g for halloysite (Hillel, 2004; Mitchell and Soga, 2005). These clay minerals do not undergo mineralogical expansion or contraction. However, the plate-like shape of kaolinite means that, in interparticle interaction, contraction or expansion can occur when subjected to variations in energy, such as applied tension (external energy) and suction (internal energy). If the kaolinite is found in aggregate structures, both contraction and expansion tend not to occur or are minimal.

The interactions between kaolinite and iron and aluminum oxides are important in aggregating and defining the physical characteristics of highly weathered soils. The negative charge present on the face of the clay minerals and the positive charge covering the iron and aluminum oxyhydroxides favor the phenomenon of aggregation as well as the interaction between aggregates. However, it should be noted that when the conditions of the environment change, for example, with the addition of lime or the infiltration of sewage water, these oxyhydroxides can be solubilized, leading to the structural collapse of the soil or affecting its resistance and deformability.

2.4.2.2.2 Micalike group

Micalike minerals are found in acidic and basic igneous, pegmatites, metamorphic, and sedimentary rocks. The micalike group comprises micas, which are primary minerals, and illite, which is a secondary mineral.

The minerals in this group have a 2:1 type structure, with layers formed by an octahedral sheet sandwiched between two tetrahedral ones. Micas are plate-shaped or

tabular, and their orientation in the soil depends on the formation of the rock or soil as well as the acting stresses. The micalike mineral plates in the soil have a preferential orientation, which creates an oriented structure and encourages anisotropic behavior in response to hydromechanical stresses.

Illite is present in soils resulting from the weathering of igneous and metamorphic rocks that are rich in muscovite, which indicates intermediate stages of weathering. The crystal structure of the clay mineral illite is similar to that of montmorillonite, but with a greater substitution of silicon tetra by aluminum. This substitution gives the crystal structure a greater charge and makes the clay mineral generally non-expansive.

Illite typically takes the form of elongated lamellae with irregular edges and an equivalent diameter ranging from 0.1 to 2 μm, and with a plate thickness as small as 3 nm. The basal interplanar distance measures approximately 10.1 Å. Illite has higher plasticity and CEC than the kaolinite group and lower than smectite, typically ranging from 10 to 40 meq/100g. The specific surface area is about 65 to 100 m^2/g. Due to these characteristics, illite is a clay mineral dominated by adsorption energy, where suction by adsorbed water is more significant than capillarity.

2.4.2.2.3 Smectite group

The smectite group are clays minerals type 2:1. They include montmorillonite, beidellite, nontronite, saponite, sauconite, and hectorite. The terms montmorillonite and smectite are often used interchangeably. This group has a theoretical formula of $Al_4Si_8O_{20}(OH)_4\ nH_2O$, where the amount of water molecules varies, resulting in basal interplanar distances that typically range from 10 Å to 40 Å. Beyond 40 Å, the layers separate, forming structures that are 10 Å thick.

Smectites are morphologically lamellar, with dimensions ranging from 0.1 mm to 2 μm and an average size of 0.5 μm. They have high SSA values that contribute to a significant reduction in soil permeability. Also, smectites increase the CEC, making the soil more sensitive to the composition of the interstitial solution. They are highly active physical-chemical clays, with high plasticity and a high capacity for expansion and contraction. Due to their high affinity with water, they enhance the soil water retention capacity and prevent water from escaping under compression.

Their impact on the hydraulic and mechanical behavior of the soil is substantial, even in small quantities. Bentonite, a clay composed mainly of clay minerals from the smectite group, is frequently mixed with natural soils to achieve low permeability without compromising strength or increasing compressibility.

2.4.2.2.4 Vermiculite group

This clay mineral belongs to the 2:1 group. The high net negative charge of the structure is due to the replacement of silicon by aluminum in the tetrahedron layer. This charge is neutralized by hydrated cations located in the interplanes. Vermiculite exhibits smaller expansion than smectite due to its lower charge density. The basal interplanar distance of the material ranges from 10 Å to 15 Å. It has a lamellar shape and a cation exchange capacity that is higher than illite but lower than smectite. The dimensions of the material range from 0.1 to 0.5 μm.

2.4.2.2.5 Chlorite group

Chlorites can be primary minerals inherited from low to medium-grade metamorphic or igneous rocks, or secondary minerals resulting from the alteration of ferromagnesian minerals. In these minerals the magnesium in the brucite layer is partially replaced by ferric

or aluminum ions. This substitution provides the positive charge necessary to neutralize the substitutions of silicon for aluminum in the tetrahedral sheets, resulting in a basal interplanar distance of 14 Å. If there are no such substitutions, the neutralization is carried out by exchangeable cations, which weakens the bond and allows it to expand to basal interplanar distances greater than 14 Å.

Chlorites typically have a lamellar shape and a surface area like that of fine micas. Their cation exchange capacity commonly ranges between 10 and 40 meq/100g, and they have a similar particle size, negative charge, and surface area to illite.

2.4.2.3 Oxides and hydroxides

When secondary in the soil, these minerals have low crystallinity associated with the speed which they are formed compared to 1:1 and 2:1 clay minerals and also with the availability of metal cations.

Hematite, one of the most widely found iron oxides in nature, is often present in deeply weathered soils, which gives them their red color. The structure of these clay minerals consists of the chemical formula Fe_2O_3, and its particles take the form of hexagonal or rhombohedral plates. Its relative density is typically 5.26.

Goethite is the most stable iron hydroxide and is commonly found in lateritic soils in Brazil, which gives them their characteristic yellow and yellowish-bronze hues. Its formation requires a more humid environment with high levels of organic matter, in contrast to hematite, which forms under opposite conditions. The mineral has a structure composed of needles and laths (elongated plates) and forms fibrous aggregates. Its relative density typically ranges from 4.26 to 4.37.

Iron and aluminum oxides and hydroxides also have a high specific surface area. Due to their high relative density, these compounds can significantly affect the dry apparent specific weight of deeply weathered soils. Therefore, it is relevant to conduct hydromechanical behavior analyses based on porosity or void ratio.

Aluminum oxides and hydroxides are common minerals found in various soils and occur particularly in hot and humid climate conditions. Diaspore, boehmite, gibbsite, and bauxite are the main aluminum oxyhydroxides, with gibbsite being the most common in tropical soils.

Gibbsite, also known as hydrargillite, is a mineral with the chemical formula $AlO(OH)_3$. It is commonly found in soils that undergo intense leaching in hot and humid climates, resulting in deep chemical weathering of aluminous minerals. Its crystals typically have a lamellar to tabular shape with pseudo-hexagonal contours, which are usually inherited from kaolinite. Gibbsite has a relative density between 2.3 and 2.4.

In tropical Brazilian soils, these minerals have a significant presence and influence on their properties and hydromechanical behavior. For example, iron oxides and hydroxides generally contribute to increasing their plasticity and aggregation.

2.4.3 Structure

Soil fabric is a term used to describe the particle sizes, shapes, and distributions, along with the arrangement of grains and grain contacts (Mitchell and Soga, 2005). In other words, soil fabric is related only to the geometrical characteristics of the particles and voids of a soil. The term structure is often used interchangeably with fabric, although it refers to the combined effects of fabric, mineralogy, and interparticle forces (Mitchell and Soga, 2005).

The fabric of bimodal tropical soils is characterized by the presence of two dominant pore-sizes. The smallest pores are located within the clay aggregates and constitute the microstructure (i.e., intra-aggregates). These micropores are usually less than 0.1 μm with a dominant pore diameter around 0.02 μm. At saturation, this length corresponds to the accumulation of 74 water molecules. This is an indication of the relevance of the adsorption mechanism in these soils.

The greatest pores form the macrostructure, pore sizes are usually higher than 5 μm. The size of the intra-aggregates pores ranges from 900 to 10,000 times lower than the inter-aggregate pores. These pores correspond to the soil voids between neighboring particles and/or clay aggregates (i.e., inter-aggregates). This range of pore network configuration results in a bimodal PSD for the Brazilian tropical soils. Fig. 2.12 shows some typical pore-size distribution curves from undisturbed specimens of these soils.

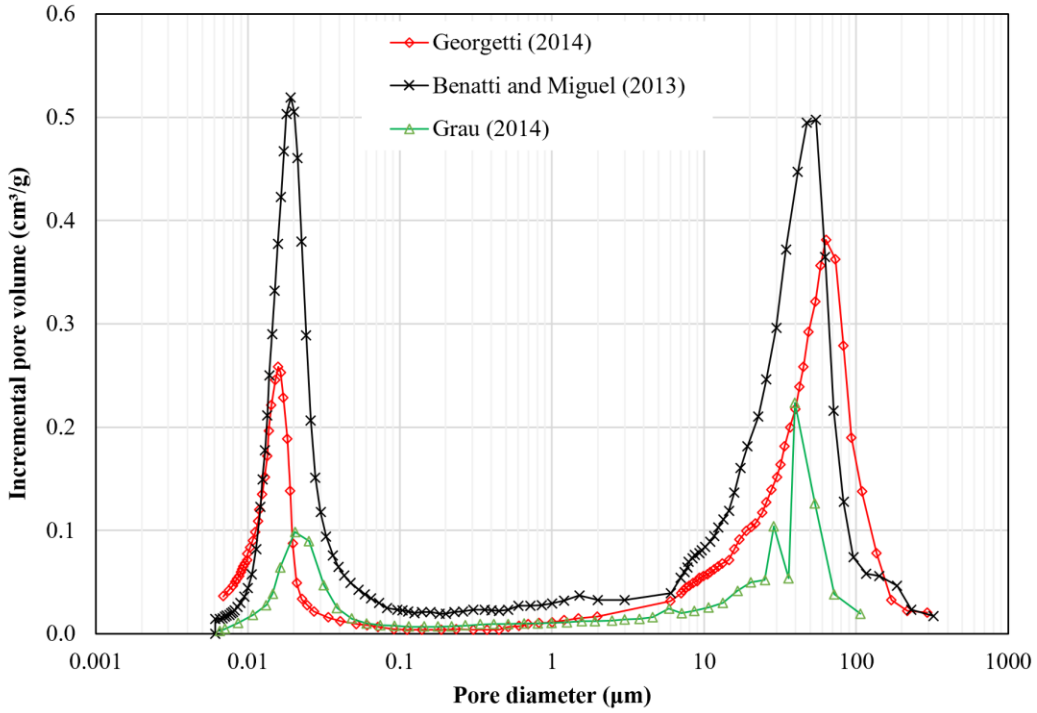

Figure 2.12 Typical PSDs of some undisturbed specimens of bimodal tropical soils

2.4.3.1 Soil Water Characteristic Curve (SWCC)

The SWCC behavior is significantly influenced by the soil structure. This means that the pore network as well the mineralogy of the clay particles are the factors controlling water storage as function of suction. As illustrated in Fig. 2.13, for bimodal tropical soils, the macrostructure controls the upper region of the SWCC where the first desorption (or transition) zone is located. The microstructure corresponds to the lower region of the SWCC that includes the second desorption zone. Both macro- and microstructures are characterized by dominant pore-sizes that determine the suction whereby most of the macro- or micropores have been drained.

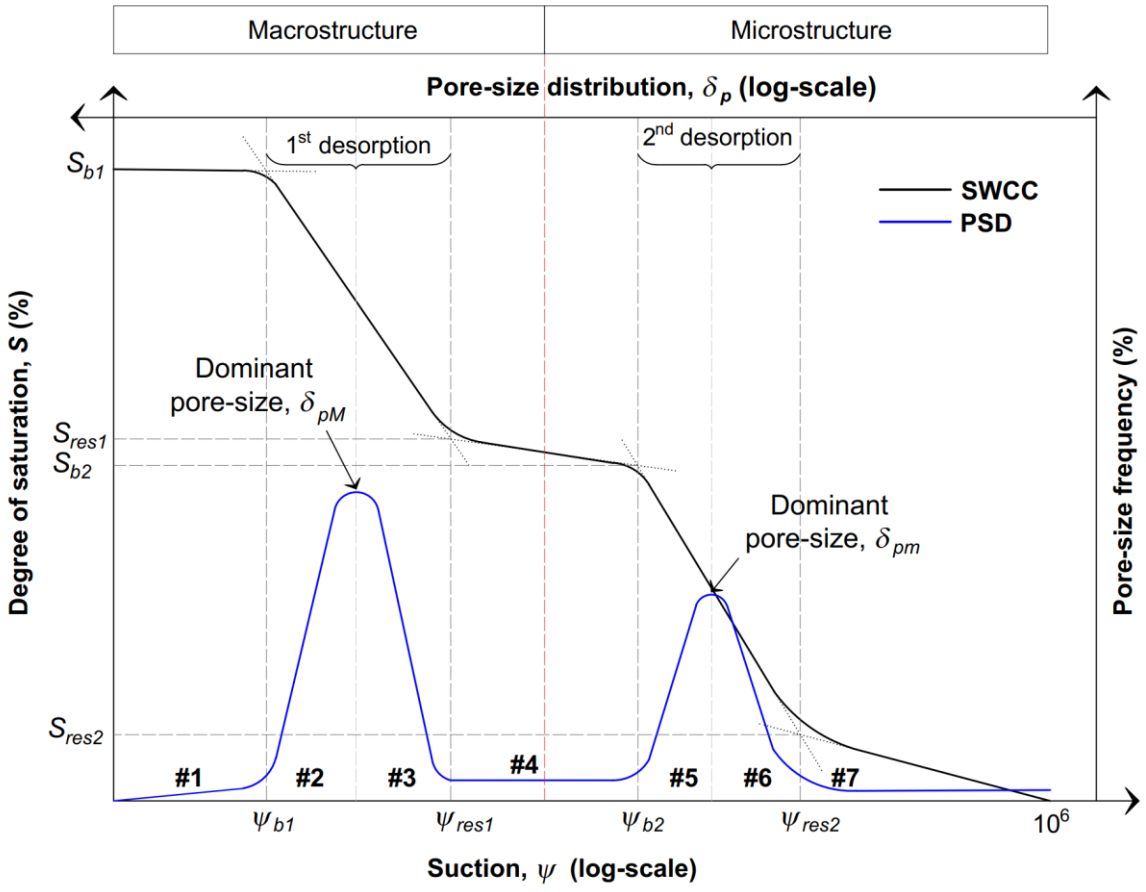

Figure 2.13 Relationship between a bimodal SWCC and its structure

The largest (not most) macropores begins to desaturate at a suction called the first air-entry value (ψ_{b1}), and its respective the degree of saturation is represented by S_{b1}. Similarly, the second air-entry value (ψ_{b2}) corresponds to the suction in which the drainage of the largest micropores takes place. At this point, the degree of saturation is expressed as S_{b2}. The suction in which only a few of the smallest macropores are saturated is called ψ_{res1}. The same definition applied to the micropores results in the ψ_{res2}. Also, the desorption rate in each transition zone is dominated by the kurtosis of the respective PSD. For a better comprehension, all these points are illustrated in Fig. 2.13.

The generic SWCC shown in Fig. 2.13 is divided into seven regions according to different characteristics in terms of air and water phases. Water storage mechanisms in each region are illustrated in Fig. 2.14. Starting from zero suction (i.e., S = 100%) up to suctions less than the first air-entry value (region #1 in Fig. 2.13 and Fig. 2.14.#1), the water phase is continuous, and the air is dissolved into water. This region is called the boundary effect zone. For suctions greater than the first air-entry value in region #2 of Fig. 2.14, air enters the macropores replacing water and forming the first capillary bridges, but the air phase is still discontinuous, as illustrated in Fig. 2.14.#2. As more water is drained with increasing suction between regions #2 and #3 in Fig. 2.13), the volume of air increases reaching a state in with both water and air phases within the macropores are continuous. This occurs at the suction that corresponds approximately to the dominant pore-size of the macropores (δ_{pM}).

Incrementations in soil suction in region #3 of Fig. 2.13 lead to a stage in which the water phase in the macropores becomes discontinuous, as illustrated in Fig. 2.14.#3. Only few macropores remain saturated and most of the water is stored in capillary bridges. At

this point, the suction is known as the first residual suction (ψ_{res1}) with its respective first degree of saturation (S_{res1}). So far, the water has flowed in liquid form and once the suctions are in region #4 of Fig. 2.13, flow occurs only in vapor form. This region corresponds to soil suctions between the macro- and micropores with little reduction in water content, albeit suctions can vary significantly. The volume of water decreases from the reduction of the scarce capillary bridges as well a few pores that remain full filled with water (Fig. 2.14.#4).

When the suction reaches a value that is high enough to trigger the drainage of the largest micropores, the second air-entry value (ψ_{b2}) is achieved. The degree of saturation at this point is represented by S_{b2}. The water phase within the micropores is continuous whereas air begins to enter inside the aggregations forming a discontinuous phase. This is the boundary between regions #4 and #5 in Fig. 2.13. Increasing the suction beyond this point results in the emergence of capillary bridges, as shown in Fig. 2.14.#5. This continues until water and air start to coexist in continuous phases at around a suction that corresponds to the dominant pore-size of the micropores (δ_{pm}). Also, the number of capillary bridges increases significantly.

After that, in region #6 of Fig. 2.13, the desorption process causes the reduction of water content up to a suction whereby the water phase turns discontinuous. Most of the micropores have been drained, as depicted in Fig. 2.14.#6. The suction and degree of saturation at this point are known as second residual suction (ψ_{res2}) and second residual degree of saturation (S_{res2}), respectively. The water storage is mainly comprised of liquid films adhered to the clay particles (i.e., adsorbed water), despite of the existence of few very small capillary bridges. Finally, the highest suctions correspond to region #7 in Fig.

2.13. The adsorption phenomenon is responsible for the remaining water with liquid films formed by up to three molecules (Fig. 2.14.#7). This degree of saturation is very low and represents a condition that is not achieved by the soil in normal conditions of soil atmosphere interaction.

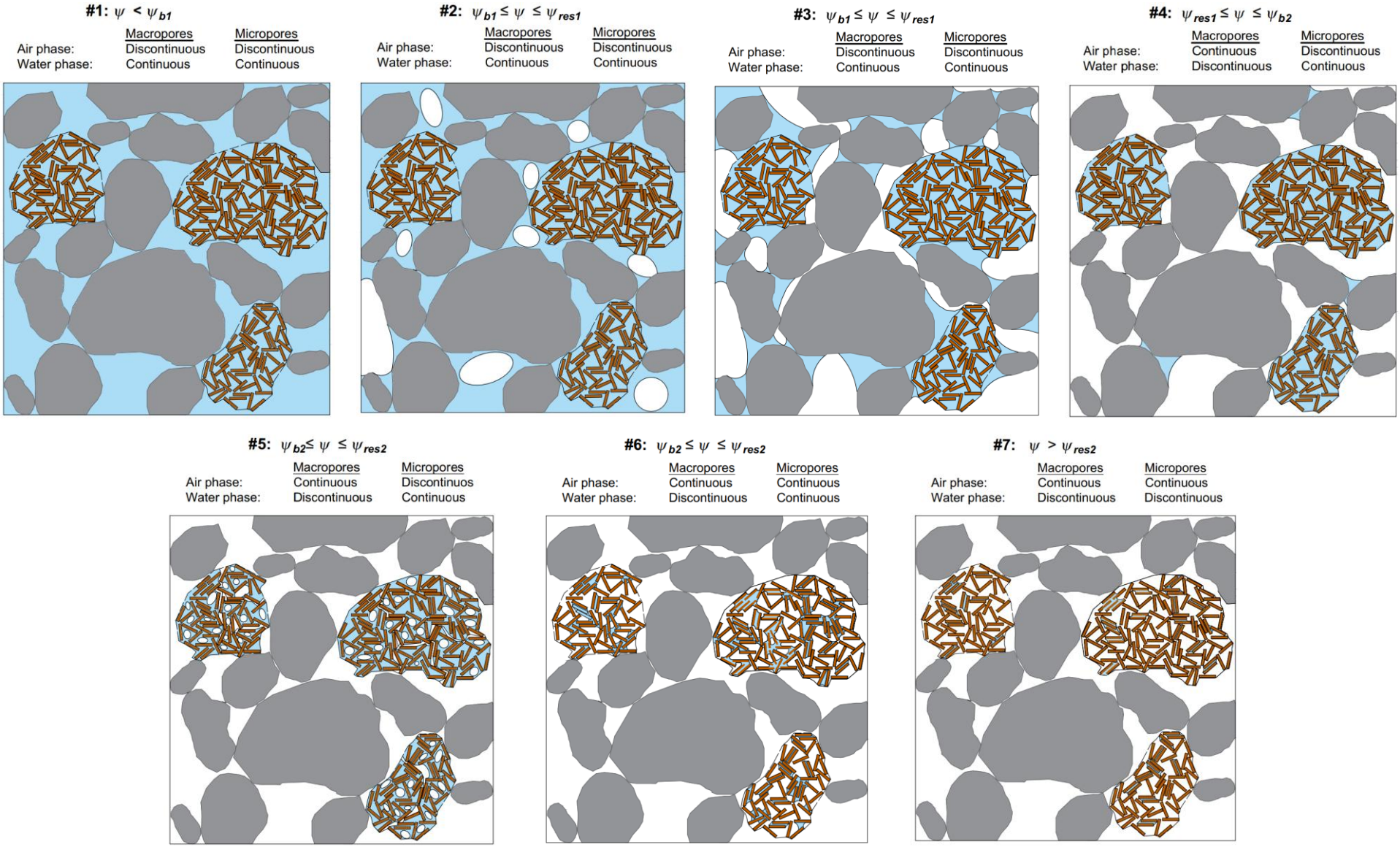

Figure 2.14 Desaturation process in a soil with double structure

2.4.3.2 Characterization techniques

A common technique to measure the pore-sizes is through MIP tests. This technique consists of the application of pressure to mercury to fill the soil voids. Each value of pressure corresponds to a pore size that is obtained using the Washburn equation and assuming pores with a cylindrical shape. The visualization of the soil fabric is possible using techniques such as Scanning Electron Microscope (SEM), Environmental SEM, X-Ray diffraction, and computed microtomography (μCT). The latter can used to obtain 2D and 3D scans that jointly with image analysis possibilities the measurement of pore-sizes. Examples of a SEM image and a μCT scan of bimodal tropical soils are shown in Fig. 2.15a and 2.15b. More details about these techniques and equipment are given by Mitchell and Soga (2005) and Romero and Simms (2008).

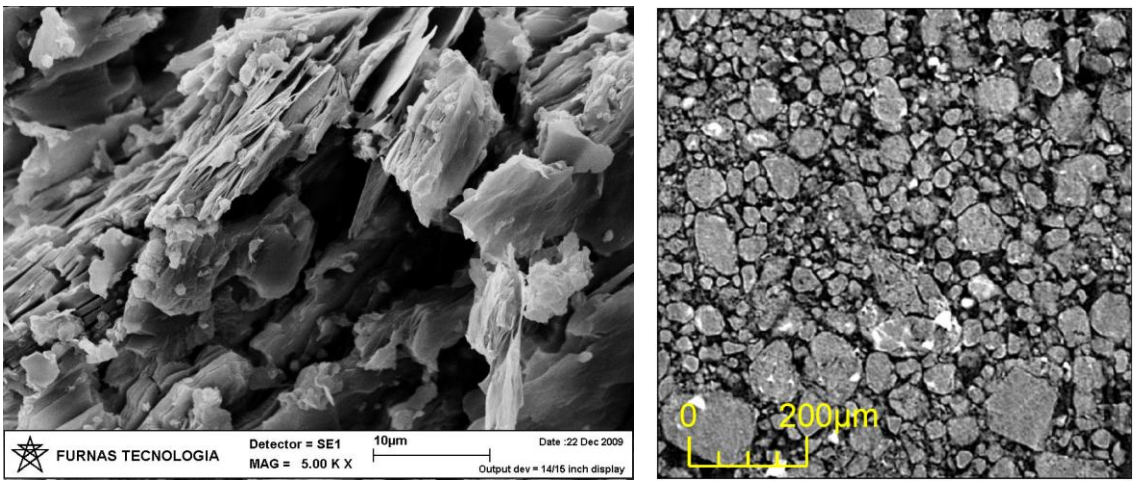

(a) (b)

Figure 2.15 (a) SEM image and (b) μCT scan of bimodal tropical soils showing its macrostructure (Araújo, 2019)

2.4.3.3 Particle analysis

The presence of clay aggregates affects significantly the GSD of tropical soils. For this reason, the particle analysis is performed by combining sieve analysis and hydrometer

test, the latter is done with (dispersed) and without (non-dispersed) the dispersing agent (i.e., sodium hexametaphosphate is the most common). The difference between the GSD in these distinct conditions is an indicative of the degree of aggregation of the soil. Nevertheless, the physical and chemical dispersion methods used in the traditional particle analysis are unable to completely undo the clay aggregates (Souza, 2020). Fig. 2.16 presents the GSD for Goiânia clayey sand illustrating the differences in particle-sizes. Notice that the particle analysis without dispersant indicates very low amount of clay particles (< 0.002 mm) whereas the test using the dispersant display about 35%.

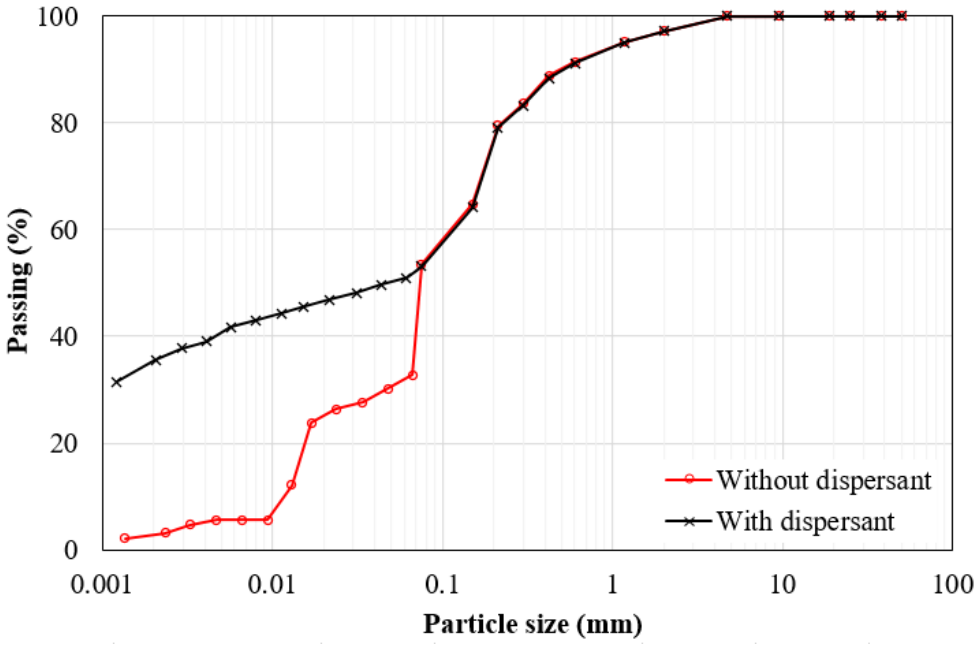

Figure 2.16 GSD for Goiânia clayey sand with and without dispersant agent (Machado, 2020)

The degree of aggregation, also known as relative aggregation (RA), refers to amount of clay aggregates in relation to the soil particles. Otálvaro et al. (2015) proposed a method to obtain the RA based on the difference between the GSD and the dispersed curve, as illustrated in Fig. 2.17:

$$RA = \frac{G_{ND} - G_D}{G_D} \times 100\% \quad (2.29)$$

where: G_{ND} is the accumulation retained non-dispersed GSD; and G_D is the accumulated retained dispersed GSD.

Similarly, the RA can also be defined using the accumulated passing curves, as illustrated in Fig. 2.18:

$$RA = \frac{G_D - G_{ND}}{G_D} \times 100\% \quad (2.30)$$

Plotting the non-cumulative retained GSD shows the particle size frequency (Fig. 2.19). The region where the non-dispersed curve is above the dispersed one corresponds to the clay aggregates. A third possibility is to calculate the RA comparing this region to the area under the dispersed curve (G_D). The RA is calculated also using Eq. 2.29.

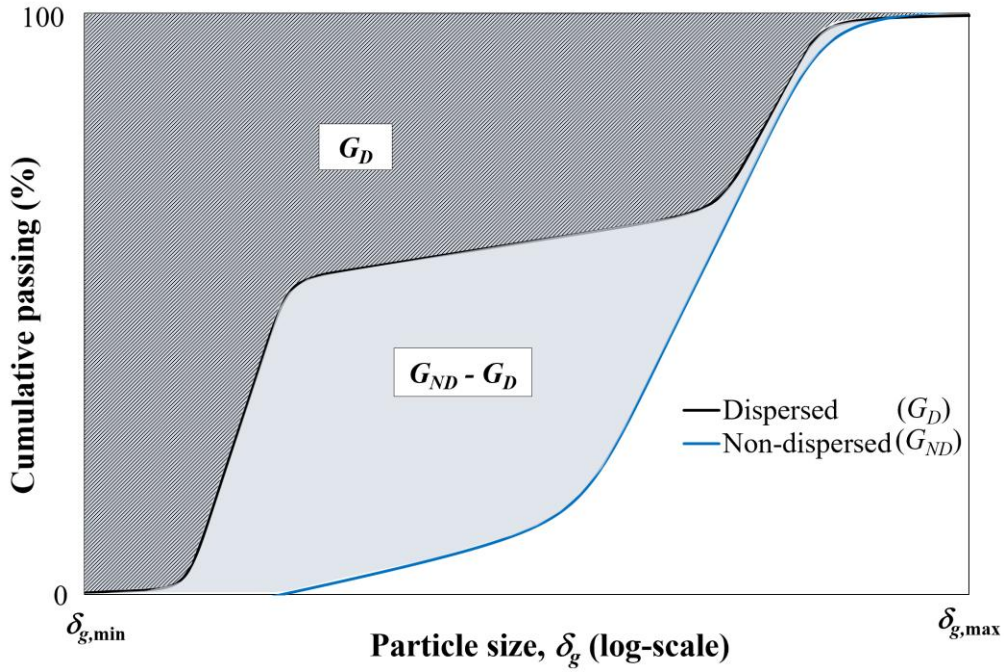

Figure 2.17 Definition of relative aggregation proposed by Otálvaro et al. (2015)

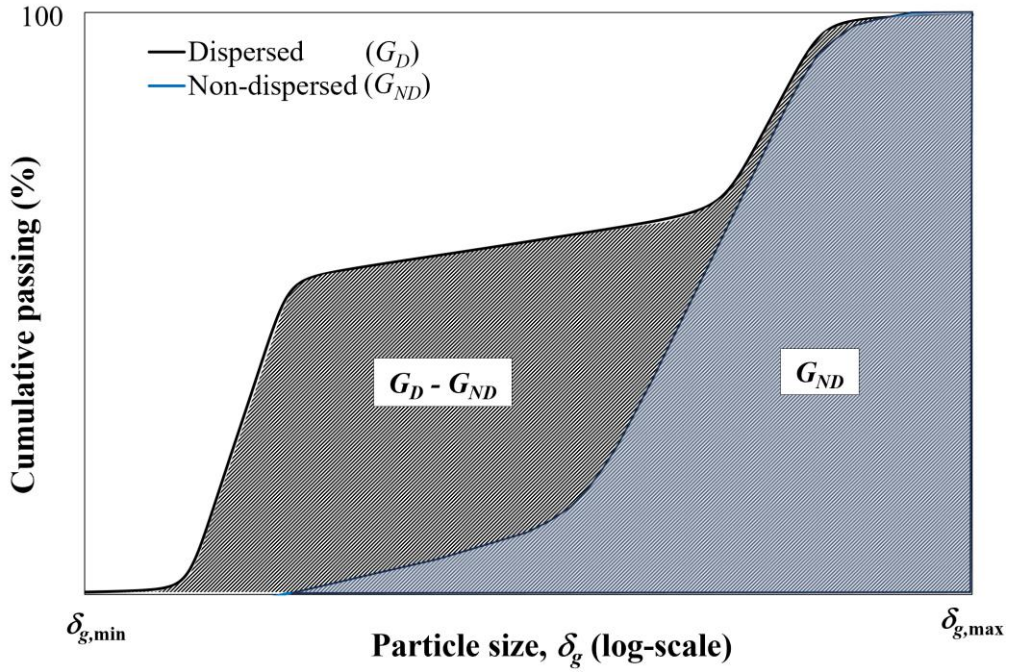

Figure 2.18 Definition of relative aggregation using the cumulative passing curves

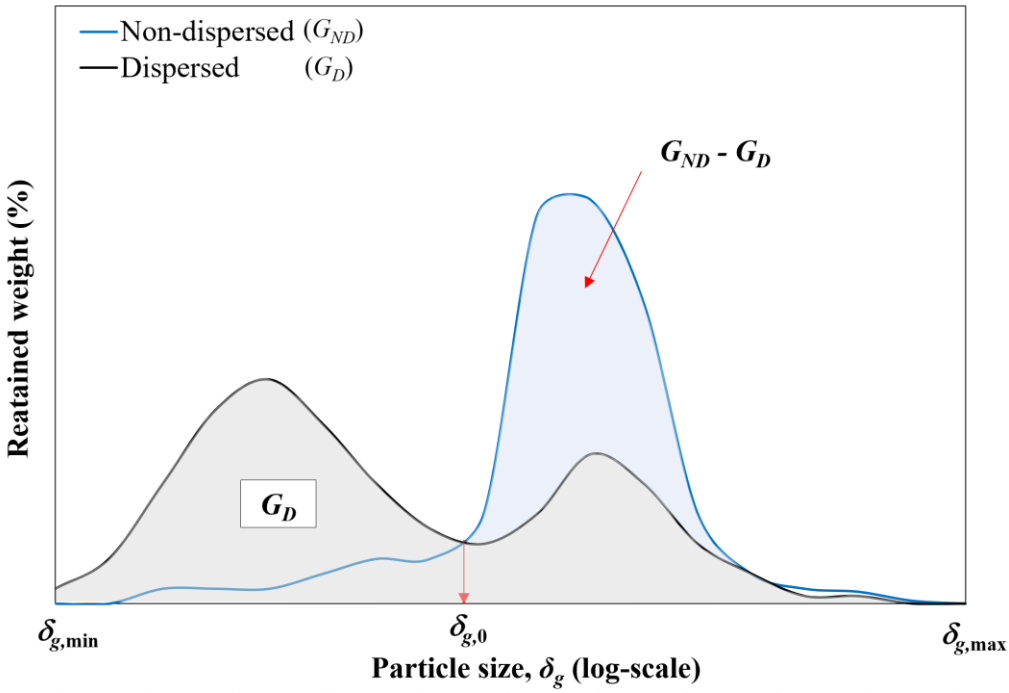

Figure 2.19 Definition of relative aggregation using the non-cumulative curves

The last method to obtain *RA* is by comparison the percentage of clay particles (i.e., < 0.002 mm) expressed by:

$$RA = 1 - \frac{\%Clay_{ND}}{\%Clay_{D}} \quad (2.31)$$

where: $\%Clay_{ND}$ is the percentage of clay particles in the non-dispersed GSD; and $\%Clay_{D}$ is the percentage of clay particles in the dispersed GSD.

2.4.3.4 Compaction influence

The fabric of a compacted soil is influenced by the method, the energy of compaction, and the initial water content. For a given energy, the initial water content determines whether the fabric is flocculated (i.e., dry of optimum) or dispersed (i.e., wet of optimum). For soils with unimodal SWCCs, this means that a soil compacted at the dry of optimum usually presents a bimodal fabric with larger pores than the same material compacted at the wet of optimum that exhibits a unimodal fabric. Fig. 2.20 depicts the pore-size distribution curves of the Jossigny silt compacted at optimum, wet and dry sides of the compaction curve. The same pattern was presented by a lean clay from Nanjing in China (Cheng et al., 2020). It is worth mentioning that despite the bimodal PSD curves of these soils, their two dominant pore-sizes are not far enough apart in order to their SWCC exhibit a bimodal shape.

For bimodal tropical soils, the influence of the initial water content is different for the micro and macrostructure. The microstructure seems to be very little sensitive to this factor while the macrostructure does not display a unique pattern (Fig. 2.21). Specimens compacted at dry of optimum can present macropores larger than those from specimens prepared at wet of optimum (Otálvaro et al., 2016; Lopes et al., 2022) and vice-versa (Santos and Esquivel, 2018).

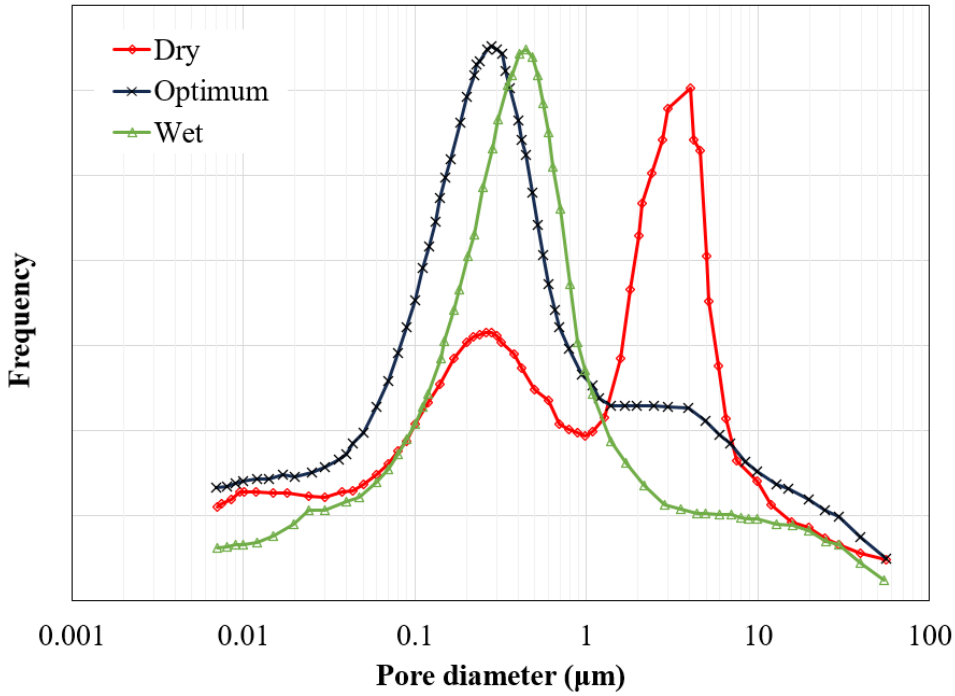

Figure 2.20 Pore-size distribution curves of Jossigny silt (Delage, 1996)

Another relevant aspect in the determination of the soil fabric is the compaction energy. Increasing the energy results in a reduction of the amount and the dominant size of the macropores. The microstructure is also unresponsive to changes in compaction energy (Otálvaro et al., 2015; Araújo, 2019), as shown in Fig. 2.22.

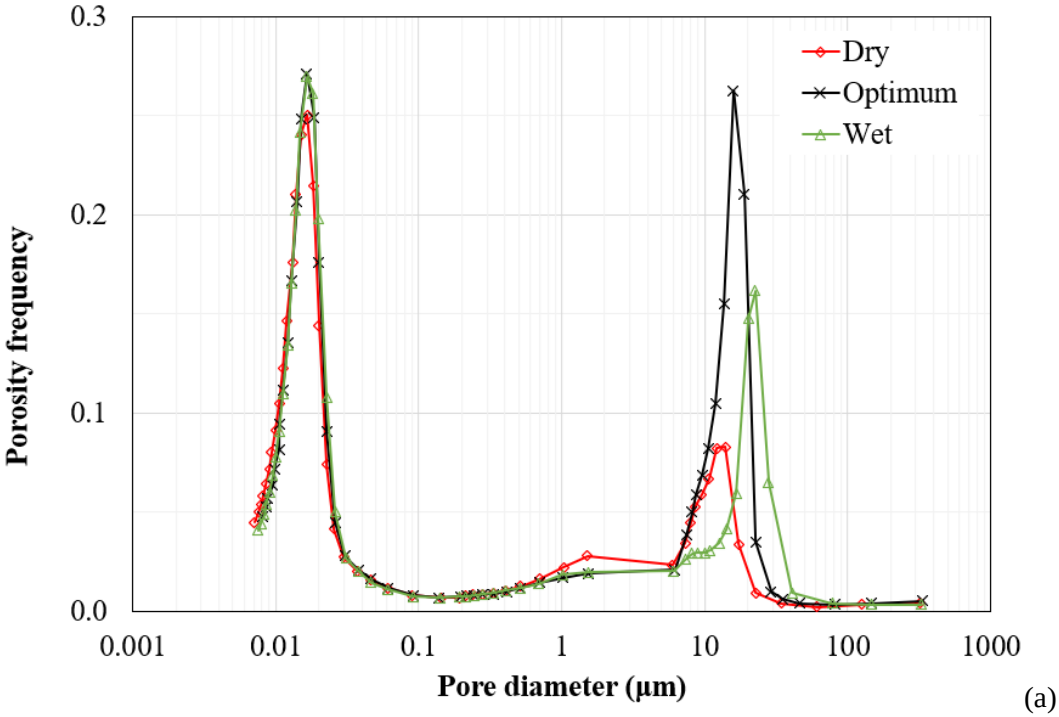

(a)

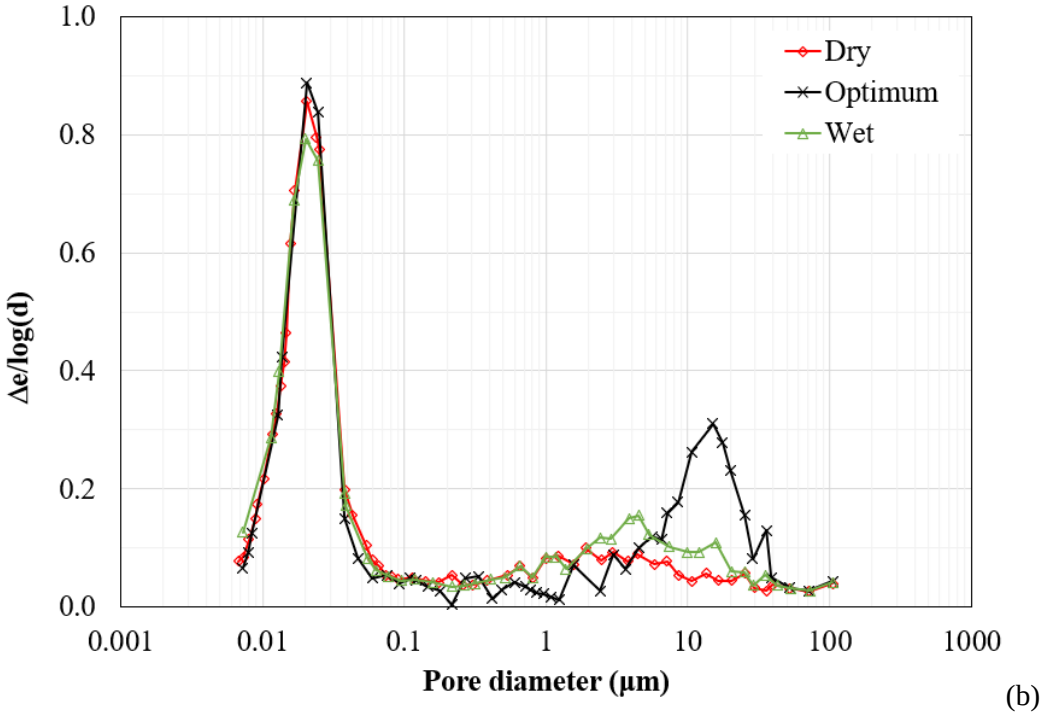

(b)

Figure 2.21 Influence of the initial water content: data from (a) Santos and Esquivel, 2018; and (b) Otálvaro et al. 2016

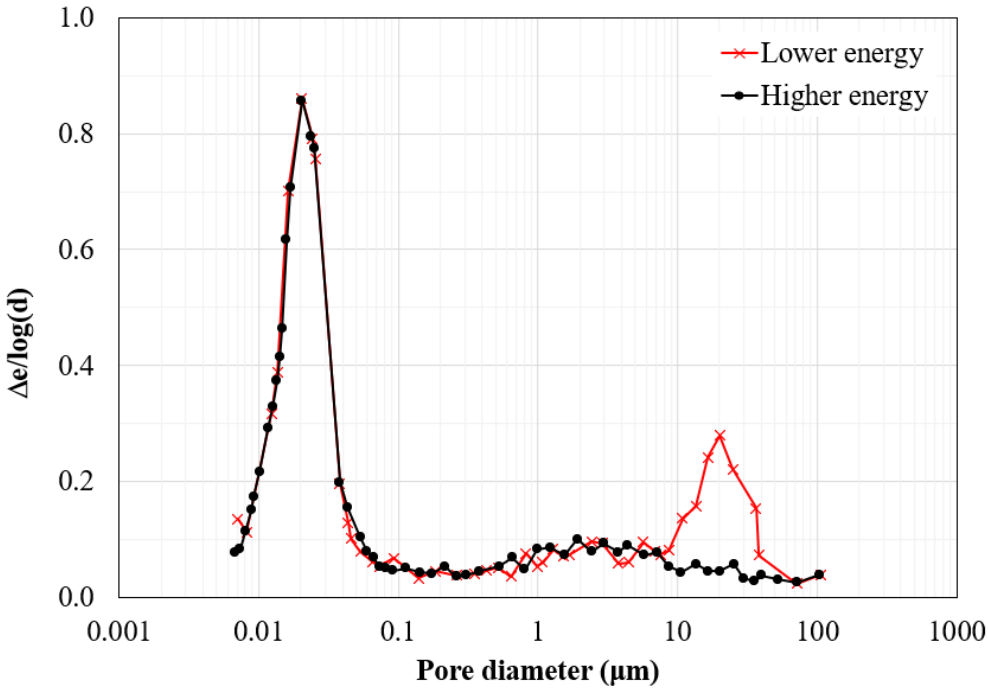

(a)

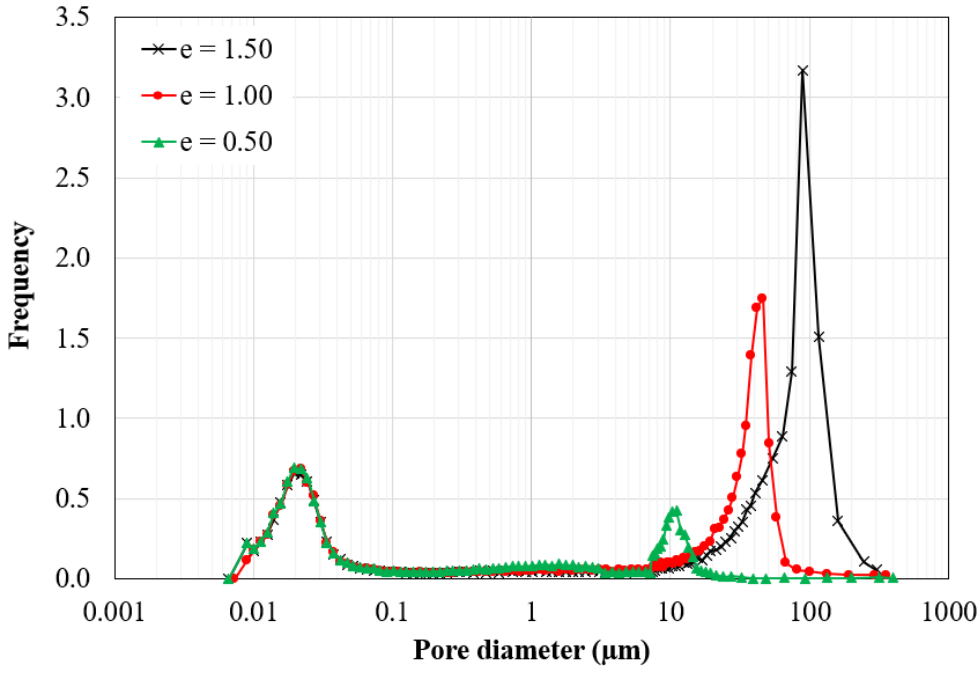

(b)

Figure 2.22 Influence of the compaction energy: data from (a) Otálvaro et al., 2016; and (b) Araújo (2019)

2.4.3.5 Disturbance and effective stress

The level of disturbance and effective stresses have similar effects on the macrostructure as those from the compaction energy. These two factors act closing the macropores. The microstructure seems to be affected according to degree of laterization of the soil, as indicated by Oliveira et al. (2019) and illustrated in Fig. 2.23a. After a given degree of laterization, data from Georgetti 2014, Mascarenha et al. (2016), Borges et al. (2019) reveal that the micropores become immune to the disturbance effects, as shown in Fig. 2.23b and 2.23c.

High effective stresses can interfere in the microstructure. The magnitude of these stresses depends on several factors related to soil origin and formation process. For example, MIP data from Lopes (2016) indicates that the microstructure of the Brasília soil begins to change for effective stresses higher than 2,000 kPa, which corresponds to a stress superior to most usual geotechnical structures (Fig. 2.24). Moreover, data from Feuerharmel (2007) indicate that the aggregates can be partially destroyed if the soil is subjected to high suctions corresponding the hygroscopic moisture.

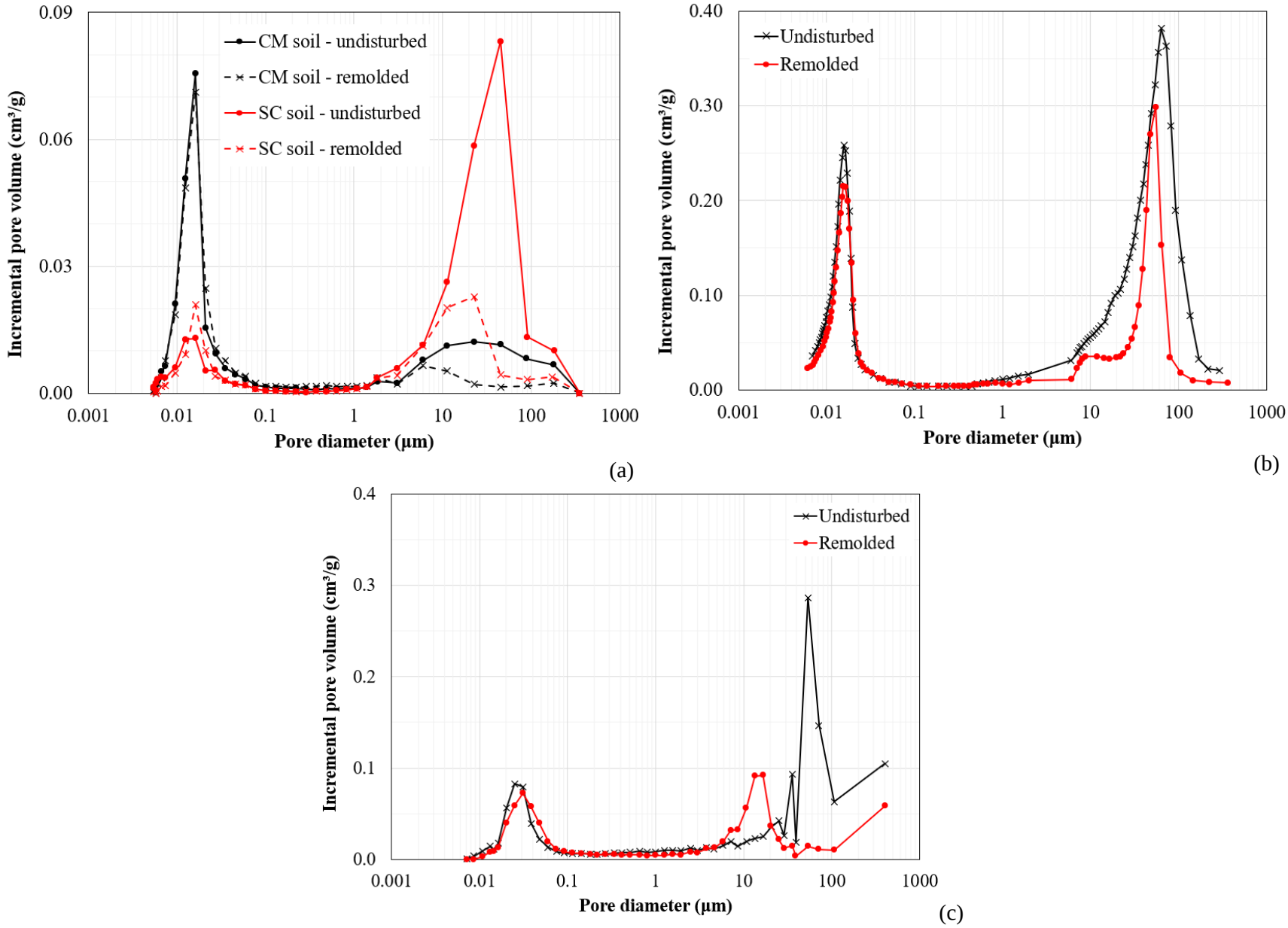

Figure 2.23 Influence of disturbance: data from (a) Oliveira et al. (2022); (b) Georgetti (2014); and (c) Borges et al. (2019)

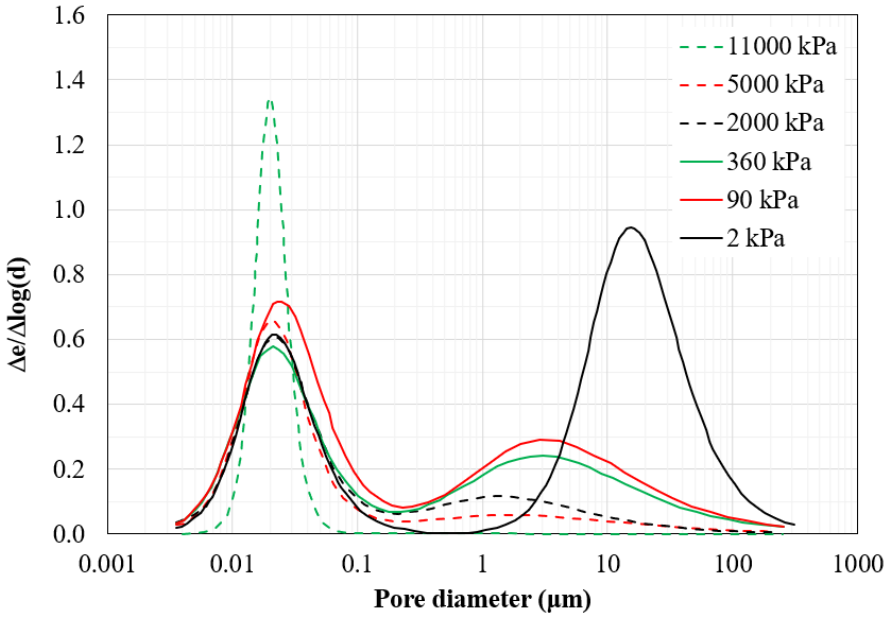

Figure 2.24 Influence of different levels of effective stress for the Brasília soil (Lopes, 2016)

References

Aitchison, G. D., 1964. Engineering concepts of moisture equilibria and moisture changes in soils. *In:* Moisture Equilibria and Moisture Changes in Soils Beneath Covered Areas, Butterworths, Sydney, 7–21.

Alves, R. D., Gitirana Jr. G. F. N., Vanapalli, S. K., 2020. Advances in the modeling of the soil–water characteristic curve using pore-scale analysis. Computers and Geotechnics. 127, 103766. https://doi.org/10.1016/j.compgeo.2020.103766

Antinoro, C., Bagarello, V., Ferro, V., Giordano, G., Iovino, M., 2014. A simplified approach to estimate water retention for Sicilian soils by the Arya–Paris model. Geoderma, 213, 226-234. http://dx.doi.org/10.1016/j.geoderma.2013.08.004

Araújo, A.G., 2019. Uso de microtomografia e porosimetria para análise de estrutura bimodal de um latossolo vermelho reconstituído. Doctoral Thesis: Departament de Civil and Environmental Engineering, Universidade Federal de Goiás, 82p.

Arya, L. M., Paris, J. F., 1981. A physicoempirical model to predict the soil moisture characteristic from particle-size distribution and bulk density data. Soil Science Society of America Journal, 45, 1023-1030. https://doi.org/10.2136/sssaj1981.03615995004500060004x

Arya, L. M., Dierolf, T. S., 1989. Predicting soil moisture characteristic from particle-size distribution: an improved method to calculate pore radii from particle radii. In: The

International Workshop on Indirect Method of Estimating Hydraulic Properties of Unsaturated Soils, Riverside, CA.

Arya, L. M., Leij, F. J., van Genuchten, M. T., Shouse, P. J., 1999. Scaling parameter to predict the soil water characteristic from particle-size distribution data. Soil Science Society of America Journal, 63, 510-519. https://doi.org/10.2136/sssaj1999.03615995006300030013x

Aubertin, M., Mbonimpa, M., Bussière, B., Chapuis, R. P., 2003. A model to predict the water retention curve from basic geotechnical properties. Canadian Geotechnical Journal. 40, 1104-1122. https://doi.org/10.1139/t03-054

Bakhshi, A., Alamdari, P., Heidari, A., Mohammadi, M., H., 2023. Estimating soil–water characteristic curve (SWCC) using machine learning and soil micro-porosity analysis. Earth Science Informatics, 16, 3839–3860. https://doi.org/10.1007/s12145-023-01131-3

Benatti, J. C. B., Miguel, M. G., 2013. A proposal of structural models for colluvial and lateritic soil profile from southwestern Brazil on the basis of their collapsible behavior. Engineering Geology. 153, 1-11. https://doi.org/10.1016/j.enggeo.2012.11.003

Benoit, B., M., 1983. The fractal geometry of nature. Henry Holt and Company, 468p.

Borges, C. R., Lopes, B. C. F., Cordão Neto, M. P., 2019. Pore size distribution of Brasilia tropical soil in 3 different initial states. In: 7th International Symposium on Deformation Characteristics of Geomaterials, Glasglow. 92, 01009. https://doi.org/10.1051/e3sconf/20199201009

Camapum de Carvalho, J., Gitirana Jr., G. F. N., Machado, S. L., Mascarenha, M. M. A., Silva Filho, F. C., Rodrigues, R. A. 2023. Solos não saturados no contexto geotécnico. Associação Brasileira de Mecânica dos Solos e Engenharia Geotécnica, São Paulo, 2nd ed.

Campos-Guereta, I., Dawson, A., Thom, N., 2021. An alternative continuous form of Arya and Paris model to predict the soil water retention curve of a soil. Advance in Water Resources. 154, 15p. Doi: https://doi.org/10.1016/j.advwatres.2021.103968

Cao, J., Jung, J., Song, X., Bate, B., 2017. On the soil water characteristic curves of poorly graded granular materials in aqueous polymer solutions. Acta Geotechnica, 13, 103-116. https://doi.org/10.1007/s11440-017-0568-7

Chan, T. P., Govindaraju, R., S., 2003. A new model for soil hydraulic properties based on a stochastic conceptualization of porous media. Water Resources Research, 39(7). https://doi.org/10.1029/2002WR001954

Chen, R., -P., Liu, P., Liu, X., -M., Wang, P., -F., Kang, X., 2019. Pore-scale model for estimating the bimodal soil–water characteristic curve and hydraulic conductivity of compacted soils with different initial densities. Engineering Geology, 260, 105199.

https://doi.org/10.1016/j.enggeo.2019.105199

Cheng, Q., Tang, C-S., Zeng, H., Zhu, C., An, N., Shi, B., 2020. Effects of microstructure on desiccation cracking of a compacted soil. Engineering Geology, 265, 105418. https://doi.org/10.1016/j.enggeo.2019.105418

Delage, P., Audiguier, M., Cui, Y. J., Howat, M. D., 1996. Microstructure of a compacted silt. Canadian Geotechnical Journal. 33(1), 150-158. https://doi.org/10.1139/t96-030

Dolinar, B., 2014. Prediction of the soil-water characteristic curve based on the specific surface area of fine-grained soils. Bulletin of Engineering Geology and the Environment. 74, 697-703. https://doi.org/10.1007/s10064-014-0664-y

Edlefsen, N. E., Anderson, A. B. C., 1943. Thermodynamics of soil moisture. Hilgardia, 15(2), 31-298. https://doi.org/10.3733/hilg.v15n02p031

Embrapa, 2014. Mapa Digital de Solos - Carbono Orgânico. https://www.embrapa.br/busca-de-noticias/-/noticia/2062813/solo-brasileiro-agora-tem-mapeamento-digital

Feuerharmel, C., Pereira, A., Gehing, W. Y. Y., Bica, A. V. D., 2006. Determination of the shear strength parameters of two unsaturated colluvium soils using the direct shear test. In: Fourth International Conference on Unsaturated Soils, Arizona. 1181–1190. https://doi.org/10.1061/40802(189)96

Fredlund, D., G., Morgenstern, N., R., Widger, R., A., 1978. The shear strength of unsaturated soils. Canadian Geotechnical Journal, 15(3), 313-321. https://doi.org/10.1139/t78-029

Fredlund, D. G., Morgenstern, N. R., 1977. Stress state variables for unsaturated soils. Journal of the Geotechnical Engineering Division, 103(5), 447-446. https://doi.org/10.1061/AJGEB6.000042

Fredlund, D. G., Xing, A., 1994. Equations for the soil-water characteristic curve. Canadian Geotechnical Journal. 31, 521-532. https://doi.org/10.1139/t94-061

Fredlund, M. D., Wilson, G. W., Fredlund, D. G., 2002. Use of the grain-size distribution for estimation of the soil-water characteristic curve. Canadian Geotechnical Journal, 39, 1103-1117. https://doi.org/10.1139/t02-049

Fredlund, D. G., Rahardjo, H., Fredlund, M. D., 2012. Unsaturated soil mechanics in engineering practice. New Jersey: John Wiley & Sons.

Gan, J., K., M., Fredlund, D., G., Rahardjo, H., 1988. Determination of the shear strength parameters of an unsaturated soil using the direct shear test. Canadian Geotechnical Journal, 25, 500-510. https://doi.org/10.1139/t88-055

Georgetti, G. B., 2014. Deformabilidade e resistência de um solo laterítico não saturado. Doctoral Thesis: Graduate program in geotechnics, Universidade de São Paulo, 130p.

Góis, F., M., B., M., Farias, M., M., Morfa, C., A., R., Costa Neto, J., A., 2023. Flow

modelling through a packing of real particles. *In:* 10th European Conference on Numerical Methods in Geotechnical Engineering, London. https://doi.org/10.53243/NUMGE2023-366

Gras, J.-P., Delenne, J.-Y., Soulié, F., Youssoufi, M. S. El., 2011. DEM and experimental analysis of the water retention curve in polydisperse granular media. Powder Technology. 208, 296-300. https://doi.org/10.1016/j.powtec.2010.08.019

Grau, E., D., A., 2014. Efeito da variação de umidade no calculo do empuxo em solos tropicais. Master Thesis: Department of Civil and Environmental Engineering, Universidade de Brasília, Distrito Federal, 105p.

Guo, L., Chen, G., Li, C., Xia, M., Gong, S., Zheng, L., 2021. A bound water model for numerical simulation of SWCC in the wide suction range based on DDA. Computers and Geotechnics, 139, 104378. https://doi.org/10.1016/j.compgeo.2021.104378

Gupta, S., C., Larson, W., E., 1979. Estimating Soil Water Retention Characteristics from Particle Size Distribution, Organic Matter Percent, and Bulk Density. Water Resources Research, 15(6), 1633-1635. https://doi.org/10.1029/WR015i006p01633

Haverkamp, R., Parlange, J. -Y., 1986. Predicting the water-retention curve from particle-size distribution. Soil science, 142(6), 325-339.

Hillel, D., 2004. Introduction to environmental soil physics. Elsevier Science, 494p.

Hoyos, L., R., Velosa, C., R., Puppala, A., J., 2014. Residual shear strength of unsaturated soils via suction-controlled ring shear testing. Engineering Geology, 172, 1-11. http://dx.doi.org/10.1016/j.enggeo.2014.01.001

Huang, G., Zhang, R., 2005. Evaluation of soil water retention curve with the pore–solid fractal model. Geoderma, 127, 52-61. https://doi.org/10.1016/j.geoderma.2004.11.016

Infante Sedano, J., A., Vanapalli, S., K., Garga, V., K., 2007. Modified Ring Shear Apparatus for Unsaturated Soils Testing. Geotechnical Testing Journal, 30(1).

Jin, T., Cai, X., Chen, Y., Jiang, S., Wei, W., 2019. A fractal-based model for soil water characteristic curve over entire range of water content. Capillarity, 2(4), 66-75. https://doi.org/10.26804/capi.2019.04.02

Khlosi, M., Cornelis, W., M., Gabriels, D., Sin, G., 2006. Simple modification to describe the soil water retention curve between saturation and oven dryness. Water Resources Research, 42, W11501. https://doi.org/10.1029/2005WR004699

Khorshidi, M., Lu, N., Khorshidi, A., 2016. Intrinsic relationship between matric potential and cation hydration. Vadose Zone Journal, 15(11), 1–12. https://doi.org/10.2136/vzj2016.01.0001

Lamorski, K., Simunek, J., Sławinsk, C., Lamorska, J., 2017. An estimation of the main wetting branch of the soil water retention curve based on its main drying branch using the machine learning method. Water Resources Research, 53, 1539-1552.

https://doi.org/10.1002/2016WR019533

Li, Y., Vanapalli, S., K., 2021. A novel modeling method for the bimodal soil-water characteristic curve. Computers and Geotechnics, 138, 104318. https://doi.org/10.1016/j.compgeo.2021.104318

Li, Y., Vanapalli, S. K., 2022. A novel modeling method for the bimodal soil-water characteristic curve. Computers and Geotechnics. 138, 104318. https://doi.org/10.1016/j.compgeo.2021.104318

Likos, W. J., Jaafar, R., 2013. Pore-scale model for water retention and fluid partitioning of partially saturated granular soil. Journal of Geotechnical and Geoenvironmental Engineering. 139(5), 724-737. https://doi.org/10.1061/(ASCE)GT.1943-5606.0000811

Lopes, B., C., F., L., 2016. Microstructural-based approach to the interpretation of clays and transitional soils behaviour. Doctoral Thesis: Department of Civil and Environmental Engineering, Universidade de Brasília, Distrito Federal, 133p.

Lopes, B., C., F., L., Kühn, V., O., Queiroz, A., C., G., Caicedo, B., Cordão Neto, M. P., 2022. Structure evaluation of a tropical residual soil under wide range of compaction conditions. Géotechnique Letters, 12(2), 106-113. https://doi.org/10.1680/jgele.21.00101

Mascarenha, M. M. A., Cordão Neto, M. P., Silva, M. T. M. G., 2016. Alternative method for analyzing hydromechanical behaviour of unsaturated soils. Soils and Rocks. 39(1), 29-39.

Machado, R. R., 2020. Ensaios pressiométricos para estimativa de parâmetros de resistência e deformabilidade de um perfil de solo tropical. Master Thesis: Departament de Civil and Environmental Engineering, Universidade Federal de Goiás, 203p.

Minasny, B., McBratney, A., B., 2002. The Neuro-m Method for Fitting Neural Network Parametric Pedotransfer Functions. Soil Science Society of America Journal, 66, 352-361. https://doi.org/10.2136/sssaj2002.3520

Mitchell, J. K., Soga, K., 2005. Fundamentals of Soil Behavior. New Jersey: Wiley.

Morrow, C., A., Moore, D., E., Lockner, D., A., 2017. Frictional strength of wet and dry montmorillonite. Journal of Geophysical Research: Solid Earth, 122(5), 3392–3409. https://doi.org/10.1002/2016JB013658

Mufti, S., Das, A., 2022. An advanced pore-scale model for simulating water retention characteristics in granular soils. Journal of Hydrology. 615, 128561. https://doi.org/10.1016/j.jhydrol.2022.128561

Nishimura, T., Fredlund, D., G., 2000. Relationship between shear strength and matric suction in an unsaturated silty soil. Unsaturated soils for Asya. Taylor and Fracis

Group: Rotterdam.

Otálvaro, I. F., Cordão Neto, M. P., Caicedo, B., 2015. Compressibility and microstructure of compacted laterites. Transportation Geotechnics. 5, 20-34. https://doi.org/10.1016/j.trgeo.2015.09.005

Oliveira, A. D., Pelaquim, F. G. P., Zanin, R. F. B., Melo, T. R., Filho, J. T., Andrello, A. C., Teixeira, R. S., 2022. The structure of tropical lateritic soils as an impacting factor in the shape of soil-water characteristic curves. Soils and Rocks. 45(2). https://doi.org/10.28927/SR.2022.070521

Or, D., Tuller, M., 1999. Liquid retention and interfacial area in variably saturated porous media: Upscaling from single-pore to sample-scale model. 35(12), 3591-3605. https://doi.org/10.1029/1999WR900262

Otálvaro, I. F., Cordão-Neto, M. P., Delage, P., Caicedo, B., 2016. Relationship between soil structure and water retention properties in a residual compacted soil. Engineering Geology. 205, 73-80. https://doi.org/10.1016/j.enggeo.2016.02.016

Pachepsky, Y. A., Timlin, D., Varallyay, G., 1996. Artificial Neural Networks to Estimate Soil Water Retention from Easily Measurable Data. Soil Science Society of America Journal, 60(3), 727-733. https://doi.org/10.2136/sssaj1996.03615995006000030007x

Pereira, S., Silva Jr., A., Mendes, T., Gitirana Jr., G., Alves, R. D., 2023. Prediction of Soil–Water Characteristic Curves in Bimodal Tropical Soils Using Artificial Neural Networks. Geotechnical Geology Engineering. https://doi.org/10.1007/s10706-023-02716-x

Phoon, K-K., Santoso, A., Quek, S-T., 2010. Probabilistic Analysis of Soil-Water Characteristic Curves. Journal of Geotechnical and Geoenvironmental Engineering, 136(3), 445-455. https://doi.org/10.1061/(ASCE)GT.1943-5606.0000222

Prakash, A., Hazra, B., Sreedeep, S., 2021. Probabilistic analysis of soil-water characteristic curve using limited data. Applied Mathematical Modelling, 89, 752-770.

Revil, A., Lu, N., 2013. Unified water isotherms for clayey porous materials. Water Resources Research. 49, 5685–5699. https://doi.org/10.1002/wrcr.20426

Rieu, M., Sposito, G., 1991. Relation pression capillaire-teneur en eau dans les milieux poreux fragmentés et identification du caractère fractal de la structure des sols. Académie des Scinces de Paris, 312, 1483-1489.

Romero, E. Simms, P. H., 2008. Microstructure investigation in unsaturated soils: a review with special attention to contribution of mercury intrusion porosimetry and environmental scanning electron microscopy. Geotechnical and Geology Engineering. 26, 707-727. https://doi.org/10.1007/s10706-008-9204-5

Saha, S., Gu, F., Luo, X., Lytton, R., L., 2018. Prediction of Soil-Water Characteristic Curve for Unbound Material Using Fredlund–Xing Equation-Based ANN Approach.

Journal of Materials in Civil Engineering, 30(5). https://doi.org/10.1061/(ASCE)MT.1943-5533.0002241

Santos, R. A., Esquivel, E., R., 2018. Saturated anisotropic hydraulic conductivity of a compacted lateritic soil. Journal of Rock Mechanics and Geotechnical Engineering, 10, 986-991. https://doi.org/10.1016/j.jrmge.2018.04.005

Satyanaga, A., Rahardjo, H., Leong, E. C., Wang, J. Y, 2013. Water characteristic curve of soil with bimodal grain-size distribution. Computers and Geotechnics. 48, 51-61. https://doi.org/10.1016/j.compgeo.2012.09.008

Saxton, K., E., Rawls, W., J., Romberger, J., S., Papendick, R., I., 1986. Estimating Generalized Soil-water Characteristics from Texture. Soil Science Society of America Journal, 50(4), 1031-1036. https://doi.org/10.2136/sssaj1986.03615995005000040039x

Schaap, M., G., Bouten, W., 1996. Modeling water retention curves of sandy soils using neural networks. Water Resources Research, 32(10), 3033-3040. https://doi.org/10.1029/96WR02278

Souza, J. C., 2020. Avaliação da relação entre a curva granulométrica e a curva característica solo-água para um solo residual bimodal sob diferentes graus de desagregação. Master Thesis: Departament de Civil and Environmental Engineering, Universidade Federal de Goiás.

Tao, G., Chen, Y., Xiao, H., Chen, Q., Wan, J., 2019. Determining Soil-Water Characteristic Curves from Mercury Intrusion Porosimeter Test Data Using Fractal Theory. Energies, 12, 752. https://doi.org/10.3390/en12040752

Terzaghi, K., 1936. The shear strength of saturated soils. Proceedings of the First International Conference on Soil Mechanics and Foundation Engineering, Cambridge, MA, Vol. 1, 54–56

Tokunaga, T., K., 2009. Hydraulic properties of adsorbed water films in unsaturated porous media. Water Resource Research, 45(6), W06415. https://doi.org/10.1029/2009WR007734

Totola, L., B., Bicalho, K., V., Hisatugu, W., H., 2023. Artificial neural networks for predicting soil water retention data of various Brazilian soils. Earth Science Informatics, 16, 3579–3595. https://doi.org/10.1007/s12145-023-01115-3

Tuller, M., Or, D., Dudley, L. M., 1999. Adsorption and capillary condensation in porous media: Liquid retention and interfacial configurations in angular pores. Water Resources Research. 35(7), 1949-1964. https://doi.org/10.1029/1999WR900098

Tuller, M., Or, D., 2005. Water films and scaling of soil characteristic curves at low water contents. Water Resources Research. 41(9), W09403. https://doi.org/10.1029/2005WR004142

Tyler, S. W., Wheatcraft, S. W., 1990. Fractal processes in soil water retention. Water Resources Research. 26(5), 1047-1054. https://doi.org/10.1029/WR026i005p01047

Vanapalli, S., K., Wright, A., Fredlund, D., G., 2000. Shear strength behavior of a silty soil over the suction range from 0 to 1,000,000 kPa. In Proc., 53rd Canadian Geotechnical Conf., 1161–1168. Montreal, QC, Canada: Canadian Geotechnical Society.

van Genuchten, M. T., 1980. A closed-form equation for predicting the hydraulic conductivity of unsaturated soils. Soil Science Society of America Journal. 44, 892-898. https://doi.org/10.2136/sssaj1980.03615995004400050002x

Wang, J-P., Hu, N., François, B., Lambert, P., 2017. Estimating water retention curves and strength properties of unsaturated sandy soils from basic soil gradation parameters. Water Resources Research. 53, 6069-6088. https://doi.org/10.1002/2017WR020411

Wang, X., Li, J., 2015. A novel liquid bridge model for estimating swcc and permeability of granular material. Power Technology. 275, 121-130. https://doi.org/10.1016/j.powtec.2015.01.044

Wang, J., -P., Li, X., Yu, H., -S., 2015. A micromechanical interpretation of the capillary effect of unsaturated granular material in a pendular state. In Computer Methods and Recent Advances in Geomechanics: Proceedings of the 14th International Conference of International Association for Computer Methods and Recent Advances in Geomechanics, 1563-1568. Taylor & Francis Books Ltd.

Wang, C., Li, S-y., He, X., Chen, Q., Zhang, H., Liu, X-y., 2021. Improved prediction of water retention characteristic based on soil gradation and clay fraction. Geoderma, 404, 115293. https://doi.org/10.1016/j.geoderma.2021.115293

You, T., Li, S., Guo, Y., Wang, C., Liu, X., Zhao, J., Wang, D., 2022. A superior soil–water characteristic curve for correcting the Arya-Paris model based on particle size distribution. Journal of Hydrology. 613, 128393. https://doi.org/10.1016/j.jhydrol.2022.128393

Yuan, C., Chareyre, B., 2022. Transitioning from the funicular to the pendular regime in granular soils. Géotechnique, 72(9), 825-931. https://doi.org/10.1680/jgeot.20.P.141

Zhang, J., Yang, S., Zhang, L., L., Zhou, M., L., 2022. Bayesian estimation of soil-water characteristic curves. Canadian Geotechnical Journal, 59, 569-582. https://doi.org/10.1139/cgj-2021-0070

Zhao, J., Li., S., Wang, C., You, T., Liu, X., Zhao, Y., 2023. A universal soil–water characteristic curve model based on the particle size distribution and fractal theory. Journal of Hydrology, 622(B), 129691. https://doi.org/10.1016/j.jhydrol.2023.129691

Zhou, W., -H., Yuen, K., -V., Tan, F., 2014. Estimation of soil–water characteristic curve and relative permeability for granular soils with different initial dry densities. Engineering Geology, 179, 1-9. http://dx.doi.org/10.1016/j.enggeo.2014.06.013

CHAPTER 3

Modeling the Bimodal SWCC of Highly Weathered Tropical Soils Using Grain-Size Information[1]

Abstract. The soil-water characteristic curve (SWCC) of highly weathered tropical soils is often bimodal, presenting two main slopes that are strongly related to the macro and micropores. The bimodal SWCC behavior is commonly attributed to fine particle aggregations that affect soil fabric and its pore-size distribution. In this paper, the relationship between basic soil properties (e.g., the Atterberg limits and the grain-size distribution) and the bimodal SWCCs are investigated using a database comprised of 40 different remolded and undisturbed soils. The proposed modeling framework is based on the relationship between the pore-size and the grain-size distributions, using a newly proposed soil property called the β-function. The findings suggest that microporosity has a strong relationship with the liquid limit whereas the total porosity varies mainly as a function of the macrostructure. The grain-size distribution curves under aggregated and disaggregated conditions offer key information on the degree of aggregation and, consequently, on the retention properties of macro and micropores. Several basic soil properties are found to be related to the desaturation zones of the micro and macropores, including the coefficient of uniformity of the fine particle range and the degree of particle aggregation. The developed model offers reasonable estimations for suctions up to approximately 20,000 kPa, with performance exceeding R^2 values of 0.80.

Key words: *pore-size distribution, particle-size distribution, pedotransfer function, water*

[1] The content of this chapter is a journal paper currently under review

retention curve, lateritic soils.

3.1 Introduction

The soil-water characteristic curve (SWCC) is typically defined as the relationship between the water content and soil suction. The SWCC is considered a key property for understanding and modeling of unsaturated soil behavior (Fredlund and Xing, 1994). The SWCC allows the determination of other hydromechanical properties, such as stress-strain relationships, the hydraulic conductivity function, and the volume change properties. Consequently, the SWCC is useful in the design of geotechnical structures that include foundations, retaining walls, slopes, cover systems, and pavements in unsaturated soils.

Multiple physicochemical aspects may influence the main soil-water storage mechanisms, which are mostly related to adsorption and capillarity phenomena (Li et al., 2024). The adsorption is closely related to the mineralogy and chemical factors, such as the cation exchange capacity and the specific surface area (Tuller and Or, 2005; Likos and Jaafar, 2013; Revil and Lu, 2013; Kyokawa, 2021). The capillarity is mainly related to the pore-size distribution (PSD), which depends on physical attributes of the soil, such as the size, shape, and arrangement of the particles (Arya and Paris, 1981; Aubertin et al., 2003; Miller et al., 2008).

Some soils present two distinct pore-size families, resulting in a bimodal SWCC. The bimodal nature of SWCCs of some soils can be associated with gap-graded grain-size distributions (GSD) or with specific soil fabric conditions (Delage and Lefebvre, 1984; Romero and Simms, 2008; Satyanaga et al., 2013). Bimodal SWCCs may also be the result of porous particles, as found in diatomaceous earth (Burger and Shackelford, 2001). It is important to note that different factors leading to bimodal SWCCs require different

modeling approaches.

Highly weathered tropical soils, also identified as lateritic soils, often exhibit bimodal SWCCs. These soils and their properties are typically associated with pedogenesis conditions marked by abundant annual precipitation combined with high temperature, being predominant in several countries, including Brazil (Huat et al., 2013; Camapum de Carvalho et al., 2023). Lateritic soils are found in regions that have predominantly rainy and dry seasons. During the rainy season, downward flux promotes the removal and transportation (i.e., leaching) of the particles of silica closer to the soil surface. During the dry season, the flow of water is reversed by means of capillary and evaporative action. Thus, the iron and aluminum ions found in deeper layers are transported towards shallower layers, where the fixation of these ions takes place. This cyclic process is fundamental for the pedogenic evolution of lateritic soils (Benatti and Miguel, 2013).

The soil layers subjected to intense cyclic wetting and desiccation become enriched with iron and aluminum oxides and hydroxides, especially goethite and gibbsite. The resulting highly weathered material forms layers with variable thickness, often extending to tens of meters (Huat et al., 2013). These lateritic soils are sometimes overlaid by concretionary laterite. These soils usually have a porous structure with clay-sized particles cemented by iron and aluminum oxides and hydroxides, forming silt to fine sand sized aggregations that impart different behavior (Otálvaro et al., 2015; Oliveira et al., 2022). Bimodal lateritic soils exhibit both cohesive and non-cohesive properties attributed to silt and clays particles, and sand-size particles, respectively. For this reason, neither the concepts of classical soil mechanics nor the common engineering classification systems are suitable for the highly weathered tropical soils (Camapum de Carvalho et al., 2023).

The SWCC of highly weathered tropical soils usually is bimodal due to the aggregations of fine particles that produce a unique structure with dual porosity (Otálvaro et al., 2016; Cordão Neto et al., 2018; Araújo, 2019). As a result, the microstructure of these soils consists of intra-aggregate pores and the macrostructure corresponds to inter-aggregate pores, as depicted in Fig. 3.1. These pore families will be referred to in this paper as micropores and macropores, respectively. Important evidence of the presence of particle aggregation is the marked difference between the grin-size distributions of the soil in the aggregated and disaggregated states. These aggregation states are established in practice by running hydrometer analysis of the soil with and without the use of mechanical and chemical dispersing agents. The ideal hydrometer testing conditions for lateritic soils have been established in the past by several studies (Gidigasu, 1976; Souza, 2020; Camapum de Carvalho et al., 2023). Important evidence of the presence of particle aggregation is when a marked difference between the GSD of the dispersed (i.e., disaggregated) and non-dispersed (i.e., aggregated) soil is observed (Camapum de Carvalho et al., 2023; Souza, 2020).

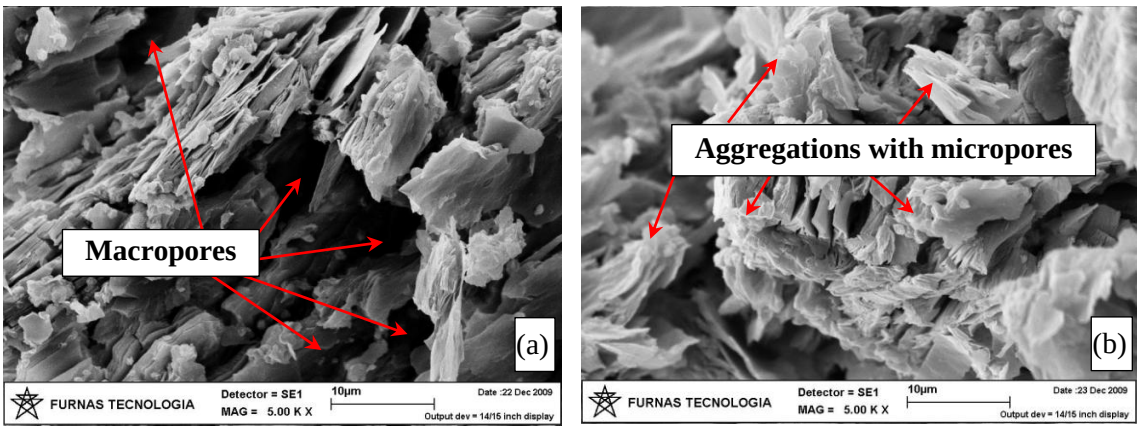

Figure 3.1 Scanning electron microscopy (SEM) pictures of a typical tropical soil: (a) the macropores and (b) the aggregations with micropores

Several previous studies have shed light into the main factors associated with the bimodal SWCCs of soils, including lateritic soils. Some investigators have observed that remolded lateritic soils may exhibit a bimodal structure, depending on the void ratio and the compaction water content (e.g., Casini et al., 2012; Kühn et al. 2022). For instance, lateritic soils compacted dry of optimum moisture content generally exhibit a fabric constituting of relatively large inter-aggregate pores and tend to have a bimodal pore-size distribution, whereas soils compacted wet of optimum tend to display a single dominant pore family (e.g., Juang and Holtz, 1986; Delage et al., 1996; Monroy et al., 2010). Several authors observed that changes in the macropores are more related to the degree of soil compaction (Li and Zhang, 2009; Monroy et al., 2010; Araújo, 2019). It has become common knowledge that highly weathered tropical soils composed of low plasticity clays tend to have micropores that are stable and do not present significant volume change (Georgetti, 2014; Araújo, 2019; Oliveira et al., 2022). Also, the dominant pore-size of the macrostructure becomes larger as the degree of aggregation increases (Miguel and Bonder, 2012).

Several models have been developed to describe and interpret bimodal SWCC behavior of different soils. Appendix A summarizes some key equations that were developed to fit or predict bimodal SWCCs. None of the presented models were specifically developed for lateritic soils. Durner (1994) presented a fitting expression that relies on the van Genuchten (1980) equation, inheriting its capabilities for describing the drainage slope and its limitation in describing the residual conditions. This expression corresponds to the sum of two unimodal SWCCs related to the micro and macrostructure. Using a similar approach, Burger and Shackelford (2001) and Zhang and Chen (2005)

modified the Fredlund and Xing (1994) equation to fit bimodal soils, overcoming the fitting limitations of van Genuchten's equation at high suctions. Gitirana Jr. and Fredlund (2004) developed a fitting equation with independent parameters, based on eight fitting parameters that correspond to the main features of the SWCC. Wijaya and Leong (2016) proposed an equation to fit bimodal SWCCs based on the connection of linear parts. This model requires 14 parameters that are obtained graphically, making the fitting process more difficult than other models.

Additional fitting models were developed for bimodal SWCCs. The van Genuchten (1980) and Fredlund and Xing (1994) models were the base for the bimodal equations proposed by Li and Vanapalli (2022) and Fang et al. (2022). The first study splits the bimodal SWCC into three stages whereas the latter merges both models into a single equation. Gao et al. (2024) relied on an exponential function combined with the Fredlund and Xing (1994) model. A pore-scale model was developed by Liu et al. (2024) with the advantage of considering the evolution of the pore structure caused by external loads. Despite the good performance of the models developed in these studies, their fitting parameters are not clearly related to physical parameters of the SWCC. This drawback is overcome by the equation developed by Zhao et al. (2023) using an exponential function, but such function has limited fitting capabilities near the curve asymptotes.

The main models available to predict bimodal SWCCs are those developed by Satyanaga et al. (2013), Hassan et al. (2022), and Pereira et al. (2023). These models are more complex than fitting equations and attempt to associate the SWCC to basic soil characterization parameters. The model by Satyanaga et al. (2013) assumes that the shape of the SWCC follows a lognormal distribution function. Regression analyses were applied

to 26 soils to determine the parameters of the SWCC as a function of the GSD curve, the saturated gravimetric water content, and the dry density. The bimodal behavior of the soils considered in these studies was attributed to the discontinuity of the GSD only and particle aggregation was not observed. The second model (Hassan et al., 2022) is based on a modification to the Arya and Paris (1981) model, with the α parameter calibrated to 90 soils samples. Unfortunately, the models by Satyanaga et al. (2013) and Hassan et al. (2022) were not intended to introduce information related to the soil microstructure and particle aggregation, making them inadequate for tropical soils typical with a double structure. Pereira et al. (2023) presented a prediction model specifically designed for bimodal tropical soils using artificial neural networks (ANNs). The authors pointed out the need to consider particle aggregation information and obtained relatively good predictions using their approach.

Several studies cited herein have contributed to the understanding of the behavior of bimodal soils, but only one of them presented a model to predict the SWCC of highly weathered tropical soils. It is also interesting to note that most studies that attempt to establish relationships between the pore structure of bimodal soils and their water retention properties focus on PSD information directly determined, using mercury intrusion porosimetry (Georgetti, 2014; Otálvaro et al., 2016; Mascarenha et al., 2016; Araújo, 2019; Kühn et al., 2021; Oliveira et al., 2022). Only a few studies rely on more practical information, such as the GSD (Satyanaga et al., 2013; Hassan et al., 2022; Pereira et al., 2023). Unfortunately, the models relying on the GSD were developed only for soils which exhibit double structure that arises from gap-graded GSDs and do not consider particle aggregation, which is a key feature of lateritic soils.

In this context, the objectives of this paper are: (i) to provide interpretations of the SWCCs of bimodal lateritic soils; (ii) to propose a new and simple approach for converting particle sizes into pore sizes, considering particle aggregation; and (iii) to present a model to predict the SWCC of bimodal lateritic soils using pore-size information inferred from the GSD curves and soil index properties.

Predictive models based on simple soil data offer preliminary information that allows viability studies and the establishment of geological and geotechnical investigation priorities in a time frame more compatible with typical project deadlines. In this sense, the approach adopted herein, based on the use of readily available simple soil data, aims to contribute to the implementation of unsaturated soil mechanics into engineering geology and geotechnical and engineering practice.

3.2 Modeling approach fundamentals

The structure of a soil can be partially characterized by its PSD, which depends primarily on particles and their arrangement. The PSD is also influenced by other factors; including stress history, wetting-drying cycles, mineralogy, and weathering processes. Several studies tried to calculate the size of pores of soils using the GSD (Arya and Paris, 1981; Fredlund et al., 2002; Likos and Lu, 2004; Likos and Jaafar, 2013; Alves et al., 2020; Zhai et al., 2023), fractal models (Tyler and Wheatcraft, 1990; Cihan et al., 2007), and discrete element methods (Wang and Li, 2015; Mufti and Das, 2022).

The present study relies mainly on the GSD to determine the PSD, along with the capillary model to quantify suction. Pore-size and its volume are inferred using the basic volume-mass relationships and the interpretation of GSDs for the aggregated and disaggregated conditions. The relationship between grain size and pore size will be defined

based on an empirical function that describes the soil fabric.

3.2.1 Estimating pore-volume from the grain-size distribution

The relationship between pore volumes and the GSD can be established based on relatively simple volume-mass equations, as described by Arya and Paris (1981). In general terms, the GSD can be represented by the functions $g(\delta_g)$ and $G(\delta_g)$, where $g(\delta_g)$ is the GSD function, $G(\delta_g)$ is the corresponding cumulative function, and δ_g is the particle diameter:

$$\int_0^{+\infty} g(\delta_g)d\delta_g = 1 \tag{3.1}$$

$$G(\delta_g) = \int_0^{\delta_g} g(\delta_g)d\delta_g \tag{3.2}$$

The typical shapes of the functions $g(\delta_g)$ and $G(\delta_g)$ for soils displaying unimodal and bimodal GSD curves are illustrated in Fig. 3.2a and 3.2b, respectively. The partition of pore-volumes is based on the area below $g(\delta_g)$ and can be quantified by the division of the GSD into finite (i.e., discrete) fractions. The void ratio (e) and the density of the solids (ρ_s) are often considered as constants. Such assumption is based on the observation that most bimodal lateritic soils usually exhibit negligible volume change resulting from suction changes during unloaded SWCC testing. The low volume change is due to the predominant presence of non-expansive minerals, such as kaolinite and gibbsite (Kühn et al., 2021; Benatti and Miguel, 2013). The modeling of volume change under confined conditions would require a more general database and is not within the scope of the present study. For a unitary total mass of particles (m_s) is unitary, the volume of voids (V_v) of a unimodal soil can be obtained by the integration or summation of Eq. 3.2 from the smallest ($\delta_{g,min}$) up to the largest particles ($\delta_{g,max}$):

$$V_v = \frac{e}{\rho_s}\int_{\delta_{g,\min}}^{\delta_{g,\max}} g(\delta_g)d\delta_g = \frac{e}{\rho_s}\Delta\delta_g \sum_{i=1}^{n} g(\delta_{g,i}) \tag{3.3}$$

where: n is the total number of fractions used in the discretization of the GSD.

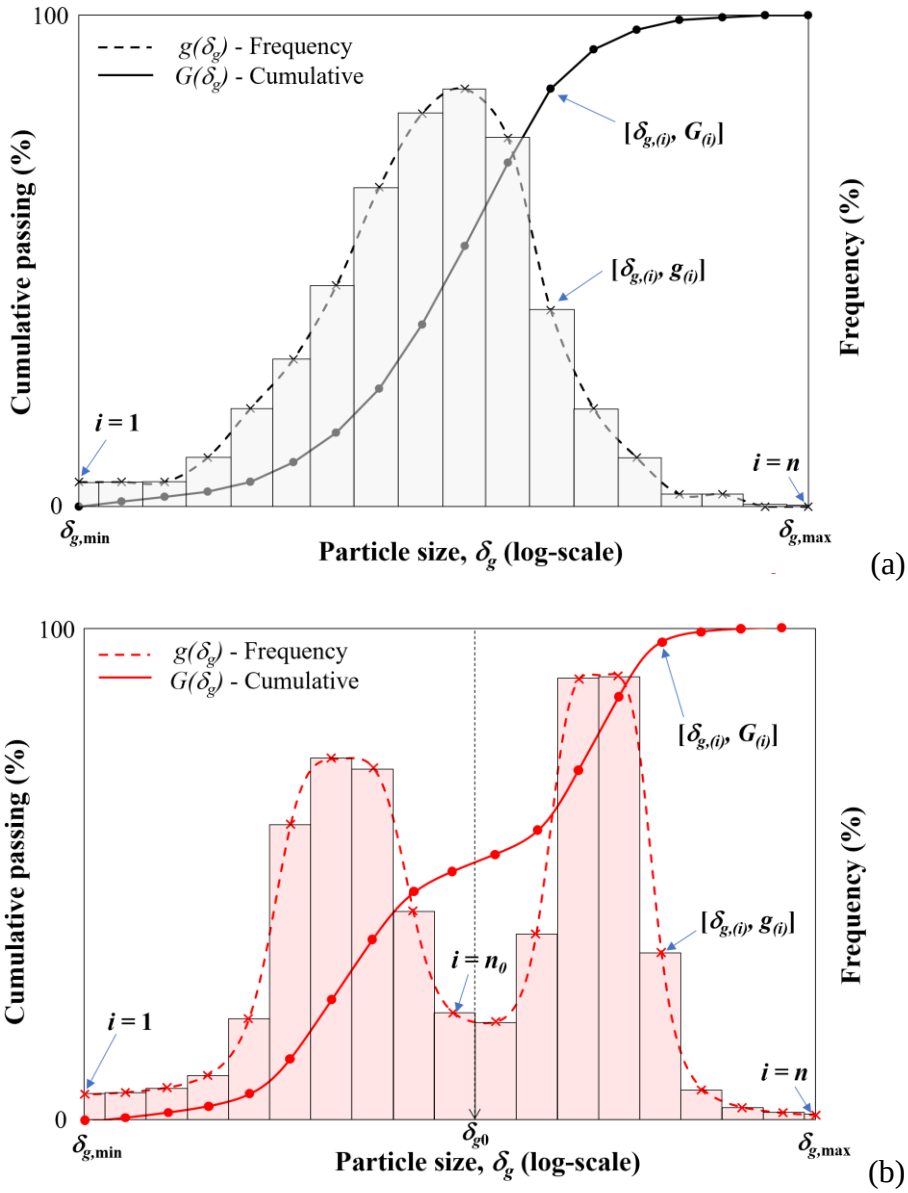

Figure 3.2 Grain-size distribution frequency g(δ_g) and cumulative G(δ_g) functions with (a) unimodal and (b) bimodal shapes

For a bimodal soil, Eq. 3.3 can be modified to account for the void ratios of the macro (e_M) and microstructure (e_m), assuming that the level of particle packing may be significantly different between inter and intra-aggregate pores:

$$V_v = \frac{e_m}{\rho_s}\int_{\delta_{g,\min}}^{\delta_{g0}} g(\delta_g)d\delta_g + \frac{e_M}{\rho_s}\int_{\delta_{g0}}^{\delta_{g,\max}} g(\delta_g)d\delta_g = \Delta\delta_g\left[\frac{e_m}{\rho_s}\sum_{i=1}^{n_0} g(\delta_{g,i}) + \frac{e_M}{\rho_s}\sum_{i=n_0+1}^{n} g(\delta_{g,i})\right] \quad (3.4)$$

where: $e_M = V_{vM}/V_s$; $e_m = V_{vm}/V_s$; V_{vM} and V_{vm} are the volumes of voids corresponding to the macro and micropores, respectively; V_s is the volume of solids; δ_{g0} is the grain size with the lowest frequency between the zones of the two dominant particle sizes; and n is its respective number of integration fractions.

3.2.2 Grain and pore-size frequency curves considering particle aggregation

The dual structure of lateritic soils is integrated within the aggregated and disaggregated GSD curves. These two GSD conditions are used as means to quantify the effect of particle aggregations in the formation of a bimodal pore structure. The aggregated and disaggregated GSD curves may be obtained by performing tests with and without chemical and mechanical dispersion methods. The adequacy of experimental methodologies in successfully dispersing and preserving aggregations should obviously be a concern and appropriate procedures must be adopted (Souza, 2020).

The association between the aggregated and disaggregated GSDs and the macro and microstructure, respectively, constitutes a fundamental hypothesis of the present study. This hypothesis was established based on: a) the evidence presented by numerous authors and summarized by Gidigasu (1976) that finer particles of highly weathered tropical soils are mostly in an aggregated state and can only be measured if disaggregation is attained; and b) the known range of suctions in the macro and micropore water retention zones of

the studied soils and the corresponding pore-sizes, calculated according to the capillary equation. These pore-size ranges offer significant evidence of the corresponding particle-size ranges that would form such pores.

The macrostructure refers to the pores formed between aggregations, with pore sizes proportional to the aggregation sizes. The microstructure refers mostly to pores located within the aggregations, with sizes proportional to the individual fine particles that form these aggregations. Therefore, it is assumed herein that the macrostructure is more closely related to the aggregated GSD whereas the microstructure can be associated with the disaggregated GSD curve.

As illustrated in Fig. 3.3a, a threshold (δ_{g0}) defining the range of particle sizes of the aggregated curve used to infer the macropores is defined by drawing two tangent lines at the first and second slopes of the aggregated GSD. The aggregated curve is re-scaled to the threshold point (P_{tA}) using Eq. 3.5 while the disaggregated GSD is rescaled from its corresponding threshold point (P_{tD}), as shown in Eq. 3.6:

$$\bar{P}_{(i)} = \bar{P}_{(i-1)} - \frac{P_{(i-1)} - P_{(i)}}{1 - P_{tA}} \tag{3.5}$$

$$\bar{P}_{(i)} = \frac{P_{(i)}}{P_{tD}} \tag{3.6}$$

where: $\bar{P}_{(i)}$ is the normalized percentage of i^{th} fraction; $\bar{P}_{(0)}$ is the normalized percentage passing of the largest particle-size = 100%; $P_{(i)}$ is the percentage of i^{th} fraction; $P_{(0)}$ is the percentage of fraction largest particle size = 100%; P_{tA} is the percentage of the threshold point at the aggregated GSD curve; P_{tD} is the percentage of the threshold point at the disaggregated GSD curve.

The combination of both GSD curves using the proposed normalization procedure

results in a bimodal grain-size frequency highlighted with red and black dashed lines in Fig. 3.3b. The relation between an infinitesimal variation in the volume of voids (dV_v) of the combined normalized GSD and a variation in the mass of particles (dg) for the macro and microstructure is given by:

$$dV_{vM} = \frac{e_M}{\rho_s}\frac{dg}{d\delta_g} \tag{3.7}$$

$$dV_{vm} = \frac{e_m}{\rho_s}\frac{dg}{d\delta_g} \tag{3.8}$$

where: subscript M and m stands for the macro- and microstructure, respectively.

In the discrete form, Eqs. 3.7 and 3.8 become:

$$V_{vM,i} = \frac{e_M}{\rho_s} g(\delta_{g,i}) \tag{3.9}$$

$$V_{vm,i} = \frac{e_m}{\rho_s} g(\delta_{g,i}) \tag{3.10}$$

where: $V_{vM,i}$ is the volume of voids of the macrostructure of the i^{th} fraction; g_i is the percentage of solids for the i^{th} fraction; and $V_{vM,i}$ is the volume of voids of the macrostructure of the i^{th} fraction.

For any given matric suction, it is assumed that pores with a corresponding air-entry value (AEV) lower than this matric suction are completely empty whereas the remainder pores are fully saturated. This dual state (i.e., filled or empty) neglects the influence of the bottleneck effect, the wetting and receding contact angles, and the existence of pendular bridges. As a result, the volumetric water content for a specific particle size or fraction (θ_i) can be calculated by multiplying the respective cumulative volume of voids with the soil dry density, starting from the smallest particle size/fraction and considering a unitary mass

of solids.

$$\theta_i = \rho_d \int_{\delta_{g,\min}}^{\delta_{g,i}} V_{vi}(\delta_g) d\delta_g = \rho_d \sum_{i=1}^{i} V_{vi} \tag{3.11}$$

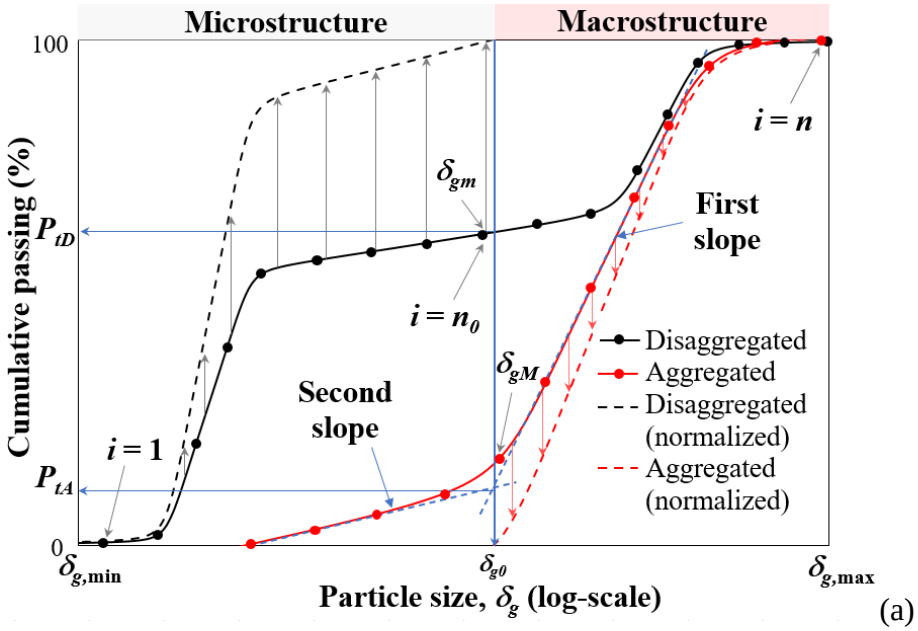

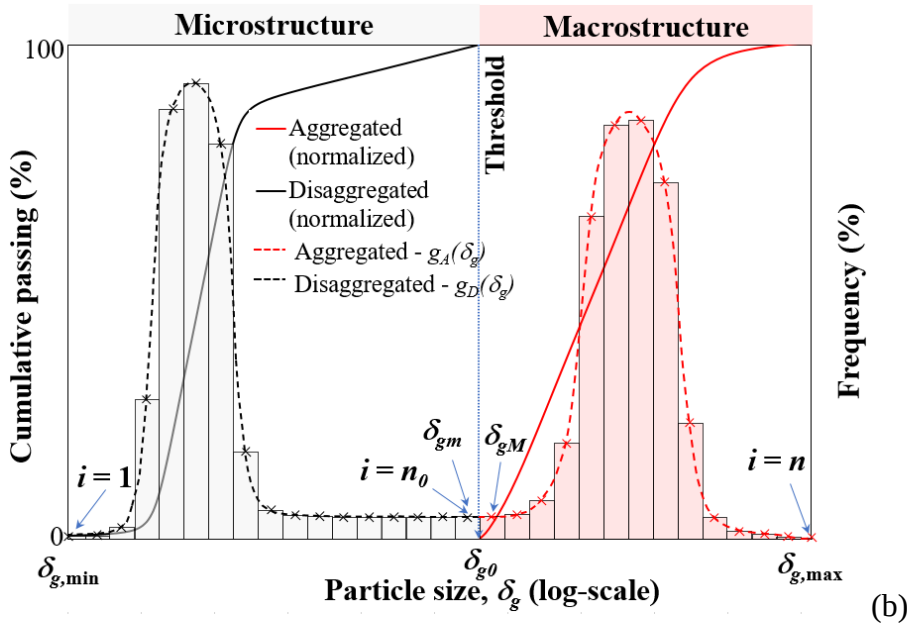

Figure 3.3 (a) Normalization procedure of the aggregated and disaggregated GSD curves; and (b) Normalized GSD curves with their respective grain-size frequency function g(δ_g)

The volumetric water contents corresponding to the micro (θ_m) or macroporosity (θ_M) of the soil may be calculated using Eq. 3.11. The first requires the establishment of $\delta_{g,i}$ equal to δ_{g0} and for the later, $\delta_{g,i}$ equal to $\delta_{g,\max}$ and $\delta_{g,\min}$ equal to δ_{g0}. The total porosity is the sum of these volumetric water contents (i.e., $\theta_m + \theta_M = n$).

3.2.3 Relationship between grain-size and pore-size

Considering the similarity between the shapes of the GSD and of the PSD curves, a fundamental soil property called β-function is introduced herein. The β-function corresponds to the ratio between particle diameter (δ_g) and pore diameter (δ_p), as follows:

$$\beta(\delta_g) = \delta_g / \delta_p \tag{3.12}$$

The β-function is presented here as a way of characterizing how the GSD influences the pore structure. In other words, β is a function that converts the GSD into a PSD. The β-function quantifies the interactions between different particle sizes and the resulting particle packing.

Figure 3.4 presents the typical general shape of the β-function for bimodal tropical soils. The β values are generally higher than 1, indicating that pores are smaller than the corresponding particle. However, the values of β depend on the nature of particle packing, which differs significantly for coarse and fine particles.

It is possible to infer typical β values based on the general particle size range and on the SWCC. For instance, coarse-grained soils with particle sizes larger than 0.074 mm are known to drain along suction ranges between 1 and 40 kPa, approximately (Alves et al., 2020; Yang and Vanapalli, 2024), resulting in β values ranging from 1 to 10. Fine-grained soils with particle sizes smaller than 0.074 mm are known to drain along suction ranges between 100 and 10,000 kPa, approximately (Gitirana Jr. and Fredlund, 2016; Yang and

Vanapalli, 2024), resulting in β values greater than 1000.

Poorly graded sands are expected to have smaller β values, when compared to well-graded sands, due to the tendency to have a lower particle packing condition. In the case of bimodal soils, particle aggregation plays an additional role because fines are merged into aggregations. The β values of micropores are usually greater than those from the macropores, as will be shown later.

The shape of the β-function shown in Fig. 3.4 suggests that it follows two power functions, one for particle sizes corresponding to the macropores and another corresponding the micropores. This behavior can be represented by the following equation:

$$\beta = \exp\left[\ln \beta_M + \frac{\ln \beta_m - \ln \beta_M}{1+\left(\delta_g / \delta_{g0}\right)^{n_c}} \right] \tag{3.13}$$

where: $\beta_M = \beta_{M0}\left(\delta_g / \delta_{g0}\right)^{\alpha_M}$; $\beta_m = \beta_{m0}\left(\delta_g / \delta_{g0}\right)^{\alpha_m}$; $\delta_{g0} = \exp\left\{\left[\ln(\delta_{gm}) + \ln(\delta_{gM})\right]/2\right\}$; β_{M0} and β_{m0} are the values corresponding to δ_{g0} of the macro and micropores, respectively; α_M is the slope of the macropores line; α_m is the slope of the micropores line; δ_{gm} is the largest particle-diameter of the micropores at the normalized disaggregated GSD; and δ_{gM} is the smallest particle-diameter of the macropores at the normalized aggregated GSD; and n_c is a parameter defining the curvature of the transition between the macro and micropores zones.

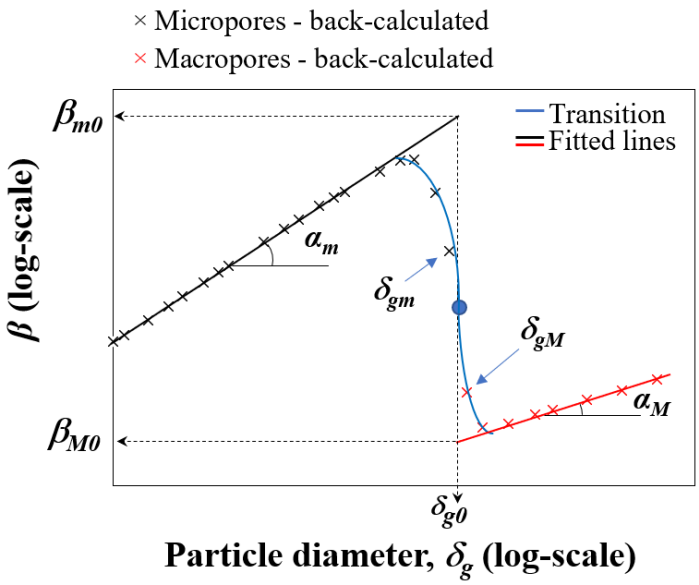

Figure 3.4 Typical β curve showing the micro-, macropore and transition zones

A value of α equal to 0 indicates that β is constant and, therefore, the soil structure remains similar along the entire particle and pore-size range. In the case of α greater than 0, the particle packing gets looser for smaller grain and pore-sizes. If the value of α is negative, the behavior is the opposite. The value of α may be related to the coefficient of uniformity, as discussed in the next sections.

3.2.4 Relationship between pore-size and pore air-entry value

The soil-water phase consists of a combination of capillary and adsorbed water (Tuller et al., 1999). Capillary water is related to the PSD. Adsorbed water refers to the water that is predominantly found at the surface of clay particles due to intermolecular forces, making it dependent on the type and amount of the clay minerals that are present in the soil (Israelachvili, 2011). The adsorbed water is strongly related to the specific surface area (Tuller and Or, 2005; Revil and Lu, 2013). Modeling of the contribution of the adsorbed water to the SWCC using specific surface area is theoretically possible. However, this information is not routinely gathered from conventional geotechnical laboratory tests.

Thus, the adsorption mechanism is only indirectly incorporated into the proposed framework, as will be discussed later.

For simplicity purpose, it is assumed herein that any particle diameter (δ_g) along the GSD curve would correspond to a pore diameter (δ_p) and an equivalent air-entry value. The air-entry value can be determined using the capillary bundle model (Arya and Paris, 1981; Arya and Dierolf, 1989; Arya et al., 1999; Fredlund et al., 2002; Alves et al., 2020; Hassan et al., 2022):

$$\left(u_a - u_w\right) = \frac{4T_s}{\delta_p} \tag{3.14}$$

where: $(u_a - u_w)$ is the matric suction; and T_s is the surface tension of water (7.2×10^{-5} kN/m).

The values of β can be back-calculated using Eqs. 3.11, 3.12 and 3.14, along with the measured SWCC. Thus, each value of β can be related to a single particle diameter. Once values of β are available along the entire particle-size range, the parameters of the β-function (Eq. 3.13) can be obtained by nonlinear regression.

3.3 Database of tropical bimodal soils

Table 3.1 presents a summary of the tropical bimodal soils database assembled using data previously published in the literature. The database has a total of 40 datasets, with several soils tested under undisturbed and remolded conditions. This database comprises soils with different geological origins including metamorphic (materials ID #1, #6, #18 to #23, and #27), sedimentary (#3, #16, #17, #24 to #26), and igneous (#2, #4, #5, #7 to #15) rocks. These soils can be identified as colluvium and residual soils from basalt (#2, #15, and #27), sandstone (#3, #16, and #17), and quartzite (#6). The locations where these soils were collected are the Midwest, Southwest, and South regions of Brazil. Most of the

materials are from the Serra Geral formation, and the Araxá and Paranoá groups.

The Serra Geral formation (135 Ma) is represented in its basal portion by extensive and thick lava packages of a basic tholeiitic nature. These basalts have an aphanitic texture, a massive structure and a black to greenish color. On top of these basaltic volcanic flows, or interspersed with them, there are acidic flows that make up the top portion of this formation. Among the acid volcanic rocks, dacites, rhyolites and rhyodacites predominate, with a grayish and reddish color (Feuerharmel, 2007).

The Araxá group is from the Neoproterozoic age (790 Ma), and primarily consists of diverse schists with subordinate layers of micaceous quartzite that exhibit shades ranging from pink to red or occasionally brown (Souza, 2020). The Paranoá group (Meso/Neoproterozoic) is comprised of purple slates with strong cleavage of ardosian. In some places, small irregular lenses of quartzite are found. Veins of milky quartz filling fractures are common (Maia et al., 2006).

These soils have varied physical, chemical, and mineralogical properties, with major oxides like SiO_2, Al_2O_3, and Fe_2O_3 comprising most of their composition in proportions that depend on the degree of laterization. Key minerals include kaolinite, quartz, goethite, hematite, and others, with characteristics influenced by geological, topographical, and atmospheric factors (Kumar et al., 2022).

The approach proposed in this study is based on the interpretation of simple soil information that can be gathered from routine geotechnical laboratory tests. For this reason, the database comprises not only information on the SWCC, but also the GSD curves (Figs. 3.5 and 3.6) and index properties.

Table 3.1 Main characteristics of the remolded specimens

Material ID	Soil ID*	Reference	USCS (disaggregated / aggregated)	Clay minerals	ρ_s (g/cm³)	w_L	w_P	Test type	ρ_d (g/cm³)	n	n_m	n_M	ψ_{b1} (kPa)	ψ_{res1} (kPa)	ψ_{b2} (kPa)	ψ_{res2} (kPa)	θ_{sat}	θ_{res1}	θ_{b2}	θ_{res2}
#1	1R1	Araújo (2019)	CL / CL	Kaolinite and hematite	2.69	0.33	0.22	Pressure plate, WP4	1.79	0.333	0.204	0.131	49.2	406.3	7000	30000	0.34	0.21	0.20	0.02
	1R2								1.35	0.500	0.193	0.342	1.7	12.3	10360	22154	0.54	0.23	0.16	0.02
	1R3								1.08	0.600	0.174	0.411	1.7	8.6	10360	22154	0.59	0.22	0.12	0.02
#2	2R1	Feuerharmel et al. (2006)	MH / MH	Kaolinite	2.86	0.74	0.57	Suction plate, filter paper	1.08	0.624	0.572	0.052	90.0	126.5	1000	80000	0.62	0.57	0.57	0.07
	2R2								1.08	0.623	0.526	0.097	14.0	28.0	1400	80000	0.62	0.54	0.51	0.09
	2U								1.07	0.625	0.489	0.136	2.2	7.2	2559	50006	0.63	0.51	0.47	0.05
#3	3R1	Feuerharmel et al. (2006)	CH / SC	Kaolinite and gibbsite	2.80	0.56	0.34		1.40	0.500	0.407	0.092	9.0	15.1	6500	50000	0.50	0.43	0.38	0.06
	3R2								1.35	0.519	0.383	0.136	4.5	8.2	2768	50000	0.52	0.39	0.38	0.04
	3U								1.40	0.500	0.380	0.120	3.0	5.9	2800	45000	0.50	0.41	0.36	0.01
#4	4R	Furman (2019)	SC / SC	Biotite	2.58	0.30	-	Filter paper	1.31	0.492	0.170	0.322	5.2	155.0	6999	23000	0.49	0.18	0.16	0.02
	4U								1.32	0.487	0.169	0.318	10.0	66.0	3428	18044	0.49	0.17	0.17	0.02
#5	5U	Furman (2019)	ML / SM	Biotite	2.65	0.29	0.23		1.25	0.528	0.260	0.268	9.1	100.3	5461	25054	0.53	0.26	0.26	0.05
#6	6R1	Otálvaro et al. (2016)	ML / SC	Kaolinite and gibbsite	2.76	0.40	0.28	Suction plate, filter paper	1.42	0.451	0.302	0.126	3.2	9.6	10000	25000	0.43	0.34	0.27	0.05
	6R2								1.50	0.448	0.324	0.123	3.4	12.0	10340	30077	0.45	0.36	0.28	0.05
	6R3								1.33	0.479	0.284	0.157	5.4	10.3	11053	35237	0.41	0.32	0.25	0.04
#7	7U	Guimarães (2002)	CL / SC	Gibbsite and kaolinite	2.74	0.38	0.28	Filter paper	1.05	0.615	0.246	0.369	2.7	5.6	4100	15000	0.62	0.28	0.20	0.04
#8	8U	Guimarães (2002)	CL / SC	Gibbsite, kaolinite, and hematite	2.73	0.36	0.26		1.06	0.611	0.219	0.392	3.0	7.0	7000	12000	0.61	0.28	0.16	0.02
#9	9U	Guimarães (2002)	CL / SC	Gibbsite and hematite	2.66	0.39	0.29		1.17	0.559	0.252	0.307	3.7	7.5	5000	16000	0.56	0.27	0.22	0.02
#10	10U	Guimarães (2002)	CL / SM	Gibbsite and hematite	2.65	0.41	0.29		1.17	0.559	0.260	0.299	1.9	10.9	7200	12500	0.56	0.30	0.22	0.03
#11	11U	Guimarães (2002)	CL / CL	Gibbsite and kaolinite	2.75	0.45	0.34		1.22	0.556	0.274	0.282	1.8	14.6	8000	10550	0.56	0.30	0.24	0.05
#12	12U	Guimarães (2002)	CL / CL	Gibbsite and kaolinite	2.63	0.44	0.33		1.22	0.535	0.282	0.253	3.2	8.0	7200	10550	0.53	0.35	0.22	0.05
#13	13U	Guimarães (2002)	CL / CL	Kaolinite and hematite	2.70	0.46	0.35		1.31	0.517	0.315	0.202	3.0	7.0	7000	12000	0.52	0.37	0.26	0.04

Material ID	Soil ID*	Reference	USCS (disaggregated / aggregated)	Clay minerals	ρ_s (g/cm³)	w_L	w_P	Test type	ρ_d (g/cm³)	n	n_m	n_M	ψ_{b1} (kPa)	ψ_{res1} (kPa)	ψ_{b2} (kPa)	ψ_{res2} (kPa)	θ_{sat}	θ_{res1}	θ_{b2}	θ_{res2}
#14	14U	Guimarães (2002)	CL / CL	Kaolinite and hematite	2.68	0.43	0.34		1.42	0.471	0.309	0.162	5.0	12.0	1500	5000	0.47	0.36	0.30	0.03
#15	15R	Oliveira et al. (2022)	MH / MH	Kaolinite and gibbsite	3.03	0.51	0.38	Pressure plate, filter paper	1.43	0.524	0.386	0.154	12.0	200.0	11000	20000	0.54	0.41	0.37	0.05
	15U								1.12	0.630	0.343	0.287	3.0	65.0	12000	20000	0.63	0.35	0.33	0.03
#16	16R	Oliveira et al. (2022)	SC / SC	Kaolinite	2.89	0.20	0.13		1.96	0.333	0.184	0.156	6.0	13.0	10000	21000	0.34	0.21	0.15	0.01
	16U								1.45	0.500	0.110	0.380	1.5	24.0	18000	28000	0.49	0.13	0.09	0.00
#17	17R	Oliveira et al. (2022)	SC / SC	Kaolinite	2.69	0.31	0.15		1.86	0.286	0.194	0.116	15.0	140.0	1000	6000	0.31	0.20	0.19	0.02
	17U								1.58	0.412	0.062	0.338	0.6	30.0	2000	5000	0.40	0.06	0.06	0.00
#18	18U	Machado (2020)	*	Gibbsite	2.74	NA	NA	Pressure plate, WP4	1.23	0.552	0.193	0.359	1.2	15.0	12000	21000	0.55	0.25	0.13	0.02
#19	19U	Machado (2020)	*	Gibbsite	2.73	NA	NA		1.25	0.541	0.195	0.346	1.1	15.0	9000	18000	0.54	0.24	0.15	0.02
#20	20U	Machado (2020)	*	Gibbsite	2.72	NA	NA		1.26	0.537	0.228	0.309	0.7	9.0	6000	16000	0.54	0.29	0.17	0.02
#21	21U	Machado (2020)	*	Gibbsite	2.75	NA	NA		1.39	0.495	0.235	0.260	1.5	9.0	5800	15000	0.49	0.30	0.17	0.02
#22	22U	Machado (2020)	*	Gibbsite	2.74	NA	NA		1.30	0.526	0.224	0.302	0.8	9.0	5800	14000	0.53	0.30	0.15	0.02
#23	23U	Machado (2020)	*	Gibbsite	2.79	NA	NA		1.37	0.510	0.240	0.270	0.6	9.0	4800	14000	0.51	0.32	0.16	0.02
#24	24U	Benatti and Miguel (2013)	CL / CL	Kaolinite	2.99	0.48	0.37	Filter paper	0.95	0.682	0.296	0.386	3.5	6.0	9000	13000	0.68	0.36	0.23	0.03
#25	25U	Benatti and Miguel (2013)	MH / MH	Kaolinite	3.08	0.50	0.38		1.13	0.632	0.292	0.340	5.0	9.0	5800	11000	0.63	0.34	0.25	0.02
#26	26U	Benatti and Miguel (2013)	CL / CL	Kaolinite	3.06	0.49	0.35		1.20	0.608	0.313	0.295	5.0	9.2	7000	13000	0.61	0.37	0.26	0.02
#27	27R	Castro et al. (2022)	ML / ML	Gibbsite and kaolinite	2.76	0.45	0.30	Pressure plate, WP4	1.29	0.533	0.293	0.240	1.0	12.3	3788	25036	0.53	0.36	0.24	0.04
	27U								1.25	0.548	0.228	0.320	4.0	584.0	4548	26000	0.55	0.23	0.23	0.04

* -R and -U stands for remolded and undisturbed, respectively. ** Not available for these materials. ψ_{b1} is the air-entry value of the macropores; ψ_{res1} is the residual suction of the macropores; ψ_{b2} is the air-entry value of the micropores; ψ_{res2} is the residual suction of the micropores; θ_{sat} is saturated volumetric water content; θ_{res1} is volumetric water content at the residual suction of the macropores; θ_{b2} is volumetric water content at the air-entry value of the micropores; and θ_{res2} is volumetric water content at the residual suction of the micropores.

Soils tested in the undisturbed condition tend to have their aggregations better preserved, resulting in SWCCs that are significantly different from those obtained from remolded specimens (Georgetti, 2014; Oliveira et al., 2022). This expected difference in water retention behavior will be investigated by considering separating the dataset into two groups, the first containing 15 remolded soils and the second involving 25 undisturbed soils.

3.3.1 Grain-size distribution curves and degree of aggregation

The GSD curves (Fig. 3.5) were determined for both disaggregated and aggregated states. The difference between these curves will be evaluated as a tool to quantify the effect of particle aggregation on the SWCC. It is important to highlight that most of the GSD curves do not present measured particle sizes that are less than 0.001 mm. Thus, most of the soils were fitted considering 0.0001 mm as the smallest particle size, which is an approximation that may affect the analyses of some disaggregated GSD curves.

A modified version of the Gitirana Jr. and Fredlund (2004) equation was used to fit the GSD curves and for the calculation of several parameters describing the GSD. The fitted GSD curves were discretized into ten parts (D_{10}, D_{20}, …, D_{90}). Since some GSD curves present a bimodal shape, two main coefficients of uniformity (C_{u1} and C_{u2}) were defined, along with a transition slope (λ). These variables were defined as follows and are based on the variables shown in Fig. 3.6a. It is worth mentioning that the steps to obtain these variables are independent of the normalization process.

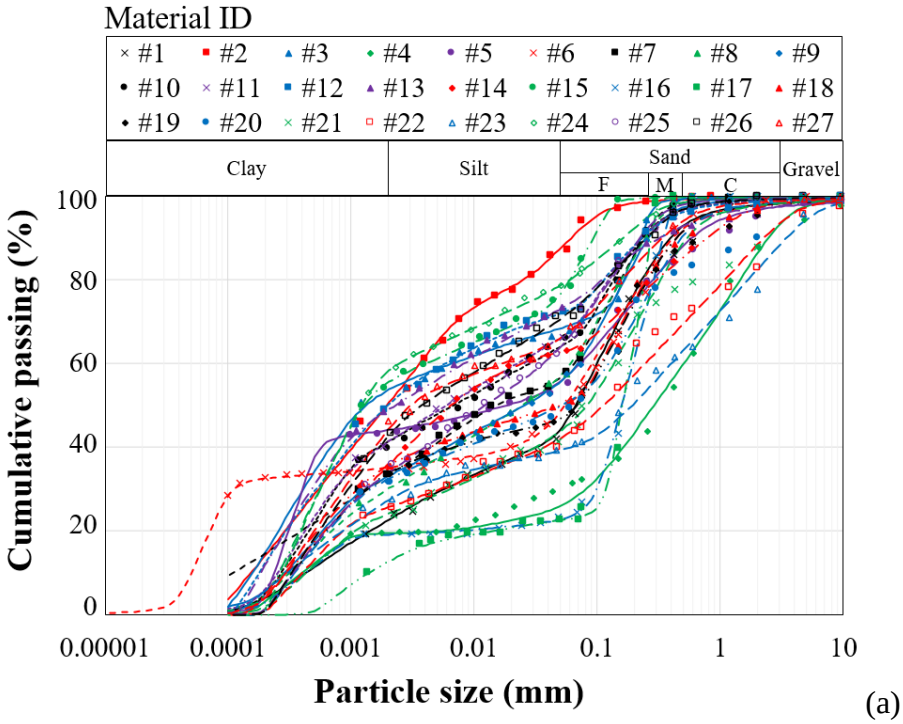

(a)

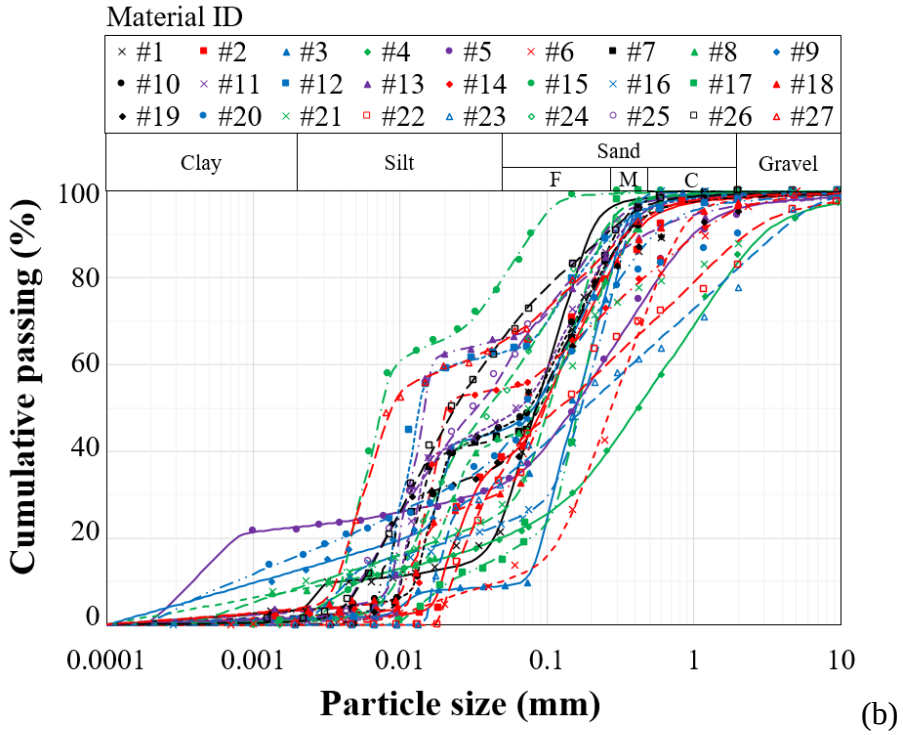

(b)

Figure 3.5 Tropical bimodal soils database: grain-size distributions obtained with (a) deflocculant (i.e., disaggregated); and (b) without deflocculant (i.e., aggregated)

$$C_{u1} = \frac{\delta_{g1}}{\delta_{g2}} \tag{3.15}$$

$$C_{u2} = \frac{\delta_{g3}}{\delta_{g4}} \tag{3.16}$$

$$\lambda = \arctan \frac{G_{g2} - G_{g3}}{\ln\left(\delta_{g2} / \delta_{g3}\right)} \tag{3.17}$$

The relative aggregation was obtained using the approach proposed by Otálvaro et al. (2015), and is defined accordingly using Eq. 3.18 and illustrated in Fig. 3.6b.

$$RA = \frac{\left| \int_{\delta_{g,\min}}^{\delta_{g,\max}} G_A(\delta_g) - G_D(\delta_g) d\delta_g \right|}{\int_{\delta_{g,\min}}^{\delta_{g,\max}} G_D(\delta_g) d\delta_g} \times 100\% \tag{3.18}$$

where: $G_A(\delta_g)$ is the function representing the aggregated GSD curve; and $G_D(\delta_g)$ is the function representing the disaggregated GSD curve.

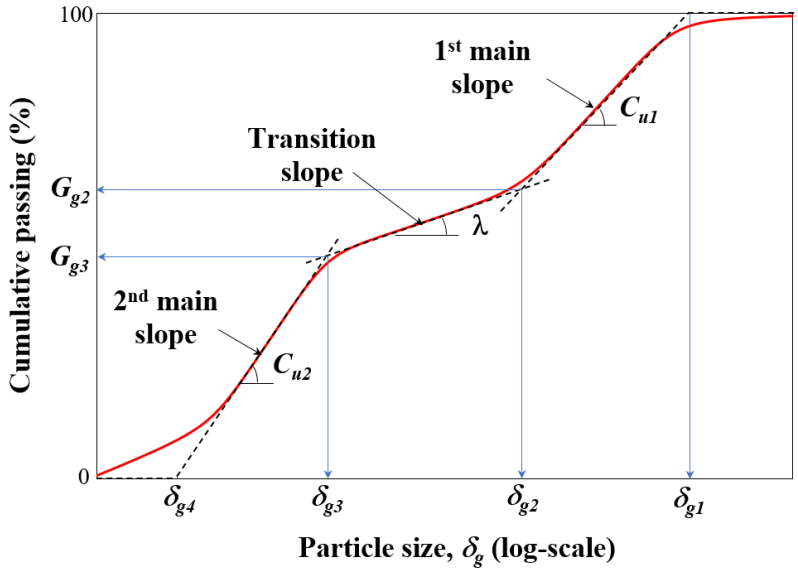

(a)

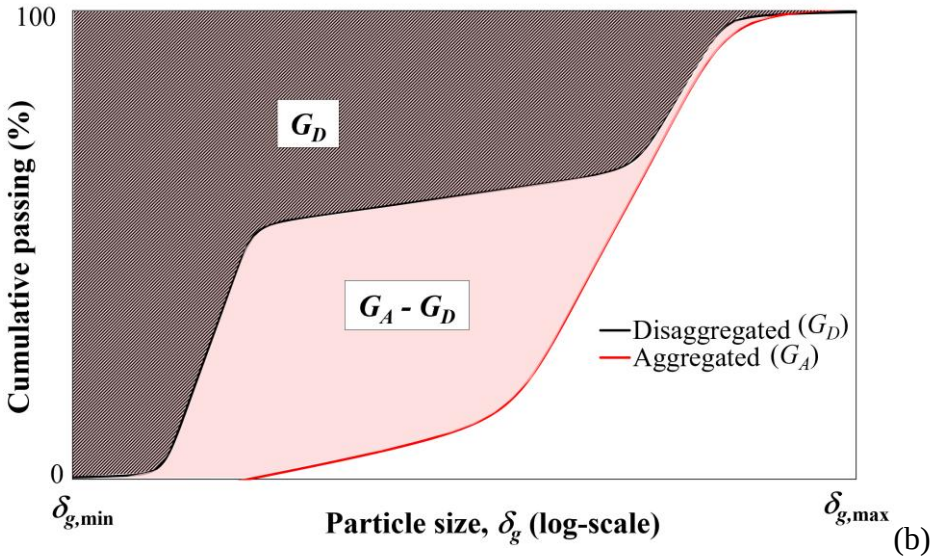

Figure 3.6 (a) Points of the GSD curve for the definition of different coefficients of uniformity; and (b) definition of relative aggregation proposed by Otálvaro et al. (2015)

3.3.2 Soil-water characteristic curves

The drying SWCCs of each dataset are shown in Fig. 3.7, along with their respective fitted curves using the Gitirana Jr. and Fredlund (2004) equation. This equation was adopted due to its great fitting capability and flexibility and because its fitting parameters have clear geometric and physical meaning. These SWCCs are used for the back-calculation of the β-function (Eq. 3.13) of each material. The relationship between the back-calculated parameters of the β-function and the basic soil properties will be investigated. The SWCC data was selected considering the number of measured points and how well-defined the entire range of macro- and micropores is.

Figures 3.7a and 3.7b demonstrate that the SWCCs of tropical bimodal soils are widely varied. The AEVs of the macro and micropores range typically from 1 to 100 kPa and from 1,000 to 18,000 kPa, respectively. The residual suctions of the macro and micropores range between 10 and 400 kPa and 20,000 to 100,000 kPa, respectively. A wide

range macro and microporosity can also be observed. Some of these soils present residual suctions of the micropores close to 100,000 kPa whereas the AEV of the macropores is frequently close to 1 kPa. These extreme values require testing procedures that are challenging to perform. As a result, some materials lack data around the first AEV and the second residual suction.

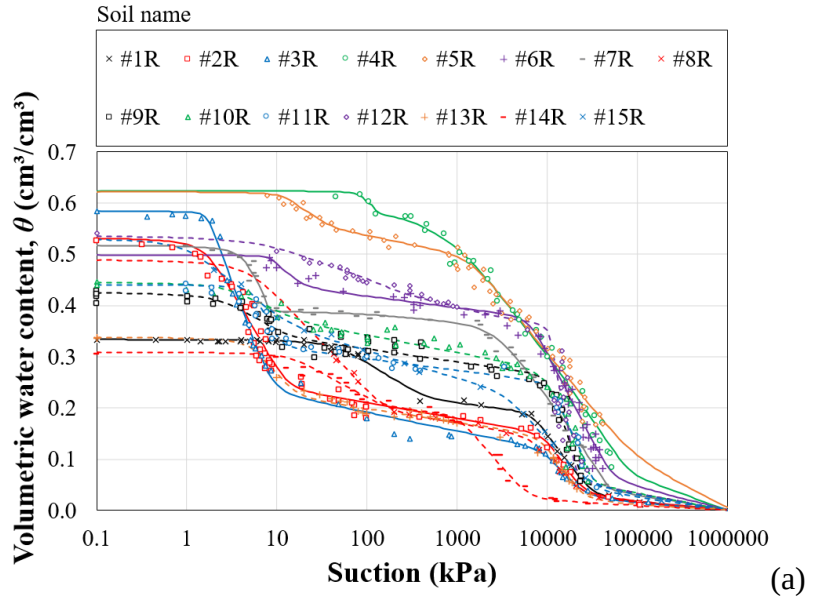

(a)

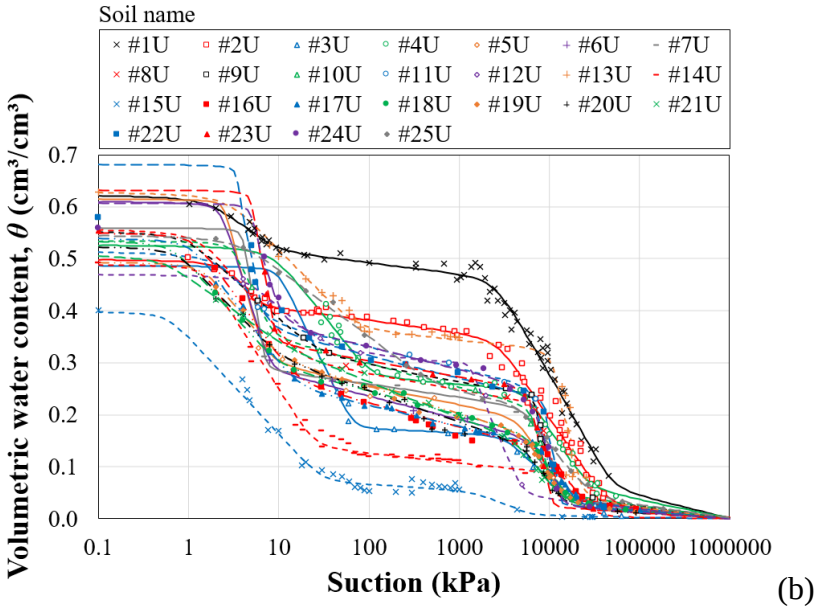

(b)

Figure 3.7 Tropical bimodal soils database: SWCCs of (a) 15 remolded soils; and (b) 25 undisturbed soils

3.4 Modeling microporosity and the β-function parameters

The key elements of the modeling framework, the β-function, was presented in Section 3.2. This function represents the relationship between the GSD and the PSD. The β-function parameters α_M, β_{M0}, α_M, and β_{m0} were determined from the experimental SWCCs shown in Section 3.3 using best-fit analyses. Figure 3.8 presents the back-calculated β-functions for all soils in the database. The β-functions were determined by taking the directly measured SWCCs and GSDs of each soil and employing Eq. 3.12 to calculate the corresponding values of β for each datapoint along the GDS. As a final step, Eq. 3.13 was fitted to each back-calculated β-function, providing a set of parameters α_M, β_{M0}, α_M, and β_{m0} for each soil.

Figure 3.8 indicated that the ranges of β values for the micro and macropores are significantly different. For the micropores, β varies from values slightly lower than 10, up to values exceeding 1000. The macropores present β values ranging from approximately 0.2 up to values slightly higher than 100. The β-functions along the micropores present positive slopes for most soils, indicating that larger particles tend to form smaller pores. The β-functions of macropores are more erratic, showing relationships between grain sizes and pores diameters that may be a result of multiple types of grains and aggregate arrangements.

The potential relationships between the β-function parameters and the other physical properties of the soil were investigated and are presented in this section. The models presented herein for the β-function parameters were established based on the following criteria: a) linear and non-linear correlation analyses were used as a first indication of

potential input variables; b) the use of relatively simple relationships with three of fewer input parameters; and c) the establishment of functions with physical meaning that can be interpreted and described, increasing the potential for relationships based on causation. Moreover, investigations of spurious relationships were also considered to avoid the selection of redundant parameters. The modeling process attempted to keep parallelism between the remolded and undisturbed dataset whenever possible.

First, linear (Pearson) and non-linear (Spearman) correlations were performed. Table 3.2 illustrates the Pearson correlation matrix showing a non-exhaustive list of the variables considered during the analyses and highlighting the five strongest correlations for each parameter of the β-function. The remaining variables and correlation matrices were suppressed for brevity purposes. The results presented in Table 3.2 were used as general guidelines for the establishment of the correlations presented in the next sections. The quality of the correlations established in the next sections will be presented in terms of the root mean square error (RMSE) and in terms of the coefficient of determination (R^2).

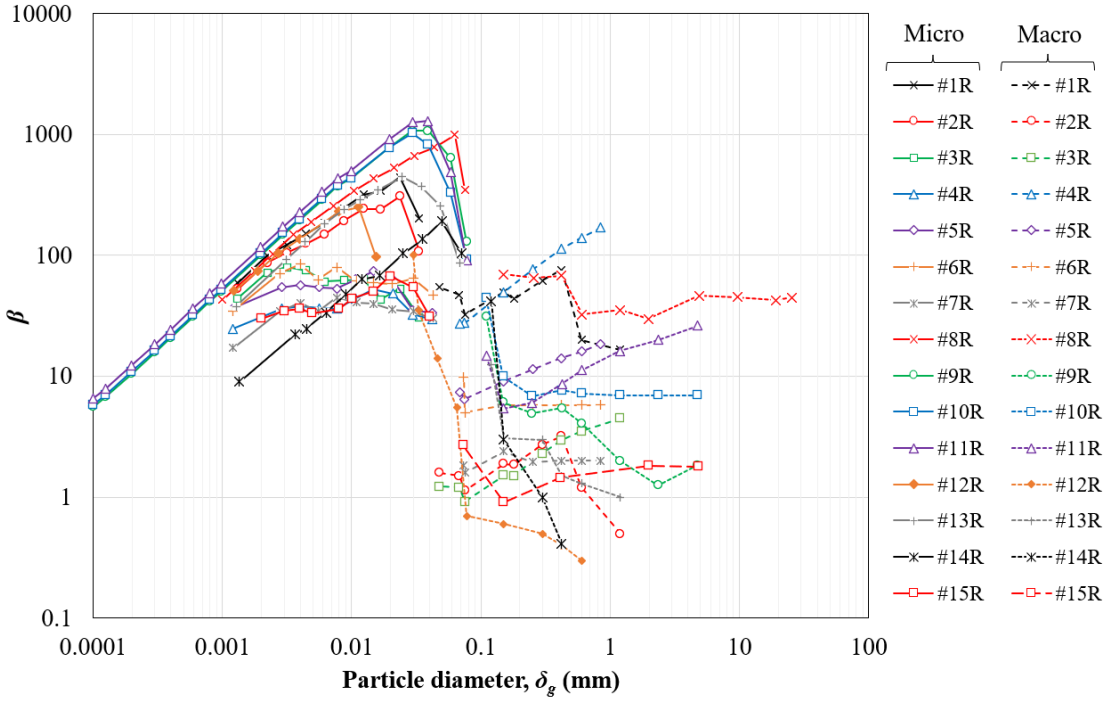

(a)

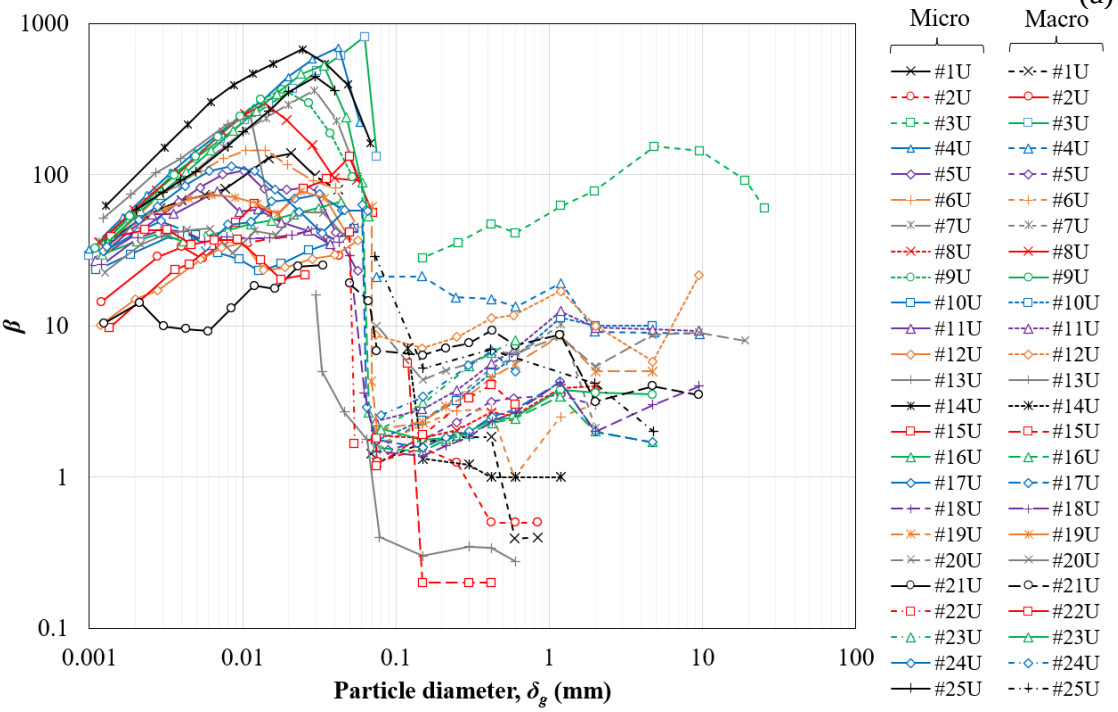

(b)

Figure 3.8. Back-calculated β-functions: (a) remolded soils; and (b) undisturbed soils

Table 3.2 Pearson correlation matrix for the main parameters of the remolded and undisturbed dataset (the best five correlations are highlighted)

	Remolded					Undisturbed				
	n_m	β_{m0}	α_m	β_{M0}	α_M	n_m	β_{m0}	α_m	β_{M0}	α_M
ρ_s	0.612	-0.216	0.007	-0.230	-0.230	0.341	0.060	0.000	-0.241	-0.122
n	0.613	-0.267	**-0.678**	-0.392	0.506	0.517	-0.058	-0.080	-0.390	0.334
n_m	1.000	-0.231	-0.365	-0.241	0.252	1.000	-0.285	-0.117	-0.348	0.369
n_M	-0.650	-0.069	-0.236	-0.031	0.111	**-0.692**	0.265	0.057	0.065	-0.119
w_L	**0.968**	-0.347	-0.530	-0.216	0.292	**0.900**	-0.365	-0.138	-0.436	0.294
w_P	**0.936**	-0.333	-0.487	-0.386	0.312	**0.865**	-0.314	-0.004	-0.524	0.241
$\delta_{g1,D}$	-0.412	0.325	0.170	**0.535**	0.005	-0.185	-0.008	-0.134	0.499	-0.080
$\delta_{g2,D}$	-0.108	-0.230	0.103	0.066	-0.361	-0.281	-0.159	-0.254	-0.020	-0.173
$\delta_{g3,D}$	0.325	-0.629	-0.788	-0.032	0.387	0.190	-0.213	0.089	-0.154	0.105
$\delta_{g4,D}$	-0.181	-0.656	-0.230	0.455	**-0.602**	-0.406	0.002	0.112	0.149	**-0.511**
$D_{10,D}$	-0.433	-0.313	0.083	**0.580**	**-0.682**	-0.642	0.027	0.104	0.247	**-0.492**
$D_{20,D}$	-0.475	-0.107	0.284	0.476	**-0.625**	-0.672	0.313	**0.259**	0.329	**-0.632**
$D_{30,D}$	-0.508	-0.019	0.333	0.466	**-0.554**	-0.678	**0.466**	**0.288**	0.404	**-0.616**
$D_{60,D}$	-0.620	0.393	0.359	**0.587**	-0.141	-0.566	0.346	0.013	**0.641**	-0.174
$D_{90,D}$	-0.518	0.309	0.144	**0.517**	0.064	-0.263	-0.056	**-0.309**	0.430	0.006
$C_{u,D}$	-0.277	**0.945**	**0.667**	-0.047	0.191	-0.420	0.230	-0.029	**0.557**	-0.066
$C_{u2,D}$	0.413	-0.541	**-0.786**	-0.114	0.516	0.043	-0.127	0.102	-0.165	0.149
λ_D	0.163	-0.549	-0.324	-0.105	-0.200	0.262	-0.097	0.090	**-0.567**	**0.434**
$\delta_{g1,A}$	-0.251	0.486	0.257	0.456	0.068	-0.126	-0.012	-0.076	0.514	-0.098
$\delta_{g2,A}$	-0.177	**0.662**	0.620	0.030	-0.108	-0.482	**0.574**	**0.461**	0.302	-0.175
$\delta_{g3,A}$	0.721	-0.568	-0.550	0.091	0.003	0.272	-0.235	-0.027	-0.348	0.232
$\delta_{g4,A}$	**0.751**	-0.586	-0.592	0.032	0.092	0.217	**-0.418**	-0.065	-0.331	0.107
$D_{10,A}$	0.375	0.230	0.185	-0.344	0.128	0.300	-0.302	-0.194	-0.146	-0.112
$D_{20,A}$	-0.153	0.641	0.534	-0.104	0.083	-0.211	0.011	-0.011	0.203	-0.306
$D_{30,A}$	-0.337	**0.875**	**0.710**	0.029	0.083	-0.472	**0.416**	0.073	0.536	-0.314
$D_{60,A}$	-0.348	**0.746**	0.554	0.308	0.057	-0.398	**0.421**	0.104	**0.708**	-0.104
$D_{90,A}$	-0.311	0.604	0.287	0.373	0.221	-0.212	-0.015	**-0.275**	0.462	0.042
$C_{u,A}$	-0.476	0.281	0.202	**0.503**	-0.017	-0.096	0.345	0.166	**0.577**	-0.048
$C_{u2,A}$	-0.021	**0.856**	**0.629**	-0.238	0.117	0.065	0.196	0.031	-0.032	0.233
λ_A	-0.581	0.257	0.517	0.489	**-0.640**	-0.296	0.013	-0.056	-0.026	0.054
$\%C_D$	**0.871**	-0.236	-0.316	-0.336	0.148	**0.795**	-0.264	-0.179	-0.301	0.247
$\%C_A$	-0.065	-0.494	-0.482	-0.258	0.252	-0.033	0.149	0.079	0.219	0.067
RA	**0.932**	-0.272	-0.438	-0.306	0.358	**0.810**	-0.258	-0.154	-0.286	0.200

$\%C_D$ is the amount of clay in percentage measured in the disaggregated GSD; and $\%C_A$ is the amount of clay in percentage measured in the aggregated GSD.

3.4.1 Microporosity

The total porosity, n, of a bimodal soil corresponds to the sum of the macro and the microporosity, as explained in Section 3.2.2. In the dataset used herein, the total porosity varied along a wide range (i.e., from 0.286 to 0.682). For remolded materials, n is related to the level of compaction which controls the amount of macro and micropores (Otálvaro et al., 2015; Georgetti, 2014; Araújo, 2019). The value of microporosity, n_m, varies along a relatively greater range (i.e., from 0.062 to 0.572) and is proportional to the degree of aggregation and percentage of fines. In short, porosity and microporosity are not strongly related to other basic soils properties such as the GSD and Atterberg limits. However, the dataset indicates that microporosity may be estimated based on other soil parameters.

The data analyses show that n_m has significant correlations with w_L (0.968 and 0.900), RA (0.932 and 0.810), and n (0.613 and 0.517), respectively for the remolded and undisturbed datasets. As both n and w_L have a similar effect on the n_m, these parameters were merged into a single parameter using their product. Based on these observations, the following equations were obtained using non-linear regression:

$$n_{m,r} = \left[2.87 - 4.94 \times \left(n \times w_L \right)^2 + 0.54 \times \ln^2 RA \right]^{-1} \tag{3.19}$$

$$n_{m,u} = 0.24 + 1.17 \times \left(n \times w_L \right)^2 - 0.012 / RA \tag{3.20}$$

where: the subscripts r and u refer to remolded and undisturbed soils; and w_L is the liquid limit.

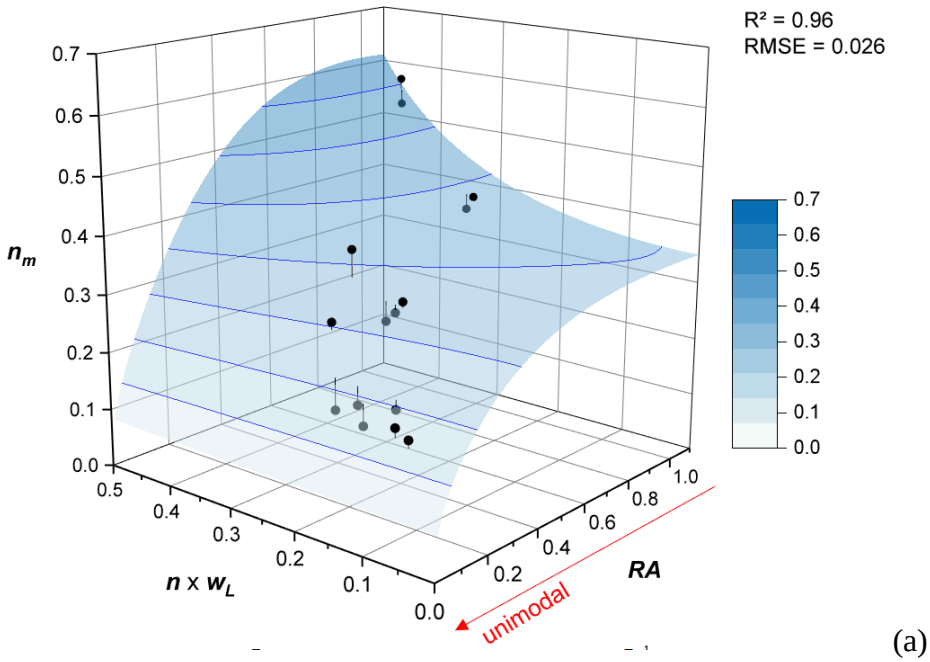

(a)

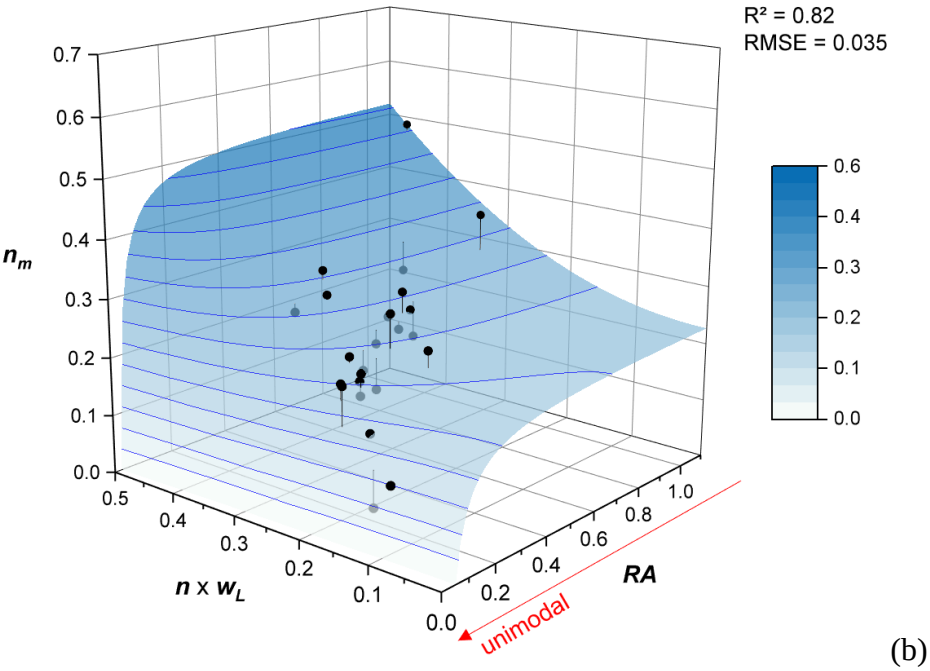

(b)

Figure 3.9 Modeling of n_m: (a) remolded soils; and (b) undisturbed soils

The regression curves (Eqs. 3.19 and 3.20) are presented as the blue surfaces shown in Fig. 3.9. The relationship between the variables presented in Fig. 3.9 have clear physical meaning. The micropores are contained in the soil aggregations formed by the cementation of clay particles. Consequently, these pore volumes are dependent on the quantity and type

of each clay mineral present in the soil, characteristics that are proportional to the liquid limit (Mitchell and Soga, 2005). The *RA* represents quantitatively the degree of aggregation and, since the microporosity corresponds to the pore volume withing the aggregations, their relationship becomes obvious. As a result, the absence of particle aggregation (i.e., *RA* = 0) would change the soil structure towards a unimodal SWCC without micropores.

3.4.2 Particle arrangement at the micropore level: β_{m0} and α_m

The parameter β_{m0} controls the β-function (Eq. 3.13) in the region of micropores, at the transition zone of the SWCC. Therefore, it influences the AEV and the residual suction of the microstructure. The β_{m0} varies notably (i.e., from 28 and 4000). The correlation and regression analyses showed different relationships for the remolded and undisturbed datasets. The value of β_{m0} for the remolded soils presented strong correlations (Table 3.2) with the coefficient of uniformity of the disaggregated GSD curve, $C_{u,D}$ (0.945). For the undisturbed soils, the correlations were weaker and involved mainly w_L. The higher dispersion for the undisturbed materials (Table 3.2) results from the complex nature of the pore structure of these soils.

The non-linear regression exercises resulted in Eqs. 3.21 and 3.22, which are illustrated in Figs. 3.10a and 3.10b.

$$\beta_{m0,r} = 603.3 - 2365.2 \times n^3 + 3.62 \times 10^{-2} \times C_{u,D}^{1.5} \quad (3.21)$$

$$\beta_{m0,u} = -973.12 - 2999.30 \times \ln^2 w_L + 985.0/w_L^{1.5} \quad (3.22)$$

where: subscripts *r* and *u* refer to remolded and undisturbed specimens; and $C_{u,D}$ is the coefficient of uniformity of the disaggregated GSD.

Equation 3.21, for remolded soils, provided reasonable goodness of fit (R^2 = 0.90 and RMSE = 0.712). It is worth mentioning that D_{10}, which is indirectly considered through

$C_{u,D}$, has been related to the AEV in several earlier studies (Kóvacs, 1981; Aubertin et al., 2003; Gallage and Uchimura, 2010; Rahardjo et al., 2012; Sakaki et al., 2014; Wang et al., 2017). Besides $C_{u,D}$, the role of total porosity, n, of the remolded materials was also considered, consistent with the findings of several authors (Araújo, 2019; Otálvaro et al., 2015; Georgetti, 2014; Oliveira et al., 2022). Fig. 3.10a demonstrates that n is especially important when its value is higher than 0.4 and $C_{u,D}$ is less than 100. This behavior is expected because a low value of $C_{u,D}$ towards unity means that the soil shows a tendency of presenting less aggregations, leading to a pore structure with fewer micropores and closer to a unimodal characteristic. For total porosities over 0.5, the influence of n increases as the $C_{u,D}$ decreases because lower values of $C_{u,D}$ mean that there is less variability in grain sizes and the packing of the particles becomes the dominant factor.

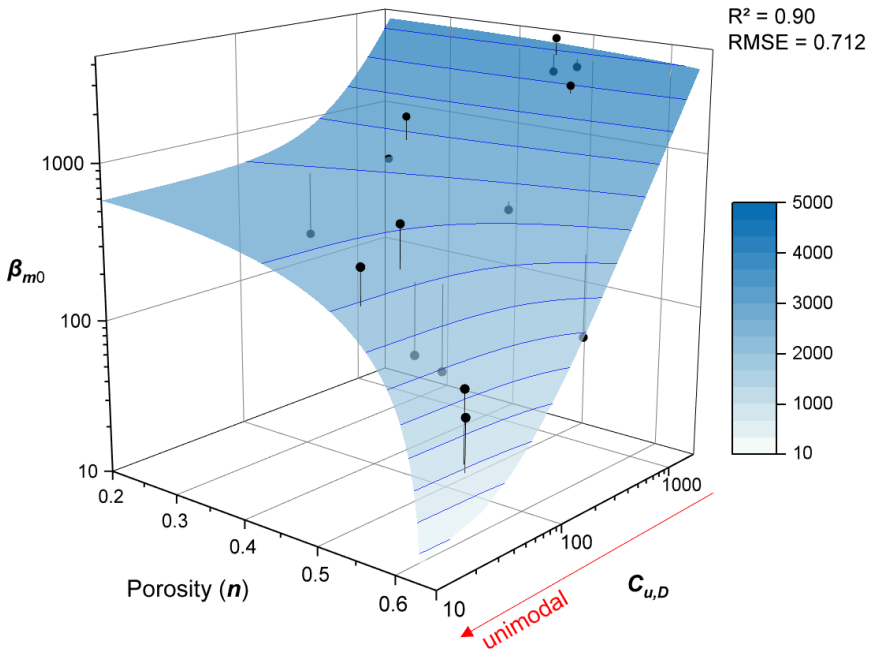

(a)

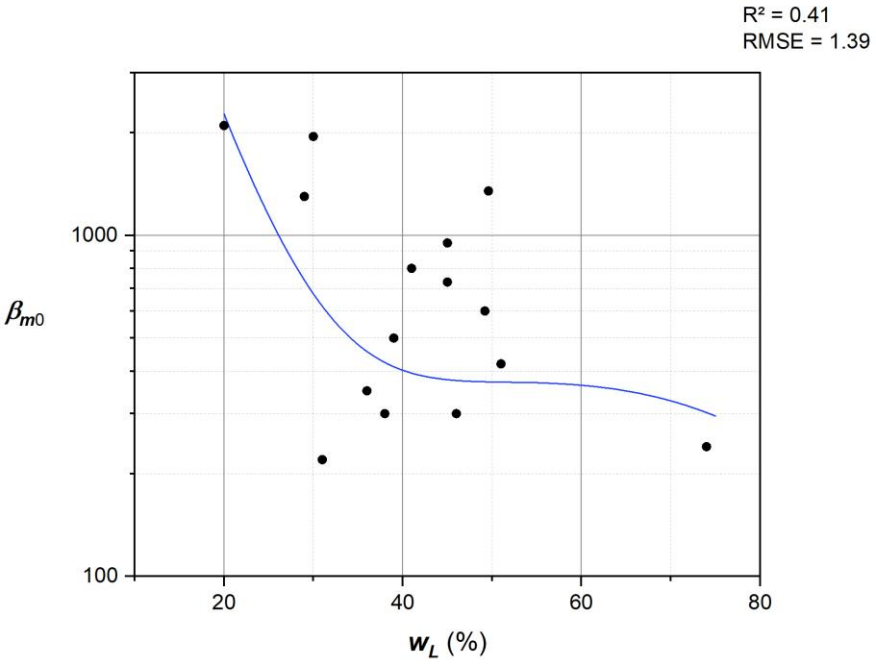
R² = 0.41
RMSE = 1.39
1000
100
β_{m0}
20
40
60
80
w_L (%)

(b)

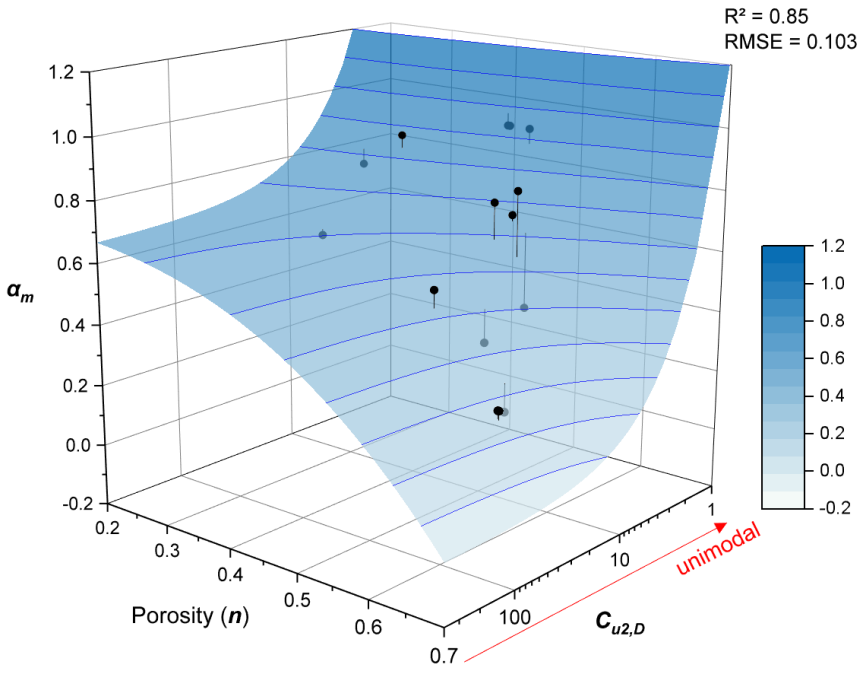
R² = 0.85
RMSE = 0.103
1.2
1.0
0.8
0.6
0.4
0.2
0.0
-0.2
α_m
0.2
0.3
0.4
0.5
0.6
0.7
Porosity (n)
1
10
100
$C_{u2,D}$
unimodal

(c)

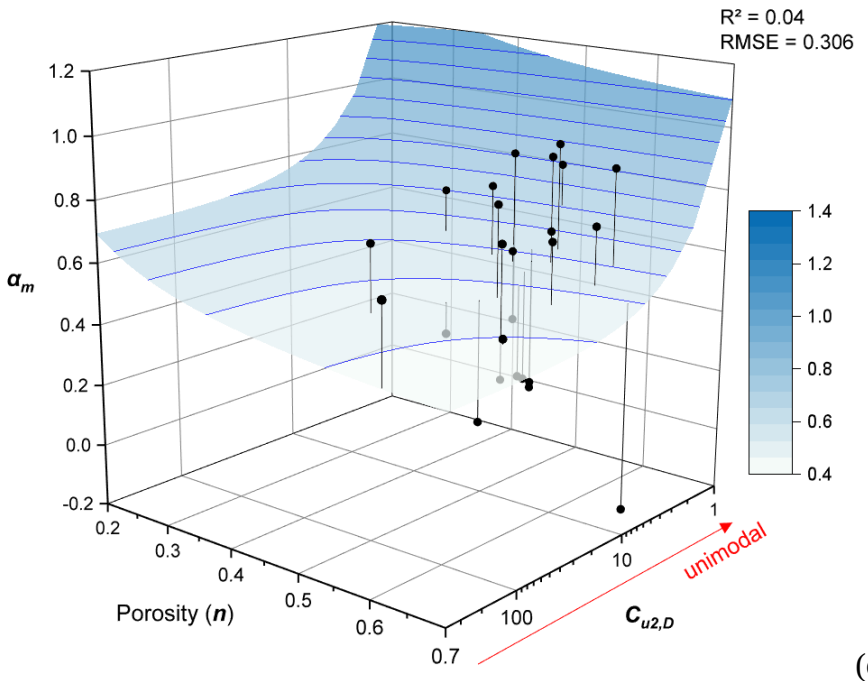

(d)

Figure 3.10 Particle arrangement at the micropore level: (a) β_{m0} of remolded soils; (b) β_{m0} of undisturbed soils; (c) α_m of remolded soils; and (d) α_m of undisturbed soils

The modest goodness of fit provided by Eq. 3.22, for undisturbed soils ($R^2 = 0.41$ and RMSE = 1.39) indicate that the selected variables were not able to capture adequately the processes associated with $\beta_{m0,u}$. Nevertheless, w_L was the best qualitative parameter to describe $\beta_{m0,u}$. None of the analyzed variables showed a strong correlation with $\beta_{m0,u}$, which can lead to the conclusion that the intrinsic variability of the undisturbed specimens originated from the soil formation process, which can lead to highly heterogeneous conditions.

The parameter α_m governs the ratio in which the micropores desaturate. Thus, the slope of the SWCC becomes steeper as α_m increases. The back-analyzed values of α_m ranged from -0.2 to 1.0, with a null value meaning that the β-function is constant along the micropores. The α_m values of the remolded and undisturbed datasets are shown in Fig. 3.10c and 3.10d and represented by Eqs. 3.23 and 3.24, respectively:

$$\alpha_{m,r} = 0.68 - 2.01 \times n^3 + 1.25/C_{u2,D} \quad (3.23)$$

$$\alpha_{m,u} = 0.325 - 0.074/n + 0.660/C_{u2,D} \quad (3.24)$$

where: n is the porosity; and $C_{u2,D}$ is the coefficient of uniformity obtained using Eq. 3.16 for the disaggregated GSD.

Equation 3.23, for the remolded soils, provided an R^2 of 0.85 and RMSE of 0.103. The analyses revealed a good correlation between α_m and both n and the second coefficient of uniformity of the disaggregated GSD ($C_{u2,D}$). The variations in the particle diameter ($\Delta\delta_g$) are proportional to the coefficient of uniformity because this variable represents the slope of the curve. As β is directly dependent of δ_g (Eq. 3.13), this expression demonstrates that variations in the values of β are controlled by α and tend to increase with C_u.

As for the undisturbed soils, the analyses indicate that none of the variables investigated holds a strong relationship with α_m. In this case, adding quantitative information about the mineralogical composition could potentially improve the results, but it would overcomplicate the implementation of this framework.

3.4.3 Particle arrangement at the macropore level: β_{M0} and α_m

The β_{M0} parameter is the variable controlling the SWCC in the zone between the AEV and the residual suction of the macrostructure. The values of β_{M0} varied from 0.6 to 45.0, which corresponds to a ratio of 75. For the AEV and the residual suction, this ratio is 150 and 99, respectively. This means that the shape of the normalized aggregated GSD curve presents a shape that is consistent with the desaturation slope of the SWCC of macropores.

Equations 3.25 and 3.26, with surfaces shown in Fig. 3.11a and 3.11b, were developed to represent the β_{M0} parameter for the remolded and undisturbed soils,

respectively:

$$\beta_{M0,r} = -3.93 + 2.85/n^2 + 1.15\delta_{g1,A}^3 \quad (3.25)$$

$$\beta_{M0,u} = -2.31 + 23.48 \times D_{60,A} + 1.22/w_L \quad (3.26)$$

Equation 3.25, for remolded soils, presented moderate performance, despite using variables which bear clear physical relationship with β_{M0}. The reduction in n leads to a decrease in the volume of macropores and results in an increase in the matric suction and in the value of β_{M0}. In the case of $\delta_{g1,A}$, the decrease of this parameter results in a reduction in β_{M0}, which means a reduction in matric suction. This behavior may sound counter-intuitive; however, soils with smaller values of $\delta_{g1,A}$ tend to have the aggregated GSD curve closer to the disaggregated curve (i.e., lower relative aggregation). In other words, a reduction in the size and/or amount of macropores originated from the aggregations causes a decrease in the matric suction and the parameter β_{M0}.

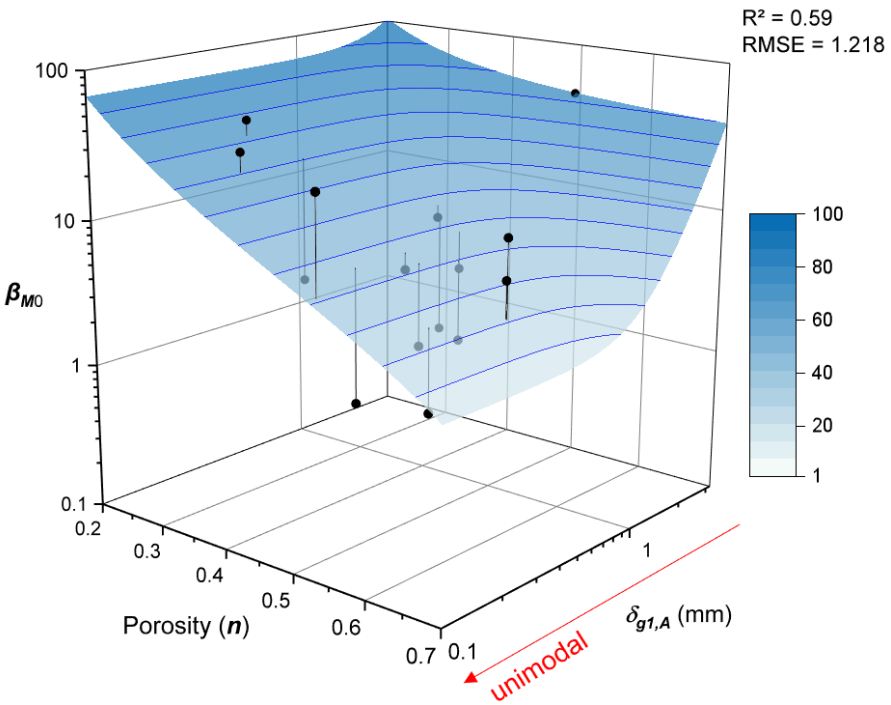

(a)

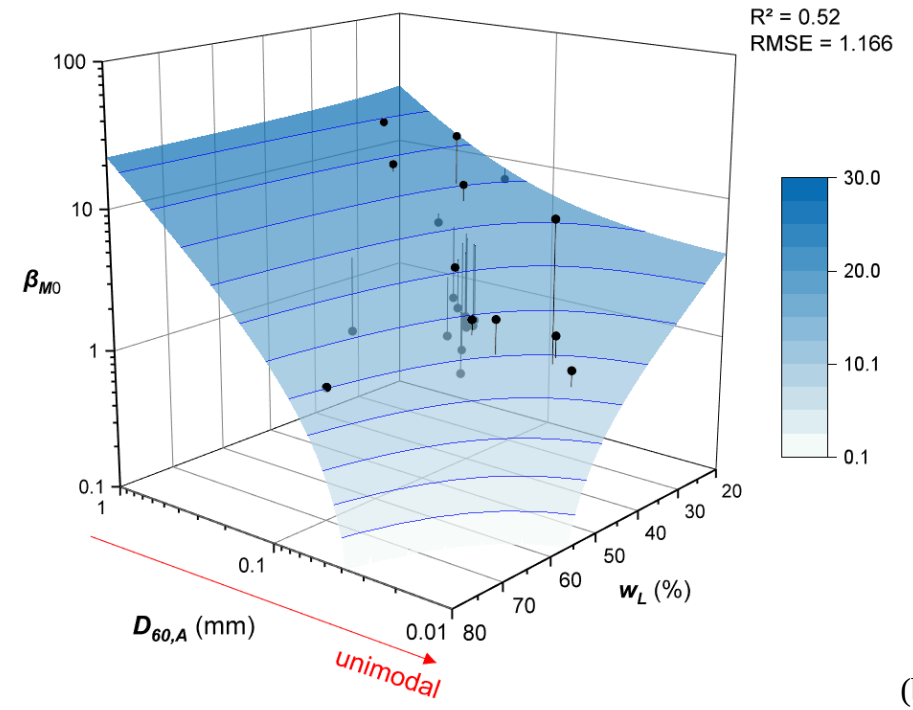
R² = 0.52
RMSE = 1.166
100
10
1
0.1
β_{M0}
30.0
20.0
10.1
0.1
1
0.1
0.01
$D_{60,A}$ (mm)
20
30
40
50
60
70
80
w_L (%)
unimodal

(b)

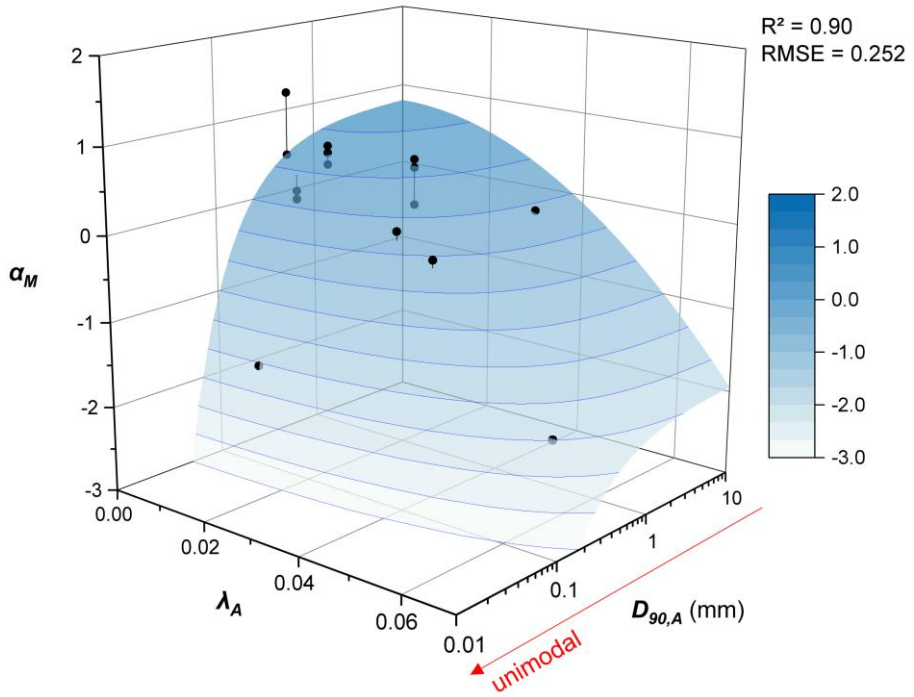
R² = 0.90
RMSE = 0.252
2
1
0
-1
-2
-3
α_M
2.0
1.0
0.0
-1.0
-2.0
-3.0
0.00
0.02
0.04
0.06
λ_A
10
1
0.1
0.01
$D_{90,A}$ (mm)
unimodal

(c)

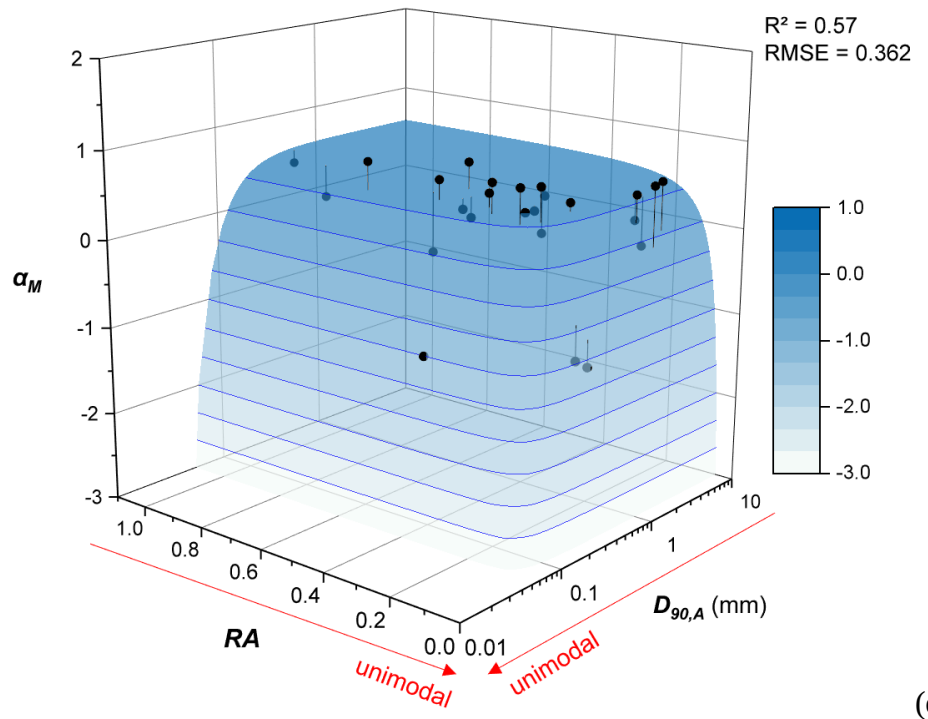

(d)

Figure 3.11 Particle arrangement at the macropore level: (a) β_{M0} of remolded soils; (b) β_{M0} of undisturbed soils; (c) α_M of remolded soils; and (d) α_M of undisturbed soils

Equation 3.26, developed for undisturbed materials, indicated that factors directly related to the level of aggregation ($D_{60,A}$ and w_L) take precedence in the pedogenesis formation process of the macrostructure. The influence of $D_{60,A}$ on β_{M0} is analogous to the influence of $\delta_{g1,A}$ of the remolded materials, in which smaller particle sizes are related to the smaller macropores. It can also be observed that with an increase in w_L, there is a reduction in β_{M0} and, therefore, in the matric suction. This means that larger values of *RA* lead to greater amounts of macropores of the largest volumes and thus reduction in the value of matric suction and β_{M0}.

The parameter α_M controls the rate of desaturations of the macropores. The values back-calculated from the datasets range from -2.0 to 1.2. The analysis of remolded soils

showed that parameters from the aggregated GSD curve control α_M. The developed correlations are shown in Fig. 3.11c and 3.11d and in Eqs. 3.27 and 3.28, for remolded and undisturbed materials, respectively:

$$\alpha_{M,r} = 0.82 - 561/\lambda_A - 0.19 \times D_{90,A} \quad (3.27)$$

$$\alpha_{M,u} = 0.60 - 8.49 \times 10^{-3} / RA^2 - 9.23 \times 10^{-3} / D_{90,A}^2 \quad (3.28)$$

Equation 3.27, for remolded soils, provided a coefficient of determination, R^2, of 0.90 and RMSE of 0.252. Both parameters, λ_A and $D_{90,A}$, bear clear physical relationships with α_M. The significance of λ_A indicates that other regions beyond the first main slope of the aggregated GSD curve cannot be disregarded. In addition, the parameter $D_{90,A}$ seems to serve as an anchor point defining the magnitude of α_M.

Equation 3.28, for undisturbed soils, provided a R^2 of 0.57 and RMSE of 0.362. Figure 3.11d shows the existence of a plateau for values of $D_{90,A}$ higher than 0.3 mm and RA over 0.20. Most of the datapoints lie within this plateau, which has an α_M value of approximately 0.60. Outside this region, the α_M values tend to be negative as the soil approaches a unimodal behavior. This may indicate that the influence of the shape of the GSD curve increases with the degree of weathering these natural soils.

3.4.4 Transition zone, n_c

The parameter n_c defines the curvature of the transition between micro and macropores in the β-function and does not have a strong physical meaning, as the previous parameters. The developed equations were design to produce smooth transitions. Equations 3.29 and 3.30 describe n_c for the remolded and undisturbed materials, respectively:

$$n_{c,r} = 20.26 - 10.98 \times \ln(\delta_{gM} / \delta_{gm}) \quad (3.29)$$

$$n_{c,u} = 20.38 - 8.31 \times \ln(\delta_{gM} / \delta_{gm}) \quad (3.30)$$

3.4.5 Procedures for estimation of the SWCC

The framework presented in Section 3.2 and the equations for the model parameters (β_{m0}, α_m, β_{M0}, α_M) provide an understanding of the fundamental relationships governing the retention properties of bimodal tropical soils. At the same time, this framework provides a prediction model for the SWCC, based on simple physical properties. The application of the proposed prediction model requires the following input data: aggregated and disaggregated GSD curves, n, and w_L. This information can be obtained from tests that are routinely performed.

The estimation of the SWCC requires the following steps:

(i) **Normalization**: the first step is to normalize the aggregated and disaggregated GSD curves following the procedure described in Section 3.2.2 and using Eqs. 3.5 and 3.6;

(ii) **GSD data acquisition**: the next step is to obtain the following parameters from the GSD curves: δ_{gm}, δ_{gM}, RA (Eq. 3.18), $C_{u,D}$, $C_{u2,D}$ (Eq. 3.16), $\delta_{g1,A}$, $D_{60,A}$, λ_A (Eq. 3.17), and $D_{90,A}$;

(iii) **Estimation of n_m**: as each GSD curve (aggregated and disaggregated) is related to a different soil structure (macro and micropores, respectively), the use of Eq. 3.19 for remolded materials or Eq. 3.20 for the undisturbed ones determine the amount of water stored within the micropores. The n_M can be obtained using the difference between the n and n_m;

(iv) **Calculations**: using each particle-size of the normalized GSD curves, calculate the volume of voids for each fraction using Eqs. 3.7 and 3.8 (continuous function)

or 3.9 and 3.10 (discrete form). The void ratio referred in those equations are related either to the micro or the macroporosity obtained in the previous step (i.e., $e_M = n_M/(1 - n)$ and $e_m = n_m/(1 - n)$). The calculation of dV_{vM} and dV_{vm} (or $V_{vm,i}$ or $V_{vM,i}$), starting from the smallest particles of the micropores (disaggregated GSD), allows to obtain the single and cumulative values of volumetric water content (Eq. 3.11);

(v) ***β*-function**: Eqs. 3.21 to 3.28 provide the variables β_{m0}, α_m, β_{M0} and α_M values used in Eq. 3.13 that are necessary to build the β-function. The fitting parameter n_c is obtained using Eqs. 3.29 and 3.30;

(vi) **Suction**: once β values corresponding to each of the points of the particle-size are available, the predicted matric suction can be obtained using Eqs. 3.12 and 3.14.

3.5 Prediction of SWCCs

This section presents an evaluation of the proposed models in terms of the prediction of the complete soil-water characteristic curves. The models' performance was quantified by comparing, in terms of RMSE and R^2 values, the predicted and the directly measured volumetric water contents. Water content values corresponding to matching suction values were interpolated using a best-fit curve (i.e., the Gitirana-Fredlund model), applied specifically to the directly measured data. This methodology allowed an unbiased consideration of experimental data dispersion and is mathematically sound, since the adopted best-fit curve adequately represented all SWCCs analyzed.

It is important to point out that the RMSE and R^2 values only account for the performance within the suction range addressed by the model. It will be shown, later in this section, that the relatively small residual region of the micropore storage was beyond the

model's prediction range.

Fig. 3.12 and 3.13 illustrate some examples of predictions that are considered representative of the entire dataset. For the remolded materials, the best prediction (R^2 = 0.983 and RMSE = 0.011) is for soil 1R1, shown in Fig. 3.12a. In the case of soil 2R2, shown in Fig. 3.12b, the prediction in the macropores region is better than in the micropores zone. Figure 3.12c, for soil 4R, illustrates a situation where the residual matric suction in the microstructure is underestimated. Figure 3.21d refers to soil 16R and indicates a situation where the model range was able to predict only a small portion of its microstructure zone because of limited GSD data. In this case, the matric suctions of the macropores are overestimated and the microporosity is in excellent agreement with the measured data. Lower volumetric water contents are sometimes overestimated.

Some predictions of the undisturbed materials are shown in Fig. 3.13. The best result is shown in Fig. 3.13a, for soil 2U (R^2 = 0.991 and RMSE = 0.027). Figures 3.13b and 3.13c illustrate results in which suctions in both macro and micropores are overestimated. It is interesting to note, however, that the partitioning between microporosity and macroporosity is well reproduced. For soil 22U, shown in Fig. 3.13d, the model provided a slight overestimation of suction for the entire SWCC. It can also be noticed that the residual region of the micropores was not captured due to unavailable GDS data for fine particles.

Figure 3.14 provides comparisons between the measured and predicted values of the proposed model, respectively for the remolded and undisturbed materials. The values of R^2 (remolded = 0.824 and undisturbed = 0.830) indicate that the model performance is similar for the remolded and undisturbed materials. There is a clear tendency for a slight

overestimation of water contents, especially when θ is between 0.2 and 0.5. Such a trend may be attributed to the greater difficulty in modeling the β-function in the transition region between micro and macrostructure. This is a region in which the shape of the curve obtained with the measured data presented greater variability (Eq. 3.13). It is also noted that for water contents lower than 0.2 the dispersion is less pronounced due to the better performance of the model in the micropores region.

The individual performance of each material is shown in Table 3.3. The best result obtained for the remolded materials (soil 1R1, RMSE = 0.011) and the worst result (soil 1R3, RMSE = 0.162) refer to the same material, compacted at different void ratios. Soil 1R3 has a relatively high void ratio of 1.5 and its data accounts for most of the points that are outside the confidence interval shown in Figure 3.14a. The overall results indicate that the model loses accuracy when the material is compacted at void ratios significantly higher than that in its natural state, because of difficulties in reproducing macropore behavior. This hypothesis is supported by the observation that the in-situ void ratio of soil 1R3 is 0.95 while soils 2R1 and 2R2 present an in-situ void ratio of 1.67.

Another noteworthy result is that it was not possible to predict the residual zone of the micropores for all soils and even transition zone of the micropores for some soils (e.g., soil 16R, Figure 3.12d). This was due to the limited range of disaggregated GSD curves. The minimum grain diameter measured was typically between 0.001 mm and 0.0001 mm (see Figure 3.3), with many GDS curves not reaching 0% passing, making the definition of parameters $C_{u,D}$ and $C_{u2,D}$ difficult. These parameters are directly related to the microstructure.

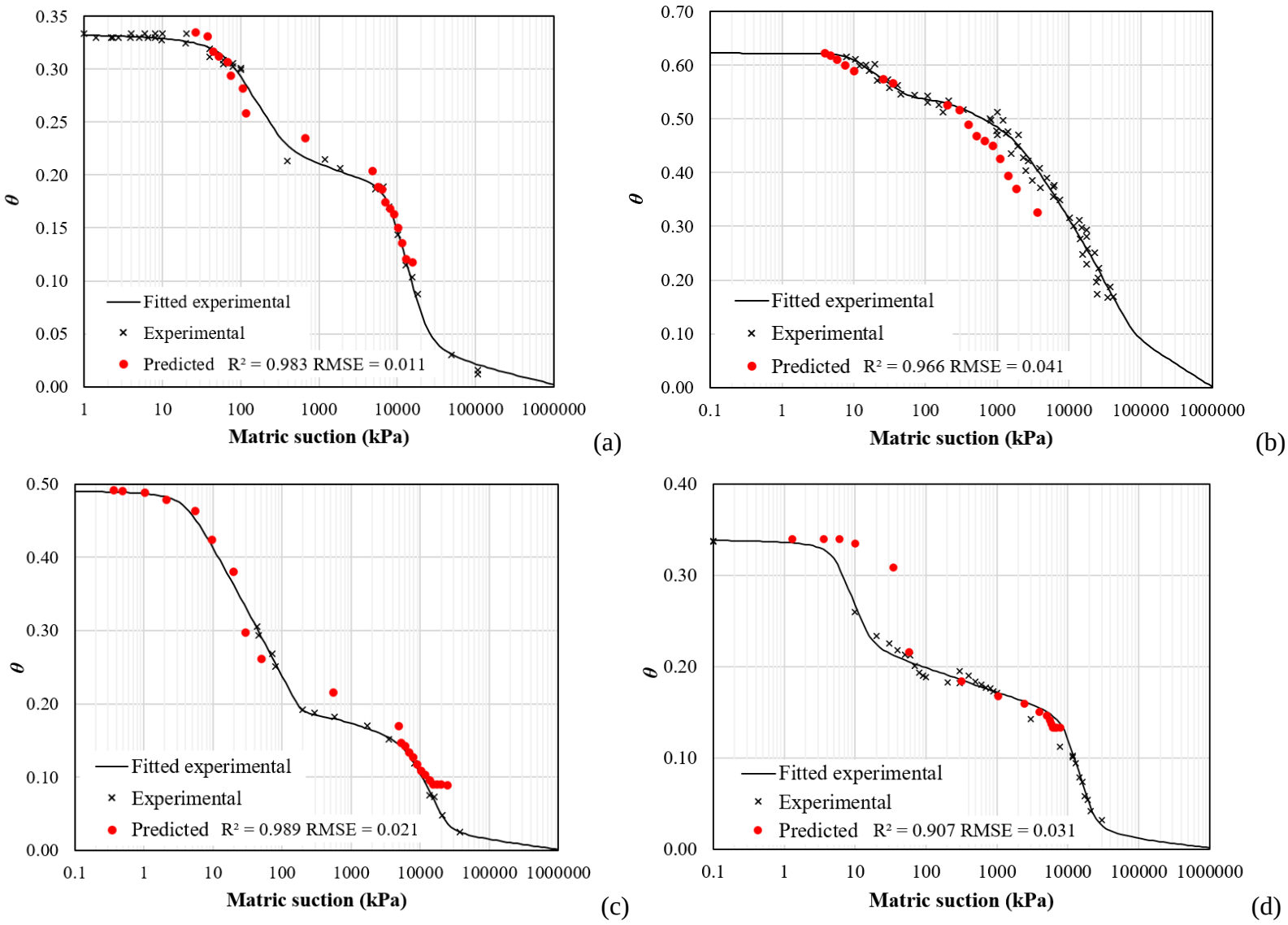

Figure 3.12 Predicted SWCCs for remolded soils: (a) 1R1, (b) 2R2, (c) 4R, and (d) 16R

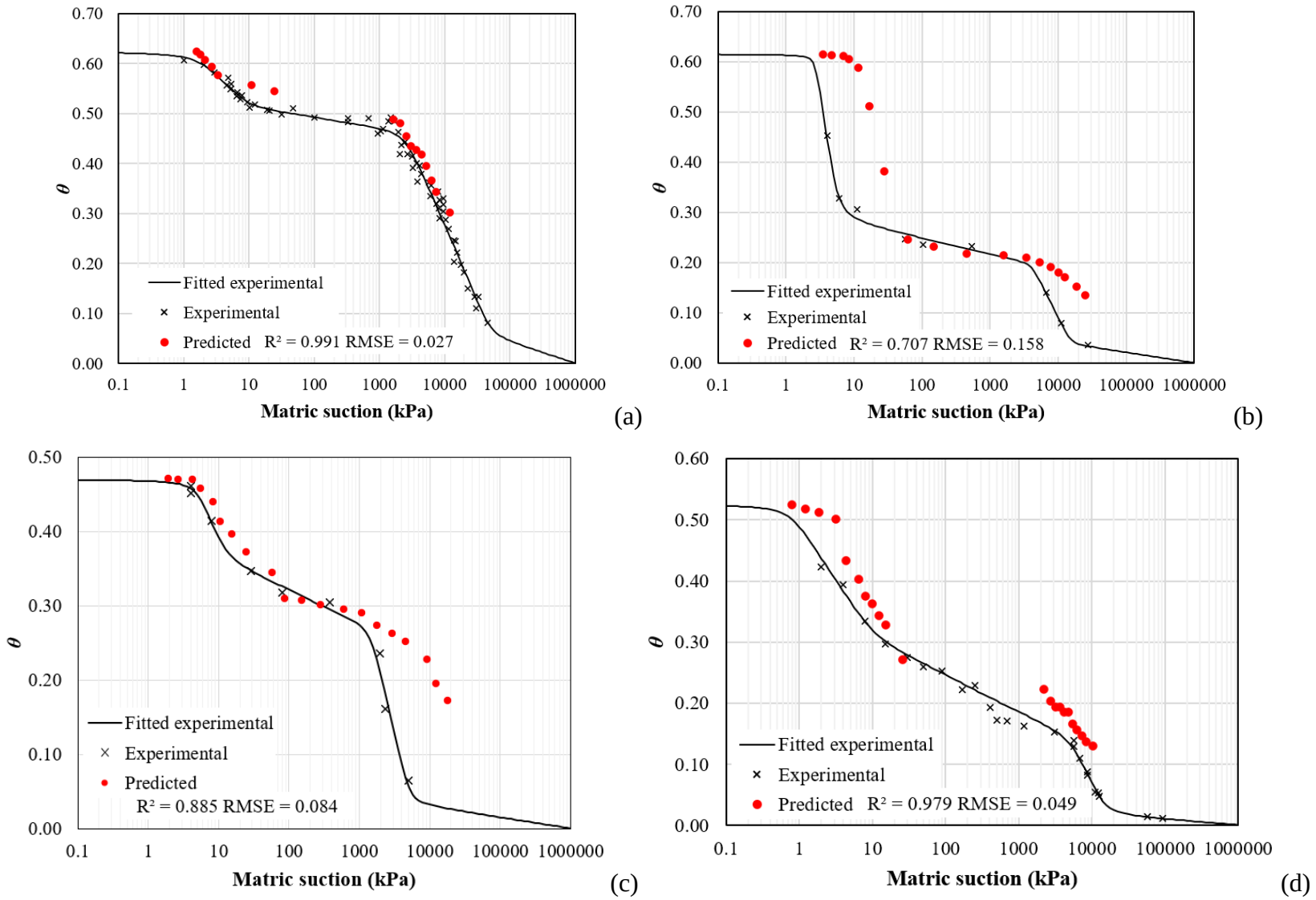

Figure 3.13 Predicted SWCCs for undisturbed soils: (a) 2U, (b) 7U, (c) 14U, and (d) 22U

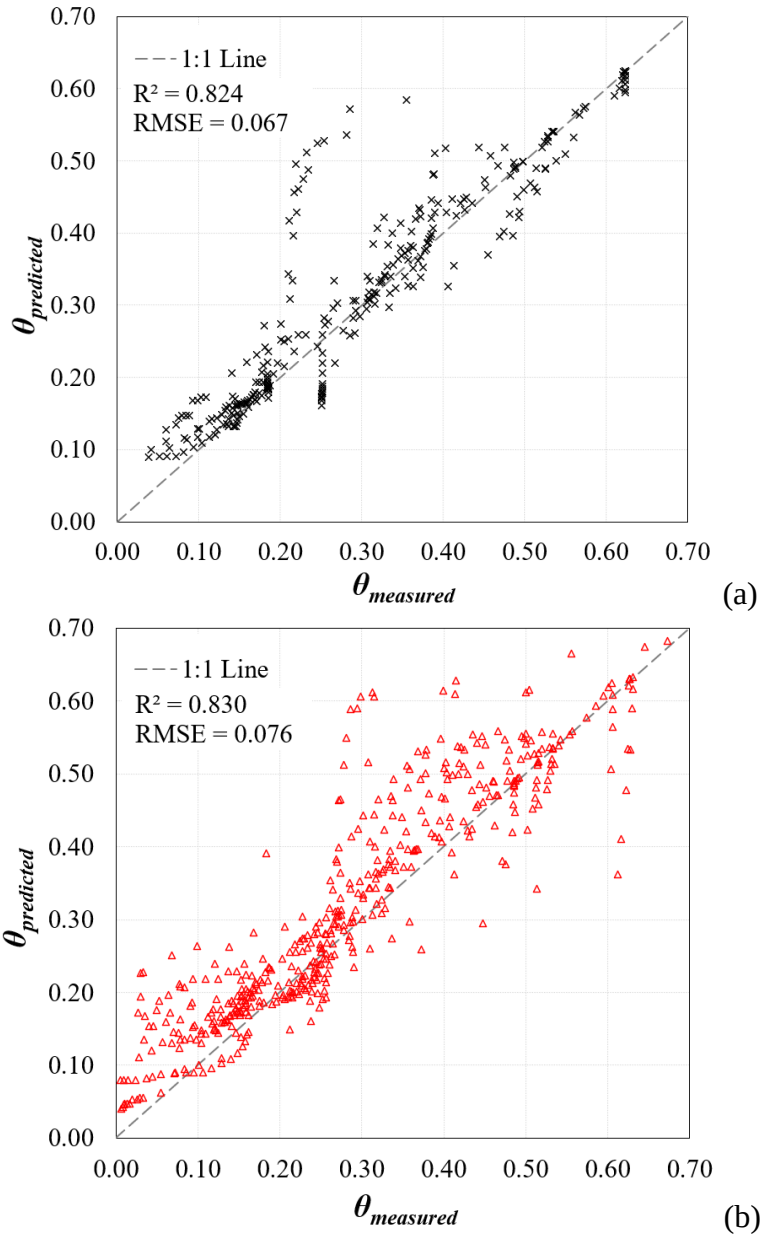

Figure 3.14 Comparison between measured and predicted volumetric water contents: (a) remolded soils; (b) undisturbed soils

It is important to note that the minimum grain-size range between 0.001 and 0.0001 mm leads to corresponding suction ranges between 10000 kPa and 100000 kPa. That means, in practice, that the limitation in the available GDS grain-size range affects the minimum water content and maximum suction that can be predicted. As a result, while the air-entry value and drainage slope of the micropores was typically within the model's

range, the residual suction for the micropores was always beyond the model's range. Fortunately, the micropore residual zone represents just a small portion of the typical bimodal SWCC of highly weather soils, thanks to their low plasticity.

Table 3.3 Performance of the proposed model demonstrated using R^2 and RMSE

Remolded		
Soil name	R^2	RMSE
1R1	0.983	0.011
1R2	0.826	0.150
1R3	0.892	0.162
2R1	0.975	0.036
2R2	0.966	0.041
3R1	0.918	0.018
3R2	0.846	0.055
4R	0.989	0.021
6R1	0.876	0.059
6R2	0.953	0.027
6R3	0.942	0.034
15R	0.879	0.035
16R	0.907	0.031
17R	0.934	0.056
27R	0.961	0.048
Overall	0.824	0.067

Undisturbed		
Soil name	R^2	RMSE
2U	0.991	0.027
3U	0.924	0.061
4U	0.935	0.051
5U	0.977	0.023
7U	0.707	0.158
8U	0.765	0.144
9U	0.827	0.078
10U	0.819	0.089
11U	0.878	0.063
12U	0.973	0.057
13U	0.937	0.049
14U	0.885	0.084
15U	0.721	0.107
16U	0.951	0.051
17U	0.905	0.072
18U	0.927	0.086
19U	0.934	0.074
20U	0.967	0.057
21U	0.967	0.033
22U	0.979	0.049
23U	0.886	0.089
24U	0.834	0.096
25U	0.930	0.052
26U	0.971	0.040
27U	0.926	0.048
Overall	0.830	0.076

The overestimation of the particle sizes constitutes another aspect of the disaggregated GSD that must be considered. As pointed out by Souza (2020), the

deflocculant agent (sodium hexametaphosphate) used in the hydrometer method is not able to destroy all aggregations. Due to this reason, some particle sizes presented in the disaggregated GSD curves may include aggregated particles.

The fittings of the variables related to the microstructure may be improved by adding information about parameters related to water adsorption (e.g., cation exchange capacity, surface specific area, or mineralogical composition). It is well known from the literature that these parameters are important for the study of soil structure (Tuller et al., 1999; Mitchell and Soga, 2005; Tuller and Or, 2005; Revil and Lu, 2013). In addition, the presence of organic matter and microorganisms may have been a factor that contributed negatively to the analyses and results of the undisturbed materials.

3.6 Conclusions

Highly weathered tropical soils are of great significance in the world because they correspond to geological conditions that are predominant in large regions of the world. These soils are common in several developing countries that require investments in resilient cities and infrastructure. In this context, the design of geotechnical structures greatly depends on the quantification of soil-atmosphere interaction and water retention properties of the soils. Several previous studies have contributed to the understanding of the main physical factors controlling the water retention properties of highly weathered tropical soils. Unfortunately, the previous models did not offer estimation models based on readily available soil properties, such as the grain-size distribution (GSD) and the Atterberg limits.

The proposed framework in this study is developed considering the coupled interactions between aggregated and disaggregated GSD curves and their association with index properties, serving as a representation of the SWCC. The hypotheses concerning the

use of aggregated and disaggregated GSD curves to respectively describe the macro- and microstructure have proven to be valid, albeit reliant on supplementary information extracted from these curves.

The parameter named relative aggregation, *RA*, used to describe quantitatively the aggregations in the soil, covers the whole aggregated and disaggregated GSD curves and provides essential information for modeling the micro and macrostructure. The slopes of the GSD curves also proved to be important for the β parameters, especially for the microstructure in which the results indicate a good correlation between such slopes the air-entry value and transition zone (i.e., desaturation slope).

Several specific particle diameters on the GSD curves stood out, including two located at the bending points of the first slope, which demonstrates the complexity of bimodal lateritic soils. The use of these various parameters leads to the conclusion that the GSD curves are fundamental to the understanding of the behavior of these soils.

The liquid limit was found to be strongly related to microstructure because it incorporates information about the amount and type of clay minerals in the soil. In addition, the porosity demonstrated to be quite important to describe the micro- and macrostructure. Such a behavior was expected for the remolded materials because the micro and macropores have a coupled influence and the n is the parameter that better represents this relation. The predictions imply that the inherent variability of the undisturbed materials is the reason their results presented performance slightly lower in comparison to those from the remolded ones.

In summary, the analyses lead to the conclusion that the structure of highly weathered tropical soils can be reasonably described through the GSD curves, the porosity, and the

liquid limit. The new approach for converting particles into pore-sizes using the β-function proved to be suitable and able to provide results with an overall R^2 over 0.8 for both remolded and undisturbed conditions. Moreover, the β-function concept can potentially be expanded in the future to other types of soils with different soil structures. These results of the present study suggest that the proposed model contributes towards better understanding of the soil structure and its relation to the SWCC of bimodal tropical soils. Most importantly, this approach can be used as a tool in the prediction of the bimodal SWCCs of lateritic soils, from which value information can be derived for the application of unsaturated soil mechanics into geotechnical practice.

References

Alves, R. D., Gitirana Jr. G. F. N., Vanapalli, S. K., 2020. Advances in the modeling of the soil–water characteristic curve using pore-scale analysis. Computers and Geotechnics. 127, 103766. https://doi.org/10.1016/j.compgeo.2020.103766

Araújo, A.G., 2019. Uso de microtomografia e porosimetria para análise de estrutura bimodal de um latossolo vermelho reconstituído. Doctoral Thesis: Department de Civil and Environmental Engineering, Universidade Federal de Goiás, 82p.

Arya, L. M., Dierolf, T. S., 1989. Predicting soil moisture characteristic from particle-size distribution: an improved method to calculate pore radii from particle radii. In: The International Workshop on Indirect Method of Estimating Hydraulic Properties of Unsaturated Soils, Riverside, CA.

Arya, L. M., Leij, F. J., van Genuchten, M. T., Shouse, P. J., 1999. Scaling parameter to predict the soil water characteristic from particle-size distribution data. Soil Science Society of America Journal, 63, 510-519. https://doi.org/10.2136/sssaj1999.03615995006300030013x

Arya, L. M., Paris, J. F., 1981. A physicoempirical model to predict the soil moisture characteristic from particle-size distribution and bulk density data. Soil Science Society of America Journal, 45, 1023-1030. https://doi.org/10.2136/sssaj1981.03615995004500060004x

Aubertin, M., Mbonimpa, M., Bussière, B., Chapuis, R. P., 2003. A model to predict the water retention curve from basic geotechnical properties. Canadian Geotechnical

Journal. 40, 1104-1122. https://doi.org/10.1139/t03-054

Benatti, J. C. B., Miguel, M. G., 2013. A proposal of structural models for colluvial and lateritic soil profile from southwestern Brazil on the basis of their collapsible behavior. Engineering Geology. 153, 1-11. https://doi.org/10.1016/j.enggeo.2012.11.003

Burger, C. A., Shackelford, C. D., 2001. Evaluating dual porosity of pelletized diatomaceous earth using bimodal soil-water characteristic curve functions. Canadian Geotechnical Journal. 38, 53-66. https://doi.org/10.1139/t00-084

Camapum de Carvalho, J., Gitirana Jr., G. F. N., Machado, S. L., Mascarenha, M. M. A., Silva Filho, F. C., 2015. Solos não saturados no contexto geotécnico. Associação Brasileira de Mecânica dos Solos e Engenharia Geotécnica, São Paulo.

Casini, F., Vaunat, J., Romero, E., Desideri, A., 2012. Consequences on water retention properties of double-porosity features in a compacted silt. Acta Geotechnica. 7, 139-150. https://doi.org/10.1007/s11440-012-0159-6

Castro, M. D., Oliveira, V. N., Mascarenha, M. M. A., Gitirana Jr., G. F. N., Luz, M. P., 2022. Análise das curvas características solo-água de amostras remoldada e indeformada de um solo laterítico não saturado. In: Anais do XX COBRAMSEG, Campinas.

Cihan, A., Perfect, E., Tyner, J. S., 2007. Water retention models for scale-variant and scale-invariant drainage of mass prefractal porous media. Vadose Zone Journal. 6, 786-792. https://doi.org/10.2136/vzj2007.0062

Cordão Neto, M. P., Hernández, O., Reinaldo, R. L., Borges, C., Caicedo, B., 2018. Study of the relationship between the hydromechanical soil behavior and microstructure of a structured soil. Earth Sciences Research Journal. 22(2), 91-101. https://doi.org/10.15446/esrj.v22n2.65640

Delage, P., Audiguier, M., Cui, Y. J., Howat, M. D., 1996. Microstructure of a compacted silt. Canadian Geotechnical Journal. 33(1), 150-158. https://doi.org/10.1139/t96-030

Delage, P., Lefebvre, G., 1984. Study of the structure of a sensitive Champlain clay and of its evolution during consolidation. Canadian Geotechnical Journal. 21(1), 21-35. https://doi.org/10.1139/t84-003

Dolinar, B., 2014. Prediction of the soil-water characteristic curve based on the specific surface area of fine-grained soils. Bulletin of Engineering Geology and the Environment. 74, 697-703. https://doi.org/10.1007/s10064-014-0664-y

Durner, W., 1994. Hydraulic conductivity estimation for soils with heterogeneous pore structure. Water Resources Research. 30(2), 211-223. https://doi.org/10.1029/93WR02676

Fang, Q., Ren, X., Zhang, B., Chen, X., Guo, Z., 2022. A flexible soil-water characteristic curve model considering physical constraints of parameters. Engineering Geology,

305, 106717. https://doi.org/10.1016/j.enggeo.2022.106717

Feuerharmel, C., Pereira, A., Gehing, W. Y. Y., Bica, A. V. D., 2006. Determination of the shear strength parameters of two unsaturated colluvium soils using the direct shear test. In: Fourth International Conference on Unsaturated Soils, Arizona. 1181–1190. https://doi.org/10.1061/40802(189)96

Feuerharmel, C., 2007. Estudo da resistência ao cisalhamento e da condutividade hidráulica de solos coluvionares não saturados da Formação Serra Geral. Doctoral Thesis: Graduate program in civil engineering. Universidade Federal do Rio Grande do Sul, 330p.

Fredlund, M. D., Wilson, G. W., Fredlund, D. G., 2002. Use of the grain-size distribution for estimation of the soil-water characteristic curve. Canadian Geotechnical Journal, 39, 1103-1117. https://doi.org/10.1139/t02-049

Fredlund, D. G., Xing, A., 1994. Equations for the soil-water characteristic curve. Canadian Geotechnical Journal. 31, 521-532. https://doi.org/10.1139/t94-061

Frydman, S., Baker, R., 2009. Theoretical soil-water characteristic curves based on adsorption, cavitation, and a double porosity model. International Journal of Geomechanics. 9(6), 250-257. https://doi.org/10.1061/(ASCE)1532-3641(2009)9:6(250)

Furman, J., 2019 Avaliação da resistência ao cisalhamento de solos tropicais brasileiros não saturados da Serra do Mar – Trecho PR-SP. Master Thesis: Graduate program in civil engineering - construction, Universidade Federal do Paraná, 113p.

Gallage, C. P. K., Uchimura, T., 2010. Effects of dry density and grain size distribution on soil-water characteristic curves of sandy soils. Soils and Foundations. 50(1), 161-172. https://doi.org/10.3208/sandf.50.161

Gao, Y., Fu, Y., Chen, J., Sun, D. A., 2024. A novel equation for simulating the bimodal soil–water retention curve of unsaturated soils. Acta Geotechnica, 1-16. https://doi.org/10.1007/s11440-024-02233-y

Georgetti, G. B., 2014. Deformabilidade e resistência de um solo laterítico não saturado. Doctoral Thesis: Graduate program in geotechnics, Universidade de São Paulo, 130p.

Gidigasu, M. D., 1976. Laterite Soil Engineering: Pedogenesis and Engineering Principles. Elsevier, New York, NY, USA. 554 p

Gitirana Jr., G. F. N., Fredlund, D. G., 2004. Soil-water characteristic curve equation with independent properties. Journal of Geotechnical and Geoenvironmental Engineering. 130(2), 209-212. https://doi.org/10.1061/(ASCE)1090-0241(2004)130:2(209)

Gitirana Jr., G. F. N., Fredlund, D. G., 2016. Statistical assessment of hydraulic properties of unsaturated soils. Soils & Rocks, 39(1), 81-95. https://doi.org/10.28927/SR.391081

Guimarães, R.C., 2002. Análise das propriedades e comportamento de um perfil de solo

laterítico aplicada ao estudo do desempenho de estacas escavadas. Master Thesis: Departament de Civil and Environmental Engineering, Universidade de Brasília, 183f.

Hassan, S. B. M., Dragonetti, G., Comegna, A., Sengouga, A., Lamaddalena, N., Coppola, A. 2022. A bimodal extension of the ARYA&PARIS approach for predicting hydraulic properties of structured soils. *Journal of Hydrology*, 610. https://doi.org/10.1016/j.jhydrol.2022.127980

Huat, B. B. K., Toll, D. G., Prassad, A., 2013. Handbook of Tropical Residual Soils Engineering. CRC Press, Taylor and Francis Group, Florida.

Israelachvili, J. N., 2011. Intermolecular and surface forces. Elsevier: 3rd Edition.

Juang, C. H., Holtz, R. D., 1986. Fabric, pore size distribution, and permeability of sandy soils. Journal of Geotechnical Engineering. 112, 855-868. https://doi.org/10.1061/(ASCE)0733-9410(1986)112:9(855)

Kühn, V. O., Lopes, B. C. F. L., Caicedo, B., Cordão-Neto, M. P., 2021. Micro-structural and volumetric behaviour of bimodal artificial soils with aggregates. Engineering Geology. 288, 106139. https://doi.org/10.1016/j.enggeo.2021.106139

Kühn, V. O., Lopes, B. C. F. L., Caicedo, B., Cordão-Neto, M. P., 2022. Mechanical behaviour of bimodal kaolin clay with aggregates. Engineering Geology. 297, 106490. https://doi.org/10.1016/j.enggeo.2021.106490

Kumar, G. S., Saini, P. K., Deoliya, R., Mishra, A. K., Negi, S. K., 2022. Characterization of laterite soil and its use in construction applications: A review. Resources, Conservation & Recycling Advances, 16. https://doi.org/10.1016/j.rcradv.2022.200120

Kyokawa, H., 2021. A double structure model for hydro-mechano-chemical behavior of expansive soils based on the surface phenomena of mineral crystals. Engineering Geology. 294, 106366. https://doi.org/10.1016/j.enggeo.2021.106366

Li, Y., Vanapalli, S. K., 2022. A novel modeling method for the bimodal soil-water characteristic curve. Computers and Geotechnics. 138, 104318. https://doi.org/10.1016/j.compgeo.2021.104318

Likos, W. J., Jaafar, R., 2013. Pore-scale model for water retention and fluid partitioning of partially saturated granular soil. Journal of Geotechnical and Geoenvironmental Engineering. 139(5), 724-737. https://doi.org/10.1061/(ASCE)GT.1943-5606.0000811

Likos, W. J., Lu, N., 2004. Hysteresis of capillary stress in unsaturated granular soil. Journal of Engineering Mechanics. 130(6), 646-655. https://doi.org/10.1061/(ASCE)0733-9399(2004)130:6(646)

Liu, J., Leung, A. K., Dong, H., Lai, N. T., 2024. A state-dependent bimodal soil water retention model considering evolutions of pore-scale soil–water interaction.

Computers and Geotechnics, 175, 106704. https://doi.org/10.1016/j.compgeo.2024.106704

Liu, Y., Zhao, Y., Vanapalli, S. K., Mehmood, M., 2024. Soil-water characteristic curve of expansive soils considering cumulative damage effects of wetting and drying cycles. Engineering Geology, 339. https://doi.org/10.1016/j.enggeo.2024.107642

Maia, P.D., Boaventura, G.R., Pires, A.C.B., 2006. Distribuição espacial de elementos-traço em sedimentos do Lago Paranoá – DF, Brasil. Geochimica Brasiliensis, 20(2), 158-174.

Machado, R. R., 2020. Ensaios pressiométricos para estimativa de parâmetros de resistência e deformabilidade de um perfil de solo tropical. Master Thesis: Departament de Civil and Environmental Engineering, Universidade Federal de Goiás, 203p.

Mascarenha, M. M. A., Cordão Neto, M. P., Silva, M. T. M. G., 2016. Alternative method for analyzing hydromechanical behaviour of unsaturated soils. Soils and Rocks. 39(1), 29-39.

Miguel, M. G., Bonder, B. H., 2012. Soil–water characteristic curves obtained for a colluvial and lateritic soil profile considering the macro and micro porosity. Geotechnical and Geological Engineering. 30, 1405–1420. https://doi.org/10.1007/s10706-012-9545-y

Miller, G.A., Khoury, C.N., Muraleetharan, K.K., Liu, C., Kibbey, T.C.G., 2008. Effects of soil skeleton deformations on hysteretic soil water characteristic curves: experiments and simulations. Water Resources Research 44, 1–10. https://doi.org/10.1029/2007WR006492

Mitchell, J. K., Soga, K., 2005. Fundamentals of Soil Behavior. New Jersey: Wiley.

Monroy, R., Zdravkovic, L., Ridley, A., 2010. Evolution of microstructure in compacted London Clay during wetting and loading. Geotechniqué. 60(2), 105-119. https://doi.org/10.1680/geot.8.P.125

Mufti, S., Das, A., 2022. An advanced pore-scale model for simulating water retention characteristics in granular soils. Journal of Hydrology. 615, 128561. https://doi.org/10.1016/j.jhydrol.2022.128561

Oliveira, A. D., Pelaquim, F. G. P., Zanin, R. F. B., Melo, T. R., Filho, J. T., Andrello, A. C., Teixeira, R. S., 2022. The structure of tropical lateritic soils as an impacting factor in the shape of soil-water characteristic curves. Soils and Rocks. 45(2). https://doi.org/10.28927/SR.2022.070521

Otálvaro, I. F., Cordão Neto, M. P., Caicedo, B., 2015. Compressibility and microstructure of compacted laterites. Transportation Geotechnics. 5, 20-34. https://doi.org/10.1016/j.trgeo.2015.09.005

Otálvaro, I. F., Cordão-Neto, M. P., Delage, P., Caicedo, B., 2016. Relationship between soil structure and water retention properties in a residual compacted soil. Engineering Geology. 205, 73-80. https://doi.org/10.1016/j.enggeo.2016.02.016

Pereira, S. A. S., Silva Jr., A. C., Mendes, T. A., Gitirana Jr., G. F. N., Alves, R. D., 2023. Prediction of soil-water characteristic curves in bimodal tropical soils using artificial neural networks. Geotechnical and Geological Engineering. https://doi.org/10.1007/s10706-023-02716-x

Rahardjo, H. Satyanaga, A., D'Amore, G. A. R., Leong, E. C., 2012. Soil–water characteristic curves of gap-graded soils. Engineering Geology. 125, 102-107. https://doi.org/10.1016/j.enggeo.2011.11.009

Revil, A., Lu, N., 2013. Unified water isotherms for clayey porous materials. Water Resources Research. 49, 5685–5699. https://doi.org/10.1002/wrcr.20426

Romero, E. Simms, P. H., 2008. Microstructure investigation in unsaturated soils: a review with special attention to contribution of mercury intrusion porosimetry and environmental scanning electron microscopy. Geotechnical and Geology Engineering. 26, 707-727. https://doi.org/10.1007/s10706-008-9204-5

Sakaki, T., Komatsu, M., Takahashi, M., 2014. Rules-of-thumb for predicting air-entry value of disturbed sands from particle size. Soil Science Society of America Journal. 78(2), 454-464. https://doi.org/10.2136/sssaj2013.06.0237n

Satyanaga, A., Rahardjo, H., Leong, E. C., Wang, J. Y, 2013. Water characteristic curve of soil with bimodal grain-size distribution. Computers and Geotechnics. 48, 51-61. https://doi.org/10.1016/j.compgeo.2012.09.008

Souza, J. C., 2020. Avaliação da relação entre a curva granulométrica e a curva característica solo-água para um solo residual bimodal sob diferentes graus de desagregação. Master Thesis: Departament de Civil and Environmental Engineering, Universidade Federal de Goiás.

Tokunaga, T. K., 2011. Physicochemical controls on adsorbed water film thickness in unsaturated geological media. Water Resources Research. 47, 12p. https://doi.org/10.1029/2011WR010676

Tuller, M., Or, D., 2005. Water films and scaling of soil characteristic curves at low water contents. Water Resources Research. 41(9), W09403. https://doi.org/10.1029/2005WR004142

Tuller, M., Or, D., Dudley, L. M., 1999. Adsorption and capillary condensation in porous media: Liquid retention and interfacial configurations in angular pores. Water Resources Research. 35(7), 1949-1964. https://doi.org/10.1029/1999WR900098

Tyler, S. W., Wheatcraft, S. W., 1990. Fractal processes in soil water retention. Water Resources Research. 26(5), 1047-1054. https://doi.org/10.1029/WR026i005p01047

van Genuchten, M. T., 1980. A closed-form equation for predicting the hydraulic conductivity of unsaturated soils. Soil Science Society of America Journal. 44, 892-898. https://doi.org/10.2136/sssaj1980.03615995004400050002x

Villibor, D. F., Nogami, J. S., Cincerre, J. R., Serra, P. R., Zuppolini Neto, A., 2009. Pavimentos de Baixo Custo para Vias Urbanas. 2nd Ed.: São Paulo.

Wang, J-P., Hu, N., François, B., Lambert, P., 2017. Estimating water retention curves and strength properties of unsaturated sandy soils from basic soil gradation parameters. Water Resources Research. 53, 6069-6088. https://doi.org/10.1002/2017WR020411

Wang, X., Li, J., 2015. A novel liquid bridge model for estimating swcc and permeability of granular material. Power Technology. 275, 121-130. https://doi.org/10.1016/j.powtec.2015.01.044

Wijaya, M., Leong, E. C., 2016. Equation for unimodal and bimodal soil–water characteristic curves. Soils and Foundations. 56(2), 291-300. https://doi.org/10.1016/j.sandf.2016.02.011

Yang, X., Vanapalli, S. K., 2024. Mechanical behavior of unsaturated soils from suction-controlled ring shear tests. Engineering Geology, 341, 107695. https://doi.org/10.1016/j.enggeo.2024.107695

Yao, L., Alves, R., Vanapalli, S., Gitirana Jr., G., 2024. Models for considering the thermo-hydro-mechanical-chemo effects on soil-water characteristic curves. Geosciences. 14(2), 38. https://doi.org/10.3390/geosciences14020038

Zhai, Q., Xiang, K., Rahardjo, H., Satyanaga, A., Dai, D., Gong, W., Zhao, X., 2023. A new domain model for estimating water distribution in soil pores during the drying and wetting processes. Engineering Geology. 322, 107180. https://doi.org/10.1016/j.enggeo.2023.107180

Zhang, L., Chen, Q., 2005. Predicting bimodal soil-water characteristic curves. Journal of Geotechnical and Geoenvironmental Engineering. 131(5), 666-670. https://doi.org/10.1061/(ASCE)1090-0241(2005)131:5(666)

Zhao, Y., Rahardjo, H., Satyanaga, A., Zhai, Q., He, J., 2023. A general best-fitting equation for the multimodal soil–water characteristic curve. Geotechnical and Geological Engineering, 41(5), 3239-3252. https://doi.org/10.1007/s10706-023-02447-z

CHAPTER 4

A simple model for the estimation of the bimodal SWCC of highly weathered tropical soils[2]

Abstract. The soil-water characteristic curve (SWCC) of highly weathered tropical (i.e., lateritic) soils is often bimodal, with distinct drainage suction ranges associated with the macrostructure and the microstructure. The nature of bimodal behavior is commonly attributed to fine particle aggregations that affect soil fabric and its pore-size distribution. This paper presents a simple model to predict the SWCC of bimodal lateritic soils based on the SWCC parameters from the Gitirana-Fredlund fitting equation. The model was developed based on nonlinear regression analyses and using a soil database consisting of 15 remolded and 25 undisturbed soils. The database contains routine geotechnical data, including index properties, grain-size distribution (GSD) curves, and drying SWCCs. The findings suggest that porosity, liquid limit, relative aggregation, and GSD parameters allow a relatively accurate estimation of the parameters of the SWCCs present in the database. The R^2 values obtained were 0.89 for remolded soils and 0.92 for undisturbed materials. The liquid limit was found to be more strongly associated with SWCC parameters describing water adsorption, while the other variables are strongly related to capillarity storage parameters.

Key words: *pore-size distribution, particle-size distribution, pedotransfer function, water retention curve, lateritic soils.*

[2] The content of this chapter is a journal paper currently under review

4.1 Introduction

Highly weathered tropical soils, also identified as lateritic soils, often exhibit bimodal soil-water characteristic curves (SWCC) due to the presence of aggregations of fine particles that produce a unique structure with dual porosity. The behavior of such soils is difficult to be explained using traditional approaches. Considering that the SWCC is the most important information for describing the hydromechanical behavior of unsaturated soils (Fredlund, 2000) and the difficulties in obtaining data measured in the field or in the laboratory (Vanapalli et al., 1999; Fredlund et al., 2012), various modeling techniques have been established to interpret and predict unimodal curves (Arya and Paris, 1981; Burger and Shackelford, 2001; Fredlund et al., 2002; Aubertin et al., 2003; Johari et al., 2006; Phoon et al., 2010; Wang et al., 2017; Han et al., 2019; Alves et al., 2020; Li and Vanapalli, 2021). Only few models have been developed for bimodal soils (Satyanaga et al., 2013; Hassan et al., 2022; Pereira et al., 2023).

The model developed by Satyanaga et al. (2013) assumes that the SWCC shape follows a lognormal distribution. Regression analyses were performed by the authors on 26 soils to determine the SWCC parameters based on characteristics of the grain size distribution (GSD) curve, saturated gravimetric water content, and dry density. The bimodal behavior observed in these soils was attributed to GSD discontinuity and particle aggregation was not considered because the model was not developed specifically for tropical soils. The model proposed by Hassan et al. (2022) is a modification of the Arya and Paris (1981) model, with the α parameter calibrated to 90 soil samples from a specific region in Italy. Significant differences between the predicted and measured α parameter were noted. However, the models by Satyanaga et al. (2013) and Hassan et al. (2022) do

not incorporate information related to soil microstructure and particle aggregation, making them inadequate for tropical soils with a double structure. Pereira et al. (2023) developed a model based on Artificial Neural Networks (ANN) using 55 tropical soils from Brazil. In terms of performance, this model was able to provide reasonable results with R^2 of 0.68. Unfortunately, this ANN model does not offer significant insights into the fundamental relationships between input and output parameters.

This paper proposes a simple prediction model for bimodal lateritic soils based on physical relationships between soil parameters. The model relies solely on information extracted from the GSD curves and index properties, resulting in simple implementation that can be readily used in geotechnical engineering practice.

4.2 Database of tropical bimodal soils

This study is based on a bimodal soils database comprising 40 materials, which was compiled from previously published data (Table 4.1). The database was divided into two sets, accordingly to specimen condition, namely: remolded or undisturbed. This separation was deemed necessary as the pore structure of these bimodal soils is significantly more variable and is easily affected by disturbance, especially at the macropore level (Georgetti, 2014; Otálvaro et al., 2016; Araújo, 2019; Oliveira et al., 2022).

Table 4.1 Main characteristics of the soils investigated

Reference	Soil ID*	USCS (disaggregated / aggregated)	w_L	w_P	ρ_d (g/cm³)	n	n_m	n_M	ψ_{b1} (kPa)	ψ_{res1} (kPa)	ψ_{b2} (kPa)	ψ_{res2} (kPa)	θ_{sat}	θ_{res1}	θ_{b2}	θ_{res2}
Araújo (2019)	1R1	CL / CL	33	22	1.79	0.333	0.204	0.131	49.2	406.3	7000	30000	0.34	0.21	0.20	0.02
	1R2				1.35	0.500	0.193	0.342	1.7	12.3	10360	22154	0.54	0.23	0.16	0.02
	1R3				1.08	0.600	0.174	0.411	1.7	8.6	10360	22154	0.59	0.22	0.12	0.02
Feuerharmel et al. (2006)	2R1	MH / MH	74	57	1.08	0.624	0.572	0.052	90.0	126.5	1000	80000	0.62	0.57	0.57	0.07
	2R2				1.08	0.623	0.526	0.097	14.0	28.0	1400	80000	0.62	0.54	0.51	0.09
	2U				1.07	0.625	0.489	0.136	2.2	7.2	2559	50006	0.63	0.51	0.47	0.05
	3R1	CH / SC	56	34	1.40	0.500	0.407	0.092	9.0	15.1	6500	50000	0.50	0.43	0.38	0.06
	3R2				1.35	0.519	0.383	0.136	4.5	8.2	2768	50000	0.52	0.39	0.38	0.04
	3U				1.40	0.500	0.380	0.120	3.0	5.9	2800	45000	0.50	0.41	0.36	0.01
Furman (2019)	4R	SC / SC	30	NP	1.31	0.492	0.170	0.322	5.2	155.0	6999	23000	0.49	0.18	0.16	0.02
	4U				1.32	0.487	0.169	0.318	10.0	66.0	3428	18044	0.49	0.17	0.17	0.02
	5U	ML / SM	29	23	1.25	0.528	0.260	0.268	9.1	100.3	5461	25054	0.53	0.26	0.26	0.05
Otálvaro et al. (2016)	6R1	ML / SC	40	28	1.42	0.451	0.302	0.126	3.2	9.6	10000	25000	0.43	0.34	0.27	0.05
	6R2				1.50	0.448	0.324	0.123	3.4	12.0	10340	30077	0.45	0.36	0.28	0.05
	6R3				1.33	0.479	0.284	0.157	5.4	10.3	11053	35237	0.41	0.32	0.25	0.04
Guimarães (2002)	7U	CL / SC	38	28	1.05	0.615	0.246	0.369	2.7	5.6	4100	15000	0.62	0.28	0.20	0.04
	8U	CL / SC	36	26	1.06	0.611	0.219	0.392	3.0	7.0	7000	12000	0.61	0.28	0.16	0.02
	9U	CL / SC	39	29	1.17	0.559	0.252	0.307	3.7	7.5	5000	16000	0.56	0.27	0.22	0.02
	10U	CL / SM	41	29	1.17	0.559	0.260	0.299	1.9	10.9	7200	12500	0.56	0.30	0.22	0.03
	11U	CL / CL	45	34	1.22	0.556	0.274	0.282	1.8	14.6	8000	10550	0.56	0.30	0.24	0.05
	12U	CL / CL	44	33	1.22	0.535	0.282	0.253	3.2	8.0	7200	10550	0.53	0.35	0.22	0.05
	13U	CL / CL	46	35	1.31	0.517	0.315	0.202	3.0	7.0	7000	12000	0.52	0.37	0.26	0.04
	14U	CL / CL	43	34	1.42	0.471	0.309	0.162	5.0	12.0	1500	5000	0.47	0.36	0.30	0.03

Reference	Soil ID*	USCS (disaggregated / aggregated)	w_L	w_P	ρ_d (g/cm³)	n	n_m	n_M	ψ_{b1} (kPa)	ψ_{res1} (kPa)	ψ_{b2} (kPa)	ψ_{res2} (kPa)	θ_{sat}	θ_{res1}	θ_{b2}	θ_{res2}
Oliveira et al. (2022)	15R	MH / MH	51	38	1.43	0.524	0.386	0.154	12.0	200.0	11000	20000	0.54	0.41	0.37	0.05
	15U				1.12	0.630	0.343	0.287	3.0	65.0	12000	20000	0.63	0.35	0.33	0.03
	16R	SC / SC	20	13	1.96	0.333	0.184	0.156	6.0	13.0	10000	21000	0.34	0.21	0.15	0.01
	16U				1.45	0.500	0.110	0.380	1.5	24.0	18000	28000	0.49	0.13	0.09	0.00
	17R	SC / SC	31	15	1.86	0.286	0.194	0.116	15.0	140.0	1000	6000	0.31	0.20	0.19	0.02
	17U				1.58	0.412	0.062	0.338	0.6	30.0	2000	5000	0.40	0.06	0.06	0.00
Machado (2020)	18U	NA	NA	NA	1.23	0.552	0.193	0.359	1.2	15.0	12000	21000	0.55	0.25	0.13	0.02
	19U	NA	NA	NA	1.25	0.541	0.195	0.346	1.1	15.0	9000	18000	0.54	0.24	0.15	0.02
	20U	NA	NA	NA	1.26	0.537	0.228	0.309	0.7	9.0	6000	16000	0.54	0.29	0.17	0.02
	21U	NA	NA	NA	1.39	0.495	0.235	0.260	1.5	9.0	5800	15000	0.49	0.30	0.17	0.02
	22U	NA	NA	NA	1.30	0.526	0.224	0.302	0.8	9.0	5800	14000	0.53	0.30	0.15	0.02
	23U	NA	NA	NA	1.37	0.510	0.240	0.270	0.6	9.0	4800	14000	0.51	0.32	0.16	0.02
Benatti and Miguel (2013)	24U	CL / CL	48	37	0.95	0.682	0.296	0.386	3.5	6.0	9000	13000	0.68	0.36	0.23	0.03
	25U	MH / MH	50	38	1.13	0.632	0.292	0.340	5.0	9.0	5800	11000	0.63	0.34	0.25	0.02
	26U	CL / CL	49	35	1.20	0.608	0.313	0.295	5.0	9.2	7000	13000	0.61	0.37	0.26	0.02
Castro et al. (2022)	27R	ML / ML	45	30	1.29	0.533	0.293	0.240	1.0	12.3	3788	25036	0.53	0.36	0.24	0.04
	27U				1.25	0.548	0.228	0.320	4.0	584.0	4548	26000	0.55	0.23	0.23	0.04

(*) R and U stand for remolded and undisturbed, respectively.

Legend: NA - not available, USCS – Unified soil classification system.

All materials selected include the following information: index properties, grain-size distribution curves, and well-defined drying SWCCs. The disaggregated (i.e., with deflocculant) and aggregated (i.e., without deflocculant) GSD curves are shown in Figs. 4.1a and 4.1b, respectively. The drying SWCCs of the remolded and undisturbed soils are shown, respectively, in Figs. 4.2a and 4.2b, along with their fitted curves using the Gitirana Jr. and Fredlund (2004) equation.

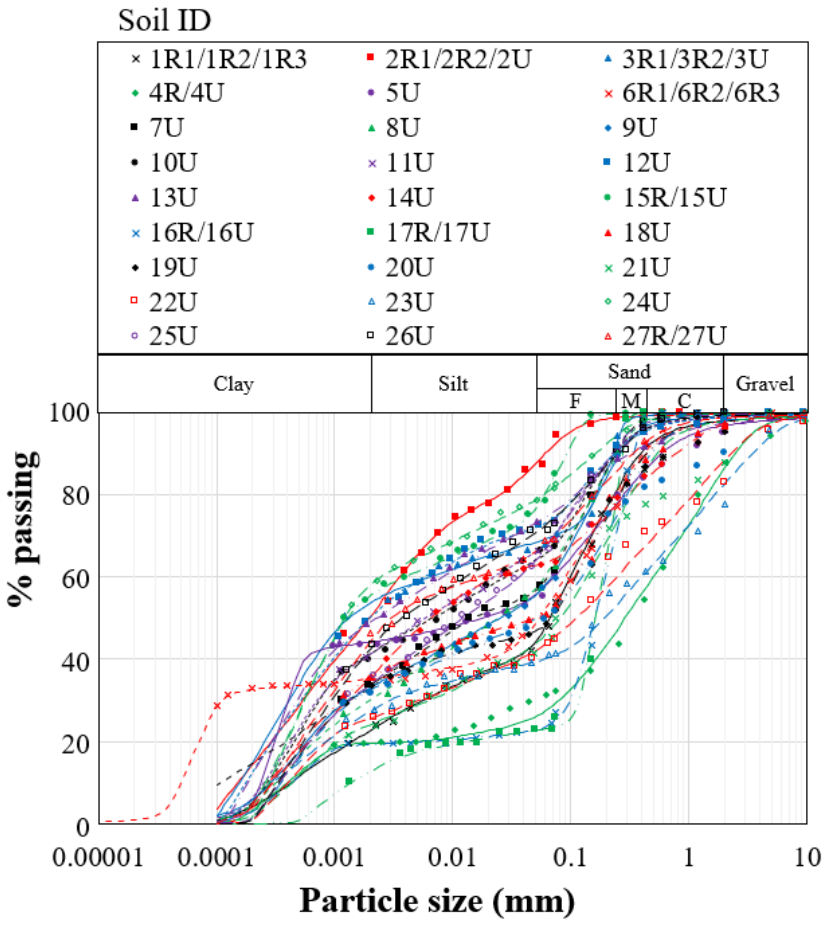

(a)

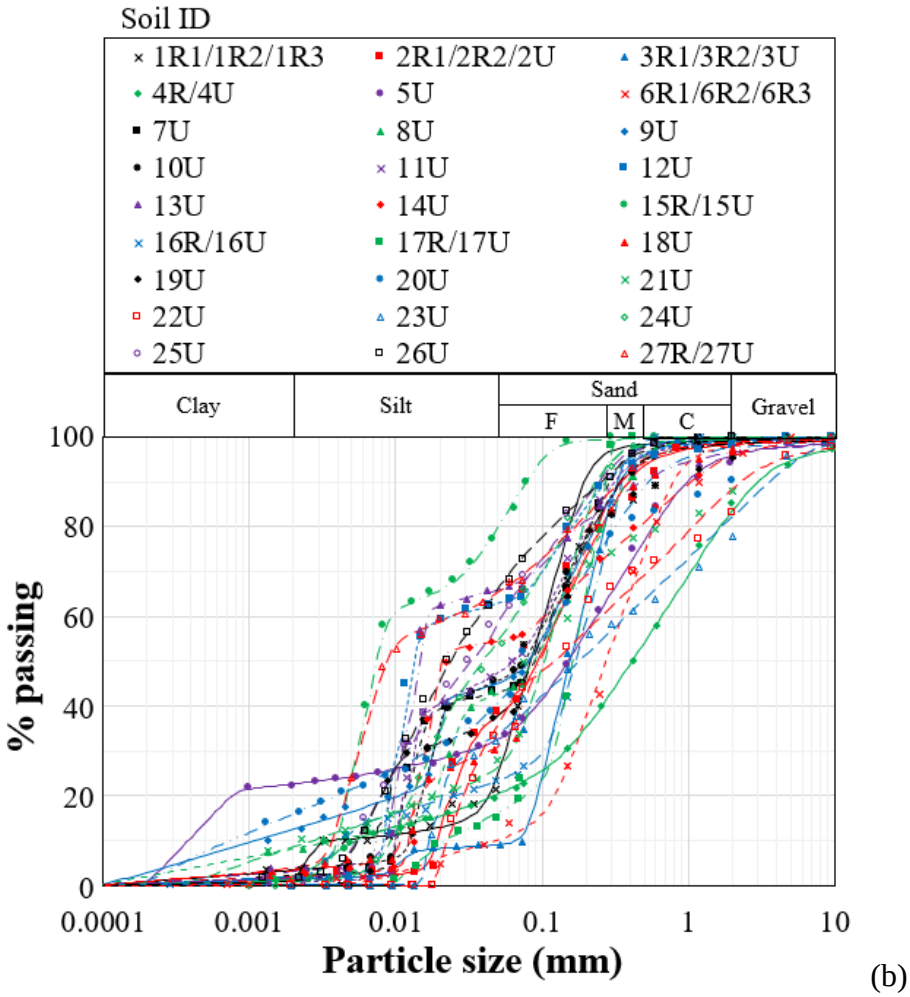

(b)

Figure 4.1 Tropical bimodal soils database: grain-size distributions obtained with (a) deflocculant (i.e., disaggregated); and (b) without deflocculant (i.e., aggregated)

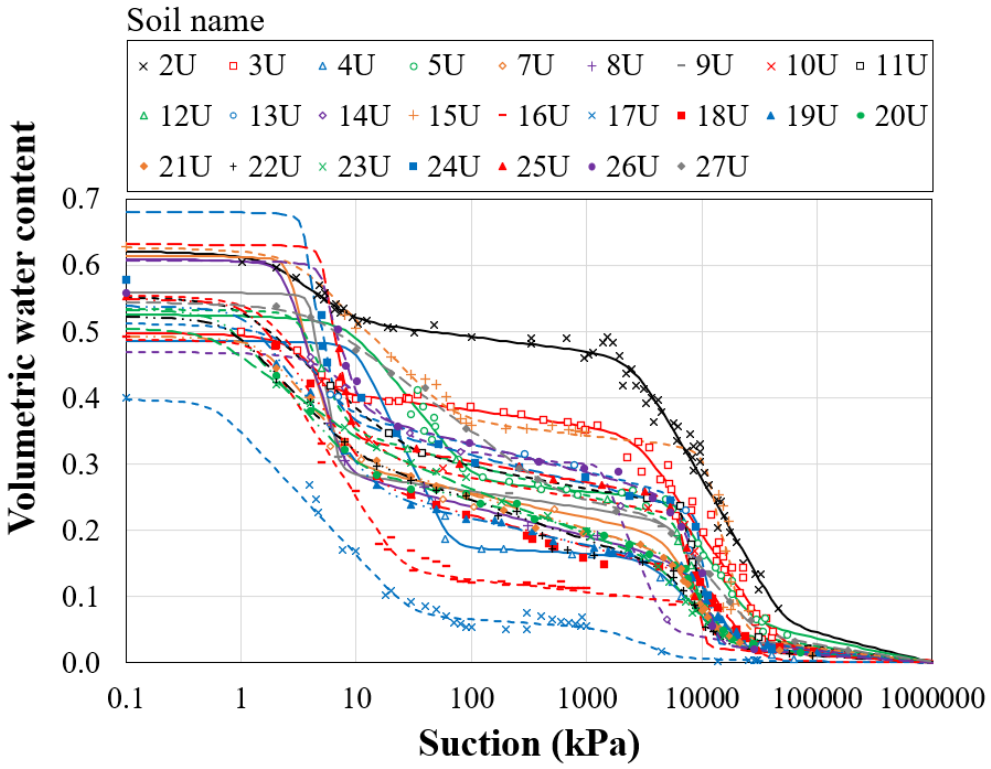

(a)

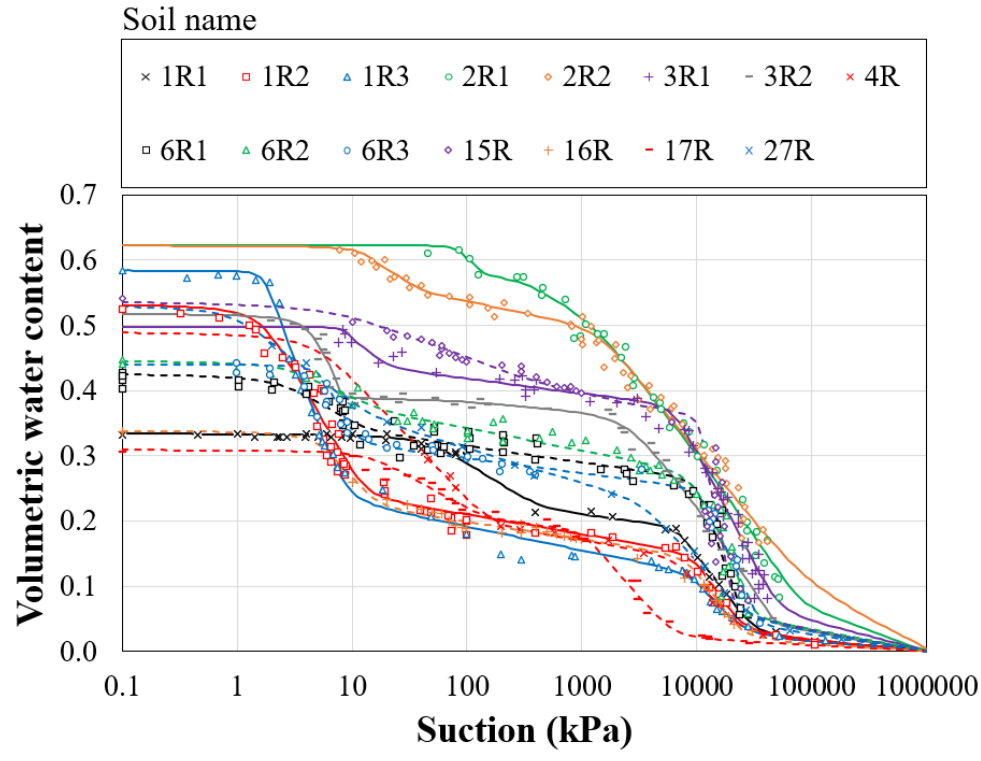

(b)

Figure 4.2 Tropical bimodal soils database: SWCCs of: a) 25 undisturbed soils; and (b) 15 remolded soils

4.3 Modeling methodology

The proposed model was developed using the parameters from the Gitirana Jr. and Fredlund (2004) equation for bimodal soils (Eq. 4.1), namely: first air-entry value (ψ_{b1}), first residual suction (ψ_{res1}), second air-entry value ψ_{b2}, and second residual suction (ψ_{res2}). Each of these parameters has its respective correspondent in terms of water content. As a result, the proposed model comprises the following four pairs of coefficients: [ψ_{b1}, θ_{sat}], [ψ_{res1}, θ_{res1}], [ψ_{b2}, θ_{b2}], and [ψ_{res2}, θ_{res2}]. This equation was chosen because its parameters are independent and correspond to the main physical and geometric features of the SWCC (Fig. 4.3a). The Gitirana-Fredlund equation, presented in terms of volumetric water content, is as follows:

$$\theta = \left[\frac{S_1 - S_2}{1+\left(\psi / \sqrt{\psi_{b1}\psi_{res1}}\right)^{d_1}} + \frac{S_2 - S_3}{1+\left(\psi / \sqrt{\psi_{res1}\psi_{b2}}\right)^{d_2}} + \frac{S_3 - S_4}{1+\left(\psi / \sqrt{\psi_{b2}\psi_{res2}}\right)^{d_3}} + S_4 \right] n \qquad (4.1)$$

$$S_i = \frac{\tan\theta_i (1+r_i^2)\ln(\psi/\psi_i^a)}{1-r_i^2\tan^2\theta_i} + (-1)^i \times \frac{(1+\tan^2\theta_i)}{(1-r_i^2\tan^2\theta_i)} \sqrt{r_i^2 \ln^2(\psi/\psi_i^a) + \frac{a^2(1-r_i^2\tan^2\theta_i)}{(1+\tan^2\theta_i)}} + S_i^a \qquad (4.2)$$

where:

$$i = 1, 2, 3, 4; \theta_i = -(\lambda_{i-1} + \lambda_i)/2; r_i = \tan[(\lambda_{i-1} - \lambda_i)/2]; \lambda_0 = 0;$$
$$\lambda_i = \arctan\{(S_i^a - S_{i+1}^a)/[\ln(\psi_{i+1}^a/\psi_i^a)]\}; S_1^a = 1; S_2^a = S_{res1};$$
$$S_3^a = S_b; S_4^a = S_{res2}; S_5^a = 0; \psi_1^a = \psi_{b1}; \psi_2^a = \psi_{res1}; \psi_3^a = \psi_{b2};$$
$$\psi_4^a = \psi_{res2}; \psi_5^a = 10^6; d_j = 2\exp[1/\ln(\psi_{j+1}^a/\psi_j^a)]; j = 1, 2, 3.$$

n is the porosity; S_{b1} is the degree of saturation corresponding to the air-entry values of the macropores; S_{res1} is the residual degree of saturation of the macropores; S_{b2} is the degree of saturation corresponding to the air-entry values of the micropores; S_{res2} is the residual

degree of saturation of the micropores; and *a* defines the sharpness of the transitions of the SWCC bending points.

The eight parameters needed to describe the SWCC were estimated using nonlinear correlation equations based on basic soil data summarized in Table 4.1. Pearson and Spearman correlations and nonlinear regression analyses were performed using the parameters from the GSD curves and index properties to obtain the best variables to describe the SWCC parameters. For each parameter, two to three variables were used in the multiple regression analyses. Additionally, the physical meaning of the variables was considered to eliminate outlier predictors. The quality of the proposed regressions was evaluated using the coefficient of determination (R^2) and the root-mean-square error (RMSE).

A modified version of the Gitirana Jr. and Fredlund (2004) equation was used to fit the GSD curves and for the calculation of several parameters describing the GSD that were used in the regression exercises. The fitted GSD curves were discretized into segments, based on nine positions (i.e., D_{10}, D_{20}, …, D_{90}). The GDS equation employed is as follows:

$$P = \left[\frac{P_1 - P_2}{1 + \left(\sqrt{d_1 d_2} / d \right)^{c_1}} + \frac{P_2 - P_3}{1 + \left(\sqrt{d_2 d_3} / d \right)^{c_2}} + \frac{P_3 - P_4}{1 + \left(\sqrt{d_3 d_4} / d \right)^{c_3}} + P_4 \right] \tag{4.3}$$

$$P_i = \frac{\tan\theta_i (1 + r_i^2) \ln(d_1 / d)}{1 - r_i^2 \tan^2 \theta_i} + (-1)^i \times \frac{(1 + \tan^2 \theta_i)}{(1 - r_i^2 \tan^2 \theta_i)} \sqrt{r_i^2 \ln^2 (d_1 / d) + \frac{a_i^2 (1 - r_i^2 \tan^2 \theta_i)}{(1 + \tan^2 \theta_i)}} + P_i^a \tag{4.4}$$

where:

$$i = 1, 2, 3, 4; \theta_i = -(\lambda_{i-1} + \lambda_i)/2; r_i = \tan[(\lambda_{i-1} - \lambda_i)/2]; \lambda_0 = 0;$$
$$\lambda_i = \arctan\{(P_i^a - P_{i+1}^a)/[\ln(d_i^a / d_{i+1}^a)]\}; P_1^a = 1; P_2^a = P_2; P_3^a = P_3;$$
$$P_4^a = P_4; P_5^a = 0; d_1^a = d_1; d_2^a = d_2; d_3^a = d_3; d_4^a = d_4;$$
$$d_5^a = d_5 = \textit{particle size at } P_5^a; d_j = 2\exp[1/\ln(d_i^a / d_{i+1}^a)]; j = 1, 2, 3.$$

Since some GSD curves present a bimodal shape, two variables representing the main slopes were created: C_{u1} and C_{u2}. These two coefficients of uniformity are defined as follows and are depicted in Fig. 4.3b.

$$C_{u1} = \delta_{g1} / \delta_{g2} \tag{4.5}$$

$$C_{u2} = \delta_{g3} / \delta_{g4} \tag{4.6}$$

Alves et al. (2024) demonstrated that the difference between aggregated and disaggregated GSDs can be used to quantify the effect of particle aggregation on the pore-size distribution and the SWCC through a parameter referred to as the relative aggregation (*RA*). Such parameter was introduced by Otálvaro et al. (2015) and represents the ratio between the difference of the area above the aggregated and disaggregated GSD curves and the area above the disaggregated GSD curve (Fig. 4.3c):

$$RA = \frac{\sum_{i=1}^{n} \left(P_{A,i} - P_{D,i}\right) \log\left(\delta_i / \delta_{i+1}\right)}{\sum_{i=1}^{n} P_{D,i} \log\left(\delta_i / \delta_{i+1}\right)} \tag{4.7}$$

where: n is the number of measured points of the grain-size distribution curve; $P_{A,i}$ is the accumulate retained percentage of the aggregated grain-size distribution at point i; $P_{D,i}$ is the accumulate retained percentage of the disaggregated grain-size distribution at point i; and δ_i is the particle diameter at point i.

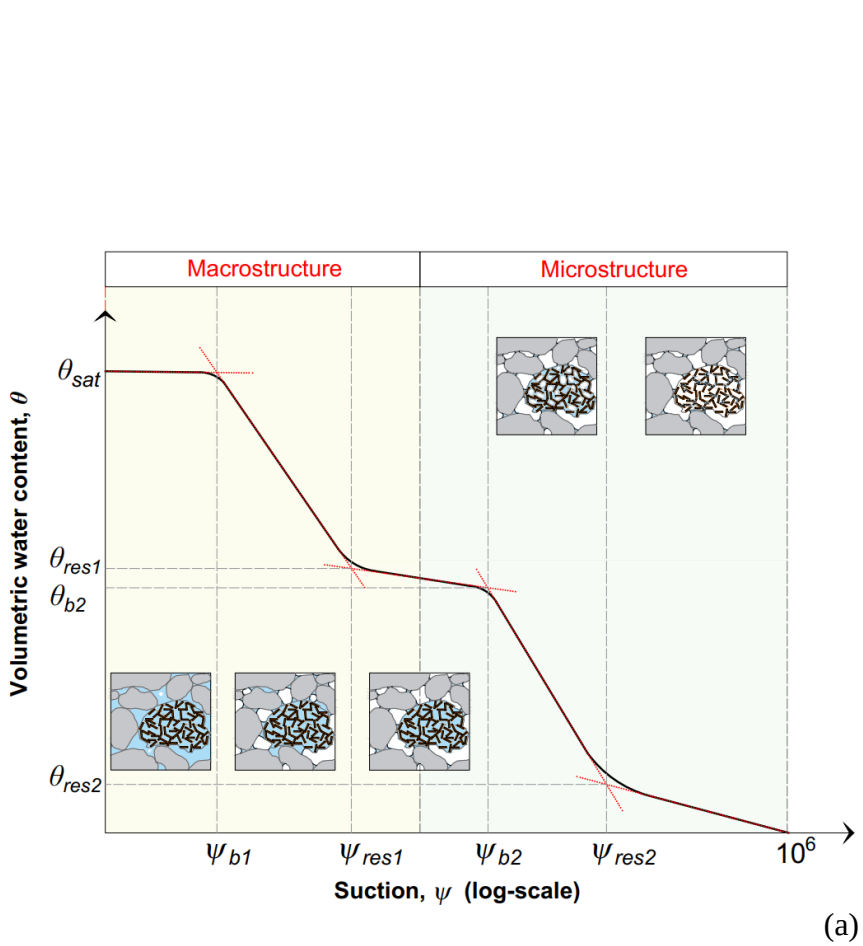

(a)

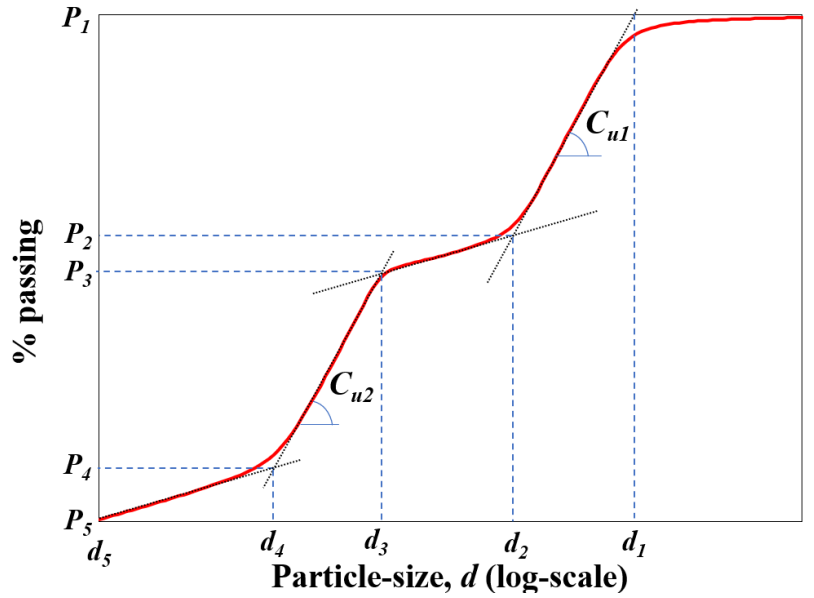

(b)

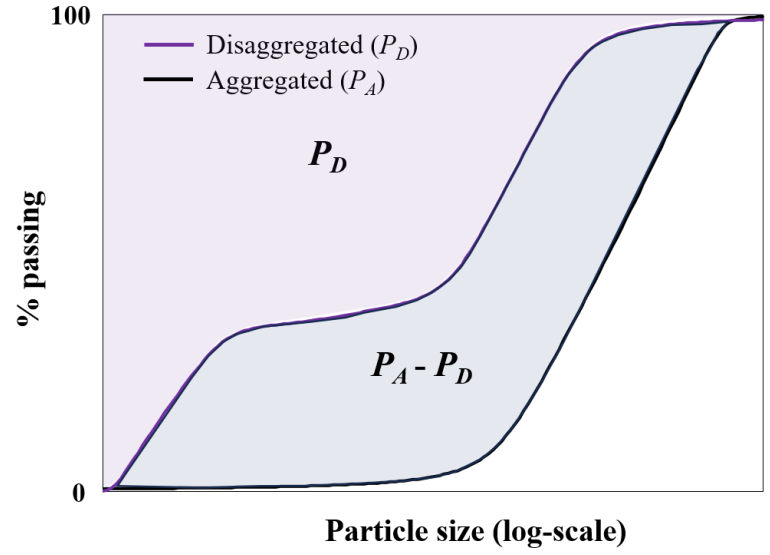

(c)

Figure 4.3 Model parameters: a) bimodal SWCC; b) GSD; and c) relative aggregation

4.4 Results

4.4.1 Volumetric water contents: θ_{res1}, θ_{b2}, and θ_{res2}

The first residual volumetric water content, θ_{res1}, corresponds to pendular water within the macropores. The parameter θ_{res1} has a wide range of values in the employed soil's database, corresponding to degrees of saturations between 16% and 92%. The regression exercises indicated that the parameters n, RA and w_L provide satisfactory descriptions of θ_{res1}, as follows:

$$\theta_{res1,r} = \left[2.524 - 7.493 \times \left(n \times w_L\right)^3 + 0.456 \times \ln^2 RA\right]^{-1} \quad (4.8)$$

$$\theta_{res1,u} = 0.461 - 3.71 \times 10^{-2} / \left(n \times w_L\right) + 9.29 \times 10^{-2} \times RA^3 \quad (4.9)$$

where: subscripts r and u stand for remolded and undisturbed, respectively.

Figures 4.4a and 4.4b present the fitted surfaces and the measured data. Equations 4.8, and 4.9 show good performance, with R^2 values of 0.95, and RMSE of 0.028 followed by an R^2 of 0.78 and RMSE of 0.041, for the remolded and undisturbed materials, respectively. The degree of aggregation, RA, is the main property controlling the residual volumetric water content of macropores, as expected. It is interesting to note that for soils that approach a unimodal structure, RA tends to zero and θ_{res1} becomes null. This is a theoretically expected limit of the proposed equations because it means that there is no water retention within the micropores when the soil has no aggregations. The variables n and w_L were found to have similar effects on θ_{res1}.

The second volumetric water content, θ_{b2}, corresponds to the stage at which the macropores are completely desaturated. The parameter θ_{b2} indicates the amount of water stored in the microstructure and is, in most cases, very similar to θ_{res1}. Compressible

aggregated may lead to larger differences between θ_{b2} and θ_{res1}. The parameter θ_{b2} has a range of values similar to that of θ_{res1}, with corresponding degrees of saturations between 15% and 92%. The following equations were proposed to estimate θ_{b2} of remolded and undisturbed materials, respectively:

$$\theta_{b2,r} = \exp\left[-0.695 + 3.154 \times \left(n \times w_L\right)^{2.5} - 0.388 / RA^{0.5}\right] \quad (4.10)$$

$$\theta_{b2,u} = 0.30 + 2.33 \times \left(n \times w_L\right)^{3} - 6.14 \times 10^{-2} / RA^{1.5} \quad (4.11)$$

Figures 4.4c and 4.4d present the fitted surfaces and the measured data for θ_{b2}. The proposed equations resulted in R^2 values of 0.93 and 0.77, and RMSE values of 0.034 and 0.041, for the remolded and undisturbed materials, respectively. These equations have a structure that is consistent with that of the equations proposed for θ_{res1} because similar physical relationships control θ_{b2}.

The second residual volumetric water content, θ_{res2}, corresponds largely to water stored in the form of adsorbed films on the clay particles forming aggregates. This interpretation of the nature of θ_{res2}, as well previous studies relating Atterberg limits to adsorption (Zhou and Lu, 2021), justifies the emergence of w_L and RA as the main variables controlling θ_{res2}. The values of θ_{res2} observed in the bimodal soil's database correspond to degrees of saturations up to 15 and 10%, for the remolded and undisturbed datasets, respectively. Based on the observed dataset, the following fitting equations were developed:

$$\theta_{res2,r} = 6.50 \times 10^{-4} + 10.33 \times 10^{-2} \times w_L - 1.19 \times 10^{-3} / RA \quad (4.12)$$

$$\theta_{res2,u} = 3.66 \times 10^{-2} - 5.47 \times 10^{-3} / w_L + 1.47 \times 10^{-2} RA \quad (4.13)$$

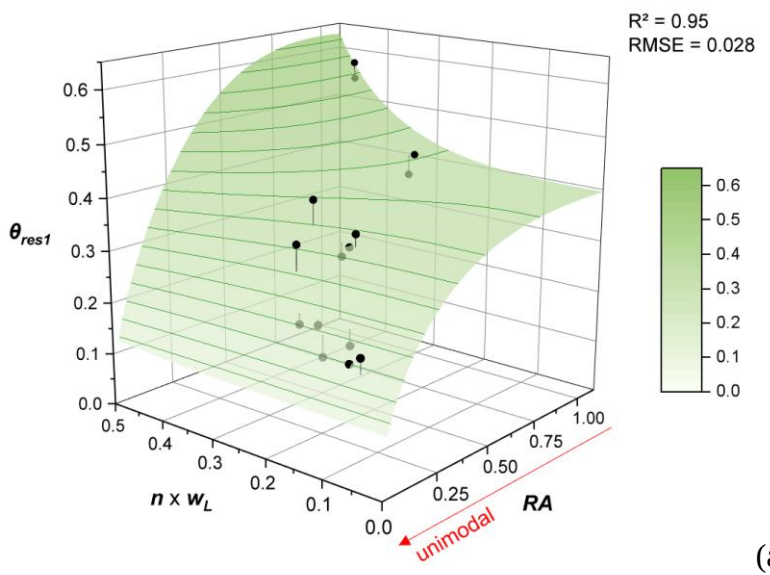
R² = 0.95
RMSE = 0.028
θres1
n x wL
RA
unimodal

(a)

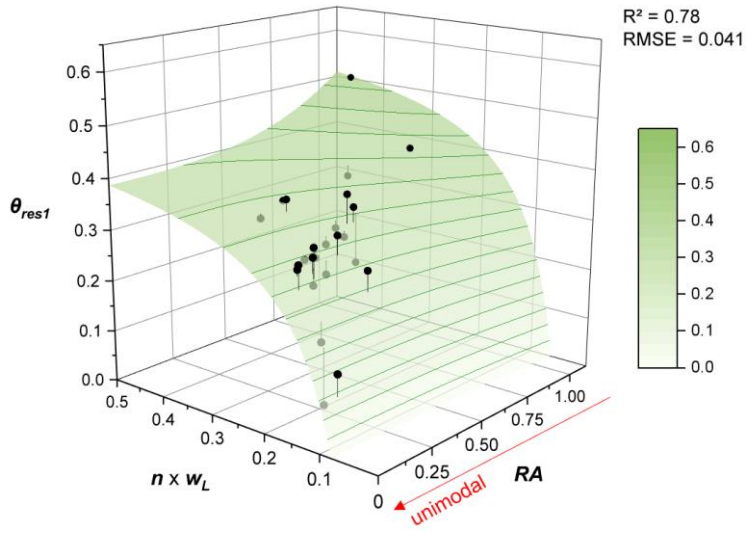
R² = 0.78
RMSE = 0.041
θres1
n x wL
RA
unimodal

(b)

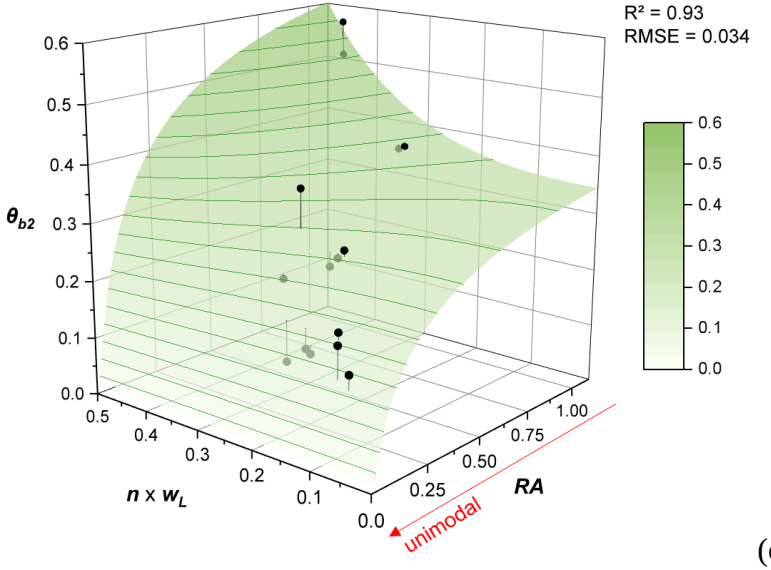
R² = 0.93
RMSE = 0.034
θb2
n x wL
RA
unimodal

(c)

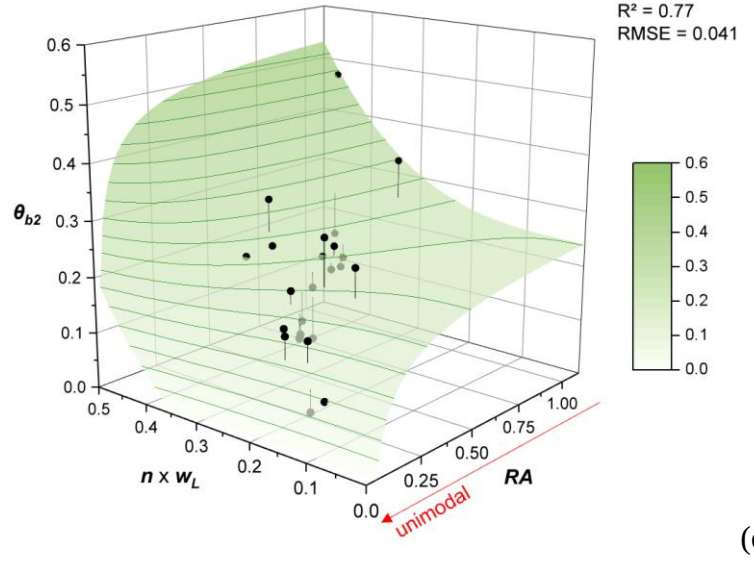
R² = 0.77
RMSE = 0.041
θb2
n x wL
RA
unimodal

(d)

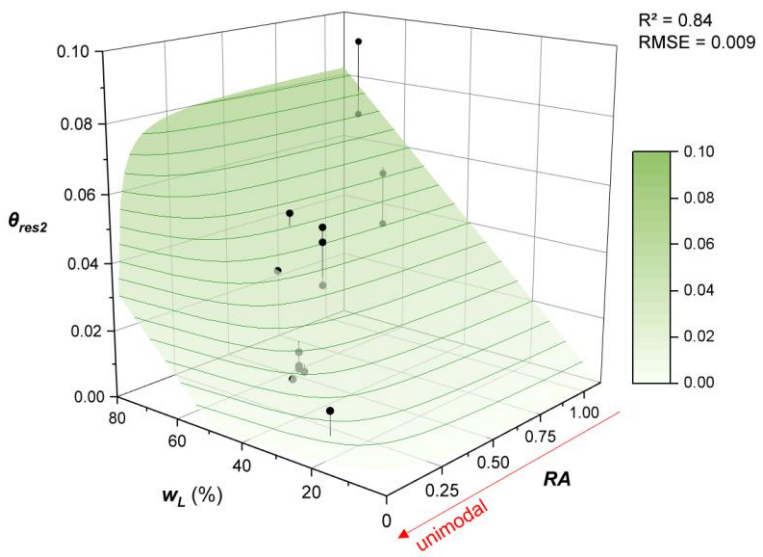

(e)

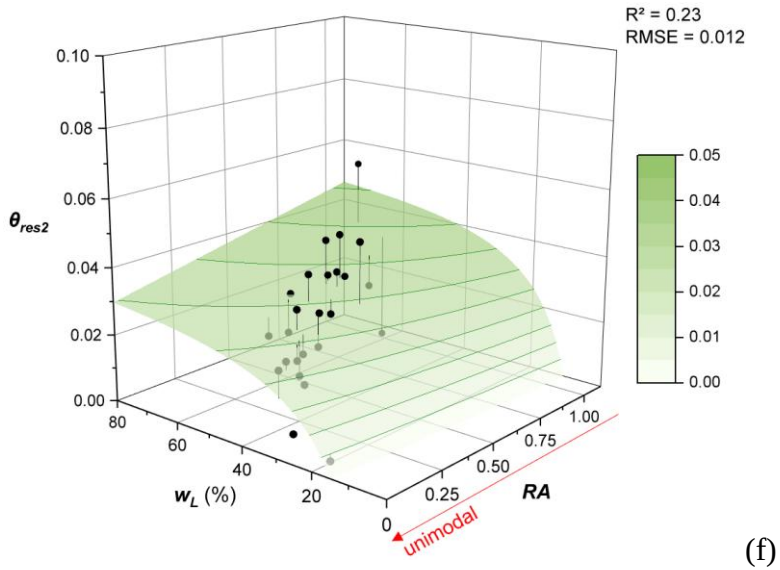

(f)

Figure 4.4 Modeling of water content parameters: a) θ_{res1} of remolded soils; b) θ_{res1} of undisturbed soils; c) θ_{b2} of remolded soils; d) θ_{b2} of undisturbed soils; e) θ_{res2} of remolded soils; and f) θ_{res2} of undisturbed soils

The fitting surfaces illustrated in Figs. 4.4e and 4.4f were generated using Eqs. 4.12 and 4.13, respectively for the remolded and undisturbed materials. The first figure indicates that w_L has a linear relationship with θ_{res2}, while *RA* values greater than 0.25 have little effect over θ_{res2}. This situation is the opposite for the undisturbed materials, where *RA* has a linear effect on θ_{res2} while w_L has minor influence when its value is higher than 50%.

4.4.2 Suction parameters for the macropore zone: first air-entry value and first residual suction, ψ_{b1} and ψ_{res1}

The first air-entry value, ψ_{b1} is the suction at which the largest macropores start to desaturate. For the soils investigated herein, ψ_{b1} varied two orders of magnitude, from values less than 1 to almost 100 kPa. Equations 4.14 and 4.15 and Figs. 4.5a and 4.5b represent ψ_{b1} for the remolded and undisturbed datasets, respectively.

$$\psi_{b1,r} = \left[-0.801+1.305\times n_M^{0.5} - 1.829/\ln(D_{10,A})\right]^{-1} \quad (4.14)$$

$$\psi_{b1,u} = \left[-1.623+2.370\times n_M^{0.5} - 3.891/\ln(D_{10,A})\right]^{-1} \quad (4.15)$$

where: n_M is the macroporosity calculated from the difference between the porosity (n) and the microporosity (n_m) (i.e., $n_M = n - n_m$).

The microporosity nm can be calculated using the following equations:

$$n_{m,r} = \left[2.87 - 4.94\times\left(n\times w_L\right)^2 + 0.54\times\ln^2 RA\right]^{-1} \quad (4.16)$$

$$n_{m,u} = 0.24+1.17\times\left(n\times w_L\right)^2 - 0.012/RA \quad (4.17)$$

Equations 4.14 and 4.15 resulted in a moderate performance, with R^2 of 0.62 and 0.26 and RMSE of 0.739 and 0.700, respectively for the remolded and undisturbed soils. From Figs. 4.5a and 4.5b it can be observed that as the macroporosity reduces and the

degree of aggregation decreases, ψ_{b1} increases significantly. As a result, the values of ψ_{b1} approach the air-entry value of the micropores, ψ_{b2}, when soils are denser and less aggregated. The parameter D_{10} is often associated with the air-entry value (ψ_b) of unimodal soils (Aubertin et al., 2003; Gallage and Uchimura, 2010; Rahardjo et al., 2012; Sakaki et al., 2014; Wang et al., 2017). Here, for lateritic soils, the parameter $D_{10,A}$ was also found to influence ψ_{b1}, but its relevance is more pronounced only for low values of n_M.

The relatively inferior performance of Eq. 4.15 can be attributed to the fact that the n_M is a variable obtained from estimations through the difference between n and n_m calculated using Eqs. 4.16 and 4.17. Thus, the errors from the calculation of n_m are propagated to the prediction of the ψ_{b1}.

The first residual suction, ψ_{res1}, may be associated with the point in which the liquid phase within the macropores becomes discontinuous. According to the measured data, the values of ψ_{res1} range from 5.9 to 584.0 kPa. Equations 4.18 and 4.19 describe ψ_{res1} for the remolded and undisturbed materials, respectively, and Figs. 4.5c and 4.5d illustrate the corresponding fitting surfaces.

$$\psi_{res1,r} = -568.90 + 85.0/n - 188.02 \times \ln(\delta_{g2,A}) \quad (4.18)$$

$$\psi_{res1,u} = -62.2 + 35.5/n + 1.2/\delta_{g2,A} \quad (4.19)$$

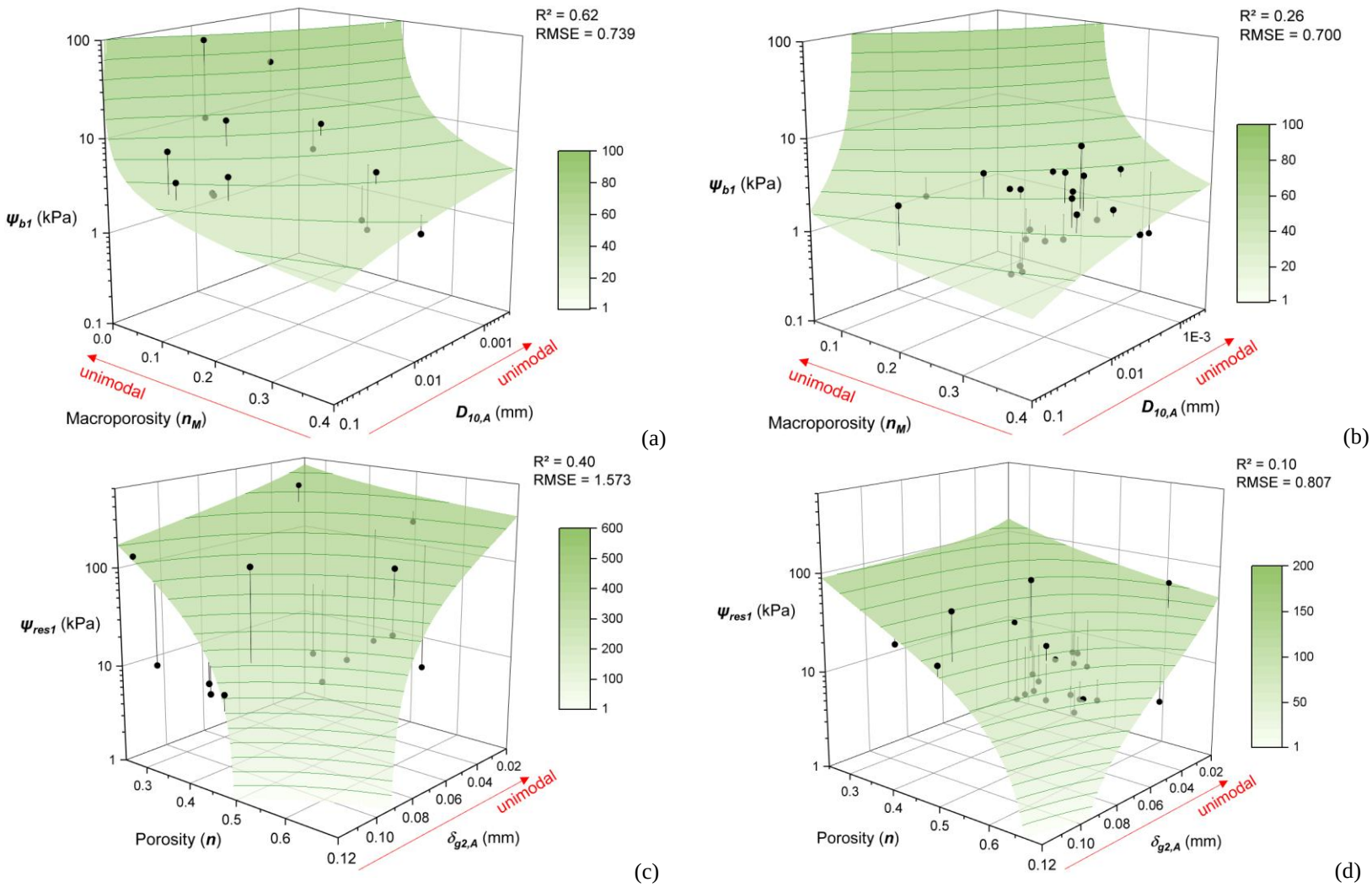

Figure 4.5 Modeling of macrostructure suction parameters: a) ψ_{b1} of remolded soils; b) ψ_{b1} of undisturbed soils; c) ψ_{res1} of remolded soils; and d) ψ_{res1} of undisturbed soils

Few variables presented correlation with ψ_{res1}, especially for the undisturbed soils. The ψ_{res1} is related to the smallest macropores, where water adsorption may be more relevant. This explains the choice of a variable that broadly represents soil structure (i.e., porosity). Lower values of n are related to higher values of ψ_{res1}. This means that compressing pores results in an increase in matric suction, as expected and in accordance with the capillary model. A similar situation occurs with $\delta_{g2,A}$ because the reduction in the particle size for a given porosity increases the number of existing pores while reducing their sizes, resulting in increased the matric suction towards to values close to the second air-entry value, ψ_{b2}. The fitting surfaces indicate that a combination of high values of $\delta_{g2,A}$ along large n values yield ψ_{res1} in a range that is commonly observed in sands (~ 10 kPa).

4.4.3 Suction parameters for the micropore zone: second air-entry value and second residual suction, ψ_{b2} and ψ_{res2}

The parameter ψ_{b2} represents the suction in which the largest micropores begin to desaturate. For the selected bimodal tropical soils, ψ_{b2} ranges from 1,000 to 18,000 kPa, with an average value around 6,500 kPa. The first residual volumetric water content, θ_{res1}, was selected as a descriptor parameter of ψ_{b2}, since it indirectly includes the information about the aggregations, mineralogy, and soil structure. Equations 4.20 and 4.21 and the fitting surfaces shown in Figs. 4.6a and 4.6b present the proposed relationships:

$$\psi_{b2,r} = 19664 - 4.29\times10^{5} D_{10,D}^{1.5} - 3.16\times10^{4} \times \theta_{res1}^{1.5} \quad (4.20)$$

$$\psi_{b2,u} = 5810 - 41.1\times\ln\left(\theta_{res1}\right)/\theta_{res1} - 8.83\times10^{10} \times D_{10,D}^{2.5} \quad (4.21)$$

These equations resulted in R^2 of 0.73 and 0.48 and RMSE of 0.314 and 0.485, respectively for the remolded and undisturbed soils. The parameter D_{10}, used in Eqs. 4.20

and 4.21, is often related to the air-entry value in unimodal soils. However. in this case, it is used to physically relate the microstructure to the disaggregated GSD.

The second residual suction, ψ_{res2} refers to the suction at which most of the water within the microstructure (i.e., within aggregations) has been drained and the remaining water is in the form of adsorbed films. At this suction, the liquid phase within the microstructure is discontinuous. The ψ_{res2} values commonly range from 5,000 to 80,000 kPa. The following equations were developed to describe ψ_{res2} of remolded and undisturbed materials:

$$\psi_{res2,r} = 13164 + 0.27 \times (C_{u2,D})^3 + 39972 \times RA \quad (4.22)$$

$$\psi_{res2,u} = 7227 + 12943 / \ln(C_{u2,D}) + 30909 \times RA^3 \quad (4.23)$$

Equations 4.22 and 4.23 demonstrated reasonable ability to fit the measured data, resulting in an R^2 of 0.95 and RMSE of 0.310 for the remolded materials and an R^2 of 0.61 and RMSE of 0.636 for undisturbed soils. Figures 4.6c and 4.6d illustrate the fitted and measured data. The aggregations in lateritic soils are comprised of arrangements of clay particles. These arrangements are somewhat quantified by the disaggregated GSD and by the microporosity. Disaggregated GSD curves showing well-graded clay particle sizes (i.e., higher values of $C_{u2,D}$) favor the formation of smaller pores. The existence of more aggregations, represented by an increase in *RA*, seems to also influence ψ_{res2}, despite the physical relationship between variables being not as clear. Based on the studies regarding adsorbed water (Tuller et al., 1999; Frydman and Baker, 2009; Tokunaga, 2011; and Dolinar, 2014), better results could be achieved if mineralogical characteristics, such as the specific surface area or the cation exchange capacity, were incorporated directly into the analyses.

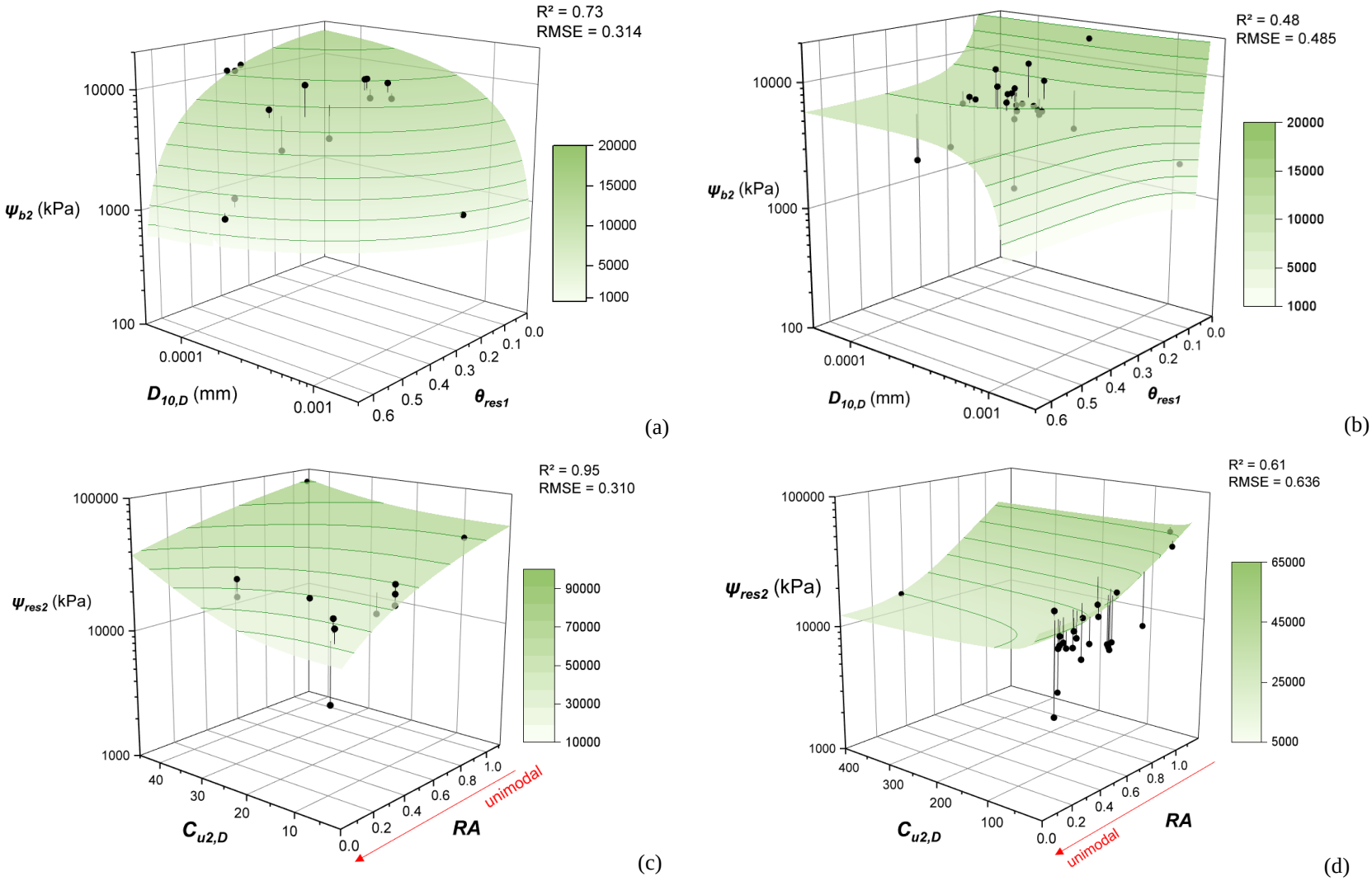

Figure 4.6 Modeling of microstructure suction parameters: a) ψ_{b2} of remolded soils; b) ψ_{b2} of undisturbed soils; c) ψ_{res2} of remolded soils; and d) ψ_{res2} of undisturbed soils

4.5 Prediction of SWCCs

Equations 4.8 to 4.23 were applied to all soils in the database to obtain the predicted SWCCs. The results are shown in Figs. 4.7 and 4.8 respectively for the remolded and undisturbed materials. The results for materials 1R1, 3R1, 6R1, 6R2, 6R3, 2U, 5U, 9U, 11U, 12U, and 20U are in excellent agreement with the measured SWCCs. In general, the predictions are satisfactory, with a slightly better performance in the micropores zone. There are three main factors that may have negatively impacted the results within the macropores zone: difficulties in obtaining a well-defined SWCC around the first air-entry value (Figs. 4.8b to 4.8e); specimens not reaching full saturation prior testing; and higher susceptibility of changes in the macropores due to external factors, such as sampling or specimen preparation.

The relative aggregation *RA* and the liquid limit w_L, presented in Eqs. 4.8-4.13, 4.16-4.17, and 4.22-4.23 are the main parameters responsible to represent the microstructure. This makes sense from a physicochemical perspective because the *RA* depicts the degree of aggregation of the soil. Thus, the more aggregated a soil is, the higher its microporosity is. The w_L indirectly incorporates the information about clay mineralogy and activity. Hence, for two soils comprised of the same predominant clay particles, the one with higher w_L exhibits a superior percentage of clay minerals and, therefore, greater microporosity. Considering also the relationship between w_L and the specific surface area (Tuller et al., 1999; Mitchell and Soga, 2005; Revil and Lu, 2013), it is hypothesized that w_L represents water stored through adsorption mechanism.

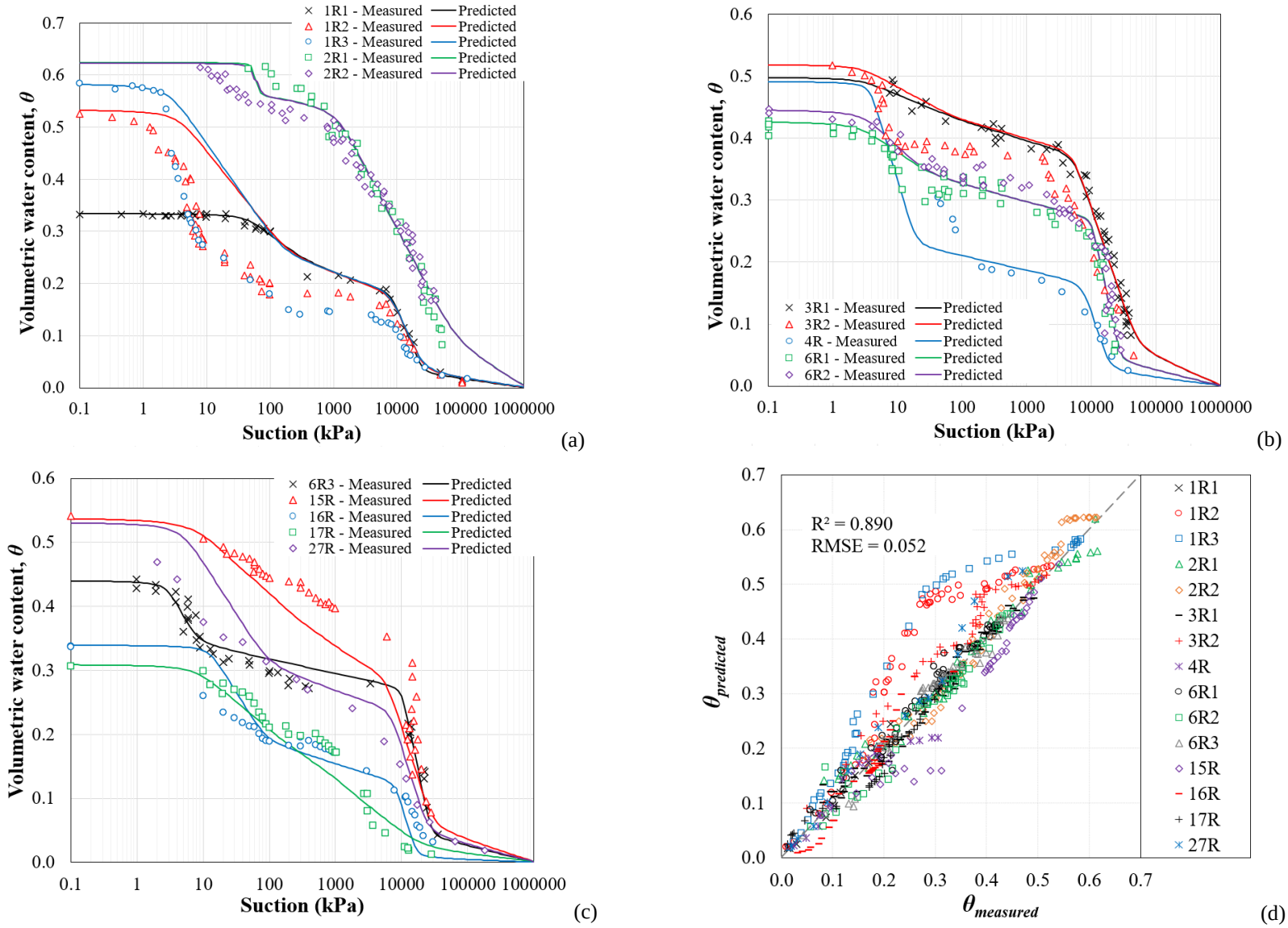

Figure 4.7 Predicted SWCCs for remolded soils: a) 1R1 to 2R2; b) 3R1 to 6R2; c) 6R3 to 27R; and d) measured and predicted volumetric water content

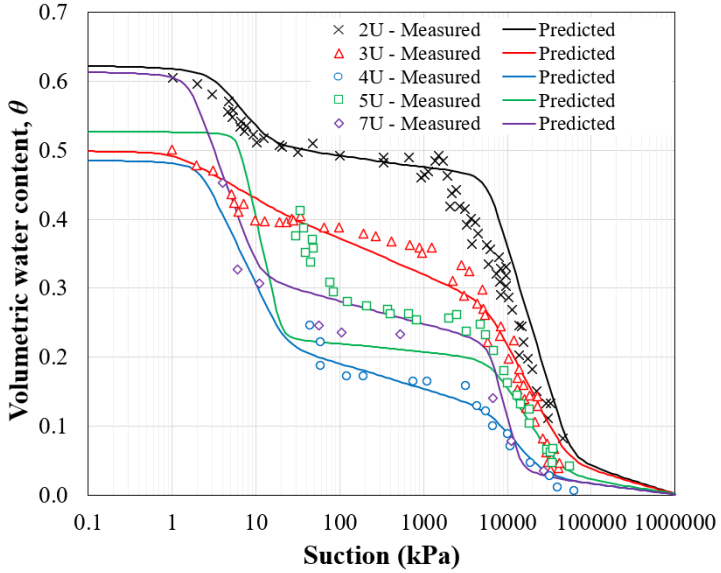
2U - Measured
3U - Measured
4U - Measured
5U - Measured
7U - Measured
Predicted
Volumetric water content, θ
Suction (kPa)
0.0
0.1
0.2
0.3
0.4
0.5
0.6
0.7
0.1
1
10
100
1000
10000
100000
1000000

(a)

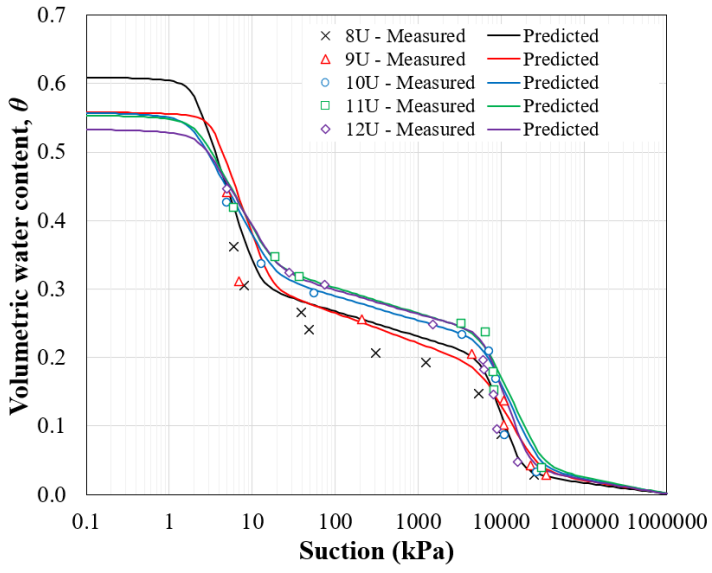
8U - Measured
9U - Measured
10U - Measured
11U - Measured
12U - Measured
Predicted
Volumetric water content, θ
Suction (kPa)
0.0
0.1
0.2
0.3
0.4
0.5
0.6
0.7
0.1
1
10
100
1000
10000
100000
1000000

(b)

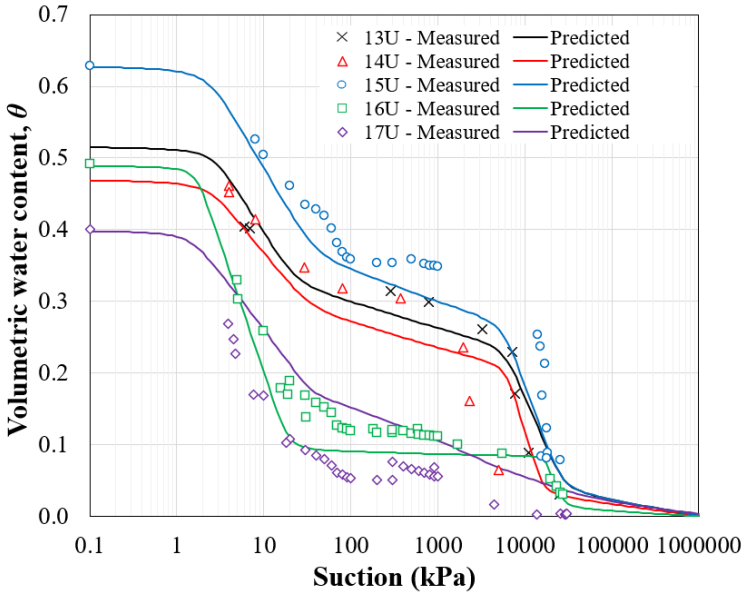
13U - Measured
14U - Measured
15U - Measured
16U - Measured
17U - Measured
Predicted
Volumetric water content, θ
Suction (kPa)
0.0
0.1
0.2
0.3
0.4
0.5
0.6
0.7
0.1
1
10
100
1000
10000
100000
1000000

(c)

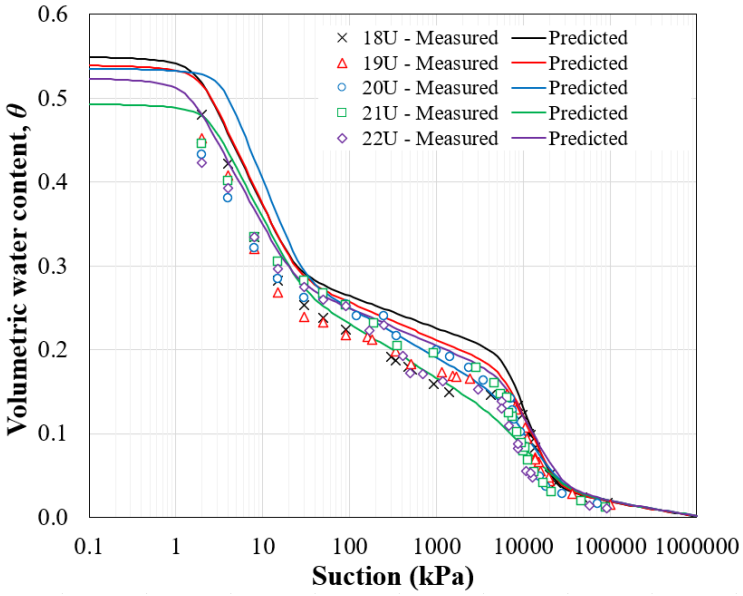
18U - Measured
19U - Measured
20U - Measured
21U - Measured
22U - Measured
Predicted
Volumetric water content, θ
Suction (kPa)
0.0
0.1
0.2
0.3
0.4
0.5
0.6
0.1
1
10
100
1000
10000
100000
1000000

(d)

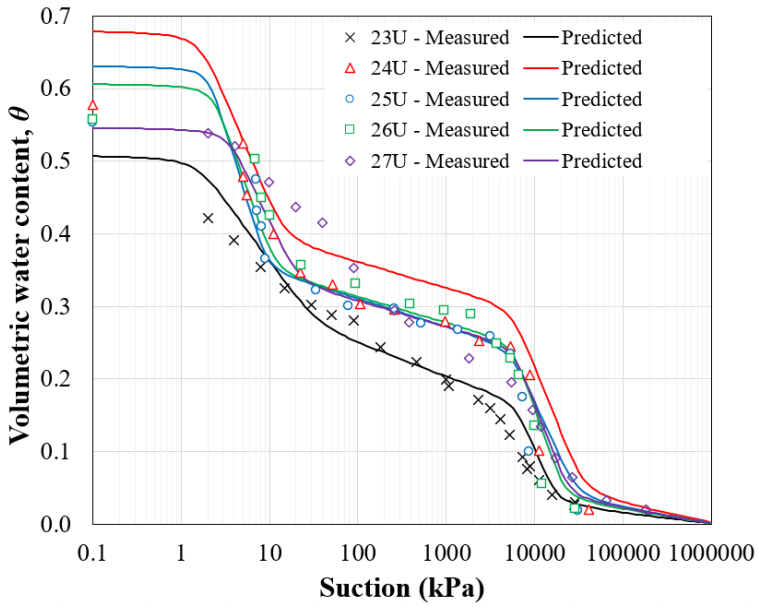

(e)

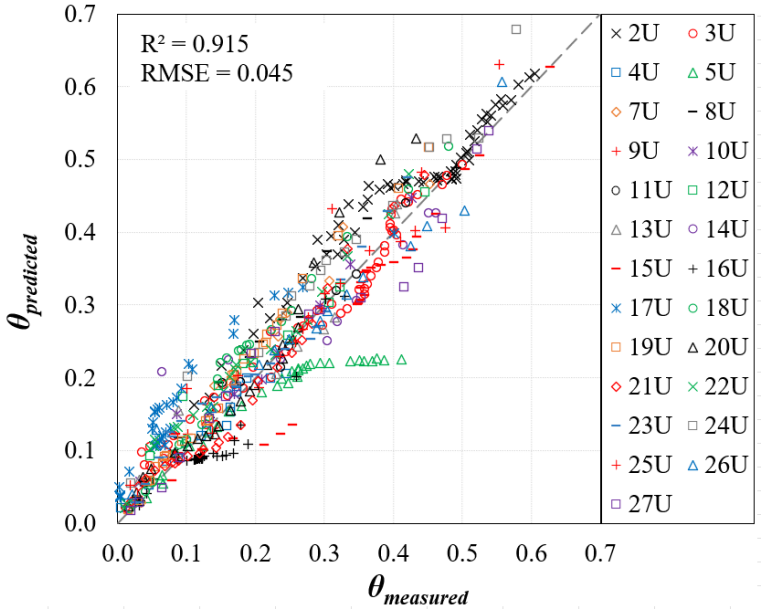

(f)

Figure 4.8 Predicted SWCCs for undisturbed soils: a) 2U to 7U; b) 8U to 12U; c) 13U to 17U; d) 18U to 22U; e) 23U to 27U; and f) measured and predicted volumetric water content

A potential improvement of the model performance within the micropores would be using GSD curves that are more representative of the presence of aggregations. Souza (2020) demonstrated that the physical and chemical dispersion used in sedimentation analysis are unable to fully disaggregate bimodal lateritic soils. Moreover, most of the sedimentation analysis results in GSD that ends in particle sizes far from 0% passing, meaning that many particle sizes are not captured in such test. Consequently, the *RA* parameter can be considered a rough estimative of degree of aggregation. On the other hand, incorporating more sophisticated techniques to calculate *RA* would require information that would make unfeasible the use of the proposed model in geotechnical engineering practice.

The overall performance of the prediction model was evaluated using the coefficient of determination (R^2) and the Root-Mean-Square-Error (RMSE). For the remolded soils, the values of R^2 and RMSE ranged from 0.837 to 0.996 and 0.007 to 0.115, respectively. For the undisturbed materials, these parameters varied from 0.832 to 0.994 and 0.016 to 0.078, respectively. The general performance of the proposed model is depicted in Figs. 4.7d and 4.8f. The overall values of R^2 (0.890 for remolded and 0.915 for undisturbed) and RMSE (0.052 for remolded and 0.045 for undisturbed) indicate a good agreement with the measured data.

4.6 Conclusions

A simple model to estimate the SWCC of bimodal lateritic soils has been proposed in this study. Only routine geotechnical information such as index properties and GSD curves were used in multiple regression analyses for the development of equations to predict the parameters from the Gitirana Jr. and Fredlund (2004) model.

The relationship between the aggregated and disaggregated GSD curves was evaluated using a parameter named relative aggregation (*RA*), which proved to be significant for the predictions of several SWCC parameters, especially for those related to the microstructure. Due to its physical significance for the bimodal structure (i.e., a decreasing *RA* means that the soil is reducing its amount of micropores of all sizes), the parameter *RA* is related to capillarity component of the matric suction.

The use of the liquid limit (w_L) to quantify microstructure parameters proved to be effective. It is known that the liquid limit is related to the specific surface area of the clay minerals and, therefore, has a clear relationship with adsorbed water.

The proposed model demonstrated strong performance, achieving an overall R^2 exceeding 0.89. These results contribute to our understanding of soil structure and its relationship with the SWCC in bimodal tropical soils. Notably, the proposed approach has significant potential for integrating unsaturated soil mechanics into geotechnical practice.

References

Alves, R. D., Gitirana Jr. G. F. N., Vanapalli, S. K., 2020. Advances in the modeling of the soil–water characteristic curve using pore-scale analysis. Computers and Geotechnics. 127, 103766. https://doi.org/10.1016/j.compgeo.2020.103766

Alves, R. D., Gitirana Jr. G. F. N., Vanapalli, S. K., 2024. Modeling the Bimodal SWCC of Highly Weathered Tropical Soils Using Grain-Size Information. Under review.

Araújo, A.G., 2019. Uso de microtomografia e porosimetria para análise de estrutura bimodal de um latossolo vermelho reconstituído. Doctoral Thesis: Department de Civil and Environmental Engineering, Universidade Federal de Goiás, 82p.

Arya, L. M., Paris, J. F., 1981. A physicoempirical model to predict the soil moisture characteristic from particle-size distribution and bulk density data. Soil Science Society of America Journal, 45, 1023-1030. https://doi.org/10.2136/sssaj1981.03615995004500060004x

Aubertin, M., Mbonimpa, M., Bussière, B., Chapuis, R. P., 2003. A model to predict the water retention curve from basic geotechnical properties. Canadian Geotechnical Journal. 40, 1104-1122. https://doi.org/10.1139/t03-054

Benatti, J. C. B., Miguel, M. G., 2013. A proposal of structural models for colluvial and lateritic soil profile from southwestern Brazil on the basis of their collapsible behavior. Engineering Geology. 153, 1-11. https://doi.org/10.1016/j.enggeo.2012.11.003

Burger, C.A., Shackelford, C.D., 2001. Soil-water characteristic curves and dual porosity of sand–diatomaceous earth mixtures. Journal of Geotechnical and Geoenvironmental Engineering, 127(9), 790–800. https://doi.org/10.1061/(ASCE)1090-0241(2001)127:9(790)

Castro, M. D., Oliveira, V. N., Mascarenha, M. M. A., Gitirana Jr., G. F. N., Luz, M. P., 2022. Análise das curvas características solo-água de amostras remoldada e indeformada de um solo laterítico não saturado. In: Anais do XX COBRAMSEG, Campinas.

Dolinar, B., 2014. Prediction of the soil-water characteristic curve based on the specific surface area of fine-grained soils. Bulletin of Engineering Geology and the Environment. 74, 697-703. https://doi.org/10.1007/s10064-014-0664-y

Feuerharmel, C., 2007. Estudo da resistência ao cisalhamento e da condutividade hidráulica de solos coluvionares não saturados da Formação Serra Geral. Doctoral Thesis: Graduate program in civil engineering. Universidade Federal do Rio Grande do Sul, 330p.

Fredlund, D. G., 2000. The implementation of unsaturated soil mechanics into geotechnical engineering. Canadian Geotechnical Journal, 37, 963-986. https://doi.org/10.1139/t00-026

Fredlund, M. D., Wilson, G. W., Fredlund, D. G., 2002. Use of the grain-size distribution for estimation of the soil-water characteristic curve. Canadian Geotechnical Journal, 39, 1103-1117. https://doi.org/10.1139/t02-049

Fredlund, D. G., Rahardjo, H., Fredlund, M. D., 2012. Unsaturated soil mechanics in engineering practice. New Jersey: John Wiley & Sons.

Frydman, S., Baker, R., 2009. Theoretical soil-water characteristic curves based on adsorption, cavitation, and a double porosity model. International Journal of Geomechanics. 9(6), 250-257. https://doi.org/10.1061/(ASCE)1532-3641(2009)9:6(250)

Furman, J., 2019 Avaliação da resistência ao cisalhamento de solos tropicais brasileiros não saturados da Serra do Mar – Trecho PR-SP. Master Thesis: Graduate program in civil engineering - construction, Universidade Federal do Paraná, 113p.

Gallage, C. P. K., Uchimura, T., 2010. Effects of dry density and grain size distribution on soil-water characteristic curves of sandy soils. Soils and Foundations. 50(1), 161-172. https://doi.org/10.3208/sandf.50.161

Georgetti, G. B., 2014. Deformabilidade e resistência de um solo laterítico não saturado. Doctoral Thesis: Graduate program in geotechnics, Universidade de São Paulo, 130p.

Gitirana Jr., G.F.N., Fredlund, D.G., 2004. Soil-water characteristic curve equation with independent properties. Journal of Geotechnical and Geoenvironmental Engineering, 130(2), 209-212. https://doi.org/10.1061/(ASCE)1090-0241(2004)130:2(209)

Guimarães, R.C., 2002. Análise das propriedades e comportamento de um perfil de solo laterítico aplicada ao estudo do desempenho de estacas escavadas. Master Thesis: Departament de Civil and Environmental Engineering, Universidade de Brasília, 183 f.

Han, Z., Vanapalli, S.K., Zou, W-L., 2019. Simple approaches for modeling hysteretic soil water retention behavior. Journal of Geotechnical and Geoenvironmental Engineering, 145(10). https://doi.org/10.1061/(ASCE)GT.1943-5606.0002148

Hassan, S. B. M., Dragonetti, G., Comegna, A., Sengouga, A., Lamaddalena, N., Coppola, A. 2022. A bimodal extension of the ARYA&PARIS approach for predicting hydraulic properties of structured soils. Journal of Hydrology, 610. https://doi.org/10.1016/j.jhydrol.2022.127980

Johari, A., Habibagahi, G., Ghahramani, A., 2006. Prediction of soil-water characteristic curve using genetic programming. Journal of Geotechnical and Geoenvironmental Engineering, 132(5), 661-665. https://doi.org/10.1061/(ASCE)1090-0241(2006)132:5(661)

Li, Y., Vanapalli, S., K., 2021. A novel modeling method for the bimodal soil-water characteristic curve. Computers and Geotechnics, 138, 104318. https://doi.org/10.1016/j.compgeo.2021.104318

Machado, R. R., 2020. Ensaios pressiométricos para estimativa de parâmetros de resistência e deformabilidade de um perfil de solo tropical. Master Thesis: Departament de Civil and Environmental Engineering, Universidade Federal de Goiás, 203p.

Mitchell, J. K., Soga, K., 2005. Fundamentals of Soil Behavior. New Jersey: Wiley.

Oliveira, A. D., Pelaquim, F. G. P., Zanin, R. F. B., Melo, T. R., Filho, J. T., Andrello, A. C., Teixeira, R. S., 2022. The structure of tropical lateritic soils as an impacting factor in the shape of soil-water characteristic curves. Soils and Rocks. 45(2). https://doi.org/10.28927/SR.2022.070521

Otálvaro, I. F., Cordão Neto, M. P., Caicedo, B., 2015. Compressibility and microstructure of compacted laterites. Transportation Geotechnics. 5, 20-34. https://doi.org/10.1016/j.trgeo.2015.09.005

Otálvaro, I. F., Cordão-Neto, M. P., Delage, P., Caicedo, B., 2016. Relationship between soil structure and water retention properties in a residual compacted soil. Engineering Geology. 205, 73-80. https://doi.org/10.1016/j.enggeo.2016.02.016

Pereira, S., Silva Jr., A., Mendes, T., Gitirana Jr., G., Alves, R. D., 2023. Prediction of Soil–Water Characteristic Curves in Bimodal Tropical Soils Using Artificial Neural Networks. Geotechnical Geological Engineering. https://doi.org/10.1007/s10706-023-02716-x

Phoon, K-K., Anastasia, S., Quek, S-T., 2010. Probabilistic analysis of soil-water characteristic curves. Journal of Geotechnical and Geoenvironmental Engineering, 136(3), 445-455. https://doi.org/10.1061/~ASCE!GT.1943-5606.0000222

Rahardjo, H. Satyanaga, A., D'Amore, G. A. R., Leong, E. C., 2012. Soil–water characteristic curves of gap-graded soils. Engineering Geology. 125, 102-107. https://doi.org/10.1016/j.enggeo.2011.11.009

Revil, A., Lu, N., 2013. Unified water isotherms for clayey porous materials. Water Resources Research. 49, 5685–5699. https://doi.org/10.1002/wrcr.20426

Sakaki, T., Komatsu, M., Takahashi, M., 2014. Rules-of-thumb for predicting air-entry value of disturbed sands from particle size. Soil Science Society of America Journal. 78(2), 454-464. https://doi.org/10.2136/sssaj2013.06.0237n

Satyanaga, A., Rahardjo, H., Leong, E. C., Wang, J. Y, 2013. Water characteristic curve of soil with bimodal grain-size distribution. Computers and Geotechnics. 48, 51-61. https://doi.org/10.1016/j.compgeo.2012.09.008

Souza, J. C., 2020. Avaliação da relação entre a curva granulométrica e a curva característica solo-água para um solo residual bimodal sob diferentes graus de desagregação. Master Thesis: Department de Civil and Environmental Engineering, Universidade Federal de Goiás.

Tokunaga, T. K., 2011. Physicochemical controls on adsorbed water film thickness in unsaturated geological media. Water Resources Research. 47, 12p. https://doi.org/10.1029/2011WR010676

Tuller, M., Or, D., Dudley, L. M., 1999. Adsorption and capillary condensation in porous media: Liquid retention and interfacial configurations in angular pores. Water Resources Research. 35(7), 1949-1964. https://doi.org/10.1029/1999WR900098

Vanapalli, S.K., Fredlund, D.G., Pufahl, D.E., 1999. The influence of soil structure and stress history on the soil-water characteristics of a compacted till. Géotechnique, 49, 143-159. https://doi.org/10.1680/geot.1999.49.2.143

Wang, J-P., Hu, N., François, B., Lambert, P., 2017. Estimating water retention curves and strength properties of unsaturated sandy soils from basic soil gradation parameters. Water Resources Research. 53, 6069-6088. https://doi.org/10.1002/2017WR020411

Zhou, B., Lu, N., 2021. Correlation between Atterberg limits and soil adsorptive water. Journal of Geotechnical and Geoenvironmental Engineering, 147(2), 04020162. https://doi.org/10.1061/(ASCE)GT.1943-5606.0002463

CHAPTER 5

Modeling the unsaturated shear strength of bimodal lateritic soils[3]

Abstract. In this study, a theoretical framework is developed for considering the evolution of soil structure for bimodal lateritic soils for providing rational explanation of the shear strength variation with respect to two independent stress state variables: net normal stress and matric suction. Most importantly, explanation with respect to shear strength contribution associated with matric suction, ϕ^b which is greater than the effective friction angle ϕ' in some lateritic soils is explained. In addition, a new model is built for predicting the shear strength that is consistent with the proposed theoretical framework. It is assumed that the changes of soil structure associated with suction affect the ϕ'. The ϕ^b was found to have two zones: one encompassing the macropores where capillarity controls water retention and another related to the micropores in which both capillarity and adsorption are relevant. A contractive shear band in drained tests is hypothesized to explain the contribution of matric suction towards shear strength that is greater than that of the net normal stress (i.e., $\phi^b > \phi'$). The proposed model is simple and provides superior comparisons to the 16 existing models including two equations developed for bimodal soils, with a coefficient of determination (R^2) greater than 0.95.

Key words: *unsaturated shear strength, prediction model, soil-water characteristic curve, highly weathered soils*.

[3] The content of this chapter is a journal paper currently under review

5.1 Introduction

The shear strength of unsaturated soils has garnered significant attention from researchers due to its fundamental role in describing soil behavior and its practical implications in the design of several geotechnical infrastructures. Various methods have been proposed to interpret and estimate unsaturated shear strength, particularly for soils with a unimodal pore structure (e.g., Vanapalli et al., 1996; Fredlund et al., 1996; Guan et al., 2010; Naghaded and Toker, 2019). Most of the models available in the literature for predicting the shear strength of unimodal soils are based on the same principles. In general, a constant effective friction angle (ϕ') is assumed, which implies that a soil pore structure is relatively constant. Matric suction (u_a - u_w) is considered either as an independent stress state variable (Fredlund et al., 1978; Toll, 1990; Vanapalli et al., 1996) or as contributing to the effective stress state (Bishop, 1959; Khalili and Khabbaz (1998); Lu et al., 2010). The contribution of matric suction to shear strength is interpreted as being dependent on the capacity of pore-water to transmit the compressive effect of matric suction. That capacity is assumed to the proportional to some measure of particle wet area that varies gradually as the soil desaturates. This approach has proven to be satisfactory for reasonable prediction of shear strength of unsaturated soils with a unimodal pore structure.

The extension of modeling concepts established for unimodal soils with a bimodal pore structure remains a challenge, especially for lateritic soils whose bimodal behavior arises from intense weathering processes. These materials can be found in tropical regions such as the South America, Central and Western Africa, Southeast Asia, and some parts of India and Australia. In Brazil, these soils cover most of the territory (De Medina et al., 2006; Huat et al., 2004), making them especially significant and have a profound influence

in geotechnical engineering practice applications. It is important to note that lateritic soils often occur in thick layers that remain unsaturated throughout the year (Fookes, 1994; Camapum de Carvalho et al., 2023). The pedogenesis of these soils is the result of many cycles of dry and wet seasons marked by abundant annual rainfalls and high temperatures. The resulting leaching, mineral deposition, dehydration and crystallization form a porous structure with clay-sized particles cemented by iron and aluminum oxides and hydroxides known as aggregations (Otálvaro et al., 2015; Oliveira et al., 2022).

The presence of aggregations in lateritic soils plays a crucial role in their behavior. Aggregations confer bimodal structure marked by two dominant pore-sizes. The soil pores within the aggregations are often referred to as micropores (or intra-aggregate pores) and those located outside the aggregations are identified as macropores (or inter-aggregate pores) (Camapum de Carvalho et al., 2023). Particle aggregation is also reflected in the soil-water characteristic curve (SWCC) of lateritic soils, which exhibits two air-entry values and two residual suctions (Camapum de Carvalho and Gitirana Jr., 2021). Particle aggregation results in significant differences between the grain-size distributions (GSD) in the aggregated or disaggregated states (Souza, 2020). Clayey lateritic soils often exhibit high hydraulic conductivity akin to sands (Pereira et al., 2005; Santos and Esquivel, 2018), high void ratios (Ortigão et al., 1996; Miguel and Vilar, 2009), and sometimes unstable cementations leading to collapsible behavior (Vilar and Rodrigues, 2011; Rodrigues et al., 2021).

The behavior of bimodal lateritic soils and the role of soil fabric have been extensively studied under remolded conditions. Several researchers have explored how initial water content during compaction influences micro and macrostructure. While the

microstructure shows minimal sensitivity to changes in water content, the macrostructure can vary significantly. Soils compacted at a water content below optimum tend to develop larger macropores compared to those compacted at water contents above optimum (Marinho et al., 2013; Otálvaro et al., 2016; Lopes et al., 2022), though some studies suggest the opposite (Santos and Esquivel, 2018). Increasing compaction energy generally reduces both the total pore volume and the size of macropores, while the microstructure remains largely unaffected (Otálvaro et al., 2015; Araújo, 2019). Furthermore, the level of disturbance and the application of effective stresses tend to close macropores, with the microstructure being influenced according to the degree of soil aggregation (Oliveira et al., 2019). Porosimetry data from soils with higher degrees of aggregation indicate that micropores are resilient to the effects of disturbance (Georgetti, 2014; Mascarenha et al., 2016; Borges et al., 2019). However, micropores are still affected by high effective stresses (Lopes, 2016) and elevated matric suctions (Feuerharmel, 2007); however, such scenarios are not typically encountered in conventional practice.

The sensitivity of the macropores to external loads and atmospheric conditions is the reason why the hydromechanical properties of bimodal lateritic soils are significantly improved when they are compacted (Villibor and Nogami, 2009). The compression of macropores leads to decreasing in the hydraulic conductivity (Feuerharmel, 2007), the reduction in the soil compressibility resulting in lower settlement (Georgetti, 2014), and an increase in shear strength (Fagundes, 2014; Georgetti, 2014). In other words, the reduction of the macropores volume augments the role of the microstructure in determining soil behavior.

Despite numerous previous studies, the effects of macro and microstructure on several key aspects of bimodal lateritic soil behavior, including shear strength, are not fully understood. For instance, some studies regarding the unsaturated shear strength have reported contribution of the matric suction to the shear strength greater than that of the net normal stress (i.e., $\phi^b > \phi'$) (Pereira, 1996; Teixeira and Vilar, 1997; Soares and Campos, 2005; Lopes et al., 2007; Feuerharmel, 2007; Kühn, 2014), which seems to be unlikely. The relationship between SWCC and shear strength failure envelope, well-established for the case of unimodal soils, is uncertain for bimodal lateritic soils. There has been limited focus on developing pedotransfer functions to model the hydromechanical behavior of bimodal lateritic soils. Furthermore, existing models for predicting unsaturated shear strength rely on artificial materials with a dual structure resulting from granulometry discontinuity (Zhao et al., 2013; Satyanaga and Rahardjo, 2019; Satyanaga et al., 2022).

This study seeks to propose a model for predicting the unsaturated shear strength of bimodal lateritic soils, founded on a theoretical framework based on the evolution of soil structure during shearing. Additionally, this research aims to clarify the rather unusual behavior documented in the literature where matric suction's impact on shear strength exceeds that of net normal stress (i.e., $\phi^b > \phi'$).

5.2 Background on unsaturated shear strength modeling

In the equation proposed by Fredlund et al. (1978), the effect of matric suction is represented by an average value for the suction range of interest, tan(ϕ^b):

$$\tau = c' + (\sigma - u_a)\tan\phi' + (u_a - u_w)\tan\phi^b \quad (5.1)$$

where: c' is the effective cohesion; $(\sigma - u_a)$ is the net normal stress; ϕ' is the effective friction angle; $(u_a - u_w)$ is the matric suction; and ϕ^b is the angle representing the contribution of the matric suction to the shear strength.

As the soil desaturates, the effect of matric suction on the shear strength diminishes. Models aiming to predict unsaturated shear strength encounter the challenge of discerning how the effectiveness of matric suction varies with changes in water content induced by increasing suction. Existing models rely heavily on the SWCC to estimate unsaturated shear strength of soils.

Table 5.1 provides a summary of these models along with their respective equations and underlying principles. However, these models exhibit several shortcomings. Many of them lack clarity regarding the adopted failure criterion or their suitability for peak or critical state conditions. Moreover, they either ignore a possible relationship between matric suction and effective friction angle, ϕ', or assume that structural changes during shearing does not affect the ϕ'. Additionally, these models typically rely on the SWCC data obtained under conditions different from those of the soil at failure, disregarding alterations in soil structure during shearing.

Many authors have shown that the effect of matric suction on shear strength is nonlinear (Donald, 1957; Bishop, 1959; Escario and Sáez, 1986; Gan and Fredlund, 1988; Vanapalli et al., 1996). The most common approach is to assume that the contribution of matric suction is related to the wet area covering the soil particles. At saturation, all particles are covered by the water, allowing the suction stress to be distributed throughout the soil structure (i.e., $\phi^b = \phi'$). Increasing the matric suction beyond the air-entry value results in desaturation of the bulk or funicular water creating some discontinuities in the

water phase and reducing the soil wet area. As a result, the capacity of distributing the suction stress to the aggregate network skeleton is diminished causing the angle ϕ^b to decrease. Hence, this approach can be generally formulated as follows:

$$\tau = c' + (\sigma - u_a)\tan\phi' + f_{Aw}(u_a - u_w)\tan\phi' \quad (5.2)$$

where: f_{Aw} in Eq. 5.2 is a function representing the ratio area of water by total area.

Comparing Eq. 5.1 and 5.2:

$$f_{Aw} = \frac{\tan\phi^b}{\tan\phi'} \quad (5.3)$$

Models based on this approach encompass various methods for representing soil structure and the water phase, such as capillary bundle, pore-scale, fractals, and others. The simplest representation of the variation in area of water is to assume that it follows the changes in water content in the SWCC. The Öberg and Sällfors (1997) model is based on the degree of saturation whereas the Lamborn (1986)/Lytton (1995) relies on the volumetric water content, but the later is valid only for high matric suctions in the transition zone. To include the entire SWCC, this model was later modified by Aubeny and Lytton (2003). The capillary component of such model in terms of degree of saturation constitutes the Zhou et al. (2016) model.

The models based on wet area led to predictions showing increasing shear strength beyond the residual suction, which is not true for some soils such as sands, silts, and some clays (Donald, 1957; Escario and Jucá, 1989). Noticing this difficulty in the residual zone, Vanapalli et al. (1996) proposed a model in which the water content is normalized with respect to the residual condition. This results in a downward in the shape of the SWCC and in the curve matric suction versus shear strength, which can be also represented

mathematically by raising the degree of saturation by a power κ greater than unity (Fredlund et al., 1996). Other alternatives include normalizing the SWCC using the residual matric suction instead of the residual water content (Bao et al., 1998) and using an exponential function (Cavalcante and Mascarenhas, 2021).

Another approach is approximating the soil structure into geometrical shapes to represent the soil structure and areas of each phase (Pham, 2022; Pham and Sutman, 2022), which allows the calculation of capillary forces between particles (Zhao et al., 2013; Zhai et al., 2019). The soil voids can be also depicted using fractals (Xu and Sun, 2001; Xu, 2004).

The Khalili and Khabbaz (1998) and Naghaded and Toker (2019) models incorporate an empirical normalization of matric suction based on the effective stress principle. There are also models based on calibrating an equation into a dataset of soils through regression analysis (Rassam and Cook, 2002; Guan et al., 2010) or artificial neural networks (Lee et al., 2003). While these models deviate from relying on the concept of wet area to predict unsaturated shear strength, they can still be expressed in terms of f_{Aw}.

Understanding the mechanical behavior of bimodal soils in general (i.e., lateritic or not) poses a greater challenge due to the existence of two desaturation zones: one for macropores and another for micropores. Prediction models developed for these materials, as summarized in Table 5.2, were built upon the approaches employed for unimodal soils, where the contribution of matric suction to shear strength varies depending on the zones of the SWCC (i.e., SWCC similarity approach). However, this hypothesis is not fully understood and lacks evidence from laboratory tests. This is why these models have such a strong subjective aspect compared to unimodal models. Moreover, these models were

devised for soils with bimodal structure resulting from gap-graded grain-size distribution, rather than the presence of aggregations as observed in bimodal lateritic soils.

The Zhao et al. (2013) model (Eq. 5.27) incorporates the normalization approach proposed by Vanapalli et al. (1996) applied to four regions of the SWCC, resulting in a failure envelope with abrupt changes at the transition between regions. When matric suction corresponds to volumetric water contents within the micropores zone, this model calculates capillary forces by assuming particles as uniform spheres. Similar approach is used in the Satyanaga et al. (2022) model, but in this case the SWCC is divided into three regions and the capillary forces are not directly calculated. A smoother and closed-form equation (Eq. 5.28) was developed by Satyanaga and Rahardjo (2019) using the first and second air-entry values to establish the zone in which the relationship between shear strength and matric suction is linear. In common, these three models make use of empirical parameters obtained from a small number of soils.

There is also a noticeable difference when comparing the average diameters of dominant pores in bimodal models to the pore sizes typically found in lateritic soils. For the firsts, the dominant diameter of the micropores is between 0.1 and 10 μm, while in lateritic soils, this value is concentrated around 0.02 μm (Benatti and Miguel, 2013; Grau, 2014; Georgetti, 2014; Lopes, 2016; Otálvaro et al., 2016; Santos and Esquivel, 2019; Araújo, 2019; Borges et al., 2019; Oliveira et al., 2022). The range corresponding to the dominant diameter of the macropores is similar in both lateritic and non-lateritic bimodal soils, with values usually between 10 and 100 μm. The result is that the ratio between the diameters of the macro and micropores of the soils used in existing models is, on average,

25 times and can reach up to 80 times. In the case of lateritic soils, this ratio is, on average, 500 times and can reach up to 5000.

Such discrepancy in microstructure can be seen by comparing the SWCCs: the second air-entry values of lateritic bimodal soils are usually greater than 1000 kPa, while for other soils this value does not reach 100 kPa. Despite all this information on pore distribution and the qualitative knowledge accumulated on the relationship between macro and microstructure summarized in the introduction, the comprehensive understanding of the interdependence of these variables and their effects on soil behavior in terms of shear strength remains did not receive the research attention it deserved. For example, the effects of the contribution of matric suction towards shear strength as well as matric suction on variations in the effective friction angle (Toll et al., 1990; Röhm and Vilar, 1995) are not fully understood from the perspective of micro to macrostructure changes.

Table 5.1 Summary of the existing models for predicting the unsaturated shear strength

Main principle	Approach	Author	Equation
Wet area	Pore-scale	Lamborn (1986) Lytton (1995)	$f_{Aw} = \theta$ (5.4) θ: volumetric water content
		Aubeny and Lytton (2003)	$f_{A_w} = \begin{cases} 1, & S = 100\% \\ \theta + \dfrac{S-85}{15}(1-\theta), & 85\% < S < 100\% \\ \theta, & S \le 85\% \end{cases}$ (5.5) S: Degree of saturation
		Pham (2022)	$f_{A_w} = \theta + S(1-\theta) + D$ (5.6) D: disturbance function
		Pham and Sutman (2022)	$f_{A_w} = (1-\theta_e)S_e$ (5.7) S_e: effective degree of saturation θ_e: effective volumetric water content
	Normalized volumetric water content	Vanapalli et al. (1996)	$f_{Aw} = \dfrac{\theta - \theta_{res}}{\theta_{sat} - \theta_{res}}$ (5.8) θ_{res}: volumetric water content at residual suction θ_{sat}: volumetric water content at saturation
		Bao et al. (1998)	$f_{Aw} = \begin{cases} 1, & (u_a - u_w) < (u_a - u_w)_b \\ \dfrac{\log(u_a - u_w)_r - \log(u_a - u_w)}{\log(u_a - u_w)_r - \log(u_a - u_w)_b}, & (u_a - u_w) \ge (u_a - u_w)_b \end{cases}$ (5.9) $(u_a - u_w)_r$: residual suction value $(u_a - u_w)_b$: air-entry value
	Semi-empirical SWCC similarity	Vanapalli et al. (1996) Fredlund et al. (1996)	$f_{Aw} = \Theta^{\kappa}$ (5.10) Θ: normalized volumetric water content defined by (= θ / θ_{sat}), which is also equal to degree of saturation S κ: fitting parameter Vanapalli et al. (2000): $\kappa = -0.0009 \cdot (PI)^2 + 0.0833PI + 0.9848$ (5.11) Garven and Vanapalli (2006): $\kappa = -0.0016(PI)^2 + 0.0975PI + 1$ (5.12) Oliveira and Marinho (2003): $\kappa = -0.0044(PI)^2 + 0.2245PI + 0.9715$ (5.13) PI: plasticity index

Main principle	Approach	Author	Equation	
	SWCC similarity	Öberg and Sällfors (1997)	$f_{Aw} = S$	(5.14)
	Fractal approach	Xu and Sun (2001) / Xu (2004)	$f_{Aw} = (u_a - u_w)_b^{(1-\zeta)} (u_a - u_w)^{\zeta-1}$ ζ is a parameter related to fractal dimension Xu and Sun (2001): $\zeta = 2D/3 - 1$ Xu (2004): $\zeta = D - 2$ D: fractal dimension	(5.15) (5.16) (5.17)
	Capillary tube analogy	Zhou et al. (2016)	$f_{A_w} = S_{cap}$ S_{cap}: degree of saturation due to capillary component	(5.18)
		Zhai et al. (2019)	$f_{A_w} = \frac{c_s}{\tan\phi'} + \frac{S - S'}{1 - S'}$ c_s: pulling stress calculated from the capillary tube model S': is the degree of saturation corresponding to suction of 3,100 kPa	(5.19)
Wet area (implicit)	SWCC similarity	Cavalcante and Mascarenhas (2021)	1) For sands: $f_{A_w} = e^{-\delta\lvert u_a - u_w\rvert}$ 2) For silts: $f_{A_w} = \begin{cases} e^{-\delta\lvert u_a - u_w\rvert}, & (u_a - u_w) \le 1/\delta \\ \frac{\exp(-1)}{\delta(u_a - u_w)}, & (u_a - u_w) > 1/\delta \end{cases}$ δ: fitting parameter related to the air-entry value	(5.20) (5.21)
Effective stress principle	Empirical	Khalili and Khabbaz (1998)	$f_{Aw} = \chi = \begin{cases} 1, & (u_a - u_w) < (u_a - u_w)_b \\ \left[\frac{(u_a - u_w)}{(u_a - u_w)_b}\right]^{\eta}, & (u_a - u_w) \ge (u_a - u_w)_b \end{cases}$ η: fitting parameter	(5.22)
	SWCC similarity	Naghaded and Toker (2019)	$f_{A_w} = \chi = \frac{(u_a - u_w)_t}{(u_a - u_w)} \left(1 - e^{\left[-(u_a - u_w)/(u_a - u_w)_t\right]}\right)$ $(u_a - u_w)_t$: transition suction	(5.23)
Regression analysis	Empirical	Rassam and Cook (2002)	$f_{A_w} = 1 - \varphi\left[(u_a - u_w) - (u_a - u_w)_b\right]^{\beta} (u_a - u_w)^{-1} \tan\phi'$ φ and β are parameters to adjust the failure envelope with the residual suction.	(5.24)

Main principle	Approach	Author	Equation	
		Guan et al. (2010)	$f_{A_w} = \begin{cases} 1, & (u_a - u_w) < (u_a - u_w)_b \\ 1 + \left[1 - (u_a - u_w)_b / (u_a - u_w)\right] b\Theta^{\kappa} & \\ & (u_a - u_w) \geq (u_a - u_w)_b \end{cases}$ b and κ are fitting parameters from regression of the SWCC and the *PI*	(5.25)
Artificial neural networks	Empirical	Lee et al. (2003)	$f_{A_w} = \frac{1}{\tan^2 \phi' \left[\frac{1}{\tan^2 \phi'} + \frac{(u_a - u_w)}{\tan \phi' C_{\max}} \right]}$ C_{max}: ultimate increment of apparent cohesion	(5.26)

Table 5.2 Prediction models for bimodal soils

Author	Equation
Zhao et al. (2013)	$\tau = c' + (\sigma - u_a)\tan\phi' + c$ $c = \begin{cases} (u_a - u_w)\tan\phi', & (u_a - u_w) \le (u_a - u_w)_{b1} \\ (u_a - u_w)(1 - S_r^{1e})\tan\phi', & (u_a - u_w)_{res1} \ge (u_a - u_w) > (u_a - u_w)_{b1} \\ \sigma_{cap} S_r^{2e}\tan\phi', & (u_a - u_w)_{b2} \ge (u_a - u_w) > (u_a - u_w)_{res1} \\ (1 - f_c)(u_a - u_w)(1 - S_r^{3e})\tan\phi', & (u_a - u_w) > (u_a - u_w)_{b2} \end{cases}$ (5.27) c: apparent cohesion $(u_a - u_w)_{b1}$, $(u_a - u_w)_{b2}$: first and second air-entry values, respectively $(u_a - u_w)_{res1}$, $(u_a - u_w)_{res2}$: first and second residual suctions, respectively S_r^{1e}, S_r^{2e}, S_r^{3e}: normalized degree of saturations of the different stages of a bimodal SWCC σ_{cap}: capillary pulling stress f_c: coarse content
Satyanaga and Rahardjo (2019)	$\tau = c' + \left[(\sigma - u_a) + (u_a - u_w)_{b1}\right]\tan\phi' + \left[2(u_a - u_w) - (u_a - u_w)_{b1} - (u_a - u_w)_{b2}\right]\tan\left(b\phi'\right) + \left[(u_a - u_w)_{b2} - (u_a - u_w)\right]\tan\left(k\phi'\right)$ (5.28) b, k: semi-empirical parameters from index properties
Satyanaga et al. (2022)	$c = \begin{cases} (u_a - u_w)\tan\phi', & (u_a - u_w) \le (u_a - u_w)_{b1} \\ (u_a - u_w)_{b1}\tan\phi' + \left[(u_a - u_w) - (u_a - u_w)_{b1}\right] b_1 \Theta^{\kappa_1}, & (u_a - u_w)_{res1} \ge (u_a - u_w) > (u_a - u_w)_{b1} \\ (u_a - u_w)_{b2}\tan\phi^{b2} + \left[e \times (u_a - u_w) - (0.2 + f_f)(u_a - u_w)_{b2}\right] b_2 \Theta^{\kappa_2}, & (u_a - u_w) > (u_a - u_w)_{b2} \end{cases}$ (5.29) b_1, k_1, b_2, k_2: semi-empirical parameters from index properties f_f: fines content

5.3 Soils investigated

Most prediction models operate on the premise of examining how shear strength behavior evolves with changes in matric suction. The analysis presented here follows a similar approach considering unsaturated shear strength data, SWCC, grain-size distribution, and specimen condition (i.e., remolded (R) or undisturbed (U)). To this end, 13 soils were analyzed, comprising 6 U and 7 R soils. These data were collected from

existing data of 7 studies, and they include soils with very distinct characteristics such as location, index properties, and classification according to the USCS. Although most bimodal lateritic materials are residual soils, some soils of this dataset are sedimentary. Also, there are 3 collapsible soils. Table 5.3 provides key information and the main characteristics of these soils.

The soils were selected based on the availability of geotechnical data that allowed the evaluation of how soil structure and aggregation level influence the mechanical behavior. In essence, for all soils selected for this study, the following set of data is available: both aggregated and disaggregated grain-size distribution curves (Fig. 5.1), index properties (Table 5.3), drying SWCC (Fig. 5.2), and unsaturated shear strength data. The role of aggregation level was assessed based on a comparison between the aggregated and disaggregated grain-size distribution curves using a parameter called relative aggregation (*RA*), as introduced by Otálvaro et al. (2015):

$$RA = \frac{\sum_{i=1}^{n}\left(P_{A,i} - P_{D,i}\right)\log\left(\delta_i / \delta_{i+1}\right)}{\sum_{i=1}^{n} P_{D,i}\log\left(\delta_i / \delta_{i+1}\right)} \tag{5.30}$$

where: n is the number of measured points of the grain-size distribution curve; $P_{A,i}$ is the accumulate retained percentage of the aggregated grain-size distribution at point i; $P_{D,i}$ is the accumulate retained percentage of the disaggregated grain-size distribution at point i; and δ_i is the particle diameter at point i.

Table 5.3 Main information and characteristics of the soils investigated

Condition	Identification	Reference	Location (city/state)	Soil	USCS (disaggregated / aggregated)	ρ_s (g/cm³)	ρ_d (g/cm³)	e	w_L	w_P	PI
Undisturbed (U)	1U	Fagundes (2014)	Bauru/São Paulo	Sedimentary collapsible	SC / SC	2.65	1.51	0.76	16	NP	-
	2U	Fernandes (2016)	Bauru/São Paulo	Sedimentary collapsible	SC / SC	2.68	1.52	0.77	20	NP	-
	3U					2.69	1.60	0.68	21	NP	-
	4U	Georgetti (2014)	São Carlos/ São Paulo	Colluvium sandstone	SC / SC	2.65	1.31	1.03	32	16	16
	5U	Feuerharmel (2007)	Timbé do Sul/Santa Catarina	Volcanic basalt colluvium	MH / MH	2.86	1.07	1.67	74	57	17
	6U			Sandstone colluvium	CH / SC	2.80	1.40	1.00	56	34	22
Remolded (R)	1R	Georgetti (2010)	São Carlos/ São Paulo	Sedimentary	SC / SC	2.69	1.68	0.60	38	21	17
	2R	Fagundes (2014)	Bauru/São Paulo	Sedimentary collapsible	SC / SC	2.65	1.85	0.43	16	NP	-
	3R	Georgetti (2014)	São Carlos/ São Paulo	Colluvium sandstone	SC / SC	2.65	1.72	0.55	32	16	16
	4R	Feuerharmel (2007)	Timbé do Sul/Santa Catarina	Volcanic basalt colluvium	MH / MH	2.86	1.08	1.65	74	57	17
	5R			Sandstone colluvium	CH / SC	2.80	1.35	1.08	56	34	22
	6R	Pereira (1996)	Pacatuba/Ceará	Residual of gneiss / collapsible	SW-SM / SC	2.64	1.50	0.76	29	17	12
	7R	Kühn (2014)	Goiânia/Goiás	--	CL / SM	2.73	1.61	0.70	45	27	18

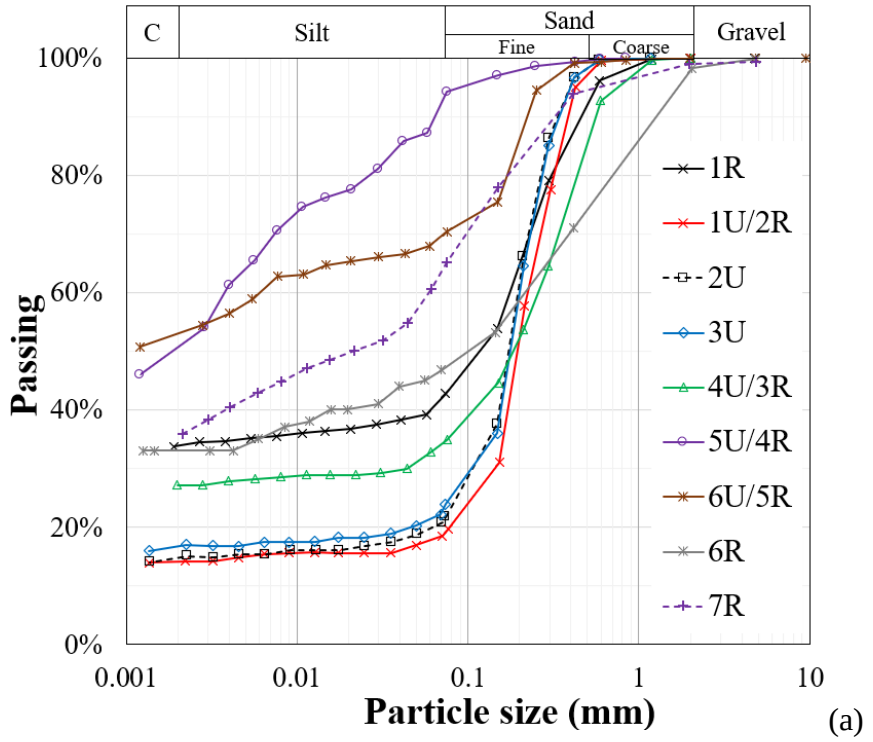

(a)

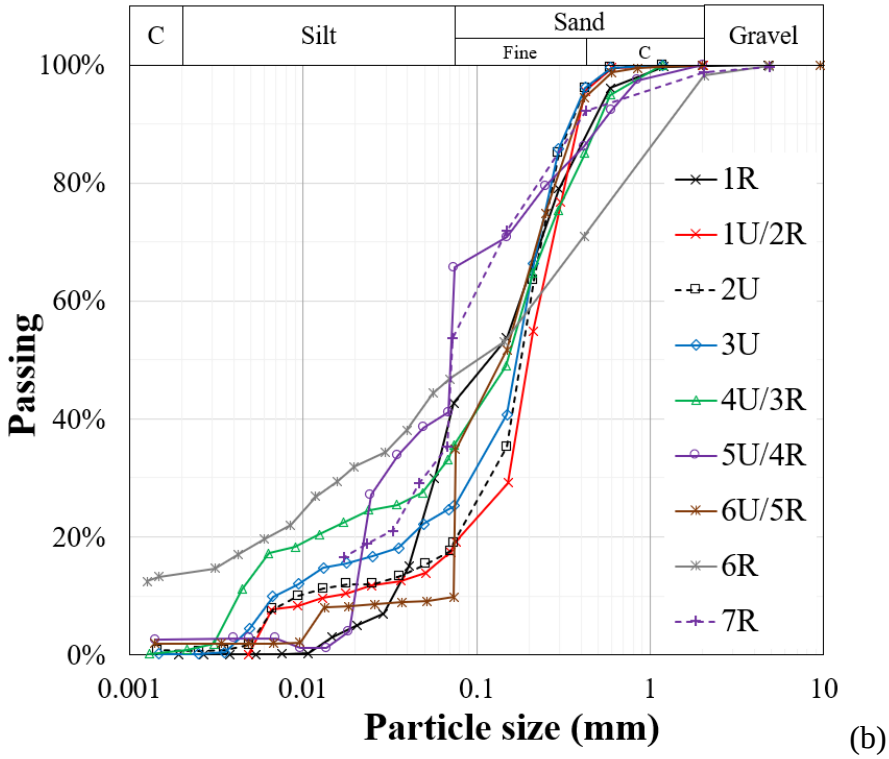

(b)

Figure 5.1 Grain-size distribution curves: (a) aggregated; and (b) disaggregated

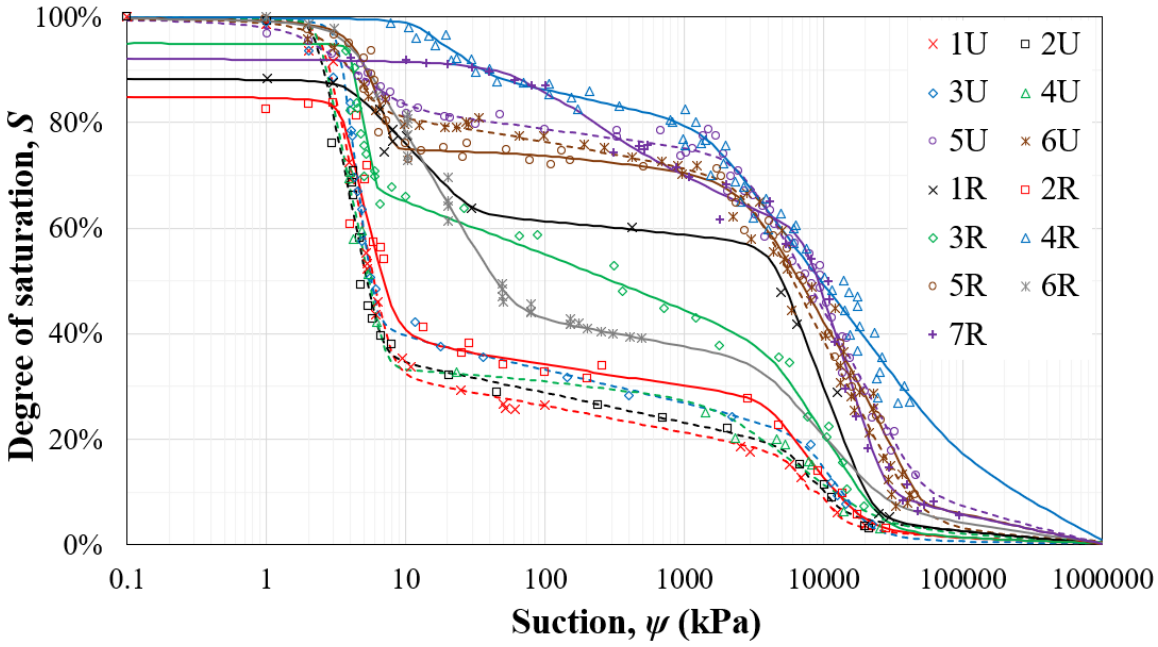

Figure 5.2 Soil-water characteristic curves of the selected soils

Remolded (R) and undisturbed (U) samples are analyzed separately due to the susceptibility of macropores to disturbances such as stress reduction, moisture fluctuations, and compaction (Feuerharmel, 2007; Georgetti, 2014; Borges et al., 2019; Oliveira et al., 2022). For soils examined under both conditions (e.g., 2R/1U and 3R/4U), it was observed that remolding enhances soil stiffness. For the shear strength data, only the maximum or peak strength was considered as failure criterion because most of the soils showed strain-hardening behavior without a clear definition of the critical state.

Table 5.4 outlines the most relevant characteristics of the shear strength tests as well as the main observations regarding the mechanical behavior of each soil. Different apparatuses were used in the tests, such as modified triaxial (CD and CW), modified direct shear and Brazilian Test - BT (i.e., diametral compression test). Tests characteristics including shear or displacement rate, suctions and net normal stresses are also presented. The SWCC parameters indicate 10 out of 13 soils were tested only under suctions outside

the macropores zone (i.e., $(u_a - u_w) < (u_a - u_w)_{res1}$), and those tested in that zone have only one or two datapoints. The effective friction angle, ϕ', for saturated conditions varied between 13.8 to 32.8º and the effective cohesion, c', showed a great dispersion, with values ranging from 0 to 27.9 kPa. The shape of the stress-strain curves did not exhibit the same pattern to those of normally consolidated ($c' = 0$) and over consolidated ($c' > 0$) clays. Further analysis of the information in Table 5.4 is presented in the following section.

Soils 4R, 5R, 6R, 7R, 5U, and 6U exhibited ϕ^b values higher than ϕ'. This unusual behavior was observed by the authors who carried out the tests and has been documented in prior studies by Teixeira and Vilar (1997), Soares and Campos (2005), and Lopes et al. (2007). Vilar (2007) suggests a potential link between the unusually high effect of matric suction and the development of cementation among particles during suction equilibrium, like the formation of a rigid crust on cut slopes following exposure to evaporation and silica deposition. However, this explanation appears inadequate as such cementation typically occurs under weather-exposed conditions where several cycles of evaporation and precipitation (i.e., drying and wetting) causes percolation of silica and fixation of iron and aluminum ions by the upward movement of water (Paraguassú and Röhm, 1991). This condition contrasts with laboratory conditions in which specimens typically maintain much higher degrees of saturation throughout testing and suction variations are significantly slower.

Table 5.4. Main characteristic of soils in terms of shear strength behavior

Soil name	*RA*	ψ_{b1} (kPa)	ψ_{res1} (kPa)	ψ_{b2} (kPa)	ψ_{res2} (kPa)	Shear strength characteristics and behavior			
						Test type / Strain or displacement rate	c' and ϕ'_0	Matric or total suction	Net normal or vertical stress
1R	0.35	5.0	16.0	4000	23000	Triaxial CW 3.3×10^{-4} %/s	c' = 14.2 kPa ϕ'_0 = 32.0º	• Tested at 0, 55-155, and 26000 kPa • $\phi^b = \phi'$ at saturation • No tests within the macropores zone • ϕ^b decreases when $(u_a - u_w) > 55$ kPa • $\phi^b \approx 0.7°$ for $(u_a - u_w) = 26000$ kPa • ϕ^b is independent of net normal stress	• Tested at 50, 150, and 300 kPa • $\phi' \approx 32°$ for all low suctions • $\phi' = 43°$ for suction of 26000 kPa • ϕ' is independent of net normal stress
2R	0.09	3.5	8.0	4000	18000	Triaxial CD 6.9×10^{-6} %/s	c' = 22.5 kPa ϕ'_0 = 30.3º	• Tested at 0, 50, 200, and 23000 kPa • $\phi^b < \phi'$ for all suctions ($\phi^b \approx 0.6\,\phi'$ at suction of 50 kPa) • No tests within the macropores zone • $\phi^b \approx 0.4°$ for $(u_a - u_w) = 23000$ kPa • ϕ^b is independent of net normal stress	• Tested at 50, 100, and 200 kPa • $\phi' \propto (u_a - u_w)$ • ϕ' is independent of net normal stress
3R	0.08	4.0	6.0	4500	25000	Triaxial CW 6.5×10^{-7} %/s	c' = 0 kPa ϕ'_0 = 31.5º	• Tested at 0, and 3-41 kPa • $\phi^b = \phi'$ for all suctions • ϕ^b is independent of net normal stress	• Tested at 50, 100, 150, 300 and 500 kPa • $\phi' \approx 31.5°$ for all suctions • ϕ' is independent of net normal stress
4R	2.04	14.0	28.0	1400	80000	Direct shear 2.03×10^{-4} mm/s	c' = 13.4 kPa ϕ'_0 = 21.1º	• Tested at 0, 50, 100, 150 and 6100 kPa • $\phi^b > \phi'$ for suctions of 50 and 100 kPa • No tests within the macropores zone • Decreases when $(u_a - u_w) \geq 150$ kPa • Increase with net vertical stress for suctions of 100 and 150 kPa • $\phi^b \approx 0.5°$ for $(u_a - u_w) = 6100$ kPa	• Tested at 25, 50, 100, and 150 kPa • $\phi' \propto (u_a - u_w)$ when $(u_a - u_w) > 50$ kPa • ϕ' is independent of net normal stress
5R	1.38	4.5	8.0	2770	50000	Direct shear 2.03×10^{-4} mm/s	c' = 18.5 kPa ϕ'_0 = 19.3º	• Tested at 0, 50, 100, 150 and 5800 kPa • $\phi^b > \phi'$ for suctions of 100 and 150 kPa at high net vertical stresses • No tests within the macropores zone • High net vertical stresses → $\phi^b \propto 1/(u_a - u_w)$	• Tested at 25, 50, 100, and 150 kPa • $\phi' \propto (u_a - u_w)$ and $\phi' \propto 1/(\sigma_v - u_a)$ • ϕ' is independent of net normal stress

Soil name	*RA*	ψ_{b1} (kPa)	ψ_{res1} (kPa)	ψ_{b2} (kPa)	ψ_{res2} (kPa)	Shear strength characteristics and behavior			
						Test type / Strain or displacement rate	c' and ϕ'_0	Matric or total suction	Net normal or vertical stress
								• Low net vertical stresses → $\phi^b \propto (u_a - u_w)$ • Convergence towards 53° at suction of 200 kPa • $\phi^b \approx 0.9°$ for $(u_a - u_w)$ = 5800 kPa	
6R	0.24	3.7	58.0	3800	25000	Direct shear 2.78×10^{-5} mm/s	c' = 3.8 kPa ϕ'_0 = 13.8º	• Tested at 0, 25, 50 and 100 kPa • $\phi^b > \phi'$ for net vertical stresses of 100, and 150 kPa • No tests within the macropores zone • $\phi^b \propto (\sigma_v - u_a)$ for $(\sigma_v - u_a) \leq 100$ kPa • ϕ^b decreases at $(\sigma_v - u_a)$ = 200 kPa	• Tested at 25, 50, 100 and 200 kPa • $\phi' \propto (u_a - u_w)$ • $\phi' \propto (\sigma_v - u_a)$ for $(u_a - u_w) \leq$ 50 kPa
7R	0.47	72.0	229.0	7400	27000	BT and Triaxial CD, CW 8.68×10^{-7} %/s for CD and 1.39×10^{-5} %/s for CW	c' = 27.9 kPa ϕ'_0 = 32.8º	• Tested at: ○ CD: 0, 100, and 200 ○ CW and BT: 70 to 61180 kPa • For low suctions (≤ 200 kPa): ○ $\phi^b > \phi'$ at suction of 100 kPa ○ ϕ^b decreases at suction of 200 kPa • For all suctions: ○ ϕ^b decreases abruptly around suction of 300 kPa ○ Peak shear strength around 6000 kPa ○ $\phi^b \approx 3°$ for suction of 14000 kPa	• Tested at: ○ CD: 20, 150, 230, and 290 kPa ○ CW: 20 and 300 kPa • For low suctions (≤ 200 kPa): ○ ϕ' = 31.7° • For all suctions: ○ ϕ' behavior is not clear, it may be constant or vary with the net confining stress accordingly to the adopted fitting procedure
1U	0.09	2.5	8	7000	11000	Triaxial CD 6.9×10^{-6} %/s	c' = 0.0 kPa ϕ'_0 = 28.3º	• Tested at 0, 50, 200, 400, and 33000 kPa • $\phi^b < \phi'$ for all suctions ($\phi^b \approx 0.25\ \phi'$ at suction of 50 kPa) • No tests within the macropores zone • $\phi^b \approx 0.1°$ for $(u_a - u_w)$ = 33000 kPa • ϕ^b is independent of net normal stress	• Tested at 50, 100, and 200 kPa • ϕ' is independent of net normal stress • ϕ' seems to be dependent of suction, but without showing a clear pattern
2U	0.09	2.2	7	7000	11000	Triaxial CD 6.9×10^{-6} %/s	c' = 4.2 kPa ϕ'_0 = 33.4º	• Tested at 0, 50, 200, and 400 kPa • $\phi^b < \phi'$ for all suctions ($\phi^b \approx 0.18\ \phi'$ at suction of 50 kPa) • No tests within the macropores zone	• Tested at 50, 100, and 200 kPa • $\phi' \approx 33.4°$ for all suctions • ϕ' is independent of net normal stress

Soil name	*RA*	ψ_{b1} (kPa)	ψ_{res1} (kPa)	ψ_{b2} (kPa)	ψ_{res2} (kPa)	Shear strength characteristics and behavior			
						Test type / Strain or displacement rate	c' and ϕ'_0	Matric or total suction	Net normal or vertical stress
								• ϕ^b is independent of net normal stress	
3U	0.07	3.3	6	9000	18000	Triaxial CD 6.9×10^{-6} %/s	c' = 5.6 kPa ϕ'_0 = 32.7º	• Tested at 0, 50, 200, and 400 kPa • $\phi^b < \phi'$ for all suctions ($\phi^b \approx 0.19\ \phi'$ at suction of 50 kPa) • No tests within the macropores zone • ϕ^b is independent of net normal stress	• Tested at 50, 100, and 200 kPa • $\phi' \approx 33.8°$ (slightly increase with suction) • ϕ' is independent of net normal stress
4U	0.08	2.4	7	2000	20000	Triaxial CW 6.5×10^{-7} %/s	c' = 0.0 kPa ϕ'_0 = 23.4º	• Tested at 0-62 kPa • $\phi^b < \phi'$ for all suctions ($\phi^b \approx 0.61\ \phi'$ at suction of 50 kPa) • ϕ^b is independent of net normal stress	• Tested at 50, 150, 300 and 150 kPa • $\phi' \approx 23.4°$ for all suctions • ϕ' is independent of net normal stress
5U	2.04	2.2	7	2560	50000	Direct shear 2.03×10^{-4} mm/s	c' = 12.4 kPa ϕ'_0 = 29.0º	• Tested at 0, 50, 100, 150 and 6500 kPa • $\phi^b > \phi'$ for suctions of 50, 100 and 150 kPa • Decreases for suctions > 100 kPa • No tests within the macropores zone • $\phi^b \approx 1.5°$ for $(u_a - u_w)$ = 6500 kPa	• Tested at 25, 50, 100, and 150 kPa • $\phi' \propto (u_a - u_w)$ for suctions ≥ 150 kPa • ϕ' is independent of net normal stress
6U	1.38	3.0	6	2800	45000	Direct shear 2.03×10^{-4} mm/s	c' = 12.7 kPa ϕ'_0 = 27.7º	• Tested at 0, 50, 100, 150 and 5600 kPa • $\phi^b > \phi'$ for suctions of 50, 100 and 150 kPa • Increases with matric suction, except for 5600 kPa • No tests within the macropores zone • $\phi^b \approx 2.3°$ at $(u_a - u_w)$ = 6500 kPa	• Tested at 25, 50, 100, and 150 kPa • $\phi' \approx 27.5°$ for all suctions, except at 5600 kPa (39.9°) • ϕ' is independent of net normal stress

where: ψ_{b1} is the first air-entry value; ψ_{res1} is the first residual suction; ψ_{b2} is the second air-entry value; ψ_{res2} is the second residual suction; and ϕ'_0 is the effective friction angle at saturation. BT stand for Brazilian test (i.e., diametral compression test).

5.4 Theoretical conceptualization of the unsaturated shear strength behavior

All soils exhibiting ϕ^b values exceeding ϕ' share certain common characteristics: the derived results were from tests performed under drained conditions, either in direct or triaxial shear tests. This detail is pivotal for elucidating the structural alterations occurring within the specimen during these tests, as outlined below.

Consider a drained test conducted at a certain water content where the water phase in the macropores is discontinuous, yet micropores are fully saturated (i.e., matric suction lies between the first residual suction and second air-entry values). Initially, the soil structure prior to shearing comprises particles and aggregations of varying dimensions, the latter possessing sizes similar to that of granular particles (Fig. 5.3a). Upon the initiation of shearing, particles and aggregations undergo rearrangement accompanied by some breakages of cementations.

As shearing progresses, when the macropores are compressed to a high degree, the soil structure reaches a state where simply rearranging particles and aggregations no longer results in volume reduction (Fig. 5.3b). Consequently, further shearing produces fragmentation of aggregations, especially within a narrow region where a shear band is being formed. This alteration in turn modifies the soil's gradation, enabling a new arrangement of particles within the shear band and subsequently reducing macropores volume (Fig. 5.3c).

While the emergence of shear bands is typically associated with dilation and strain-softening behavior (Desrues and Viggiani, 2004; Yang and Vanapalli, 2023), it is noteworthy that contractive shear bands have been observed in clays (Hicher et al., 1994;

Jiang et al., 2010) and soft rocks (Bésuelle et al., 2000; El Bied et al., 2002). As the size of macropores gradually approaches that of the larger micropores, and considering that aggregations remain saturated, there is a rise in the degree of saturation within the shear band, even under constant matric suction. This transition triggers discontinuous portions of the water phase to increase their connectivity and continuity, thereby increasing the wetted area and the effect of matric suction, expressed in terms of ϕ^b (Fig. 5.3d).

Assuming that the water phase is predominantly continuous within the microstructure found along the shear band, this creates a network resembling a skeleton of aggregations surrounding granular particles, sustained by matric suction. It is crucial to note that these packets of aggregates where the water phase is continuous cannot transfer the compressive effect of matric suction to granular particles due to the substantial size disparity between micro and macropores. As evidenced by several authors using mercury intrusion porosimetry (MIP) tests of bimodal lateritic soils, micropore sizes are between 500 and 5000 times smaller than macropores (Benatti and Miguel, 2013; Grau, 2014; Georgetti, 2014; Lopes, 2016; Otálvaro et al., 2016; Santos and Esquivel, 2019; Araújo, 2019; Borges et al., 2019; Mendes and Marinho, 2020; Oliveira et al., 2022). Consequently, water storage mechanisms at the micropore scale are primarily related to adsorption, while capillarity governs at the macropore scale. Given that this network aggregate skeleton operates independently of direct contact between granular particles, it does not contribute to shear strength when net normal stress increases. Therefore, it is plausible for the value of ϕ^b to surpass that of ϕ' within the shear band.

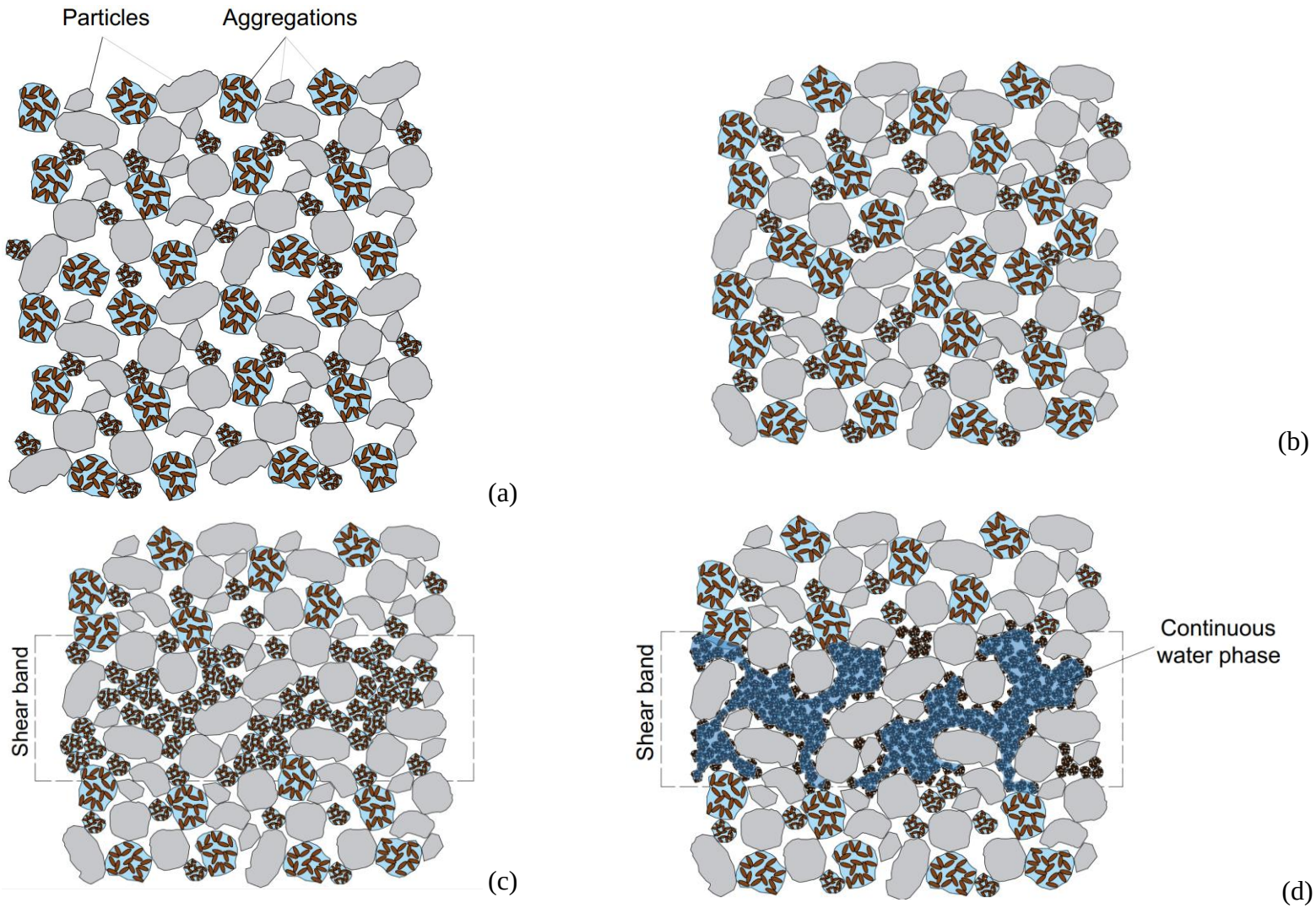

Figure 5.3 Changes in the bimodal structure of lateritic soils during shearing in drained conditions: (a) initial state; (b) structure rearrangement and contraction during initial shearing stages; (c) formation of the shear band; and (d) emergence of regions with continuous water phase within the shear band

Two possible results are observed after the initial macropore compression described herein. These results depend on the net total stresses, as shown in Fig. 5.4. Under sufficiently high net normal stresses, the soil undergoes significant axial strains or horizontal displacements, gradual volumetric reduction and an increase in shear stress, without exhibiting a peak deviator or shear stress (i.e., strain-hardening). Conversely, under low net normal stresses, further breakage of aggregations within the shear band is not observed. In such instances, additional volumetric changes are negligible as the remaining aggregations are very small, resembling the fine fraction. Coupled with loose fines, this condition facilitates particles sliding along an almost linear trajectory in the failure plane, thereby reaching critical state.

In the CW triaxial tests shown in Fig. 5.4, as the degree of saturation increases within the shear band, the matric suction decreases. Since pore-air pressure (u_a) remains constant, the pore-water pressure (u_w) within the shear band surpasses that in its vicinity, prompting outflow. If shear occurs slowly enough to enable hydraulic equilibrium, failure will coincide with the monitored matric suction in the test. However, if shearing is rapid, the matric suction along the failure plane will be that within the shear band, potentially leading to an underestimation of the contribution of matric suction to shear strength (i.e., reduction in ϕ^b).

This process, describing the formation of the aggregate network skeleton occurs only when micropores are saturated, and there remains residual water within macropores, facilitating connections between non-contacting aggregations. Extending this theoretical concept, it is assumed that the matric suction at the onset of micropore desaturation corresponds to the threshold beyond which the aggregate network skeleton cannot emerge.

This assumption is confirmed by comparing the behavior exhibited by all investigated soils with $\phi^b > \phi'$ (i.e., 4R, 5R, 5U, and 6U) to their respective SWCCs shown in Fig. 5.6, except for material 7R. Nonetheless, Fig. 5.2 illustrates that the SWCC of material 7R lacks a clear definition of the first residual suction.

In the shearing phase of drained tests, the behavior concerning ϕ' is dependent of degree of aggregation, confirming the observation presented by Kühn et al. (2022). Soils exhibiting a higher degree of aggregation imply that, following the breakage of aggregations, granular particles are often surrounded by aggregations and have minimal direct contact with other granular particles. Consequently, ϕ' is predominantly influenced by the properties of the aggregations, analogous to the impact of increased fines in granular soils (Cabalar, 2011; Muawia, 2013; Nagaraj, 2016; Kim et al., 2018). Therefore, ϕ' may decrease with an increase in net normal stress, leading to more aggregation breakage, as observed in soils 5R and 6R. Since aggregation sizes can significantly reduce after breakage, the relative number of contacts between particles and aggregations decreases.

For 5 out of 7 remolded soils and for 4 out of 6 undisturbed soils, the effective friction angle ϕ' was found to vary approximately linearly with suction in logarithmic scale, as depicted in Fig. 5.5a and 5.5b. However, materials 3R, 7R, 2U, and 4U exhibited nearly constant ϕ' values. It is plausible that the suctions applied in these tests were insufficient to induce significant structural changes capable of altering ϕ'. Notably, soils exhibiting the most pronounced increases in ϕ' with suction were those with the highest relative aggregation (*RA*). Conversely, soils 3R, 2U, 3U, and 4U displayed the lowest *RA* values (Table 5.4), supporting the hypothesis that ϕ' is predominantly influenced by the aggregations, as previously discussed.

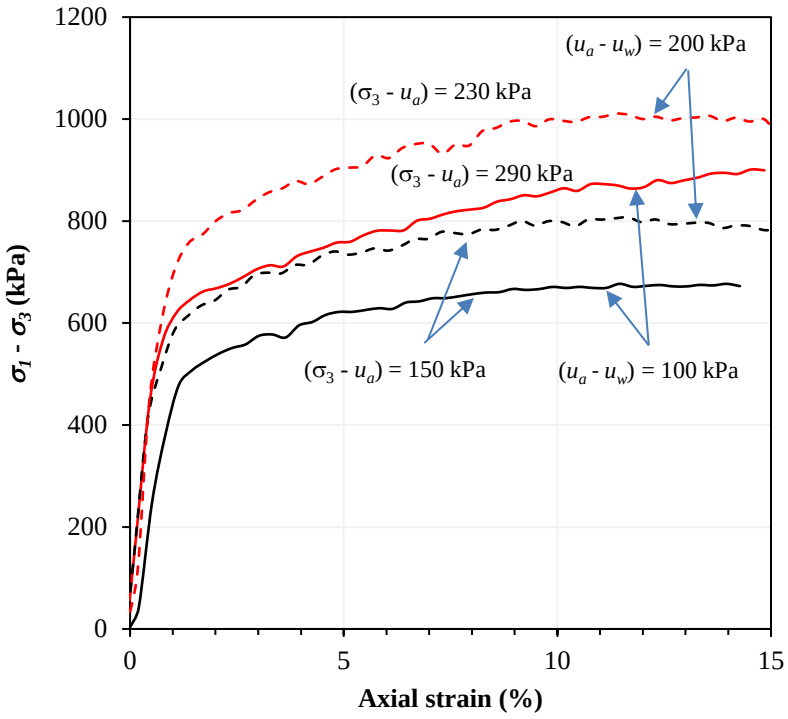
1200
1000
800
600
400
200
0
0
5
10
15
σ1 - σ3 (kPa)
Axial strain (%)
(ua - uw) = 200 kPa
(σ3 - ua) = 230 kPa
(σ3 - ua) = 290 kPa
(σ3 - ua) = 150 kPa
(ua - uw) = 100 kPa

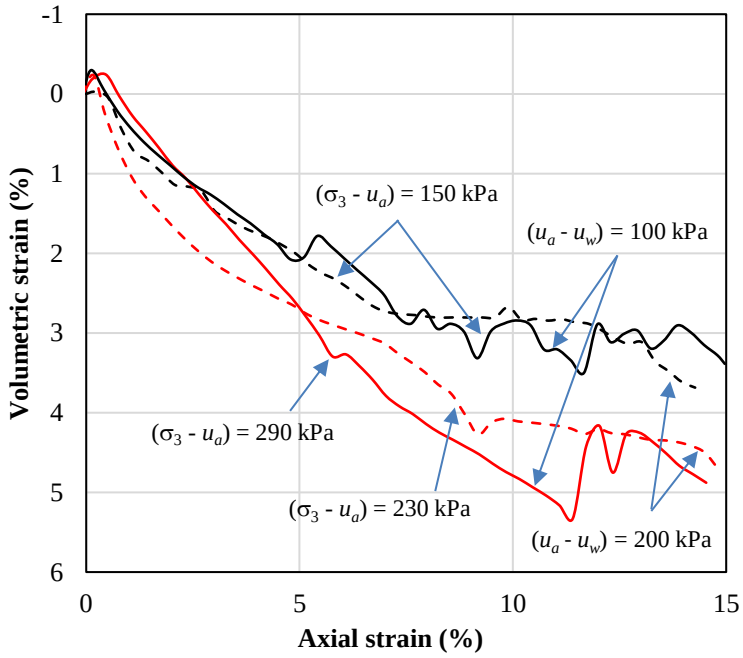
-1
0
1
2
3
4
5
6
0
5
10
15
Volumetric strain (%)
Axial strain (%)
(σ3 - ua) = 150 kPa
(ua - uw) = 100 kPa
(σ3 - ua) = 290 kPa
(σ3 - ua) = 230 kPa
(ua - uw) = 200 kPa

(a)

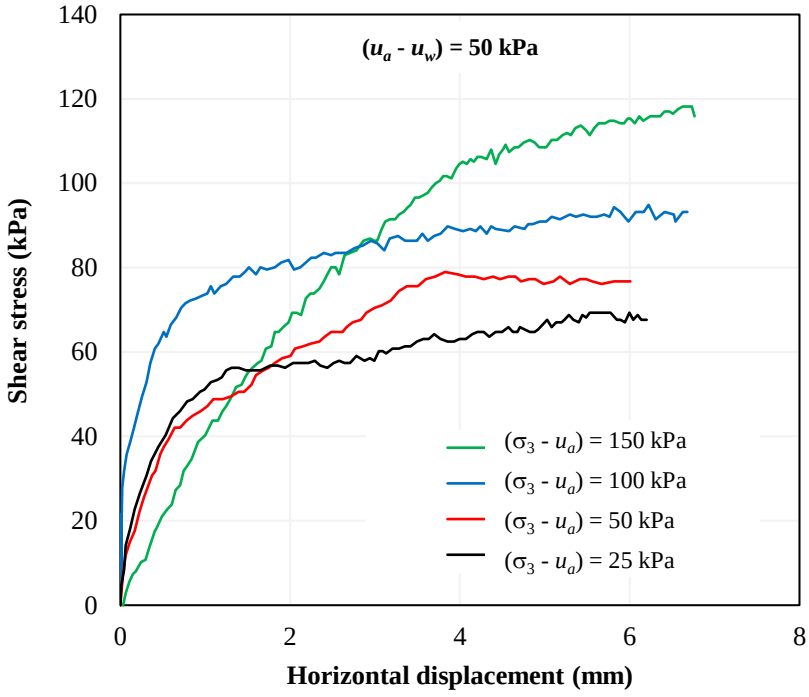
$(u_a - u_w)$ = 50 kPa
Shear stress (kPa)
Horizontal displacement (mm)
$(\sigma_3 - u_a)$ = 150 kPa
$(\sigma_3 - u_a)$ = 100 kPa
$(\sigma_3 - u_a)$ = 50 kPa
$(\sigma_3 - u_a)$ = 25 kPa

(b)

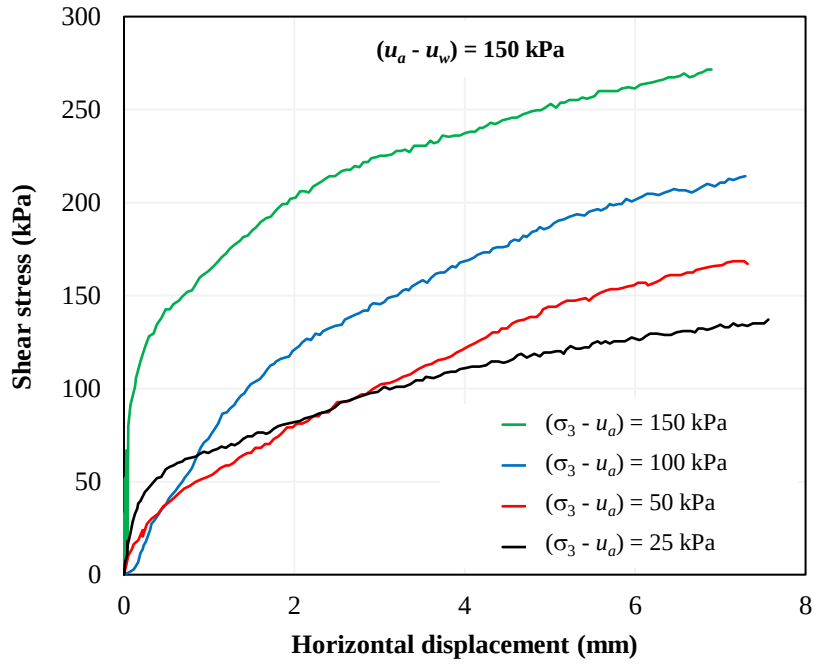
$(u_a - u_w)$ = 150 kPa
Shear stress (kPa)
Horizontal displacement (mm)
$(\sigma_3 - u_a)$ = 150 kPa
$(\sigma_3 - u_a)$ = 100 kPa
$(\sigma_3 - u_a)$ = 50 kPa
$(\sigma_3 - u_a)$ = 25 kPa

(c)

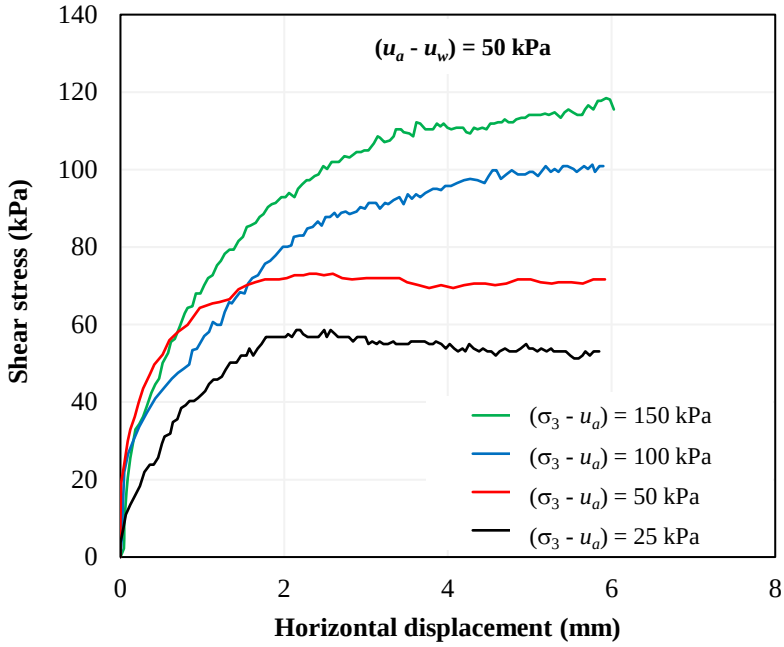

(d)

Figure 5.4 Strains and displacements of soils: (a) 7R; (b) 4R with matric suction of 50 kPa; (c) 4R with matric suction of 150 kPa; and (d) 6U with matric suction of 50 kPa

In poorly aggregated soils, there are numerous points of contact between granular particles, primarily influencing ϕ'. With fewer aggregations present, the formation of an aggregate network skeleton becomes less likely. Consequently, the water phase may only become continuous in small, isolated regions. As a result, the contribution of increased suction to resistance cannot exceed that of increased net normal stress (i.e., $\phi^b \leq \phi'$). In other words, the higher the percentage of fines forming aggregates, the higher the effect of macro and microstructural affects leading to the formation of a shear band that intensifies the effect of matric suction.

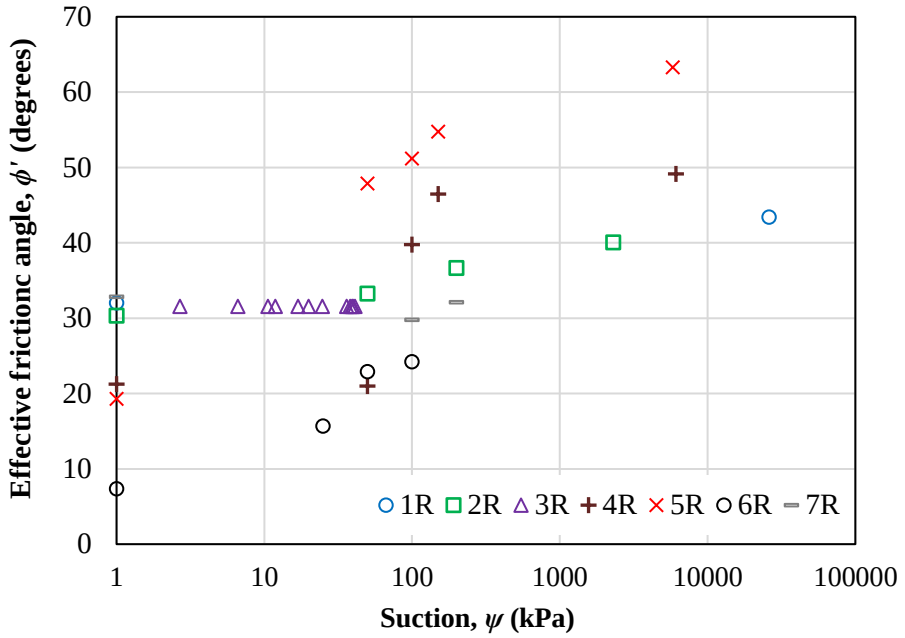

(a)

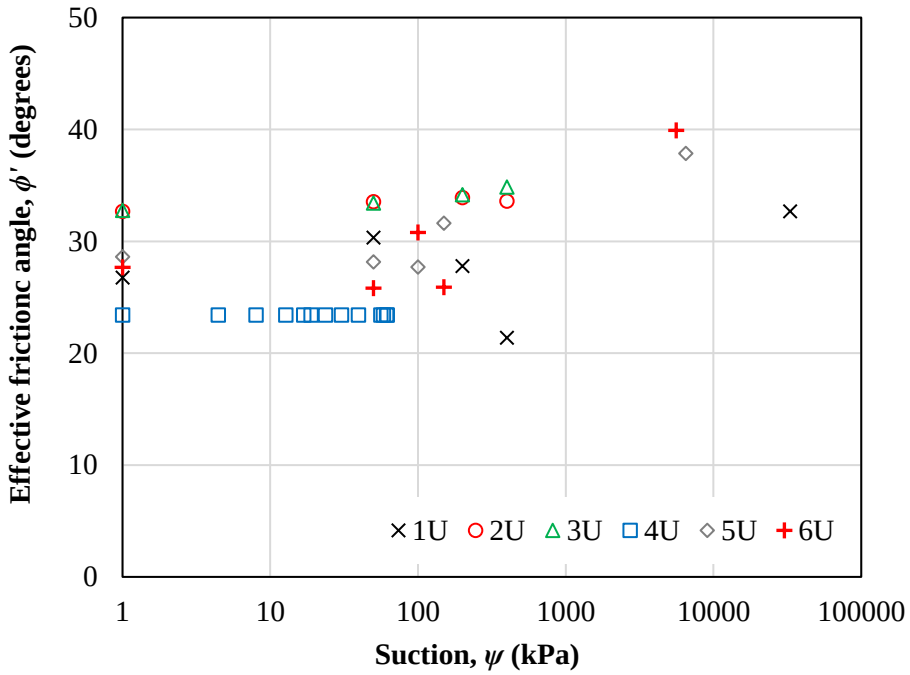

(b)

Figure 5.5 Effective friction angle ϕ' as function of suction: (a) remolded; and (b) undisturbed soils

The dataset analyzed herein indicates that the angle ϕ^b is deemed equivalent to ϕ' for matric suctions lower than the suction at complete saturation of micropores, $(u_a - u_w)_m$. This

assumption is based on observations of soils 1R, 2R, 4R, 5R, 6R, 2U, 3U, 5U, and 6U, where a reduction in ϕ^b occurs at suctions greater than their respective $(u_a - u_w)_{res1}$, as shown in Fig. 5.6. For the remainder soils, assessing possible variations in ϕ^b was challenging as tests were conducted at suctions higher than the desaturation region between macro and micropores. Therefore, it is reasonable to consider that $(u_a - u_w)_m$ corresponds to the average between $(u_a - u_w)_{res1}$ and $(u_a - u_w)_{b2}$ represented on a logarithmic scale:

$$\left(u_a - u_w\right)_m = 10^{\left[\log\left(u_a - u_w\right)_{b2} + \log\left(u_a - u_w\right)_{res1}\right]/2} \tag{5.31}$$

At high suctions between $(u_a - u_w)_{b2}$ and $(u_a - u_w)_{res2}$, the values of ϕ^b approach zero (Fig. 5.6), indicating that further increases in suction cease to impact the shear strength. It is important to note that ϕ^b does not actually reach zero, since it is defined as a secant angle and because doing so would nullify all contributions accumulated from lower suctions. Despite the limited data in the micropores residual region, the most suitable assumption for the analyzed soils appears to be that shear strength becomes constant beyond a suction value $(u_a - u_w)_f$. This value corresponds to the midpoint between $(u_a - u_w)_{b2}$ and $(u_a - u_w)_{res2}$, both represented in logarithmic scale.

$$\left(u_a - u_w\right)_f = 10^{\left[\log\left(u_a - u_w\right)_{b2} + \log\left(u_a - u_w\right)_{res2}\right]/2} \tag{5.32}$$

In unimodal soils, it is customary to neglect the contribution of suction in the residual section. This is because the remainder water in the pores forms very small pendular rings, constituting a discontinuous phase that hinders the distribution of capillary stresses throughout the soil. On the other hand, in bimodal lateritic soils, adsorption accounts for a significant portion of water storage in micropores. With an average micropore diameter of 20 nm (Benatti and Miguel, 2013; Otálvaro et al., 2016; Oliveira et al., 2022) and

considering that the influence of intermolecular forces responsible for adsorption extends up to distances of 10 nm (Tuller et al., 1999; Israelachvili, 2011), it can be estimated that roughly half of the micropore water volume is stored through this mechanism. However, the effects of adsorption on shear strength are disregarded due to their insignificance or limited understanding. Therefore, the definition provided for $(u_a - u_w)_f$ and described by Eq. 5.32 is reasonable and carries clear physical significance.

Figure 5.6 indicates that the soils tested under high suctions exhibit an abrupt decrease in ϕ^b from $(u_a - u_w)_m$, but the limited data does not allow any correlation with the shape of the SWCC within the range between $(u_a - u_w)_m$ and $(u_a - u_w)_f$. For soil 7R, tested at various suctions approaching the micropore residual zone, the fitted curve showing suction versus ϕ^b on a semi-log scale (Fig. 5.7) resembles the van Genuchten (1980) model. A similar shape was previously observed by Gan and Fredlund (1988) for unimodal soils.

Although these structural changes conceptualized here align with observations for explaining the mechanical behavior of the studied bimodal soils, further investigation of the microstructure using, for instance, imaging techniques, is needed to validate these hypotheses.

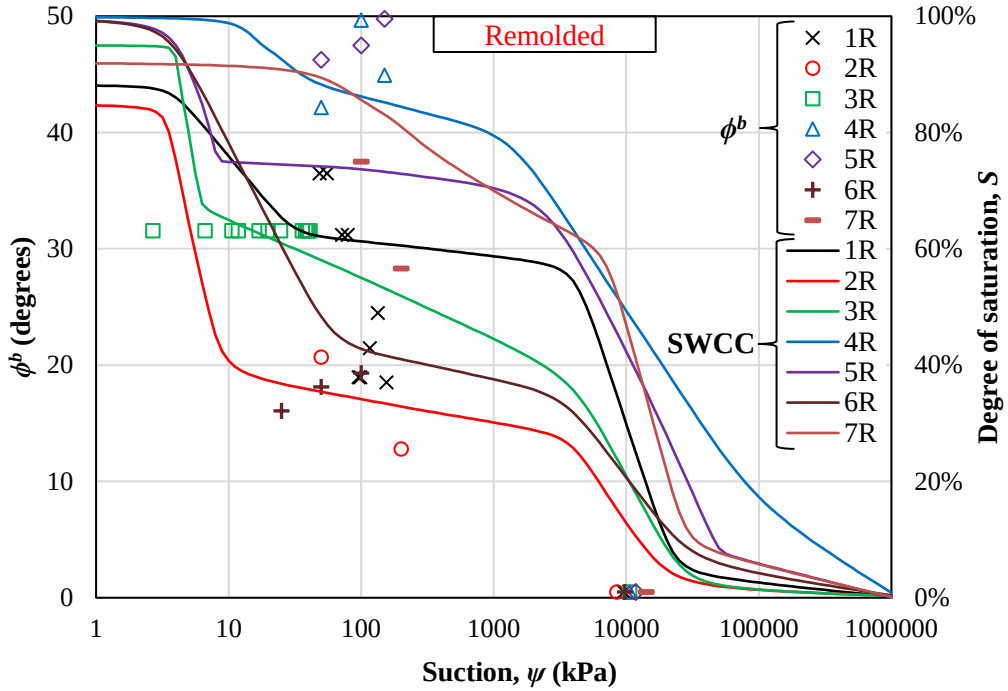

(a)

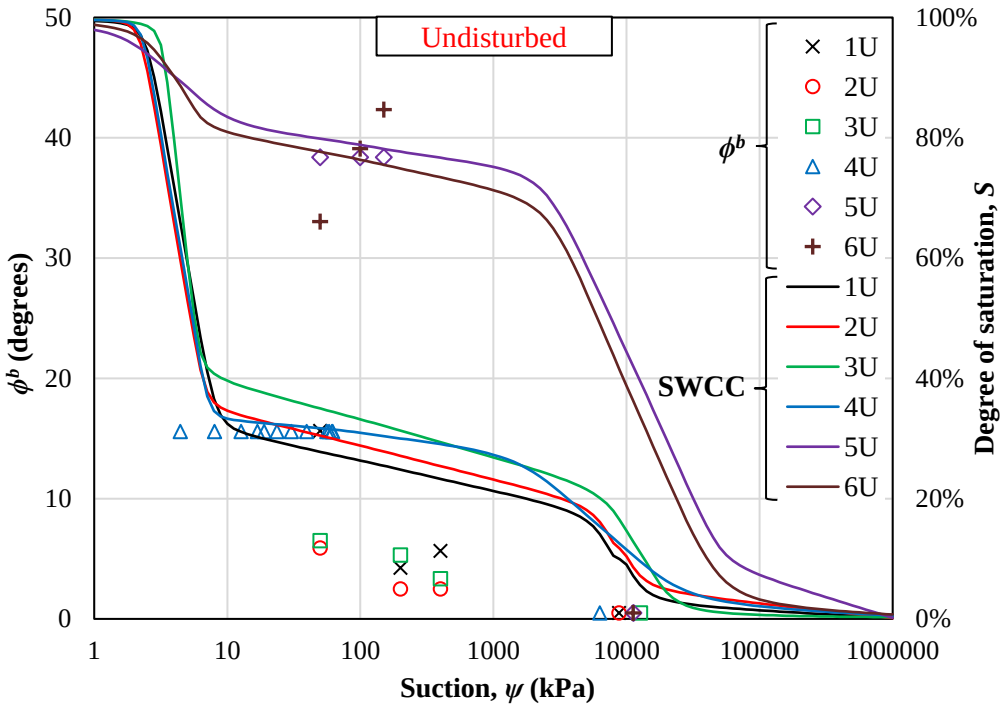

(b)

Figure 5.6 Relationship between ϕ^b and the SWCC: (a) remolded; and (b) undisturbed soils

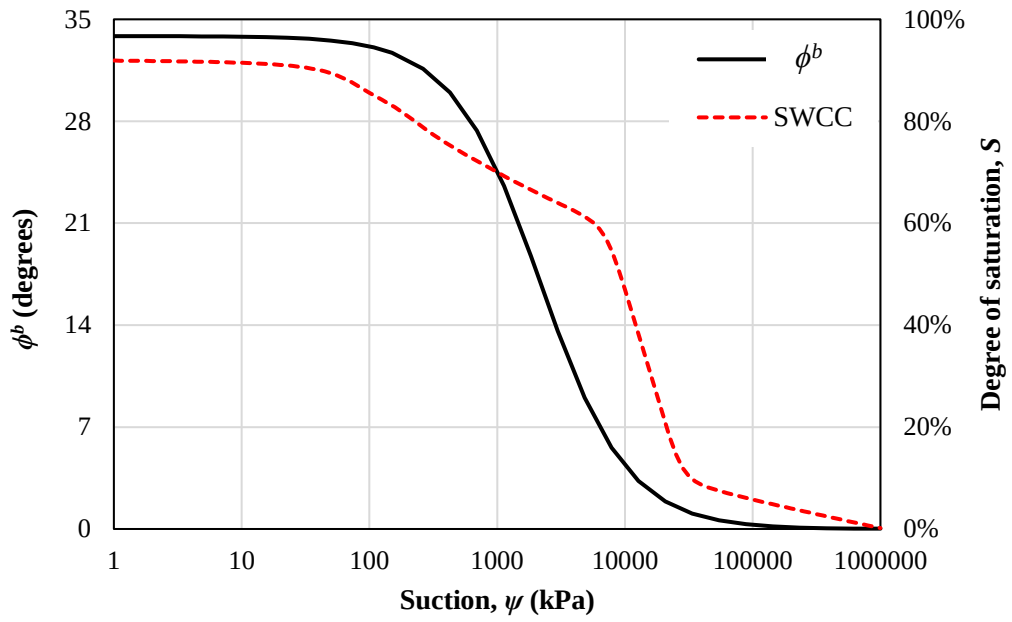

Figure 5.7 Relationship between ϕ^b and the SWCC of soil 7R based on best-fit curve of the shear strength data

5.5 Modeling the unsaturated shear strength

The conceptualization of soil structure behavior outlined in the previous section forms the basis for defining the following observations and assumptions in the proposed shear strength prediction model.

The angle ϕ^b will always be less than or equal to the effective friction angle ϕ'. Although some soils exhibited ϕ^b values exceeding those of ϕ' (e.g., 4R, 5R, 6R, 7R, 5U, and 6U), this limit must be imposed to represent the soil behavior to physical concepts rather than to specific laboratory conditions that may not be fully representative of the actual behavior.

Analyses in the literature using the SWCC to interpret the shear strength behavior often neglect structural changes resulting from the shearing process. SWCCs are typically determined from drying paths under unconfined conditions, whereas the soil at failure may

have undergone different stress paths leading to significant structural alterations. In bimodal lateritic soils, the primary structural changes occur in the macropores, as discussed earlier, leading to alterations in ϕ^b and ϕ'. Variations in ϕ^b within the suction range of the macropores may be disregarded (Fig. 5.8c), but changes in ϕ' values must be considered.

The common approach adopted by previous prediction models involves using an extended Mohr-Coulomb failure envelope with parameters that individually account for the influence of matric suction and net normal stress. To streamline the proposed model, a modified version of the Fredlund et al. (1978) equation (Eq. 5.1) is used by introducing ϕ' and ϕ^b, as depicted in Fig. 5.8. The equation to predict ϕ' was formulated considering that ϕ' is linearly proportional to the logarithm of suction (Fig. 5.8b). This relationship is expressed using a parameter λ, which was found to be associated with the relative aggregation (*RA*) of the soil, as shown in Fig. 5.9. Consequently, ϕ' (in degrees) can be expressed as:

$$\phi' = \phi'_0 + \lambda \ln\left(u_a - u_w\right) \tag{5.33}$$

where: ϕ'_0 is the effective friction angle at saturation.

The factor λ was computed for each soil through regression analysis and then compared with *RA* values according to the soil condition (i.e., remolded or undisturbed). Noticing the proportionality between the two parameters, λ is assumed to be represented by:

$$\lambda = b + d \times RA \tag{5.34}$$

where: b and d are fitting parameters, b is 0.157 and 0, and d is 1.09 and 2.97, respectively for undisturbed and remolded soils.

The observed decrease in ϕ^b is related to the desaturation of micropores, as discussed in the previous section. Moreover, the shape of the SWCC is commonly used to estimate the wet area of the particles and, consequently, the effective contribution of matric suction to shear strength. For the soils investigated, the variation in ϕ^b did not prove to be related to the shape of the SWCC in the range between $(u_a - u_w)_m$ and $(u_a - u_w)_f$. Consequently, the van Genuchten (1980) model was adopted to describe the behavior of ϕ^b between $(u_a - u_w)_m$ and $(u_a - u_w)_f$. Therefore, ϕ^b (in degrees) can be expressed as:

$$\phi^b = \frac{\phi'_0 - \phi^b_f}{\left[1 + a\left(u_a - u_w\right)^n\right]^{1-1/n}} + \phi^b_f \qquad (5.35)$$

where: ϕ'_0 is the effective friction angle at saturation in degrees; ϕ^b_f is the value of ϕ^b at suction $(u_a - u_w)_f$ in degrees; a is a fitting parameter related to the inflection point between the asymptotes; and n is a fitting parameter related to the slope of the curve.

Equation 5.35, used to describe ϕ^b, incorporates two fitting parameters, denoted as a and n, which correspond to the inflection point between the two asymptotes and the curve's slope, respectively. The evolution of ϕ^b is illustrated in Fig. 5.8c and described as follows: initially, ϕ^b is equivalent to ϕ'_0 up to $(u_a - u_w)_m$, then ϕ^b reduces to a minimum value ϕ^b_f at $(u_a - u_w)_f$. Tests carried out at suctions close to $(u_a - u_w)_f$ indicate that the value of ϕ^b_f is approximately 0.5º.

Parameter a controls the position of the curve depicted in Fig. 5.8c. Consequently, an obvious relationship emerges between a and $(u_a - u_w)_{b2}$. Back analyses reveal that a can be calculated from Eq. 5.35 (in kPa) without differentiation between remolded and undisturbed soils. On the other hand, the evaluation of parameter n is more complex due to its physical significance, which entails representing how the contribution of matric suction

diminishes during the desaturation of micropores. Since only soil 7R was tested at various suctions in the micropores zone, it was not possible to carry out a more detailed analysis to develop a possible relationship between *n* and the SWCC. However, the values of *n* equal to 4.25 and 2.03 proved to be adequate for undisturbed and remolded soils, respectively.

$$a = 1.91\times10^{-4}\exp\left[9.29\times10^{-4}\left(u_a - u_w\right)_{b2}\right] \tag{5.36}$$

A relationship between the decrease in ϕ^b and the shape of the SWCC in the range between $(u_a - u_w)_m$ and $(u_a - u_w)_f$, represented by the parameter *n* was pursued. However, such a relationship was not found and there are two reasons why this relationship is either absent or not clear: (i) the boundaries $(u_a - u_w)_m$ and $(u_a - u_w)_f$ are inadequate or (ii) the microstructure geometry and the water storage mechanisms is overly complex and does not allow the establishment of a clear relationship between ϕ^b and the desaturation of the micropores. Regarding reason (i), the shear strength data as well the theoretical justification relating the size of micropores to the influence of intermolecular forces causing adsorption provide compelling arguments in favor of the selected threshold $(u_a - u_w)_f$, as discussed previously. On the other hand, the limit $(u_a - u_w)_m$ may be questionable, since it falls within a region where shear strength data is scarce. If this limit were close or equivalent to $(u_a - u_w)_{b2}$, a relationship between ϕ^b and the shape of the SWCC could easily be ascertained; however, the data indicates that $(u_a - u_w)_m$ is closer to $(u_a - u_w)_{res1}$.

Finally, the shear strength envelope, in terms of apparent cohesion and matric suction, features only two regions (Fig. 5.8d): one linear and the other nonlinear, similar to that commonly exhibited by unimodal soils.

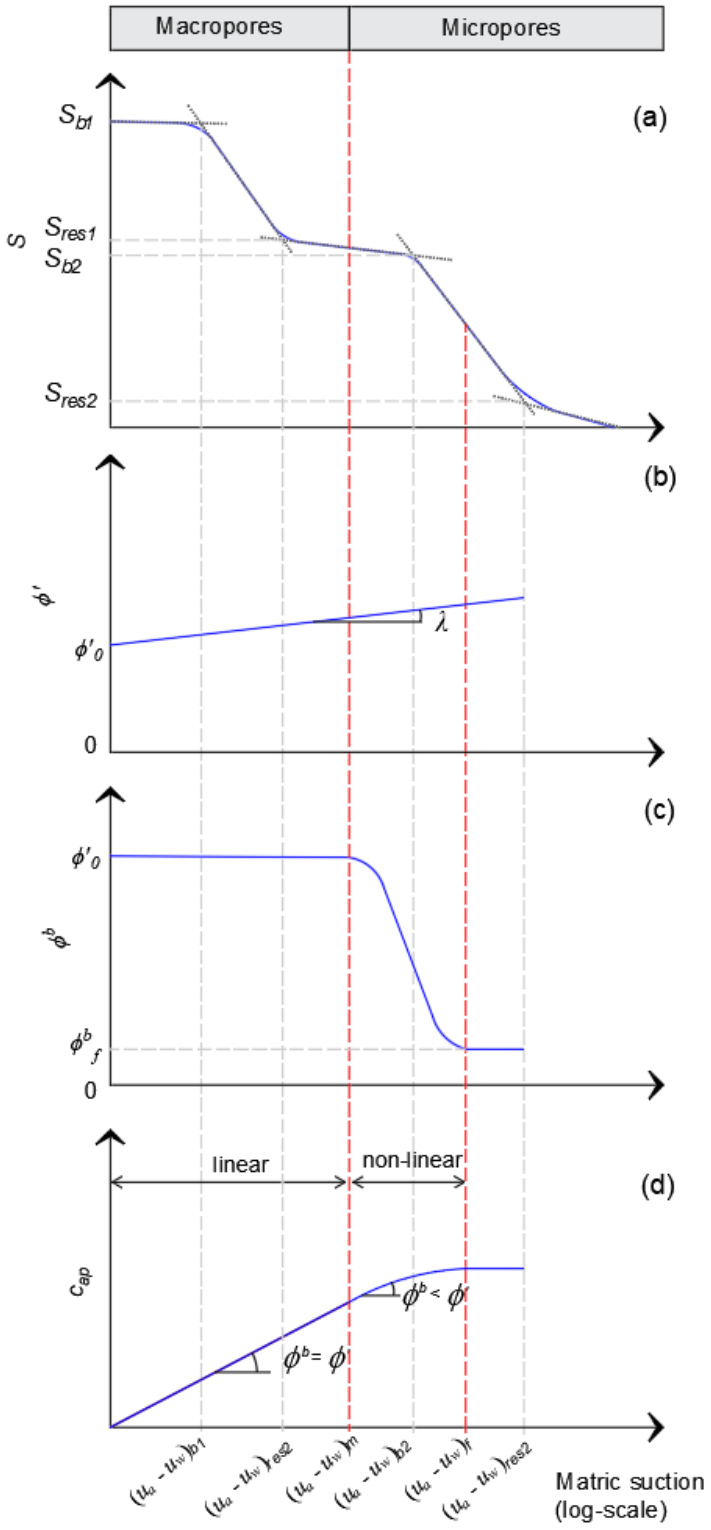

Figure 5.8 Shear strength parameters accordingly to the adopted hypothesis: (a) bimodal SWCC; (b) non-linearity of ϕ'; (c) non-linearity of ϕ^b; and (d) apparent cohesion, c_{ap}

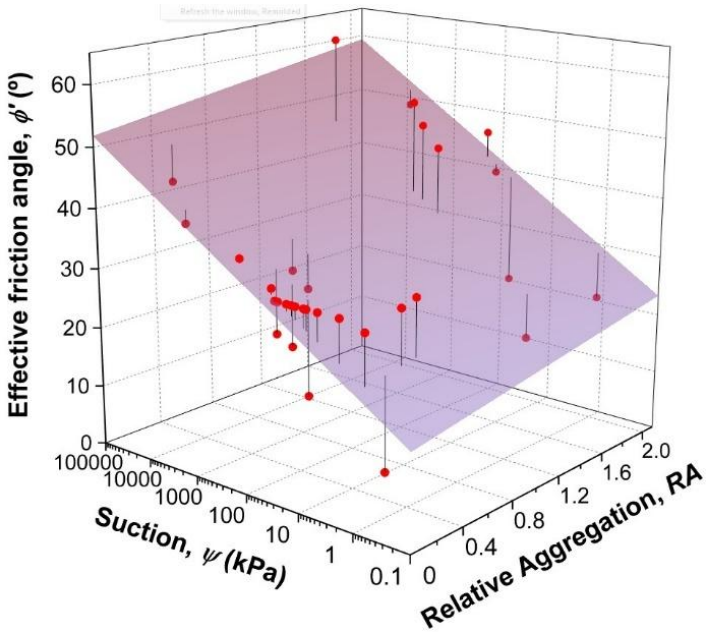

(a)

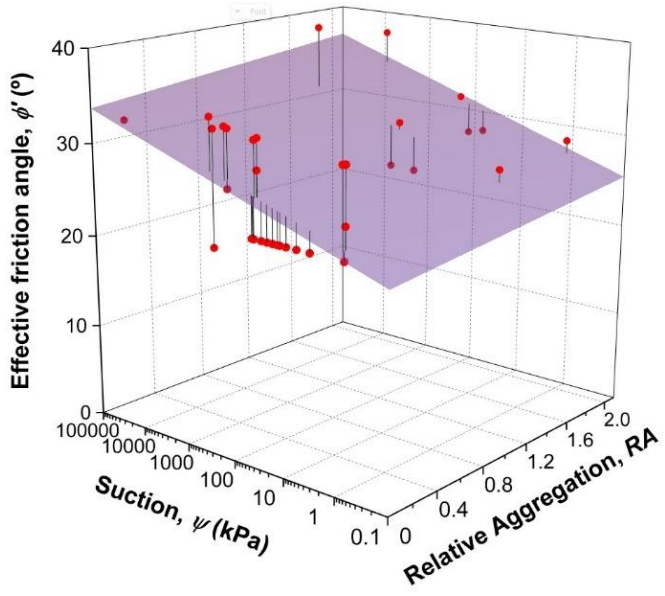

(b)

Figure 5.9 Relationship between ϕ', suction, and relative aggregation of: (a) remolded; and (b) undisturbed soils

5.6 Model performance and comparison to previous models

Figures 5.10 and 5.11 illustrate the results for the predictions for the remolded and undisturbed soils, respectively. The model parameters are presented in Table 5.5. The

proposed model presents good predictions for most soils. The highest dispersions were obtained for materials 4R, 5R, 1U and 6U, being the materials with the highest levels of soil aggregation. Particularly for soils 4R, 5R, 5U, and 6U, it was noted that the shear strength tends to be underestimated. This outcome was anticipated, given that these materials demonstrated a significant increase in both ϕ' and ϕ^b with matric suction, while the proposed model imposes a constraint on the value of ϕ^b to ϕ'_0.

The comparison between measured and predicted data is depicted in Fig. 5.12a and 5.12b for remolded and undisturbed soils, respectively. While both sets exhibit similar R^2 values, the Root Mean Square Error (RMSE) for remolded soils is nearly double of that of undisturbed soils. This discrepancy can be attributed partly to the generally higher shear strength values observed for remolded soils. Additionally, the model demonstrates great accuracy for shear strengths up to 100 kPa, commonly associated with low matric suctions and net normal stresses, where the structural changes in the soils are less pronounced.

The performance of the proposed model was compared with several existing models in the literature, extending evaluations to include models designed for unimodal soils because of two reasons: (i) unimodal models are also commonly used for predicting the shear strength ignoring bimodal nature of laterites; (ii) due to the scarcity of models developed for bimodal soils. It is worth mentioning that the application of unimodal models that require the determination of the air-entry value and residual suction was based on the use of the first air-entry value and the second residual suction. This methodology provided the best results for each model.

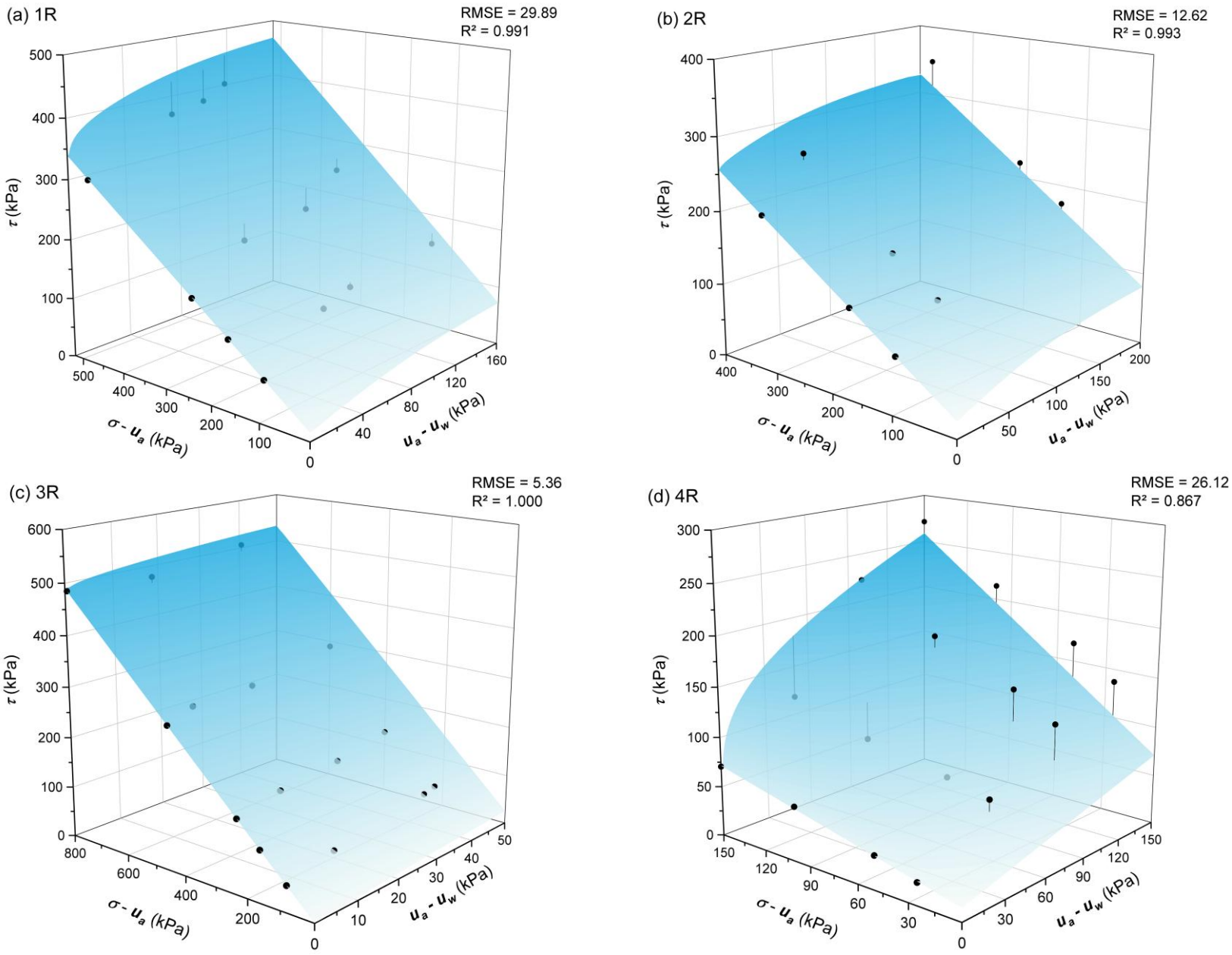
(a) 1R
RMSE = 29.89
R² = 0.991
τ (kPa)
σ - ua (kPa)
ua - uw (kPa)
(b) 2R
RMSE = 12.62
R² = 0.993
τ (kPa)
σ - ua (kPa)
ua - uw (kPa)
(c) 3R
RMSE = 5.36
R² = 1.000
τ (kPa)
σ - ua (kPa)
ua - uw (kPa)
(d) 4R
RMSE = 26.12
R² = 0.867
τ (kPa)
σ - ua (kPa)
ua - uw (kPa)

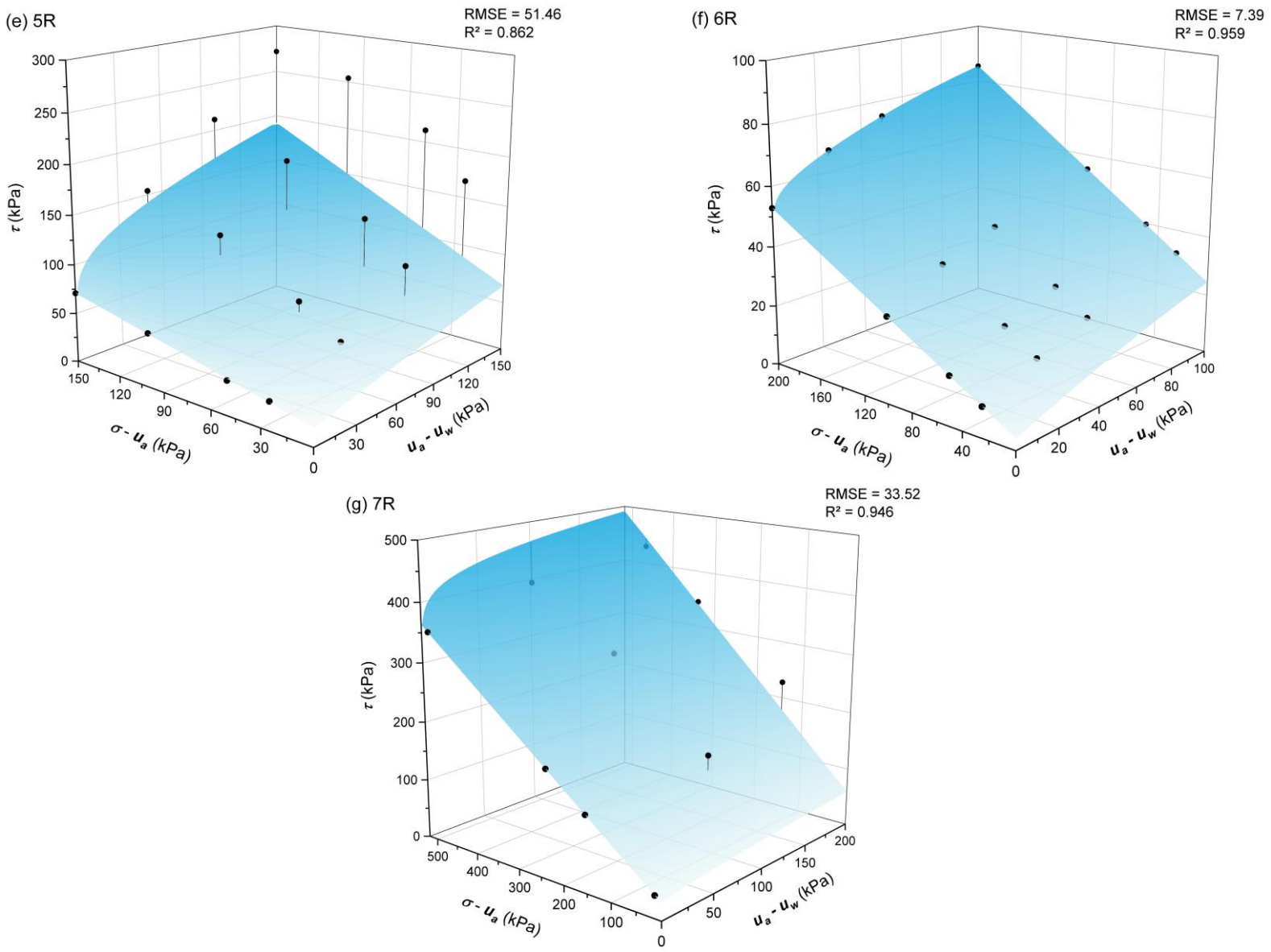

Figure 5.10 Predicted (surface) and measured (points) extended shear strength envelope for remolded soils: (a) 1R; (b) 2R; (c) 3R; (d) 4R; (e) 5R; (f) 6R; (g) 7R

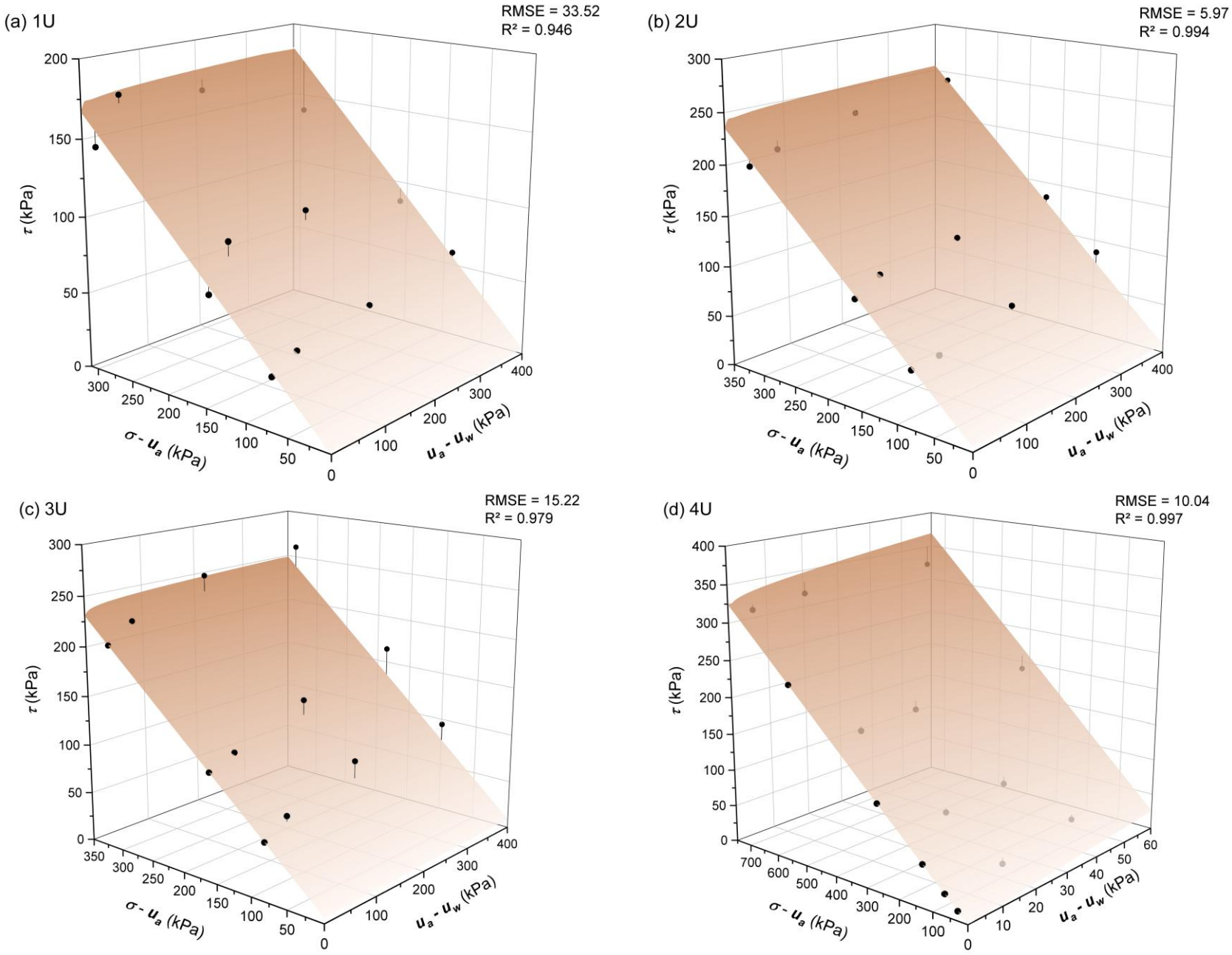
(a) 1U
RMSE = 33.52
R² = 0.946
τ (kPa)
σ - u_a (kPa)
u_a - u_w (kPa)
(b) 2U
RMSE = 5.97
R² = 0.994
τ (kPa)
σ - u_a (kPa)
u_a - u_w (kPa)
(c) 3U
RMSE = 15.22
R² = 0.979
τ (kPa)
σ - u_a (kPa)
u_a - u_w (kPa)
(d) 4U
RMSE = 10.04
R² = 0.997
τ (kPa)
σ - u_a (kPa)
u_a - u_w (kPa)

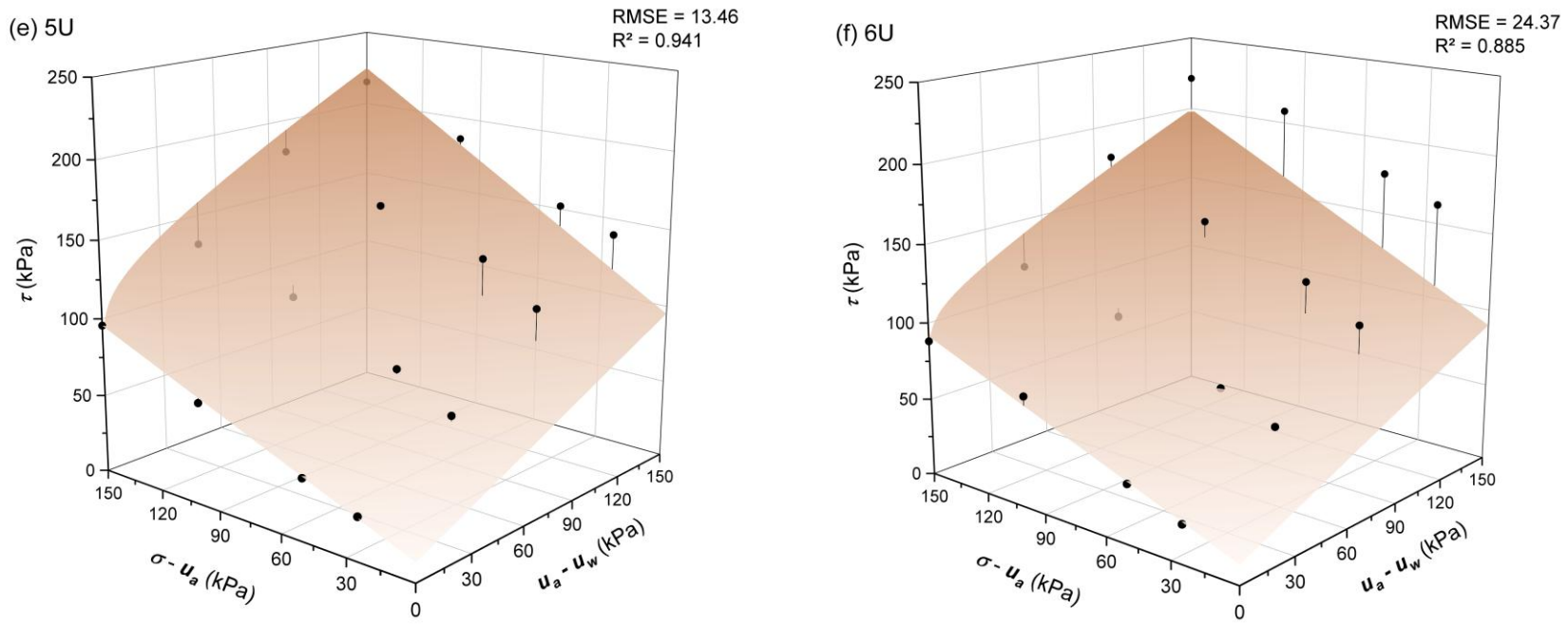

Figure 5.11 Predicted (surface) and measured (points) extended shear strength envelope for undisturbed soils: (a) 1U; (b) 2U; (c) 3U; (d) 4U; (e) 5U; and (f) 6U

Table 5.5 Model parameters

Soil name	$(u_a - u_w)_m$ (kPa)	$(u_a - u_w)_f$ (kPa)	a (kPa)	λ
1U	237	8775	0.1272	0.251
2U	237	8775	0.1272	0.254
3U	232	12728	0.8152	0.229
4U	119	6325	0.0012	0.241
5U	136	11313	0.0021	2.370
6U	129	11225	0.0026	1.652
1R	253	9592	0.0078	1.044
2R	179	8485	0.0078	0.258
3R	164	10607	0.0125	0.230
4R	198	10583	0.0007	6.040
5R	151	11765	0.0025	4.080
6R	469	9747	0.0065	0.694
7R	1303	14135	0.1845	1.379

Figure 5.13 illustrates the performance of all models, demonstrating the superiority of the proposed model. In terms of RMSE, for remolded soils, the proposed model was 40% more accurate than the Naghaded and Toker (2019) model, which was the second-best performing model. Note that most models exhibited similar performances, with RMSE values around 50 kPa. For undisturbed soils, the proposed model presented a 50% improvement over the Vanapalli et al. (1996) model, which ranked second in terms of performance. Conversely, existing models developed for gap-graded soils exhibited comparatively poorer results, probably that they were developed using limited data sets of materials whose microstructures are very different from those of bimodal lateritic soils. The discussion in this paragraph is to mainly highlight the limitations of using the existing models in the literature towards predicting the shear strength of lateritic bimodal soils. It is

also important to point out that the equations developed for predicting the shear strength of unsaturated soils presently available in the literature were developed with different objectives and for different soils and conditions; in other words, they were not exclusively developed for lateritic bimodal soils.

The proposed model tends to underestimate shear strength as the degree of soil aggregation increases. To overcome this limitation, it is necessary to consider increasing values of ϕ^b for matric suctions lower than $(u_a - u_w)_m$.

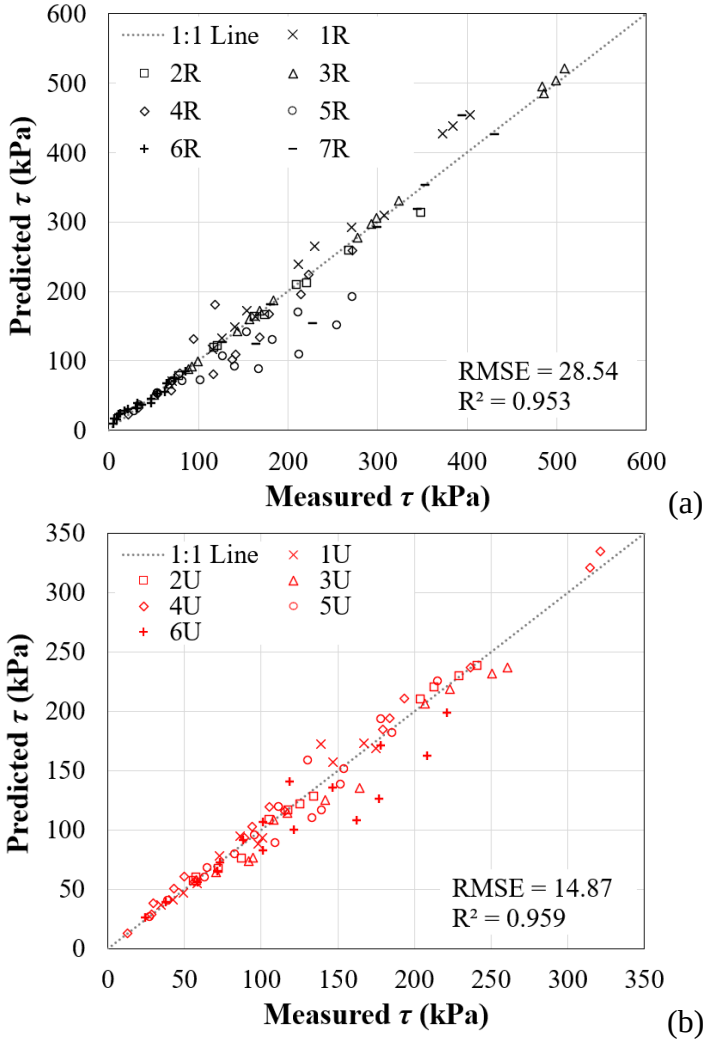

Figure 5.12 Measured versus predicted shear strength for soils: (a) remolded; and (b) undisturbed

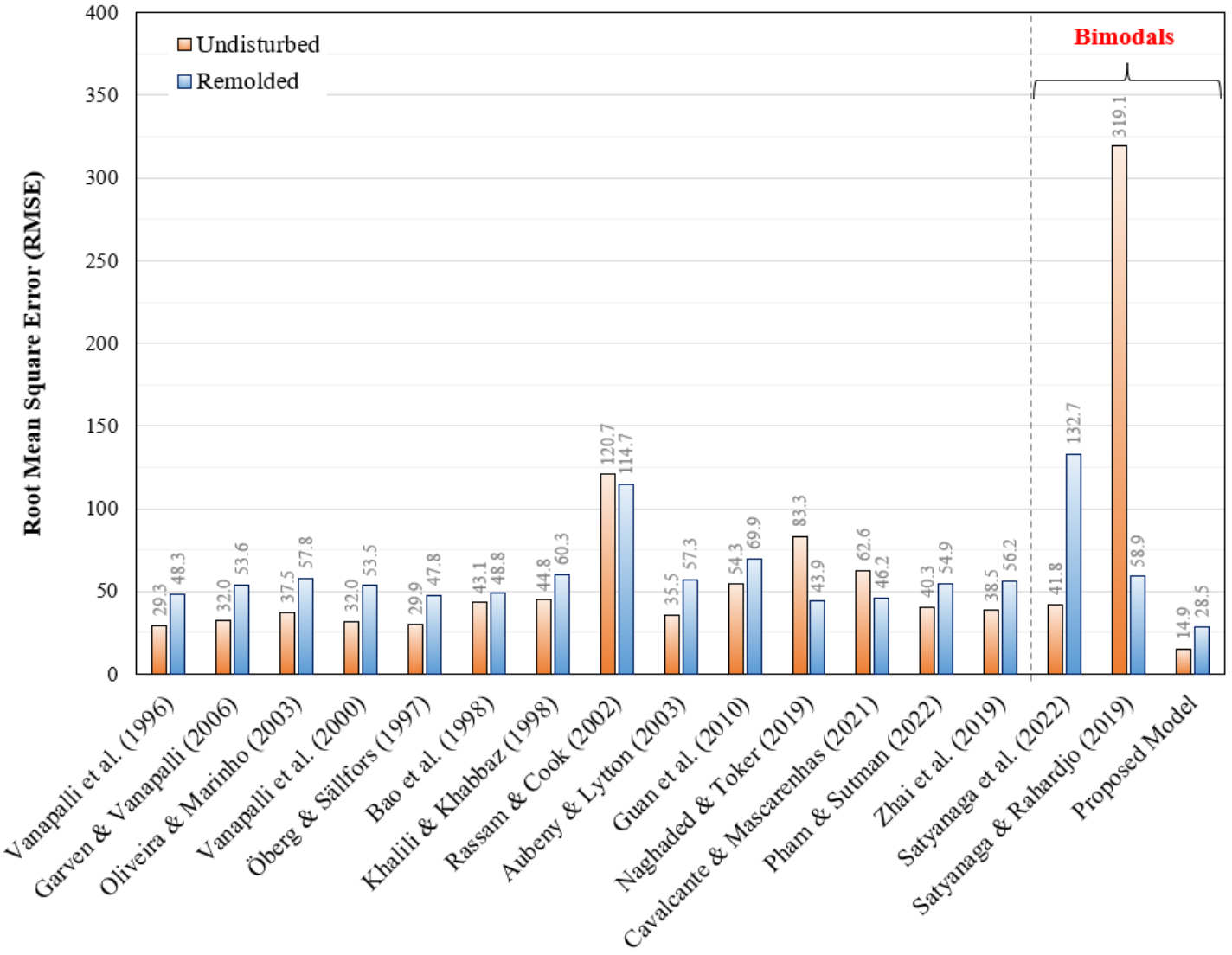

Figure 5.13 Performance of some existing models and the proposed approach

5.7 Conclusions

This study introduces a theoretical framework delineating the structural evolution of bimodal lateritic soils during shearing, offering insights into modeling unsaturated shear strength and elucidating the anomaly of matric suction contribution to the shear strength (i.e., $\phi^b > \phi'$). The analyses conducted reveal several key findings:

- Examples of ϕ^b values surpassing ϕ' as documented in literature and found in this study were consistently observed in drained tests. This behavior is believed to occur solely in specimens subjected to suctions exceeding the first air-entry value and due to the emergence of a contractive shear band. Within this band, macropores are filled with broken aggregations, increasing degree of saturation and creating regions with continuous water phases encompassing the microstructure. Consequently, the shear strength attributed to matric suction is governed by aggregations within these saturated areas, while the impact of ϕ' is constrained by direct contact between particles and aggregations. However, this proposed approach needs further validation;
- The influence of net normal stress contribution to shear strength is influenced by matric suction. Generally, an approximately linear correlation was observed between ϕ' values and the logarithm of matric suction, attributable to soil hardening induced by macropores closure with increased matric suction;
- The failure envelope, in terms of apparent cohesion and matric suction, appears to exhibit two distinct regions: a linear zone extending from saturation to the beginning of the micropores region $(u_a - u_w)_m$, and a non-linear zone encompassing the preceding limit to the midpoint of the micropores transition zone $(u_a - u_w)_f$;

- The proposed model for unsaturated strength prediction is straightforward to implement and yields promising results for bimodal lateritic soils, necessitating solely information regarding aggregated and disaggregated grain-size distribution, and SWCC. Comparative analysis with other models, including bimodal approaches, demonstrated its significant superior performance. However, the model could be improved by recalibrating the fitting parameters (a, b, d and ϕ^b_f) if more soils tested with suctions in the micropores region were considered. The hypotheses used in the model development constitute a framework that can be easily adapted to improve predictions through using a larger dataset. The poor results from the existing models for bimodal soils indicate their unsuitability for use with highly weathered tropical soils.

References

Araújo, A.G., 2019. Uso de microtomografia e porosimetria para análise de estrutura bimodal de um latossolo vermelho reconstituído. Doctoral Thesis: Departament de Civil and Environmental Engineering, Universidade Federal de Goiás, 82p.

Aubeny, C., Lytton, R., 2003. Estimating strength versus location and time in high-plasticity clays. Texas Transportation Institute, College Station, Texas.

Bao, C., Gong, B., Zhan, L., 1998. Properties of unsaturated soils and slope stability of expansive soils. Proceedings of the Second International Conference on Unsaturated Soils (UNSAT 98). Beijing, China. 1: 71-98.

Benatti, J., C., B., Miguel, M., G., 2013. A proposal of structural models for colluvial and lateritic soil profile from southwestern Brazil on the basis of their collapsible behavior. Engineering Geology. 153, 1-11. https://doi.org/10.1016/j.enggeo.2012.11.003

Bésuelle, P., Desrues, J., Raynaud, S., 2000. Experimental characterisation of the localisation phenomenon inside a Vosges sandstone in a triaxial cell. International Journal of Rock Mechanics and Mining Sciences,37(8), 1223-1237. https://doi.org/10.1016/S1365-1609(00)00057-5

Bishop, A., W., 1959. The principle of effective stress. Teknisk Ukeblad, 106(39), 859-863

Borges, C. R., Lopes, B. C. F., Cordão Neto, M. P., 2019. Pore size distribution of Brasilia

tropical soil in 3 different initial states. In: 7th International Symposium on Deformation Characteristics of Geomaterials, Glasglow. 92, 01009. https://doi.org/10.1051/e3sconf/20199201009

Cabalar, A., F., 2011. The Effects of Fines on the Behaviour of a Sand Mixture. Geotechnical and Geological Engineering, 29, 91–100. https://doi.org/10.1007/s10706-010-9355-z

Camapum de Carvalho, J., Gitirana Jr., G. F. N., 2021. Unsaturated soils in the context of tropical soils. Soils and Rock, 44(3), 25p. https://doi.org/10.28927/SR.2021.068121

Camapum de Carvalho, J., Gitirana Jr., G. F. N., Machado, S. L., Mascarenha, M. M. A., Silva Filho, F. C., Rodrigues, R. A. 2023. Solos não saturados no contexto geotécnico. Associação Brasileira de Mecânica dos Solos e Engenharia Geotécnica, São Paulo, 2nd ed.

Cavalcante, A., L., B., Mascarenhas, P., V., S., 2021. Efficient approach in modeling the shear strength of unsaturated soil using soil water retention curve. Acta Geotechnica, 16:3177-3186. https://doi.org/10.1007/s11440-021-01144-6

De Medina, J., Motta, L., M., G., Santos, J., D., G., D., 2006. Deformability characteristics of Brazilian laterites. Geotechnical and Geological Engineering, 24, 949–971. https://doi.org/10.1007/s10706-005-8507-z

Desrues, J., Viggiani, G., 2004. Strain localization in sand: an overview of the experimental results obtained in Grenoble using stereophotogrammetry. Internatinal Journal for Numerical Analytical Methods in Geomechanics, 28, 279-321. https://doi.org/10.1002/nag.338

Donald, I., B., 1957. Effective stresses in unsaturated non-cohesive soils with controlled negative pore pressure, Master's thesis, University of Melbourne, Melbourne, Australia.

El Bied, A., Sulem, J., Martineau, F., 2002. Microstructure of shear zones in Fontainebleau sandstone. International Journal of Rock Mechanics and Mining Sciences, 39(7), 917-932. https://doi.org/10.1016/S1365-1609(02)00068-0

Escario, V., Jucá, J., F., T., 1989. Strength and Deformation of Partially Saturated Soils. Proceedings of the 12th International Conference on Soil Mechanics and Foundation Engineering, Rio de Janeiro, 2, 43-46.

Escario, V., Sáez, J., 1986. The shear strength of partly saturated soils. Géotechnique, 36(3), 453-456. https://doi.org/10.1680/geot.1986.36.3.453

Fagundes, L., S., 2014. Avaliação da resistência ao cisalhamento de um solo tropical não saturado. Master Thesis: Graduate program in civil and environmental engineering, Universidade Estadual Paulista, 102p.

Fernandes, J., F., 2016. Resistência e deformabilidade de um solo não saturado a partir de

ensaios triaxiais. Master Thesis: Graduate program in civil and environmental engineering, Universidade Estadual Paulista, 144p.

Feuerharmel, C., 2007. Estudo da resistência ao cisalhamento e da condutividade hidráulica de solos coluvionares não saturados da Formação Serra Geral. Doctoral Thesis: Graduate program in civil engineering. Universidade Federal do Rio Grande do Sul, 330p.

Fookes, P., G., 1994. A review: Genesis and classification of tropical soils for engineers. Proceedings of the Geotechnics in the African Environment, Balkema, Rotterdam, Netherlands, 423-442.

Fredlund, D., G., Morgenstern, N., R., Widger, R., A., 1978. The shear strength of unsaturated soils. Canadian Geotechnical Journal, 15(3), 313-321. https://doi.org/10.1139/t78-029

Fredlund, D., G., Xing, A., Fredlund, M., D., and Barbour, S., L., 1996. Relationship of the unsaturated soil shear strength to the soil-water characteristic curve. Canadian Geotechnical Journal, 33(3): 440-448. https://doi.org/10.1139/t96-065

Gan, K., J., Fredlund, D., G., 1988. Multistage direct shear testing of unsaturated soils. Geotechnical Testing Journal, 11(2), 132-138. https://doi.org/10.1520/GTJ10959J

Georgetti, G. B., 2010. Resistência de um solo não saturado a partir de ensaios com teor de umidade constante (CW). Master Thesis: Graduate program in geotechnics, Universidade de São Paulo, 108p.

Georgetti, G. B., 2014. Deformabilidade e resistência de um solo laterítico não saturado. Doctoral Thesis: Graduate program in geotechnics, Universidade de São Paulo, 130p.

Grau, E., D., A., 2014. Efeito da variação de umidade no calculo do empuxo em solos tropicais. Master Thesis: Department of Civil and Environmental Engineering, Universidade de Brasília, Distrito Federal, 105p.

Guan, G., S., Rahardjo, H., Choon, L., E., 2010. Shear strength equations for unsaturated soil under drying and wetting. Journal of Geotechnical and Geoenvironmental Engineering, 136(4). https://doi.org/10.1061/(ASCE)GT.1943-5606.0000261

Hicher, P., Y., Wahyudi, H., Tessier, D., 1994. Microstructural analysis of strain localization in clay. Computers and Geotechnics, 16, 205-222. https://doi.org/10.1016/0266-352X(94)90002-7

Huat, B. B. K., Toll, D. G., Prassad, A., 2013. Handbook of Tropical Residual Soils Engineering. CRC Press, Taylor and Francis Group, Florida.

Israelachvili, J. N., 2011. Intermolecular and surface forces. Elsevier: 3rd Edition.

Jiang, M-j., Peng, L-c., Zhu, H-h., Lin, Y-x., Huang, L-j., 2010. Microscopic investigation on shear band of marine clay in Zhuhai, China. Rock and Soil Mechanics, 31(7), 2017-2023.

Khalili, N., Khabbaz, M., H., 1998. Technical Note: A unique relationship for χ for the determination of the shear strength of unsaturated soils. Géotechnique, 48(5): 681-687. https://doi.org/10.1680/geot.1998.48.5.681

Kim, D., Nam, B., H., Youn, H., 2018. Effect of clay content on the shear strength of clay–sand mixture. International Journal of Geo-Engineering, 9. https://doi.org/10.1186/s40703-018-0087-x

Kühn, V. O. 2014. Resistência ao cisalhamento de um solo tropical não saturado considerando altas sucções. Master thesis, Universidade Federal de Goiás, Goiânia, Goiás, Brazil.

Kühn, V. O., Lopes, B. C. F. L., Caicedo, B., Cordão-Neto, M. P., 2022. Mechanical behaviour of bimodal kaolin clay with aggregates. Engineering Geology. 297, 106490. https://doi.org/10.1016/j.enggeo.2021.106490

Lamborn, M., J., 1986. A micromechanical approach to modeling partly saturated soils. Master Thesis: Texas A & M University, Texas, 546p.

Lee, S., J., Lee, S., R., Kim, Y., S. 2003. An approach to estimate the unsaturated shear strength using artificial neural network and hyperbolic formulation. Computers and Geotechnics, 489-503. https://doi.org/10.1016/S0266-352X(03)00058-2

Lopes, M. B. L., Campos, T. M. P., Antunes, F. S., Villar, L. F. S. 2007. Influência da sucção na resistência ao cisalhamento de um solo residual de filito da Região Metropolitana de Belo Horizonte (MG). In: VI Simpósio Brasileiro de Solos Não Saturados.

Lopes, B., C., F., L., Kühn, V., O., Queiroz, A., C., G., Caicedo, B., Cordão Neto, M., P., 2022. Structure evaluation of a tropical residual soil under wide range of compaction conditions. Géotechnique Letters, 12(2), 106-113. https://doi.org/10.1680/jgele.21.00101

Lopes, B., C., F., L., 2016. Microstructural-based approach to the interpretation of clays and transitional soils behaviour. Doctoral Thesis: Department of Civil and Environmental Engineering, Universidade de Brasília, Distrito Federal, 133p.

Lu, N., Jonathan, W. G., David, T. W., 2010. A closed-form equation for effective stress in unsaturated soil. Water Resources Research, 46, W05515. https://doi.org/10.1029/2009WR008646

Lytton, R., L., 1995. Keynote Address: Foundations and Pavements on Unsaturated Soils, Proceedings of the First International Conference on Unsaturated Soils (UNSAT 95).

Marinho, F., A., M., Oliveira, O., M., Adem, H., Vanapalli, S., 2013. Shear strength behavior of compacted unsaturated residual soil. International Journal of Geotechnical Engineering, 7(1), 9p. https://doi.org/10.1179/1938636212Z.00000000011

Mascarenha, M. M. A., Cordão Neto, M. P., Silva, M. T. M. G., 2016. Alternative method

for analyzing hydromechanical behaviour of unsaturated soils. Soils and Rocks. 39(1), 29-39. http://dx.doi.org/10.28927/SR.391029

Mendes, R., M., Marinho, F., A., M., 2020. Soil water retention curves for residual soils using traditional methods and MIP. Geotechnical and Geological Engineering, 38, 5167-5177. https://doi.org/10.1007/s10706-020-01354-x

Miguel, M., G., Vilar, O., M., 2009. Study of the water retention properties of a tropical soil. Canadian Geotechnical Journal, 46, 1084-1092. https://doi.org/10.1139/T09-039

Muawia, A., D., 2013. Effects of Clay and Moisture Content on Direct Shear Tests for Clay-Sand Mixtures. Advances in Materials Science and Engineering, 562726. https://doi.org/10.1155/2013/562726

Nagaraj, H., B., 2016. Influence of gradation and proportion of sand on stress–strain behavior of clay–sand mixtures. International Journal of Geo-Engineering, 7. https://doi.org/10.1186/s40703-016-0033-8

Naghaded, R., A., Toker, N., K., 2019. Exponential equation for predicting shear strength envelope of unsaturated soils. International Journal of Geomechanics, 19(7). https://doi.org/10.1061/(ASCE)GM.1943-5622.0001435

Öberg, A., L., Sallfors, G., 1997. Determination of shear strength parameters of un-saturated silts and sands based on the water retention curve. Geotechnical Testing Journal, 20(1), 40-48. https://doi.org/10.1520/GTJ11419J

Oliveira, A. D., Pelaquim, F. G. P., Zanin, R. F. B., Melo, T. R., Filho, J. T., Andrello, A. C., Teixeira, R. S., 2022. The structure of tropical lateritic soils as an impacting factor in the shape of soil-water characteristic curves. Soils and Rocks. 45(2). https://doi.org/10.28927/SR.2022.070521

Ortigão, J., A., R., Cunha, R., P., Alves. L., S., 1996. In situ tests in Brasília porous clay. Canadian Geotechnical Journal, 33, 189-198. https://doi.org/10.1139/t96-035

Otálvaro, I. F., Cordão Neto, M. P., Caicedo, B., 2015. Compressibility and microstructure of compacted laterites. Transportation Geotechnics. 5, 20-34. https://doi.org/10.1016/j.trgeo.2015.09.005

Otálvaro, I. F., Cordão-Neto, M. P., Delage, P., Caicedo, B., 2016. Relationship between soil structure and water retention properties in a residual compacted soil. Engineering Geology. 205, 73-80. https://doi.org/10.1016/j.enggeo.2016.02.016

Paraguassú, A., B., Rohm, S., A. 1991. Movimento da agua no solo sob efeito da temperatura e a sua influência na cimentação de superfícies de sedimentos arenosos. In Atas. São Paulo: Sbg.

Pereira, J., H., F., 1996. Numerical analysis of the mechanical behavior of collapsing earth dams during first reservoir filling. Doctoral Thesis: Department of Civil Engineering, University of Saskatchewan, 448p.

Pereira, J., H., F., Fredlund, D., G., Cordão Neto, M. P., Gitirana Jr., G., F., N., 2005. Hydraulic behavior of collapsible compacted gneiss soil. Journal of Geotechnical and Geoenvironmental Engineering, 131(10), 1264-1273. https://doi.org/10.1061/(ASCE)1090-0241(2005)131:10(1264)

Pham, T., A., 2022. Micromechanical-based shear strength equation considering the stress-state effect for unsaturated soils. International Journal of Geomechanics, 22(9). https://doi.org/10.1061/(ASCE)GM.1943-5622.0002495

Pham, T., A., Sutman, M., 2022. An analytical model for predicting the shear strength of unsaturated soils. Proceedings of the Institution of Civil Engineers – Geotechnical Engineering. https://doi.org/10.1680/jgeen.21.00135

Rassam, D., W., Cook, F., J., 2002. Predicting the shear strength envelope of unsaturated soils. Geotechnical Testing Journal, 28: 215-220. https://doi.org/10.1520/GTJ11365J

Röhm, S., A., Vilar, O., M., 1995. Shear strength of an unsaturated sandy soil. Proceedings of the First International Conference on Unsaturated Soils (UNSAT 95), 189-193.

Rodriges, R., A., Soares, F., V., P., Sanchez, M., 2021. Settlement of footings on compacted and natural collapsible soils upon loading and soaking. Journal of Geotechnical and Geoenvironmental Engineering, 147(4). https://doi.org/10.1061/(ASCE)GT.1943-5606.0002479

Santos, R. A., Esquivel, E., R., 2018. Saturated anisotropic hydraulic conductivity of a compacted lateritic soil. Journal of Rock Mechanics and Geotechnical Engineering, 10, 986-991. https://doi.org/10.1016/j.jrmge.2018.04.005

Satyanaga, A., Rahardjo, H., 2019. Unsaturated shear strength of soil with bimodal soil-water characteristic curve. Géotechnique, 69(9), 828-832. https://doi.org/10.1680/jgeot.17.P.108

Satyanaga, A., Bairakhmetov, N., Kim, J., R., Moon, S-W., 2022. Role of bimodal water retention curve on the unsaturated shear strength. Applied Science, 12, 1266. https://doi.org/10.3390/app12031266

Soares, R. M., Campos, T. M. P. 2005. Resistência ao cisalhamento de um solo coluvionar não saturado da cidade do Rio de Janeiro. In: IV Conferência Brasileira sobre Estabilidade de Encostas, Salvador, Bahia, Brazil.

Souza, J. C., 2020. Avaliação da relação entre a curva granulométrica e a curva característica solo-água para um solo residual bimodal sob diferentes graus de desagregação. Master Thesis: Department de Civil and Environmental Engineering, Universidade Federal de Goiás.

Teixeira, R., S., Vilar, O., M., 1997. Shear strength of an unsaturated compacted soil. Proceedings of the 3rd Brazilian Symposium on Unsaturated Soils, Rio de Janeiro, 1, 161-169

Toll, D., G., 1990. A framework for unsaturated soil behaviour. Géotechnique, 40(1), 31-44. https://doi.org/10.1680/geot.1990.40.1.31

Tuller, M., Or, D., Dudley, L. M., 1999. Adsorption and capillary condensation in porous media: Liquid retention and interfacial configurations in angular pores. Water Resources Research. 35(7), 1949-1964. https://doi.org/10.1029/1999WR900098

Vanapalli, S., K., Fredlund, D., G., Pufahl, D., E., Clifton, A., W., 1996. Model for the prediction of shear strength with respect to soil suction. Canadian Geotechnical Journal, 33(3), 379-392. https://doi.org/10.1139/t96-060

van Genuchten, M., T., 1980. A closed-form equation for predicting the hydraulic conductivity of unsaturated soils. Soil Science Society of America Journal. 44, 892-898. https://doi.org/10.2136/sssaj1980.03615995004400050002x

Vilar, O., M., 2007. An expedite method to predict the shear strength of unsaturated soils. Soils and Rocks, 30(1), 51-61. https://doi.org/10.28927/SR.301051

Vilar, O., M., Rodrigues, R., A., 2011. Collapse behavior of soil in a Brazilian region affected by a rising water table, 48(2). https://doi.org/10.1139/T10-065

Villibor, D. F., Nogami, J. S. 2009. Pavimentos econômicos: tecnologia do uso dos solos finos lateríticos. Arte & Ciência, São Paulo, São Paulo, Brazil.

Xu, Y., Sun, D., 2001. Determination of expansive soil strength using a fractal model. Fractals, 9 (1), 51-60. https://doi.org/10.1142/S0218348X01000506

Xu, Y., 2004. Fractal approach to unsaturated shear strength. Journal of Geotechnical and Geoenvironmental Engineering, 130 (3), 264-273. https://doi.org/10.1061/(ASCE)1090-0241(2004)130:3(264)

Yang, X., Vanapalli, S., K., 2023. Mechanisms of modeling methods of strain-softening behavior of unsaturated soils. International Journal of Geomechanics, 23(5): 03123001. https://doi.org/10.1061/IJGNAI.GMENG-7934

Zhai, Q., Rahardjo, H., Satyanaga, A., Dai, G., 2019. Estimation of unsaturated shear strength from soil–water characteristic curve. Acta Geotechnica, https://doi.org/10.1007/s11440-019-00785-y

Zhao, H., F., Zhang, L., M., Fredlund, D., G., 2013. Bimodal shear-strength behavior of unsaturated coarse-grained soils. Journal of Geotechnical and Geoenvironmental Engineering, 139(12), 2070-2081. https://doi.org/10.1061/(ASCE)GT.1943-5606.0000937

Zhou, A., Huang, R., Sheng, D., 2016. Capillary water retention curve and shear strength of unsaturated soils. Canadian Geotechnical Journal, 53, 974-987. https://doi.org/dx.doi.org/10.1139/cgj-2015-0322

CHAPTER 6

Summary and Conclusions

6.1 Summary

The focus of this thesis has been directed towards developing rational methods for interpretation and was well as tools for predicting the hydromechanical behavior of unsaturated soils in tropical regions. Both qualitative and quantitative the relationship and effects of aggregations with micro and microporosity, as well as how this is reflected in the SWCC and the unsaturated shear strength are explained considering the influence of aggregations on the behavior of bimodal lateritic soils, particularly from Brazil, which are significantly different from that of soils with a unimodal structure.

The most common way of visualizing the presence of aggregations is through the comparison of aggregated and disaggregated GSD, which have inherent limitations when carrying out sieve and sedimentation analysis, such as approximating the shape of the particle to a sphere and restricting the smallest perceptible sizes based on Stokes' Law. This means that any method used to quantify aggregations based on such analyses presents uncertainties that could be avoided if more rigorous measurement tests, such as imaging techniques (X-ray microtomography and laser diffraction), were adopted. However, the adoption of these more advanced techniques, although potentially leading to greater theoretical rigor, would hinder the dissemination of the proposed methods in engineering practice applications, since they would require information that is not part of the common scope in geotechnical laboratories. Despite this, the good results obtained from the analyses

suggest that the method chosen based on the relative difference between the aggregate and disaggregate GSD curves is suitable for the objectives proposed herein:

(1) Soil structure:

i. The relationship between macro and microstructure is reflected in the porosity of the soil. Consequently, macroporosity can be obtained from the difference between the porosity and the microporosity estimated using the relative aggregation (*RA*) and the liquid limit. This is possible because disturbances in soil structure resulting from drying and wetting cycles, compaction, and increasing or relieving stress, have little influence on variations in micropores (i.e. variations in volume are mainly due to changes in macrostructure), as detailed in Chapter 2. The greater preservation of soil structure, especially aggregations, in undisturbed specimens led to the separation of analyses and the development of models in remolded and undisturbed conditions.

(2) The SWCC of highly weathered bimodal soils:

The first prediction model proposed, described in Chapter 3, was based on a framework which, using the capillary tube model, makes it possible to relate aggregated and disaggregated GSD curves to the bimodal PSD curves and, consequently, to the SWCC. This model only requires index properties and the referred granulometries to be implemented. Using an equation that relates the diameter of each particle to a pore diameter, called β-function, the aggregated GSD is used to obtain the SWCC in the

macropores region, while the disaggregated GSD allows the prediction in the macropores range. From this approach, it was observed that:

ii. The level or degree of soil aggregation, represented by the relative aggregation (*RA*), proved to be closely related to microporosity. As microstructure includes the pores contained within the aggregations, the physical meaning of this relationship is evident. Another variable that showed a strong link with microporosity was the liquid limit (w_L) due to its physical-chemical nature. Aggregations are generally formed by clusters of clay particles and the greater the specific surface area of the clay mineral, the greater the capacity to retain water stored in the micropores in form of adsorption. Thus, the capillary component of the water stored in the microstructure is more closely related to relative aggregation, while the adsorption component has more affinity to the liquid limit.

iii. The analyses carried out using characteristics extracted from the aggregated and disaggregated GSD, along with the assumption that these curves are more linked to macro and microstructure respectively, indicate that the GSD curves allow to obtain information about PSD and contribute to the understanding of the behavior of the soils investigated.

iv. Porosity plays a crucial role in this context, as it is the only variable that distinguishes soils in volumetric terms. This is especially important in remolded soils, in which samples compacted at different energies result in distinct structures that are not related either to the GSD curves or the liquid limit.

v. The first proposed model, based on the β-function, was able to provide good results with coefficients of determination (R^2) greater than 0.80, for both remolded and undisturbed soils. Considering the Root Mean Squared Error (RMSE) as a performance indicator, the predictions for the remolded dataset resulted in 13.4% greater adherence to the measured data than the undisturbed soils.

vi. It is recognized that using the same dataset to obtain the parameters of the β-function and then using the same data in the predictions is a limitation. However, this choice was preferable given the relatively small number of materials in each dataset (15 remolded and 25 undisturbed). Whether the decision was made to create a dataset to be used only for predictions and measuring the performance of the models, relevant information could be lost in the development processes.

vii. Another limitation of this model is directly related to the GSD curves. The number of points in the predicted SWCC depends on the number of points in the aggregated and disaggregated GSD curves. More data points would contribute towards better definition of the predicted SWCC, which is not a continuous curve. As mentioned earlier, the GSD of bimodal lateritic soils, especially the disaggregated one, are often far from reaching passing percentages close to 0%, which results in predictions limited to the smallest suctions in the micropores region.

The second SWCC prediction model is based on the regression of the parameters used in the fitting equation proposed by Gitirana Jr. and Fredlund (2004), as detailed in

Chapter 4. This model also requires index properties and GSD information as input data, but its application is more straightforward and simpler, especially in the steps related to the GSD curves. The following comments can be drawn from this method:

viii. The three variables mentioned above, relative aggregation, liquidity limit and porosity, also stood out in this case. In addition, the diameter corresponding to 10% passing (D_{10}) showed a strong relationship with the air-entry values, which is often reported in the literature for unimodal soils.

ix. In terms of performance, the second model proved to be superior with R^2 exceeding 0.89. The same limitation regarding the use of the same dataset for both calibration and prediction described for the first model also applies. Considering the performance in terms of RMSE, an opposite trend can be seen in relation to the first model: the undisturbed soils presented results 15.6% higher than those of the remolded ones.

x. For each model, the great similarity in performance between remolded and undisturbed materials may be an indication that the size of each dataset is adequate. Although the dataset for undisturbed soils is significantly larger, this does not mean that it could be reduced to the same size of that of remolded soils, since the formation process of undisturbed soils leads to intrinsic variability in their structure.

xi. One aspect that may have contributed to reducing the performance of the models in the region close to the first air-entry value was the greater difficulty in obtaining well-defined SWCCs in this region. Generally, the suctions of

the first air-entry value are between 0.1 and 10 kPa, a range in which errors and dispersions inherent to measurement techniques are more relevant.

xii. The results of the two proposed models could be improved by incorporating mineralogical information such as specific surface area or cation capacity exchange. However, the need for tests that are not part of the geotechnical routine would make it difficult to implement these models in practice, similar to what was discussed about the limitations of GSD curves.

(3) The shear strength of highly weathered bimodal soils:

The unsaturated shear strength behavior of bimodal lateritic soils was investigated with two key objectives in mind: (i) explain values of ϕ^b greater than ϕ'; and (ii) develop a simple prediction model capable of provide reasonable results. These two objectives were achieved in Chapter 5 from which the comments below can be withdrawn.

xiii. Soils exhibiting values of ϕ^b exceeding ϕ' were consistently observed in drained tests. Such behavior is believed to occur exclusively in specimens subjected to suctions greater than the first air-entry value and is attributed to the formation of a contractive shear band during the shearing phase. Within this band, macropores become filled with fragmented aggregations, increasing the degree of saturation and creating regions where continuous water phases surround the granular particles. This creates a “skeleton” in these full saturated regions that governs the shear strength associated with matric suction whereas outside the shear band the specimen remains unsaturated. The influence of ϕ' is limited to direct contact between particles

and aggregations in the shear band. However, this proposed theory requires further validation.

xiv. The data indicates that the contribution of net normal stress to shear strength is affected by matric suction. A generally linear relationship was observed between ϕ' values and the logarithm of matric suction, which can be attributed to soil hardening caused by the closure of macropores as matric suction increases.

xv. The division of the SWCC in different zones accordingly to its notorious points – ψ_{b1}, ψ_{res1}, ψ_{b2}, and ψ_{res2} –, used by previous studies in bimodal soils to describe the failure envelope in terms of apparent cohesion and matric suction, has proven inadequate for bimodal lateritic soils. In fact, such envelope appears to have two distinct regions: a linear zone extending from full saturation to the beginning of the micropores region $(u_a - u_w)_m$, and a non-linear zone starting from the preceding limit and extended to the midpoint of the micropores transition zone $(u_a - u_w)_f$. However, this relationship in the non-linear zone is unclear for two possible reasons in certain scenarios: (a) the boundaries $(u_a - u_w)_m$ and $(u_a - u_w)_f$ may be inadequate, or (b) the complexity of microstructure geometry and water storage mechanisms may prevent the establishment of a clear relationship between ϕ^b and micropore desaturation with the data available. Regarding reason (a), both the shear strength data and theoretical justification linking micropores size to the influence of intermolecular forces, responsible for adsorption, strongly support the chosen threshold $(u_a - u_w)_f$. Conversely, the limit $(u_a - u_w)_m$ may

be questionable, as it falls within a region with limited shear strength data. In case of such limit were closer or equivalent to $(u_a - u_w)_{b2}$, a relationship between ϕ^b and the shape of the SWCC could be more easily determined. Yet, the data suggests that $(u_a - u_w)_m$ is closer to $(u_a - u_w)_{res1}$.

xvi. It was proposed a new predicting model relying on the Fredlund et al. (1978) equation for the extended Mohr-Coulomb failure envelope. The angle ϕ^b is estimated using an expression in the form of the van Genuchten (1980) equation. At saturation, ϕ^b is considered equivalent to the effective friction angle ϕ' from the saturated tests. Then, ϕ^b decreases with suction at a rate determined by $(u_a - u_w)_{b2}$. At suction corresponding to $(u_a - u_w)_f$, the value of ϕ^b becomes constant to approximately 0.5º. The effective friction angle ϕ' is assumed to be dependent of the relative aggregation and to increase with suction. This model is simple and requires only basic geotechnical information such as GSD curves and the SWCC.

xvii. Comparisons between 16 models from the literature and the proposed predicting model showed a superior performance of the latter. Many unimodal models performed better than the two bimodal ones, reinforcing that they are unsuitable for lateritic soils. The overall results point out to a goodness-of-fit in terms of R^2 greater than 0.95. For soils highly aggregated, the model tends to underestimate shear strength. Assuming increasing values of ϕ^b for matric suctions lower than $(u_a - u_w)_m$ is an alternative to overcome this condition, but more experimental data within this range is necessary to support such assumption.

6.2 Suggestions for future research

Considering the limitations and the theoretical aspects that lack data for their validation or refutation, the following suggestions for future work are made:

(1) The evaluation of the performance of the SWCC and the unsaturated shear strength models based on original data, either by collecting and/or performing new tests, preferably with bimodal laterite soils from other regions;

(2) It is hypothesized that the development of new prediction models based on artificial intelligence for bimodal lateritic soils, supported by the analyses and theoretical interpretations of the factors influencing the SWCC discussed in this study, has the potential to achieve better results, given the high regression capability of such approach; and

(3) Unsaturated shear strength tests in drained conditions along image techniques to verify the hypothesis of the contractive shear band and the emergence of a "skeleton" responsible for the peculiar behavior of ϕ^b. Moreover, unsaturated shear strength tests in several suctions duly spaced apart in the range of $(u_a - u_w)_{b1}$ to $(u_a - u_w)_{res2}$ to further investigate: the relationship between ϕ' and ϕ^b with suction, especially the variations of ϕ^b within the macropores region. Such tests can potentially provide more information for a more accurate calibration of the fitting parameters of the proposed model (i.e., *b*, *d*, *a*, and *n*).

References

Fredlund, D., G., Morgenstern, N., R., Widger, R., A., 1978. The shear strength of unsaturated soils. Canadian Geotechnical Journal, 15(3), 313-321. https://doi.org/10.1139/t78-029

Gitirana Jr., G.F.N., Fredlund, D.G., 2004. Soil-water characteristic curve equation with independent properties. Journal of Geotechnical and Geoenvironmental Engineering, 130(2), 209-212. https://doi.org/10.1061/(ASCE)1090-0241(2004)130:2(209)

Souza, J. C., 2020. Avaliação da relação entre a curva granulométrica e a curva característica solo-água para um solo residual bimodal sob diferentes graus de desagregação. Master Thesis: Department de Civil and Environmental Engineering, Universidade Federal de Goiás.

van Genuchten, M., T., 1980. A closed-form equation for predicting the hydraulic conductivity of unsaturated soils. Soil Science Society of America Journal. 44, 892-898. https://doi.org/10.2136/sssaj1980.03615995004400050002x

Appendix A - Fitting and predicting models for bimodal SWCCs

Reference	Equation
Durner (1994)	$\theta = (\theta_s - \theta_r)\left\{ w_m \left[\frac{1}{1+(a_m\psi)^{n_m}} \right]^{m_m} + w_M \left[\frac{1}{1+(a_M\psi)^{n_M}} \right]^{m_M} \right\} + \theta_r$ (A.1) where: θ is the volumetric water content; θ_s is the saturated volumetric water content; θ_r is the residual volumetric water content; w_m is the weight factor of the micropores; w_M is the weight factor of the macropores; α_m, n_m and m_m are fitting parameters of the micropores; α_M, n_M and m_M are fitting parameters of the macropores; and ψ is the suction.
Burger and Shackelford (2001) and Zhang and Chen (2005)	$\theta = p_M n_{pM}\left[1 - \frac{\ln\left(1+\frac{\psi}{\psi_{res1}}\right)}{\ln\left(1+\frac{10^6}{\psi_{res1}}\right)} \right]\left\{ \frac{1}{\ln\left[\exp(1) + \left(\frac{\psi}{a_M}\right)^{n_M} \right]} \right\}^{m_M} + p_m n_{pm}\left[1 - \frac{\ln\left(1+\frac{\psi}{\psi_{res2}}\right)}{\ln\left(1+\frac{10^6}{\psi_{res2}}\right)} \right]\left\{ \frac{1}{\ln\left[\exp(1) + \left(\frac{\psi}{a_m}\right)^{n_m} \right]} \right\}^{m_m}$ (A.2) where: p_M is the volumetric percentage of the macropores; p_m is the volumetric percentage of the micropores; n_{pM} is the porosity component of the macropores; n_{pm} is the porosity component of the micropores; ψ_{res1} is the residual suction of the macropores; and ψ_{res2} is the residual suction of the micropores.
Gitirana Jr. and Fredlund (2004)	$\theta = \left[\frac{S_1 - S_2}{1+\left(\psi / \sqrt{\psi_{b1}\psi_{res1}}\right)^{d_1}} + \frac{S_2 - S_3}{1+\left(\psi / \sqrt{\psi_{res1}\psi_{b2}}\right)^{d_2}} + \frac{S_3 - S_4}{1+\left(\psi / \sqrt{\psi_{b2}\psi_{res2}}\right)^{d_3}} + S_4 \right] n$ (A.3) where: $S_i = \frac{\tan\theta_i (1+r_i^2)\ln(\psi/\psi_i^a)}{1 - r_i^2\tan^2\theta_i} + (-1)^i \times \frac{(1+\tan^2\theta_i)}{(1-r_i^2\tan^2\theta_i)}\sqrt{r_i^2\ln^2(\psi/\psi_i^a) + \frac{a^2(1-r_i^2\tan^2\theta_i)}{(1+\tan^2\theta_i)}} + S_i^a$ $i = 1, 2, 3, 4; \theta_i = -(\lambda_{i-1} + \lambda_i)/2; r_i = \tan[(\lambda_{i-1} - \lambda_i)/2]; \lambda_0 = 0; \lambda_i = \arctan\{(S_i^a - S_{i+1}^a)/[\ln(\psi_{i+1}^a/\psi_i^a)]\};$ $S_1^a = 1; S_2^a = S_{res1}; S_3^a = S_b; S_4^a = S_{res2}; S_5^a = 0; \psi_1^a = \psi_{b1}; \psi_2^a = \psi_{res1}; \psi_3^a = \psi_{b2}; \psi_4^a = \psi_{res2}; \psi_5^a = 10^6;$ $d_j = 2\exp[1/\ln(\psi_{j+1}^a/\psi_j^a)]; j = 1, 2, 3.$

Reference	Equation
	n is the porosity; S_{res1} is the residual degree of saturation of the macropores; S_b is the degree of saturation corresponding to the air-entry values of the micropores; S_{res2} is the residual degree of saturation of the micropores; ψ_{b1} is the air-entry value of the macropores; ψ_{b2} is the air-entry value of the micropores; and a defines the sharpness of the transitions of the bending points.
Satyanaga et al. (2013)	$$\theta = \left(1 - \frac{\ln\left(1+\frac{\psi}{\psi_r}\right)}{\ln\left(1+\frac{10^6}{\psi_r}\right)}\right)\left[\theta_r + (\theta_{s1}-\theta_{s2})\left(1 - erfc\frac{\ln\left(\frac{\psi_{b1}-\psi}{\psi_{b1}-\psi_{m1}}\right)}{s_1}\right) + (\theta_{s2}-\theta_r)\left(1 - erfc\frac{\ln\left(\frac{\psi_{b2}-\psi}{\psi_{b2}-\psi_{m2}}\right)}{s_2}\right)\right] \quad (A.4)$$ where: ψ_r is the residual suction; θ_{s1} is the saturated volumetric water content of the macropores; θ_{s2} is the saturated volumetric water content of the micropores; ψ_{m1} is the suction at the inflection point of the macropores; ψ_{m2} is the suction at the inflection point of the micropores; s_1 represents the standard deviation of the macropores; s_2 represents the standard deviation of the micropores. $s_1 = \theta_{s1}\exp\sqrt{\frac{\sum_{i=1}^{n}\ln\frac{\psi_i}{\mu}}{n}}$; $s_2 = \theta_{s2}\exp\sqrt{\frac{\sum_{i=1}^{n}\ln\frac{\psi_i}{\mu}}{n}}$; n is the total number of points of suction; ψ_i is the suction at point i; and μ is the geometric mean of suction.
Wijaya and Leong (2016)	$$\theta = \theta_s - m_1(x-x_1) - R_2(x)(m_2-m_1) - R_3(x)(m_3-m_2) - R_4(x)(m_4-m_3) - R_5(x)(m_5-m_4) \quad (A.5)$$ where: m_i is the slope of each linear segment of the SWCC; $x = \log\psi$; $x_1 = \log\psi_0$ being ψ_0 the suction when $\theta = \theta_s$; R_i is the ramp function of each linear segment given as $R_i = \frac{1}{2}\left\langle (x-x_1) + \frac{1}{c_i}\ln\left\{\frac{\cosh\left[c_i(x-x_i)\right]}{\cosh\left[c_i(x_i-x_1)\right]}\right\}\right\rangle$; $c_i = \frac{2}{\log\left(\frac{\psi_{i+}}{\psi_{i-}}\right)}$ being ψ_{i+} the suction where the SWCC merges into linear segment i and ψ_{i-} the suction where the SWCC separates from linear segment i - 1.
Costa and Cavalcante (2021)	$$\theta = \theta_r + (\theta_s - \theta_r)\left[\lambda\exp\left(-\delta_1|\psi|\right) + (1-\lambda)\exp\left(-\delta_2|\psi|\right)\right] \quad (A.6)$$ where δ_1 and δ_2 are fitting hydraulic parameters corresponding to the macropores and micropores; and λ is the weight factor corresponding to the macropores;

Reference	Equation
Hassan et al. (2022)	$\theta_{(m/M)} = \left[\sum_{j=1}^{i} V_{v(m/M)}\right] / V$; $\psi_{i(m/M)} = \frac{2T_s \cos\upsilon}{\rho_w g r_{i(m/M)}}$; (A.7) where: subscript *i* stands for the fraction of the particle/aggregation-size distribution curve; *m* stands for microporosity and *M* for macroporosity; V_v is the volume of voids; *V* is the total volume; T_s is the surface tension of water; *v* is the contact angle; ρ_w is the density of water; *g* is the gravity acceleration; *r* is the pore radius defined as: $r_{i(m/M)} = R_i[4e_{(m/M)} n_{i(m/M)}^{1-\alpha}]^{0.5} / 6$; and n_i the number of particles/aggregations of each fraction defined as: $n_{i(m/M)} = 3V_{v(m/M)} \big/ 4\pi R_i^3$; *R* is the particle/aggregation radius.
Li and Vanapalli (2022)	$\frac{\theta_I - \Delta\theta_{sp}^H + (1-\alpha^H)\Delta\theta_M - \theta_r}{\Delta\theta_{Lp}^H - \alpha^H \Delta\theta_M} = \left[\frac{1}{1+\left(a_{v1}\psi\right)^{n_{v1}}}\right]^{m_{v1}}$ for $\psi \le \psi_A$ (A.8) $\frac{\theta_{III} - \theta_r}{\Delta\theta_{sp}^H - (1-\alpha^H)\Delta\theta_M} = \left[\frac{1}{1+\left(a_{v3}\psi\right)^{n_{v3}}}\right]^{m_{v3}}$ for $\psi \ge \psi_B$ (A.9) $\theta_{II} = (1-\beta^{HD})\theta_I + \beta^{HD}\theta_{III}$ for $\psi_A < \psi < \psi_B$ (A.10) where: $\alpha^H = \frac{1}{\psi_B - \psi_A}\int_{\psi_A}^{\psi_B} \beta^{HD}(\psi) d\psi$; θ_I, θ_{II},and θ_{III} are the volumetric water content in stages I, II and III, respectively; ψ_A is the residual suction of the macropores; ψ_B is the air-entry value of the micropores; $\Delta\theta^H_{sp}$ is the volumetric water content between the residual suctions; $\Delta\theta^H_{Lp}$ is the difference between the volumetric water contents at saturation (θ_s) and the residual suction of the macropores (θ_{Ma}); $\Delta\theta_M$ is the difference between the volumetric water contents at the residual suction of the macropores (θ_{Ma}) and the air-entry value of the micropores (θ_{Mb}); a_{v1}, n_{v1} and m_{v1} and fitting parameters of stage I; a_{v3}, n_{v3} and m_{v3} and fitting parameters of stage III; and β^{HD} is floating parameter related to stage II.

Appendix B - Estimated SWCCs based on the general (Chapter 3) and simplified (Chapter 4) models

Note: the application of the simplified model to the undisturbed materials soil names #16 to #21 was performed using an estimative of the liquid limit (w_L).

- **Remolded materials**

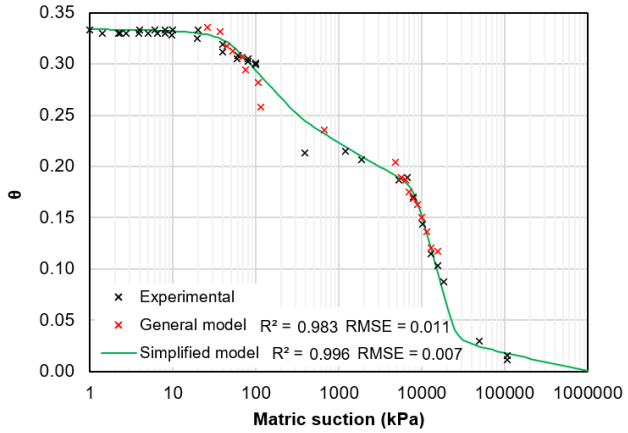

Figure B.1. Predicted SWCCs for soil 1R1

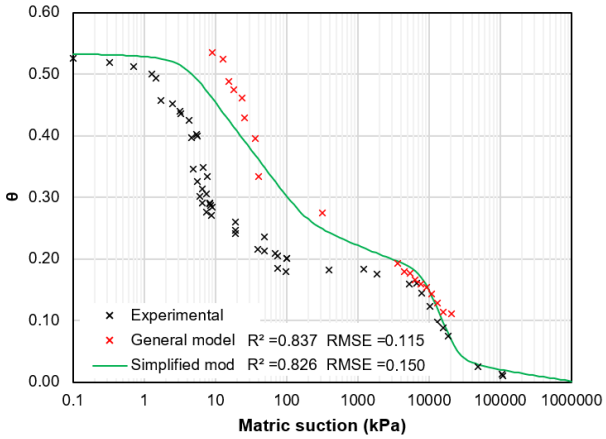

Figure B.2. Predicted SWCCs for soil 1R2

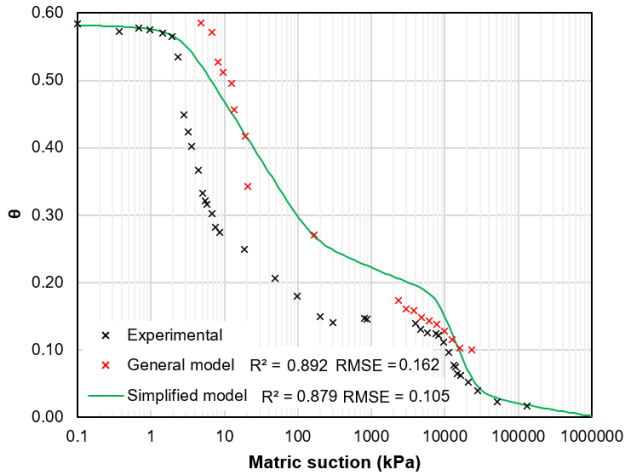

Figure B.3. Predicted SWCCs for soil 1R3

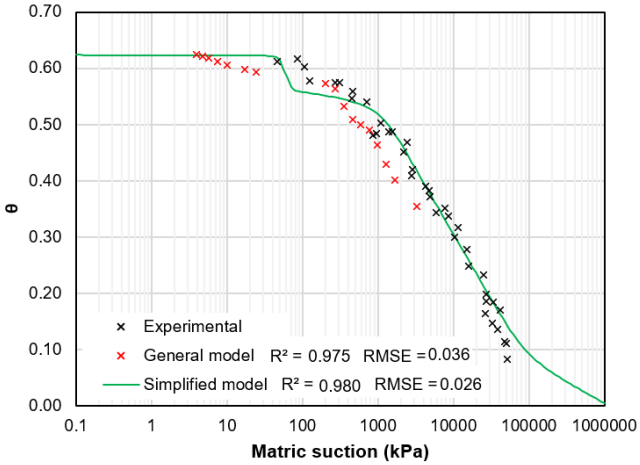

Figure B.4. Predicted SWCCs for soil 2R1

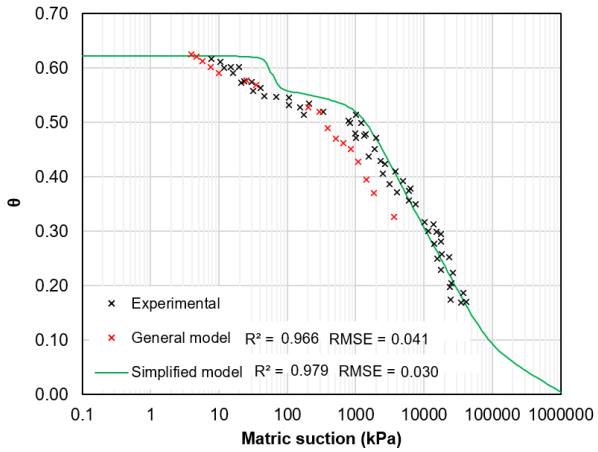

Figure B.5. Predicted SWCCs for soil 2R2

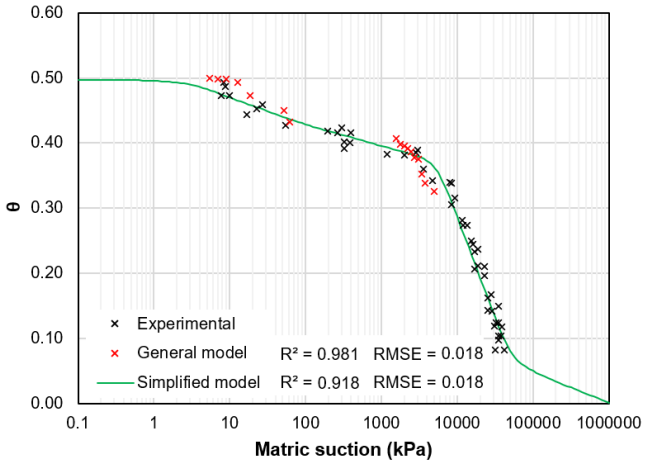

Figure B.6. Predicted SWCCs for soil 3R1

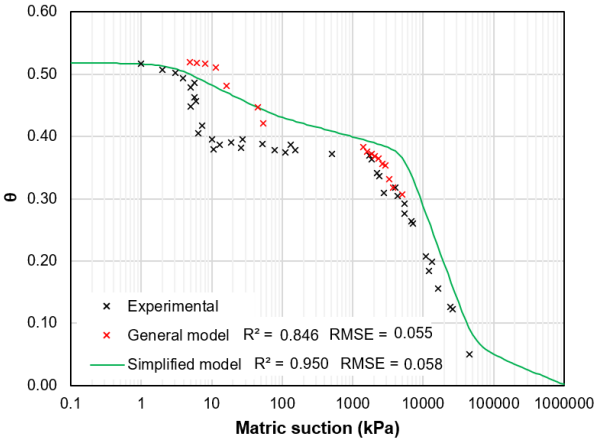

Figure B.7. Predicted SWCCs for soil 3R2

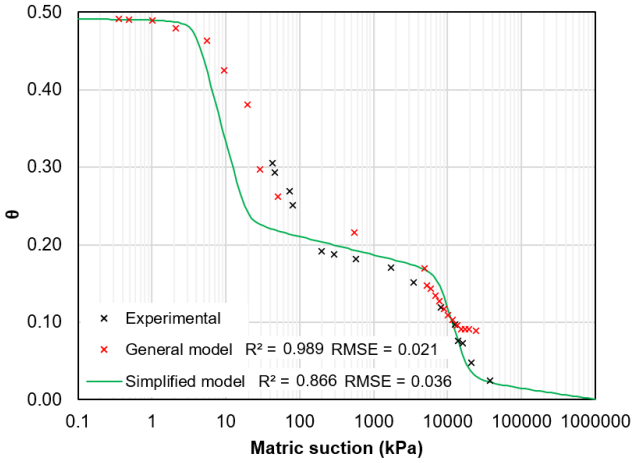

Figure B.8. Predicted SWCCs for soil 4R

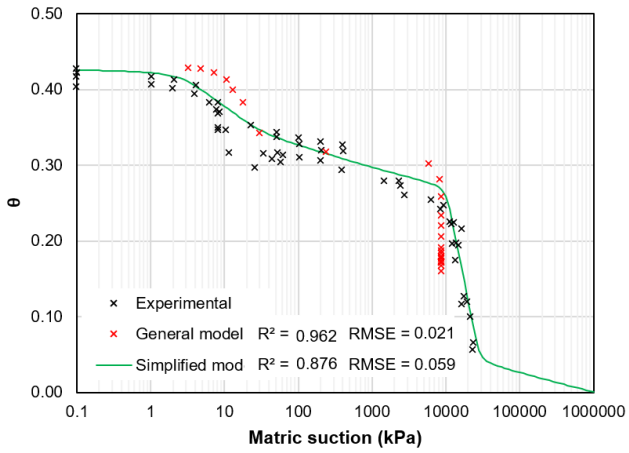

Figure B.9. Predicted SWCCs for soil 6R1

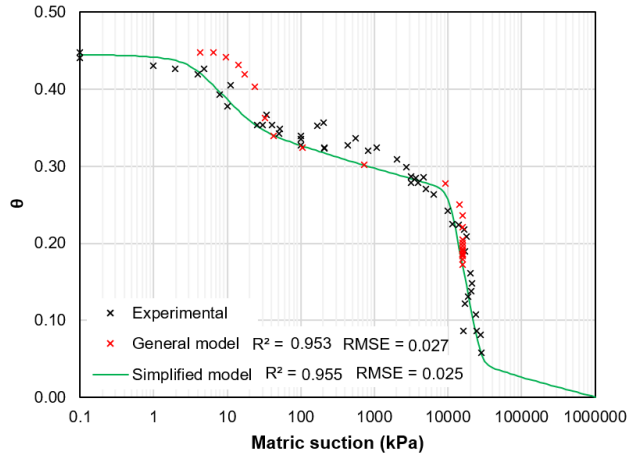

Figure B.10. Predicted SWCCs for soil 6R2

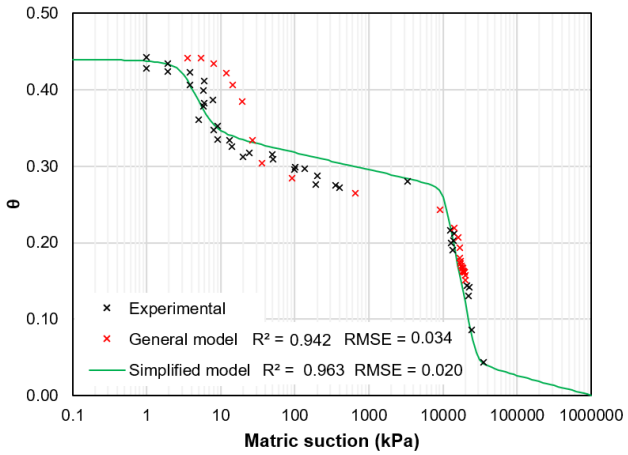

Figure B.11. Predicted SWCCs for soil 6R3

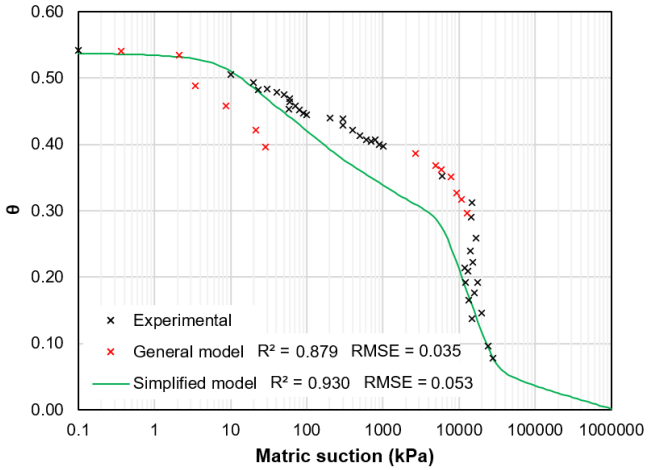

Figure B.12. Predicted SWCCs for soil 15R

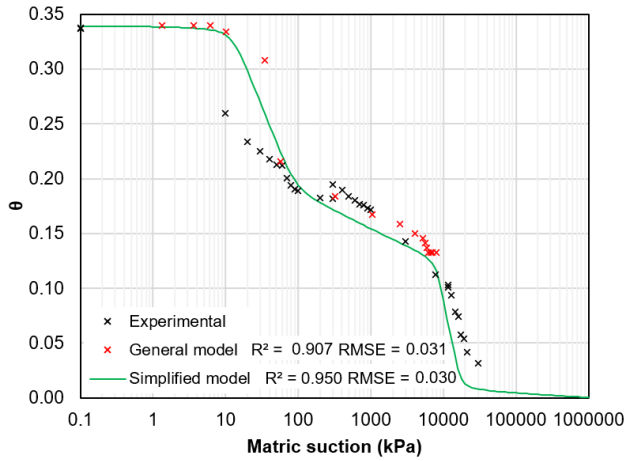

Figure B.13 Predicted SWCCs for soil 16R

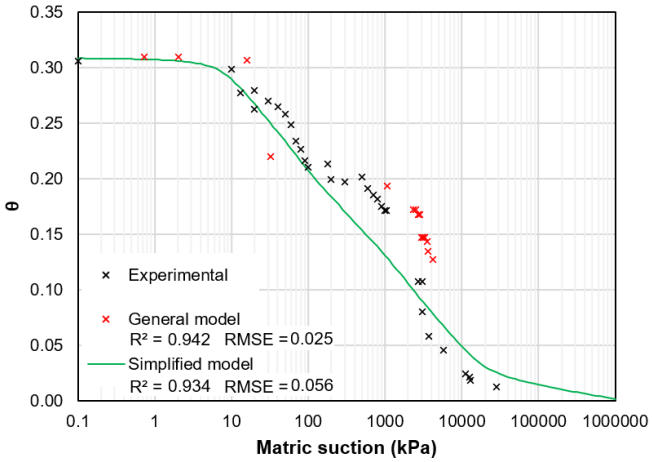

Figure B.14. Predicted SWCCs for soil 17R

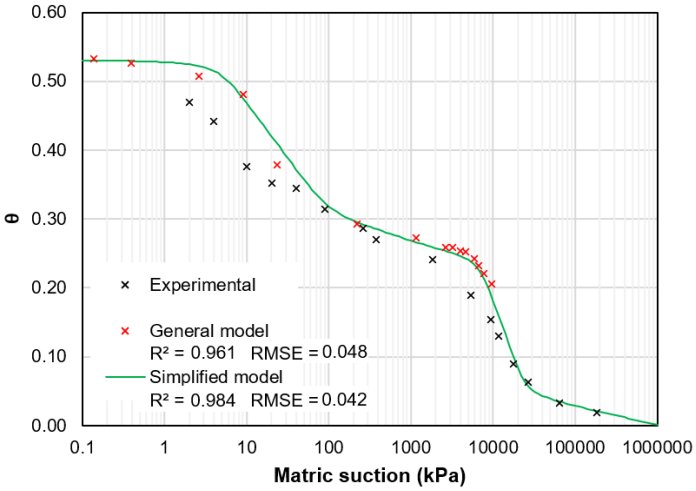

Figure B.15. Predicted SWCCs for soil 27R

- **Undisturbed materials**

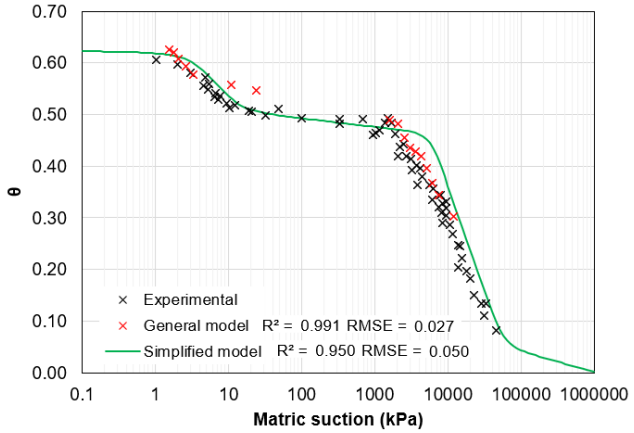

Figure B.16. Predicted SWCCs for soil 2U

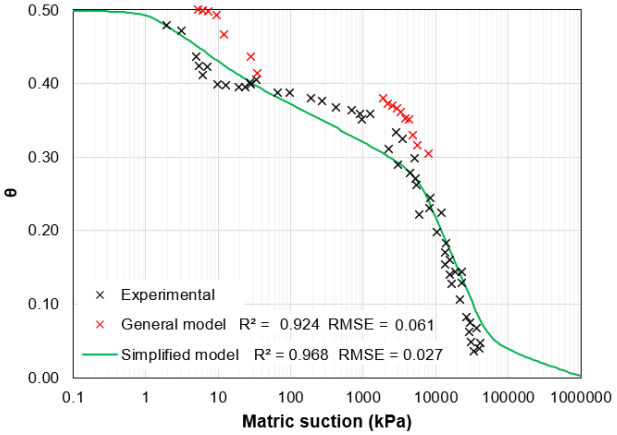

Figure B.17. Predicted SWCCs for soil 3U

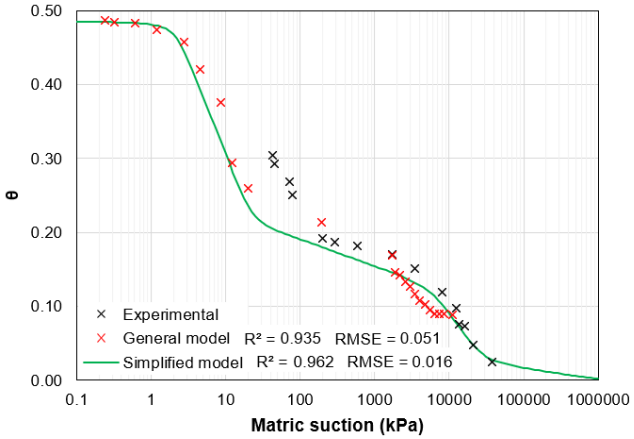

Figure B.18. Predicted SWCCs for soil 4U

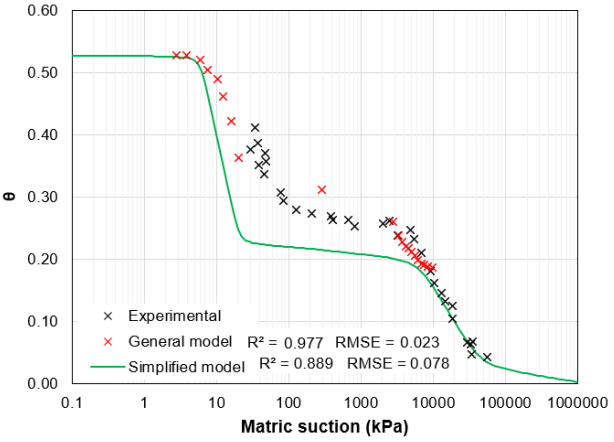

Figure B.19. Predicted SWCCs for soil 5U

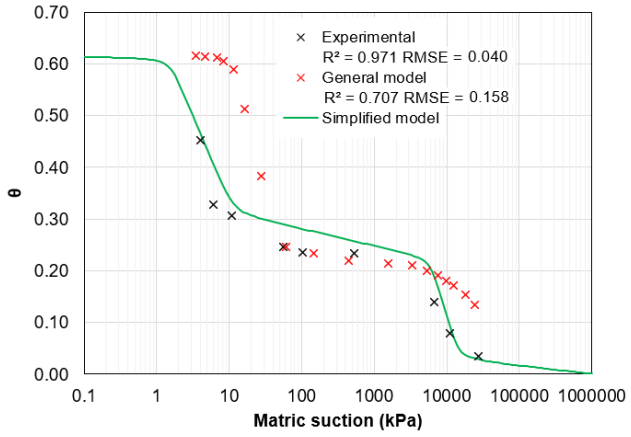

Figure B.20. Predicted SWCCs for soil 7U

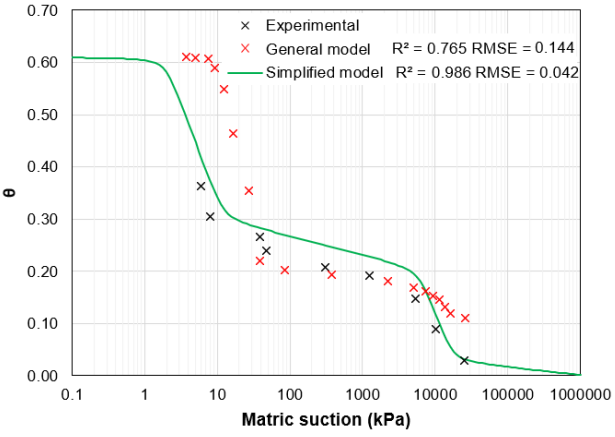

Figure B.21. Predicted SWCCs for soil 8U

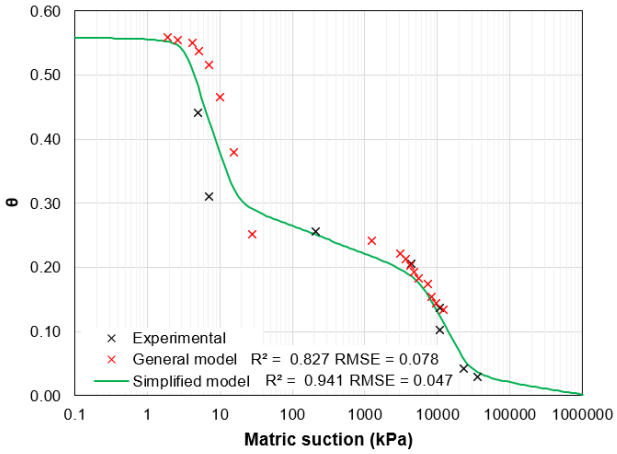

Figure B.22. Predicted SWCCs for soil 9U

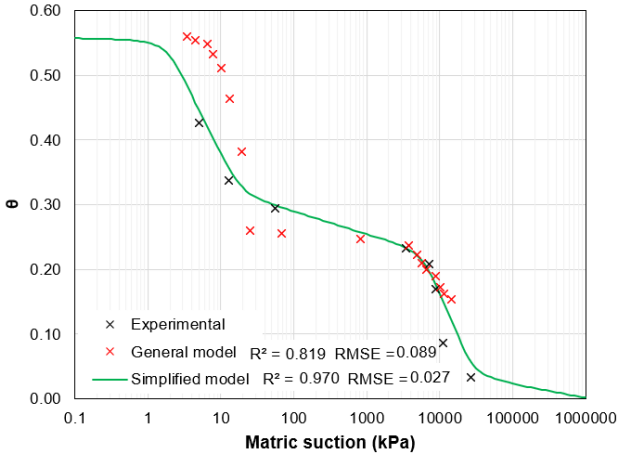

Figure B.23. Predicted SWCCs for soil 10U

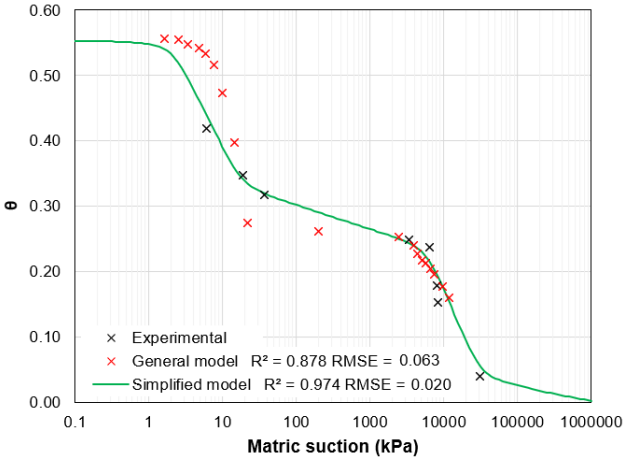

Figure B.24. Predicted SWCCs for soil 11U

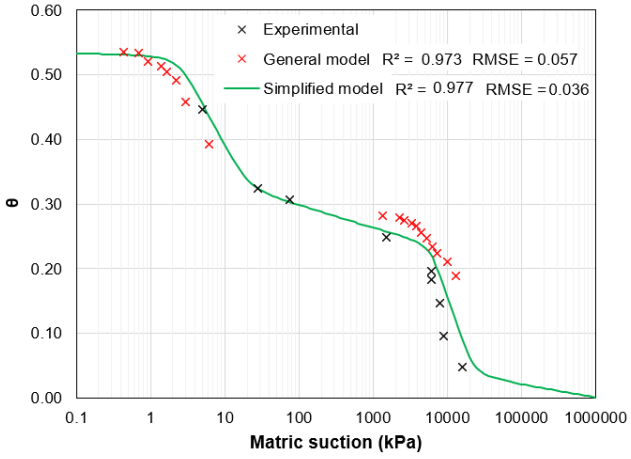

Figure B.25. Predicted SWCCs for soil 12U

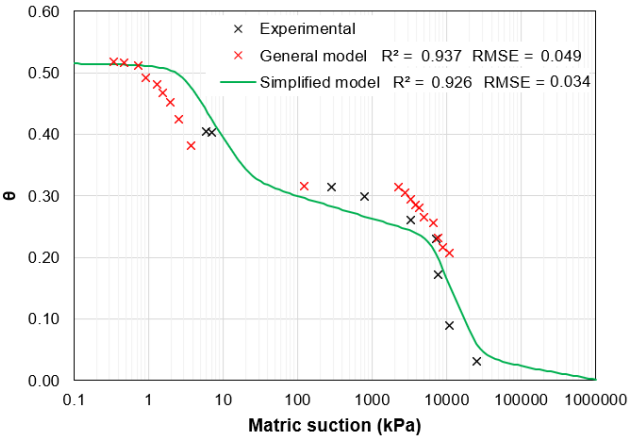

Figure B.26. Predicted SWCCs for soil 13U

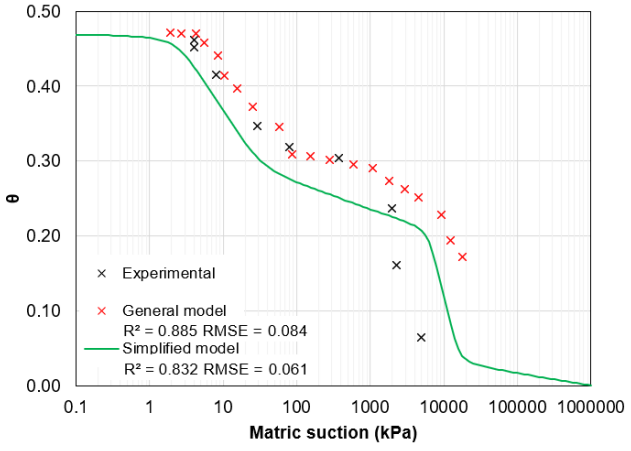

Figure B.27. Predicted SWCCs for soil 14U

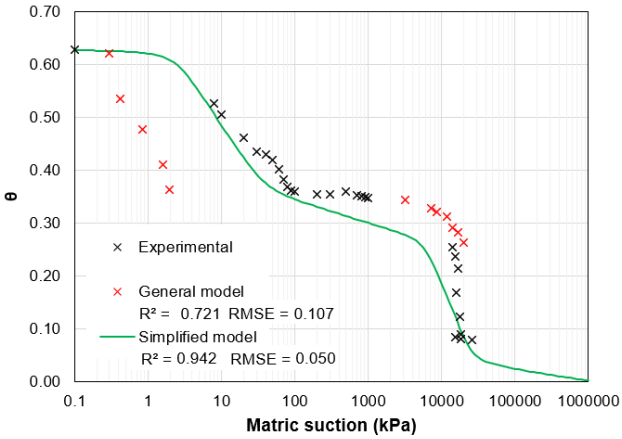

Figure B.28. Predicted SWCCs for soil 15U

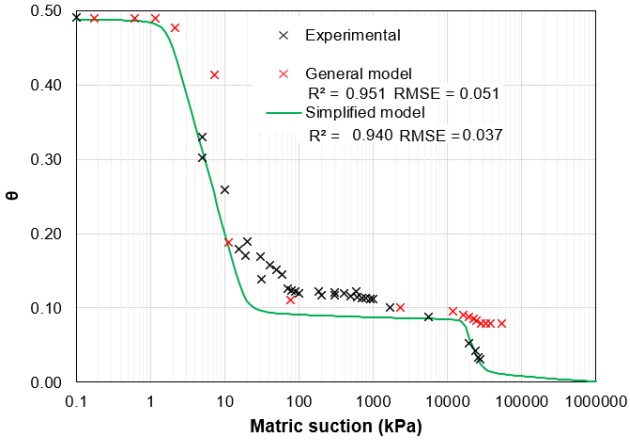

Figure B.29. Predicted SWCCs for soil 16U

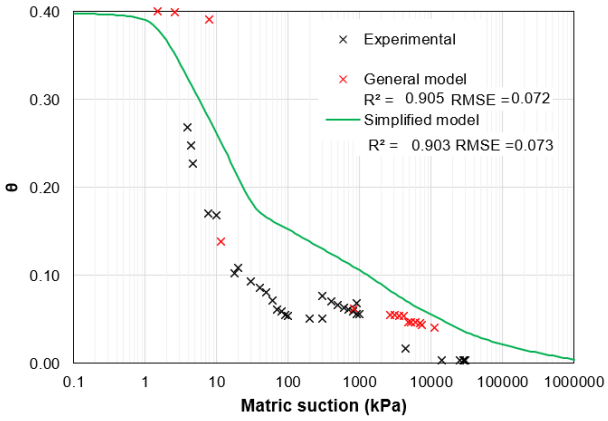

Figure B.30. Predicted SWCCs for soil 17U

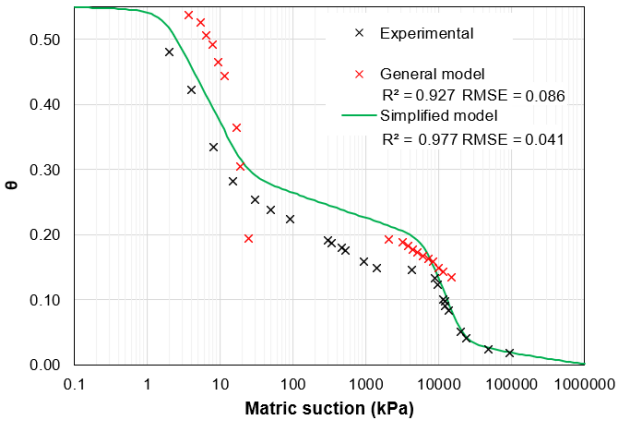

Figure B.31. Predicted SWCCs for soil 18U

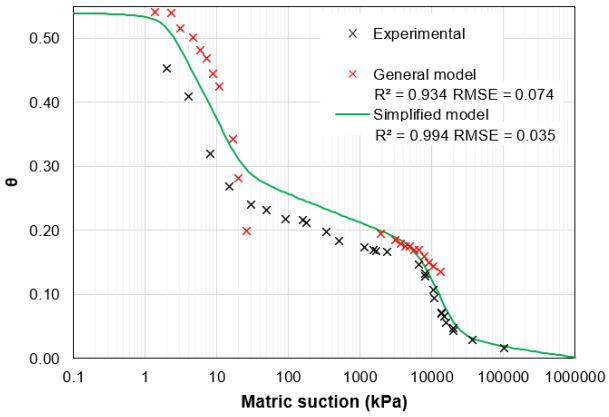

Figure B.32. Predicted SWCCs for soil 19U

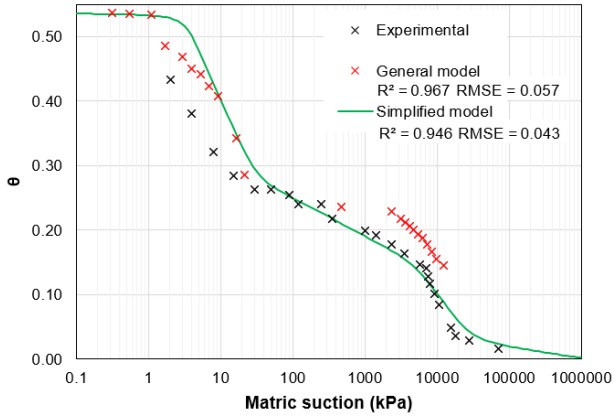

Figure B.33. Predicted SWCCs for soil 20U

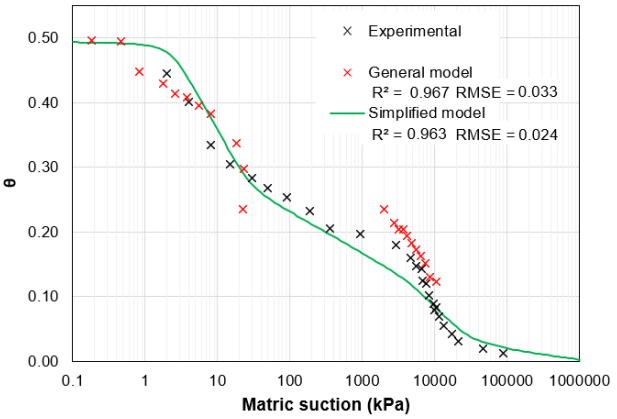

Figure B.34. Predicted SWCCs for soil 21U

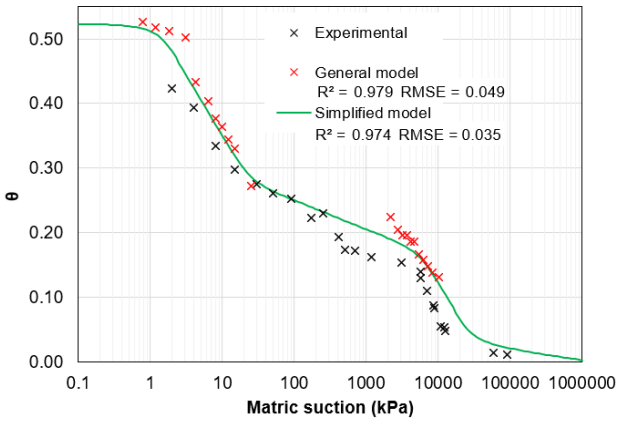

Figure B.35. Predicted SWCCs for soil 22U

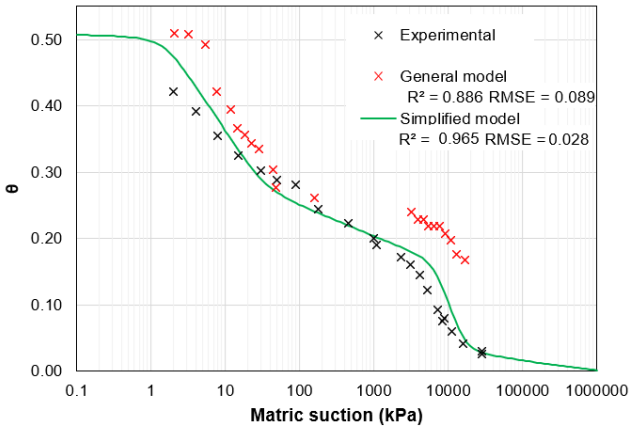

Figure B.36. Predicted SWCCs for soil 23U

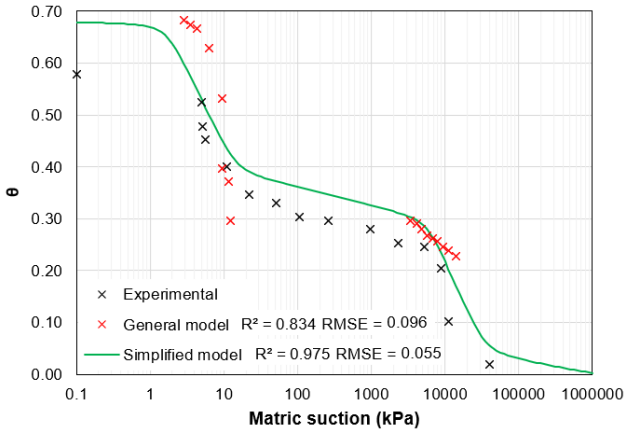

Figure B.37. Predicted SWCCs for soil 24U

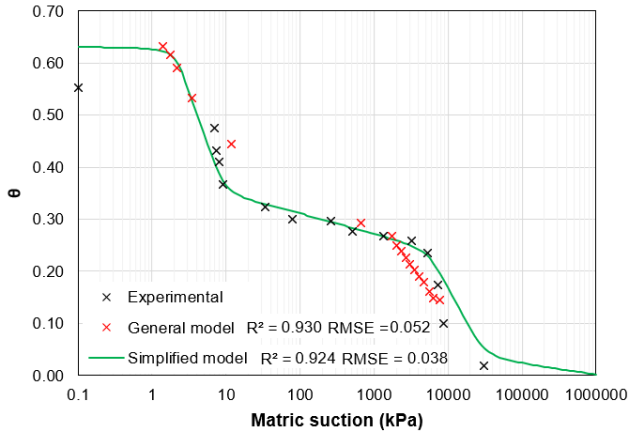

Figure B.38. Predicted SWCCs for soil 25U

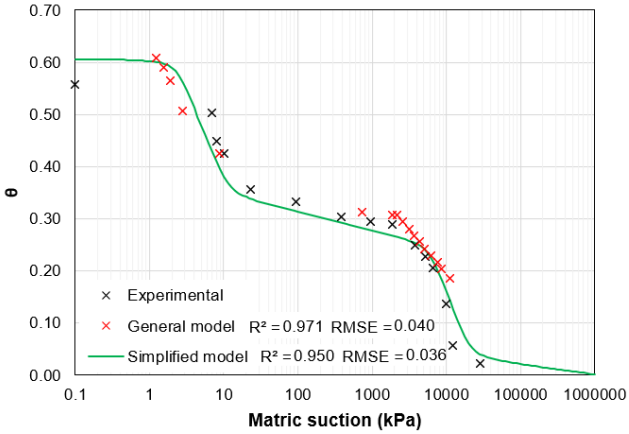

Figure B.39. Predicted SWCCs for soil 26U

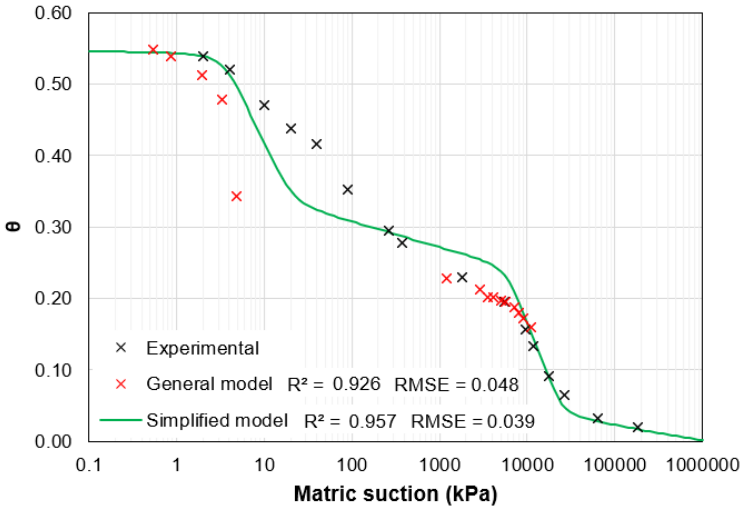

Figure B.40. Predicted SWCCs for soil 27U

Appendix C- Information, analysis, and laboratory data of soils used in the unsaturated shear strength investigation

C.1 Georgetti (2010) – 1R

- Soil basic information and characteristics
  - Specimen condition: remolded
  - Void ratio (e_0) = 0.60
  - Density of solids (ρ_s) = 2.69
  - Dry density (ρ_d) = 1.68
  - Liquid limit (w_L) = 38%
  - Plastic limit (w_P) = 21%
  - USCS = SC (disaggregated) / SC (aggregated)

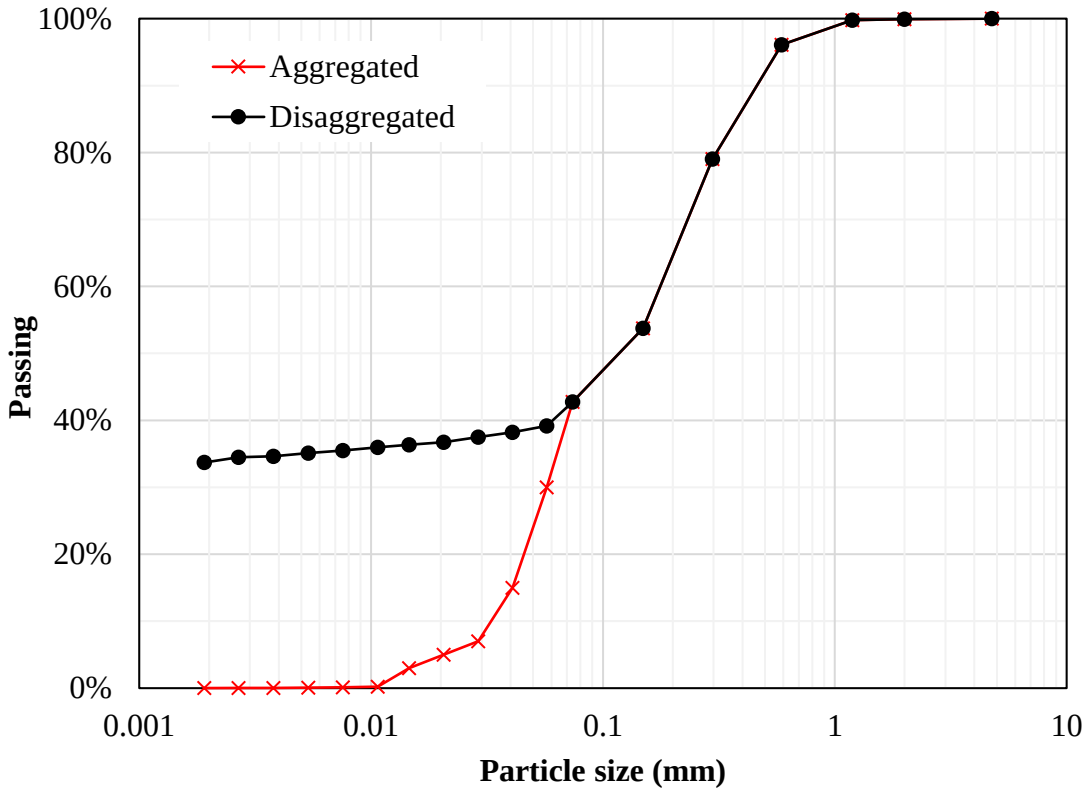

Figure C. 1. Grain-size distribution curve of soil 1R

- SWCC

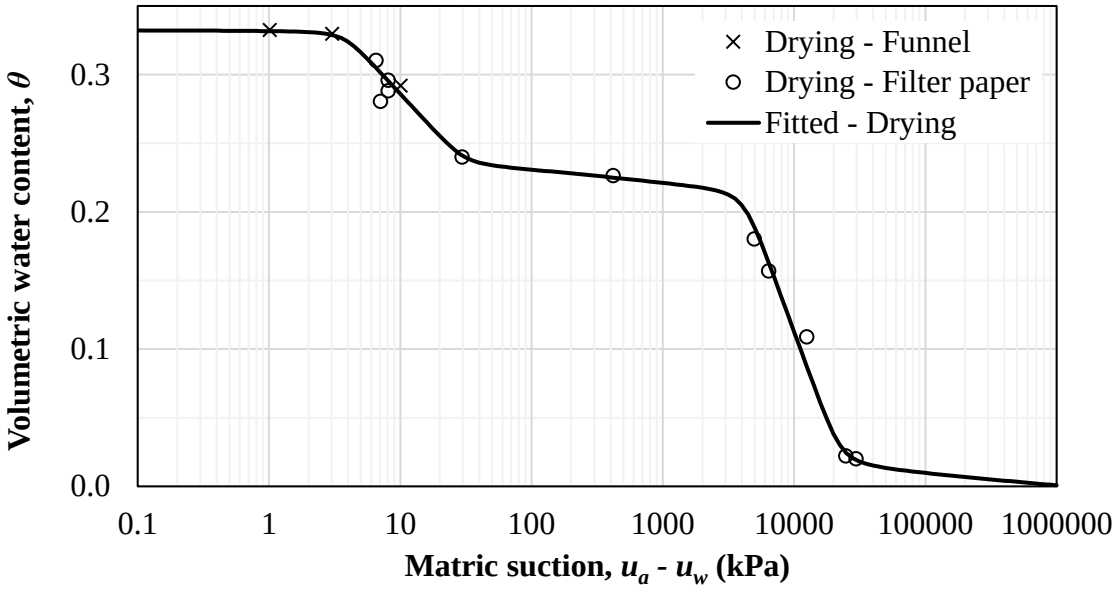

Figure C. 2. Drying soil-water characteristic curve of soil 1R

- Shear strength data
  - Initial void ratio (e_0) = 0.60
  - Type: modified triaxial CW
  - Volume measurement: NA
  - Shear velocity: 0.02 mm/min ($3.3x10^{-4}$ %/s)

i) $u_a - u_w$ = 0 kPa

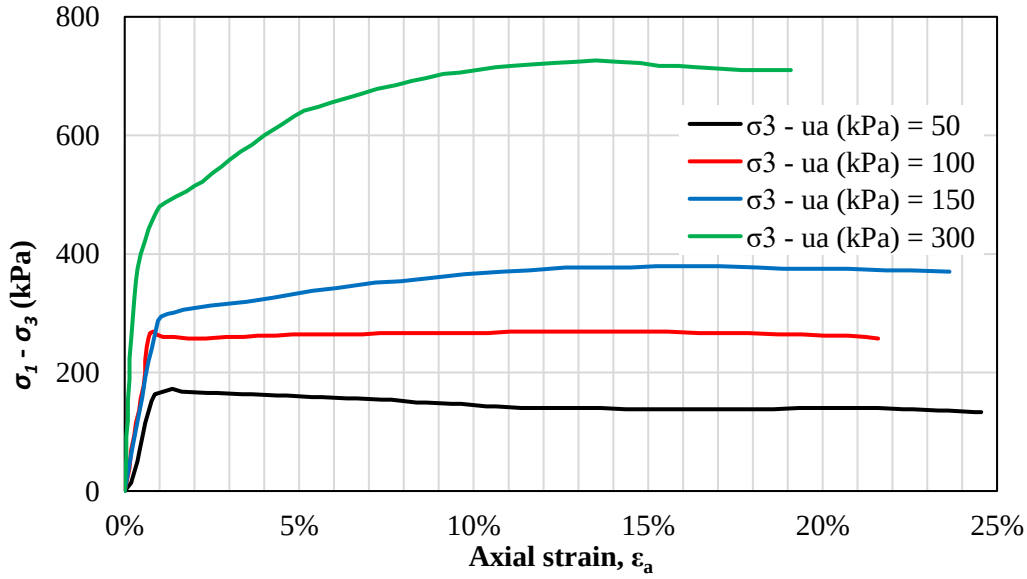

Figure C. 3. Axial strain versus deviator stress of saturated tests of soil 1R

ii) $\sigma_3 - u_a = 50$ kPa

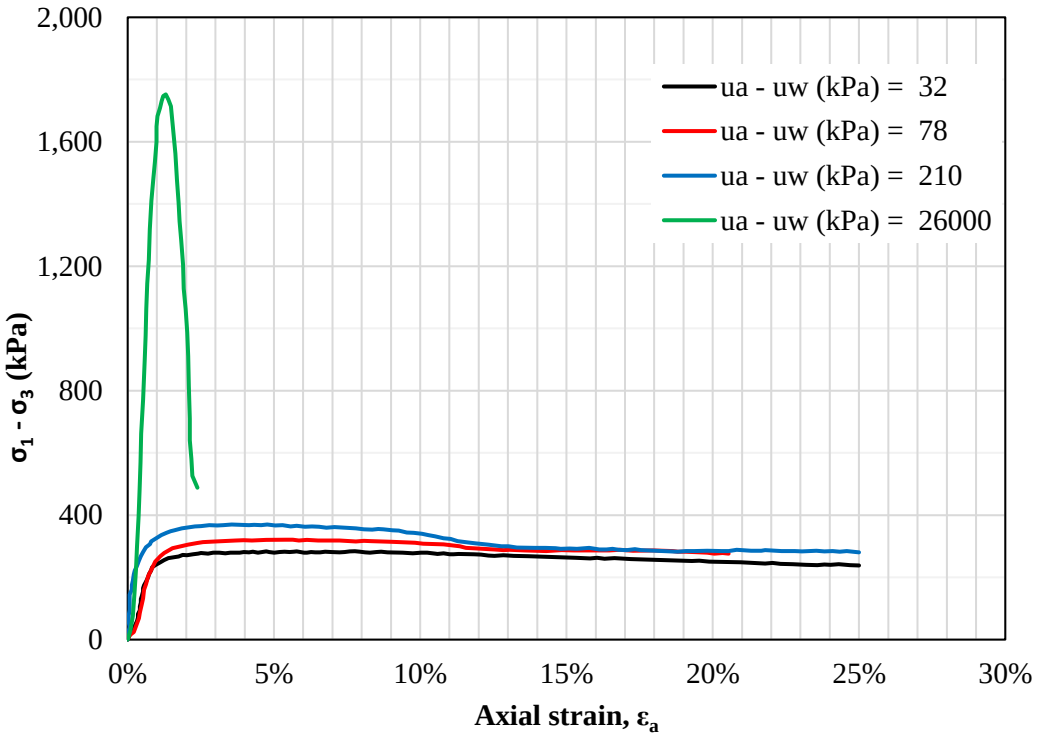

Figure C. 4. Axial strain versus deviator stress with ($\sigma_3 - u_a$) = 50 kPa of soil 1R

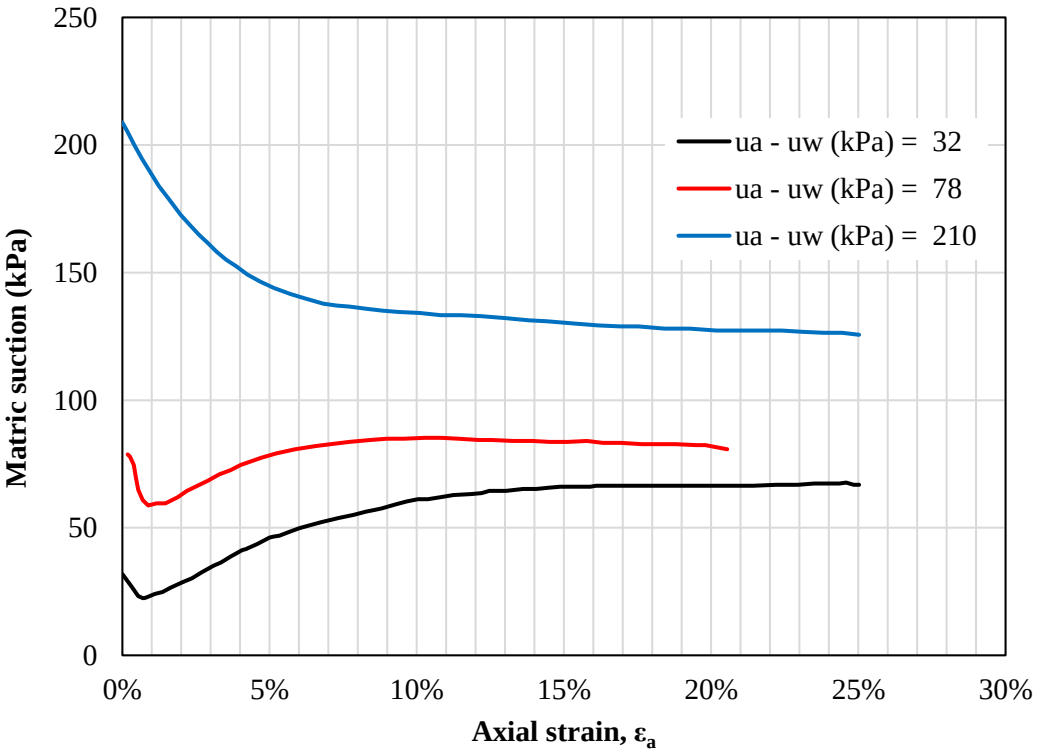

Figure C. 5. Axial strain versus matric suction with ($\sigma_3 - u_a$) = 50 kPa of soil 1R

iii) σ_3 - u_a = 150 kPa

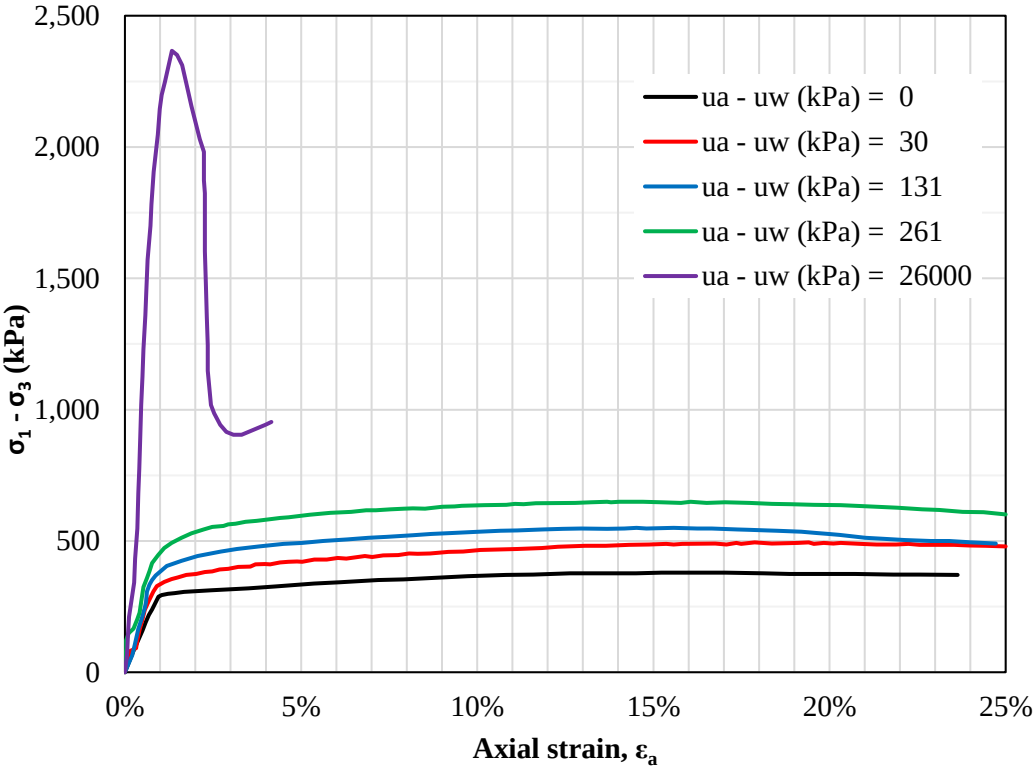

Figure C. 6. Axial strain versus deviator stress with (σ_3 - u_a) = 150 kPa of soil 1R

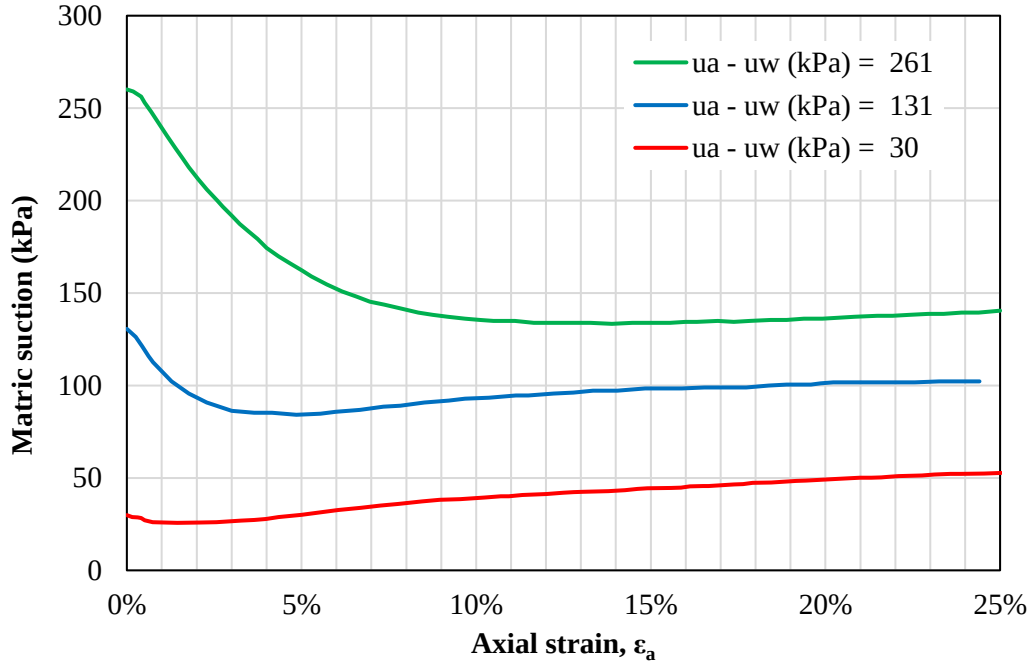

Figure C. 7. Axial strain versus matric suction with (σ_3 - u_a) = 150 kPa of soil 1R

iv) σ_3 - u_a = 300 kPa

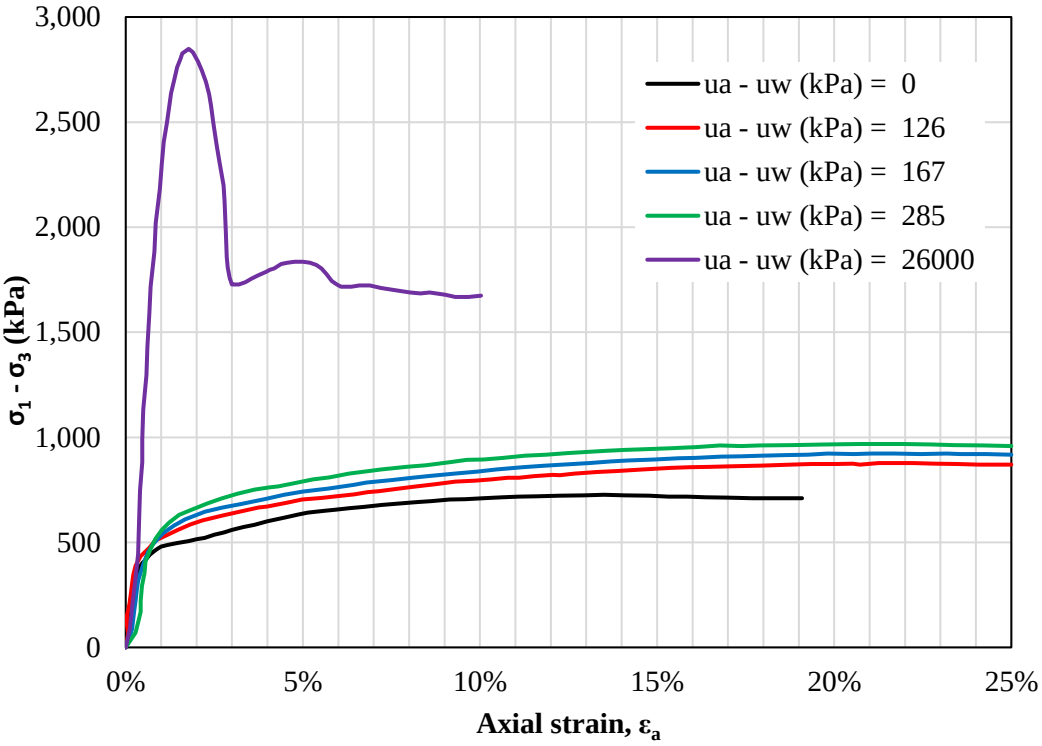

Figure C. 8. Axial strain versus deviator stress with (σ_3 - u_a) = 300 kPa of soil 1R

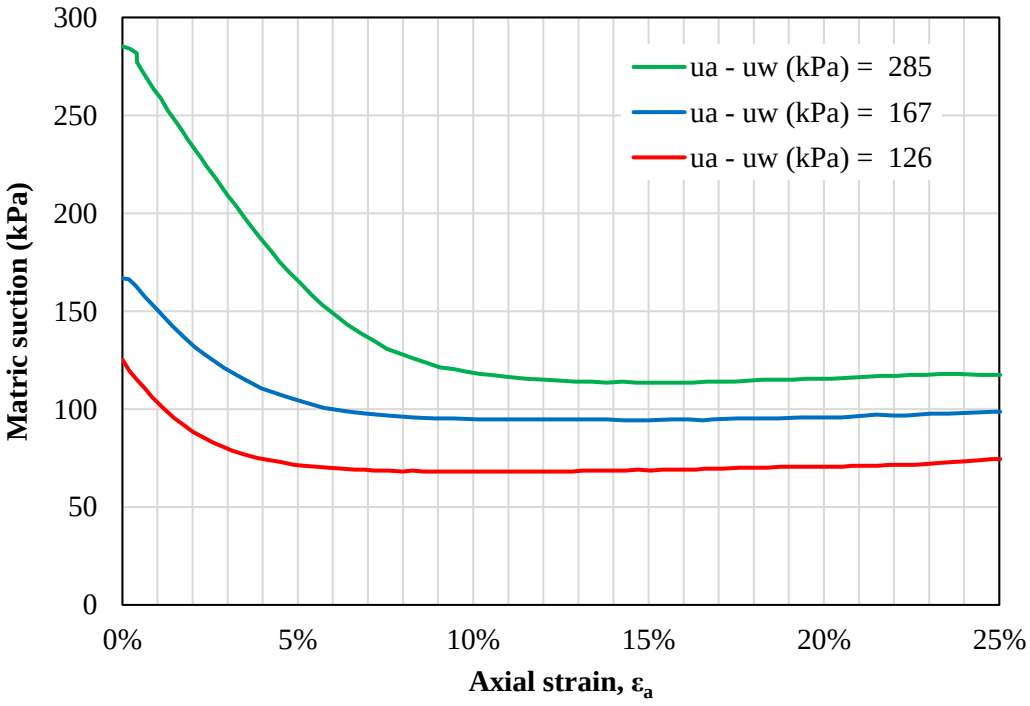

Figure C. 9. Axial strain versus matric suction with (σ_3 - u_a) = 300 kPa of soil 1R

- Failure criterion: peak or maximum shear stress

The data from the shear strength tests for peak failure criterion is presented in Table C.1:

Table C. 1. Shear strength data of soil 1R for peak failure criterion

$\sigma_1 - \sigma_3$ (kPa)	$\sigma_3 - u_a$ (kPa)	$u_a - u_w$ (kPa) Initial	$u_a - u_w$ (kPa) Final	t (kPa)	s* (kPa)
172.4	50	0	0	86.2	136.2
284.1	50	32	55	142.1	192.1
321.0	50	78	79	160.5	210.5
370.0	50	210	155	185.0	235.0
1752.3	50	26000	26000	876.1	926.1
269.0	100	0	0	134.5	234.5
379.3	150	0	0	189.7	339.7
494.5	150	30	49	247.3	397.3
549.9	150	131	98	274.9	424.9
649.2	150	261	133	324.6	474.6
2366.4	150	26000	26000	1183.2	1333.2
726.4	300	0	0	363.2	663.2
877.3	300	126	72	438.7	738.7
922.7	300	167	96	461.3	761.3
968.1	300	285	116	484.0	784.0
2848.4	300	26000	26000	1424.2	1724.2

In order to obtain the shear parameters, the data were arranged accordingly to similar final matric suctions. Table C.2 depicts the data after this procedure:

Table C. 2. Shear strength data of soil 1R for peak failure criterion after data arrangement based on similar values of matric suction

$\sigma_1 - \sigma_3$ (kPa)	$\sigma_3 - u_a$ (kPa)	$u_a - u_w$ (kPa)	t (kPa)	s* (kPa)
172.4	50	0	86.2	136.2
269.0	100		134.5	234.5
379.3	150		189.7	339.7
726.4	300		363.2	663.2
284.1	50	52	142.1	192.1
494.5	150		247.3	397.3
321.0	50	75	160.5	210.5
877.3	300		438.7	738.7
549.9	150	97	274.9	424.9
922.7	300		461.3	761.3
1752.3	50	26000	876.1	926.1
2366.4	150		1183.2	1333.2
2848.4	300		1424.2	1724.2

The graph in terms of *s** and *t* (Fig. C.10) points out to a linear relationship between these variables. As a result, the angle ψ' has a unique value for each matric suction. Fig. C.10 also presents the fitting equations from which the intercepts (*d*) can be obtained.

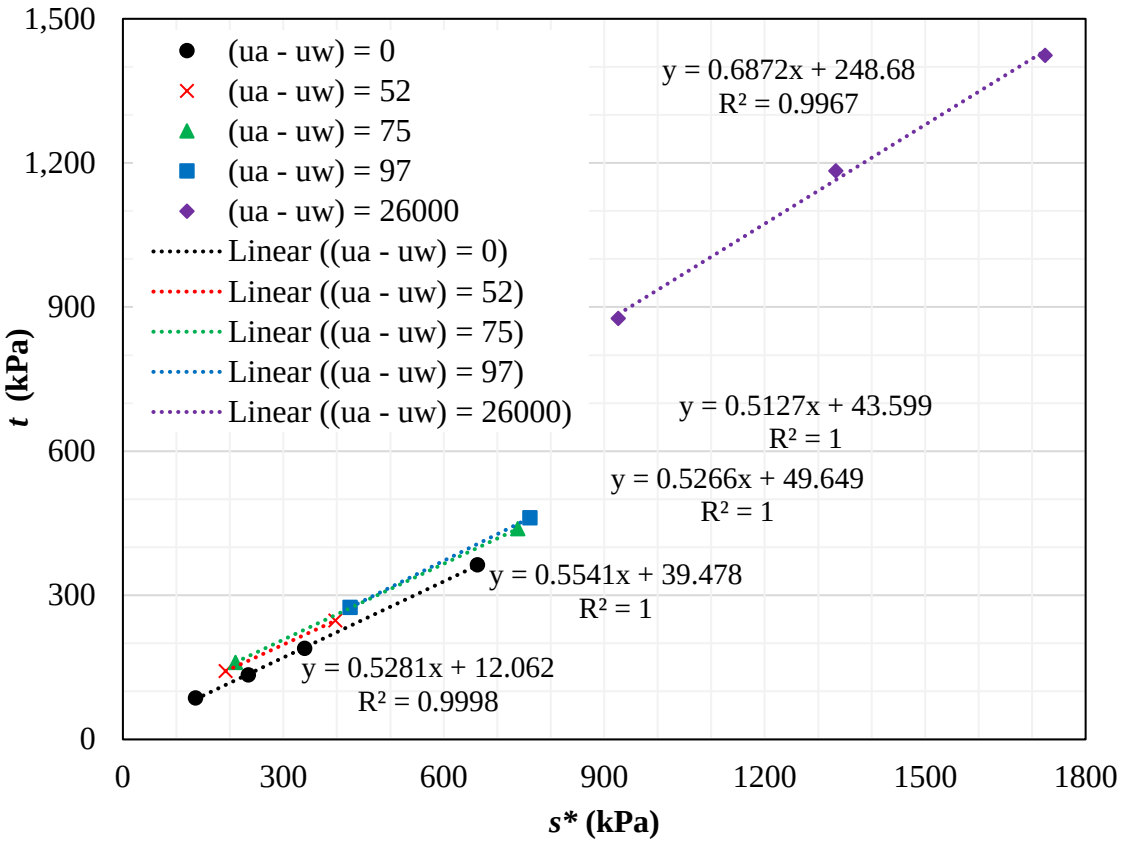

Figure C. 10. Failure envelope in terms of s* and t of soil 1R

To obtain the values of ψ^b, it was performed a fitting procedure based on the minimization of the squared errors of *t* by changing the values of ψ^b. For the tests that were not grouped according to similar matric suctions, the parameters *d* and ψ' were obtained through interpolation. Table C.3 shows all the shear strength parameters after performing the aforementioned procedures.

Table C. 3. Shear strength parameters of soil 1R for peak failure criterion

$\sigma_1 - \sigma_3$ (kPa)	$\sigma_3 - u_a$ (kPa)	$u_a - u_w$ (kPa)	t (kPa)	s* (kPa)	d (kPa)	ψ'	ϕ'	c_{app} (kPa)	ψ^b	ϕ^b	t fitted	Error²	σ_f (kPa)	τ_f (kPa)
172.4	50	0	86.2	136.2	12.1	27.8	31.9	14.2	0.0	0.0	84.0	4.9E+00	90.7	70.6
284.1	50	55	142.1	192.1	39.5	27.1	30.8	46.0	31.3	36.5	144.0	3.8E+00	119.2	126.1
321.0	50	79	160.5	210.5	49.6	27.8	31.8	58.4	26.5	31.2	162.4	3.6E+00	126.0	140.2
370.0	50	155	185.0	235.0	75.0	29.0	33.6	90.1	15.4	18.5	185.0	2.2E-09	132.5	154.3
1752.3	50	26000	876.1	926.1	248.7	34.5	43.4	342.3	0.5	0.7	876.1	5.7E-08	324.0	634.1
269.0	100	0	134.5	234.5	12.1	27.8	31.9	14.2	0.0	0.0	135.9	2.0E+00	163.5	115.9
379.3	150	0	189.7	339.7	12.1	27.8	31.9	14.2	0.0	0.0	191.4	3.1E+00	239.5	163.1
494.5	150	49	247.3	397.3	39.5	27.1	30.8	46.0	31.3	36.5	245.3	3.8E+00	270.5	211.7
549.9	150	98	274.9	424.9	43.6	29.0	33.6	52.4	15.8	19.0	275.3	1.4E-01	272.6	229.4
649.2	150	133	324.6	474.6	70.0	29.0	33.6	84.1	20.4	24.5	324.6	7.1E-11	294.7	271.1
2366.4	150	26000	1183.2	1333.2	248.7	34.5	43.4	342.3	0.6	0.8	1183.2	4.3E-08	520.1	857.2
726.4	300	0	363.2	663.2	12.1	27.8	31.9	14.2	0.0	0.0	362.3	8.6E-01	471.4	307.3
877.3	300	72	438.7	738.7	49.6	27.8	31.8	58.4	26.5	31.2	436.8	3.6E+00	507.6	372.0
922.7	300	96	461.3	761.3	43.6	29.0	33.6	52.4	15.8	19.0	461.0	1.4E-01	505.7	383.7
968.1	300	116	484.0	784.0	65.0	29.0	33.6	78.1	17.9	21.5	484.0	7.5E-11	515.8	403.3
2848.4	300	26000	1424.2	1724.2	248.7	34.5	43.4	342.3	0.5	0.7	1424.2	5.2E-08	745.5	1032.2

SSE	2.6E+01
RMSE	1.27
R^2	1.000

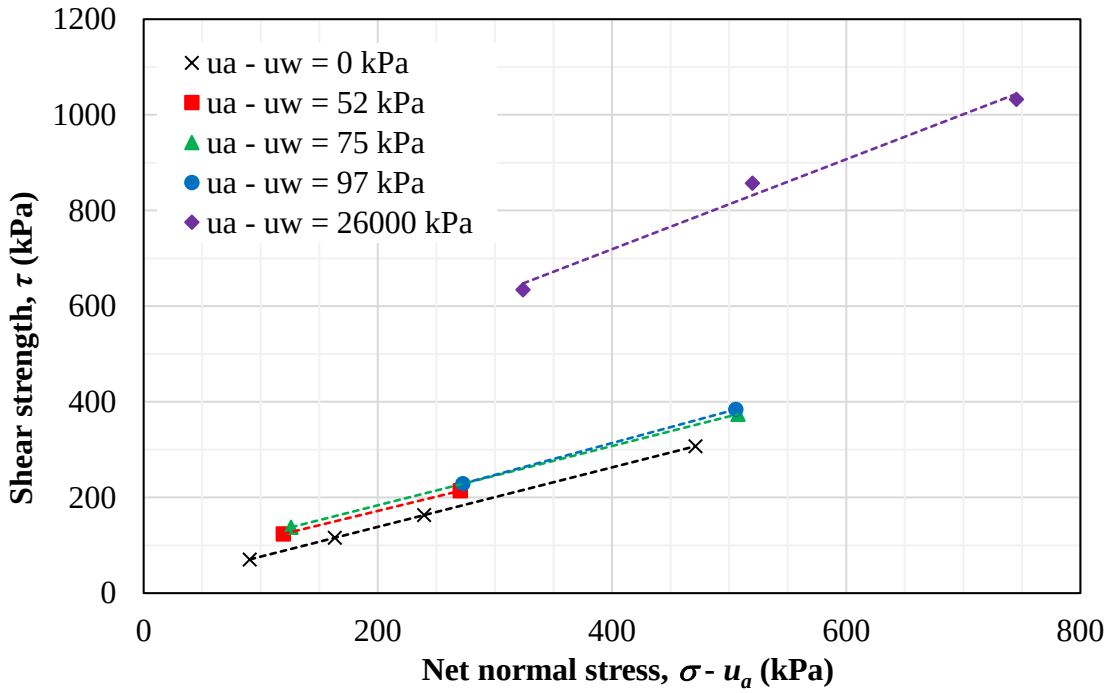

Figure C. 11. Failure envelope in terms of (σ - u_a) and τ of soil 1R

The values presented in Table C.3 indicate that ϕ^b does not change with the net confining stress and decrease as long the matric suction increases. For matric suctions up to 155 kPa, it is safe to assume that ϕ' is about 32.0º. Although Table C.3 presents some values of ϕ^b greater than ϕ' for matric suctions of 49 and 55 kPa, this does not constitute a problem because this behavior can be attributed to the fitting procedure. Assuming ϕ^b equal to ϕ' for these two tests would result in a RMSE of 2.15, and this error corresponds to 0.49% of the average values of *t*. In other words, this error is negligible in comparison to the inherent variability of the soil, sampling, testing and fitting.

The data from Table C.3 were fitted using the Modified Bi-Hyperbolic model for low (≤ 155 kPa) and all matric suctions. The fitting parameters are presented in Table C.4. For low suctions, the R^2 and RMSE are respectively 0.997 and 6.2 whereas for all suctions, they are 0.991 and 25.6, respectively. These goodness-of-fit points out to a great adherence of the model to the data. The extended Mohr-Coulomb failure surfaces for low and all matric suctions are depicted in Fig. C.12 and C.13, respectively.

Table C. 4. Parameters obtained for the Modified Bi-Hyperbolic model of soil 1R at peak failure

	Low suctions	All suctions
c' (kPa)	14.2	14.2
ϕ' (degrees)	32.0	32.0
ϕ^b (degrees)	31.8	31.8
τ_{ult1} (kPa)	4.13×10^{10}	6.53×10^{7}
τ_{ult2} (kPa)	3.07×10^{2}	5.26×10^{2}
τ_{peak} (kPa)	124.0	98.5
T_{ult} (kPa)	124.0	98.5
s_b	157.0	499.2
n	65.8	1
a_1	1.600	1.600
b_1	2.42×10^{-11}	1.53×10^{-8}
a_2	1.611	1.611
b_2	3.42×10^{-3}	1.96×10^{-3}

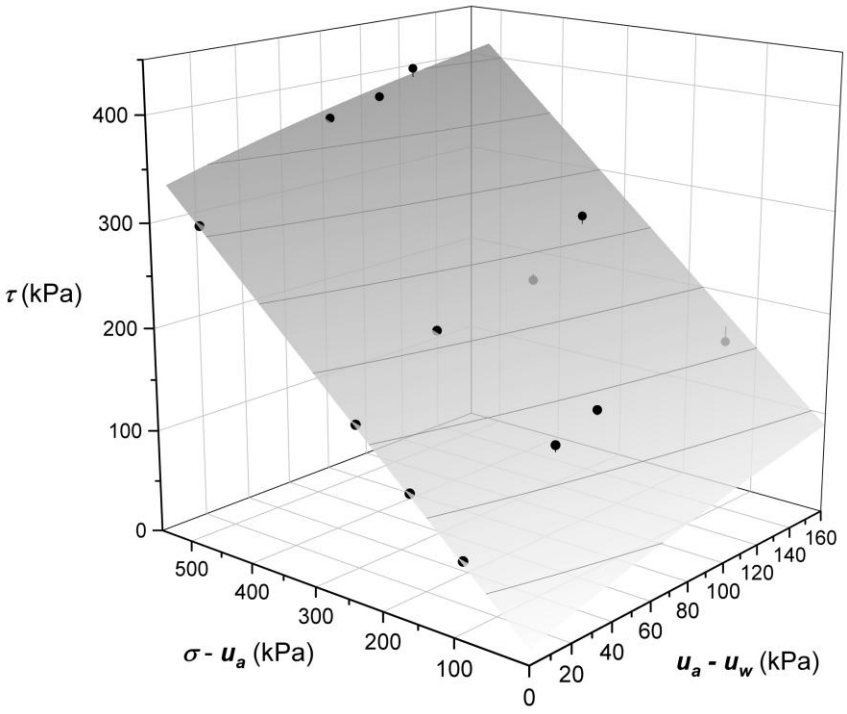

Figure C. 12. Extended Mohr-Coulomb failure surface fitted using the Modified Bi-Hyperbolic model of soil 1R for low matric suctions (≤ 155 kPa)

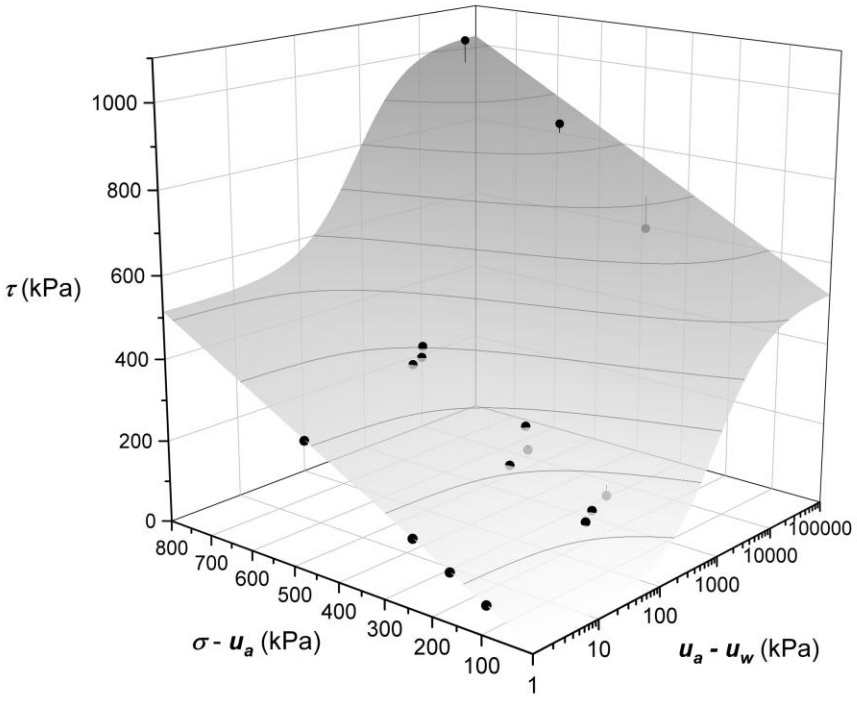

Figure C. 13. Extended Mohr-Coulomb failure surface fitted using the Modified Bi-Hyperbolic model of soil 1R for all matric suctions

- General comments

The graphs showing axial strain versus deviator stress indicate that most of the curves presented strain-hardening behavior (Figs. C.3-4, C.6-8). In summary, the shear strength parameters considering peak shear strength as failure criterion points out:

- At first, the angle ϕ^b is equal to ϕ'. For matric suctions between 52 and 75 kPa, ϕ^b begins to reduce. Also, ϕ^b is independent of the net normal stress;
- The angle ϕ' increases with the matric suction, but it is remains constant ($\approx 32.0°$) for matric suctions under 155 kPa.

C.2 Fagundes (2014) – 2R and 1U

- Soil basic information and characteristics
    - Void ratio (e_0) = 0.43 (remolded); 0.76 (undisturbed)
    - Density of solids (ρ_s) = 2.649
    - Dry density (ρ_d) = 1.853 (remolded); 1.508 (undisturbed)
    - Liquid limit (w_L) = 15.5%
    - Plastic limit (w_P) = NP
    - USCS = SC (disaggregated) / SC (aggregated)

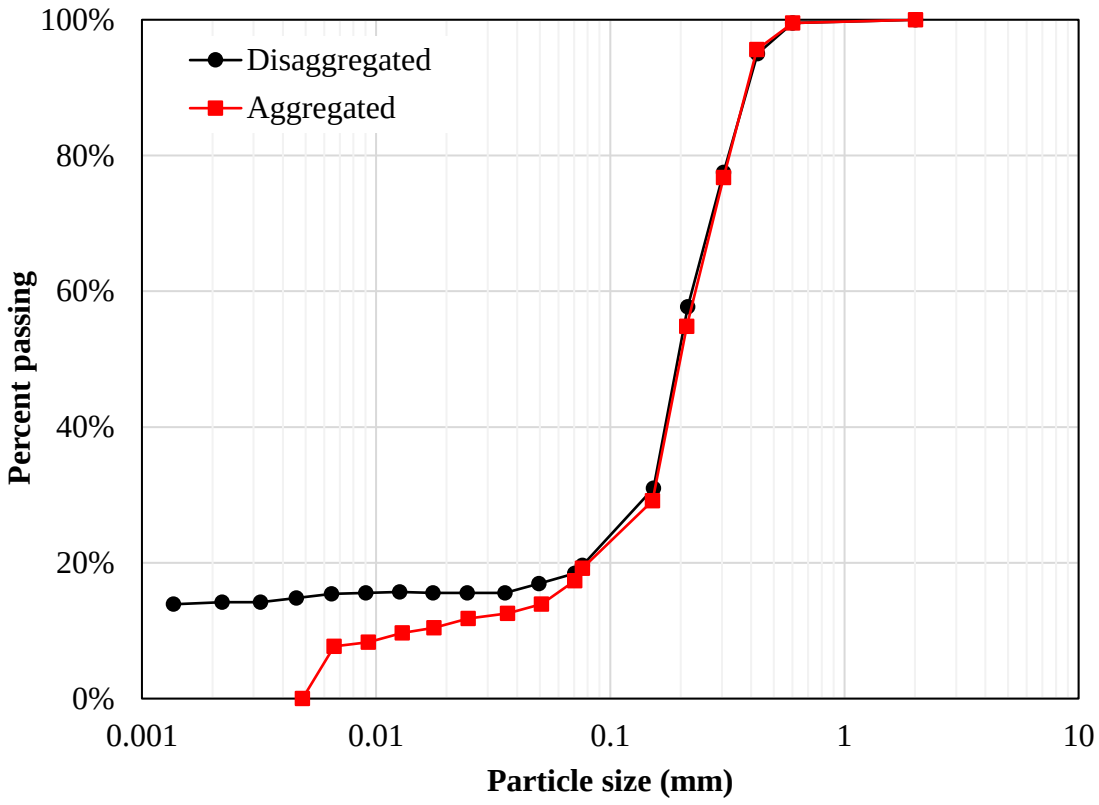

Figure C. 14. Grain-size distribution curve of soils 2R and 1U

- SWCC

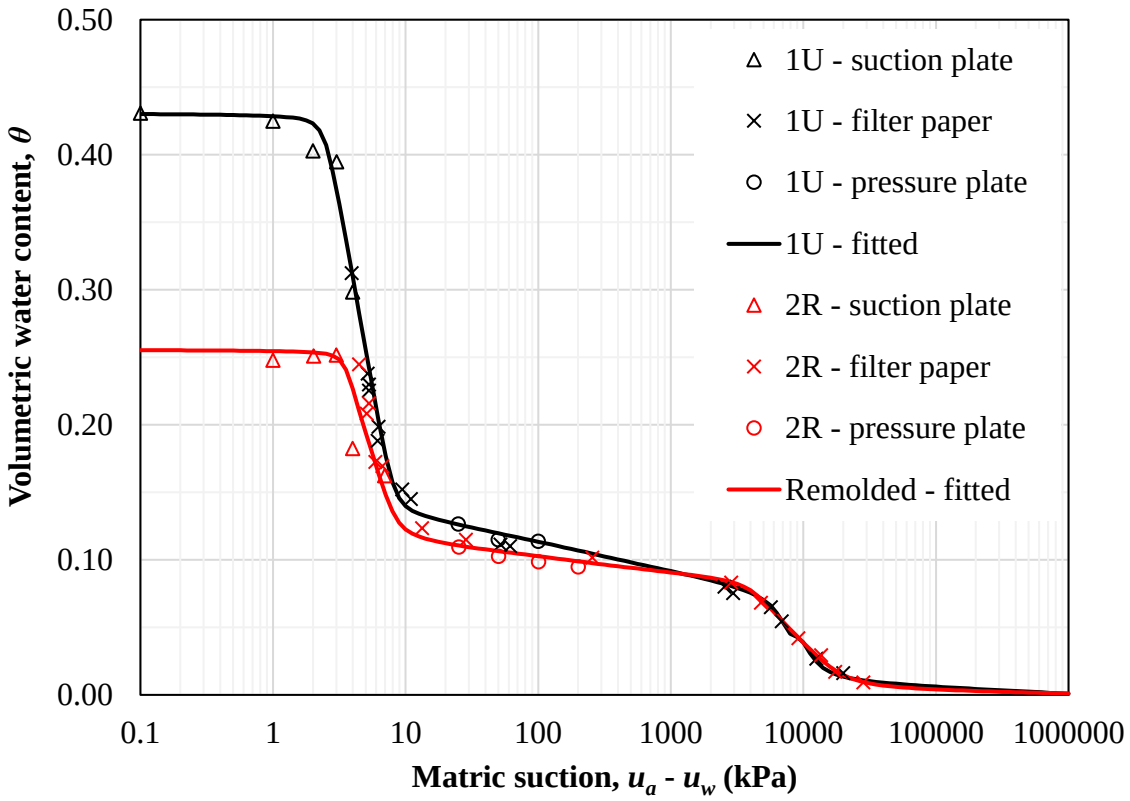

Figure C. 15. Soil-water characteristic curves of soils 2R and 1U

- Shear strength data: 2R
  - Initial void ratio (e_0) = 0.43
  - Type: modified triaxial CD
  - Volume measurement: double-walled cell
  - Shear velocity: 0.05 mm/min
  - USCS = SC-SC

i) $u_a - u_w = 0$ kPa

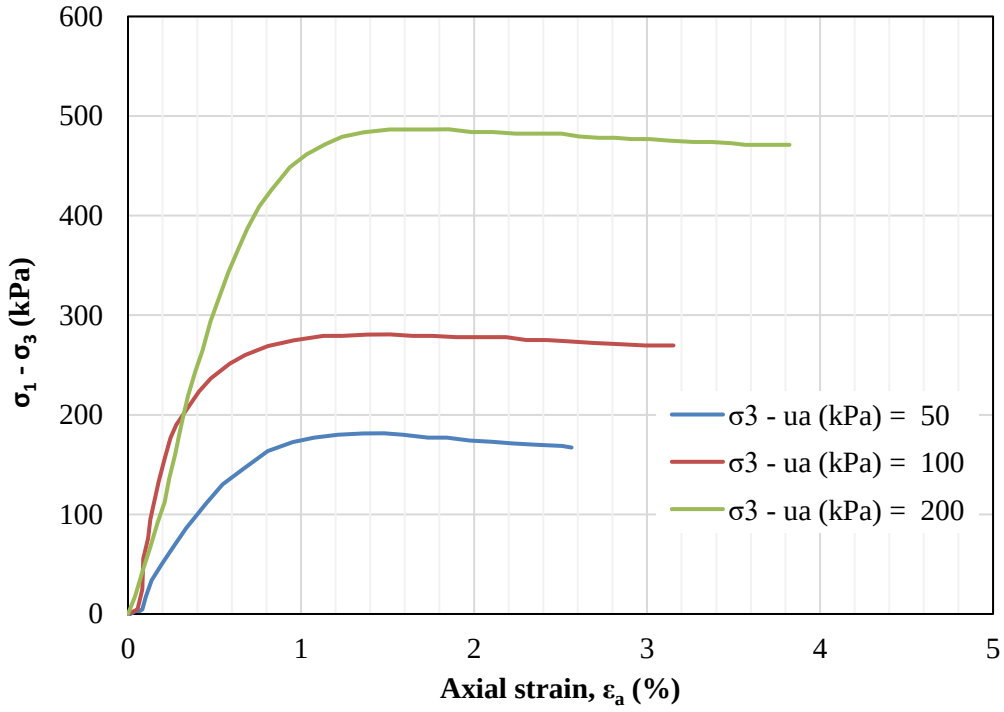

Figure C. 16. Axial strain versus deviator stress of saturated tests of soil 2R

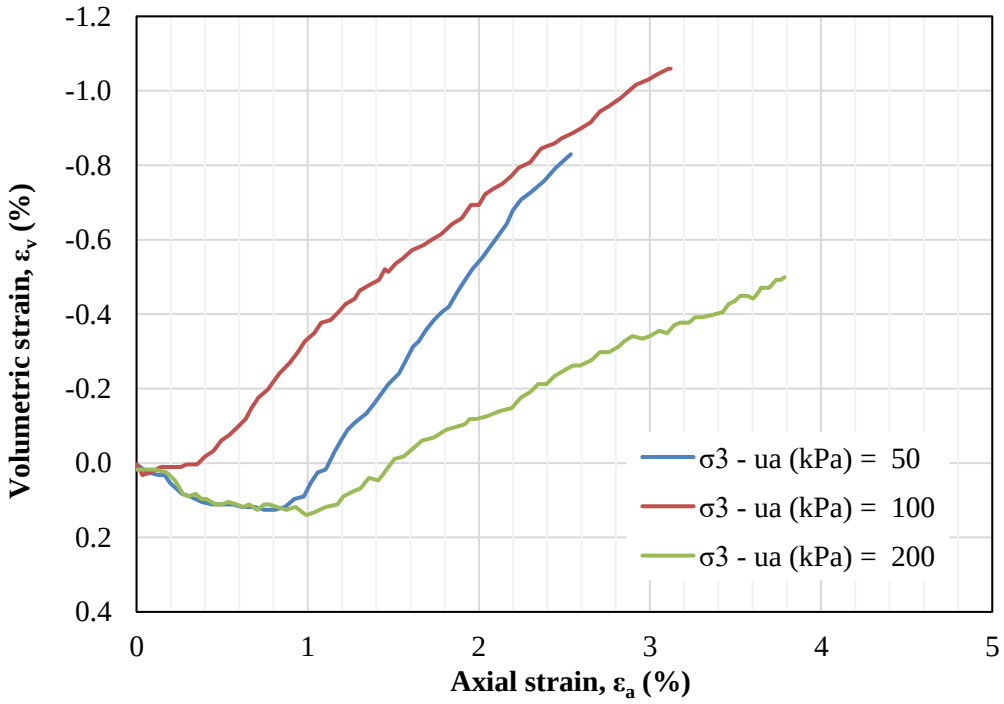

Figure C. 17. Axial strain versus volumetric strain of saturated tests of soil 2R

ii) $u_a - u_w$ = 50 kPa

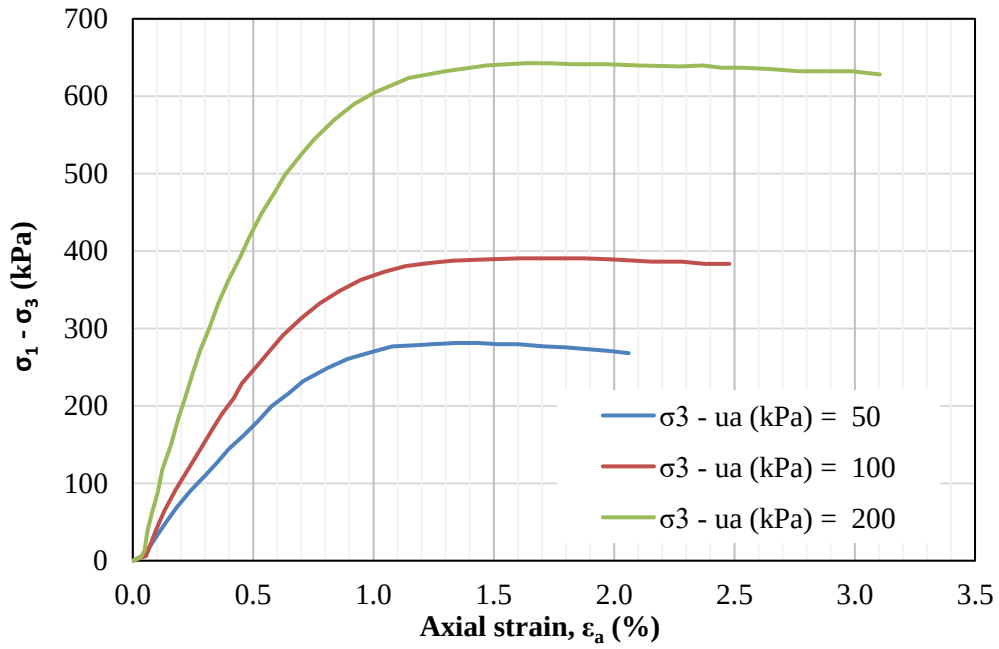

Figure C. 18. Axial strain versus deviator stress of tests with (u_a - u_w) = 50 kPa of soil 2R

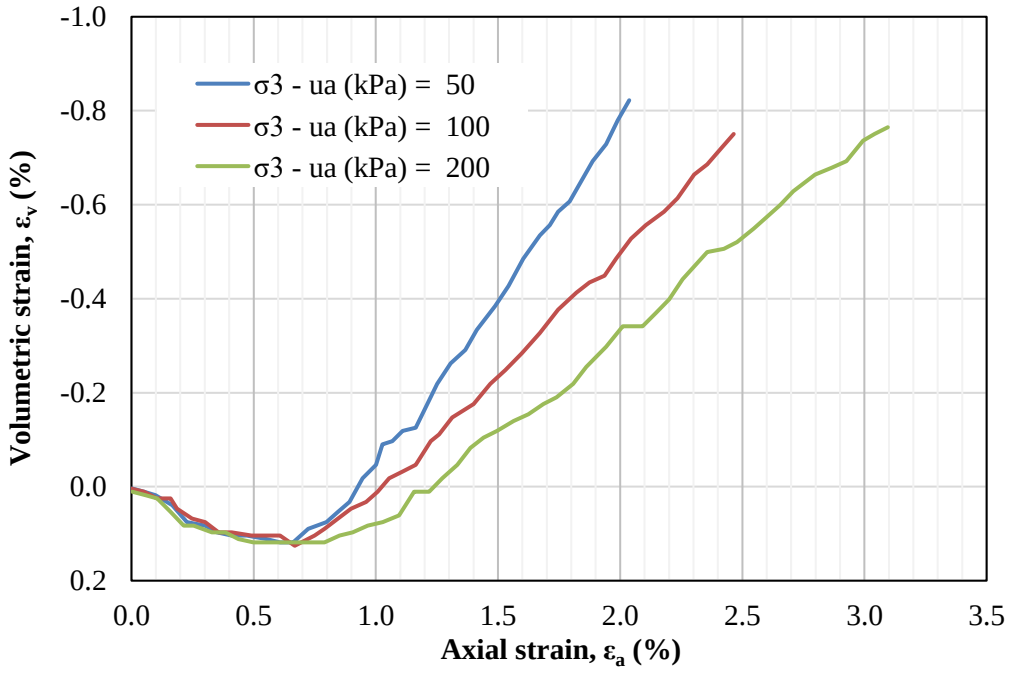

Figure C. 19. Axial strain versus volumetric strain of tests with (u_a - u_w) = 50 kPa of soil 2R

iii) $u_a - u_w$ = 200 kPa

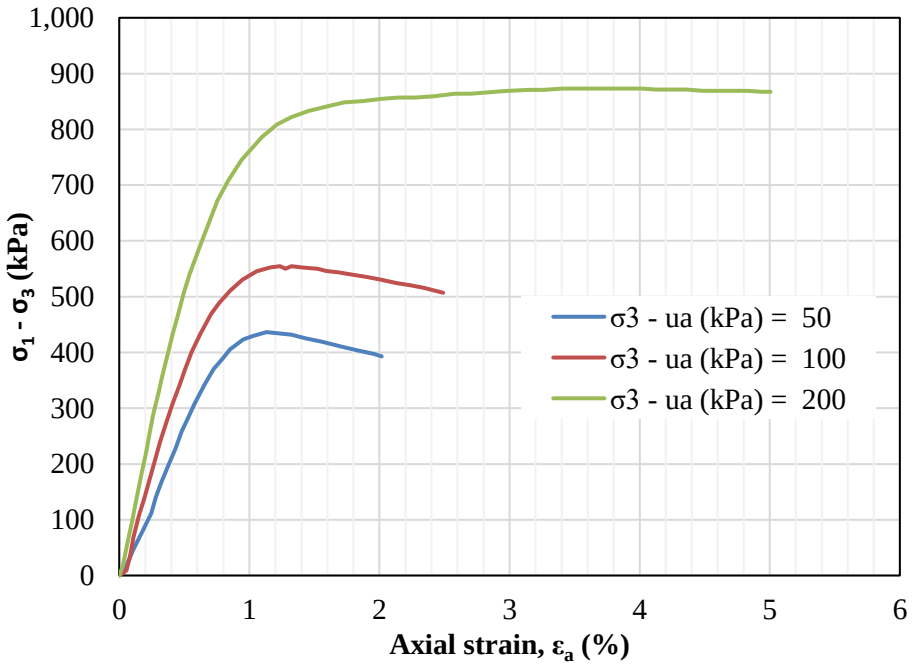

Figure C. 20. Axial strain versus deviator stress of tests with (u_a - u_w) = 200 kPa of soil 2R

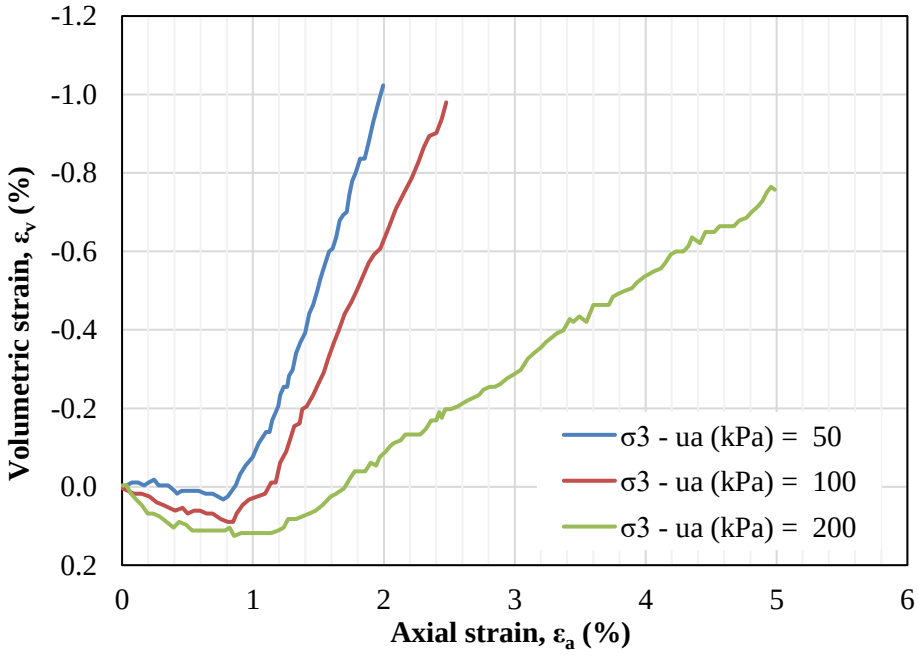

Figure C. 21. Axial strain versus volumetric strain of tests with (u_a - u_w) = 200 kPa of soil 2R

iv) $u_a - u_w$ = 23000 kPa

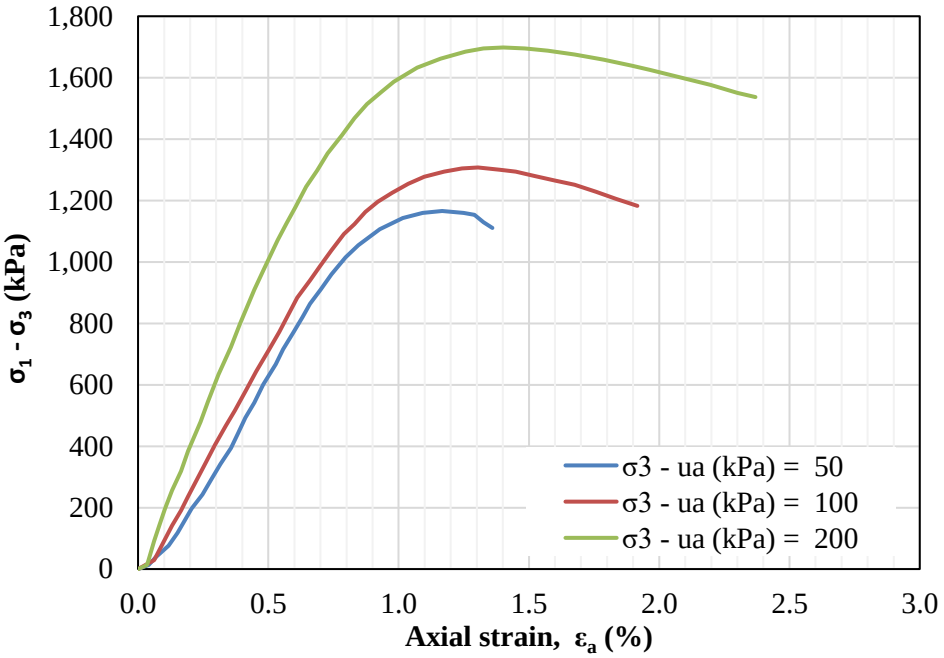

Figure C. 22. Axial strain versus deviator stress of tests with (u_a - u_w) = 23000 kPa of soil 2R

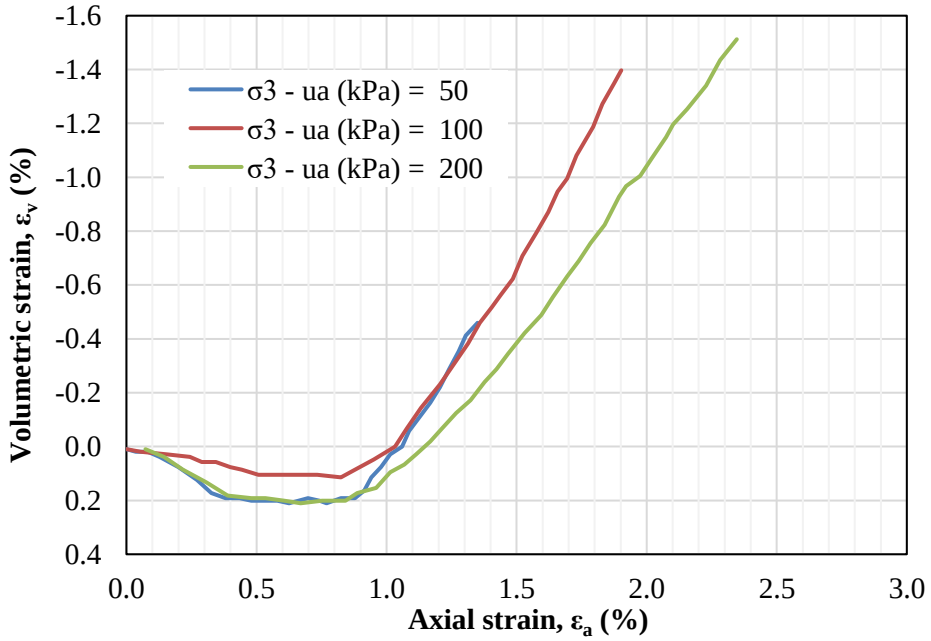

Figure C. 23. Axial strain versus volumetric strain of tests with (u_a - u_w) = 23000 kPa of soil 2R

- Failure criterion: maximum or peak shear stress

The data from the tests for maximum shear strength as failure criterion is presented in Table C.5.

Table C. 5. Shear strength parameters of soil 2R for peak failure criterion

$\sigma_1 - \sigma_3$ (kPa)	$\sigma_3 - u_a$ (kPa)	$u_a - u_w$ (kPa)	t (kPa)	s* (kPa)	d (kPa)	ψ'	ϕ'	c_{app} (kPa)	ψ^b	ϕ^b	t fitted	Error²	σ_f (kPa)	τ_f (kPa)
181.5	50		90.7	140.7						0.0	90.5	6.9E-02	95.1	78.1
280.7	100	0	140.4	240.4	19.4	26.8	30.3	22.5		0.0	140.8	1.5E-01	169.3	121.5
486.7	200		243.3	443.3						0.0	243.2	1.7E-02	320.6	210.0
281.2	50		140.6	190.6					18.5	22.1	140.6	1.3E-10	113.7	117.3
390.5	100	50	195.3	295.3	35.0	28.7	33.2	41.9	15.6	18.7	195.3	7.2E-11	188.5	162.9
642.6	200		321.3	521.3					17.8	21.3	321.3	2.1E-10	345.4	268.4
436.3	50		218.1	268.1					10.9	13.6	218.1	1.0E-09	138.6	174.1
554.6	100	200	277.3	377.3	55.6	30.8	36.6	69.3	9.3	11.6	277.3	9.9E-10	212.5	221.5
873.3	200		436.6	636.6					10.5	13.1	436.6	1.3E-09	376.7	349.4
1166.1	50		583.0	633.0					0.4	0.5	583.0	2.4E-08	259.2	444.5
1307.3	100	23000	653.7	753.7	172.7	32.8	40.1	225.6	0.4	0.5	653.6	2.2E-08	334.4	498.6
1698.2	200		849.1	1049.1					0.4	0.5	849.1	2.3E-08	504.0	648.2

SSE	0.24
R^2	1.00
RMSE	0.14

The failure envelope in terms of *s** and *t* shown in Fig. C.24 indicates a constant value of ψ' for each matric suction. To obtain the values of ψ^b, it was performed a fitting procedure based on the minimization of the squared errors of *t* by changing the values of ψ^b.

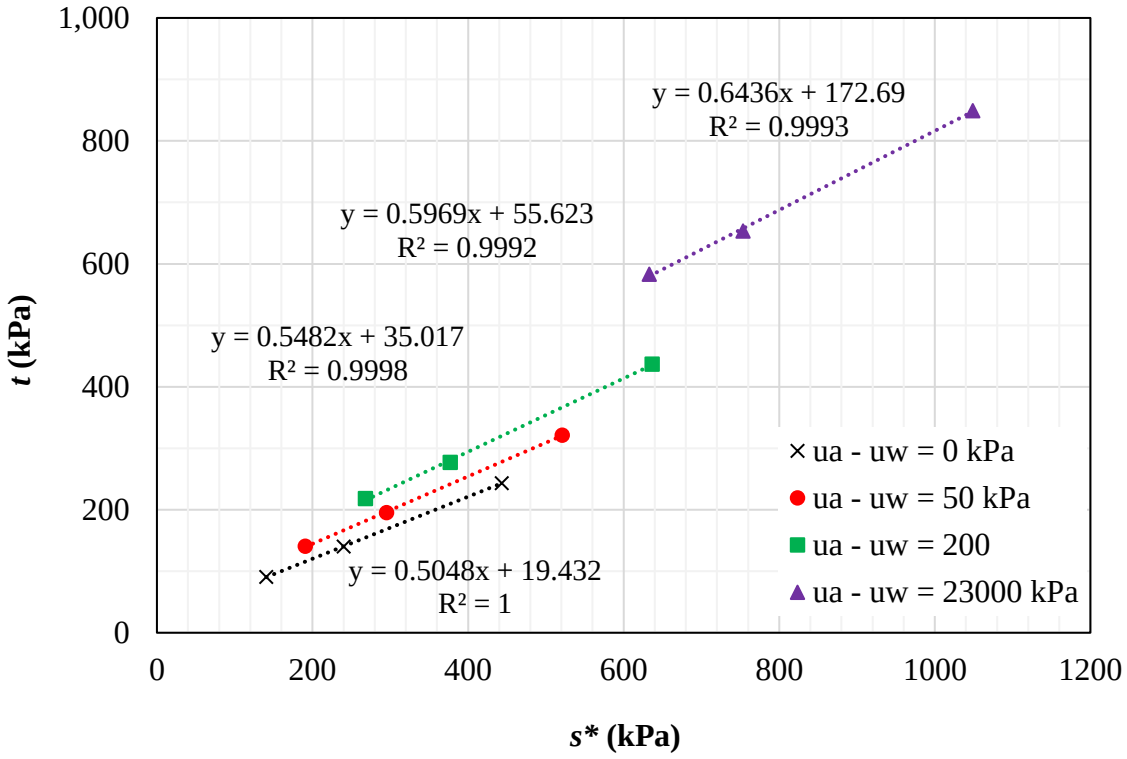

Figure C. 24. Failure envelope in terms of *s and *t* of soil 2R**

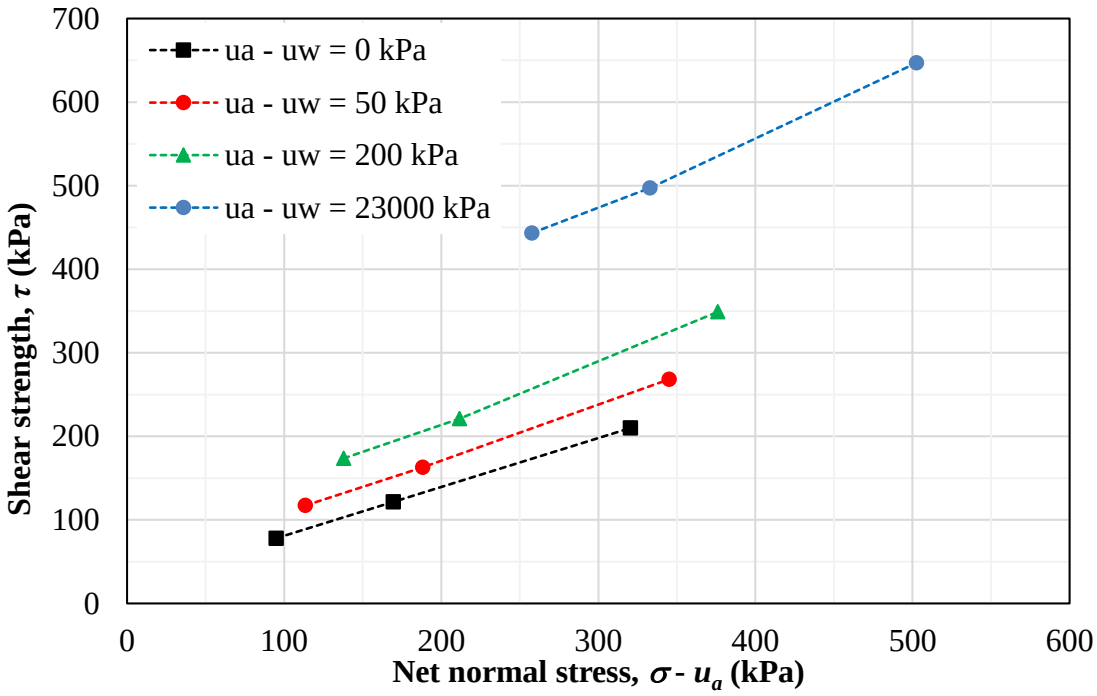

Figure C. 25. Failure envelope in terms of (σ - u_a) and τ of soil 2R

The values presented in Table C.5 indicate that ϕ^b does not change with the net confining stress and decrease as long the matric suction increases. For matric suctions of 50, 200 and 23000 kPa, ϕ^b are 20.7º, 12.8º and 0.5º, respectively.

The data from Table C.5 were fitted using the Modified Bi-Hyperbolic model for low (≤ 200 kPa) and all matric suctions. The fitting parameters are presented in Table C.6. For low suctions, the R^2 and RMSE are respectively 0.992 and 8.8 whereas for all suctions, they are 0.997 and 9.8, respectively. These goodness-of-fit points out to a great adherence of the model to the data. The extended Mohr-Coulomb failure surfaces for low and all matric suctions are depicted in Fig. C.26 and C.27, respectively.

Table C. 6. Parameters obtained for the Modified Bi-Hyperbolic model of soil 2R

	Low suctions	All suctions
c' (kPa)	22.5	0.0
ϕ' (degrees)	31.7	35.2
ϕ^b (degrees)	32.3	39.2
τ_{ult1} (kPa)	2.69×10^{7}	7.61×10^{9}
τ_{ult2} (kPa)	5.75×10^{2}	1.16×10^{9}
τ_{peak} (kPa)	179.4	1020.5
s_b	114.2	0.0
n	99.8	176.2
a_1	1.617	1.416
b_1	3.71×10^{-8}	1.31×10^{-10}
a_2	1.583	1.227
b_2	1.18×10^{-3}	8.65×10^{-10}

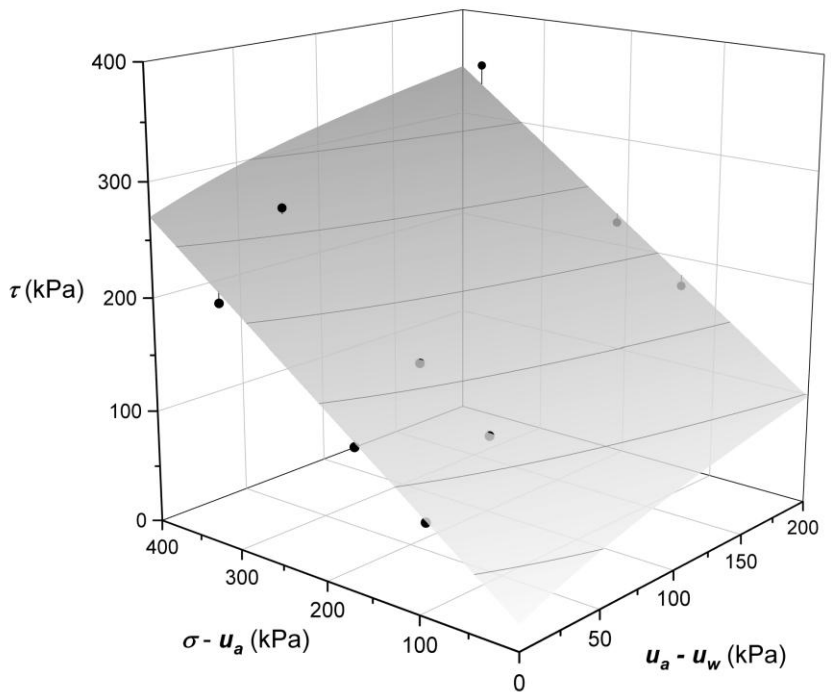

Figure C. 26. Extended Mohr-Coulomb failure surface fitted using the Modified Bi-Hyperbolic model of soil 2R for low matric suctions (≤ 200 kPa)

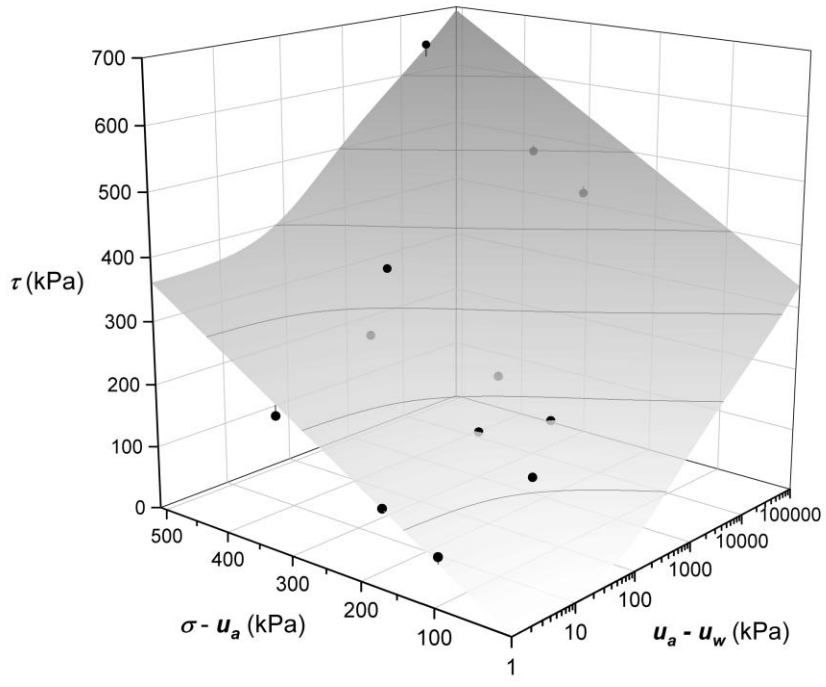

Figure C. 27. Extended Mohr-Coulomb failure surface fitted using the Modified Bi-Hyperbolic model of soil 2R for all matric suctions

- General comments

The graphs showing the axial strain versus deviator stress indicate that most of the curve showed strain-hardening behavior (Figs. C.16, C.18, C.20 and C.22). Some curves exhibited peak followed by a slight decrease in the deviator stress. In summary, the shear strength parameters considering maximum shear strength as failure criterion indicate:

- The angle ϕ^b is inferior than ϕ' for all tests. However, the lowest matric suction in the unsaturated tests is 50 kPa, which is higher than the first residual suction (20 kPa). Hence, it is possible that ϕ^b is equal or higher than ϕ' for matric suctions under 50 kPa;
- Both angles ϕ' and ϕ^b are dependent of the suction, the first increases while the later decreases. They are also unaffected by the net normal stress;
- For high suctions over than the second residual suction (20000 kPa), ϕ^b approaches zero ($\approx 0.4°$).

- Shear strength data: 1U
  - Initial void ratio (e_0) = 0.76
  - Type: modified triaxial CD
  - Volume measurement: double-walled cell
  - Shear velocity: 0.05 mm/min

i) $u_a - u_w$ = 0 kPa

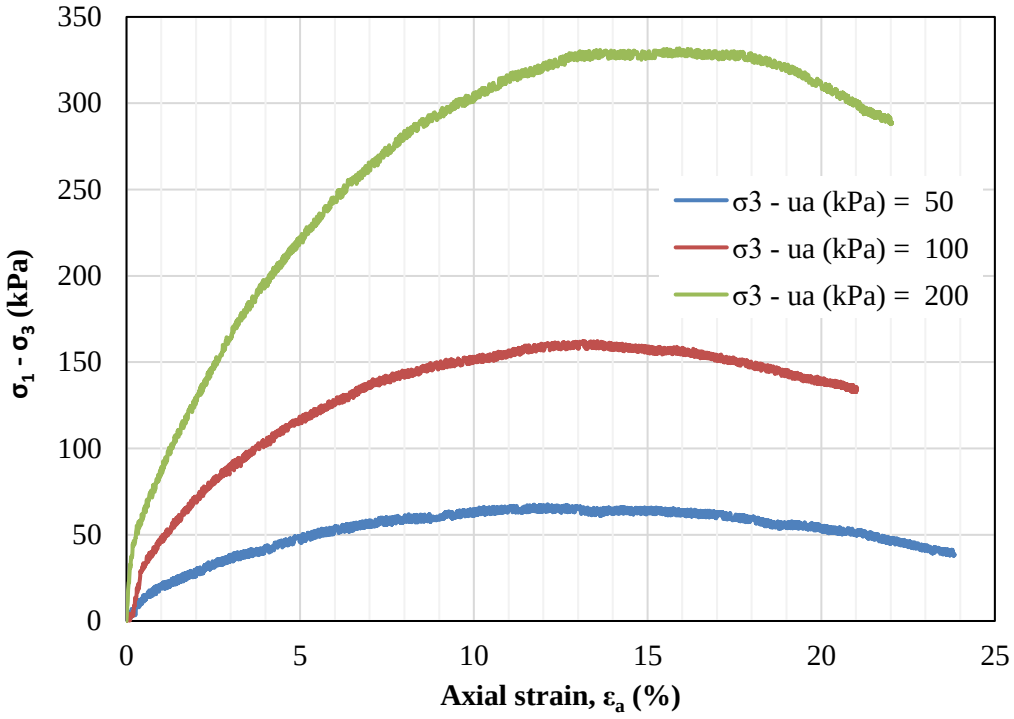

Figure C. 28. Axial strain versus deviator stress of saturated tests of soil 1U

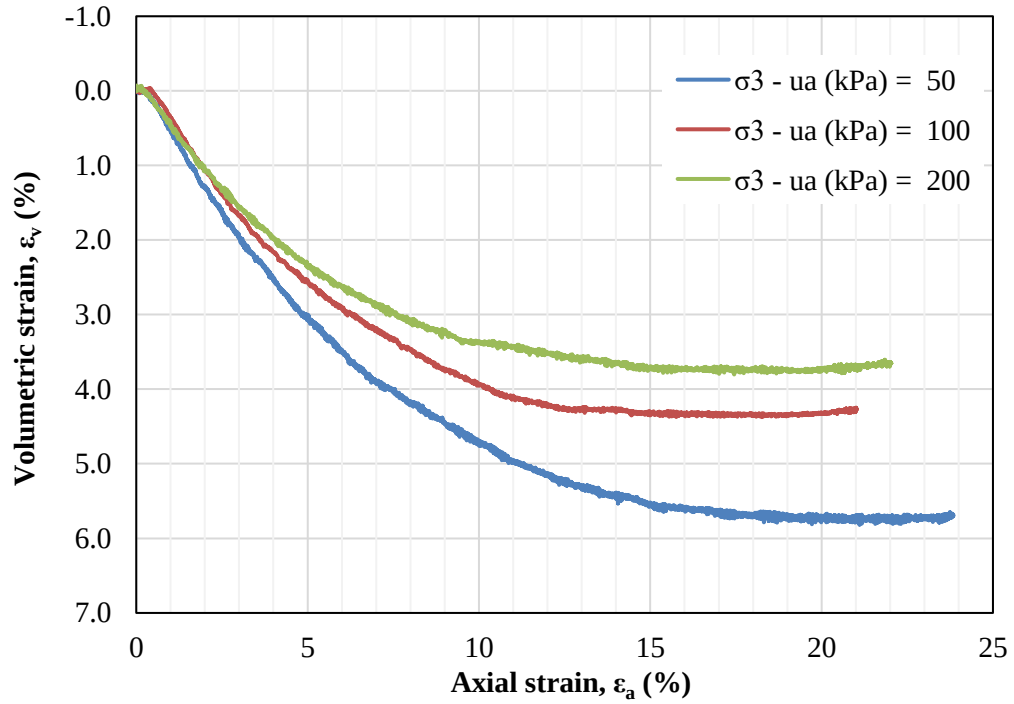

Figure C. 29. Axial strain versus volumetric strain of saturated tests of soil 1U

ii) $u_a - u_w$ = 50 kPa

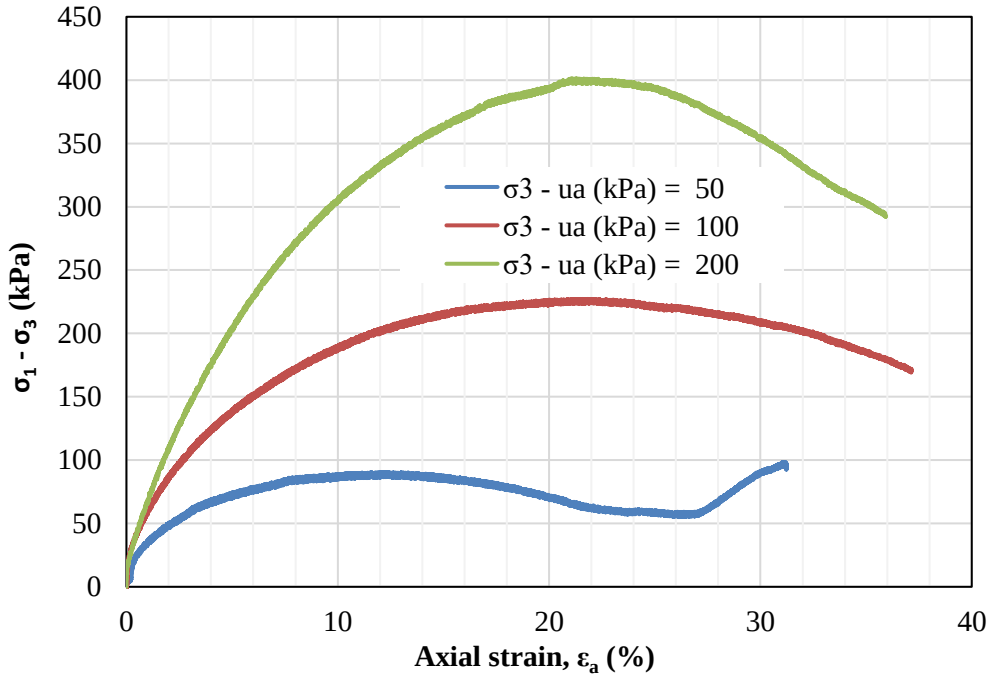

Figure C. 30. Axial strain versus deviator stress of tests with (u_a - u_w) = 50 kPa of soil 1U

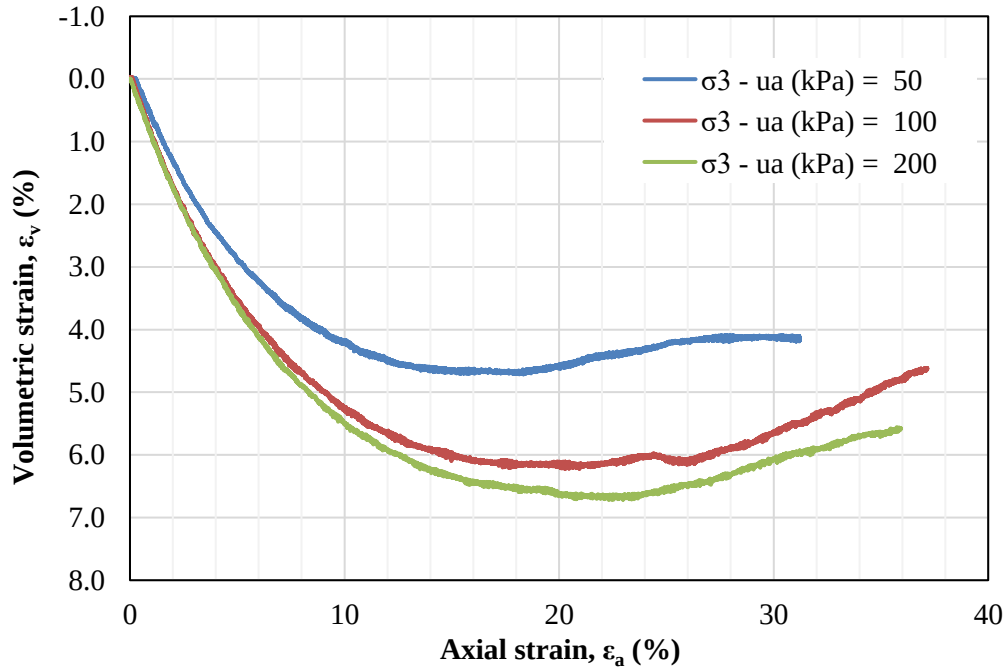

Figure C. 31. Axial strain versus volumetric strain of tests with (u_a - u_w) = 50 kPa of soil 1U

iii) $u_a - u_w$ = 200 kPa

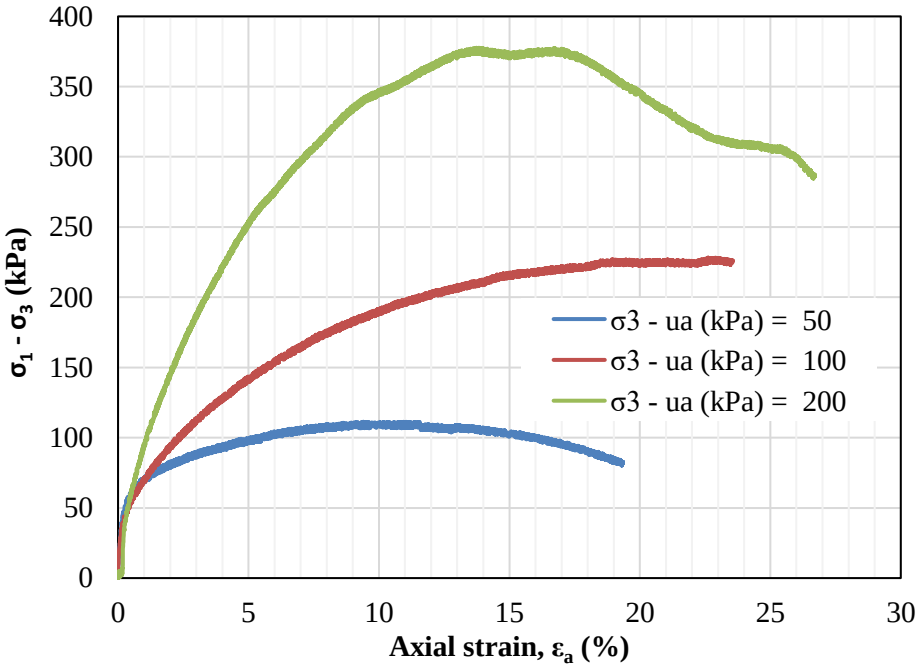

Figure C. 32. Axial strain versus deviator stress of tests with (u_a - u_w) = 200 kPa of soil 1U

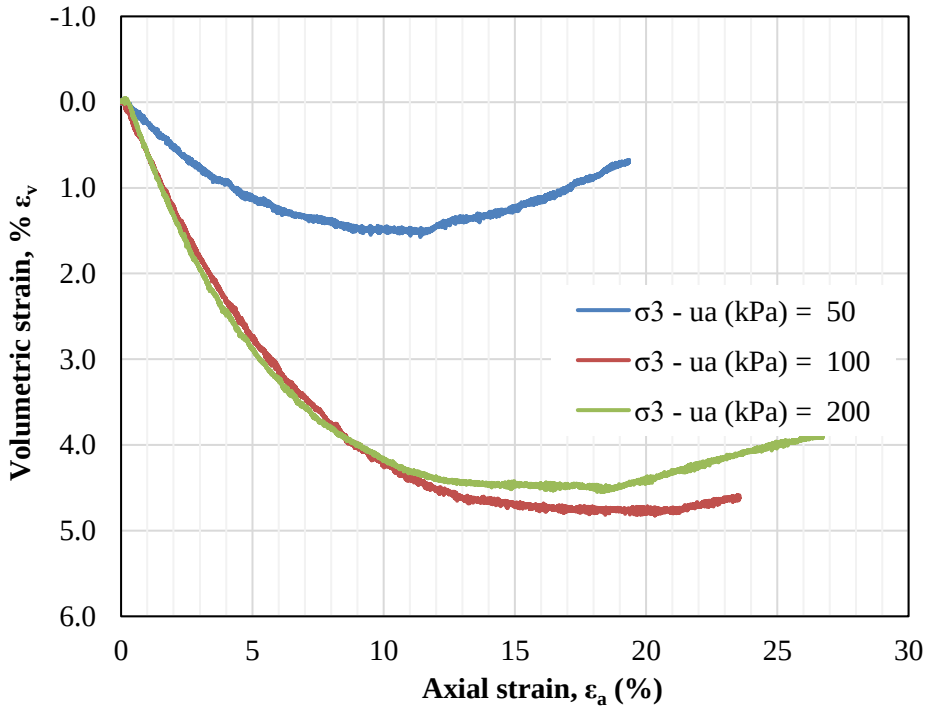

Figure C. 33. Axial strain versus volumetric strain of tests with (u_a - u_w) = 200 kPa of soil 1U

iv) $u_a - u_w$ = 400 kPa

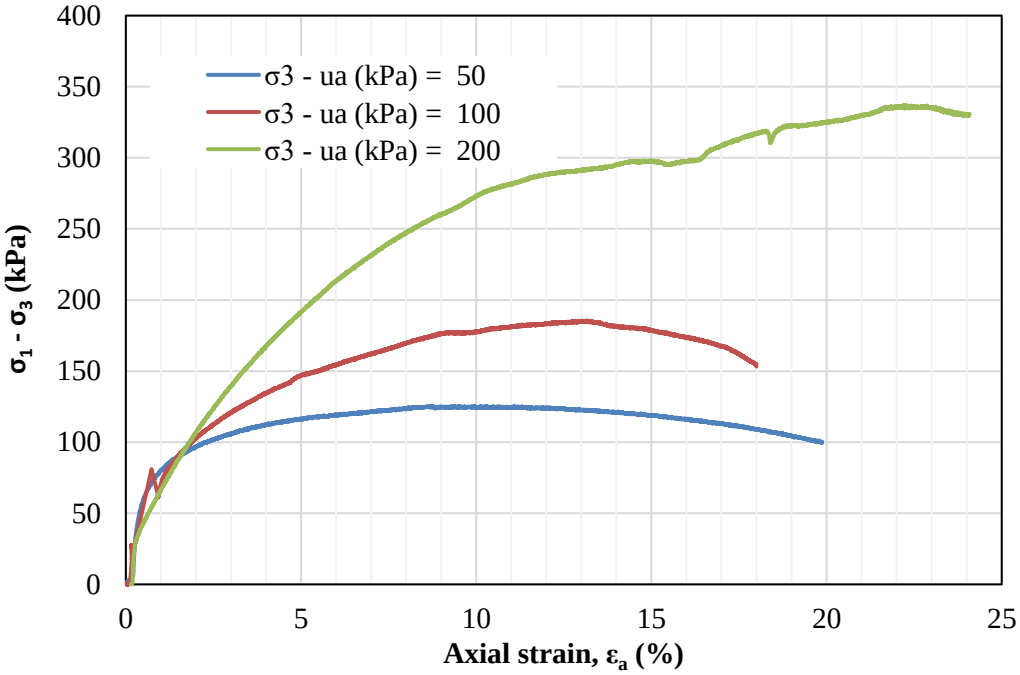

Figure C. 34. Axial strain versus deviator stress of tests with (u_a - u_w) = 400 kPa of soil 1U

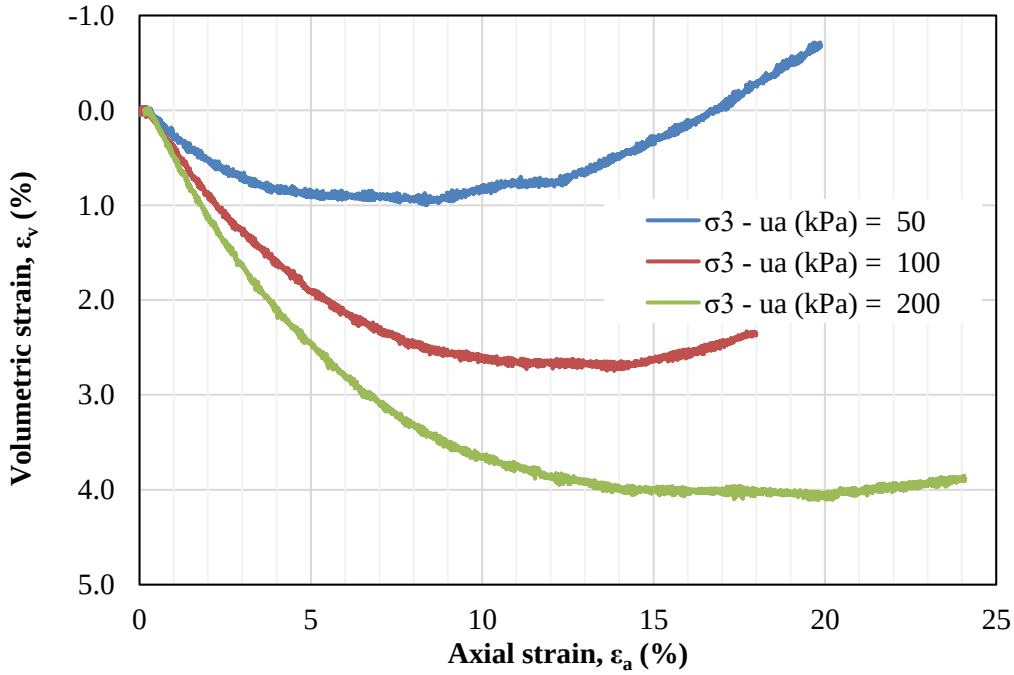

Figure C. 35. Axial strain versus volumetric strain of tests with (u_a - u_w) = 400 kPa of soil 1U

v) $u_a - u_w$ = 33000 kPa

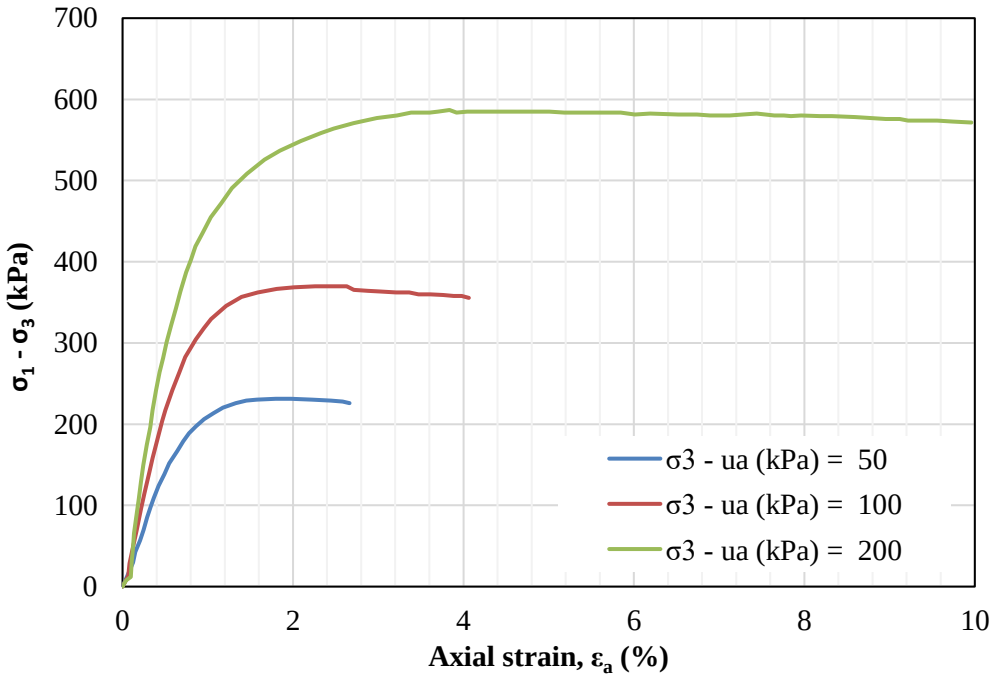

Figure C. 36. Axial strain versus deviator stress of tests with (u_a - u_w) = 33000 kPa of soil 1U

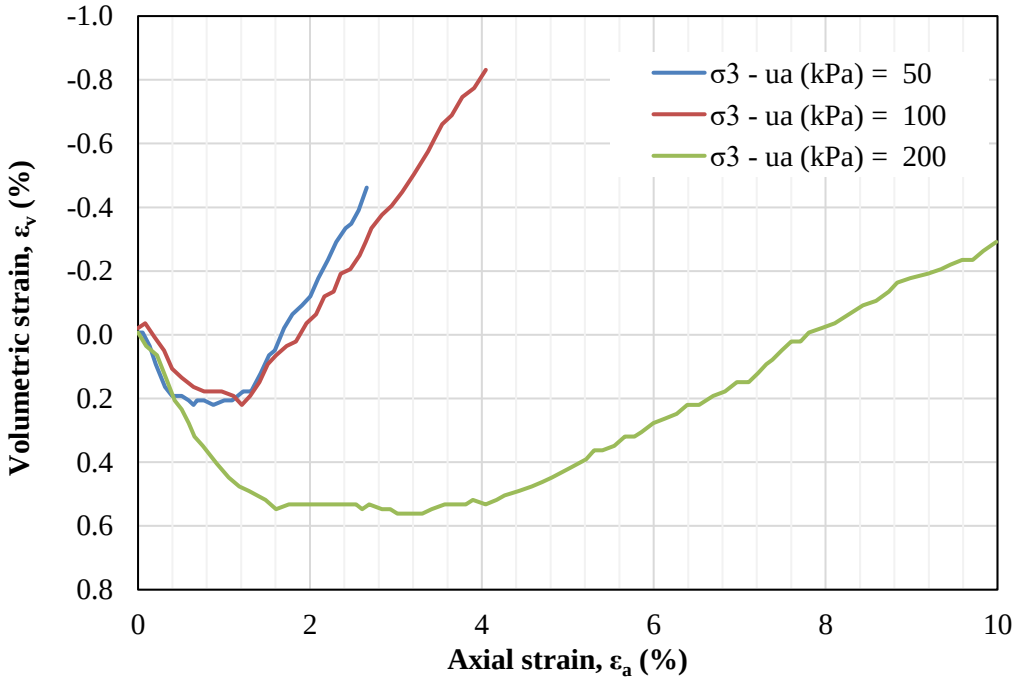

Figure C. 37. Axial strain versus volumetric strain of tests with (u_a - u_w) = 33000 kPa of soil 1U

- Failure criterion: maximum or peak shear stress

The data from the shear strength tests for peak failure criterion is presented in Table C.7.

Table C. 7. Shear strength parameters of soil 1U for peak failure criterion

$\sigma_1 - \sigma_3$ (kPa)	$\sigma_3 - u_a$ (kPa)	$u_a - u_w$ (kPa)	t (kPa)	s* (kPa)	d (kPa)	ψ'	ϕ'	c_{app} (kPa)	ψ^b	ϕ^b	t fitted	Error²	σ_f (kPa)	τ_f (kPa)
67.6	50		33.8	83.8					0.0		37.7	1.6E+01	68.6	34.6
162.3	100	0	81.1	181.1	0.00	24.2	26.9	0.0	0.0		81.6	1.9E-01	144.6	72.9
331.8	200		165.9	365.9					0.0		164.8	1.3E+00	291.2	146.9
90.7	50		45.3	95.3					0.0	0.0	48.1	7.9E+00	72.4	42.4
227.3	100	50	113.7	213.7	0.45	26.8	30.3	0.5	6.6	7.6	113.7	3.3E-11	156.3	98.1
401.5	200		200.7	400.7					0.0	0.0	202.4	2.6E+00	299.4	175.1
111.2	50		55.6	105.6					1.8	2.1	55.6	5.7E-11	79.7	49.2
228.2	100	200	114.1	214.1	9.37	25.0	27.8	10.6	4.1	4.6	114.1	1.4E-10	160.9	100.9
377.7	200		188.8	388.8					2.1	2.4	188.8	7.6E-11	300.8	167.1
125.4	50		62.7	112.7					3.1	3.3	62.7	5.8E-10	89.8	58.4
185.6	100	400	92.8	192.8	21.95	20.0	21.4	23.6	3.2	3.5	92.8	6.4E-10	158.9	86.4
298.2	200		149.1	349.1					3.1	3.3	149.1	6.8E-10	294.7	138.8
231.3	50		115.6	165.6					0.0	0.1	115.6	7.1E-10	103.2	97.3
369.8	100	33000	184.9	284.9	28.09	28.4	32.7	33.4	0.1	0.1	184.9	8.0E-10	185.1	155.6
586.9	200		293.5	493.5					0.0	0.1	293.5	5.4E-10	335.0	247.0

SSE	2.7E+01
R^2	1.000
RMSE	1.35

The failure envelope in terms of *s** and *t* shown in Fig. C.38 indicates a constant value of ψ' for each matric suction. To obtain the values of ψ^b, it was performed a fitting procedure based on the minimization of the squared errors of *t* by changing the values of ψ^b. For $(\sigma_3 - u_a) = 50$ with $(u_a - u_w) = 50$ kPa, it was assumed failure at the first peak in the curve presented in Fig. C.30. For $(\sigma_3 - u_a) = 200$ with $(u_a - u_w) = 400$ kPa, it was assumed a peak failure around 15% of axial strain presented in Fig. C.34.

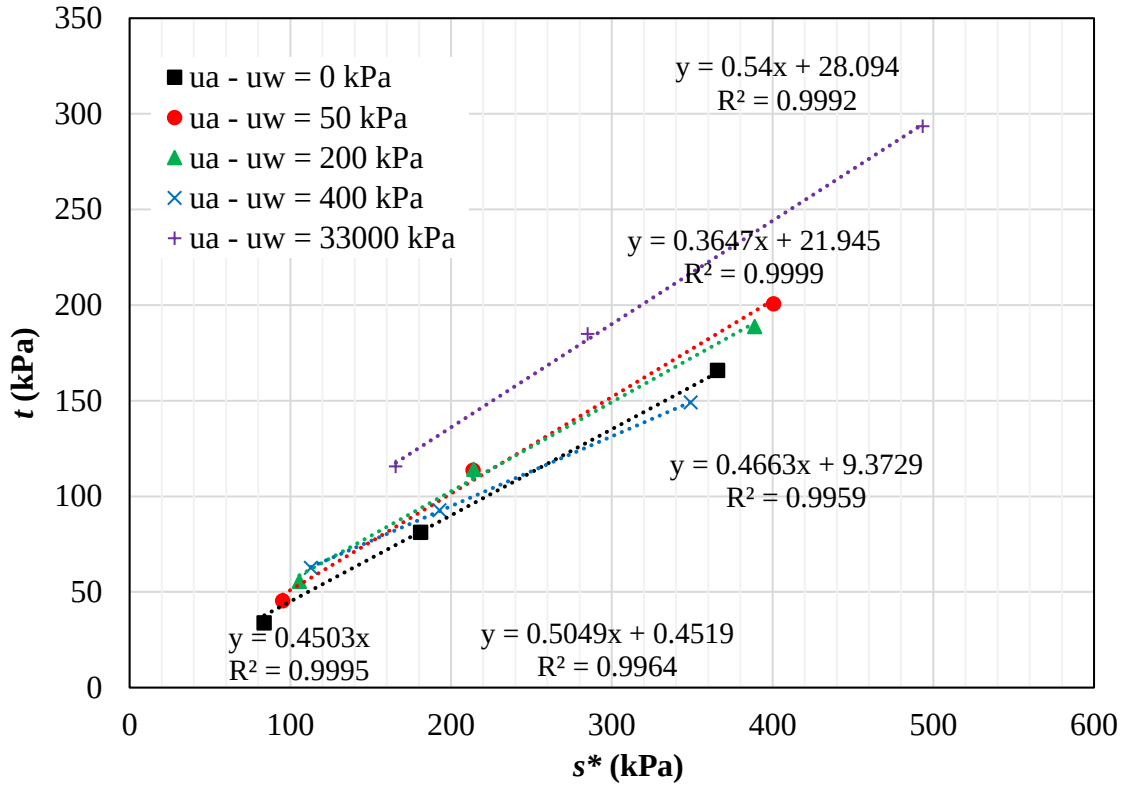

Figure C. 38. Failure envelope in terms of *s and *t* of soil 1U**

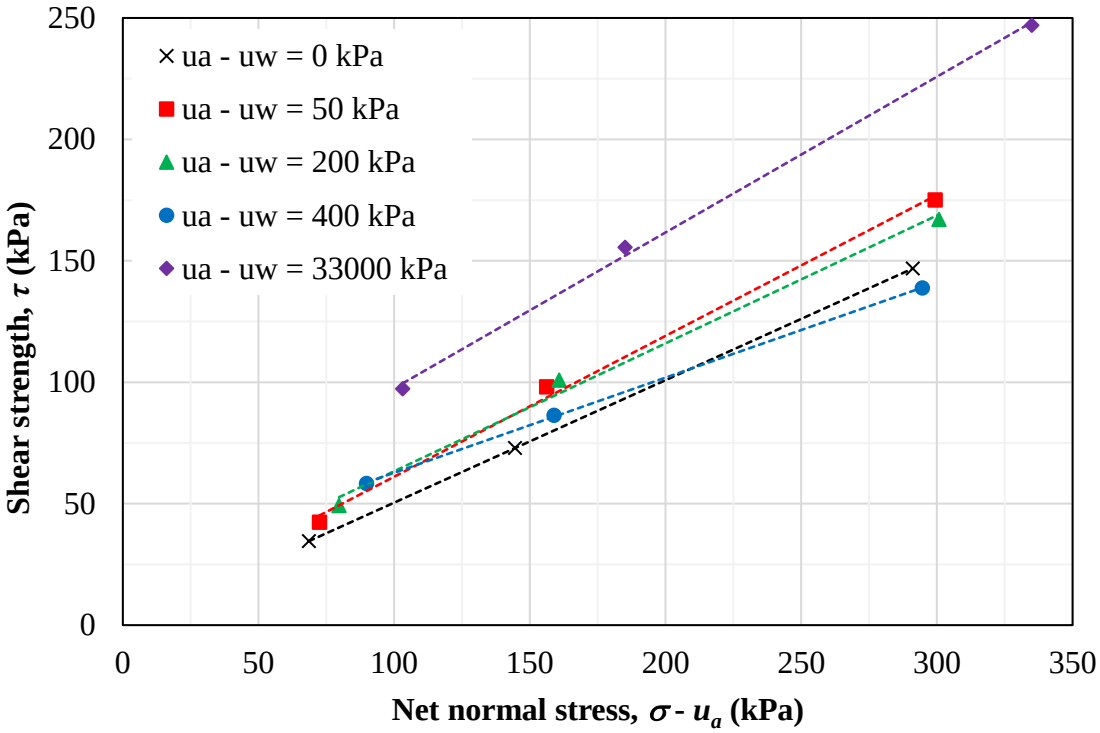

Figure C. 39. Failure envelope in terms of (σ - u_a) and τ of soil 1U

The values presented in Table C.7 indicate that ϕ^b does not change with the net confining stress and decrease as long the matric suction increases. For matric suctions of 50 kPa, the fitting resulted in two null ϕ^b values, but considering the inherent variability of the tests, it is reasonable to assume these ϕ^b values are similar to that of 7.6º. Thus, for matric suctions of 50, 200, 400 and 33000 kPa, ϕ^b are 7.6º, 3.0º, 3.4º and 0.1º, respectively. The data from Table C.7 were fitted using the Modified Bi-Hyperbolic model for low (≤ 400 kPa) and all matric suctions. For low suctions, the R^2 and RMSE are respectively 0.969 and 9.1 whereas for all suctions, they are 0.969 and 10.2, respectively. These goodness-of-fit points out to mean errors of 9.3 and 9.1%, respectively. Although such errors are not particularly high, the fitted surfaces indicate a significative dispersion for some points. The fitting parameters are presented in Table C.8 and the extended Mohr-Coulomb failure surfaces for low and all matric suctions are depicted in Fig. C.40 and C.41, respectively.

Table C. 8. Parameters obtained for the Modified Bi-Hyperbolic model of soil 1U

	Low suctions	All suctions
c' (kPa)	0.0	0.0
ϕ' (degrees)	26.8	28.5
ϕ^b (degrees)	7.4	1.9
τ_{ult1} (kPa)	5.94E+03	1.10E+07
τ_{ult2} (kPa)	4.00E+01	1.10E+05
τ_{peak} (kPa)	263.9	74.3
s_b	0.0	0.0
n	370.1	10.2
a_1	1.978	1.839
b_1	1.68×10^{-4}	9.06×10^{-8}
a_2	7.750	30.346
b_2	2.50×10^{-2}	9.13×10^{-6}

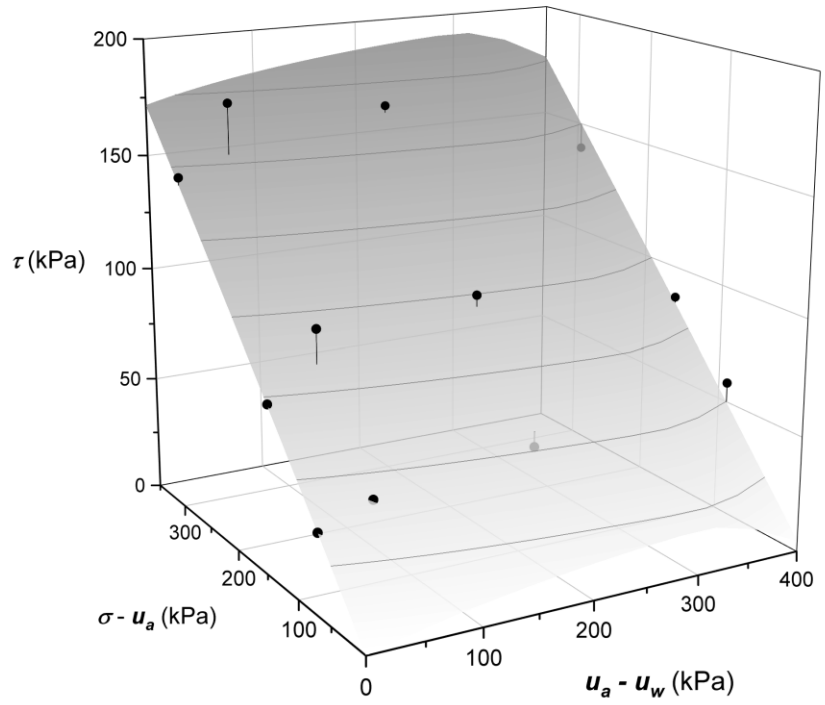

Figure C. 40. Extended Mohr-Coulomb failure surface fitted using the Modified Bi-Hyperbolic model of soil 1U for low matric suctions (≤ 400 kPa)

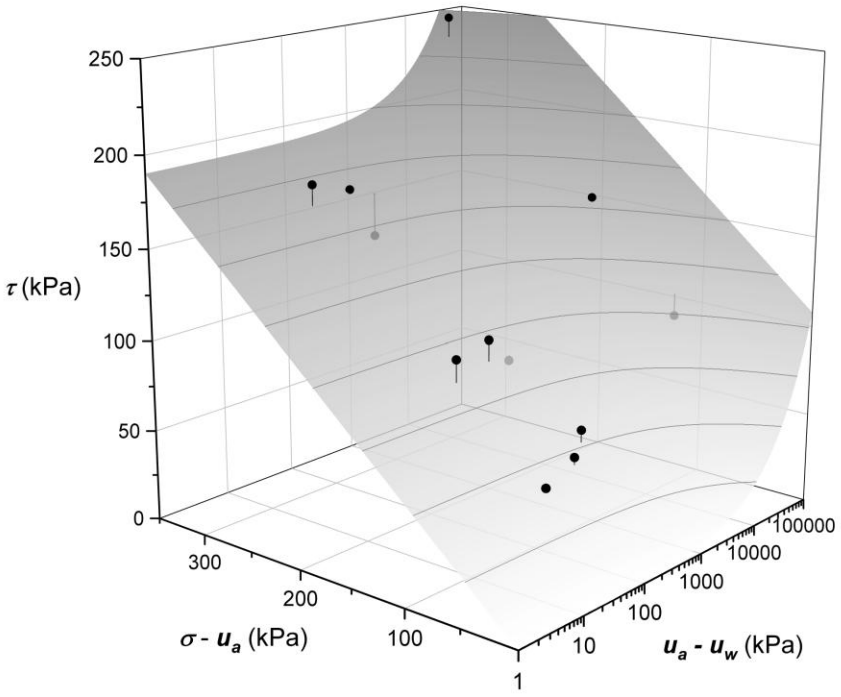

Figure C. 41. Extended Mohr-Coulomb failure surface fitted using the Modified Bi-Hyperbolic model of soil 1U for all matric suctions

- General comments

The graphs showing axial strain versus deviator stress indicate that most of the curves presented strain-hardening behavior (Figs. C.28, C.30, C.32, C.34 and C.36). Some tests were performed until significative axial strains surpassing 20%. In summary, the shear strength parameters considering peak shear strength as failure criterion points out:

- The angle ϕ^b is lower than ϕ', however, the maximum ϕ^b obtained is equivalent to $0.25\phi'$ for matric suction of 50 kPa, which is superior than the first residual suction (8 kPa), as shown in Table C.7 and Fig. C.15;
- The angle ϕ' seems to decrease for matric suctions over 50 kPa, but it increases again for high suctions;
- For high suctions over than the second air-entry value (11000 kPa), ϕ^b approaches zero ($\approx 0.1°$), as shown in Table C.7;
- The magnitude of the axial strains indicate that the specimens presented ductile behavior.

C.3 Georgetti (2014) – 3R and 4U

- Soil basic information and characteristics
    - Void ratio (e_0) = 0.55 (remolded); 1.03 (undisturbed)
    - Density of solids (ρ_s) = 2.65
    - Dry density (ρ_d) = 1.72 (remolded); 1.31 (undisturbed)
    - Liquid limit (w_L) = 32%
    - Plastic limit (w_P) = 16%
    - USCS = SC (disaggregated) / SC (aggregated)

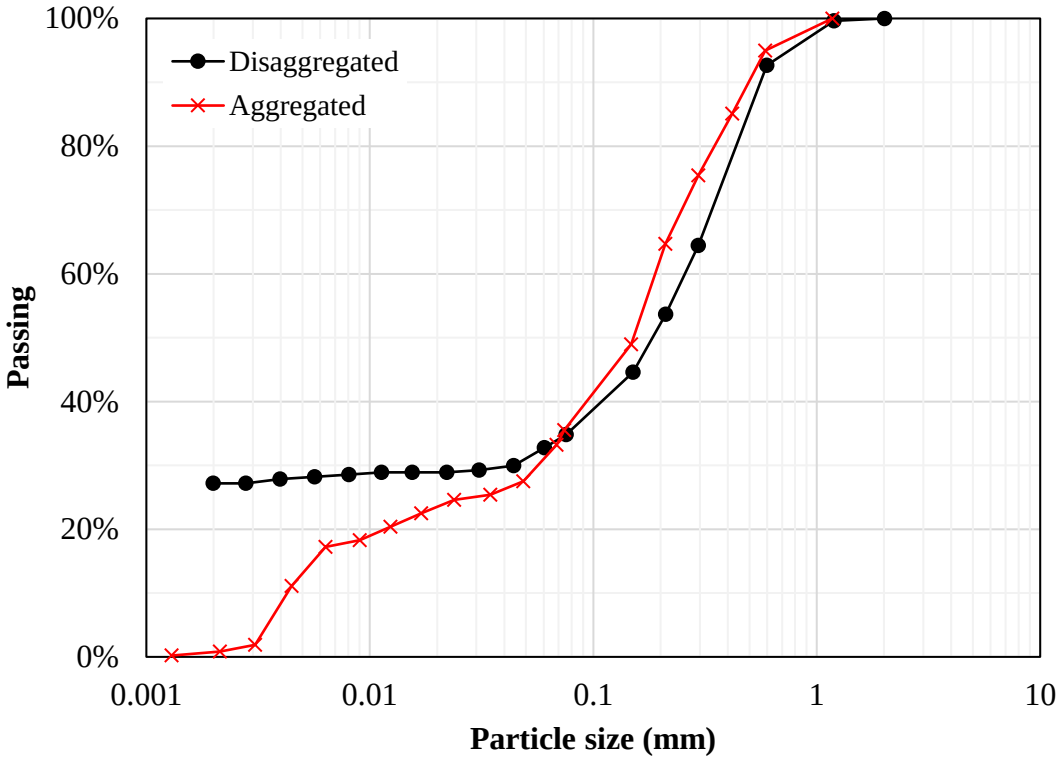

Figure C. 42. Grain-size distribution curve of soil 3R and 4U

- SWCC

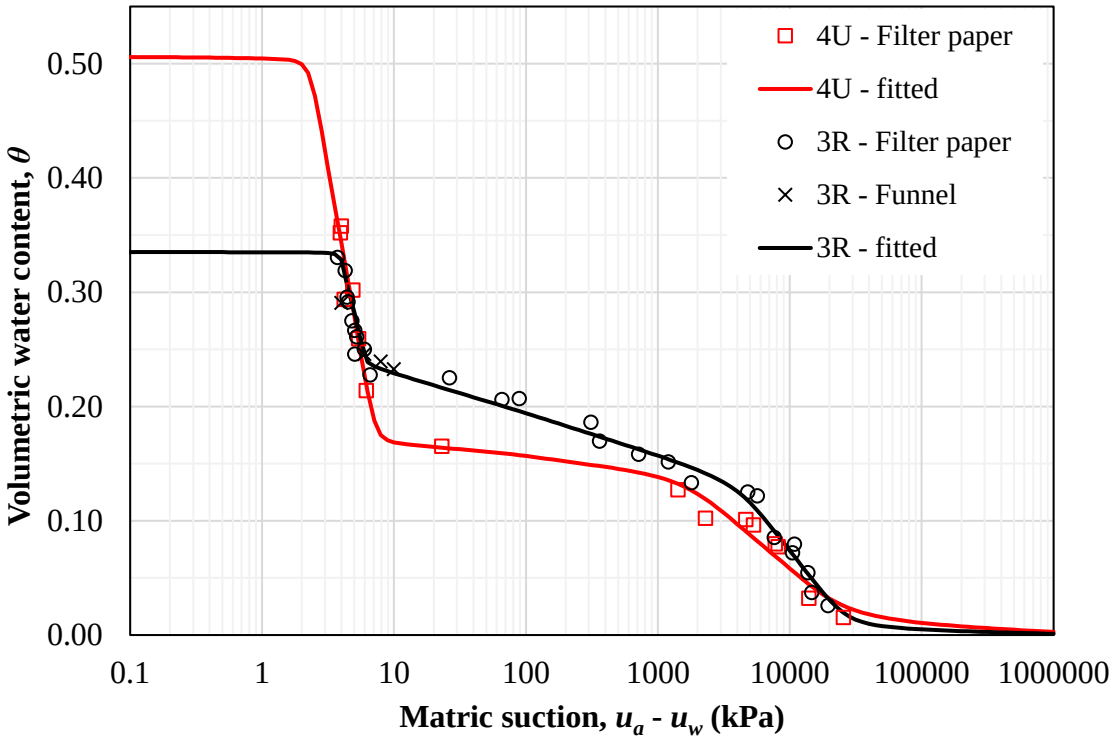

Figure C. 43. Soil-water characteristic curves of soils 3R and 4U

- Shear strength data: 3R
  - Initial void ratio (e_0) = 0.55
  - Type: modified triaxial CW multistage
  - Volume measurement: double walled cell
  - Shear velocity: 0.004 mm/min

i) $u_a - u_w = 0$ kPa

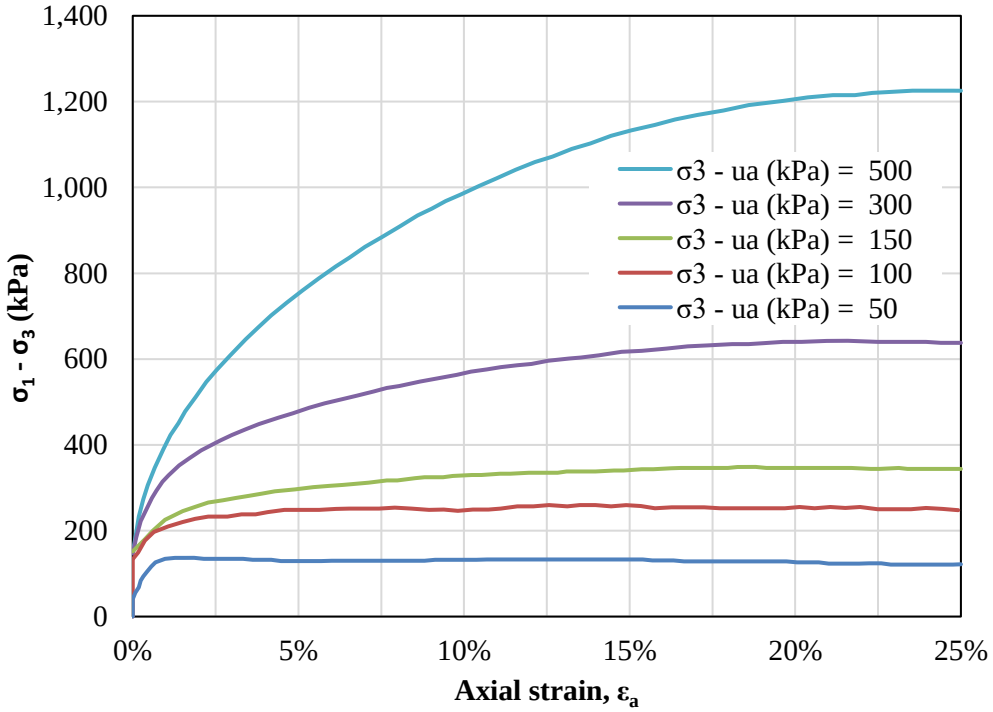

Figure C. 44. Axial strain versus deviator stress of saturated tests of soil 3R

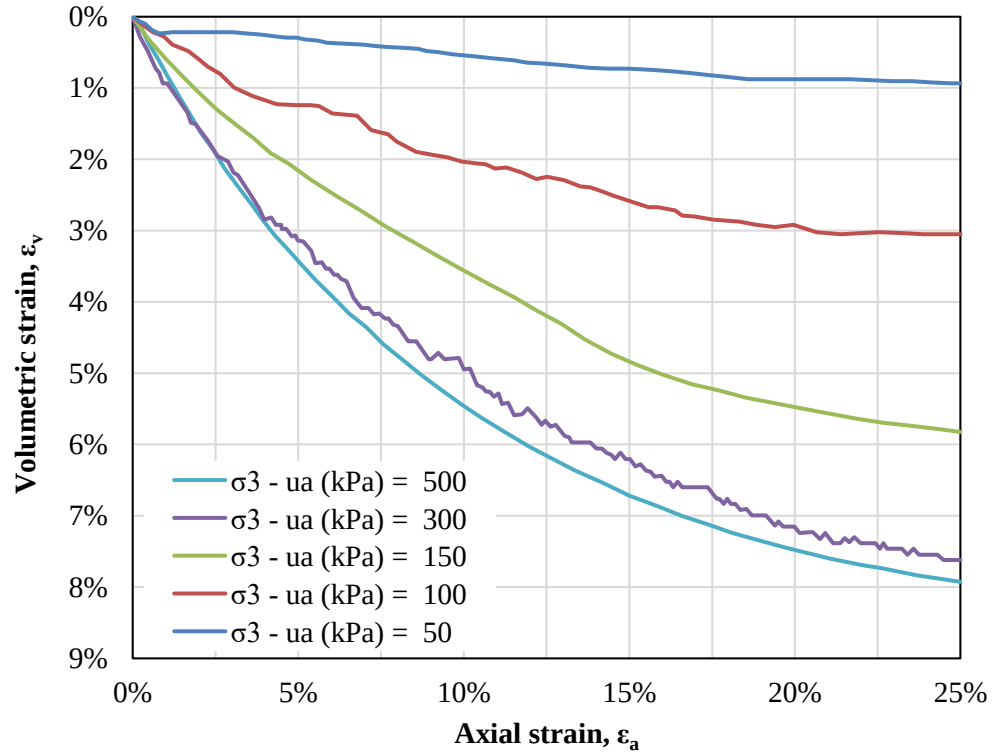

Figure C. 45. Axial strain versus volumetric strain of saturated tests of soil 3R

ii) $u_a - u_w$ = 15 kPa (initial)

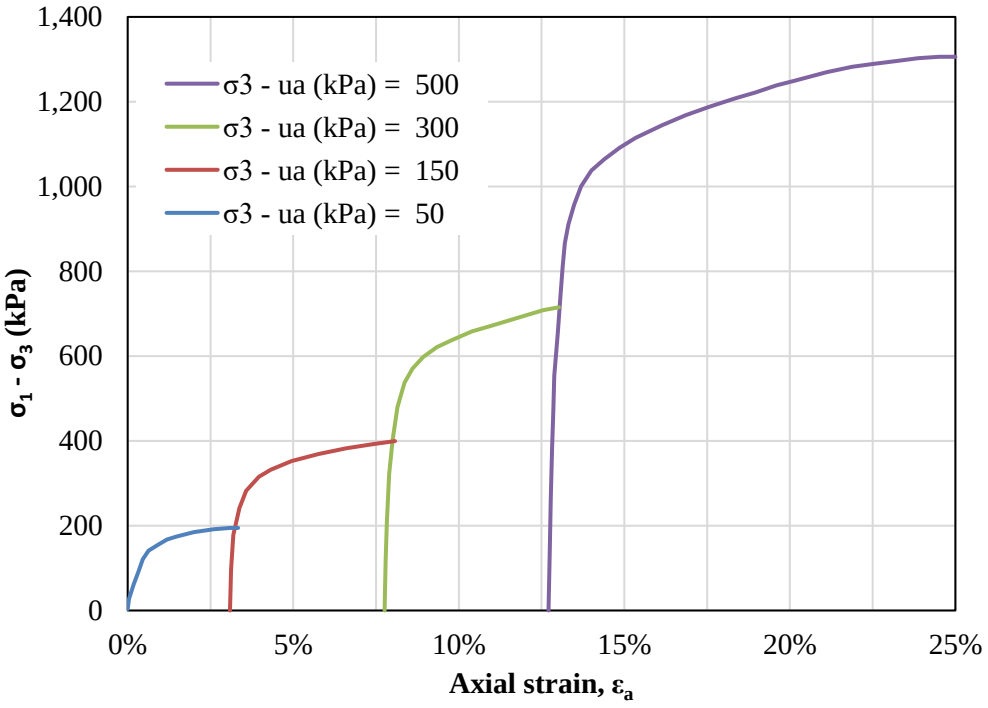

Figure C. 46. Axial strain versus deviator stress of unsaturated triaxial tests with initial matric suction of 15 kPa of soil 3R

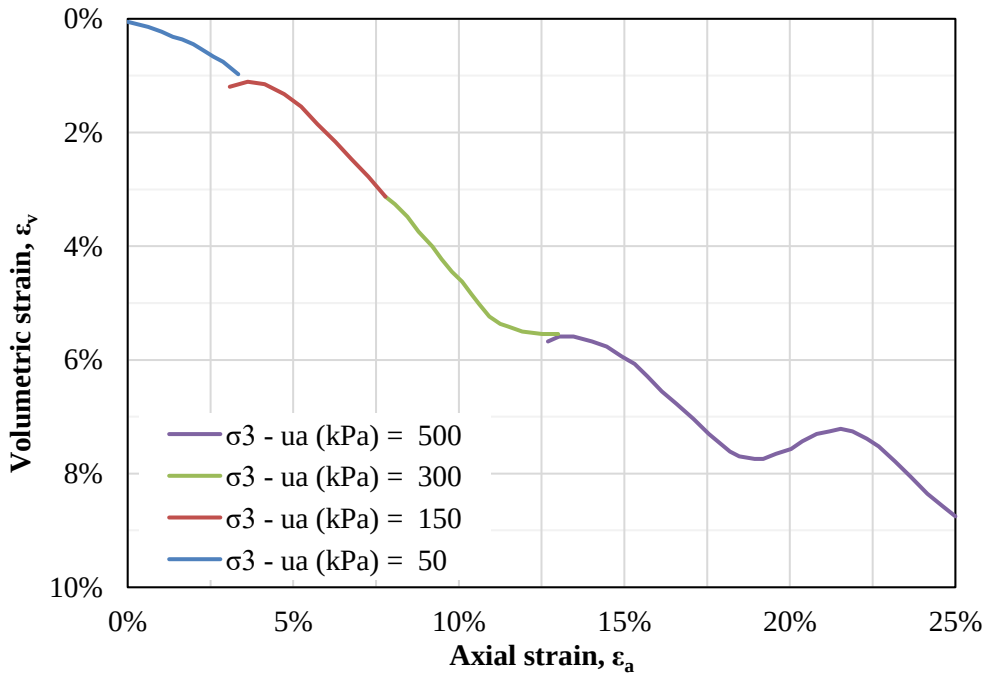

Figure C. 47. Axial strain versus volumetric strain of unsaturated triaxial tests with initial matric suction of 15 kPa of soil 3R

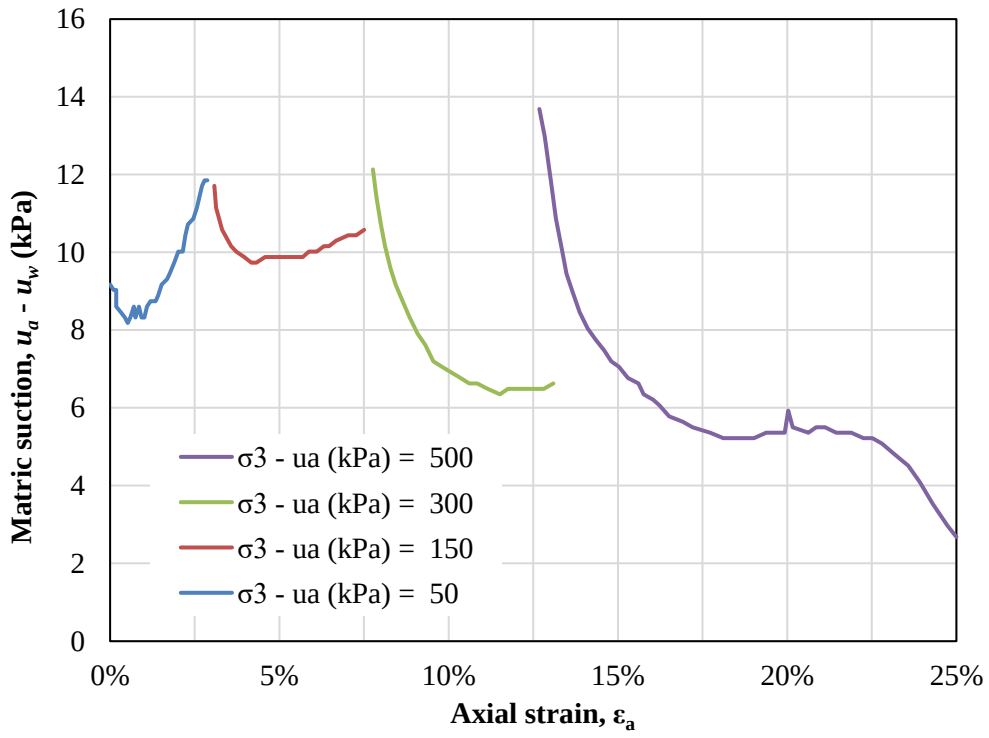

Figure C. 48. Axial strain versus matric suction of unsaturated triaxial tests with initial matric suction of 15 kPa of soil 3R

iii) $u_a - u_w$ = 40 kPa (initial)

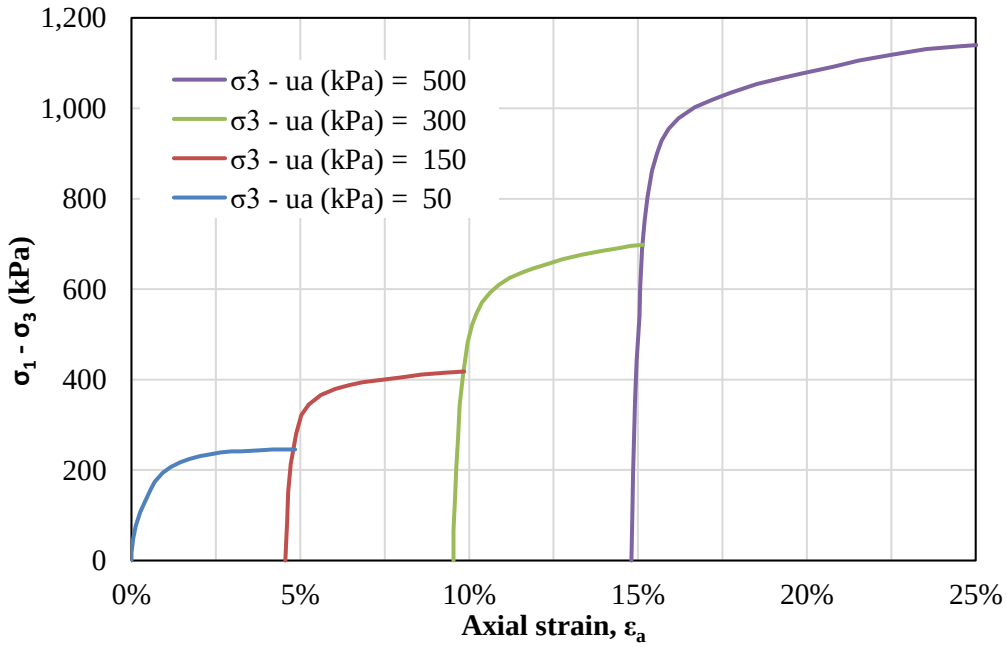

Figure C. 49. Axial strain versus deviator stress of unsaturated triaxial tests with initial matric suction of 40 kPa of soil 3R

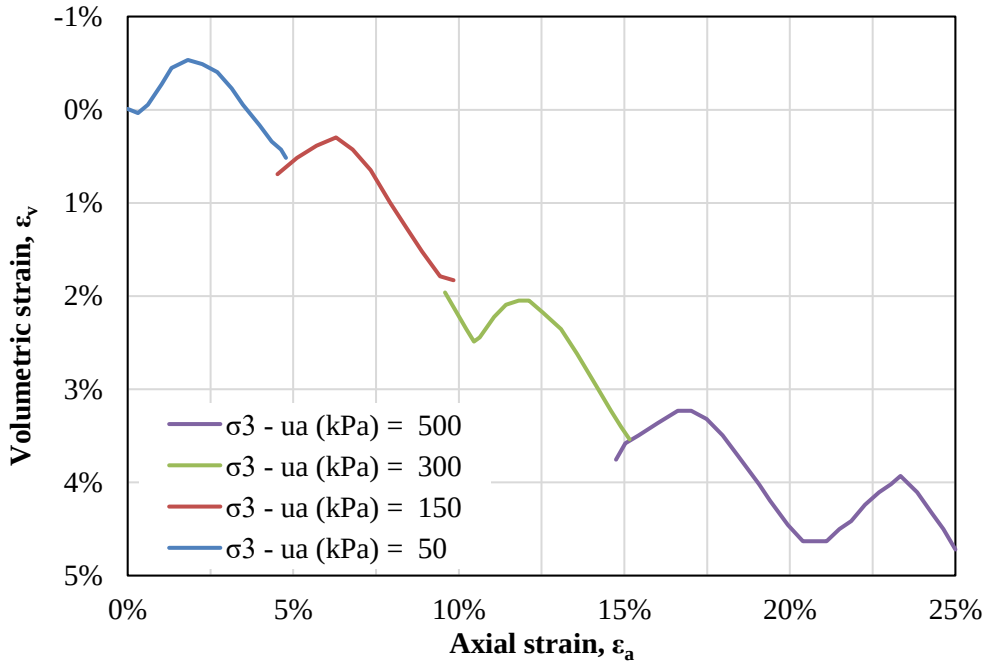

Figure C. 50. Axial strain versus volumetric strain of unsaturated triaxial tests with initial matric suction of 40 kPa of soil 3R

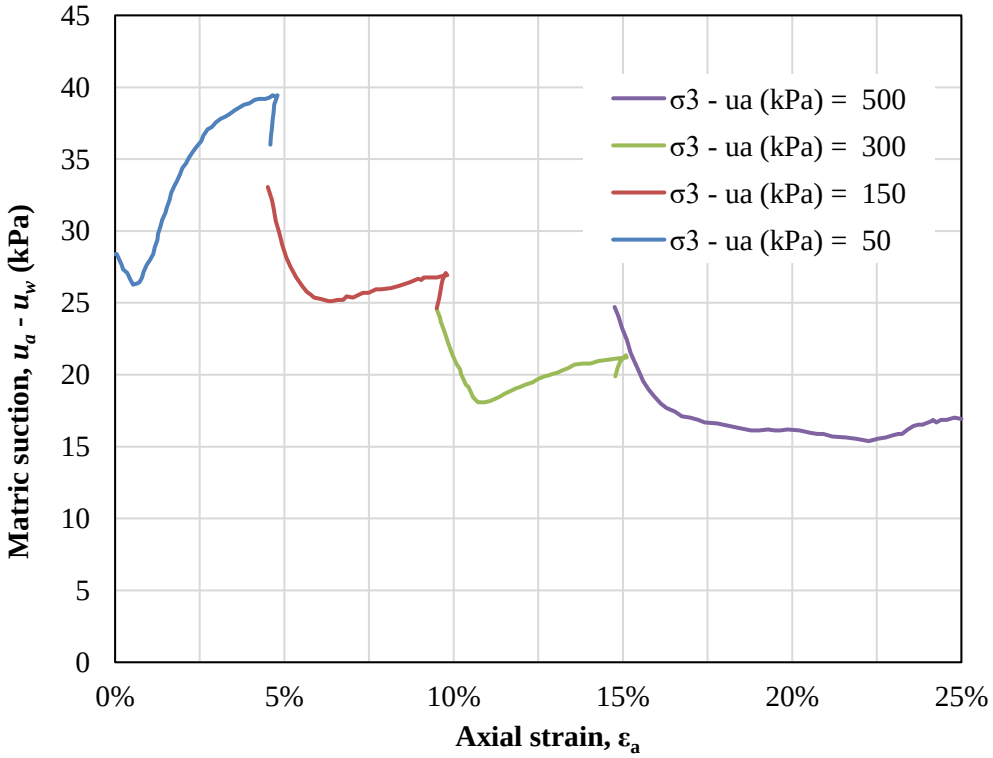

Figure C. 51. Axial strain versus matric suction of unsaturated triaxial tests with initial matric suction of 40 kPa of soil 3R

iv) $u_a - u_w$ = 100 kPa (initial)

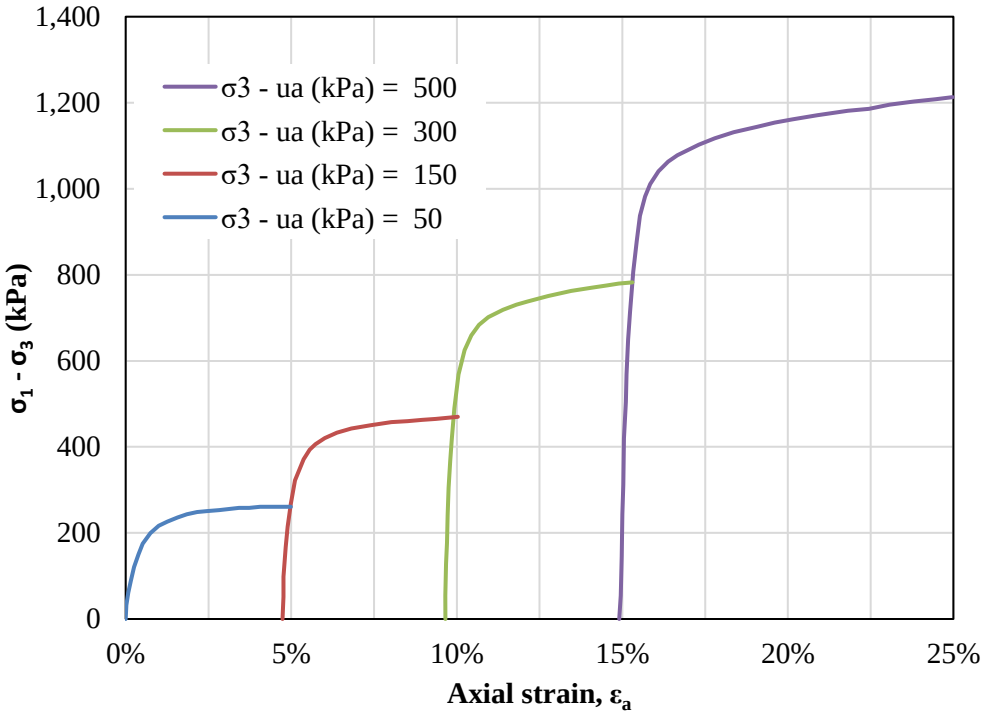

Figure C. 52. Axial strain versus deviator stress of unsaturated triaxial tests with initial matric suction of 100 kPa of soil 3R

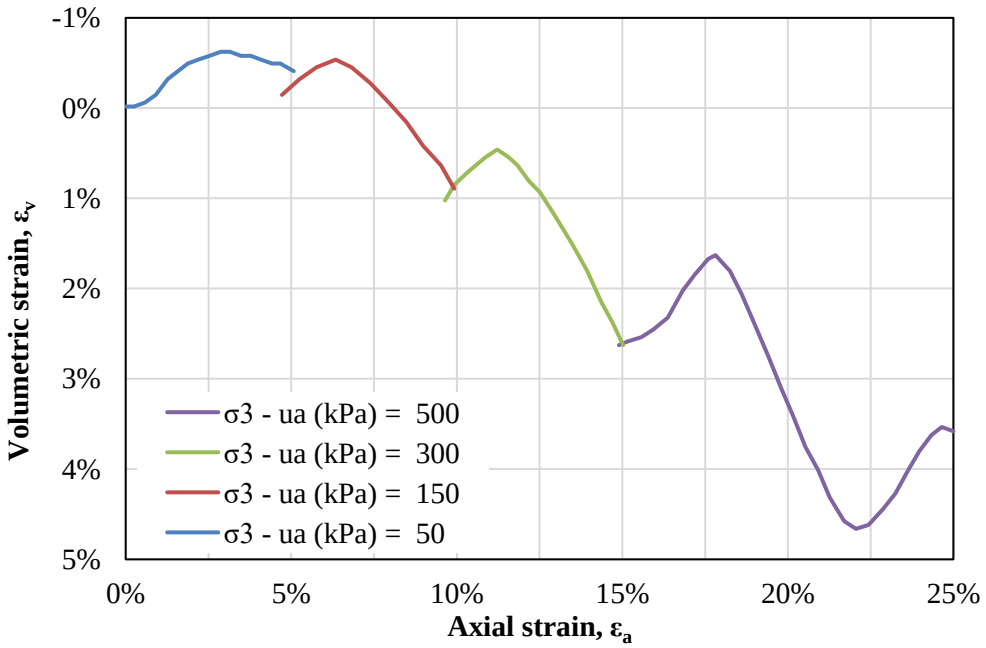

Figure C. 53. Axial strain versus volumetric strain of unsaturated triaxial tests with initial matric suction of 100 kPa of soil 3R

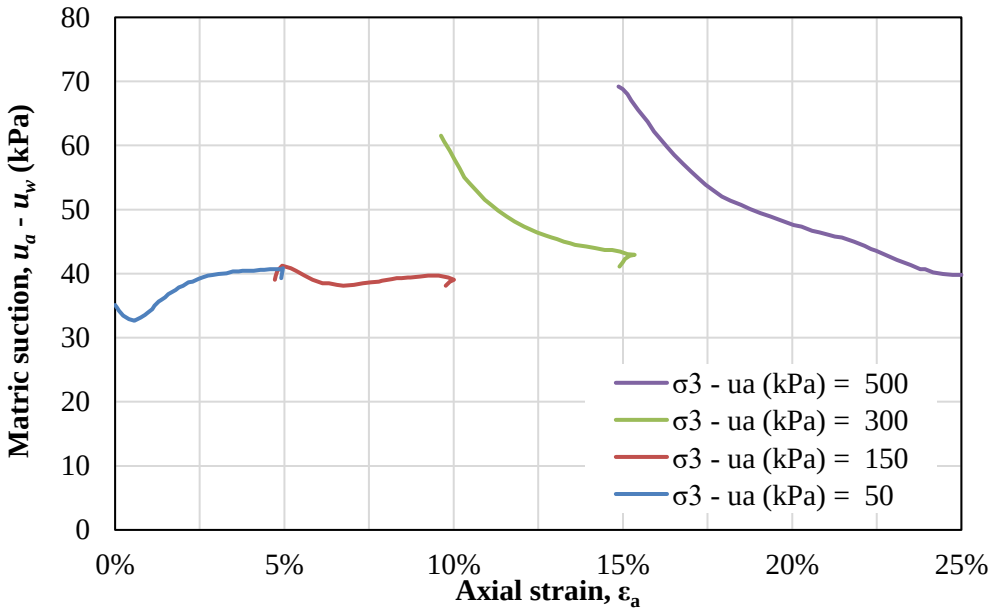

Figure C. 54. Axial strain versus matric suction of unsaturated triaxial tests with initial matric suction of 100 kPa of soil 3R

- Failure criterion: maximum shear stress

The data from the tests for maximum shear strength as failure criterion are presented in Table C.9.

Table C. 9. Shear strength data of soil 3R for maximum stress

$\sigma_1 - \sigma_3$ (kPa)	$\sigma_3 - u_a$ (kPa)	$u_a - u_w$ (kPa) Initial	$u_a - u_w$ (kPa) Final	t (kPa)	s* (kPa)
136.9	50	0	0	68.4	118.4
259.7	100		0	129.9	229.9
348.7	150		0	174.4	324.4
642.7	300		0	321.3	621.3
1225.3	500		0	612.7	1112.7
194.7	50	15	11.9	97.4	147.4
399.5	150		10.6	199.8	349.8
715.1	300		6.6	357.6	657.6
1306.0	500		2.7	653.0	1153.0
245.6	50	40	36.0	122.8	172.8
418.0	150		24.6	209.0	359.0
698.0	300		19.9	349.0	649.0
1139.7	500		16.9	569.8	1069.8
260.8	50	100	39.3	130.4	180.4
469.9	150		38.1	235.0	385.0
782.4	300		41.1	391.2	691.2
1213.0	500		39.8	606.5	1106.5

In order to obtain the shear parameters, the data were arranged accordingly to similar final matric suctions. Table C.10 depicts the data after this procedure:

Table C. 10. Shear strength data of soil 3R for maximum shear stress after data arrangement based on similar values of matric suction

$\sigma_1 - \sigma_3$ (kPa)	$\sigma_3 - u_a$ (kPa)	$r = u_a - u_w$ (kPa)	t (kPa)	s* (kPa)
136.9	50	0	68.4	118.4
259.7	100	0	129.9	229.9
348.7	150	0	174.4	324.4
642.7	300	0	321.3	621.3
1225.3	500	0	612.7	1112.7
194.7	50	11.9	97.4	147.4
399.5	150	10.6	199.8	349.8
698.0	300	19.9	349.0	649.0
1139.7	500	16.9	569.8	1069.8
245.6	50	36.0	122.8	172.8
260.8	50	39.3	130.4	180.4
469.9	150	38.1	235.0	385.0
782.4	300	41.1	391.2	691.2
1213.0	500	39.8	606.5	1106.5

The graph in terms of s^* and t (Fig. C.55) points out to a linear relationship between these variables. As a result, the angle ψ' has a unique value for each matric suction. Fig. C.55 also presents the fitting equations from which the intercepts (d) can be obtained.

For the tests that were not grouped according to similar matric suctions, the parameters d and ψ' were obtained through interpolation. The best fit results in some values of ϕ^b slightly greater than ϕ' ($\approx 0.3°$), this is not inconsistent because this behavior can be attributed to the fitting procedure. Assuming ϕ^b equal to ϕ' resulted in a RMSE of 12.5, and this error corresponds to 4.5% of the average values of t. In other words, this error is negligible in comparison to the inherent variability of the soil, sampling, testing, data digitalization and fitting. Table C.11 shows all the shear strength parameters after performing the aforementioned procedures.

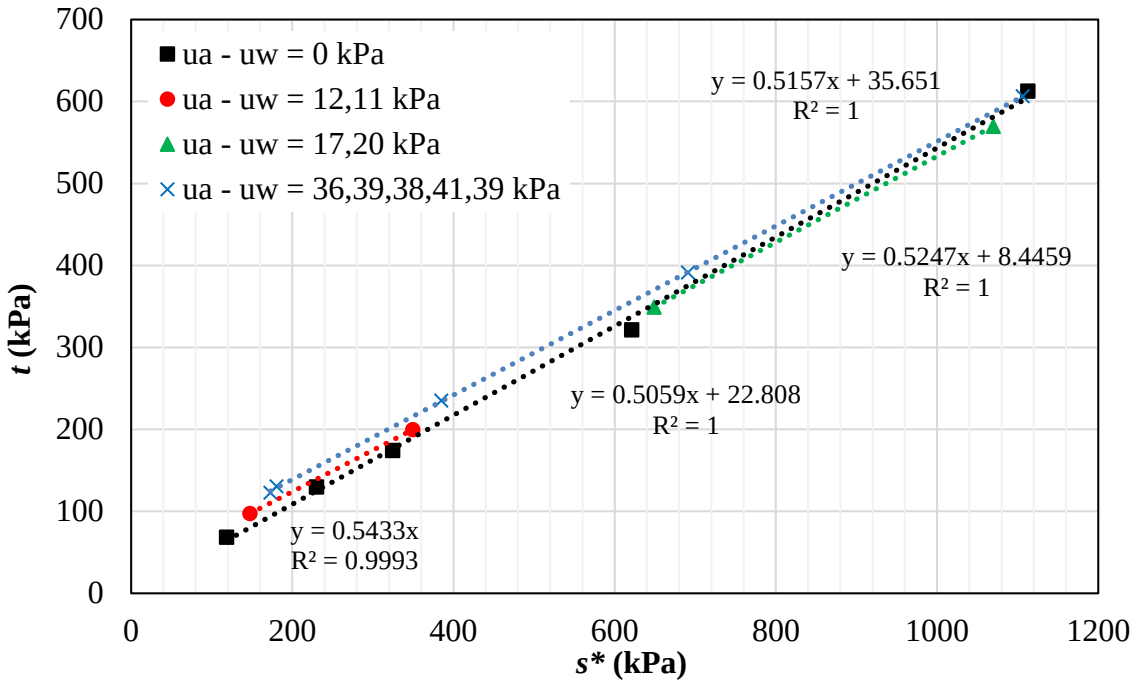

Figure C. 55. Failure envelope in terms of s* and t of soil 3R

Table C. 11. Shear strength parameters of soil 3R for maximum stress as failure criterion

$\sigma_1 - \sigma_3$ (kPa)	$\sigma_3 - u_a$ (kPa)	$u_a - u_w$ (kPa)	t (kPa)	s* (kPa)	d (kPa)	ψ'	ϕ'	c_{app} (kPa)	ψ^b	ϕ^b	t - fitted	Error²	σ_f (kPa)	τ_f (kPa)
136.9	50	0	68.4	118.4	0.0	27.6	31.5	0.0			61.9	4.3E+01	82.7	50.7
259.7	100	0	129.9	229.9	0.0	27.6	31.5	0.0			120.1	9.6E+01	162.0	99.3
348.7	150	0	174.4	324.4	0.0	27.6	31.5	0.0			169.4	2.4E+01	233.3	142.9
642.7	300	0	321.3	621.3	0.0	27.6	31.5	0.0			324.5	1.0E+01	453.5	277.9
1225.3	500	0	612.7	1112.7	0.0	27.6	31.5	0.0			581.2	9.9E+02	792.6	485.7
194.7	50	11.9	97.4	147.4	22.8	27.6	31.5	26.7	26.9	31.5	83.0	2.1E+02	96.5	66.4
399.5	150	10.6	199.8	349.8	22.8	27.6	31.5	26.7	26.9	31.5	188.1	1.4E+02	245.4	156.9
715.1	300	6.6	357.6	657.6	18.5	27.6	31.5	21.7	26.9	31.5	346.8	1.2E+02	470.7	292.5
1306.0	500	2.7	653.0	1153.0	10.0	27.6	31.5	11.7	26.9	31.5	603.6	2.4E+03	811.8	499.1
245.6	50	36.0	122.8	172.8	35.7	27.6	31.5	41.8	26.9	31.5	108.5	2.0E+02	108.6	88.7
418.0	150	24.6	209.0	359.0	31.0	27.6	31.5	36.4	26.9	31.5	200.0	8.1E+01	249.8	168.2
698.0	300	19.9	349.0	649.0	8.4	27.6	31.5	9.9	26.9	31.5	349.1	5.5E-03	466.7	298.2
1139.7	500	16.9	569.8	1069.8	8.4	27.6	31.5	9.9	26.9	31.5	567.4	5.9E+00	772.1	483.5
260.8	50	39.3	130.4	180.4	35.7	27.6	31.5	41.8	26.9	31.5	114.2	2.6E+02	112.3	92.9
469.9	150	38.1	235.0	385.0	35.7	27.6	31.5	41.8	26.9	31.5	220.4	2.1E+02	262.2	184.1
782.4	300	41.1	391.2	691.2	35.7	27.6	31.5	41.8	26.9	31.5	381.9	8.7E+01	486.8	323.5
1213.0	500	39.8	606.5	1106.5	35.7	27.6	31.5	41.8	26.9	31.5	598.2	7.0E+01	789.6	508.3

SSE	4986.39
R^2	0.997
RMSE	17.13

The values presented in Table C.11 indicate that ϕ' and ϕ^b does not change with the net confining stress or the matric suction. The values of ϕ' and ϕ^b are 31.5º. It worth mentioning that none of the tests reached matric suctions over than 50 kPa, indicating the micropores were always fully saturated. Moreover, taking into account the accumulated volumetric changes that reduced the overall void ratio of the specimens, the possible increase in the first residual suction may resulted the specimens to fail with the macropores partially saturated. Fig. C.56 presents the failure envelope in terms of net normal stress and shear strength.

The data from Table C.11 were fitted using the Modified Bi-Hyperbolic. The fitting parameters are presented in Table C.12. The goodness-of-fit obtained are R^2 = 1.000 and RMSE = 0.0, indicating that the Modified Bi-Hyperbolic model is adequate to represent quite well the shear strength envelope for this material. The extended Mohr-Coulomb failure surfaces is depicted in Fig. C.57.

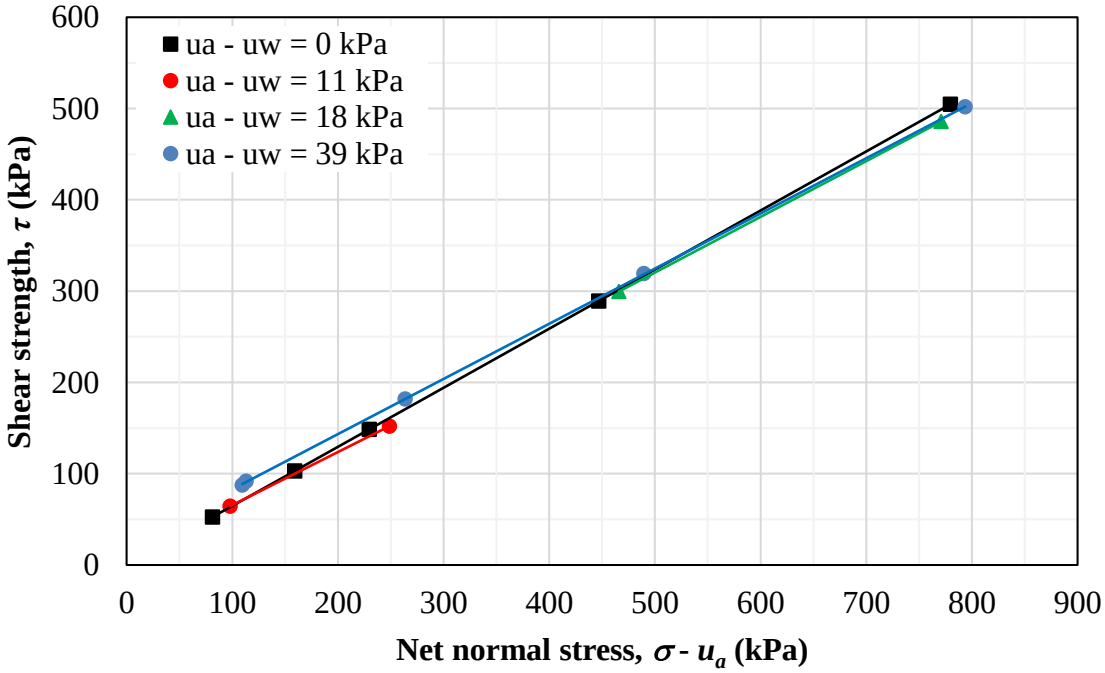

Figure C. 56. Failure envelope in terms of (σ - u_a) and τ of soil 3R

Table C. 12. Parameters obtained for the Modified Bi-Hyperbolic model

c' (kPa)	0.0	s_b	1.0
ϕ' (degrees)	31.5	n	1.1
ϕ^b (degrees)	32.5	a_1	1.632
τ_{ult1} (kPa)	3.51×10^{7}	b_1	2.85×10^{-8}
τ_{ult2} (kPa)	3.40×10^{5}	a_2	1.570
τ_{peak} (kPa)	0.0	b_2	2.94×10^{-6}
τ_{ult} (kPa)	0.0		

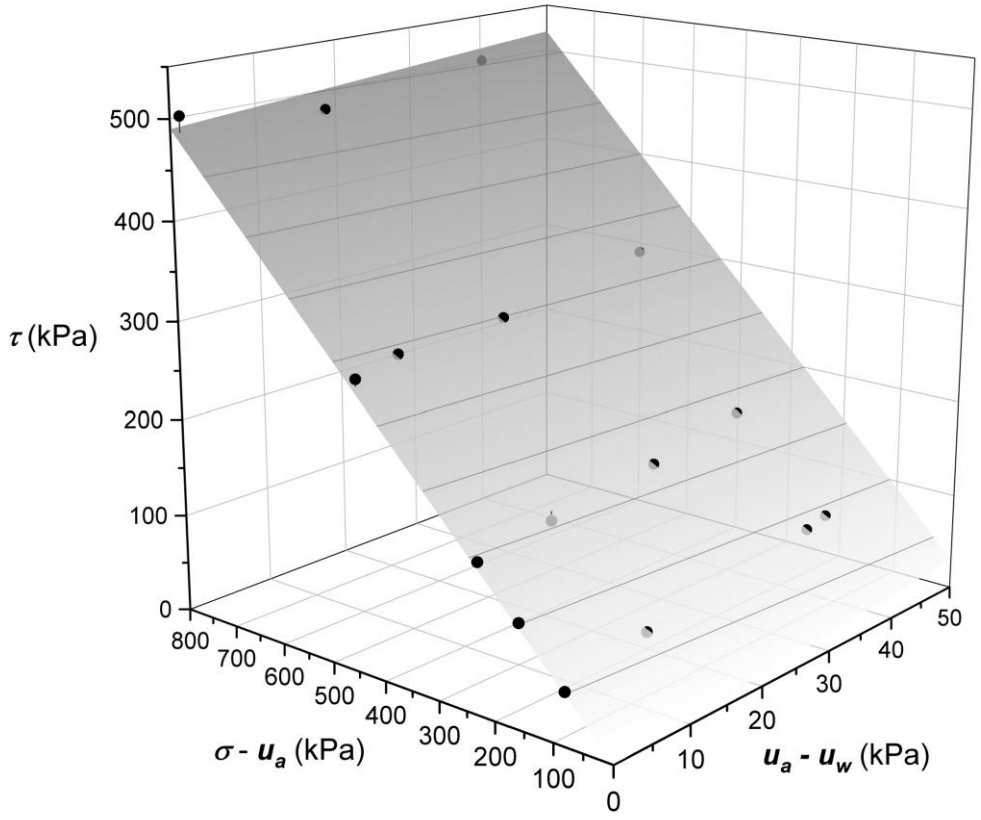

Figure C. 57. Extended Mohr-Coulomb failure surface fitted using the Modified Bi-Hyperbolic model of soil 3R

- General comments

The graphs showing the axial strain versus deviator stress indicate strain-hardening behavior (Figs. C.44, C.46, C.49 and C.52). In summary, the shear strength parameters considering maximum shear strength as failure criterion indicate:

- The angle ϕ^b and ϕ' are equivalent and constant within the stress range of the tests (Table C.9);
- As none of the tests reached matric suctions over than 50 kPa, and taking into account the accumulated volumetric changes that reduced the overall void ratio of the specimens (Figs. C.45, C.47, C.50 and C.53), it is possible that the first residual suction increased leading to the specimens to fail with the macropores partially saturated.

- Shear strength data: 4U
  - Initial void ratio (e_0) = 1.07
  - Type: modified triaxial CW multistage
  - Volume measurement: double walled cell
  - Shear velocity: 0.004 mm/min

i) $u_a - u_w$ = 0 kPa

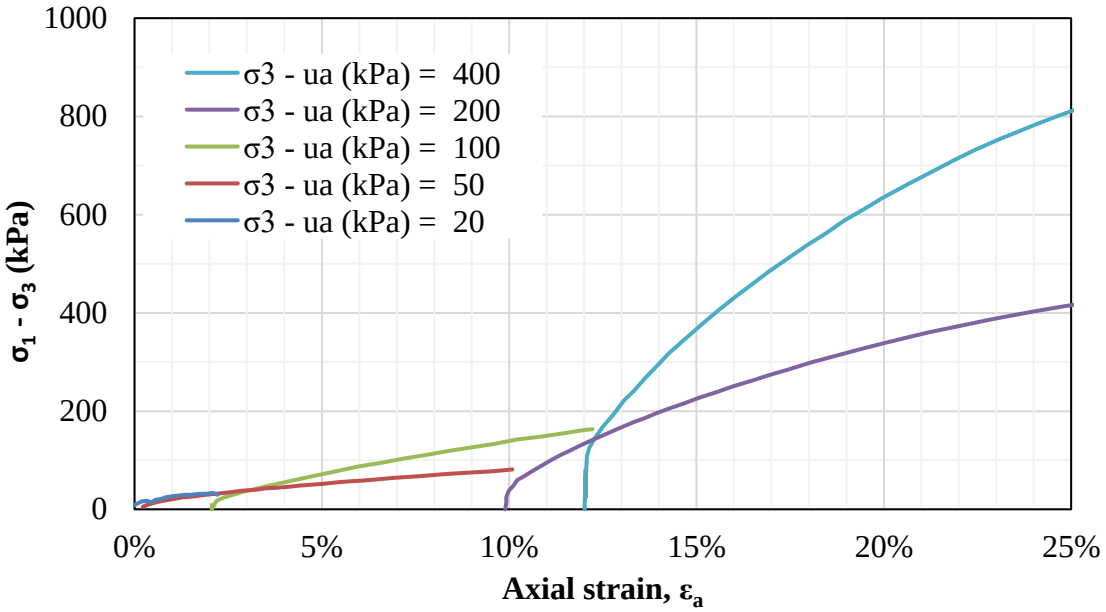

Figure C. 58. Axial strain versus deviator stress of saturated tests of soil 4U

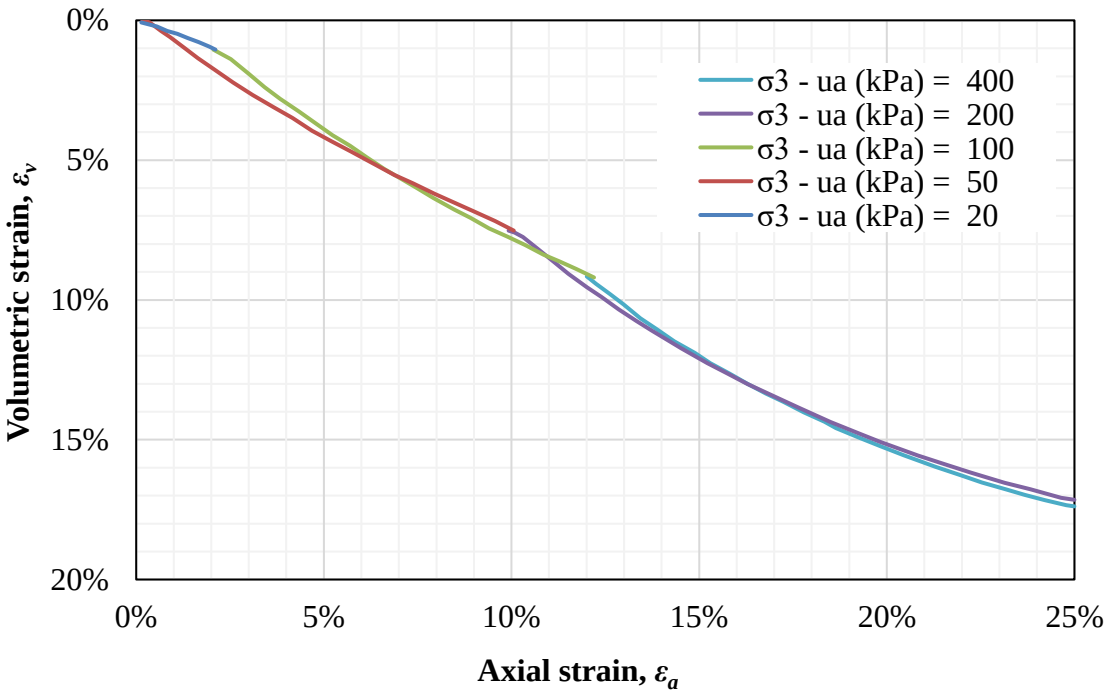

Figure C. 59. Axial strain versus volumetric strain of saturated tests of soil 4U

ii) $u_a - u_w$ = 15 kPa (initial)

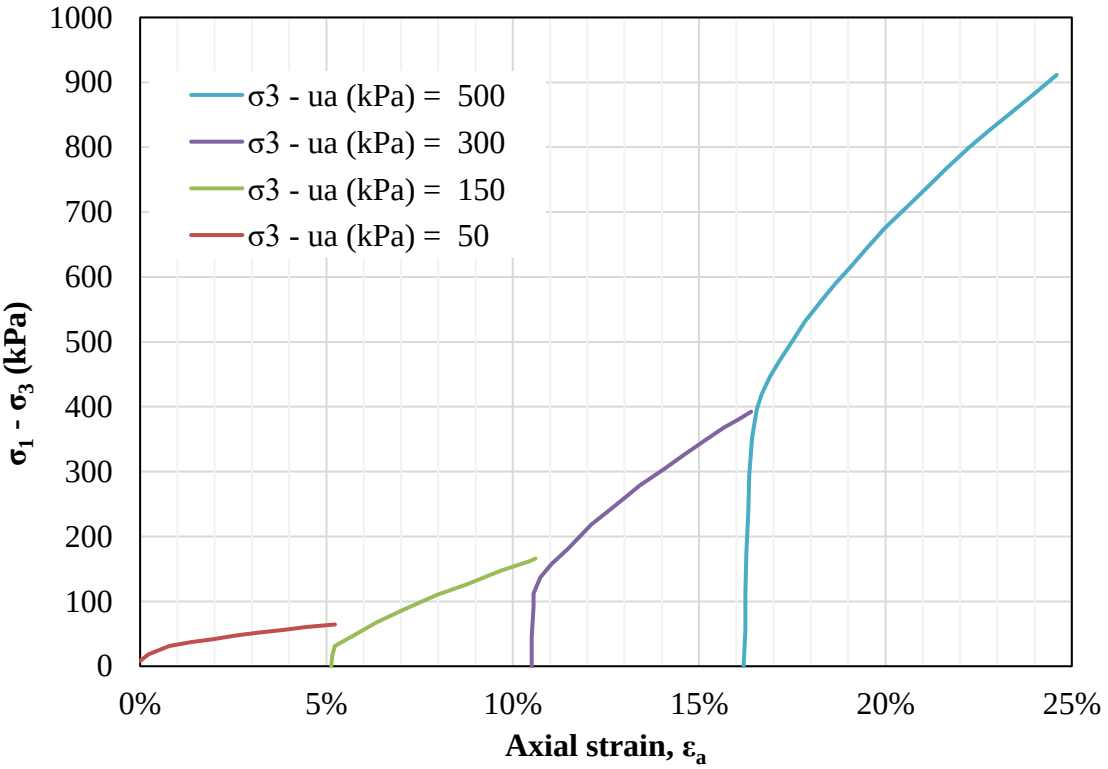

Figure C. 60. Axial strain versus deviator stress of unsaturated triaxial tests with initial matric suction of 15 kPa of soil 4U

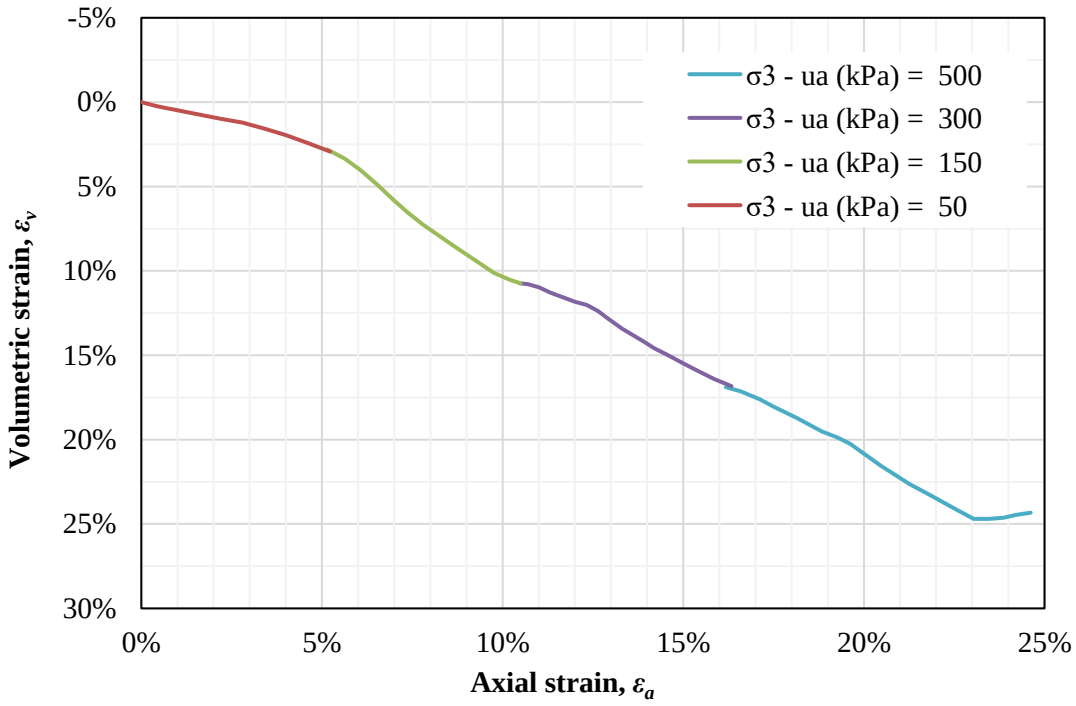

Figure C. 61. Axial strain versus volumetric strain of unsaturated triaxial tests with initial matric suction of 15 kPa of soil 4U

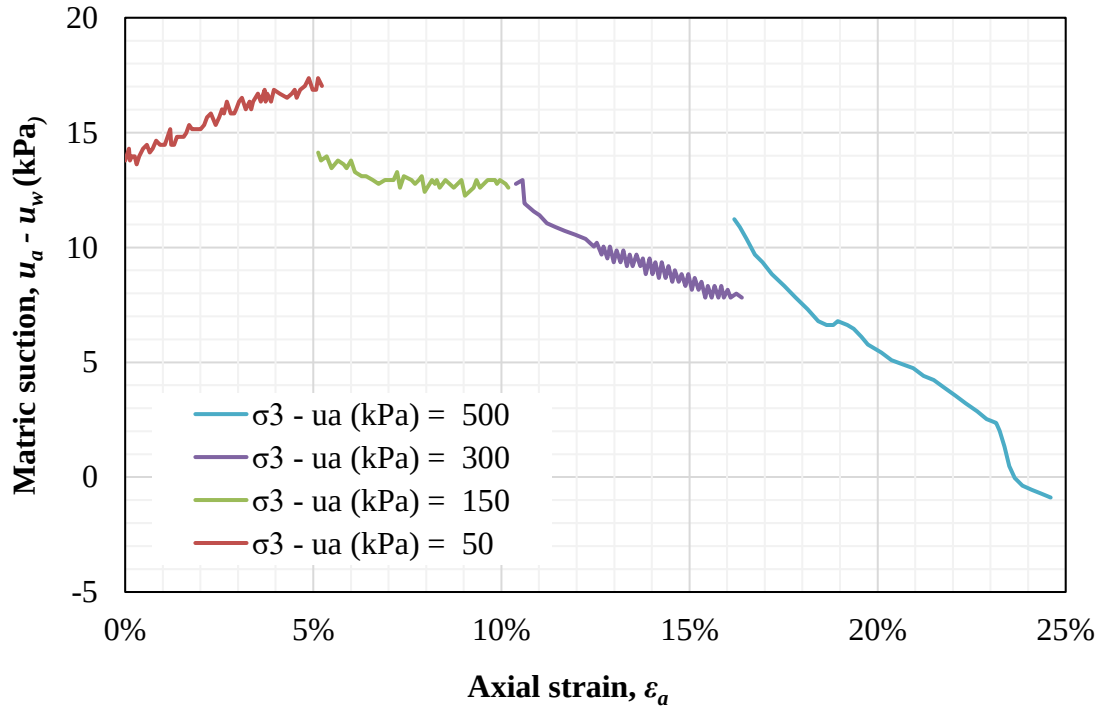

Figure C. 62. Axial strain versus matric suction of unsaturated triaxial tests with initial matric suction of 15 kPa of soil 4U

iii) $u_a - u_w$ = 40 kPa (initial)

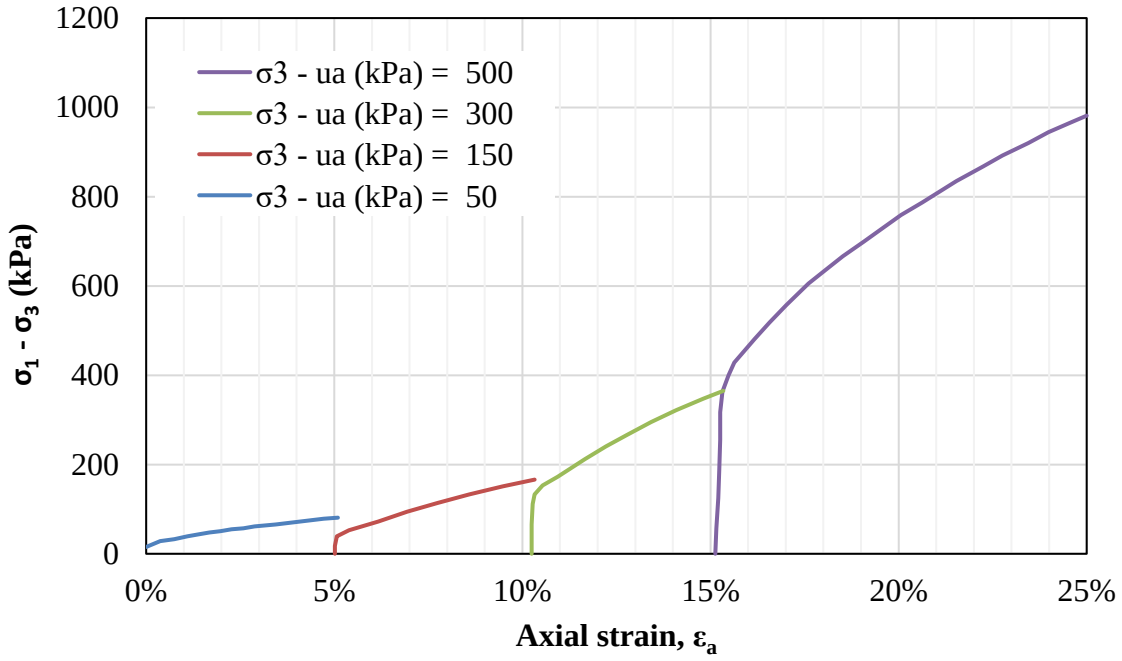

Figure C. 63. Axial strain versus deviator stress of unsaturated triaxial tests with initial matric suction of 40 kPa of soil 4U

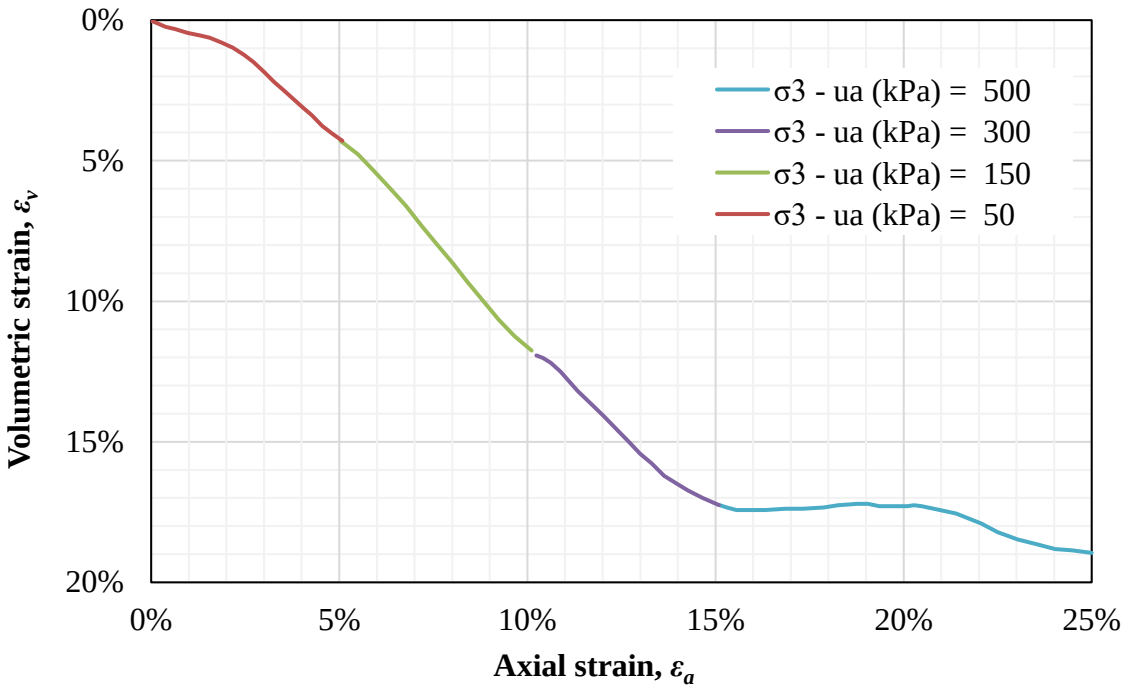

Figure C. 64. Axial strain versus volumetric strain of unsaturated triaxial tests with initial matric suction of 40 kPa of soil 4U

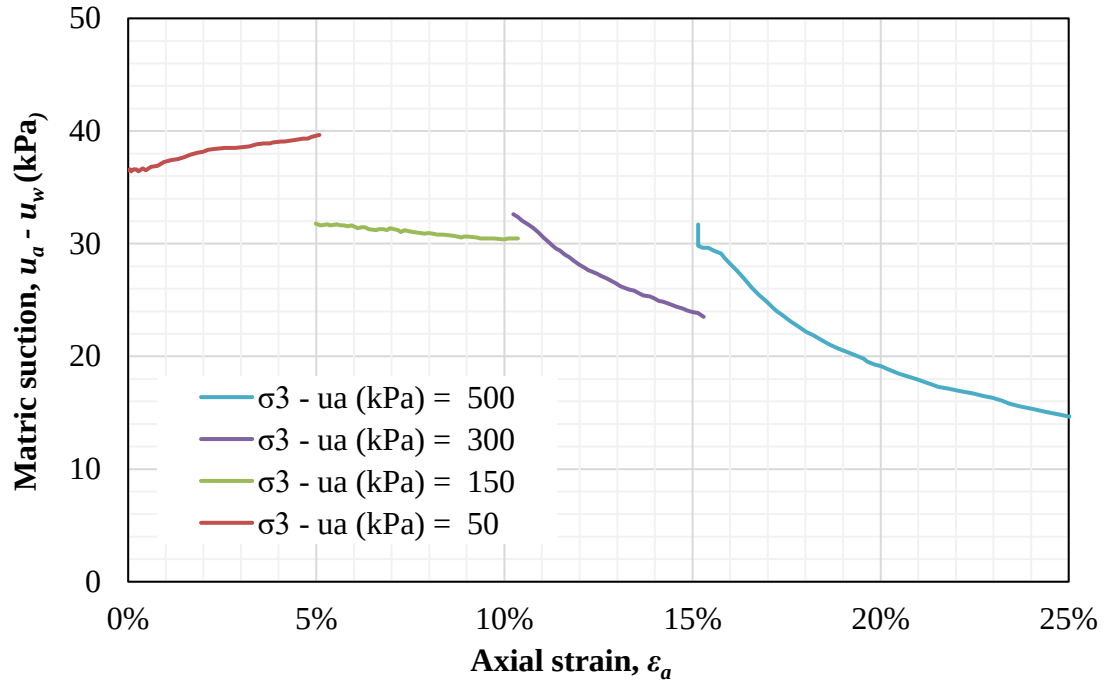

Figure C. 65. Axial strain versus matric suction of unsaturated triaxial tests with initial matric suction of 40 kPa of soil 4U

iv) $u_a - u_w$ = 80 kPa (initial)

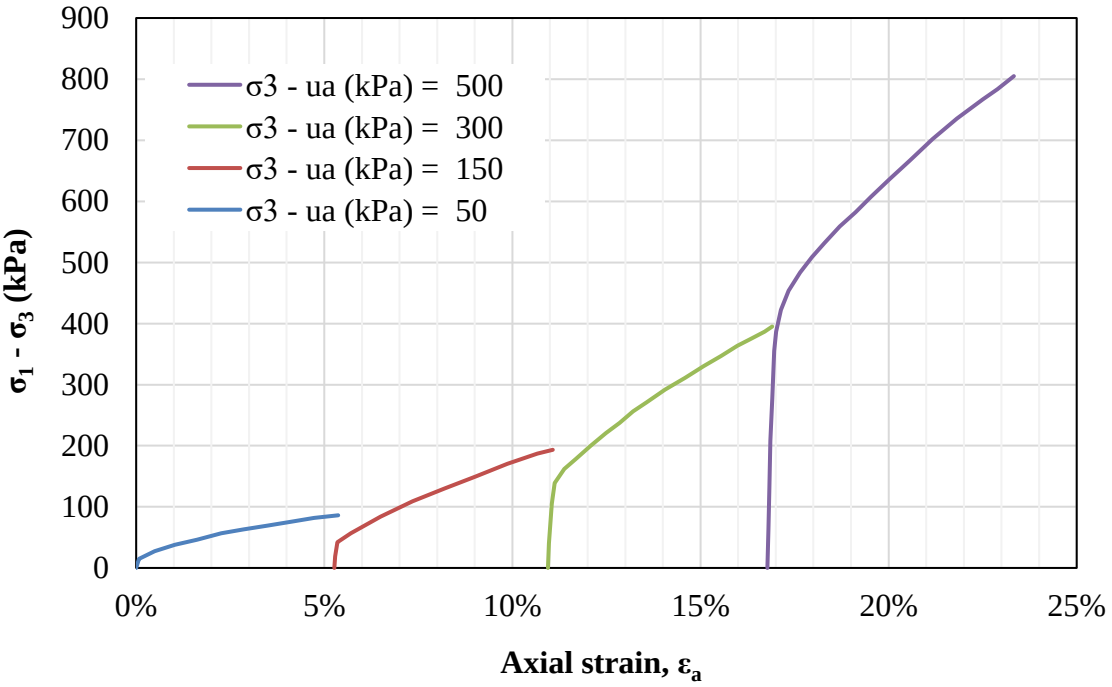

Figure C. 66. Axial strain versus deviator stress of unsaturated triaxial tests with initial matric suction of 80 kPa of soil 4U

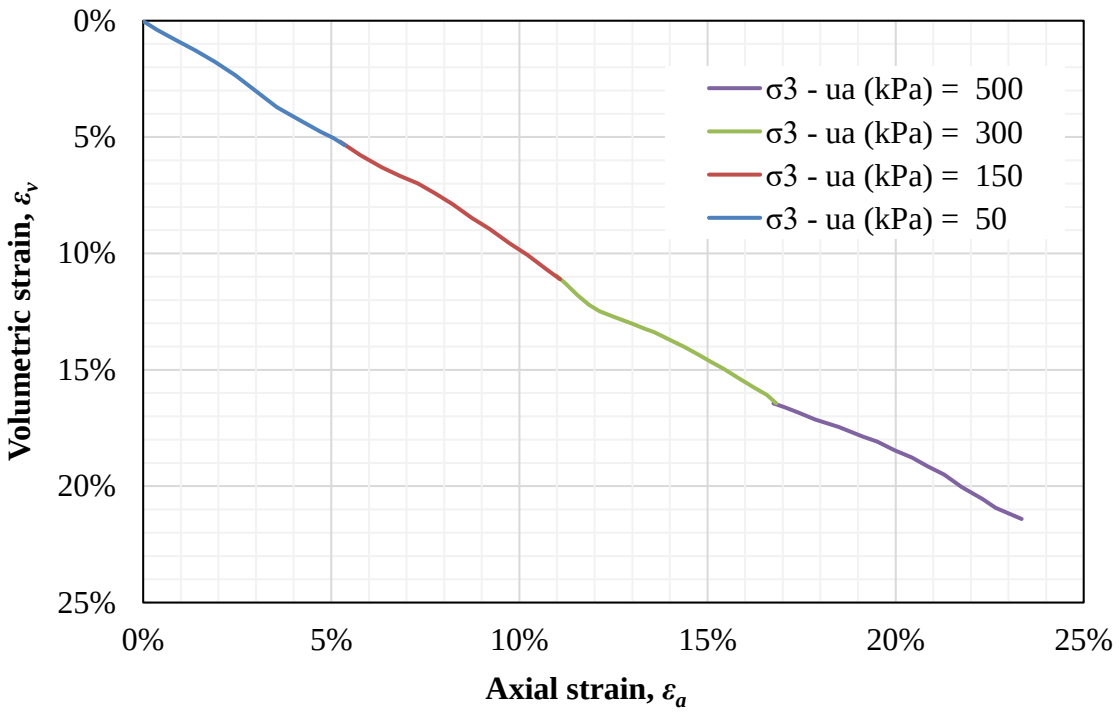

Figure C. 67. Axial strain versus volumetric strain of unsaturated triaxial tests with initial matric suction of 80 kPa of soil 4U

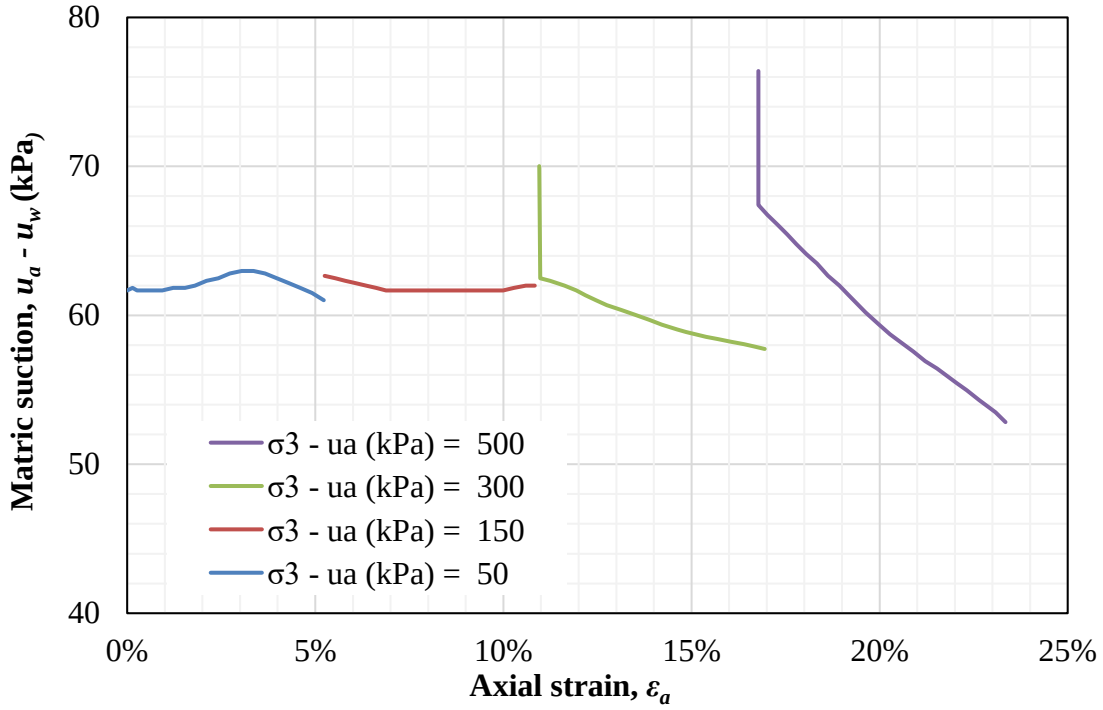

Figure C. 68. Axial strain versus matric suction of unsaturated triaxial tests with initial matric suction of 80 kPa of soil 4U

- Failure criterion: 5% normalized axial strain

The data from the shear strength tests for 5% normalized axial strain as failure criterion is presented in Table C.13. Because the tests were performed in multistage, this criterion accounted 5% of axial strain with respect to the initial axial strain.

Table C. 13. Shear strength data of soil 4U for 5% axial strain

$\sigma_1 - \sigma_3$ (kPa)	$\sigma_3 - u_a$ (kPa)	$u_a - u_w$ (kPa) Initial	$u_a - u_w$ (kPa) Final	t (kPa)	s* (kPa)
29.8	20	0	0.00	14.9	34.9
53.2	50		0.00	26.6	76.6
101.8	100		0.00	50.9	150.9
222.2	200		0.00	111.1	311.1
488.0	400		0.00	244.0	644.0
63.2	50	15	16.86	31.6	81.6
155.8	150		12.72	77.9	227.9
361.5	300		8.02	180.8	480.8
742.6	500		4.44	371.3	871.3
80.3	50	40	39.58	40.2	90.2
160.6	150		30.38	80.3	230.3
361.9	300		23.64	180.9	480.9
761.7	500		18.92	380.9	880.9
83.7	50	80	61.37	41.9	91.9
178.7	150		61.81	89.3	239.3
362.2	300		58.27	181.1	481.1
733.7	500		55.96	366.8	866.8

In order to obtain the shear parameters, the data were arranged accordingly to similar final matric suctions. Table C.14 depicts the data after this procedure:

Table C. 14. Shear strength data of soil 4U for 5% axial strain after arrangement based on similar values of matric suction

$\sigma_1 - \sigma_3$ (kPa)	$\sigma_3 - u_a$ (kPa)	$u_a - u_w$ (kPa)	t (kPa)	s* (kPa)
29.8	20.0	0.0	14.9	34.9
53.2	50.0	0.0	26.6	76.6
101.8	100.0	0.0	50.9	150.9
222.2	200.0	0.0	111.1	311.1
488.0	400.0	0.0	244.0	644.0
63.2	50.0	16.9	31.6	81.6
761.7	500.0	18.9	380.9	880.9

$\sigma_1 - \sigma_3$ (kPa)	$\sigma_3 - u_a$ (kPa)	$u_a - u_w$ (kPa)	t (kPa)	s* (kPa)
83.7	50.0	61.4	41.9	91.9
178.7	150.0	61.8	89.3	239.3
362.2	300.0	58.3	181.1	481.1
733.7	500.0	56.0	366.8	866.8

The graph in terms of *s** and *t* (Fig. C.69) points out to a linear relationship between these variables. As a result, the angle ψ' has a unique value for each matric suction. Fig. C.69 also presents the fitting equations from which the intercepts (*d*) can be obtained.

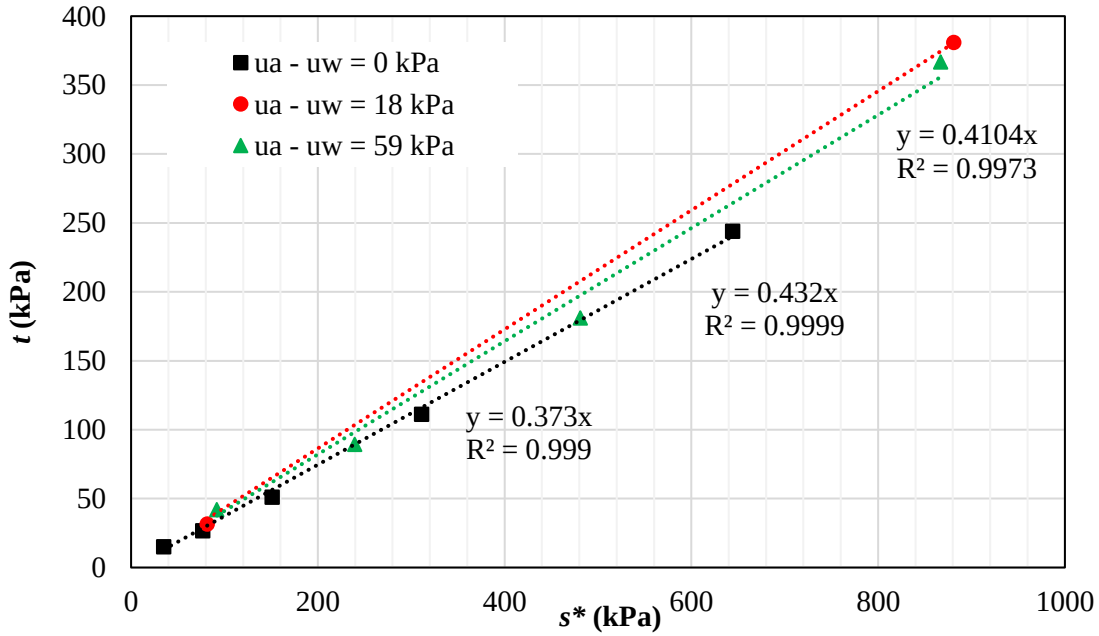

Figure C. 69. Failure envelope in terms of s* and t of soil 4U

Although the values of ϕ' varied with the matric suction, the difference between these values are small. Thus, the angle ϕ' was assumed as 23.4º as a result of the average obtained from Fig. C.69. Each ϕ^b was calculated from assuming values that best fitted the measured data presented in Table C.13. This process minimized the errors while resulting in ϕ^b that were either unrealistic high or zero, with no clear pattern. In this case, it was considered ϕ^b as the average of the back-calculated values leading to 14.3º. The mean error in relation to

the average values of *t* is 10.5%. Table C.15 shows all the shear strength parameters after performing the aforementioned procedures.

Table C. 15. Shear strength parameters of soil 4U for 5% axial strain

$\sigma_1 - \sigma_3$ (kPa)	$\sigma_3 - u_a$ (kPa)	$u_a - u_w$ (kPa)	t (kPa)	s* (kPa)	d (kPa)	ψ'	ϕ'	c_{app} (kPa)	ψ^b	ϕ^b	t - fitted	Error²	σ_f (kPa)	τ_f (kPa)
29.8	20	0.00	14.9	34.9	0.0	21.7	23.4	0.0		0.0	13.9	1.10E+00	29.0	12.5
53.2	50	0.00	26.6	76.6	0.0	21.7	23.4	0.0		0.0	30.4	1.45E+01	66.0	28.6
101.8	100	0.00	50.9	150.9	0.0	21.7	23.4	0.0		0.0	59.9	8.15E+01	130.7	56.6
222.2	200	0.00	111.1	311.1	0.0	21.7	23.4	0.0		0.0	123.6	1.55E+02	267.0	115.5
488.0	400	0.00	244.0	644.0	0.0	21.7	23.4	0.0		0.0	255.8	1.38E+02	547.1	236.8
63.2	50	16.86	31.6	81.6	0.0	21.7	23.4	0.0	14.3	0.0	36.7	2.62E+01	69.0	29.9
155.8	150	12.72	77.9	227.9	0.0	21.7	23.4	0.0	14.3	15.6	93.8	2.51E+02	197.0	88.8
361.5	300	8.02	180.8	480.8	0.0	21.7	23.4	0.0	14.3	15.6	193.0	1.49E+02	409.0	179.2
742.6	500	4.44	371.3	871.3	0.0	21.7	23.4	0.0	14.3	15.6	347.2	5.82E+02	723.8	314.5
80.3	50	39.58	40.2	90.2	0.0	21.7	23.4	0.0	14.3	15.6	45.9	3.29E+01	74.2	43.2
160.6	150	30.38	80.3	230.3	0.0	21.7	23.4	0.0	14.3	15.6	99.2	3.58E+02	198.4	94.3
361.9	300	23.64	180.9	480.9	0.0	21.7	23.4	0.0	14.3	15.6	197.0	2.59E+02	409.1	183.6
761.7	500	18.92	380.9	880.9	0.0	21.7	23.4	0.0	14.3	1.1	354.7	6.87E+02	729.6	316.1
83.7	50	61.37	41.9	91.9	0.0	21.7	23.4	0.0	14.3	4.3	52.1	1.05E+02	75.2	37.1
178.7	150	61.81	89.3	239.3	0.0	21.7	23.4	0.0	14.3	0.0	110.8	4.61E+02	203.9	88.2
362.2	300	58.27	181.1	481.1	0.0	21.7	23.4	0.0	14.3	0.0	205.9	6.16E+02	409.2	177.1
733.7	500	55.96	366.8	866.8	0.0	21.7	23.4	0.0	14.3	12.3	358.5	6.90E+01	721.1	324.3
											SSE	3986.30		
											R^2	0.991		
											RMSE	15.31		

It worth mentioning that the tests reached the maximum matric suctions of 62 kPa, indicating the micropores were always fully saturated. Also, the data indicates that the matric suction has little influence on the shear strength within its range. Moreover, taking into account the accumulated volumetric changes that reduced the overall void ratio of the specimens, the possible increase in the first residual suction may resulted the specimens to fail with the macropores partially saturated. Fig. C.70 presents the failure envelope in terms of net normal stress and shear strength.

The data from Table C.15 were fitted using the Modified Bi-Hyperbolic. The fitting parameters are presented in Table C.16. The goodness-of-fit obtained (R^2 = 1.000 and RMSE = 1.7) indicate a great data adherence. The extended Mohr-Coulomb failure surfaces is depicted in Fig. 16.

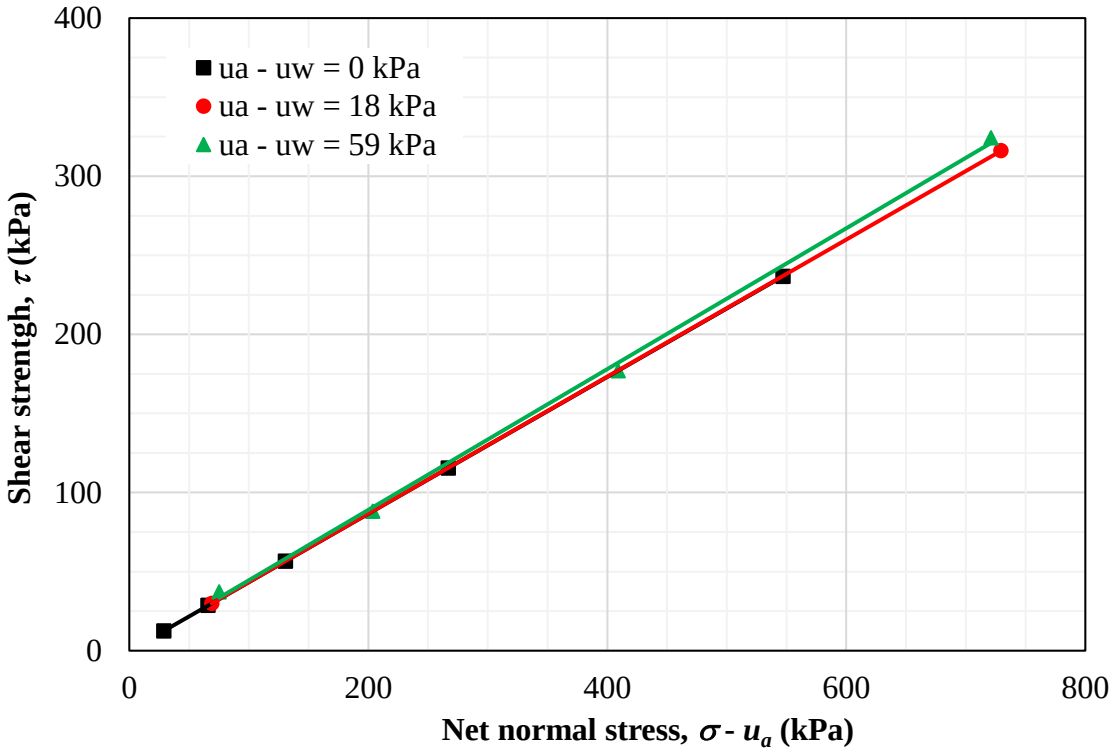

Figure C. 70. Failure envelope in terms of (σ - u_a) and τ of soil 4U

Table C. 16. Parameters obtained for the Modified Bi-Hyperbolic model of soil 4U

c' (kPa)	0.0	s_b	56.8
ϕ' (degrees)	23.3	n	130.7
ϕ^b (degrees)	14.6	a_1	2.321
τ_{ult1} (kPa)	4.35×10^{7}	b_1	2.30×10^{-8}
τ_{ult2} (kPa)	2.93×10^{5}	a_2	3.838
τ_{peak} (kPa)	0.0	b_2	3.42×10^{-6}
τ_{ult} (kPa)	0.0		

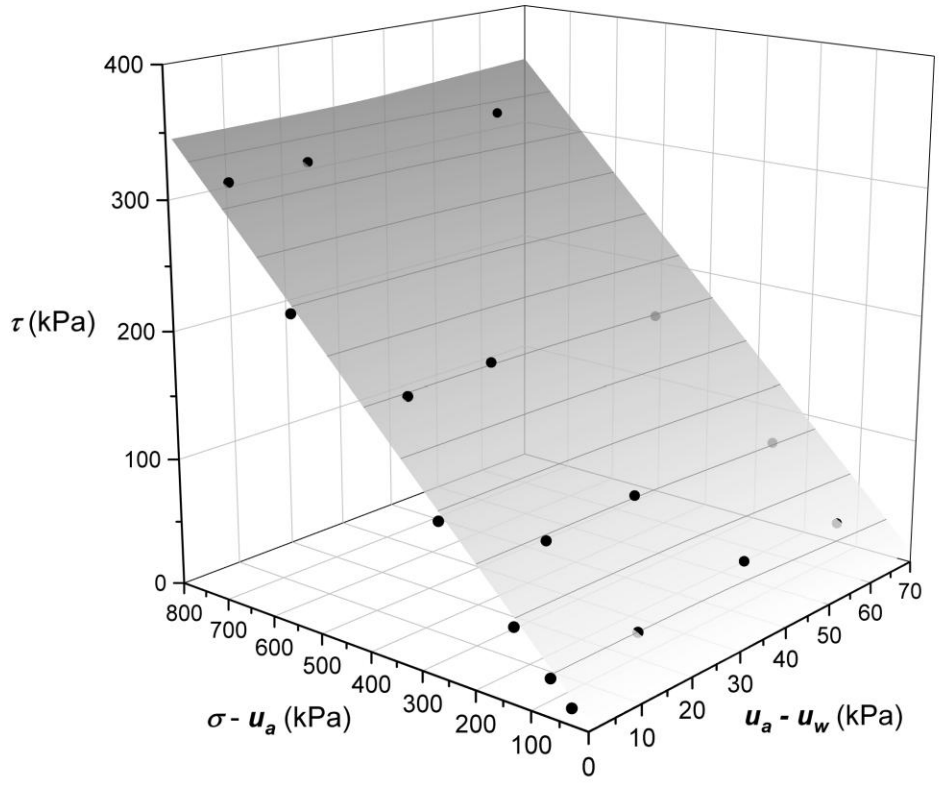

Figure C. 71. Extended Mohr-Coulomb failure surface fitted using the Modified Bi-Hyperbolic model of soil 4U

- General comments

As the tests were performed in multistage and the axial strain versus deviator stress curves did not show a well-defined peak (strain-hardening), the failure criterion that seems to be more suitable is constant strain at 5% of relative axial strain (Figs. C.58, C.60, C.63 and C.66). In summary, the shear strength parameters considering this failure criterion indicate:

- The angle ϕ^b is lower than ϕ', however, the maximum ϕ^b obtained is equivalent to 0.61ϕ' for matric suction of 56 kPa, which is superior than the first residual suction (8 kPa), as shown in Table C.13 and Fig. C.43;
- The angle ϕ' is constant and equal to 23.4°.

C.4 Feuerharmel (2007) – 4R and 5U

- Soil basic information and characteristics
  - Void ratio (e_0) = 1.65 (remolded); 1.67 (undisturbed)
  - Density of solids (ρ_s) = 2.86
  - Dry density (ρ_d) = 1.08 (remolded); 1.07 (undisturbed)
  - Liquid limit (w_L) = 74%
  - Plasticity limit (w_P) = 57%
  - USCS = MH (disaggregated) / MH (aggregated)

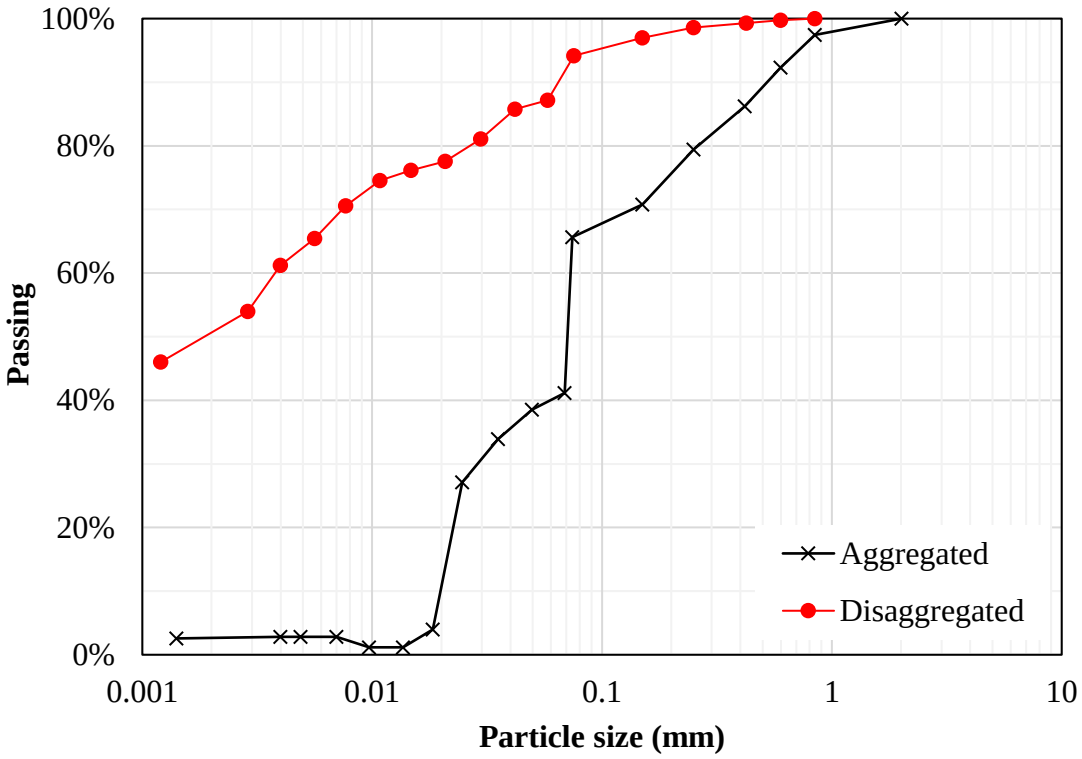

Figure C. 72. Grain-size distribution curve of soil 4R

- Soil-water characteristic curve

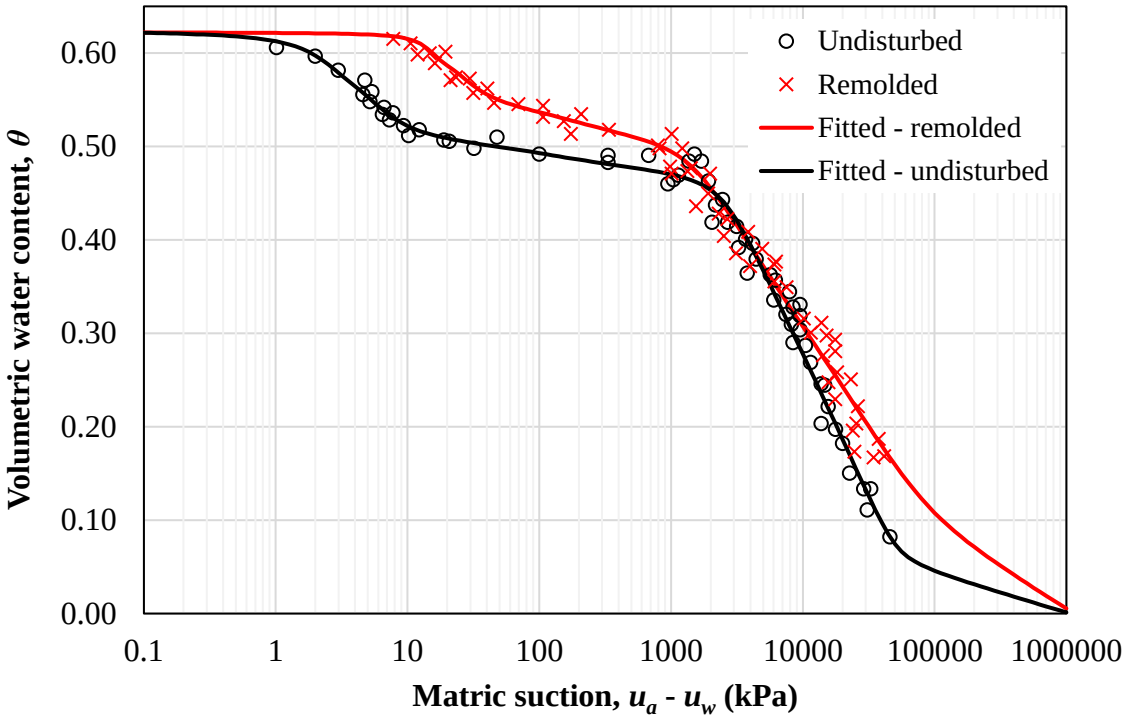

Figure C. 73. Soil-water characteristic curve of soils 4R and 5U

- Shear strength data: 4R
  - Initial void ratio (e_0) = 1.65
  - Type: modified direct shear
  - Shear velocity: 2.03×10^{-4} mm/s

i) $u_a - u_w$ = 0 kPa

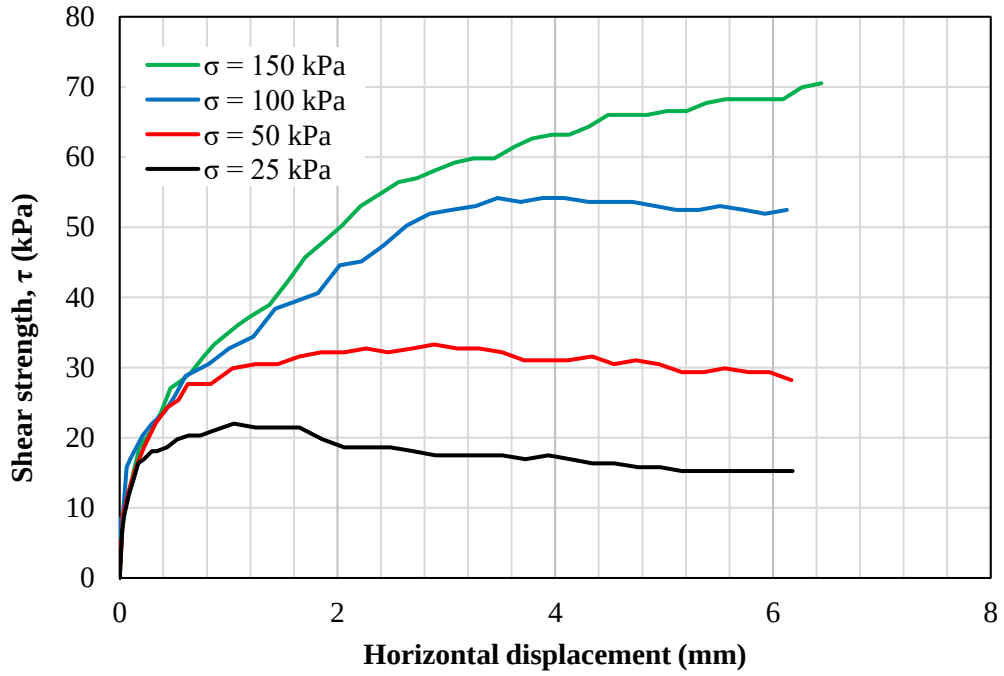

Figure C. 74. Horizontal displacement versus shear strength of saturated tests of soil 4R

ii) $u_a - u_w$ = 50 kPa

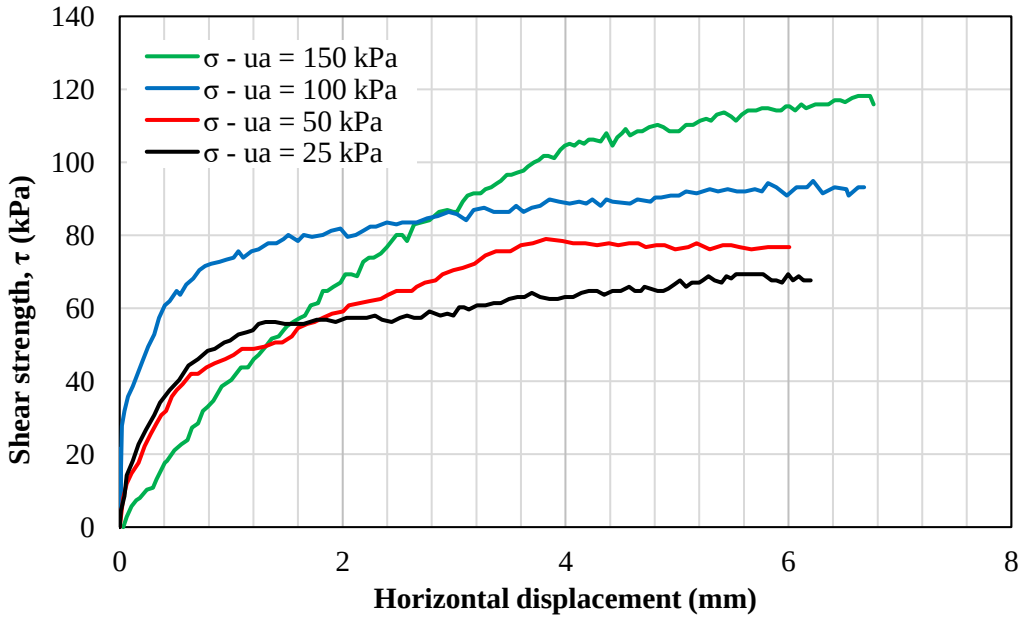

Figure C. 75. Horizontal displacement versus shear strength of tests with (u_a - u_w) = 50 kPa of soil 4R

iii) $u_a - u_w$ = 100 kPa

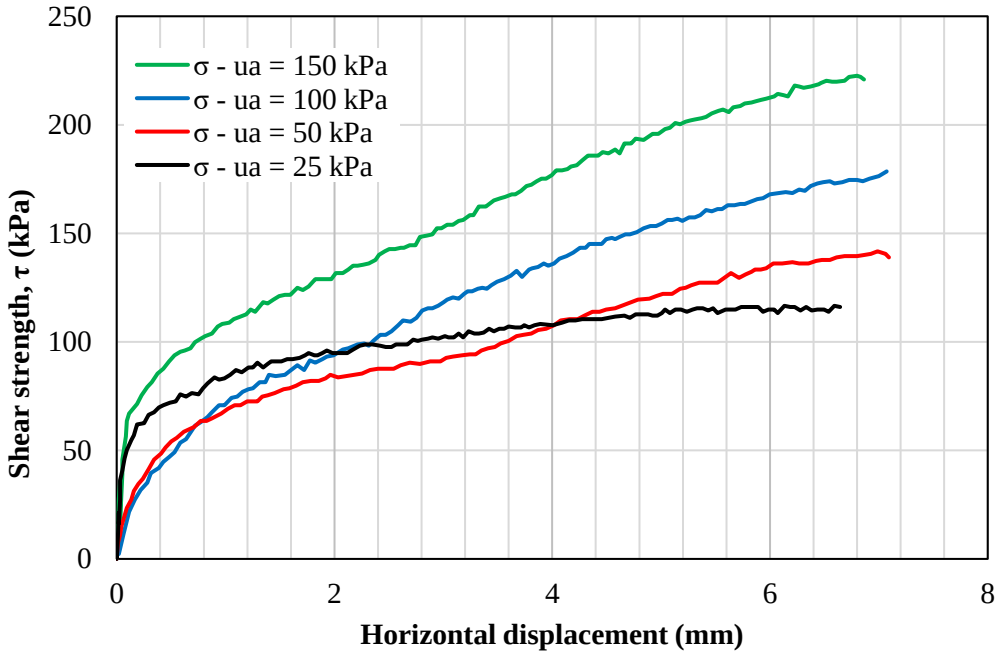

Figure C. 76. Horizontal displacement versus shear strength of tests with (u_a - u_w) = 100 kPa of soil 4R

iv) $u_a - u_w$ = 150 kPa

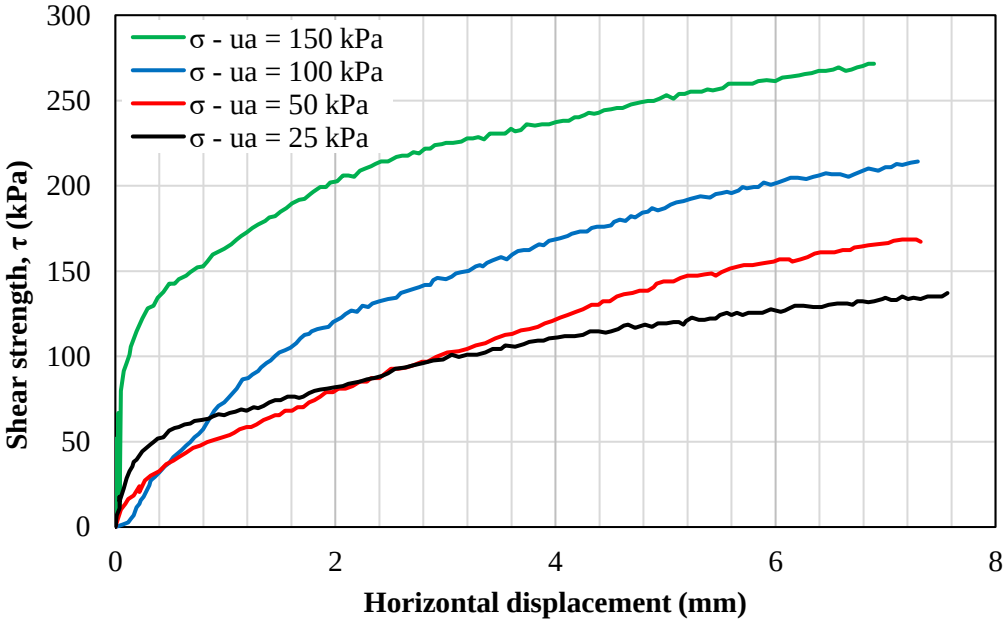

Figure C. 77. Horizontal displacement versus shear strength of tests with (u_a - u_w) = 150 kPa of soil 4R

v) $u_a - u_w$ = 6100 kPa

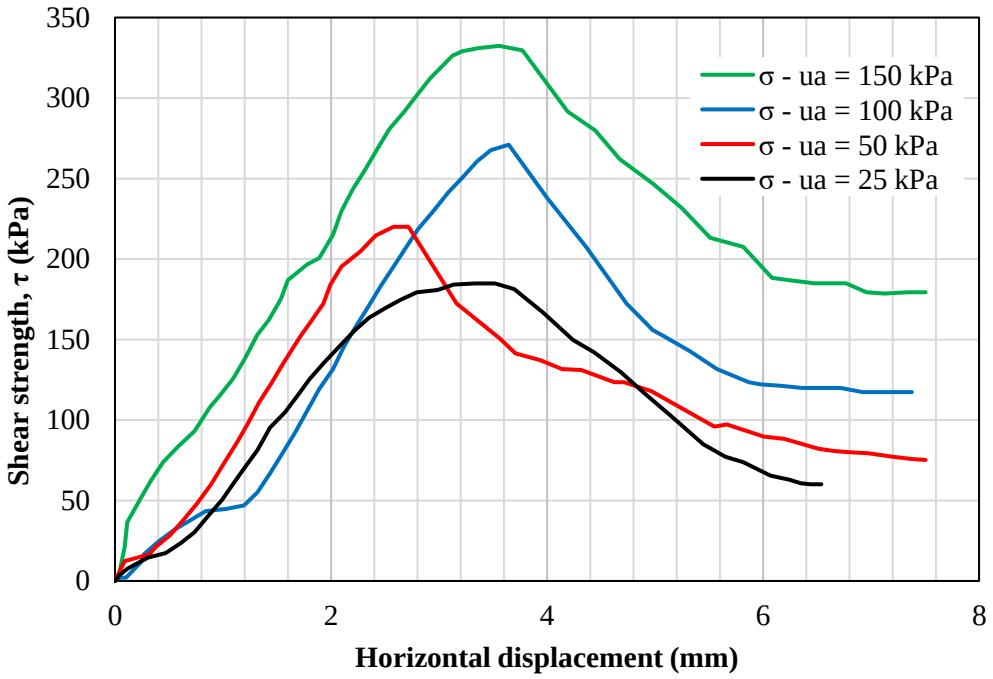

Figure C. 78. Horizontal displacement versus shear strength of tests with (u_a - u_w) = 6100 kPa of soil 4R

- Failure criterion: maximum or peak shear stress

The data from the tests for maximum or peak shear stress as failure criterion is presented in Table C.17. The graph of the shear strength as function of the net vertical stress (Fig. C.79) indicates that ϕ' has a unique value for each matric suction. Also, the increment in matric suction results in an increase in ϕ'. The angle ϕ^b was calculated assuming the saturated condition (i.e., secant) and the previous matric suction (i.e. tangent) as reference. For matric suctions of 100 and 150 kPa, ϕ^b tangent increases with the net vertical stress whereas it remains practically constant for matric suctions of 50 and 6100 kPa. Moreover, the relation ϕ^b/ϕ' is greater than 1 when the matric suction is equal or less than 100 kPa.

Table C. 17. Shear strength parameters of soil 4R at maximum or peak shear stress

τ (kPa)	σ - u_a (kPa)	u_a - u_w (kPa)	c_{app} (kPa)	ϕ'	ϕ^b (tan)	ϕ^b (sec)	ϕ^b(tan)/ϕ'
22.0	25	0	13.4	21.3			
33.3	50						
54.2	100						
70.5	150						
69.3	25	50	59.2	21.0	43.4	43.4	2.1
79.0	50				42.4	42.4	2.0
94.9	100				39.2	39.2	1.9
118.2	150				43.6	43.6	2.1
116.6	25	100	97.3	39.7	43.4	43.4	1.1
141.7	50				51.4	47.3	1.3
178.5	100				59.1	51.2	1.5
222.6	150				64.4	56.7	1.6
137.1	25	150	112.3	46.5	22.3	37.5	0.5
168.5	50				28.2	42.0	0.6
214.2	100				35.5	46.9	0.8
271.5	150				44.4	53.3	1.0
184.8	25	6100	158.1	49.2	0.5	1.5	0.0
220.0	50				0.5	1.8	0.0
271.0	100				0.5	2.0	0.0
332.4	150				0.6	2.5	0.0

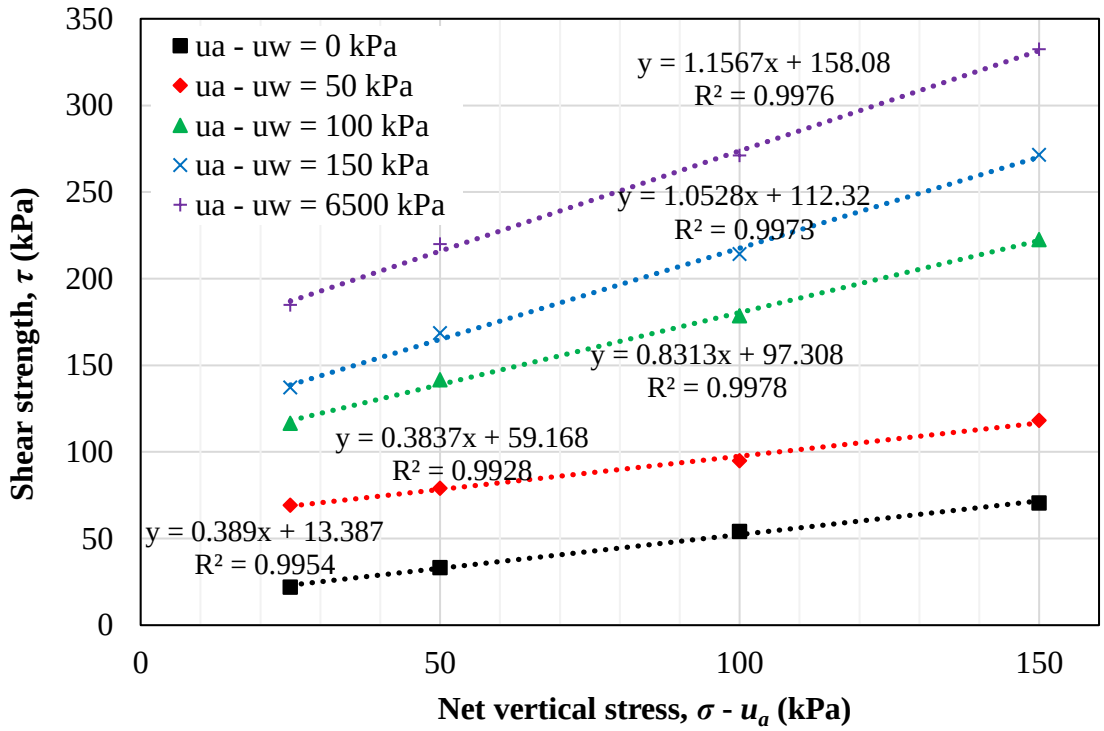

Figure C. 79. Failure envelope in terms of net vertical stress (σ_v - u_a) and τ of soil 4R at maximum or peak shear stress

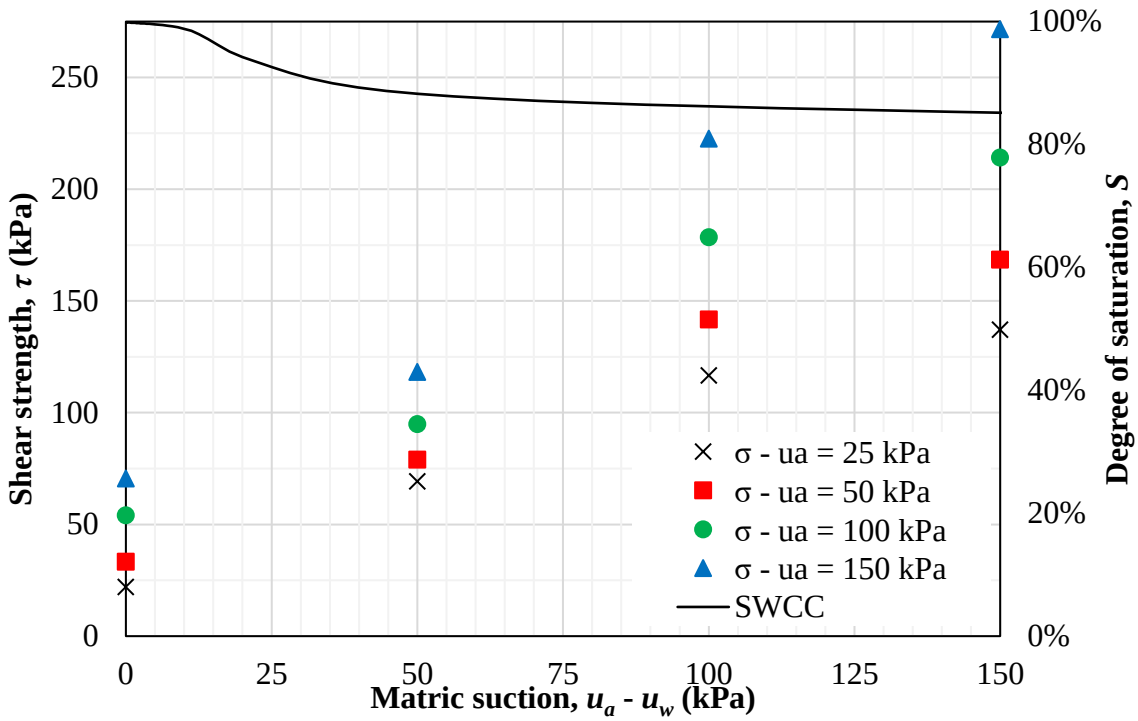

Figure C. 80. Failure envelope in terms of matric suction ($u_a - u_w$) and τ of soil 4R at maximum or peak shear stress

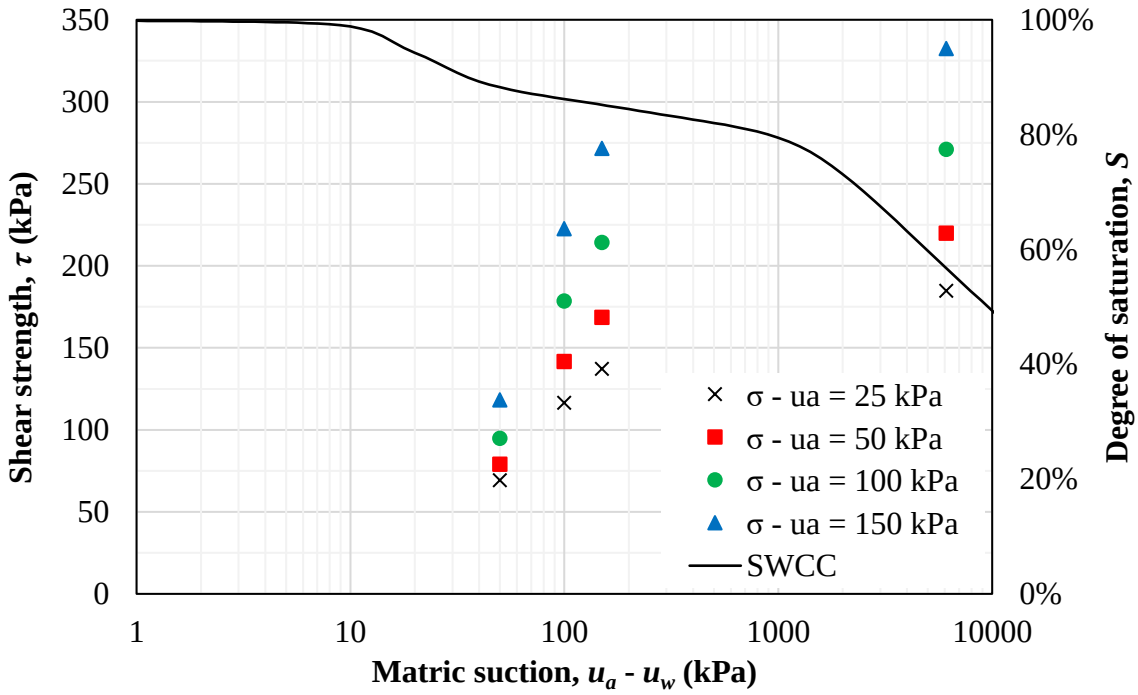

Figure C. 81. Failure envelope in terms of matric suction ($u_a - u_w$) and τ for soil #4R in monolog scale at maximum or peak shear stress

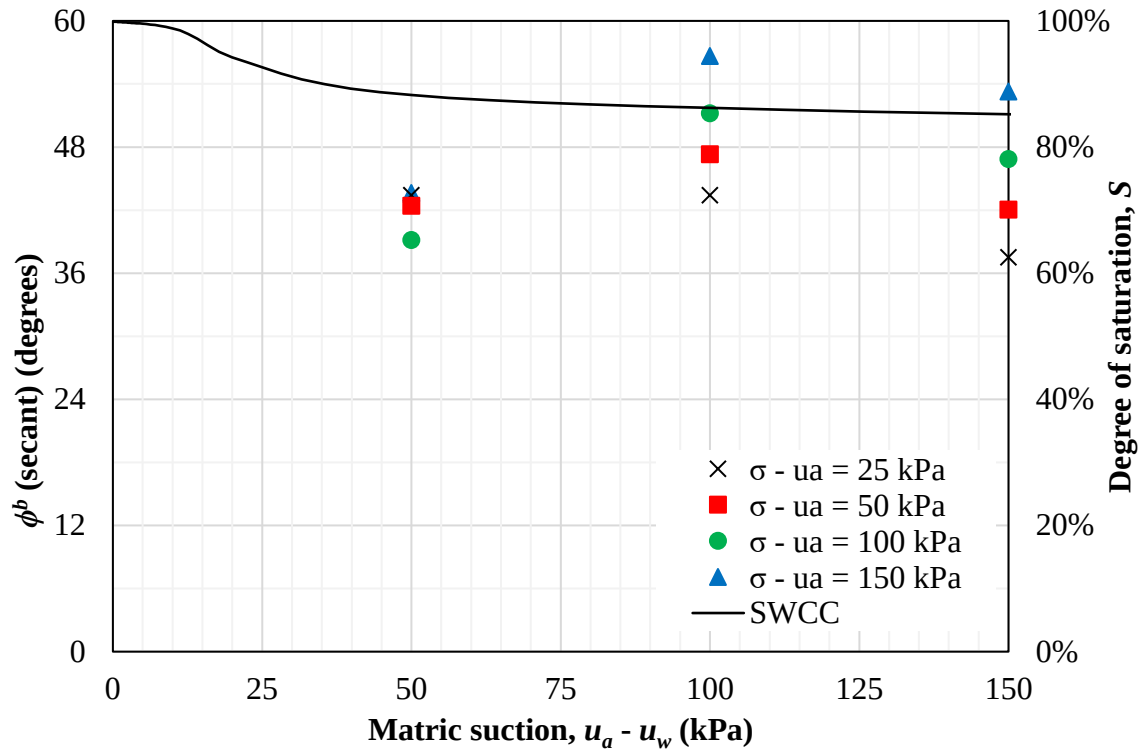

Figure C. 82. Variation of the angle ϕ^b secant as function of the matric suction ($u_a - u_w$) of soil 4R at maximum or peak shear stress

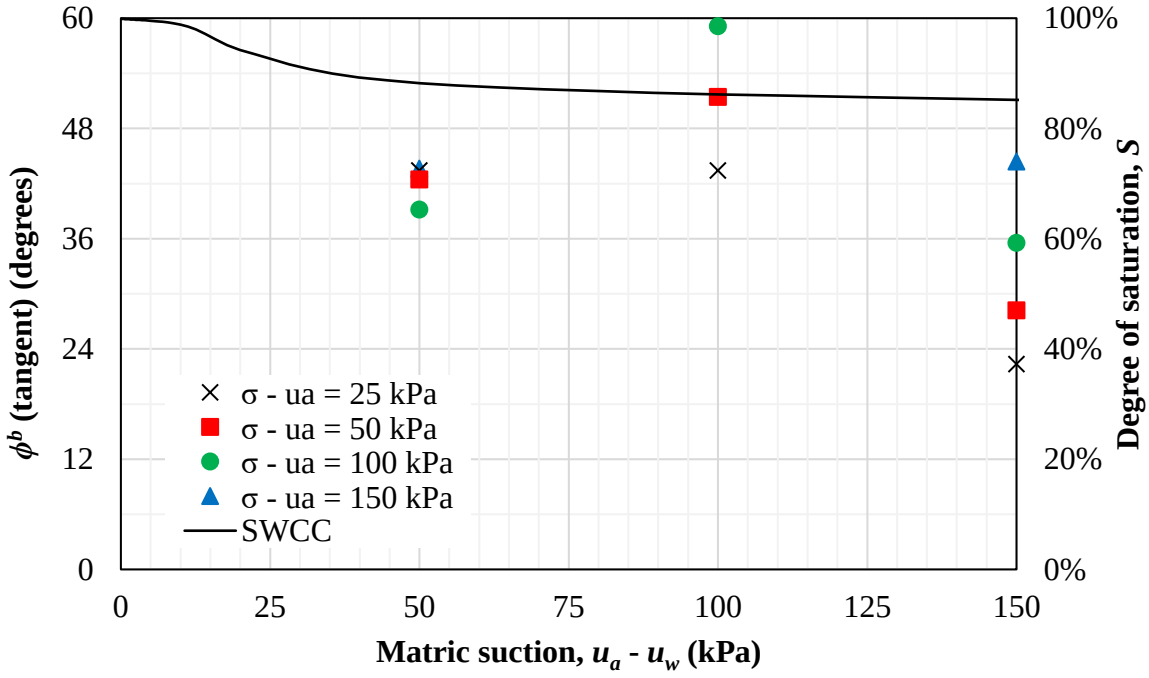

Figure C. 83. Variation of the angle ϕ^b tangent as function of the matric suction ($u_a - u_w$) of soil 4R at maximum or peak shear stress

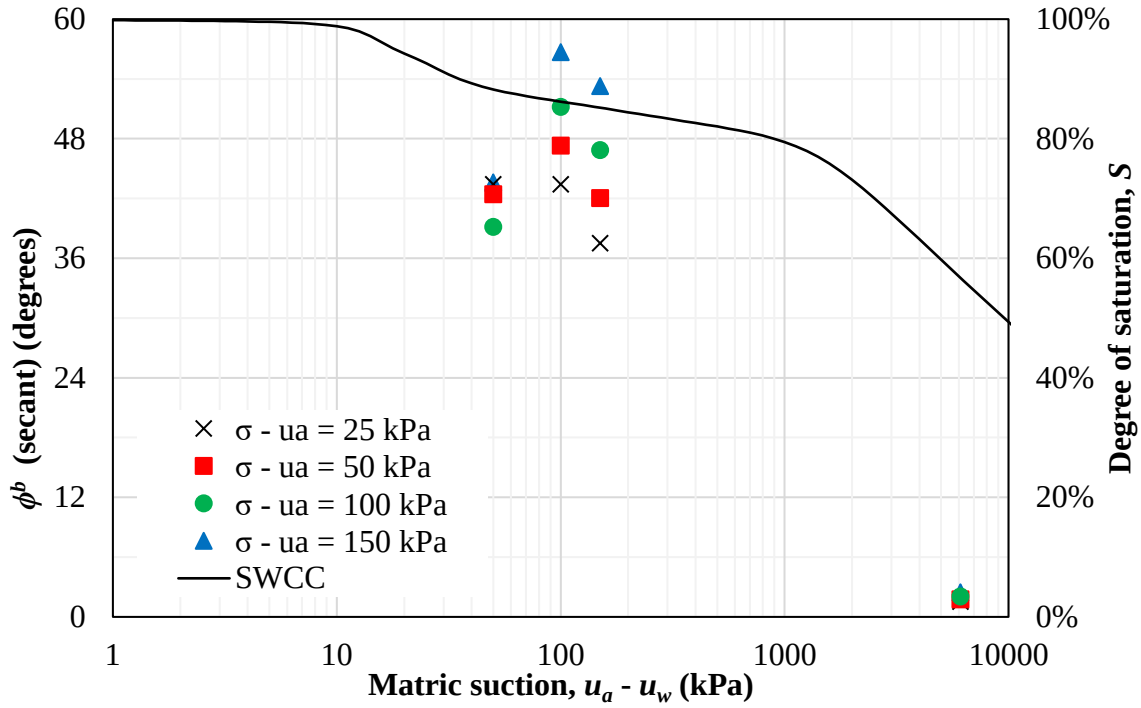

Figure C. 84. Variation of the angle ϕ^b secant as function of the matric suction ($u_a - u_w$) of soil 4R in monolog scale at maximum or peak shear stress

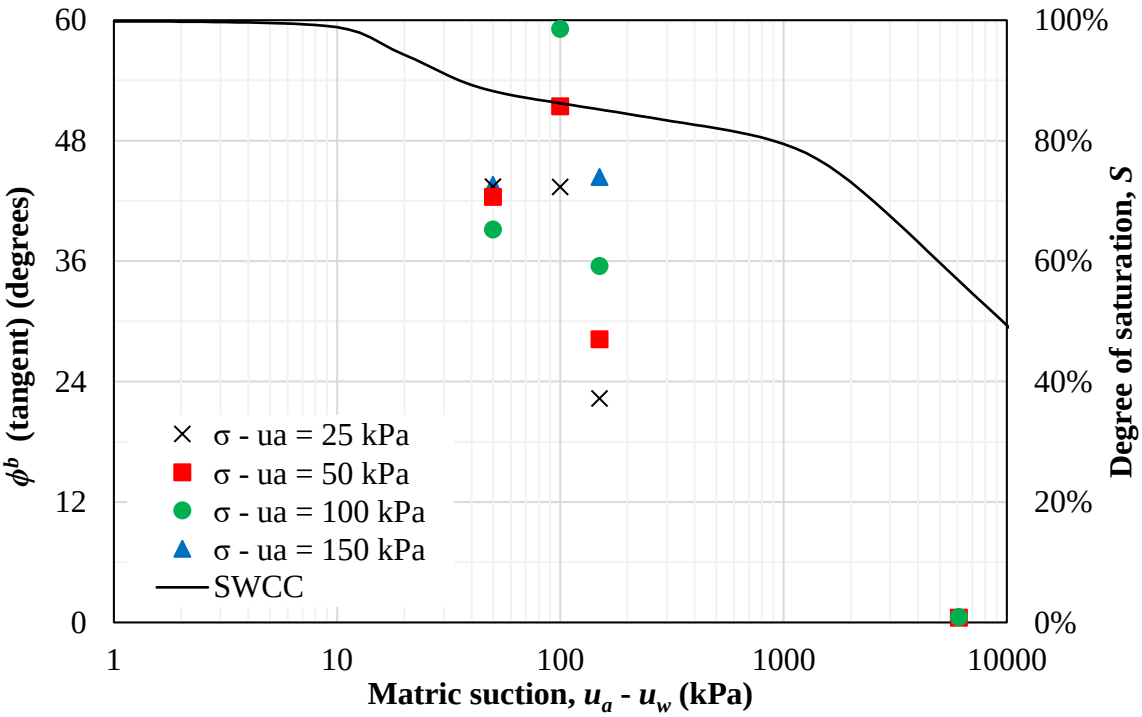

Figure C. 85. Variation of the angle ϕ^b tangent as function of the matric suction ($u_a - u_w$) of soil 4R in monolog scale at maximum or peak shear stress

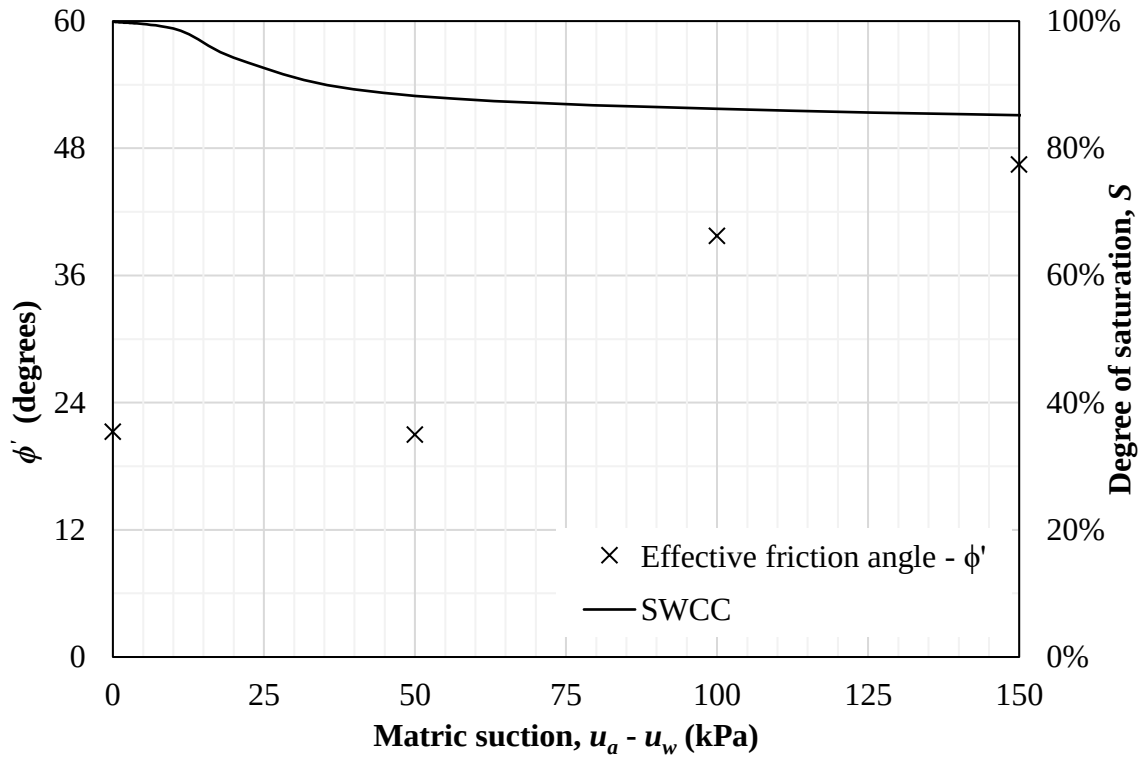

Figure C. 86. Variation of the angle ϕ' as function of the matric suction ($u_a - u_w$) of soil 4R at maximum or peak shear stress

The data from Table C.17 were fitted using the Modified Bi-Hyperbolic model for low (≤ 150 kPa) and all matric suctions. The fitting parameters are presented in Table C.18. For low suctions, the R^2 and RMSE are respectively 0.945 and 16.8 whereas for all suctions, they are 0.956 and 18.8, respectively. Although these R^2 are high, the RMSE indicate a mean error respectively for low and all suctions of 13.5 and 12.5%, which are significant. The extended Mohr-Coulomb failure envelopes are illustrated in Figs. C.87 and C.88 for low and all suctions, respectively.

Table C. 18. Parameters obtained for the Modified Bi-Hyperbolic model for maximum or peak shear stress

	Low suctions	All suctions
c' (kPa)	0.0	0.0
ϕ' (degrees)	30.9	33.6
ϕ^b (degrees)	47.3	45.1
τ_{ult1} (kPa)	4.68 x10^5	6.23E+04
τ_{ult2} (kPa)	2.66 x10^3	6.89E+04
τ_{ult} (kPa)	9.5	148.9
τ_{peak} (kPa)	9.5	46974.1
s_b	104.5	1087.4
n	3.0	2.0
a_1	1.669	1.505
b_1	2.14 x10^{-6}	1.61x10^{-5}
a_2	0.922	0.997
b_2	3.77 x10^{-4}	1.45x10^{-5}

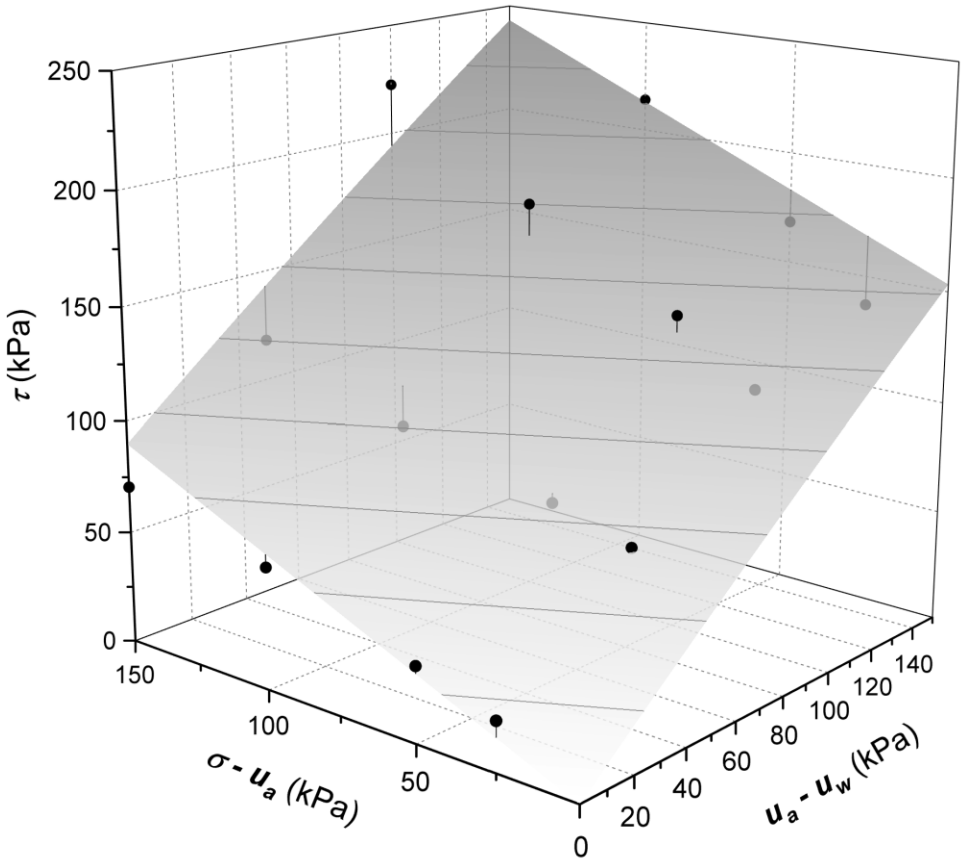

Figure C. 87. Extended Mohr-Coulomb failure surface using the Modified Bi-Hyperbolic model of soil 4R at maximum or peak shear stress in low suctions

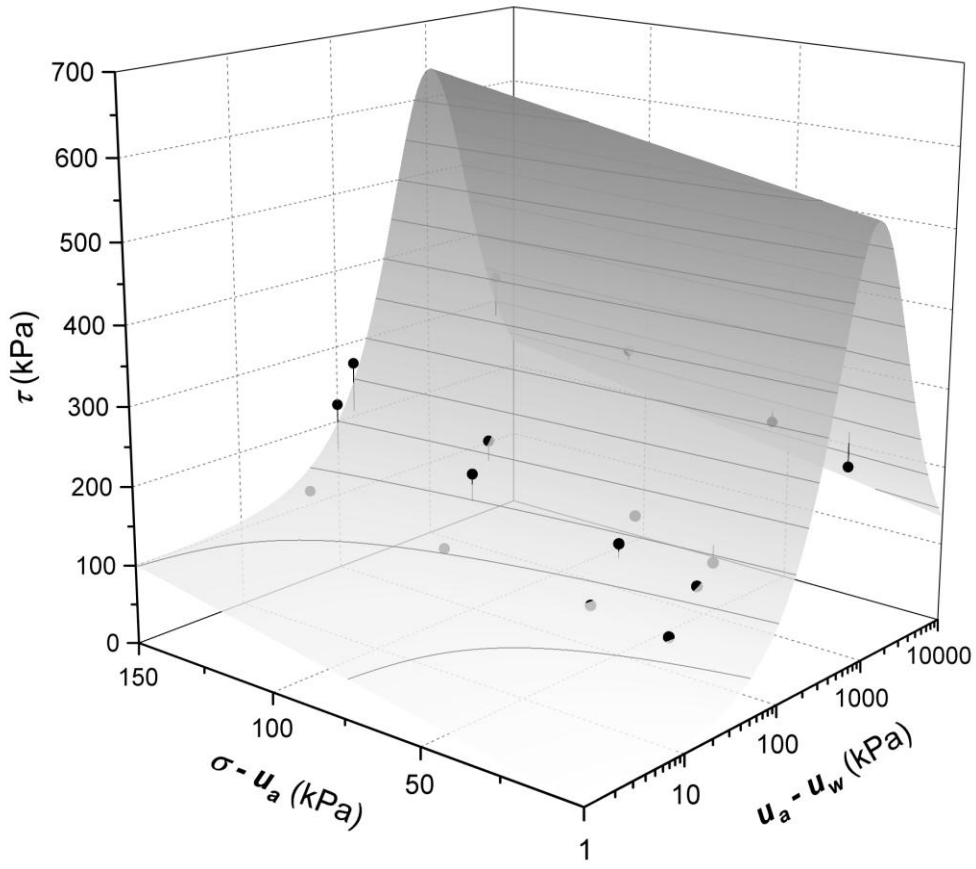

Figure C. 88. Extended Mohr-Coulomb failure surface using the Modified Bi-Hyperbolic model of soil 4R at maximum or peak shear stress in all suctions

- General comments

The graphs showing the horizontal displacement versus the shear stress indicate strain-hardening behavior (Figs. C.74 to C.77), except for suctions of 6100 kPa that exhibited peak and residual shear strength (Fig. C.78). In summary, the shear strength parameters considering maximum or peak shear stress as failure criterion indicate:

- The angle ϕ^b is greater than ϕ' for matric suctions of 100 and 150 kPa (Table C.17);
- The angle ϕ' starts to increase with matric suction at 100 kPa, which is superior than the first residual suction (28 kPa) (Fig. C.86);

- For matric suction of 50 kPa, the angle ϕ^b is independent of the net normal stress while for higher suctions, ϕ^b increases with the net normal stress. The highest values of ϕ^b were obtained from suctions of 100 kPa. From this point, the values of ϕ^b started to decrease (Fig. C.82).
- For high suctions over than the second air-entry value (1400 kPa), ϕ^b approaches zero (≈ 0.5°), as shown in Fig. C.85.

- Shear strength data: 5U
  - Initial void ratio (e_0) = 1.67
  - Type: modified direct shear
  - Shear velocity: 2.03×10^{-4} mm/s

i) $u_a - u_w$ = 0 kPa

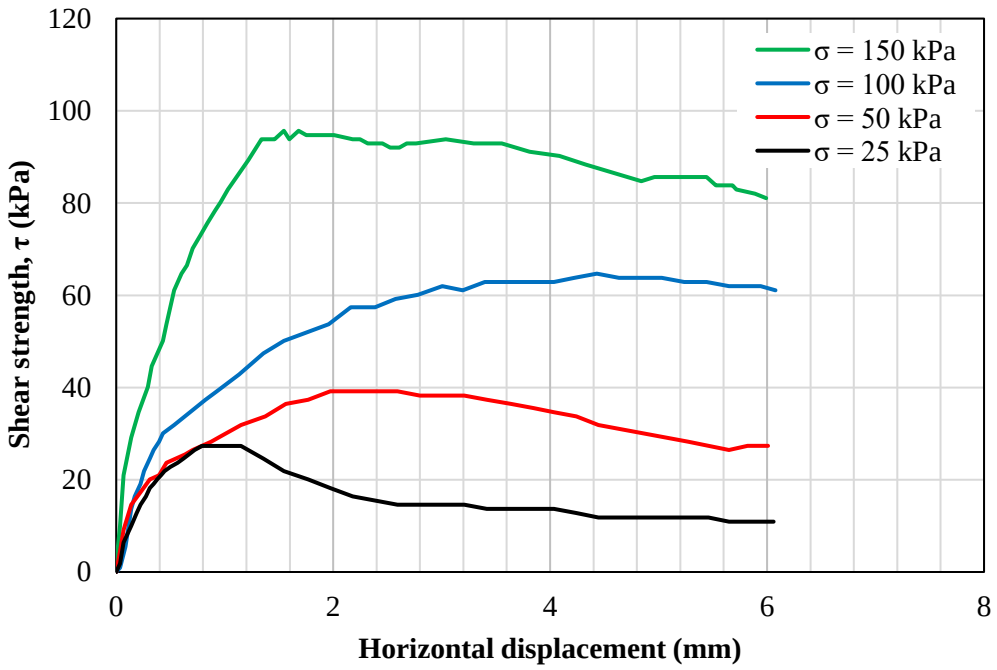

Figure C.89. Horizontal displacement versus shear strength of saturated tests of soil 5U

ii) $u_a - u_w$ = 50 kPa

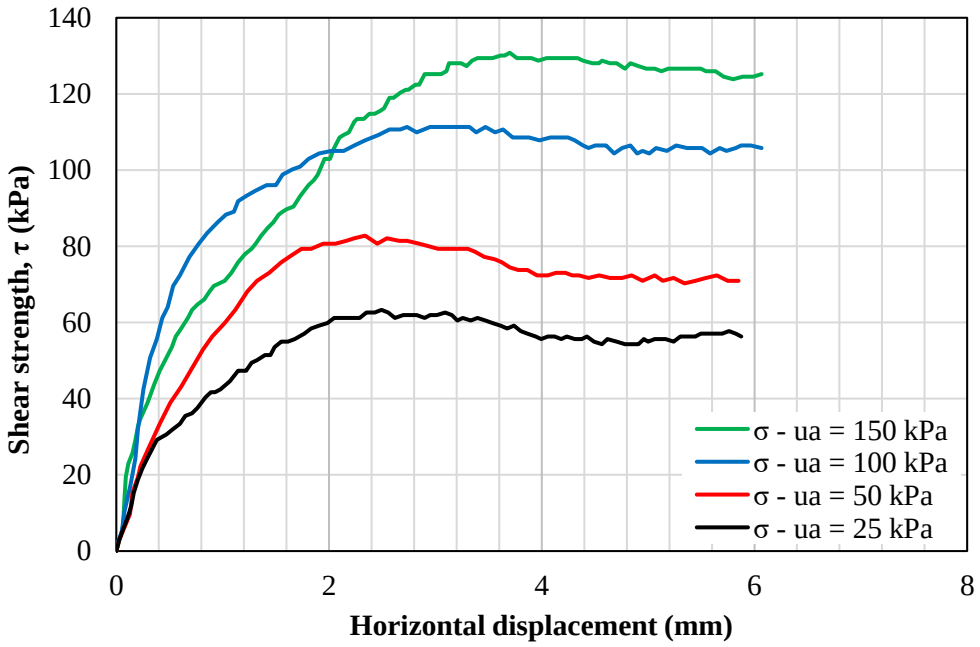

Figure C.90. Horizontal displacement versus shear strength of tests with (u_a - u_w) = 50 kPa of soil 5U

iii) $u_a - u_w$ = 100 kPa

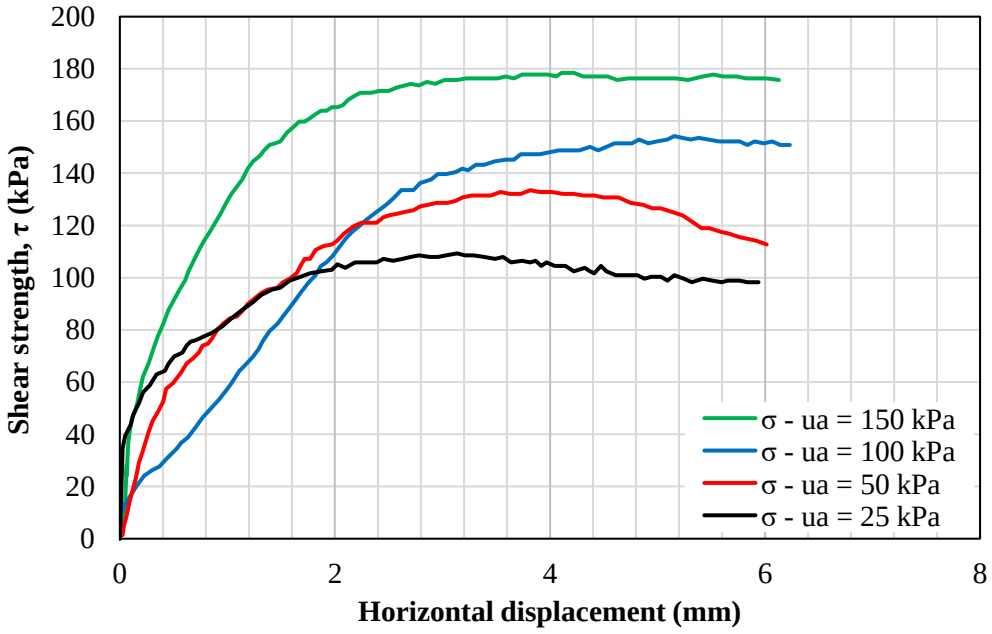

Figure C.91. Horizontal displacement versus shear strength of tests with (u_a - u_w) = 100 kPa of soil 5U

iv) $u_a - u_w$ = 150 kPa

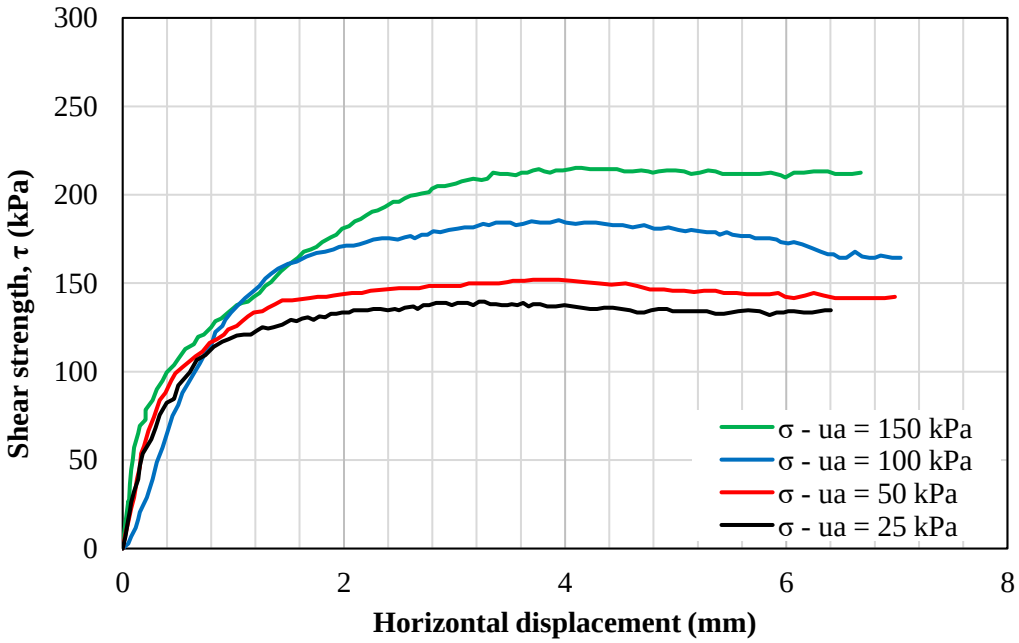

Figure C.92. Horizontal displacement versus shear strength of tests with (u_a - u_w) = 150 kPa of soil 5U

v) $u_a - u_w$ = 6500 kPa

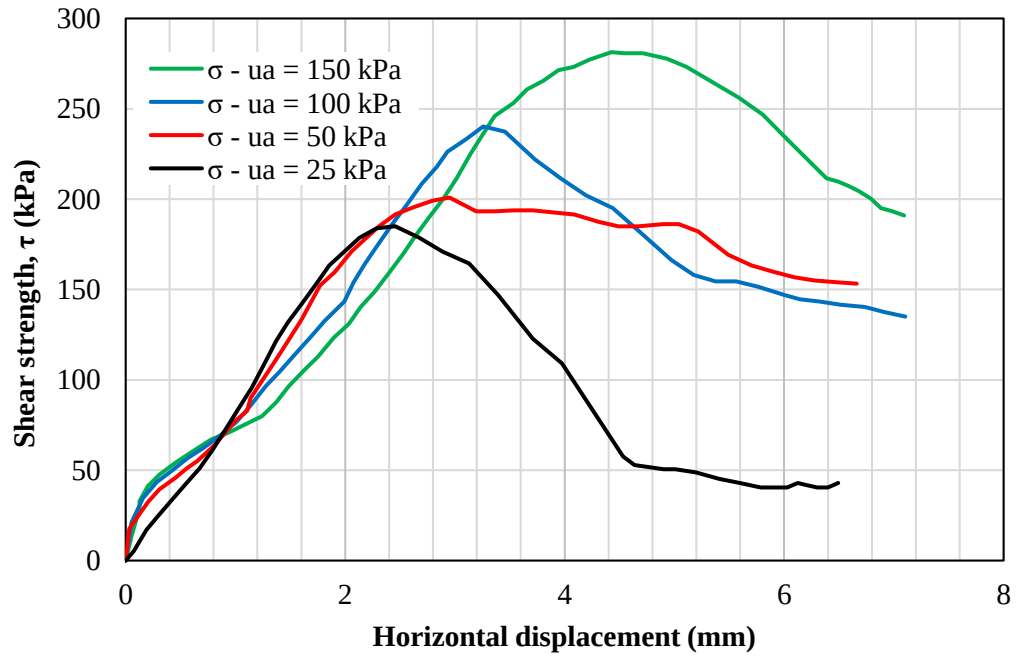

Figure C.93. Horizontal displacement versus shear strength of tests with (u_a - u_w) = 6500 kPa of soil 5U

- Failure criterion: maximum or peak shear stress

The data from the tests for maximum or peak shear stress as failure criterion is presented in Table C.19. The plot of the shear strength as function of the net vertical stress (Fig. C.94) indicates that ϕ' has a unique value for each matric suction. The values of ϕ' seems to increase when the matric suction is greater than 100 kPa. Also, the relationship between the matric suction and the shear strength depicted in Fig. C.95 points out to constant values of ϕ^b at each net vertical stress for matric suctions up to 150 kPa. The angle ϕ^b was calculated assuming the slope of the best-fit linear equation (i.e., secant) and the previous matric suction (i.e. tangent) as reference. Moreover, except for matric suction of 6500 kPa, the relation ϕ^b/ϕ' is always greater than 1.

Table C.19. Shear strength parameters of soil 5U at maximum or peak shear stress

τ (kPa)	σ - u_a (kPa)	u_a - u_w (kPa)	c_{app} (kPa)	ϕ'	ϕ^b (sec)	ϕ^b (tan)	ϕ^b(tan)/ϕ'
27.3	25	0	12.40	28.6	37.4		1.3
39.2	50				37.9		1.3
64.7	100				39.1		1.4
95.7	150				39.1		1.4
63.3	25	50	53.60	28.1	37.4	35.7	1.3
82.8	50				37.9	41.1	1.3
111.3	100				39.1	43.0	1.4
130.8	150				39.1	35.1	1.4
109.3	25	100	101.20	27.7	37.4	39.3	1.4
133.5	50				37.9	43.3	1.4
154.2	100				39.1	41.8	1.4
178.5	150				39.1	39.6	1.4
139.6	25	150	123.07	31.6	37.4	36.8	1.2
152.0	50				37.9	36.9	1.2
185.7	100				39.1	38.9	1.2
215.2	150				39.1	38.6	1.2
185.0	25	6500	163.75	37.8	1.4	1.4	0.0
200.9	50				1.4	1.4	0.0
240.2	100				1.5	1.5	0.0
281.4	150				1.6	1.6	0.0

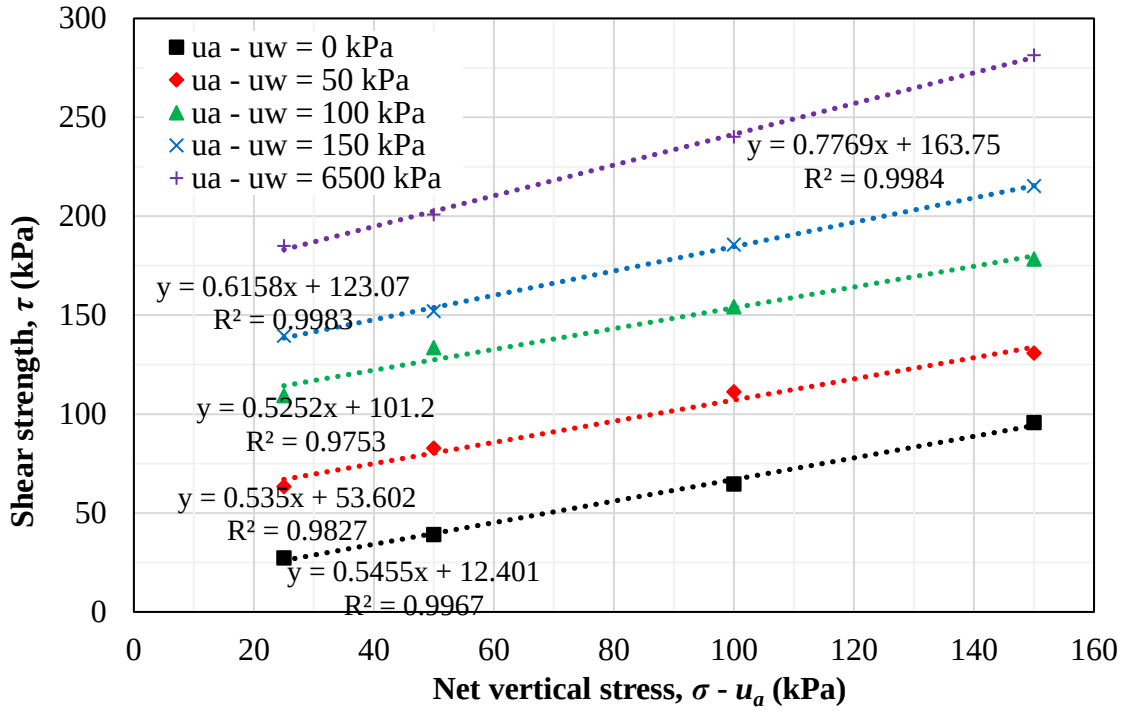

Figure C.94. Failure envelope in terms of net vertical stress (σ_v - u_a) and τ for soil #5U at maximum or peak failure

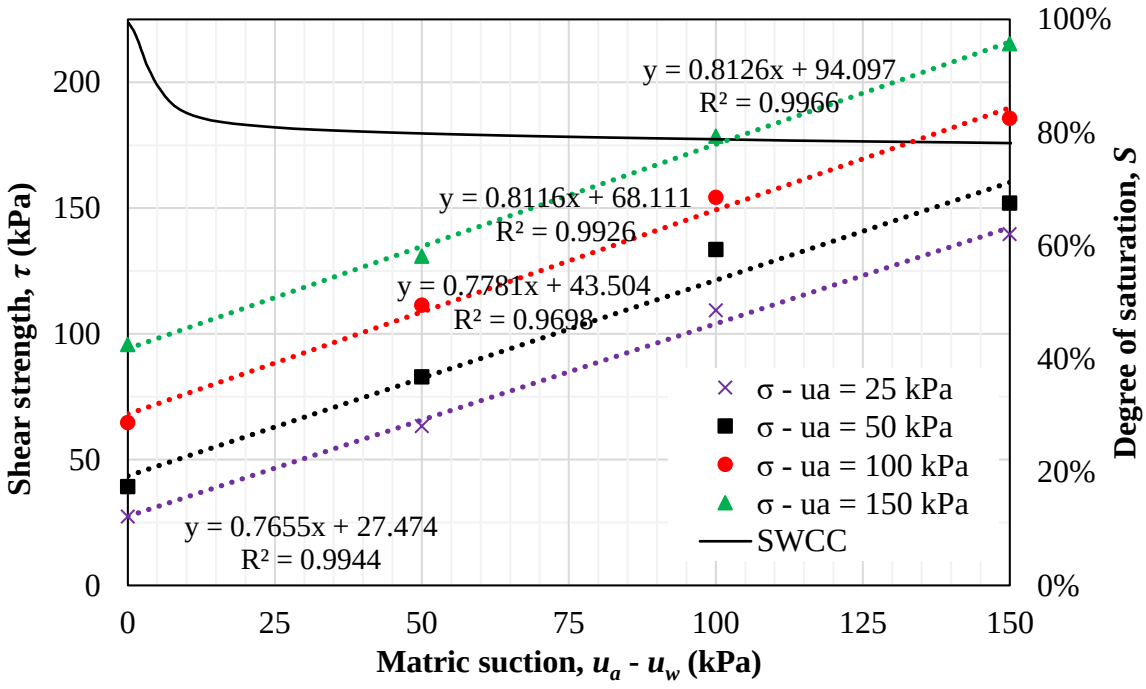

Figure C.95. Failure envelope in terms of matric suction (u_a - u_w) and τ for soil #5U at maximum or peak failure

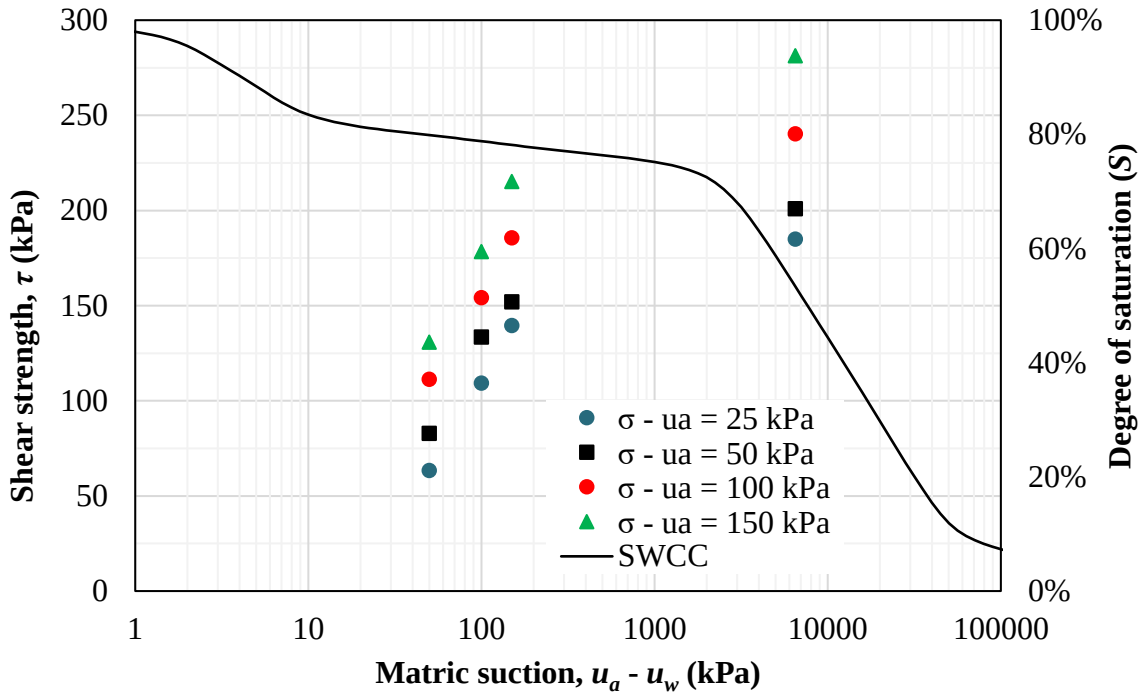

Figure C.96. Failure envelope in terms of matric suction (u_a - u_w) and τ for soil #5U at maximum or peak failure in monolog scale

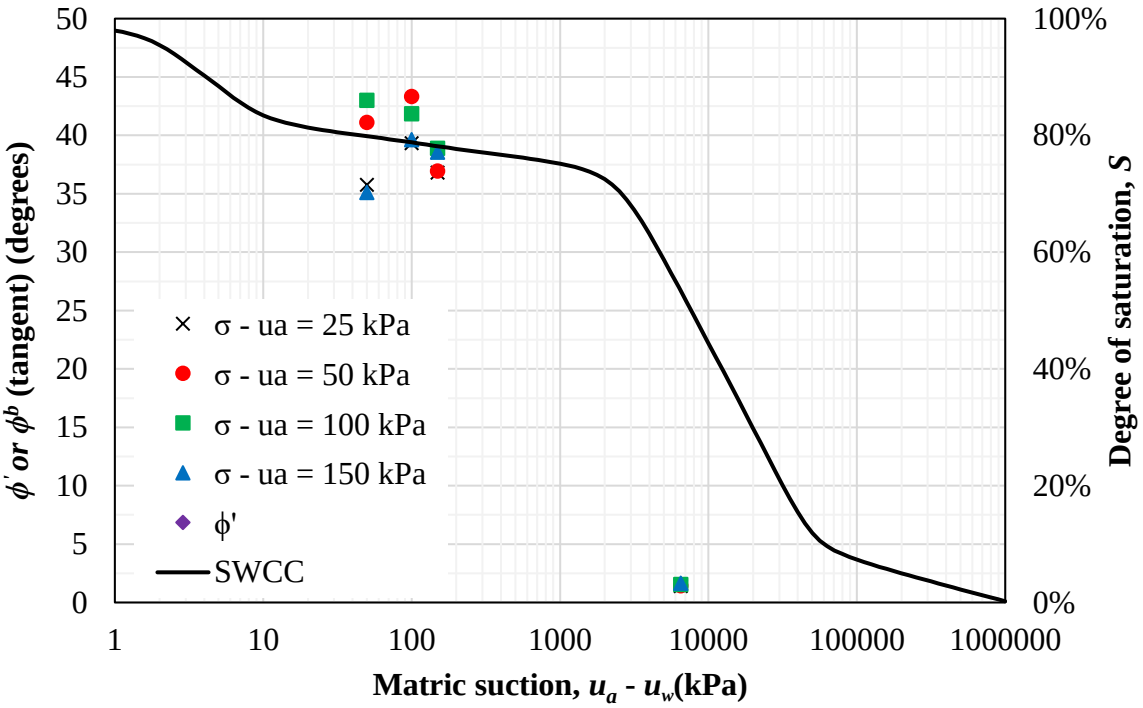

Figure C.97. Variation of the angle ϕ^b tangent as function of the matric suction (u_a - u_w) of soil 5U in monolog scale at maximum or peak shear stress

The data from Table C.19 were fitted using the Modified Bi-Hyperbolic model for low (≤ 150 kPa) and all matric suctions. The fitting parameters are presented in Table C.20. For low suctions, the R^2 and RMSE are respectively 0.993 and 4.3 whereas for all suctions, they are 0.974 and 10.6, respectively. These goodness-of-fit points out to mean errors of 3.7 and 7.6%, respectively. Although such errors are not particularly high, the fitted surface for all suctions indicate a relevant dispersion for some points. The extended Mohr-Coulomb failure surfaces for low and all matric suctions are depicted in Fig. C.98 and C.99, respectively.

Table C.20. Parameters obtained for the Modified Bi-Hyperbolic model for maximum or peak shear strength

	Low suctions	All suctions
c' (kPa)	10.6	3.6
ϕ' (degrees)	29.1	31.0
ϕ^b (degrees)	43.9	60.9
τ_{ult1} (kPa)	5.03 x10^5	5.06E+5
τ_{ult2} (kPa)	6.90 x10^2	1.84E+2
τ_{ult} (kPa)	0.2	0.2
τ_{peak} (kPa)	0.2	0.2
s_b	100.0	100.0
n	1.0	1.0
a_1	1.800	1.667
b_1	1.99 x10^{-6}	1.98x10^{-6}
a_2	1.041	0.557
b_2	1.47 x10^{-3}	5.54x10^{-3}

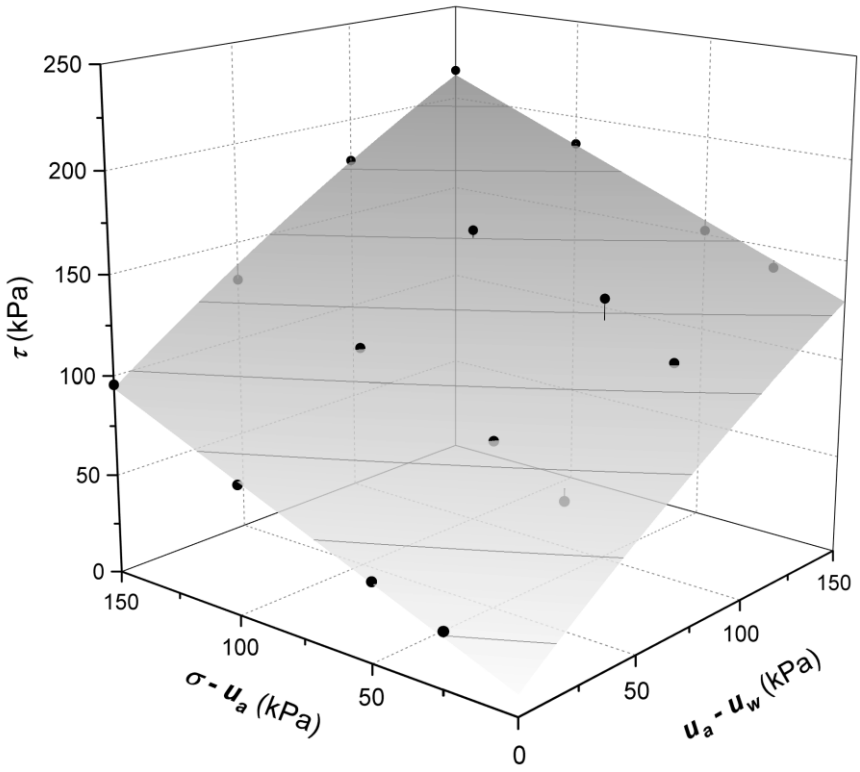

Figure C.98. Extended Mohr-Coulomb failure surface fitted using the Modified Bi-Hyperbolic model of soil #5U for low matric suctions (≤ 150 kPa) at maximum or peak failure

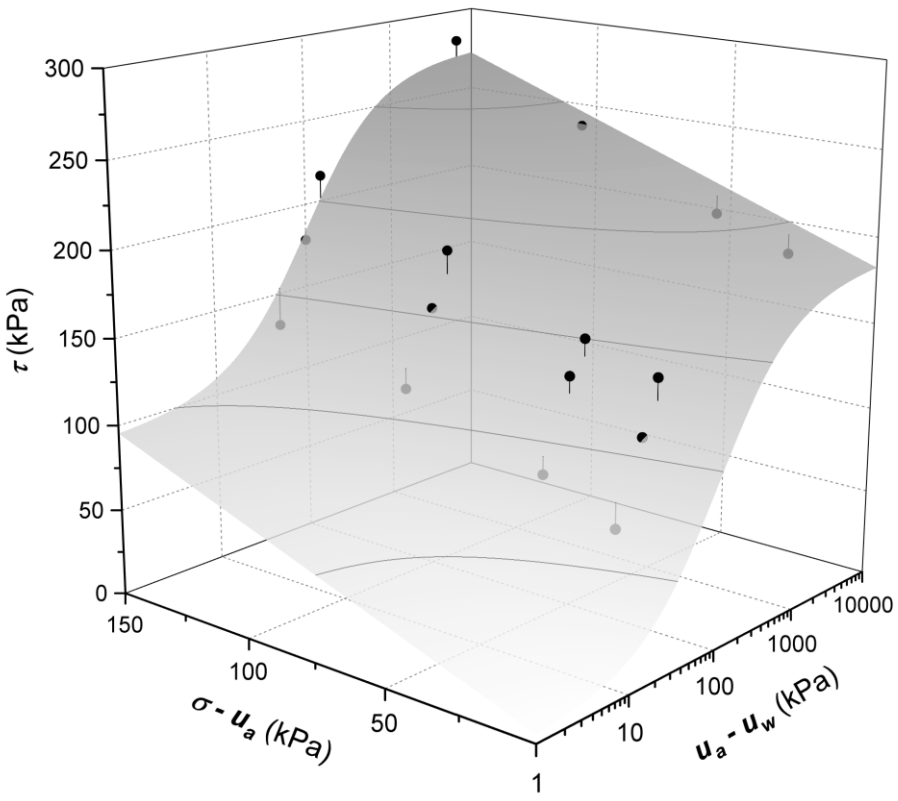

Figure C.99. Extended Mohr-Coulomb failure surface fitted using the Modified Bi-Hyperbolic model of soil #5U for all matric suctions at maximum or peak failure

- General comments

The graphs showing axial strain versus deviator stress indicate that most of the curves presented strain-hardening behavior (Figs. C.89 to C.92). For suction of 6500 kPa, the curves showed a clear peak (Fig. C.93). In summary, the shear strength parameters considering peak shear strength as failure criterion points out:

i. The angle ϕ^b is greater than ϕ' for matric suctions of 50, 100 and 150 kPa (Table C.19);

ii. The angle ϕ' increases for suctions ≥ 150 kPa (Table C.19);

iii. The angle ϕ^b increases with matric suction up to approximately 100 kPa. From this point, ϕ^b decreases and seems to converge to a single value independently

of the net normal stress (Fig. C.97). Also, ϕ^b appears to exhibit a peak between net normal stress of 50 and 100 kPa;

iv. For high suctions over than the second air-entry value (2560 kPa), ϕ^b is on average 1.5° (Fig. C.97).

C.5 Feuerharmel (2007) – 5R and 6U

- Soil basic information and characteristics
  - Void ratio (e_0) = 1.08 (remolded); 1.00 (undisturbed)
  - Density of solids (ρ_s) = 2.80
  - Dry density (ρ_d) = 1.35 (remolded); 1.40 (undisturbed)
  - Liquid limit (w_L) = 56%
  - Plasticity limit (w_P) = 34%
  - USCS = CH (disaggregated) / SC (aggregated)

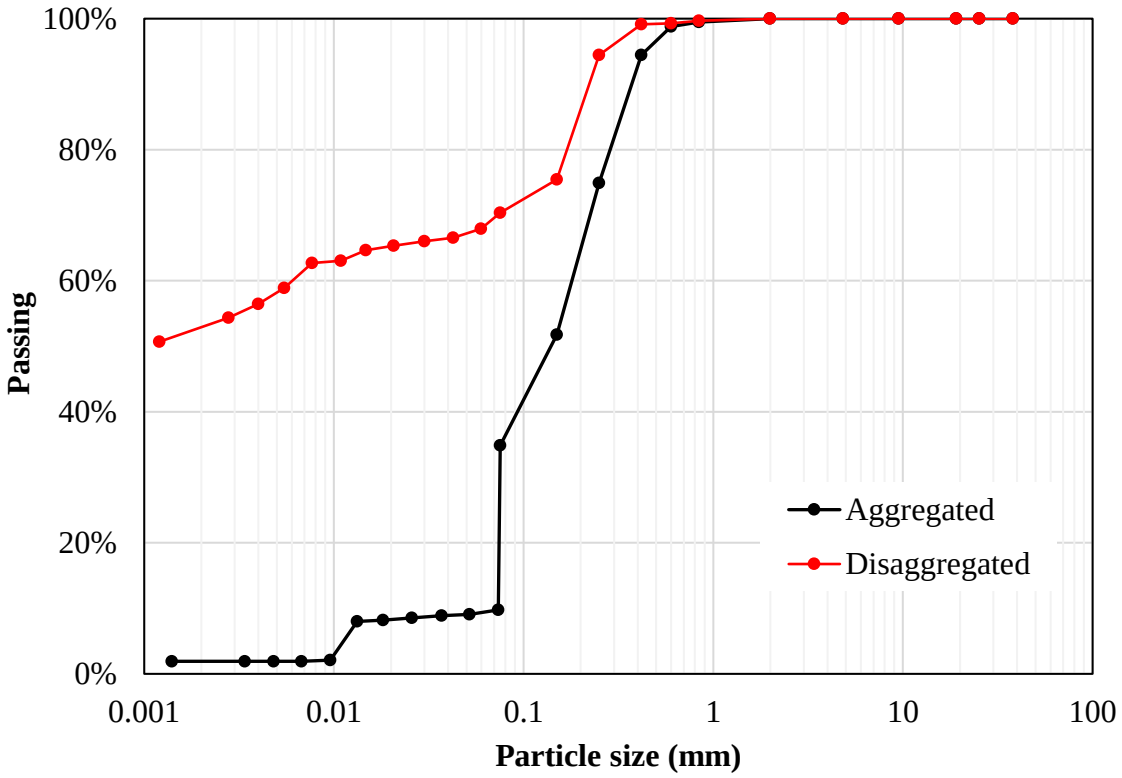

Figure C.100. Grain-size distribution curve of soil 5R

- Soil-water characteristic curve

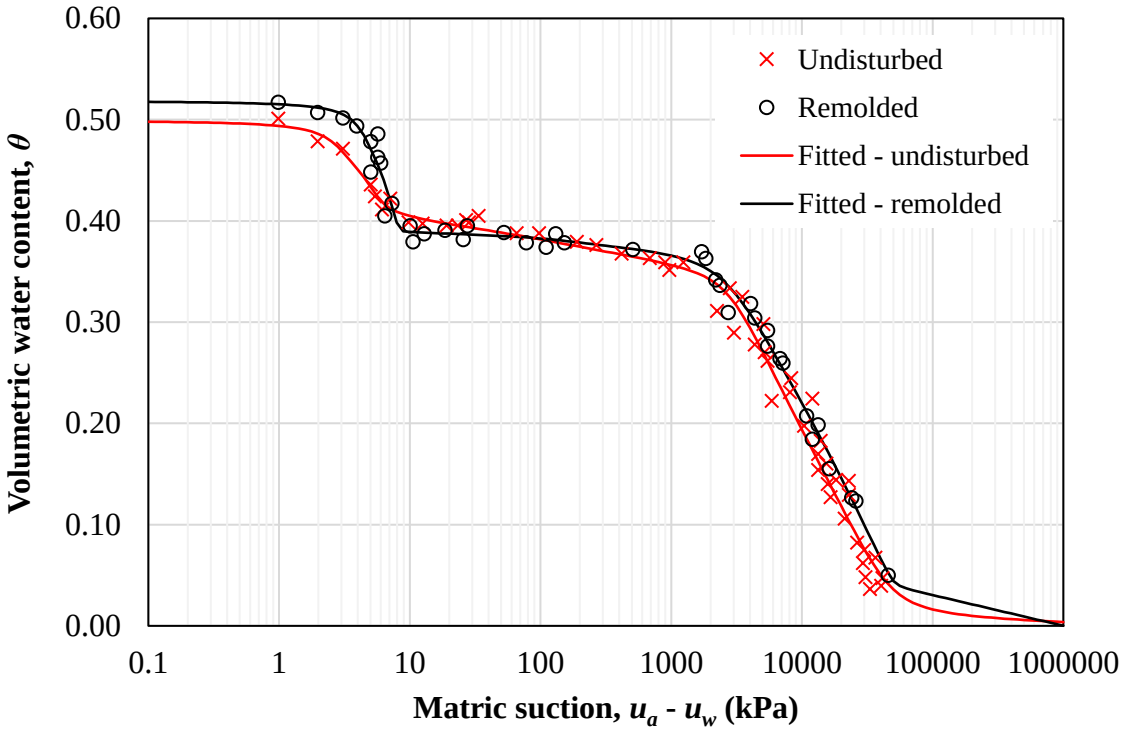

Figure C.101. Soil-water characteristic curve of soils 5R and 6U

- Shear strength data: 5R
  - Initial void ratio (e_0) = 1.08
  - Type: modified direct shear
  - Shear velocity: 2.03×10^{-4} mm/s

i) $u_a - u_w$ = 0 kPa

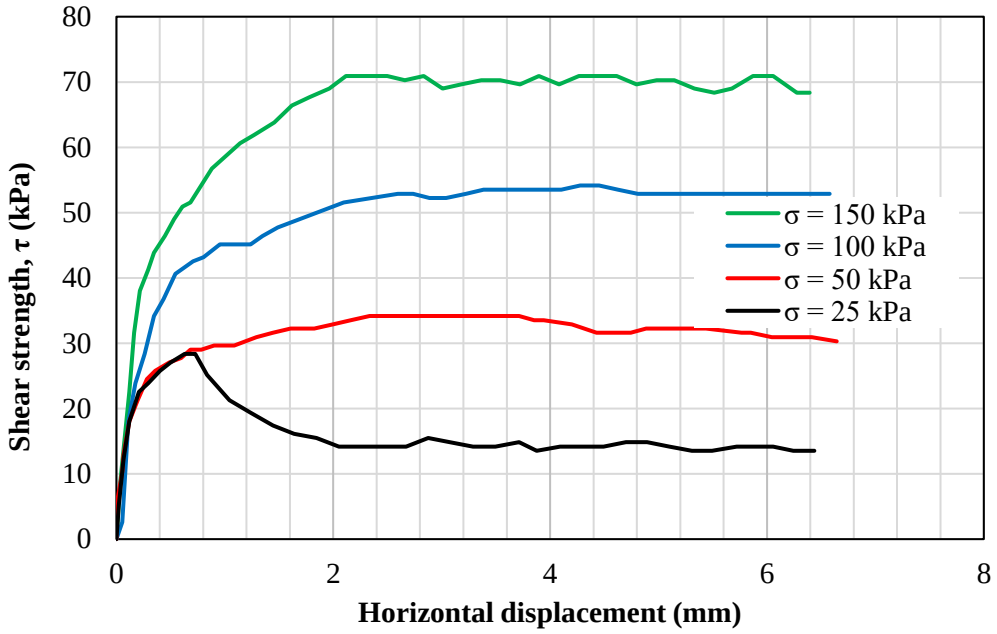

Figure C.102. Horizontal displacement versus shear strength of saturated tests of soil 5R

ii) $u_a - u_w$ = 50 kPa

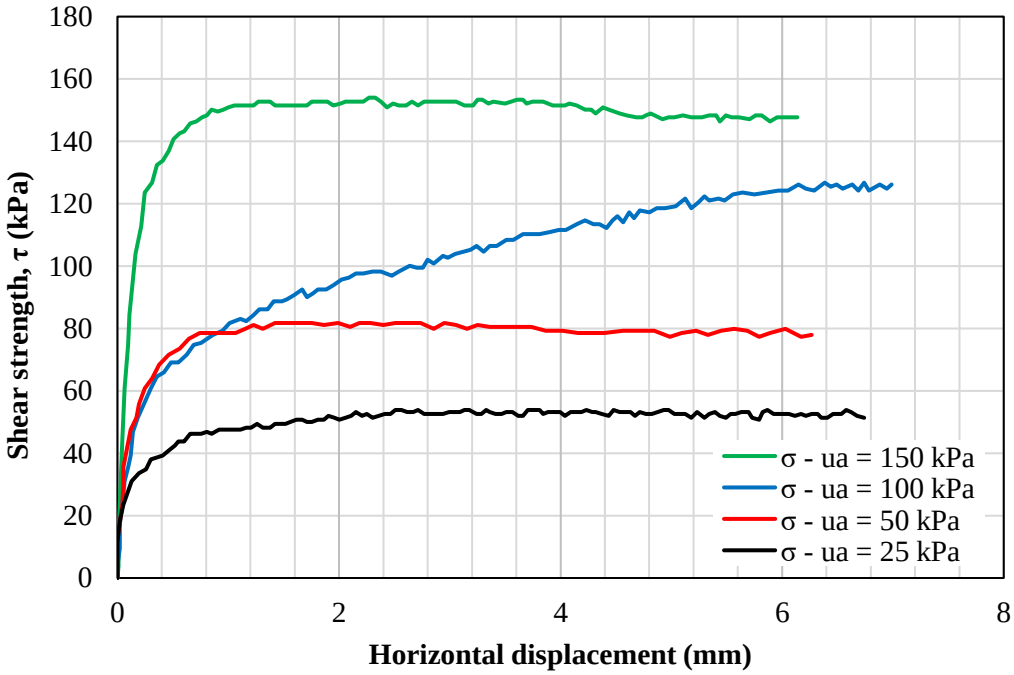

Figure C.103. Horizontal displacement versus shear strength of tests with (u_a - u_w) = 50 kPa of soil 5R

iii) $u_a - u_w$ = 100 kPa

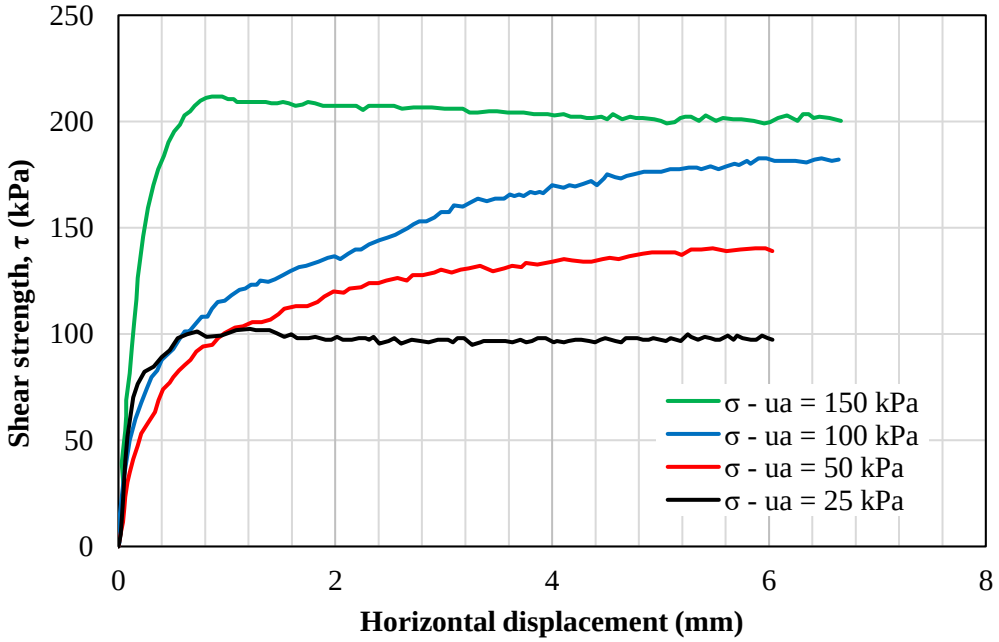

Figure C.104. Horizontal displacement versus shear strength of tests with (u_a - u_w) = 100 kPa of soil 5R

iv) $u_a - u_w$ = 150 kPa

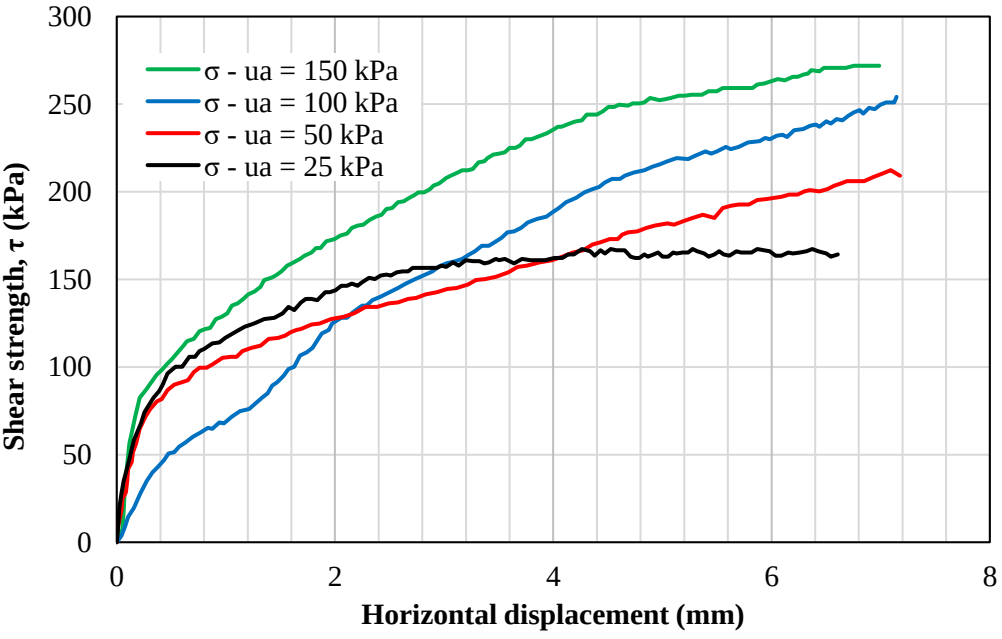

Figure C.105. Horizontal displacement versus shear strength of tests with (u_a - u_w) = 150 kPa of soil 5R

v) $u_a - u_w$ = 5800 kPa

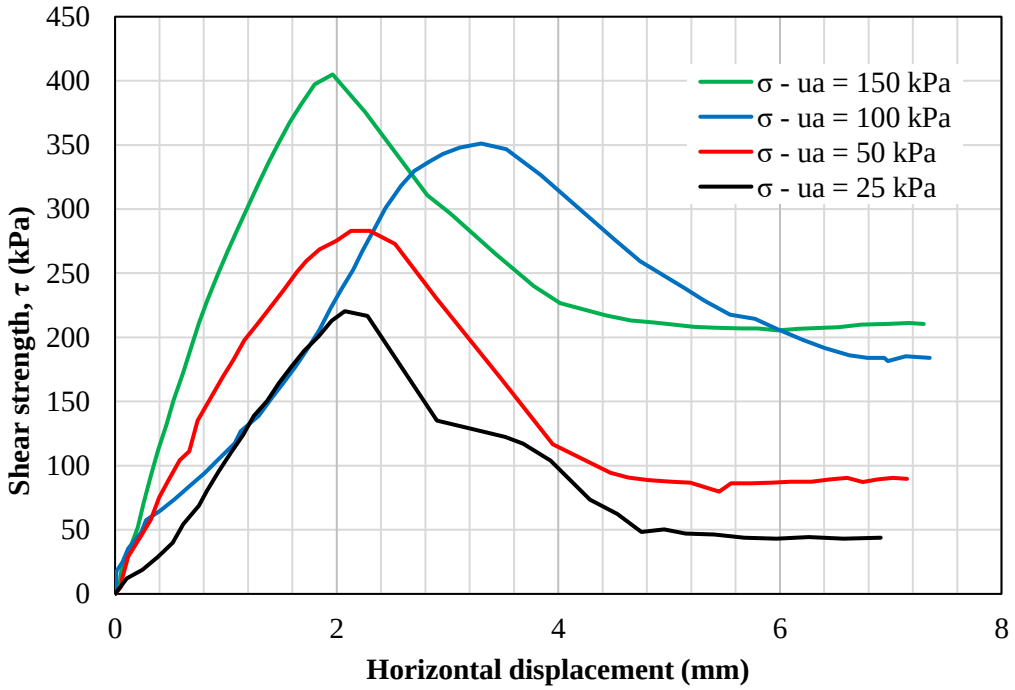

Figure C.106. Horizontal displacement versus shear strength of tests with (u_a - u_w) = 5800 kPa of soil 5R

- Failure criterion: maximum or peak shear stress

The data from the tests for maximum or peak shear stress as failure criterion are presented in Table C.21. For each matric suction other than 0 kPa, the cohesions were obtained by fitting the data assuming a polynomial equation of order 2. This was motivated because the tests exhibited a non-linear behavior of the effective friction angle with respect to the net vertical stress, as depicted by Fig. C.107.

Table C.21. Shear strength parameters for soil 5R at maximum or peak failure

τ (kPa)	σ - u_a (kPa)	u_a - u_w (kPa)	c_{app} (kPa)	ϕ' (sec)	ϕ' (tan)	ϕ^b (sec)	ϕ^b (tan)	ϕ^b(tan)/ ϕ'(tan)
28.4	25	0	18.5	19.3	21.6			
34.2	50				13.1			
54.2	100				21.8			
70.9	150				18.5			
53.9	25	50	21.0	52.7	52.7	27.0	27.0	0.5

τ (kPa)	σ - u_a (kPa)	u_a - u_w (kPa)	c_{app} (kPa)	ϕ' (sec)	ϕ' (tan)	ϕ^b (sec)	ϕ^b (tan)	ϕ^b(tan)/ ϕ'(tan)
81.8	50			50.5	48.1	43.6	43.6	0.9
126.8	100			46.6	42.0	55.4	55.4	1.3
154.0	150			41.6	28.6	59.0	59.0	2.1
102.4	25			55.3	55.3	36.5	44.1	0.8
140.3	50	100	66.2	56.0	56.6	46.7	49.5	0.9
182.7	100			49.3	40.3	52.1	48.2	1.2
211.7	150			44.1	30.2	54.6	49.1	1.6
167.3	25			60.7	60.7	42.8	52.4	0.9
212.3	50	150	122.8	60.8	60.9	49.9	55.2	0.9
254.2	100			52.7	39.9	53.1	55.0	1.4
271.9	150			44.8	19.5	53.3	50.3	2.6
220.4	25			66.0	66.0	1.9	0.5	0.0
283.0	50	5800	164.3	67.2	68.2	2.5	0.7	0.0
351.1	100			61.9	53.7	2.9	1.0	0.0
405.0	150			58.1	47.1	3.3	1.3	0.0

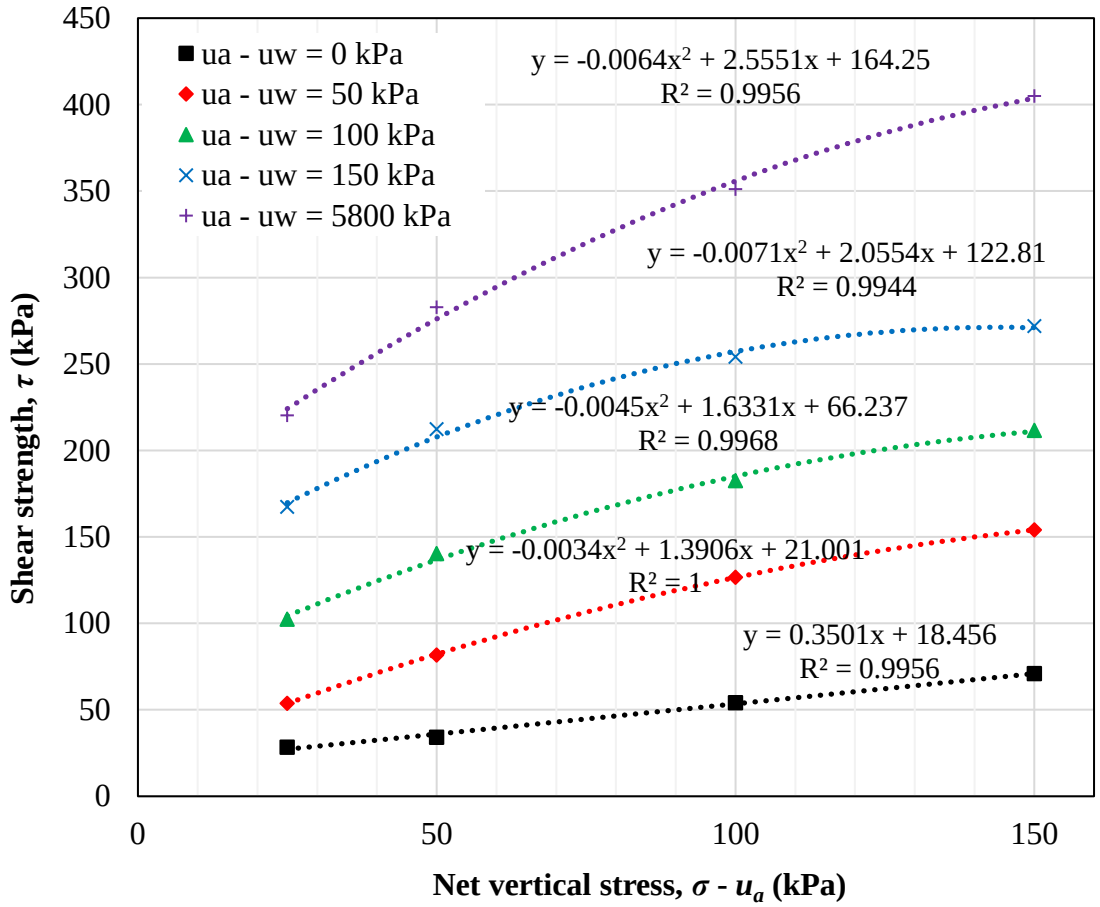

Figure C.107. Failure envelope in terms of net vertical stress (σ_v - u_a) and τ for soil 5R at maximum or peak failure

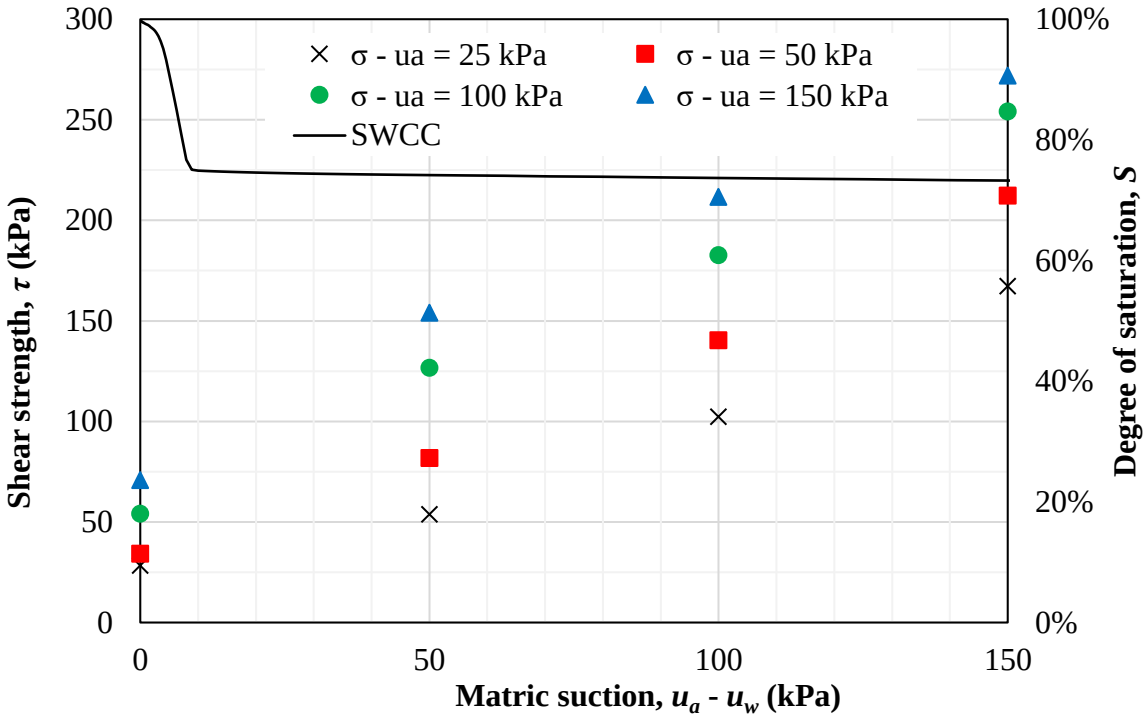

Figure C.108. Failure envelope in terms of matric suction (u_a - u_w) and τ for soil 5R at maximum or peak failure

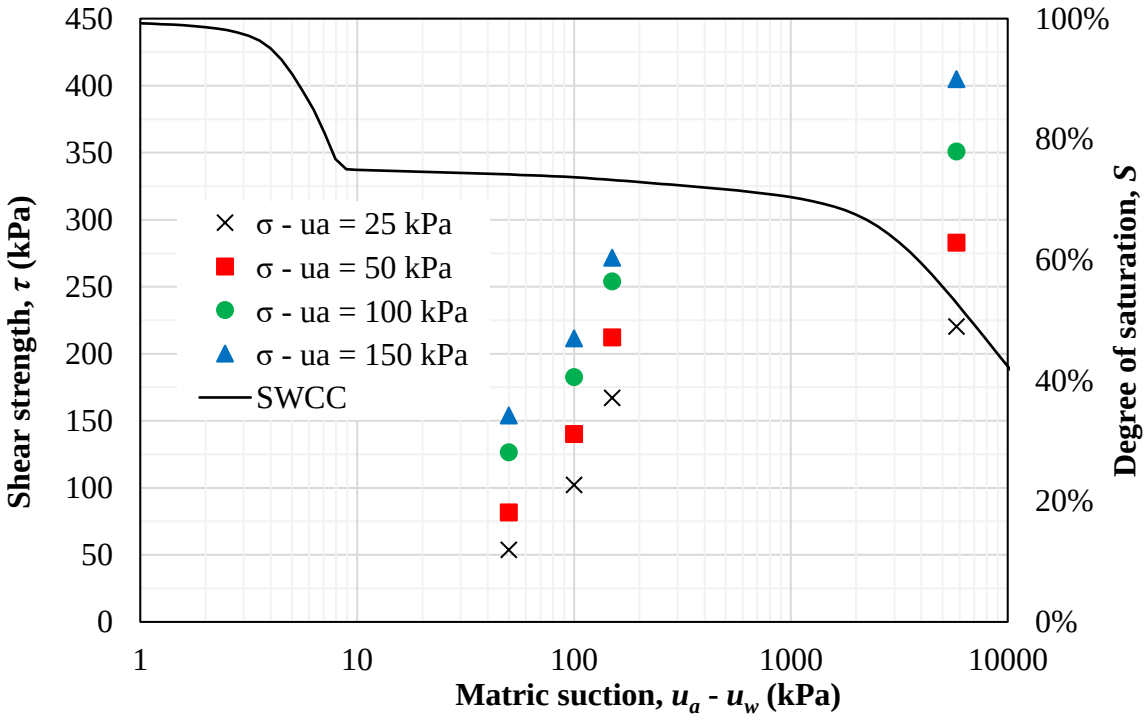

Figure C.109. Failure envelope in terms of matric suction (u_a - u_w) and τ for soil 5R at maximum or peak failure in monolog scale

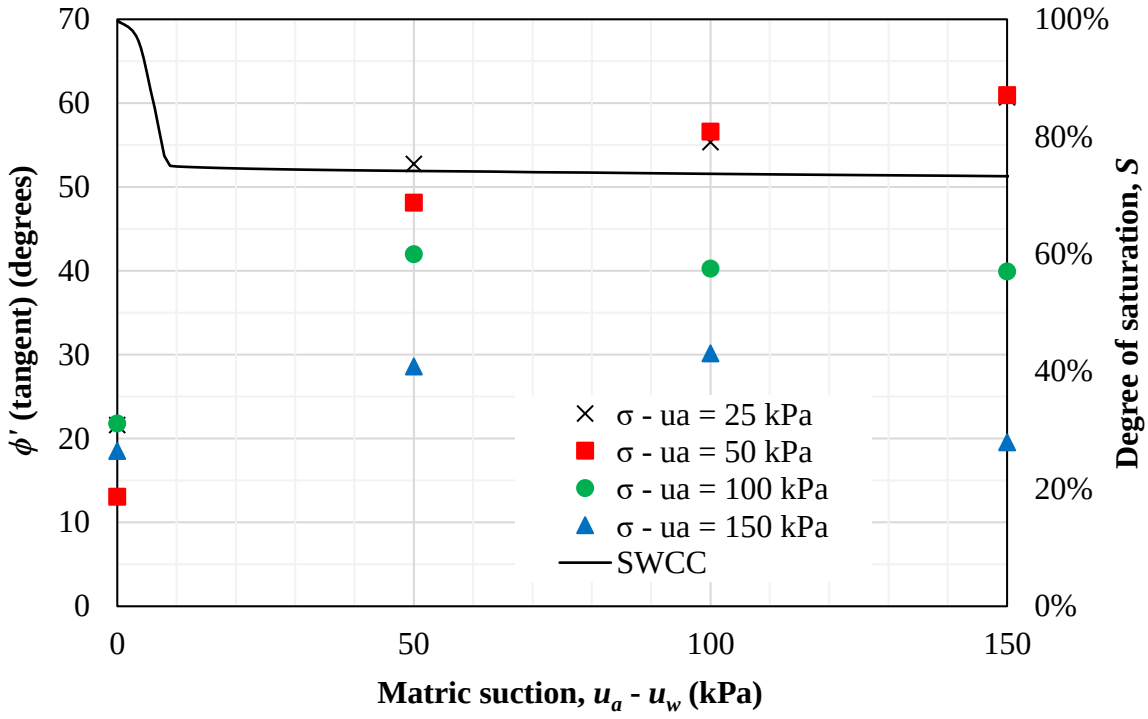

Figure C.110. Variation of the angle ϕ' tangent as function of the matric suction (u_a - u_w) for soil 5R at maximum or peak failure

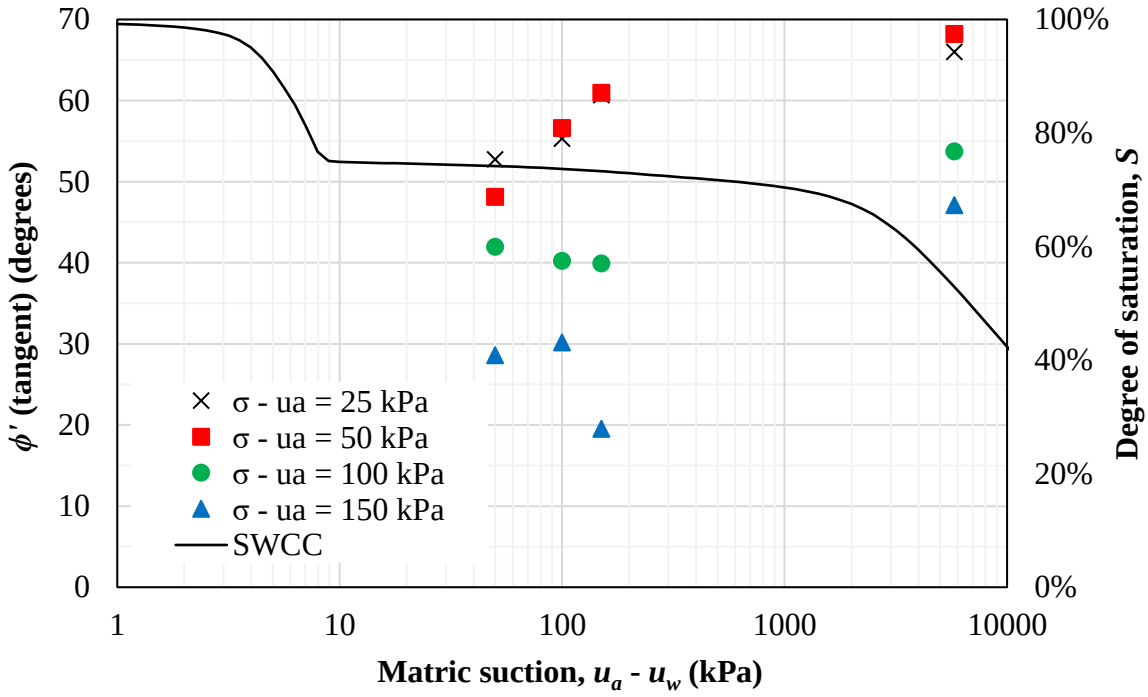

Figure C.111. Variation of the angle ϕ' tangent as function of the matric suction (u_a - u_w) for soil 5R in monolog scale at maximum or peak failure

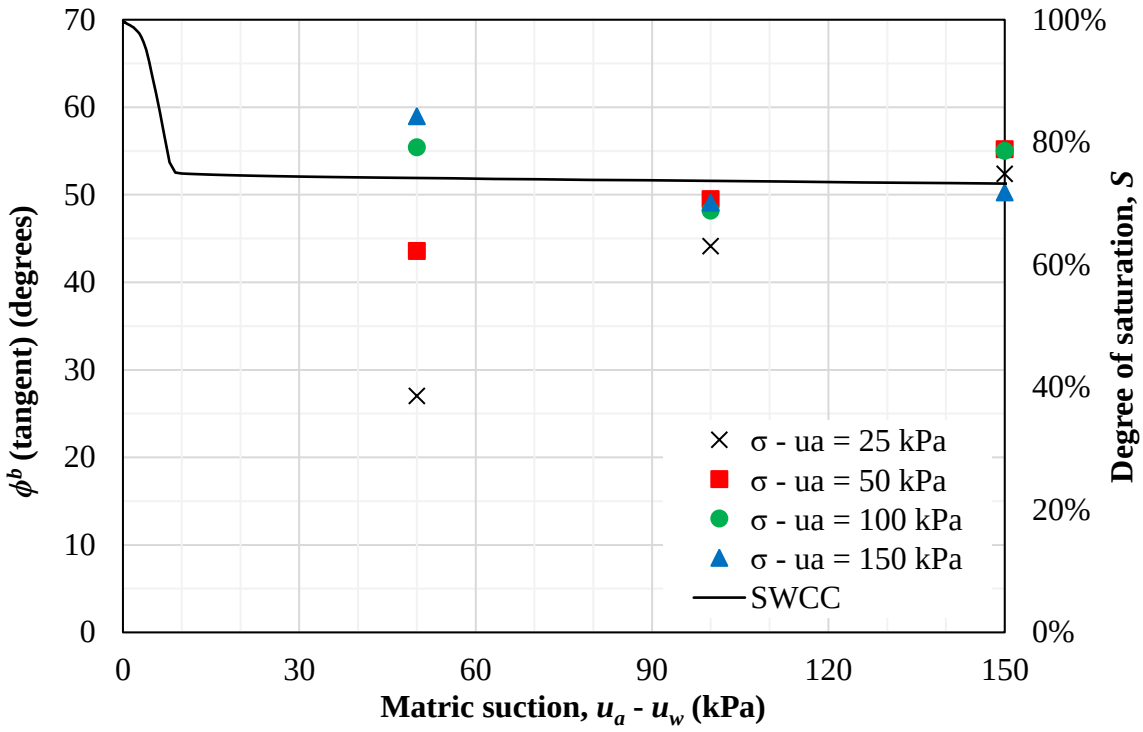

Figure C.112. Variation of the angle ϕ^b tangent as function of the matric suction (u_a - u_w) for soil 5R at maximum or peak failure

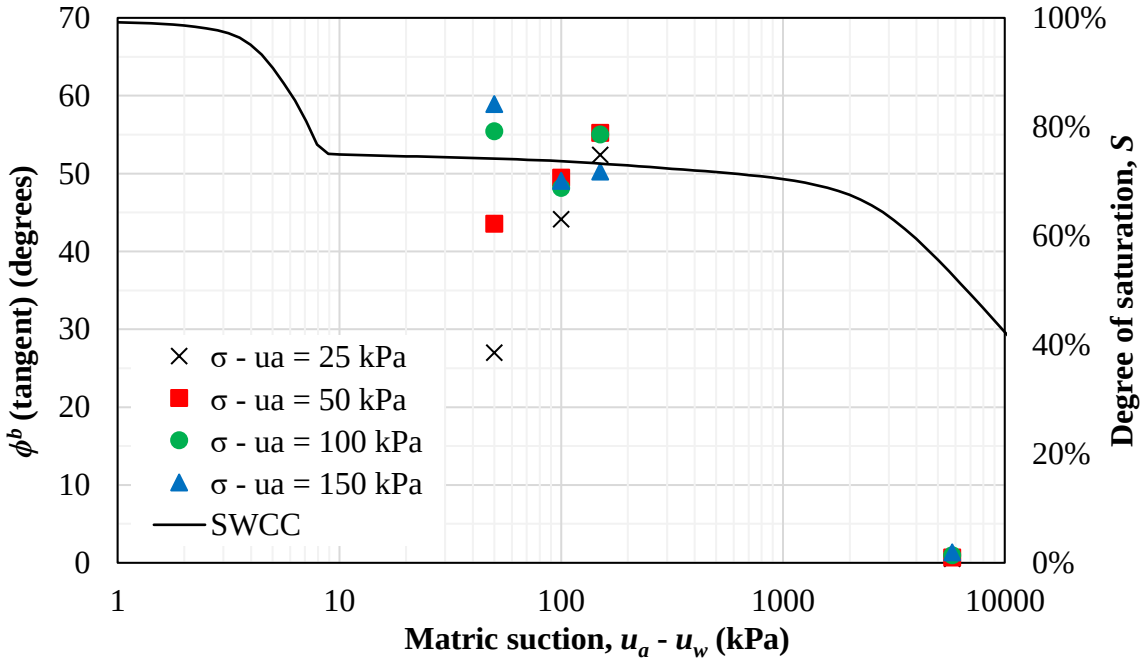

Figure C.113. Variation of the angle ϕ^b tangent as function of the matric suction (u_a - u_w) for soil 5R in monolog scale at maximum or peak failure

The data from Table C.21 were fitted using the Modified Bi-Hyperbolic model for low (≤ 150 kPa) and all matric suctions. The fitting parameters are presented in Table C.22. For low suctions, the goodness-of-fit obtained are R^2 = 0.971 and RMSE = 13.7 whereas for all suctions are R^2 = 0.939 and RMSE = 27.1. Although the values of R^2 are relatively high, the respective mean errors of 10.2 and 15.9% as well the dispersion showed in Figs. C.114 and C.115 indicates that the Modified Bi-Hyperbolic model is inadequate to represent the shear strength envelope for this material.

Table C.22. Parameters obtained for the Modified Bi-Hyperbolic model at maximum or peak failure

	Low suctions	All suctions
c' (kPa)	0.0	0.0
ϕ' (degrees)	32.1	35.2
ϕ^b (degrees)	48.7	62.7
τ_{ult1} (kPa)	2.88×10^{10}	2.88E+10
τ_{ult2} (kPa)	3.86×10^{5}	2.69E+02
τ_{ult} (kPa)	0.0	17.6
τ_{peak} (kPa)	0.0	17.6
s_b	100.0	100.0
n	1.0	1.0
a_1	1.595	1.419
b_1	3.47×10^{-11}	3.47×10^{-11}
a_2	0.879	0.516
b_2	2.59×10^{-6}	3.72×10^{-3}

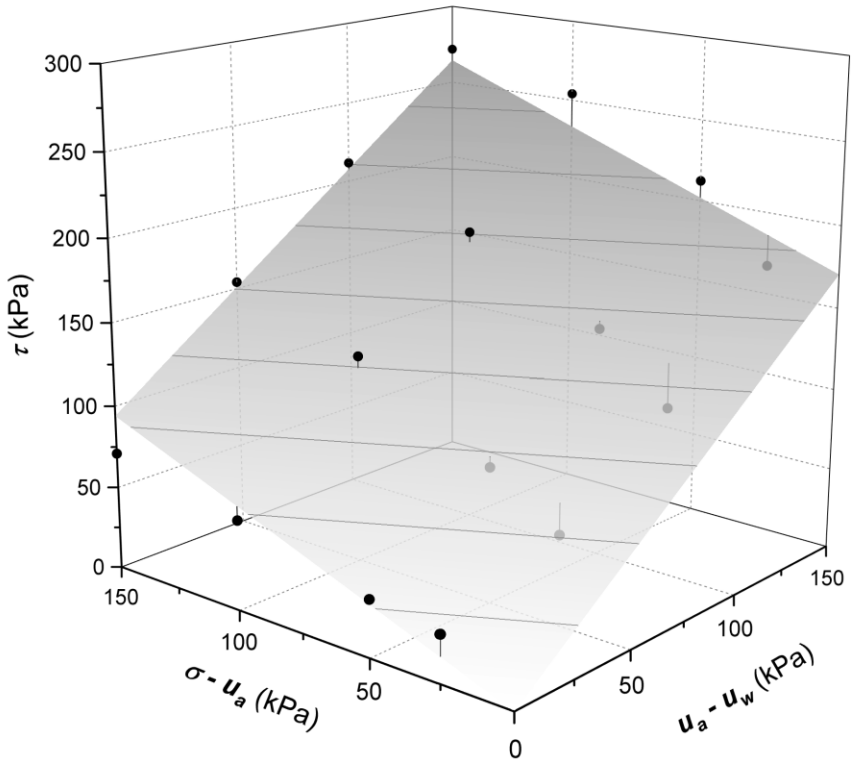

Figure C.114. Extended Mohr-Coulomb failure surface using the Modified Bi-Hyperbolic model for soil 5R at maximum or peak failure criterion for low suctions (≤ 150 kPa)

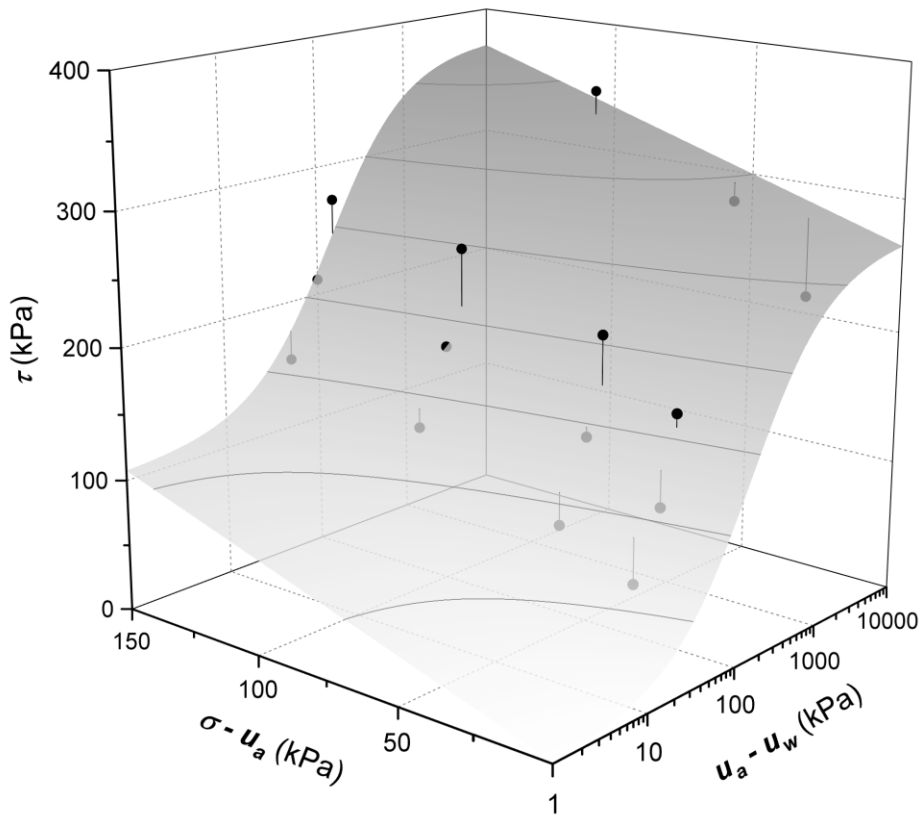

Figure C.115. Extended Mohr-Coulomb failure surface using the Modified Bi-Hyperbolic model for soil 5R at maximum or peak failure criterion for all suctions

- General comments

The graphs showing the horizontal displacement versus the shear stress indicate overall strain-hardening behavior (Figs. C.102 to C.106), with a few exceptions. In summary, the shear strength parameters considering maximum or peak shear stress as failure criterion indicate:

  - The angle ϕ^b is greater than ϕ' for net normal stresses of 100 and 150 kPa (Table C.21), except for suction of 5800 kPa;
  - The angle ϕ' increase with matric suction and decreases with net normal stress (Figs. C.110 and C.111);

- The angle ϕ^b increases with the net normal stress. The effect of the matric suction is dependent of the net normal stress. Higher net normal stresses cause decrease in ϕ^b as the matric suction increases whereas lower net normal stress results in increase of ϕ^b as the suction also increases. It seems that ϕ^b converges to a constant value around 53° close to matric suctions of 200 kPa (Fig. C.112);
- For high suctions over than the second air-entry value (2770 kPa), ϕ^b approaches zero (≈ 0.9°), as shown in Fig. C.113.

- Shear strength data: 6U
  - Initial void ratio (e_0) = 1.00
  - Type: modified direct shear
  - Shear velocity: 2.03×10^{-4} mm/s

i) $u_a - u_w$ = 0 kPa

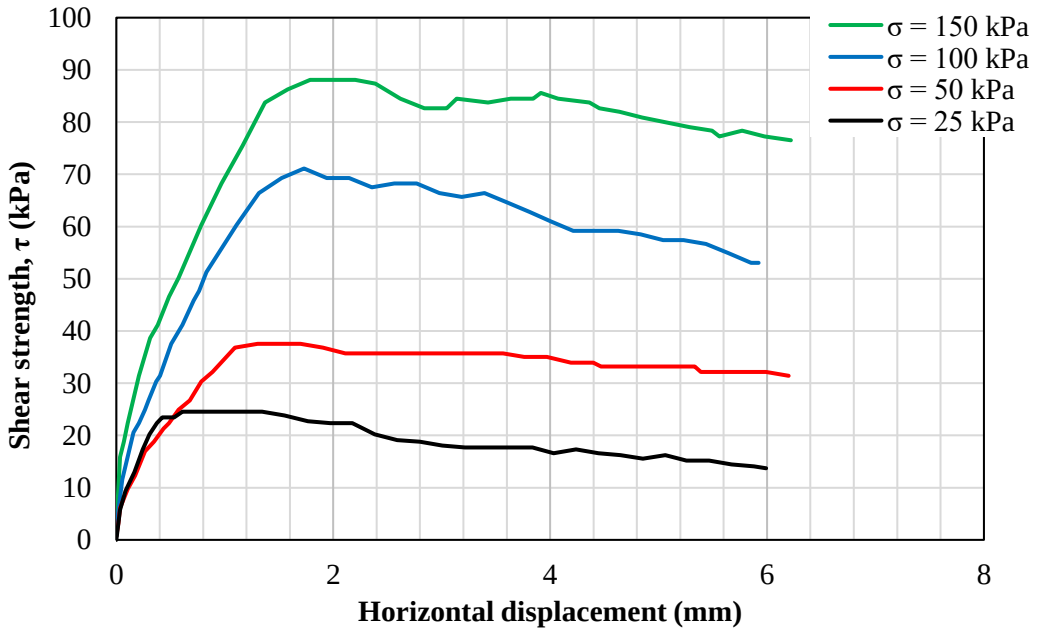

Figure C.116. Horizontal displacement versus shear strength of saturated tests of soil 6U

ii) $u_a - u_w$ = 50 kPa

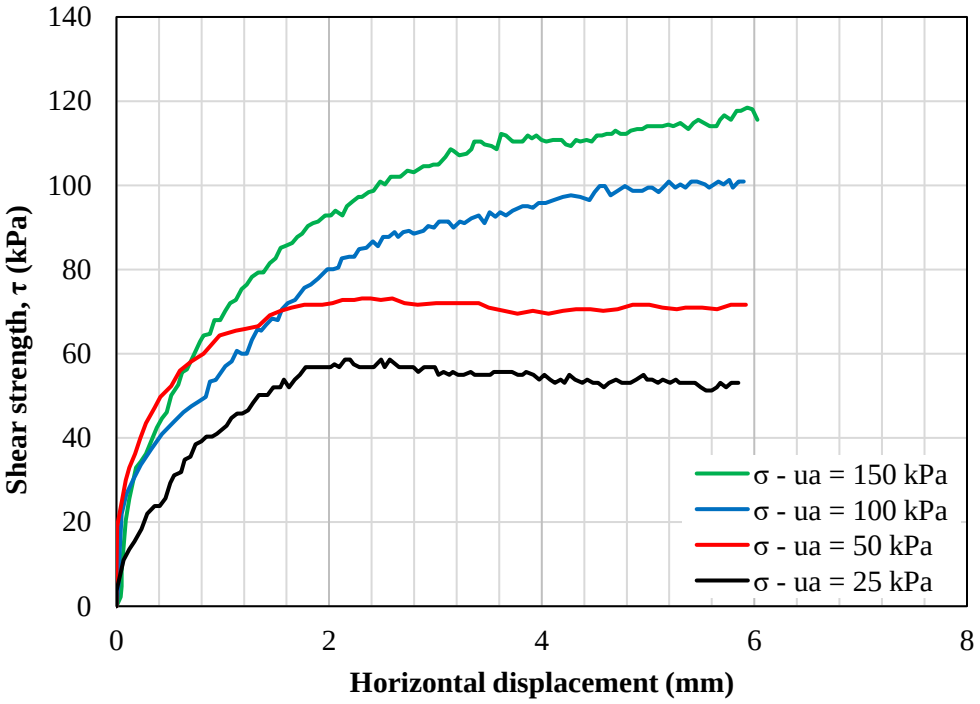

Figure C.117. Horizontal displacement versus shear strength of tests with (u_a - u_w) = 50 kPa of soil 6U

iii) $u_a - u_w$ = 100 kPa

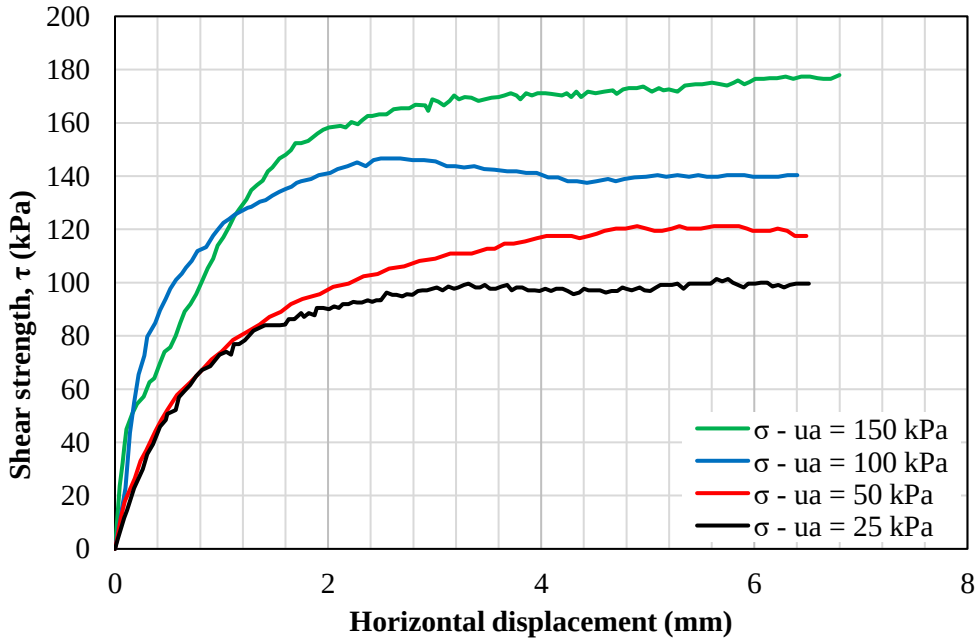

Figure C.118. Horizontal displacement versus shear strength of tests with (u_a - u_w) = 100 kPa of soil 6U

iv) $u_a - u_w$ = 150 kPa

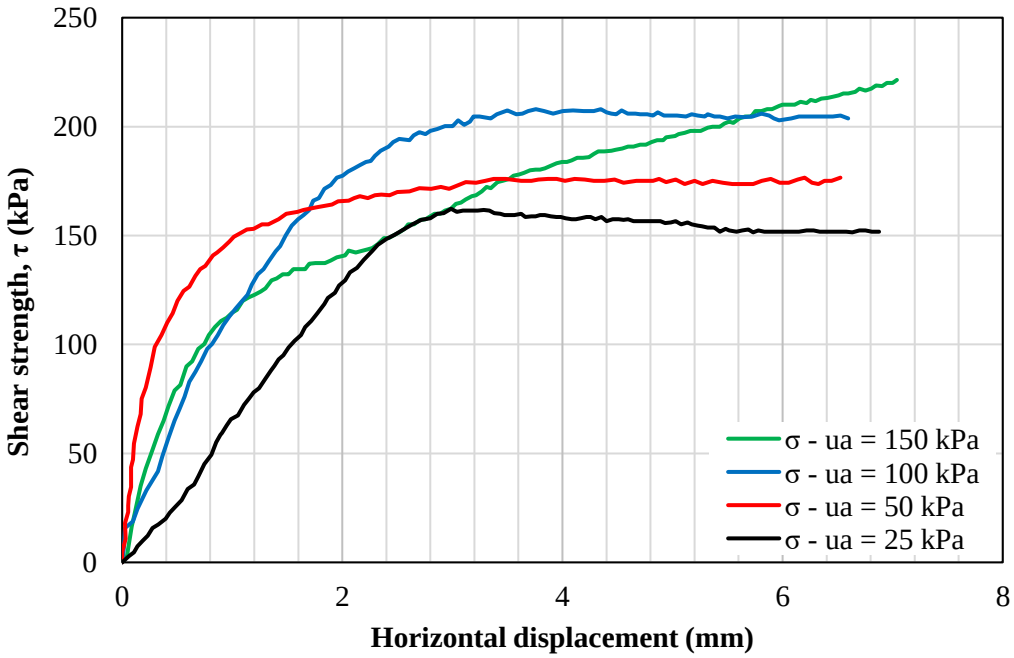

Figure C.119. Horizontal displacement versus shear strength of tests with (u_a - u_w) = 150 kPa of soil 6U

v) $u_a - u_w$ = 5600 kPa

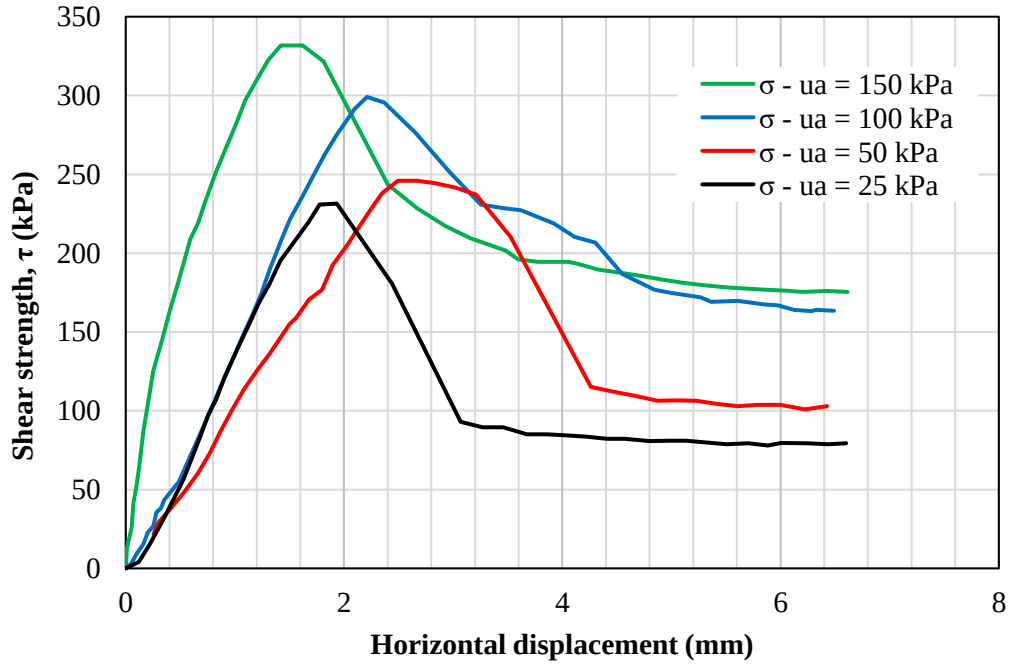

Figure C.120. Horizontal displacement versus shear strength of tests with (u_a - u_w) = 5600 kPa of soil 6U

- Failure criterion: maximum or peak shear stress

The data from the tests for maximum or peak shear stress as failure criterion is presented in Table C.23. The plot of the shear strength as function of the net vertical stress (Fig. C.121) indicates that ϕ' has a unique value for each matric suction. The values of ϕ' seems to quite dispersed, for suctions up to 150 kPa, ϕ' is on average 27.5°. For the suction of 5600 kPa, ϕ' is 39.9º. Also, the relationship between the matric suction and the shear strength depicted in Fig. C.122 points out that ϕ^b increases with the matric suction, except for suction of 5600 kPa. Moreover, the relation ϕ^b/ϕ' is always greater than 1 for matric suctions of 50, 100 and 150 kPa.

Table C.23. Shear strength parameters for soil 6U for maximum or peak failure criterion

τ (kPa)	σ - u_a (kPa)	u_a - u_w (kPa)	c_{app} (kPa)	ϕ'	ϕ^b (sec)	ϕ^b (tan)	ϕ^b/ϕ'
24.55	25	0	12.71	27.7			0.0
37.55	50						0.0
71.12	100						0.0
88.09	150						0.0
58.61	25	50	48.55	25.8	34.3	34.3	1.3
73.13	50				35.4	35.4	1.4
101.28	100				31.1	31.1	1.2
118.46	150				31.3	31.3	1.2
101.35	25	100	88.36	30.8	37.5	40.5	1.3
121.20	50				39.9	43.9	1.4
146.62	100				37.1	42.2	1.4
177.94	150				41.9	49.9	1.6
162.29	25	150	152.61	25.9	42.6	50.6	2.0
176.57	50				42.8	47.9	1.9
208.00	100				42.4	50.8	2.0
221.43	150				41.6	41.0	1.6
231.41	25	5600	209.05	39.9	2.1	0.7	0.0
245.91	50				2.1	0.7	0.0
299.08	100				2.3	1.0	0.0
331.77	150				2.5	1.2	0.0

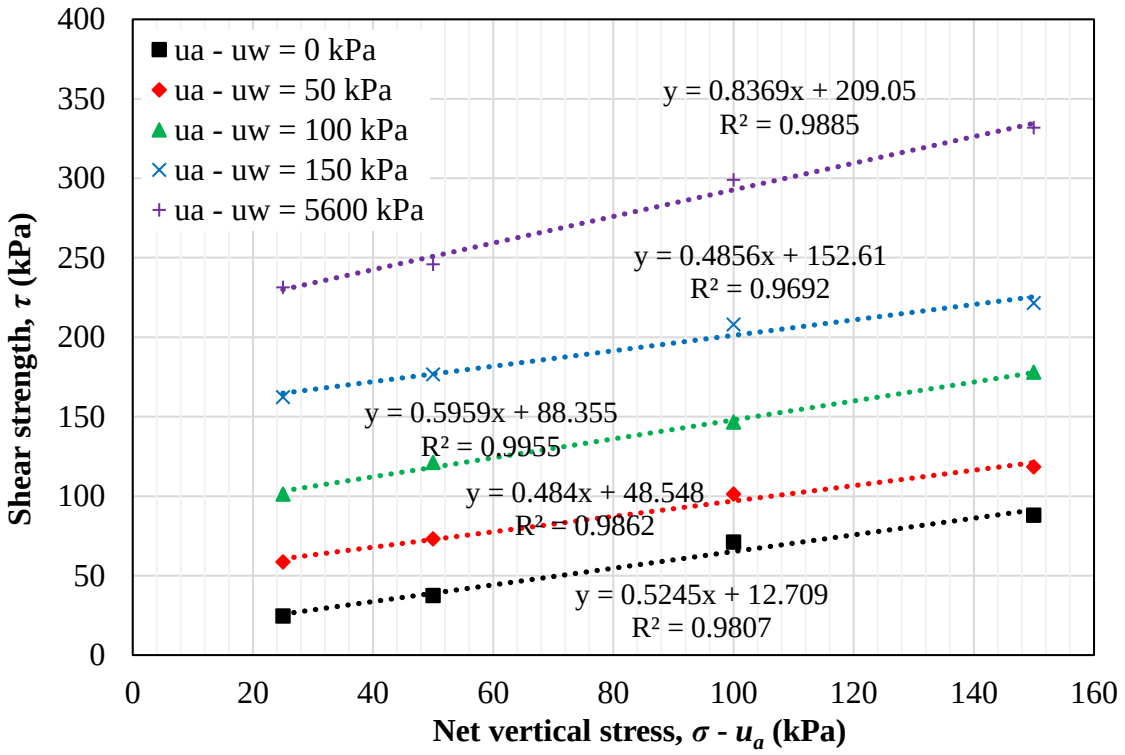

Figure C.121. Failure envelope in terms of net vertical stress (σ_v - u_a) and τ for soil 6U at maximum or peak failure

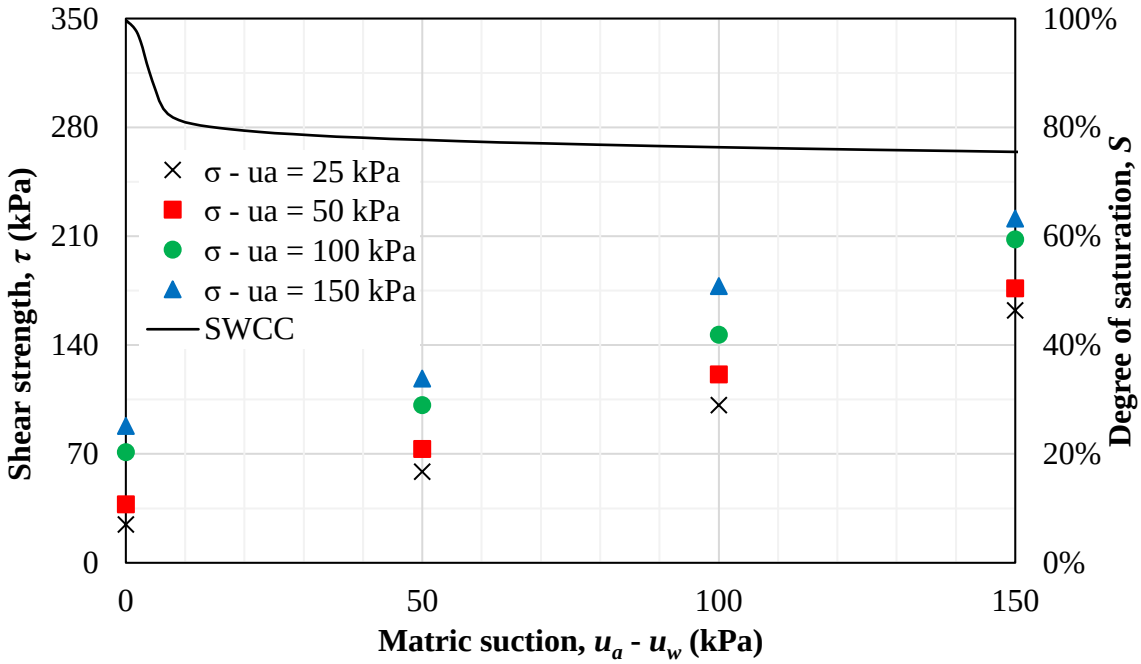

Figure C.6.122. Failure envelope in terms of matric suction (u_a - u_w) and τ for soil 6U at maximum or peak failure

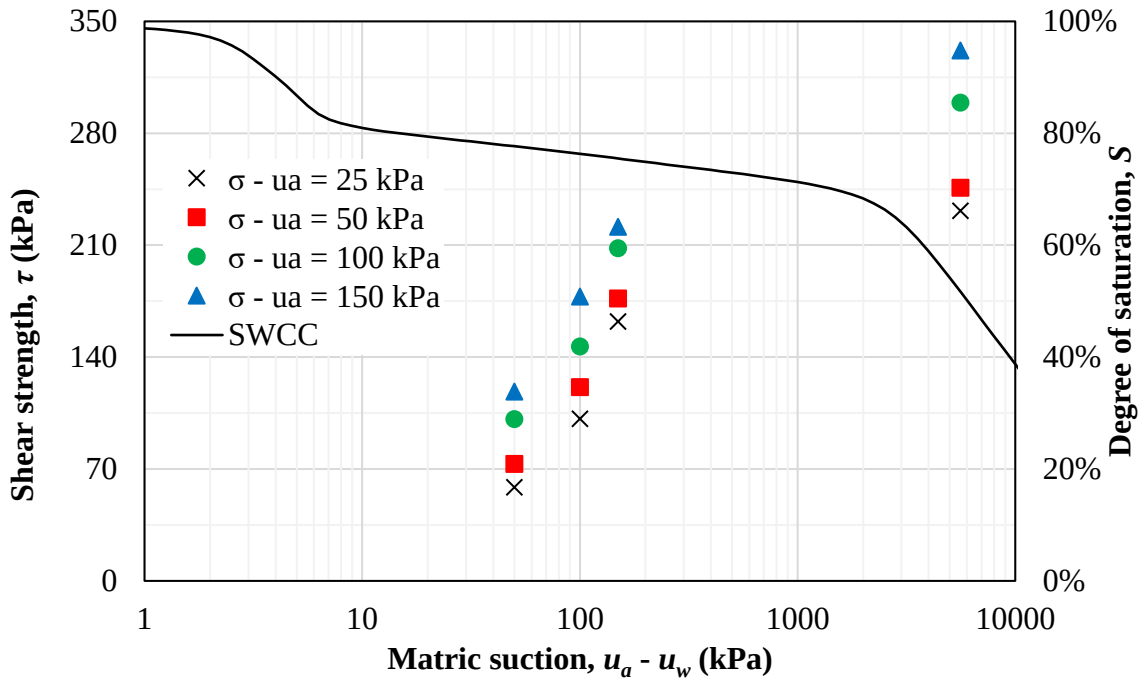

Figure C.123. Failure envelope in terms of matric suction (u_a - u_w) and τ for soil 6U at maximum or peak failure in monolog scale

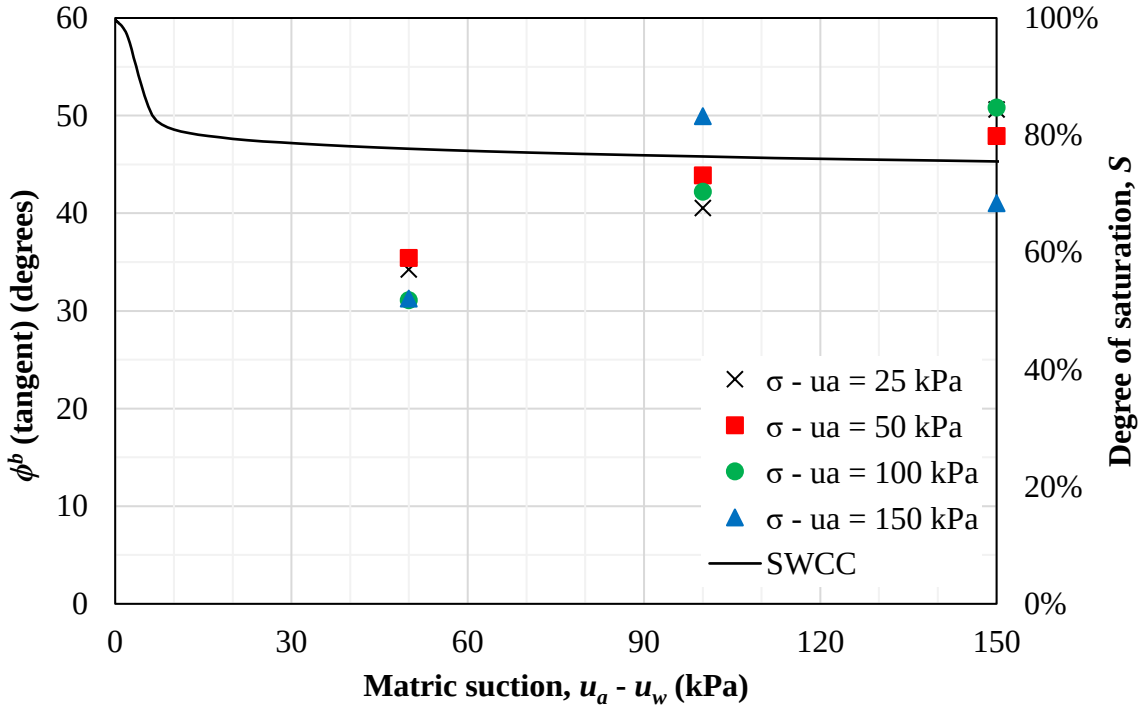

Figure C.124. Variation of the angle ϕ^b tangent as function of the matric suction (u_a - u_w) for soil 6U at maximum or peak failure

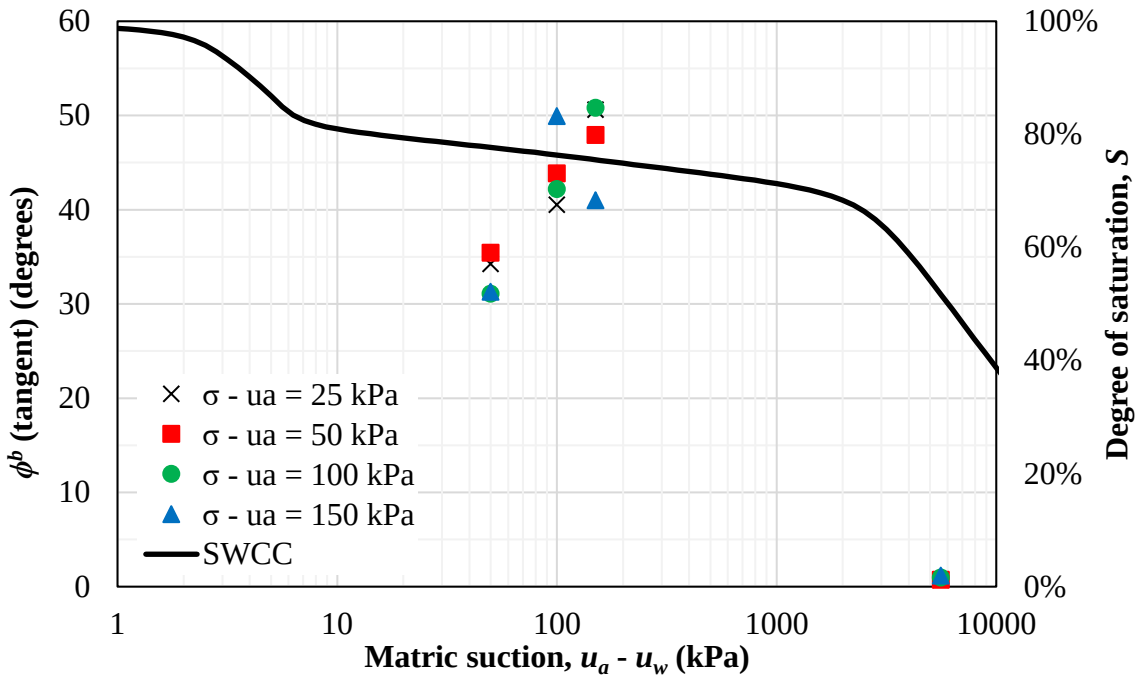

Figure C.125. Variation of the angle ϕb tangent as function of the matric suction (u_a - u_w) for soil 6U at maximum or peak failure in monolog scale

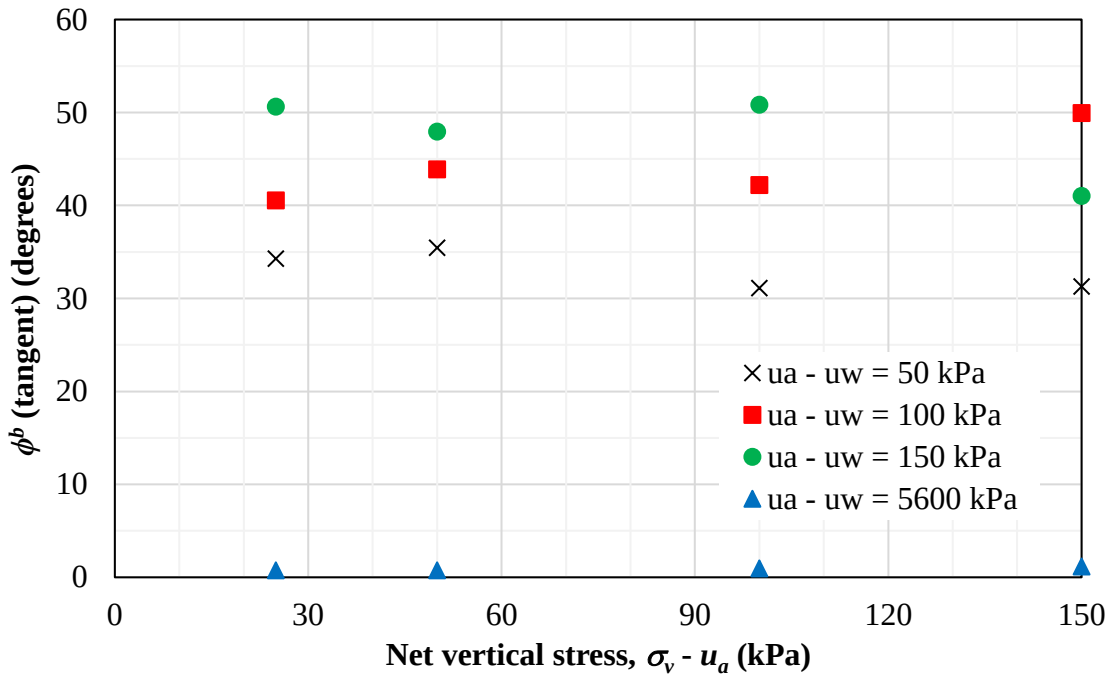

Figure C.126. Variation of the angle ϕb tangent as function of the net vertical stress (σ_v -u_a) for soil 6U at maximum or peak failure

The data from Table C.23 were fitted using the Modified Bi-Hyperbolic model for low (≤ 150 kPa) and all matric suctions. The fitting parameters are presented in Table C.24. For low suctions, the R^2 and RMSE are respectively 0.987 and 6.6 whereas for all suctions, they are 0.988 and 9.1, respectively. These goodness-of-fit points out to mean errors of 5.6 and 6.1%, respectively. The extended Mohr-Coulomb failure surfaces for low and all matric suctions are depicted in Fig. C.127 and C.128, respectively.

Table C.24. Parameters obtained for the Modified Bi-Hyperbolic model for maximum or peak shear strength

	Low suctions	All suctions
c' (kPa)	0.0	0.0
ϕ' (degrees)	38.0	30.7
ϕ^b (degrees)	42.5	43.4
τ_{ult1} (kPa)	2.89×10^{2}	3.43E+5
τ_{ult2} (kPa)	2.34×10^{9}	5.94E+3
τ_{ult} (kPa)	0.0	0.0
τ_{peak} (kPa)	859.4	859.7
s_b	48463.4	2034.1
n	134.1	2.4
a_1	1.279	1.687
b_1	3.46×10^{-3}	2.92×10^{-6}
a_2	1.092	1.056
b_2	4.27×10^{-10}	1.68×10^{-4}

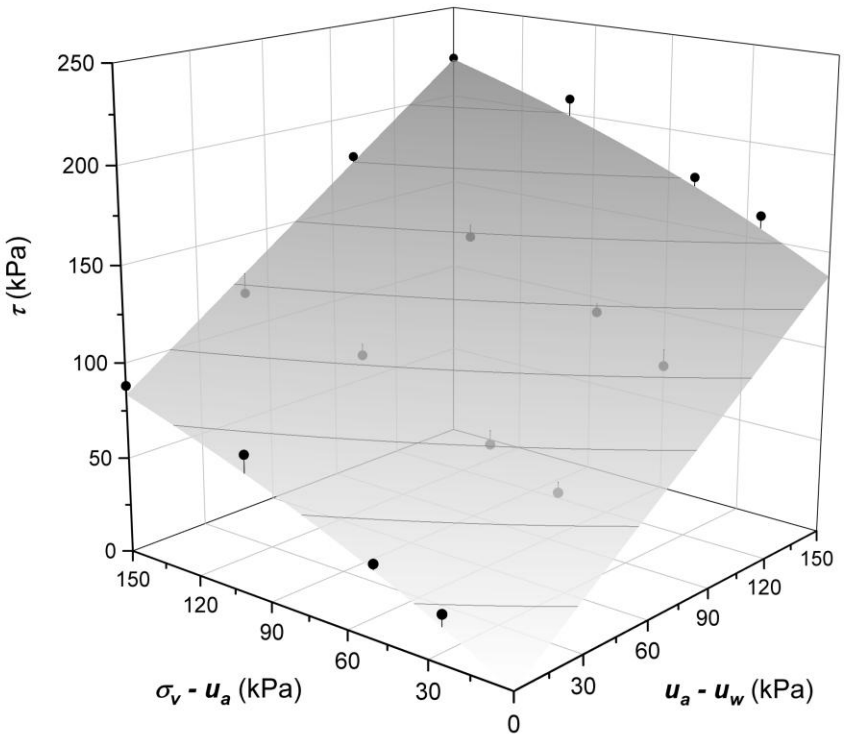

Figure C.127. Extended Mohr-Coulomb failure surface fitted using the Modified Bi-Hyperbolic model of soil #6U for low matric suctions (≤ 150 kPa) at maximum or peak failure

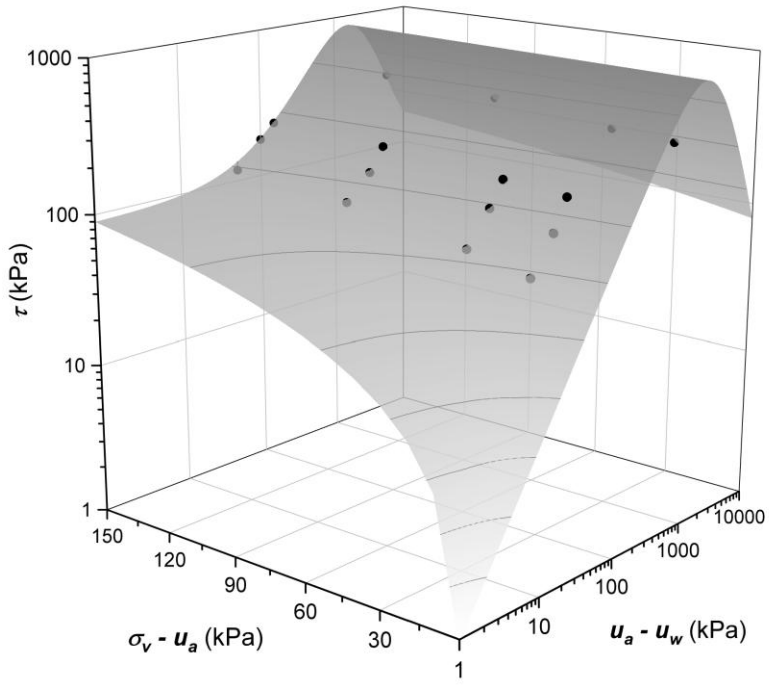

Figure C.128. Extended Mohr-Coulomb failure surface fitted using the Modified Bi-Hyperbolic model of soil #6U for all matric suctions at maximum or peak failure

- General comments

The graphs showing axial strain versus deviator stress indicate that most of the curves presented strain-hardening behavior (Figs. C.116 to C.119). For suction of 5600 kPa, the curves showed a clear peak (Fig. C.120). In summary, the shear strength parameters considering peak shear strength as failure criterion points out:

v. The angle ϕ^b is greater than ϕ' for matric suctions of 50, 100 and 150 kPa (Table C.23);

vi. The angle ϕ' seems to be relatively constant around 27.5° for suctions up to 150 kPa. When suction is 5600 kPa, ϕ' is 39.9º (Figs. C.124 and C.125);

vii. The angle ϕ^b increases with matric suction up, except for suction of 5600 kPa.

viii. For high suctions over than the second air-entry value (2800 kPa), ϕ^b is on average 0.9° (Fig. C.125).

C.6 Pereira (1996) – 6R

- Soil basic information and characteristics
  - Void ratio (e_0) = 0.76
  - Density of solids (ρ_s) = 2.64
  - Dry density (ρ_d) = 1.50
  - Liquid limit (w_L) = 29%
  - Plasticity limit (w_P) = 17%
  - USCS = SW-SM (disaggregated) / SC (aggregated)

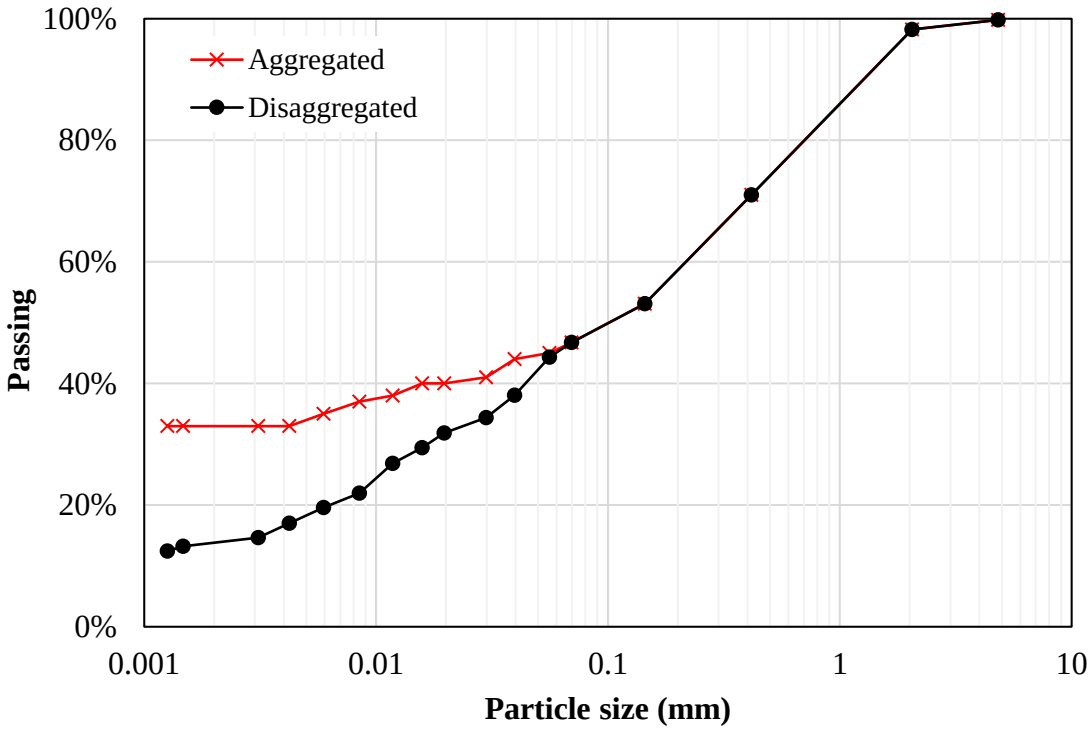

Figure C.129. Grain-size distribution curve of soil 6R

- Soil-water characteristic curve

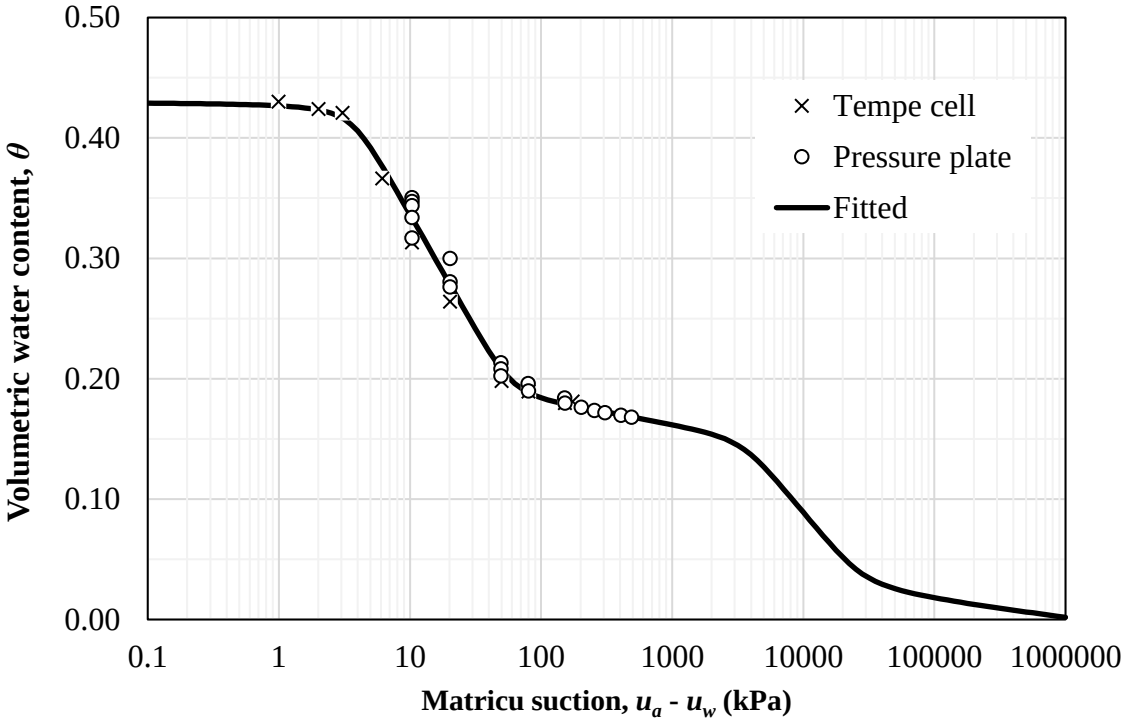

Figure C.130. Soil-water characteristic curve of soil 6R

- Shear strength data
  - Initial void ratio (e_0) = 0.76
  - Type: modified direct shear
  - Shear velocity: 2.78×10^{-5} mm/s

i) $u_a - u_w$ = 0 kPa

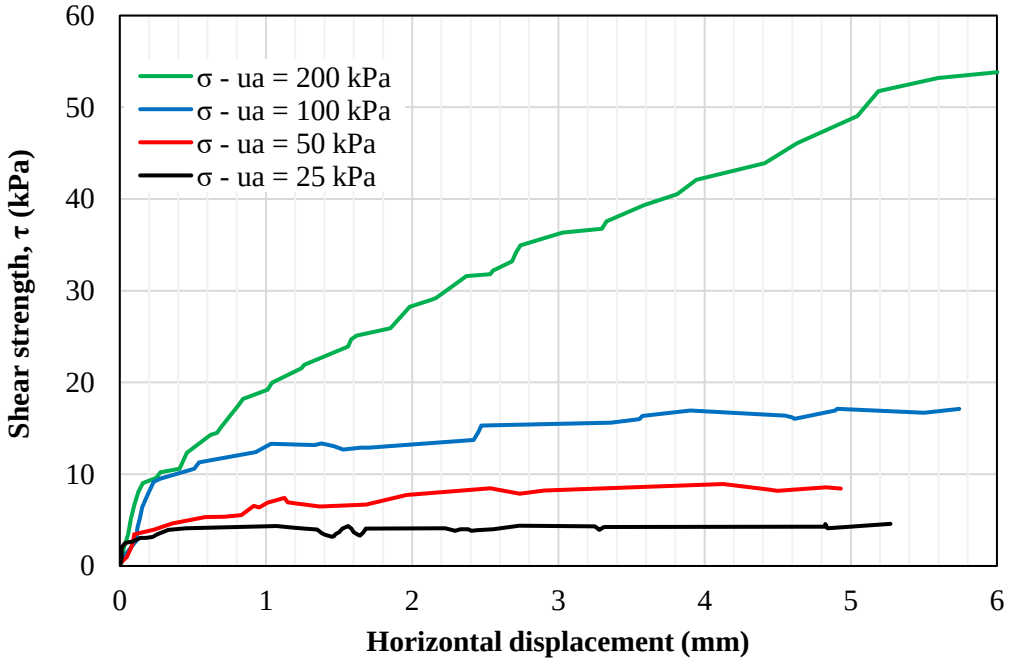

Figure C.131. Horizontal displacement versus shear strength of saturated tests of soil 6R

ii) $u_a - u_w$ = 25 kPa

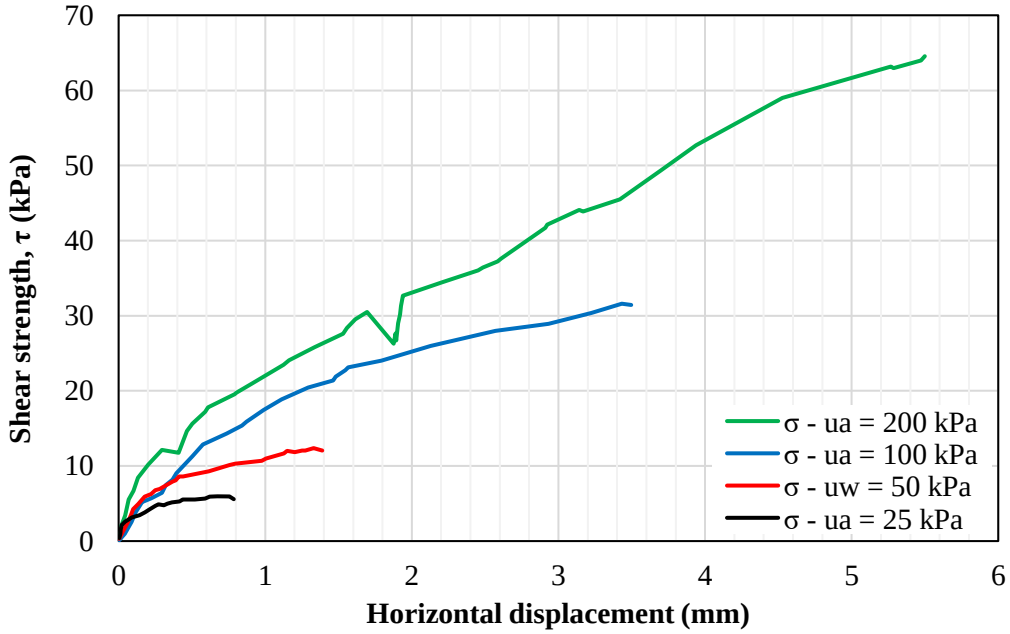

Figure C.132. Horizontal displacement versus shear strength of tests with (u_a - u_w) = 25 kPa of soil 6R

iii) $u_a - u_w$ = 50 kPa

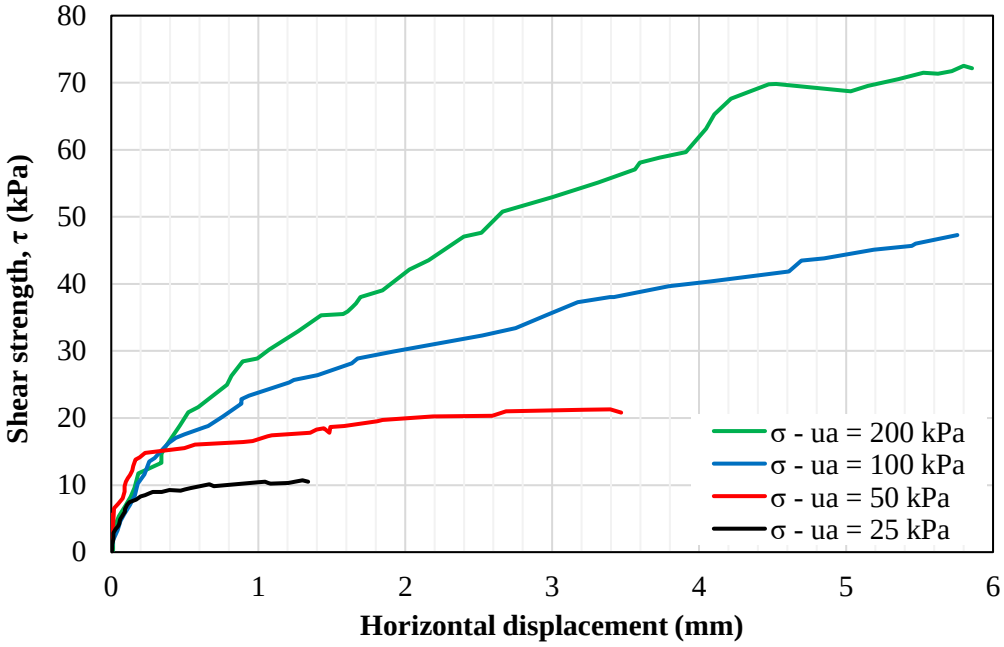

Figure C.133. Horizontal displacement versus shear strength of tests with (u_a - u_w) = 50 kPa of soil 6R

iv) $u_a - u_w$ = 100 kPa

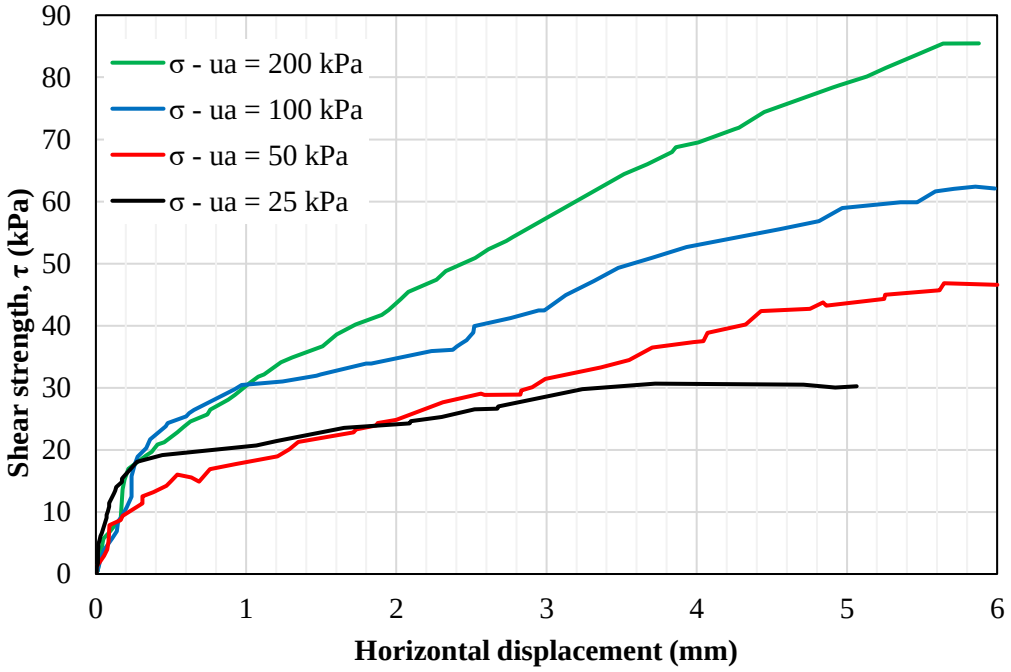

Figure C.134. Horizontal displacement versus shear strength of tests with (u_a - u_w) = 100 kPa of soil 6R

- Failure criterion: maximum shear stress

The data from the tests for maximum shear stress as failure criterion are presented in Table C.25. The plot of the shear strength as function of the net vertical stress (Fig. C.135) indicates that ϕ' varies with the matric suction and the net vertical stress. The angles ϕ^b and ϕ' were calculated assuming the saturated condition (i.e., secant) and the previous matric suction (i.e. tangent) as reference. Moreover, the relation ϕ^b/ϕ' for tangent angles is greater than 1 for high levels of net vertical stresses.

Table C.25. Shear strength parameters for soil 6R at maximum shear stress

τ (kPa)	$\sigma - u_a$ (kPa)	$u_a - u_w$ (kPa)	c_{app} (kPa)	ϕ' (tan)	ϕ' (sec)	ϕ^b (tan)	ϕ^b (sec)	ϕ^b(tan)/ ϕ'(tan)
4.6	25	0	3.8	1.8	1.8			
8.9	50			9.8	5.9			
17.1	100			9.3	7.6			
53.8	200			20.2	14.0			
5.9	25	25	0.0	13.4	13.4	3.1	3.1	0.2
12.4	50			14.4	13.9	7.8	7.8	0.5
31.6	100			21.0	17.5	30.1	30.1	1.4
64.6	200			18.2	17.9	23.2	23.2	1.3
10.7	25	50	0.0	23.2	23.2	10.8	7.0	0.5
21.3	50			22.9	23.1	19.6	13.9	0.9
47.3	100			27.5	25.3	32.1	31.1	1.2
72.5	200			14.2	19.9	17.7	20.5	1.2
30.7	25	100	18.7	25.5	25.5	21.8	14.6	0.9
46.8	50			32.9	29.3	27.1	20.8	0.8
62.4	100			17.3	23.6	16.8	24.4	1.0
85.5	200			13.0	18.4	14.5	17.6	1.1

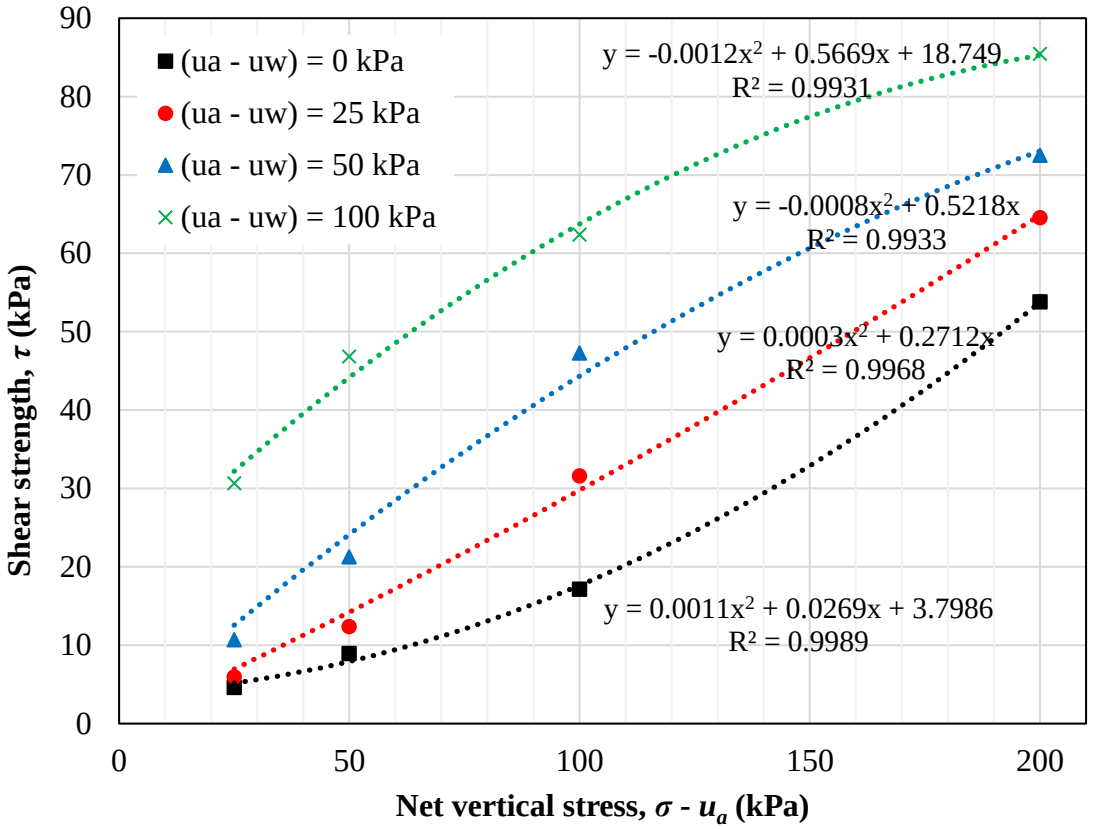

Figure C.135. Failure envelope in terms of net vertical stress (σ_v - u_a) and τ for soil 6R

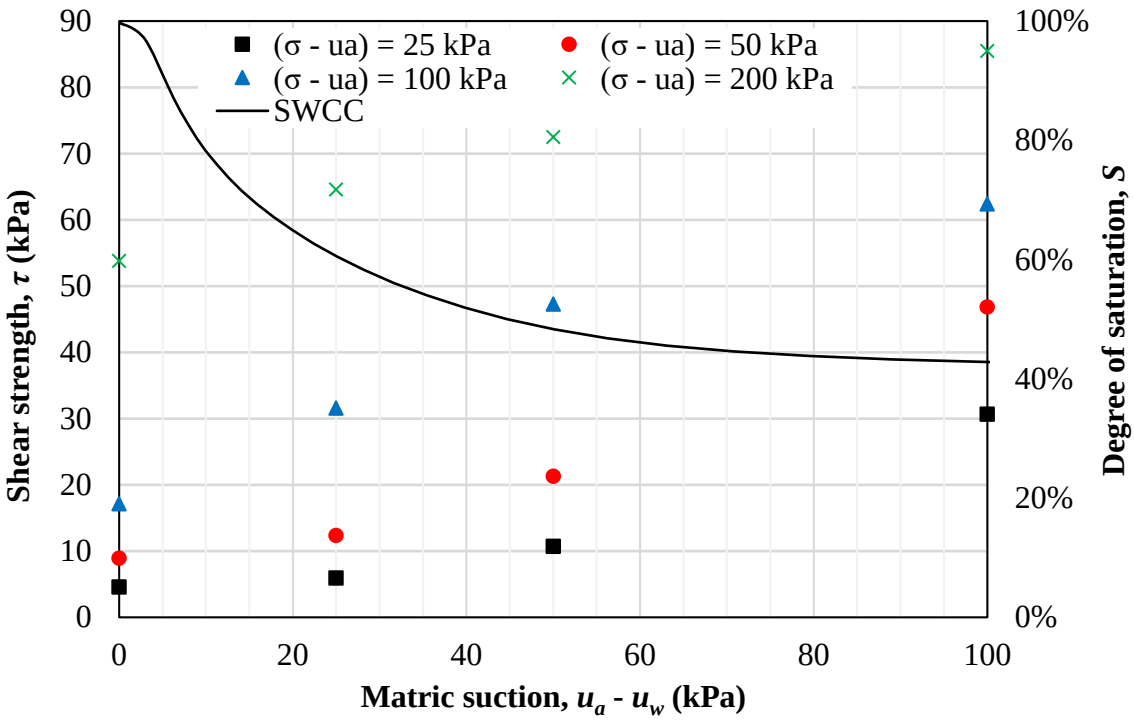

Figure C.136. Failure envelope in terms of matric suction ($u_a - u_w$) and τ for soil 6R

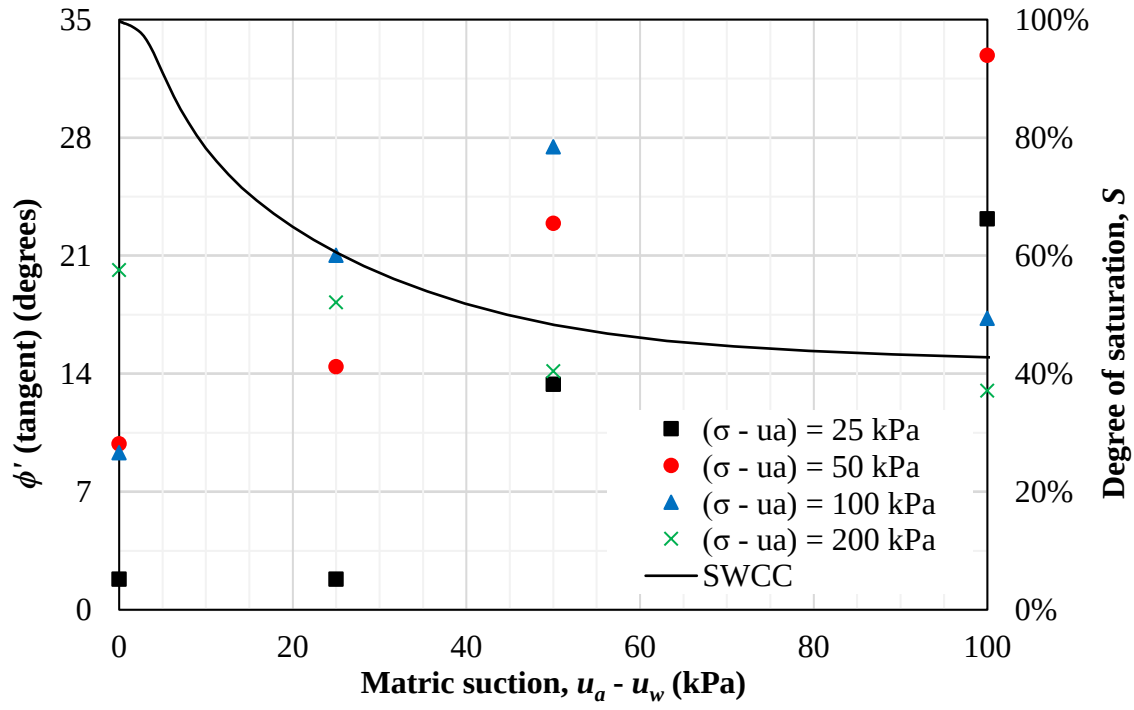

Figure C.137. Variation of the angle ϕ' tangent as function of the matric suction (u_a - u_w) for soil 6R

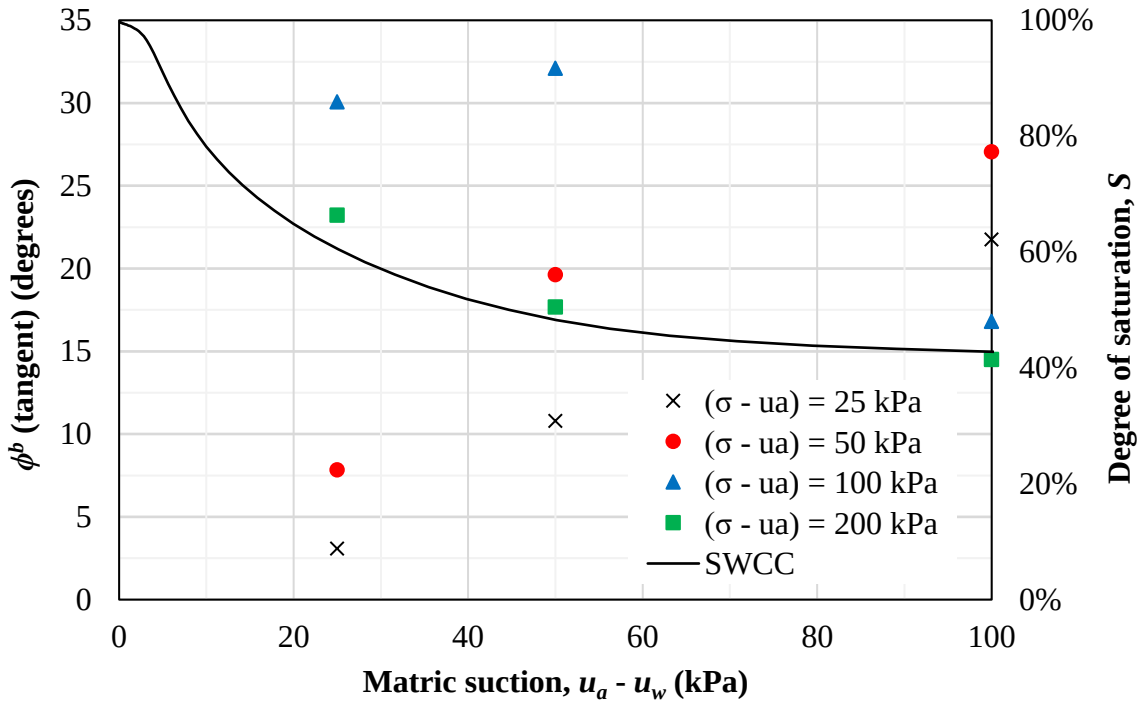

Figure C.138. Variation of the angle ϕ^b tangent as function of the matric suction (u_a - u_w) for soil 6R

The data from Table C.25 were fitted using the Modified Bi-Hyperbolic model. The fitting parameters are presented in Table C.26. The extended Mohr-Coulomb failure surface is shown in Fig. C.139. The goodness-of-fit obtained are R^2 = 0.975 and RMSE = 6.0. Although the R^2 is high, the mean error of 16.6% as well the dispersion showed in Fig. C.139 indicates that the Modified Bi-Hyperbolic model is inadequate to represent the shear strength envelope for this material.

Table C.26. Parameters obtained for the Modified Bi-Hyperbolic model for peak shear strength

c' (kPa)	0.0	s_b	50.0
ϕ' (degrees)	15.3	n	20.0
ϕ^b (degrees)	16.0	a_1	3.660
τ_{ult1} (kPa)	1.00E+07	b_1	$1.00x10^{-7}$
τ_{ult2} (kPa)	1.00E+07	a_2	3.487
τ_{ult} (kPa)	1999.9	b_2	$1.00x10^{-7}$
τ_{peak} (kPa)	1999.9		

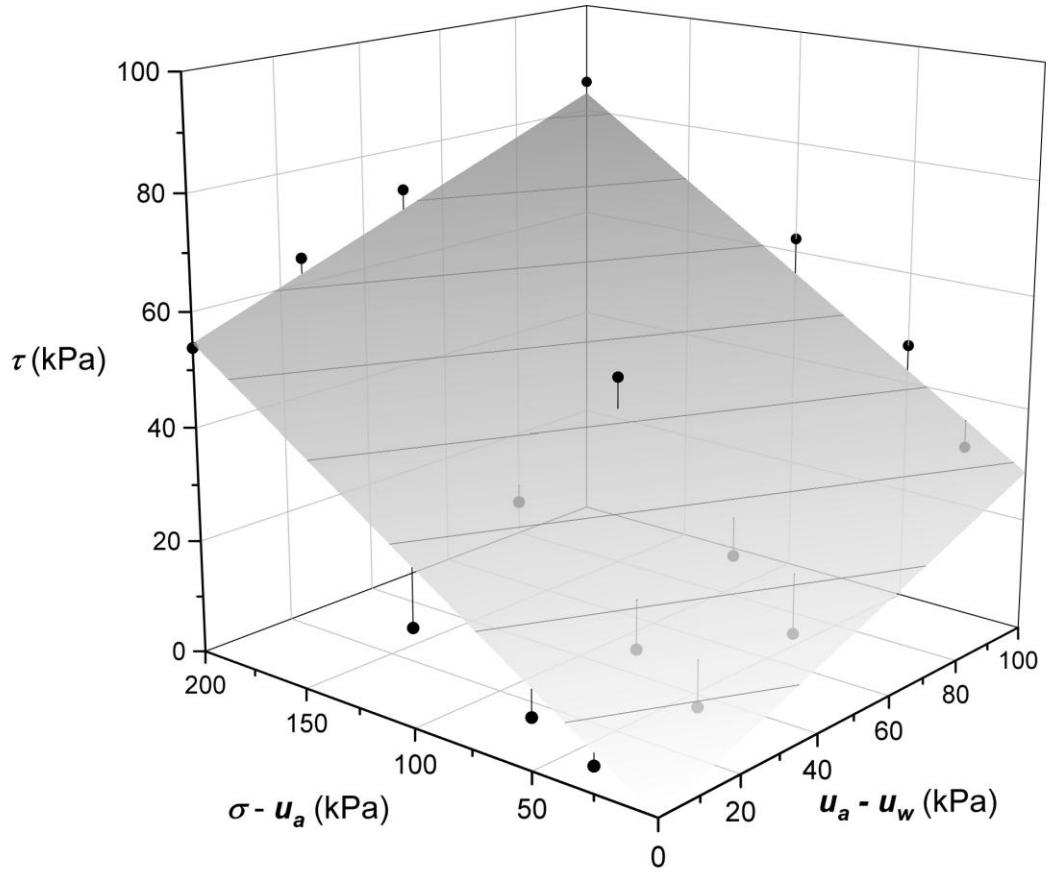

Figure C.139. Extended Mohr-Coulomb failure surface using the Modified Bi-Hyperbolic model for soil 6R

- General comments

The graphs showing the horizontal displacement versus the shear stress indicate strain-hardening behavior (Figs. C.131 to C.134). In summary, the shear strength parameters considering maximum shear strength as failure criterion indicate:

  - The angle ϕ^b is greater than ϕ' for net normal stresses of 100 and 200 kPa (Table C.25);
  - Both angles ϕ' and ϕ^b tangent seems to increase with suction and net normal stress. At some point between net normal stresses of 100 and 200 kPa

combined to matric suctions between 50 and 100 kPa, the soil exhibits an opposite behavior with ϕ' and ϕ^b decreasing (Figs. C.114 and C.115);

- It worth mentioning that the first air-entry value and the first residual suction are 4 and 58 kPa, respectively (Fig. C.107). Therefore, the change in the soil behavior mentioned in (ii) probably took place at a matric suction with the transition between the desaturation of the macro and micropores.

C.7 Kühn (2014) – 7R

- Soil basic information and characteristics
  - Void ratio (e_0) = 0.70
  - Density of solids (ρ_s) = 2.73
  - Dry density (ρ_d) = 1.61
  - Liquid limit (w_L) = 45%
  - Plasticity limit (w_P) = 27%
  - USCS = CL (disaggregated) / SM (aggregated)

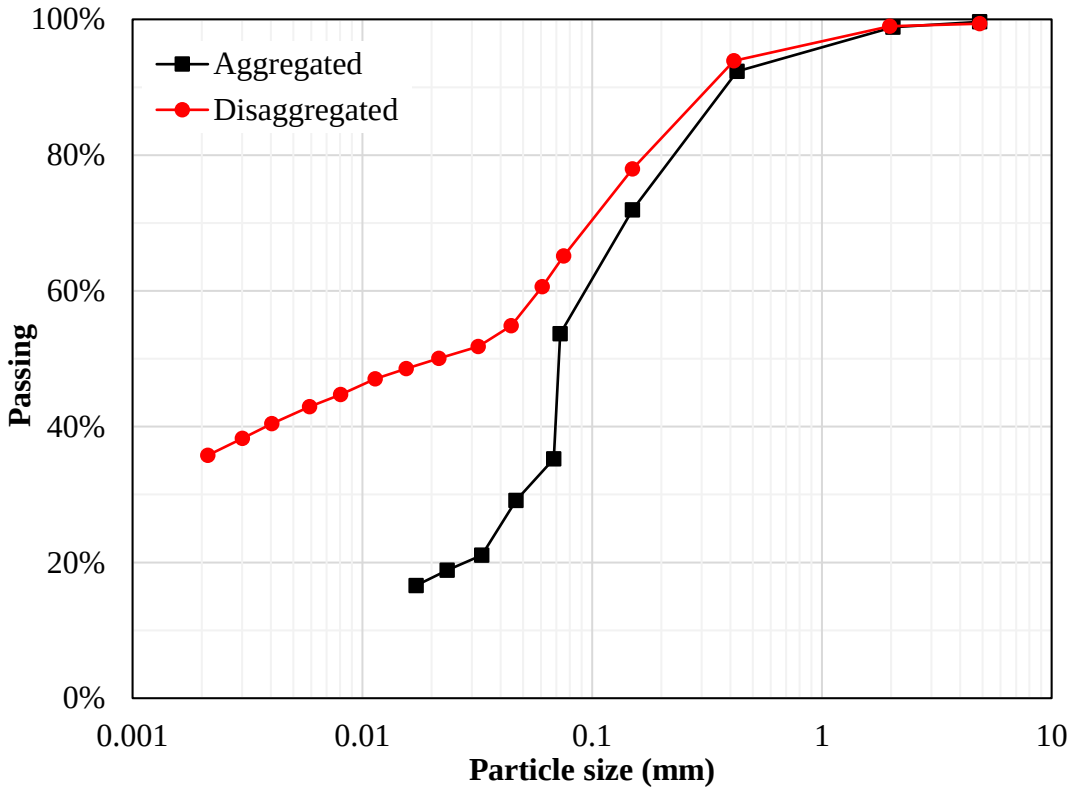

Figure C.140. Grain-size distribution curve of soil 7R

- Soil-water characteristic curve

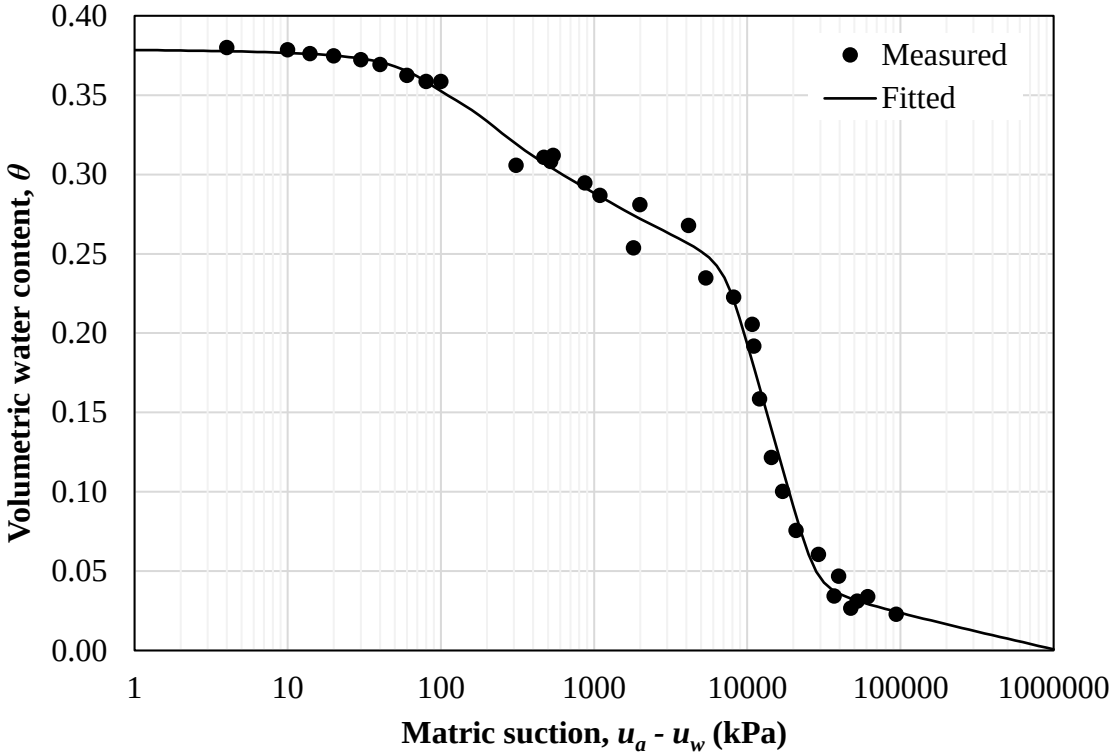

Figure C.141. Soil-water characteristic curve of soil 7R

- Shear strength data
  - Initial void ratio (e_0) = 0.641
  - Type: modified triaxial CD and CW, and BT
  - Volume measurement: double walled cell
  - Shear velocity: 3.96×10^{-3} mm/min (CD); 6.355×10^{-2} mm/min (CW)

i) $u_a - u_w$ = 0 kPa

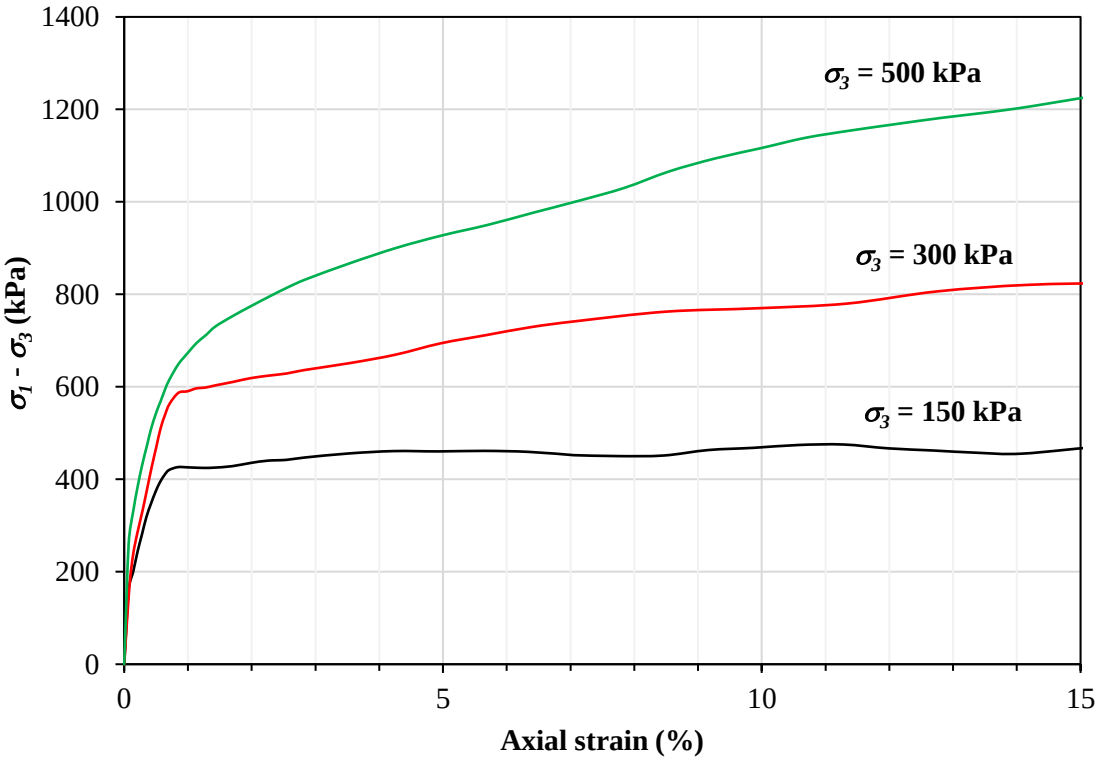

Figure C.142. Axial strain versus deviator stress of saturated triaxial tests of soil 7R

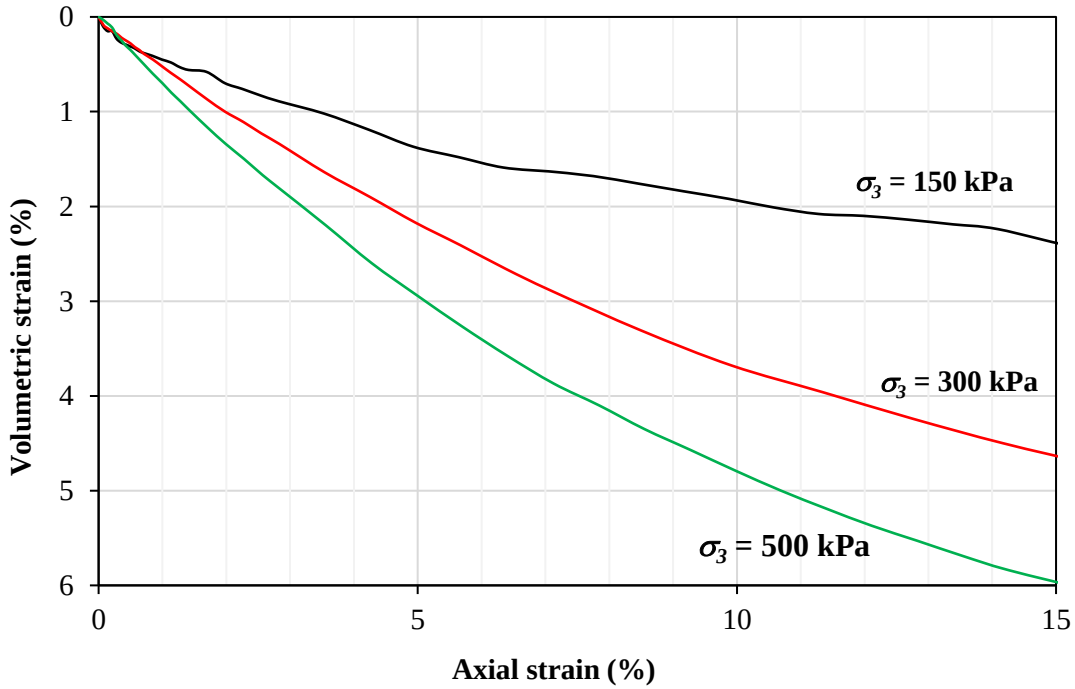

Figure C.143. Axial versus volumetric strain of saturated triaxial tests of soil 7R

ii) $u_a - u_w$ = 100 kPa (CD)

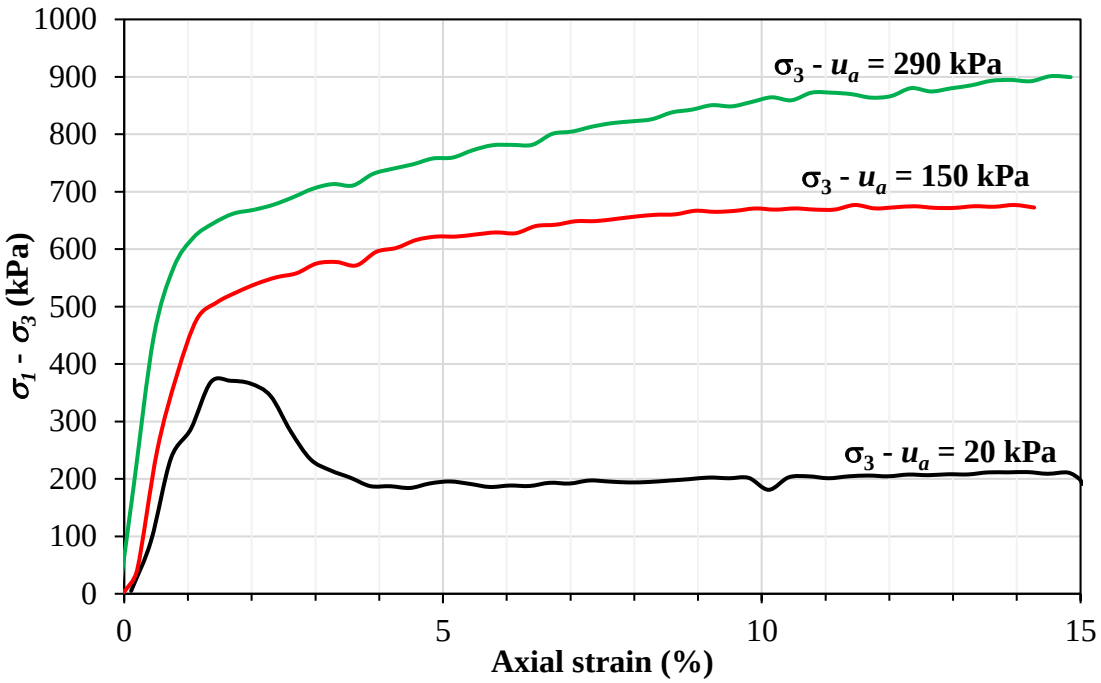

Figure C.144. Axial strain versus deviator stress for tests with (u_a - u_w) = 100 kPa of soil 7R

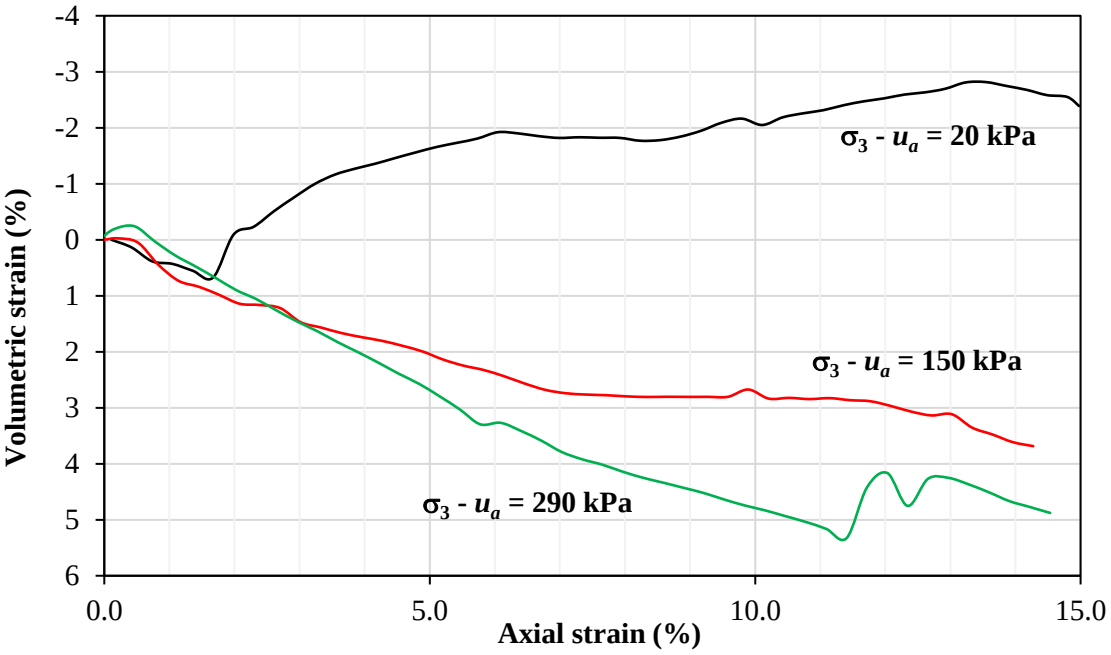

Figure C.145. Axial versus volumetric strain for tests with (u_a - u_w) = 100 kPa of soil 7R

iii) $u_a - u_w$ = 200 kPa (CD)

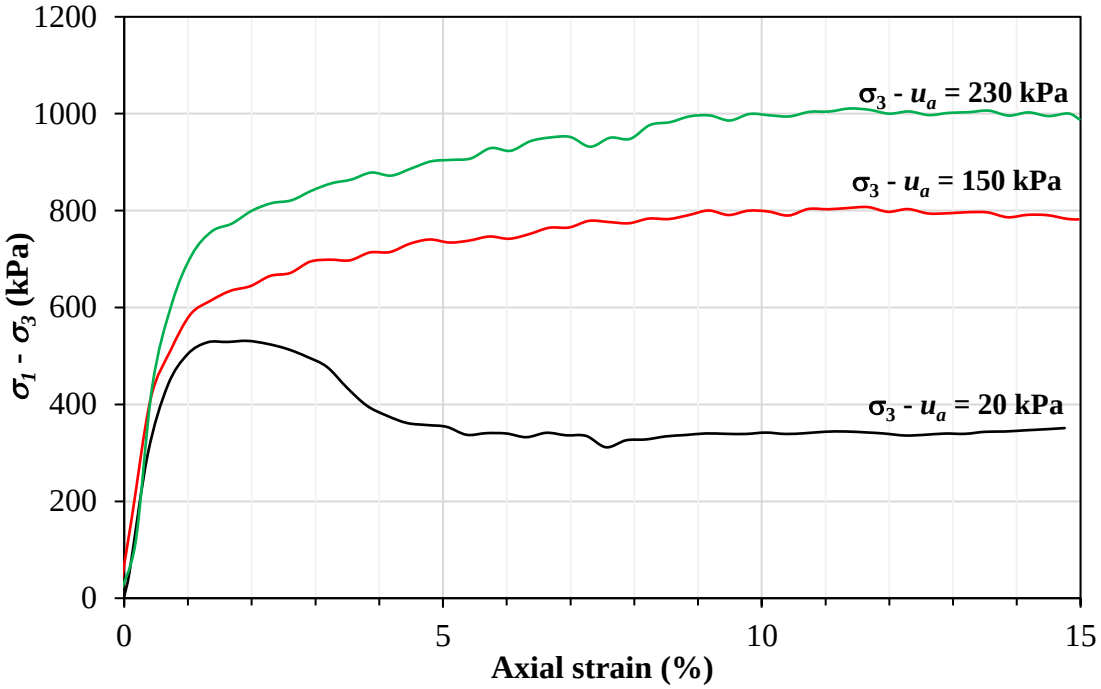

Figure C.146. Axial strain versus deviator stress for tests with (u_a - u_w) = 200 kPa of soil 7R

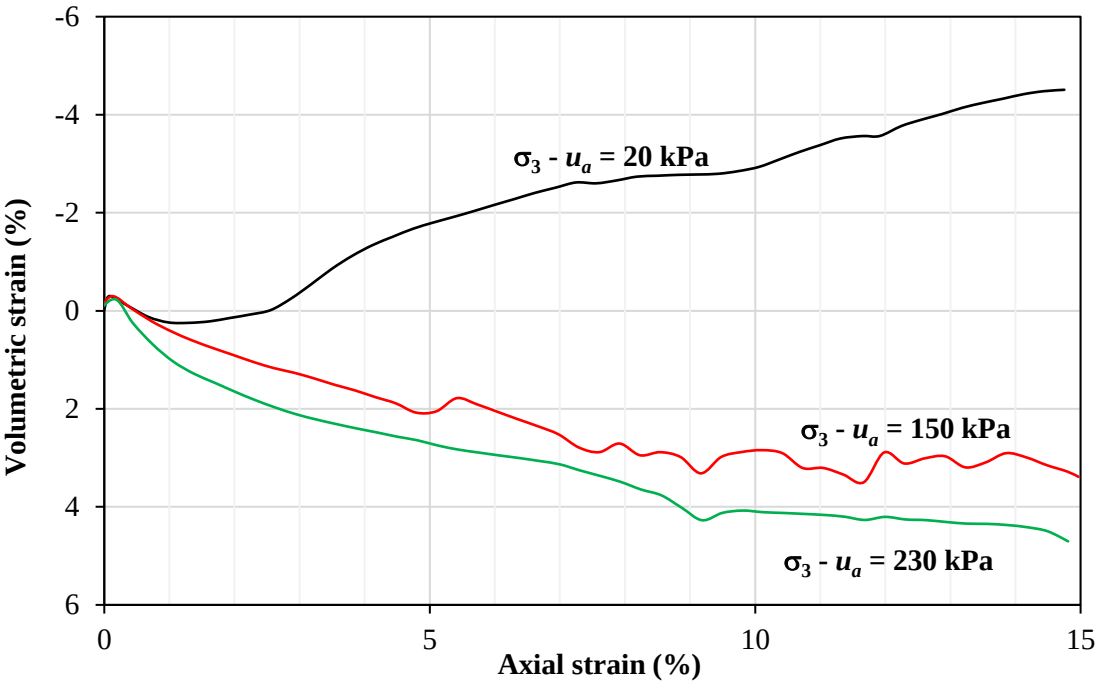

Figure C.147. Axial versus volumetric strain for tests with (u_a - u_w) = 200 kPa of soil 7R

iv) σ - u_a = 20 kPa (CW)

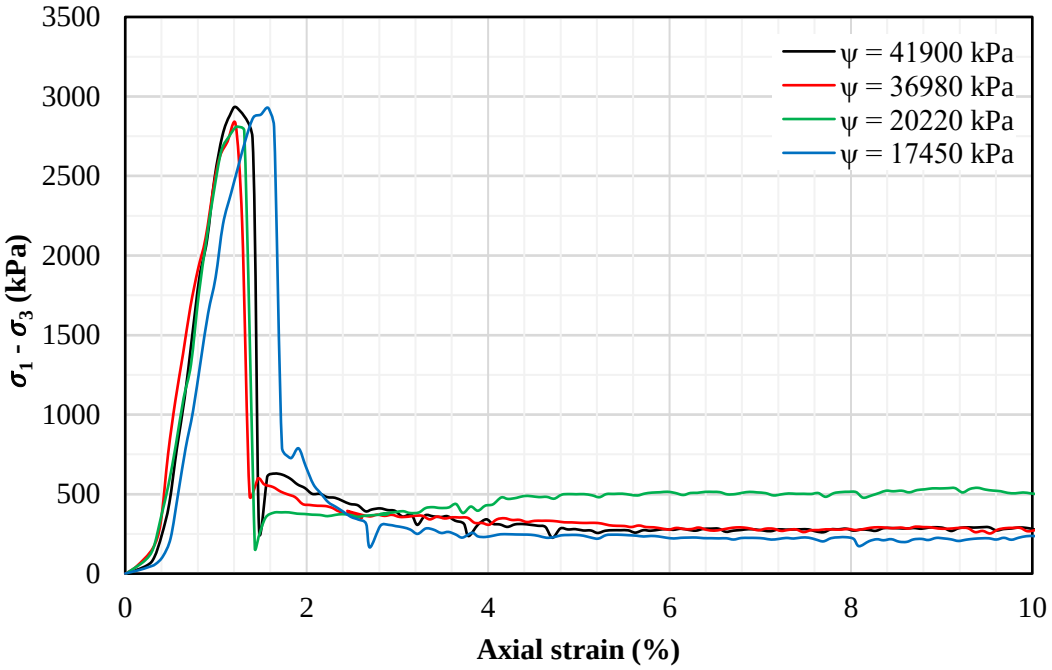

Figure C.148. Axial strain versus deviator stress for CW tests with different suctions of soil 7R

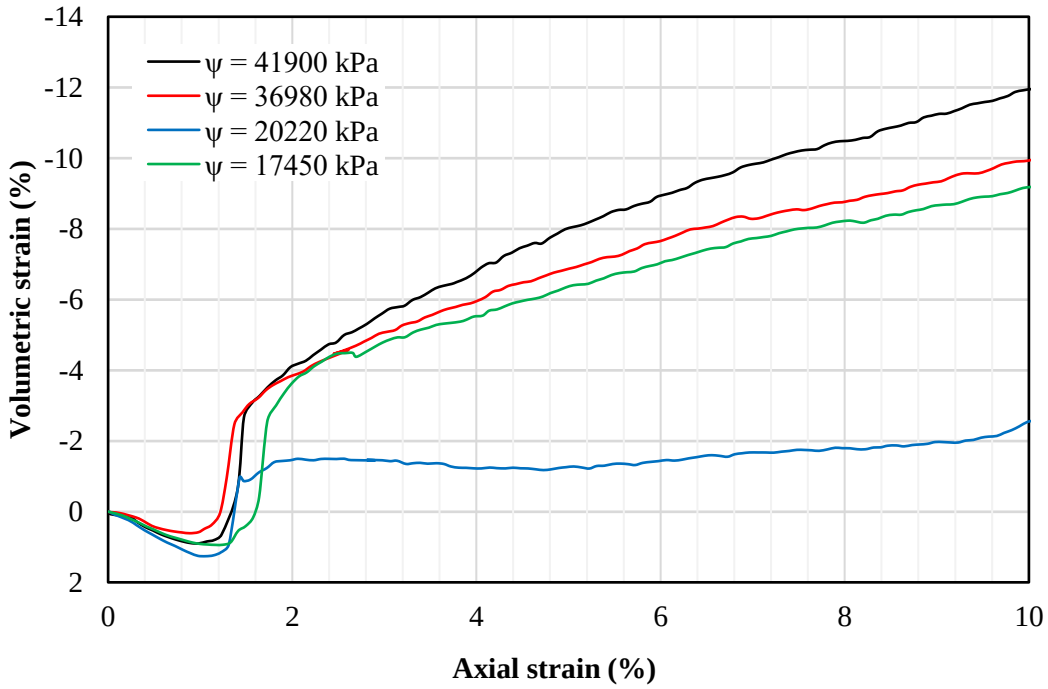

Figure C.149. Axial versus volumetric strain for CW tests with different suctions of soil 7R

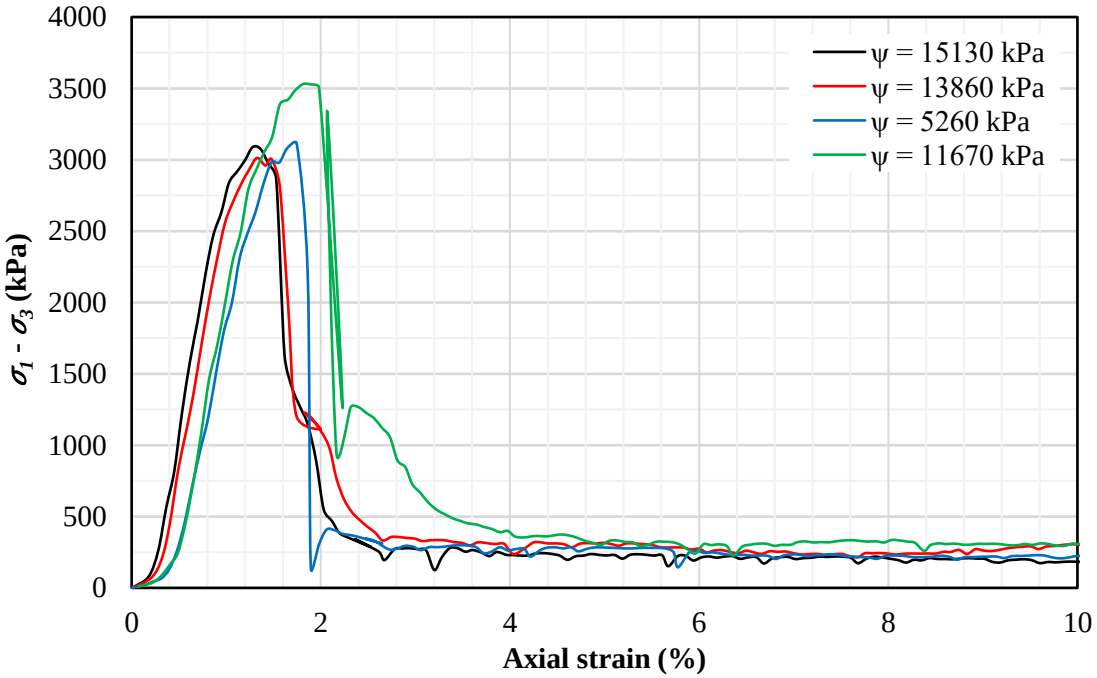

Figure C.150. Axial strain versus deviator stress for CW tests with different suctions of soil 7R

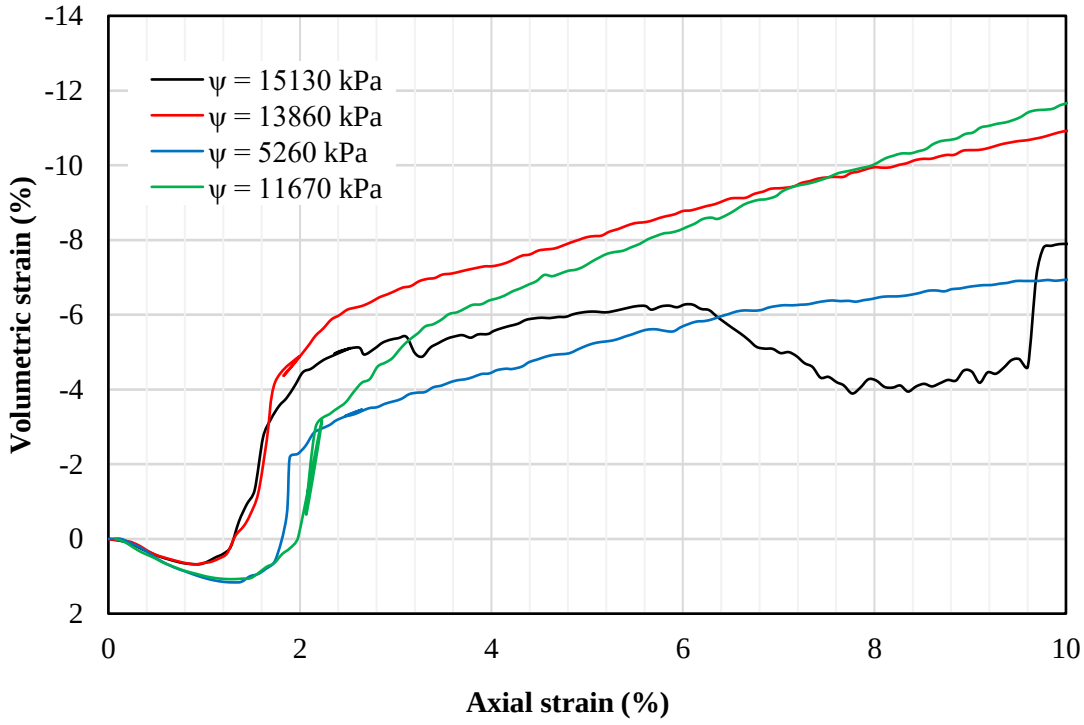

Figure C.151. Axial versus volumetric strain for CW tests with different suctions of soil 7R

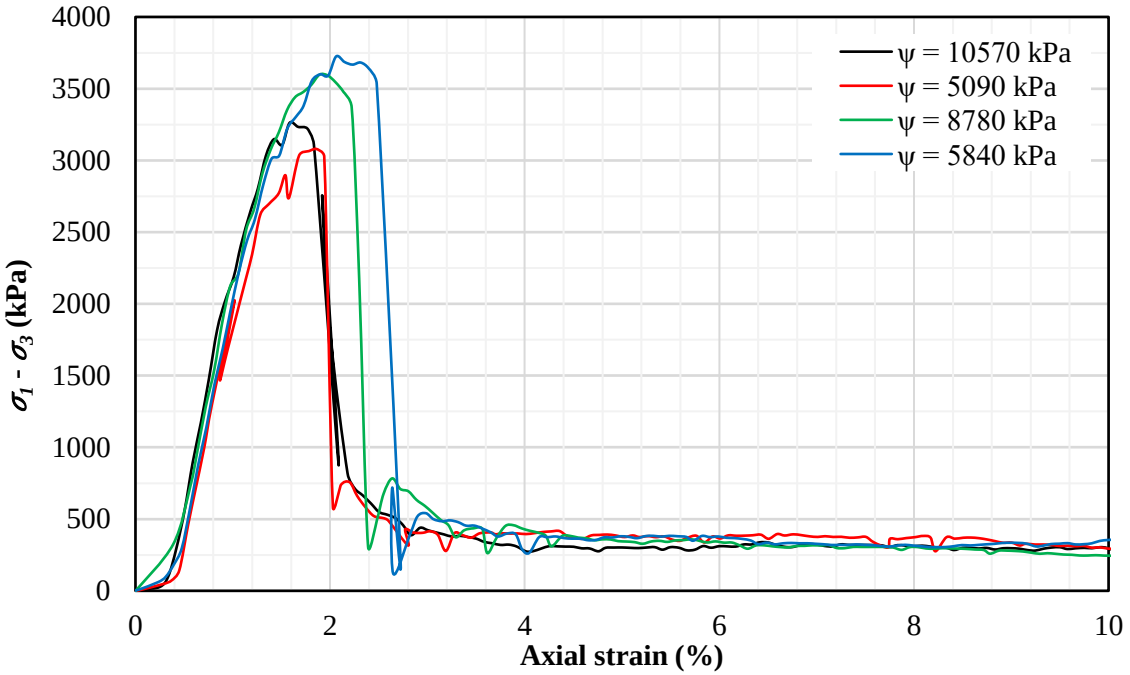

Figure C.152. Axial strain versus deviator stress for CW tests with different suctions of soil 7R

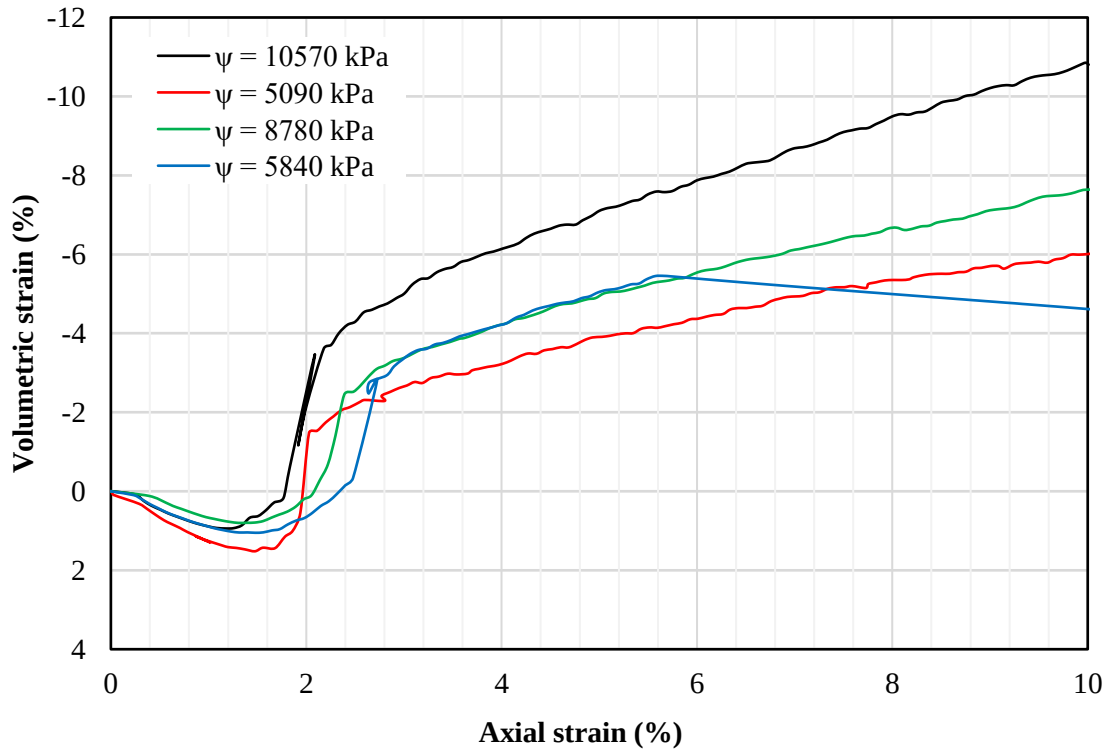

Figure C.153. Axial versus volumetric strain for CW tests with different suctions of soil 7R

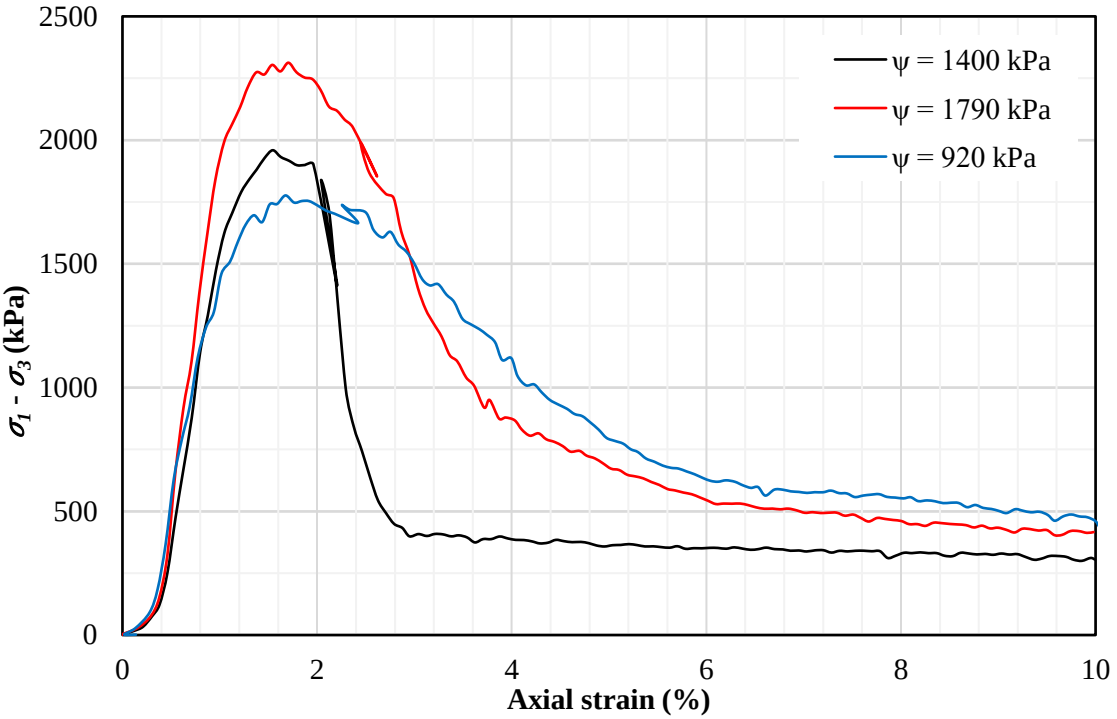

Figure C.154. Axial strain versus deviator stress for CW tests with different suctions of soil 7R

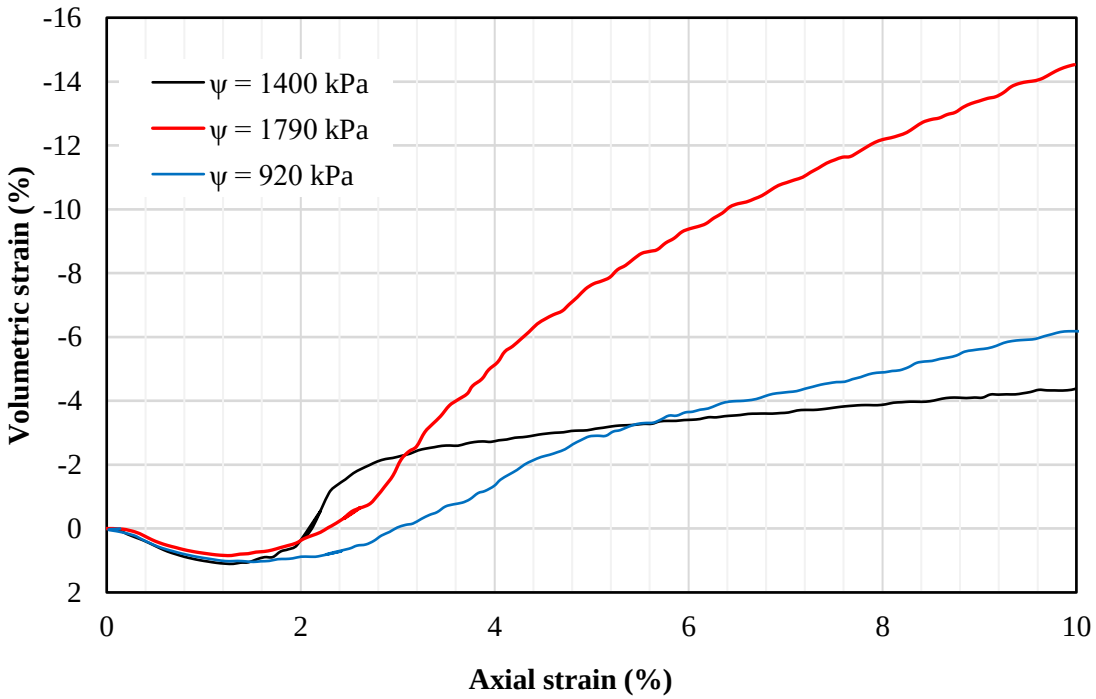

Figure C.155. Axial versus volumetric strain for CW tests with different suctions of soil 7R

v) σ - u_a = 300 kPa (CW)

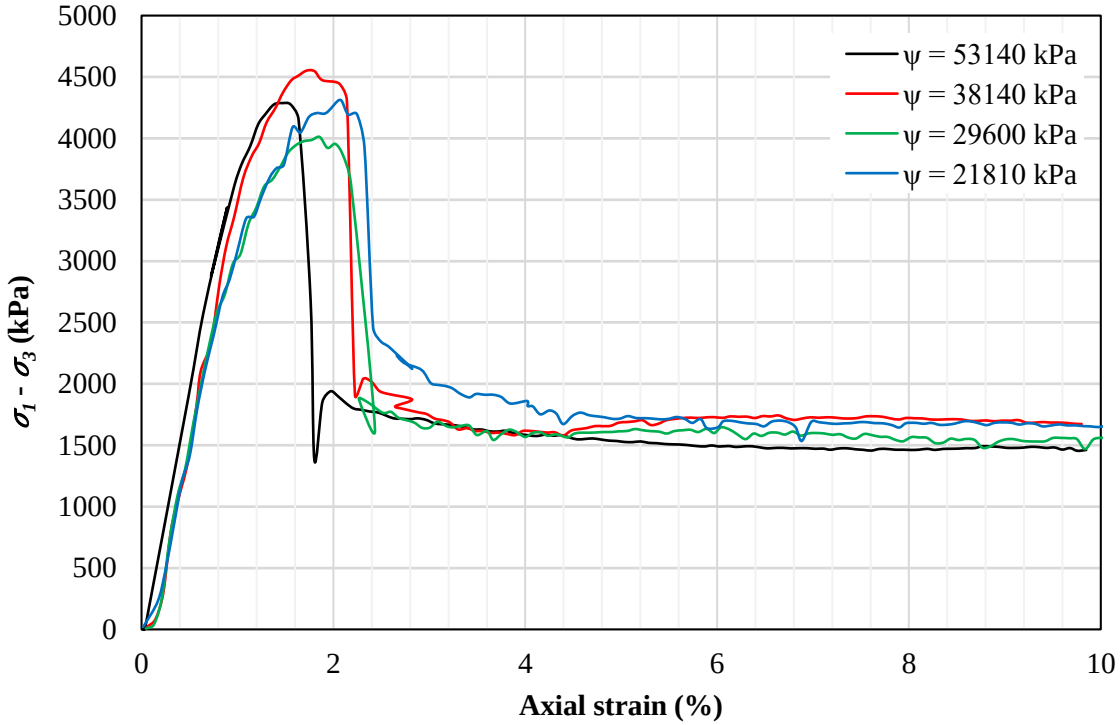

Figure C.156. Axial strain versus deviator stress for CW tests with different suctions of soil 7R

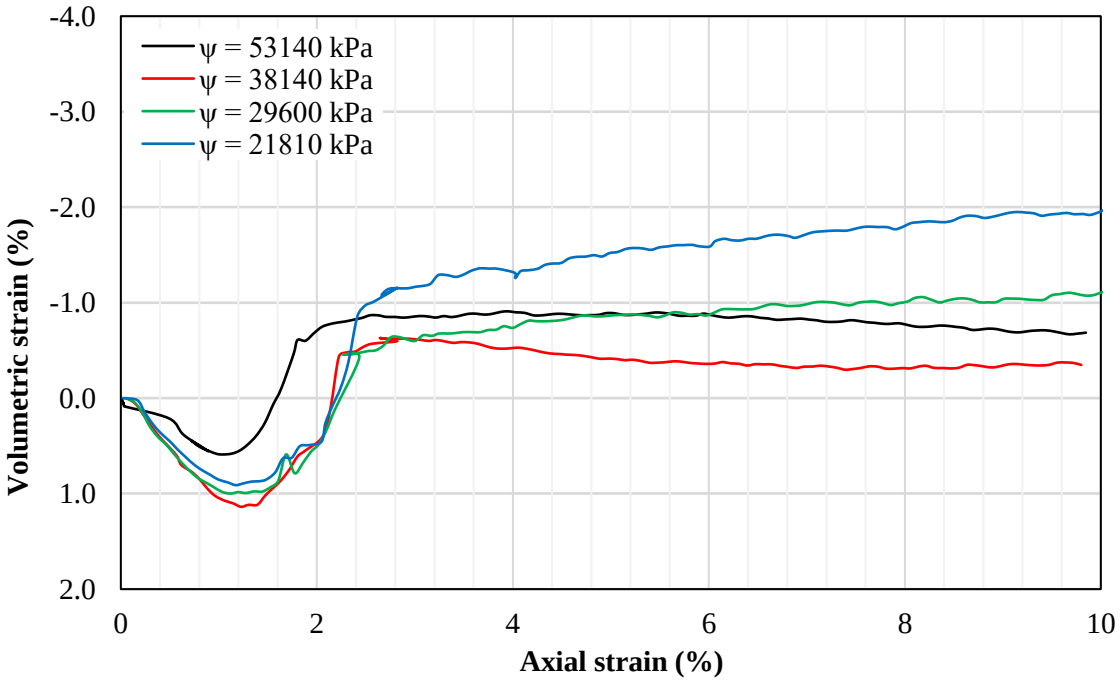

Figure C.157. Axial versus volumetric strain for CW tests with different suctions of soil 7R

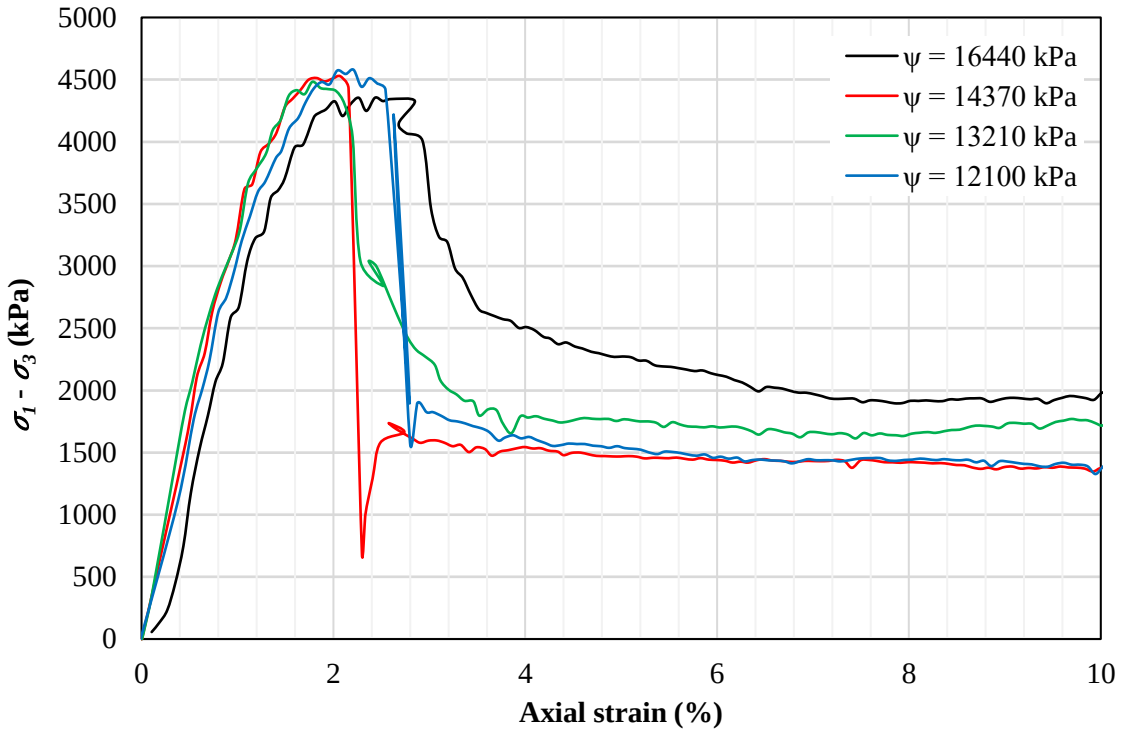

Figure C.158. Axial strain versus deviator stress for CW tests with different suctions of soil 7R

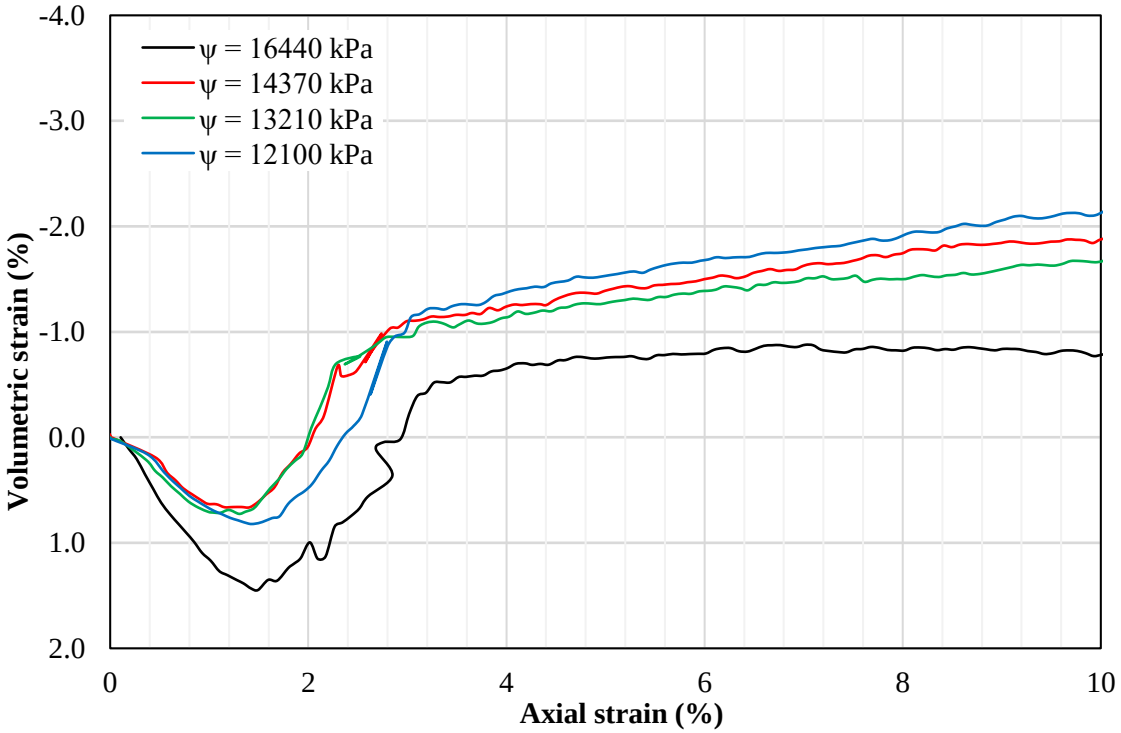

Figure C.159. Axial versus volumetric strain for CW tests with different suctions of soil 7R

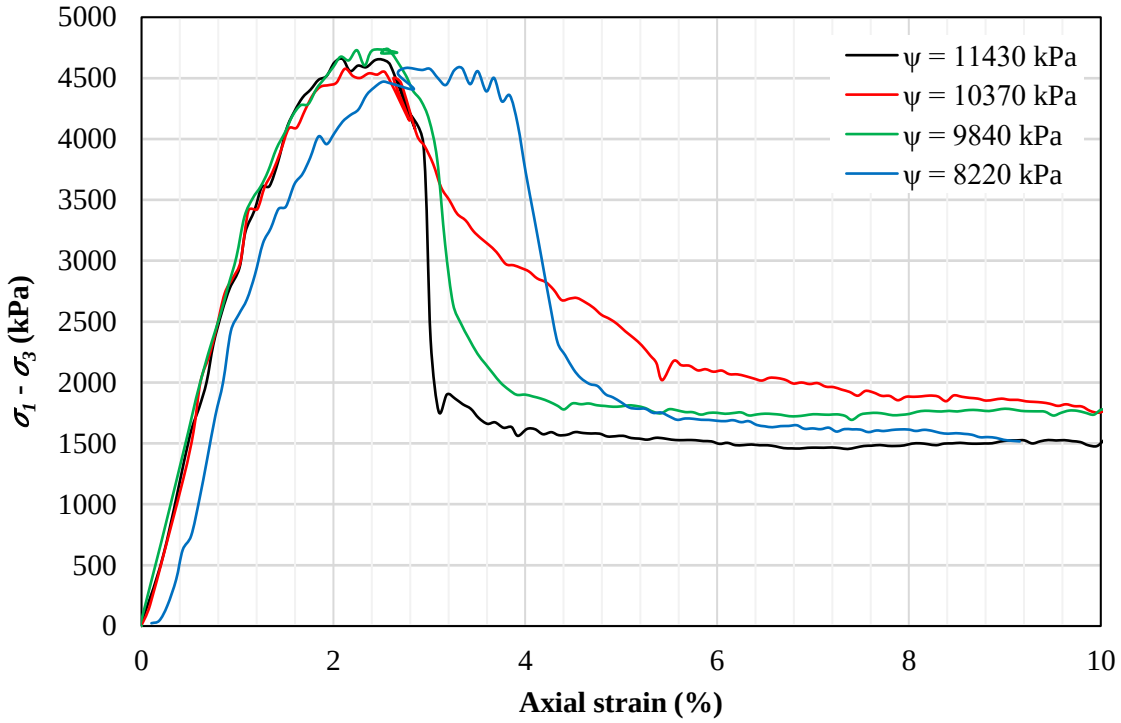

Figure C.160. Axial strain versus deviator stress for CW tests with different suctions of soil 7R

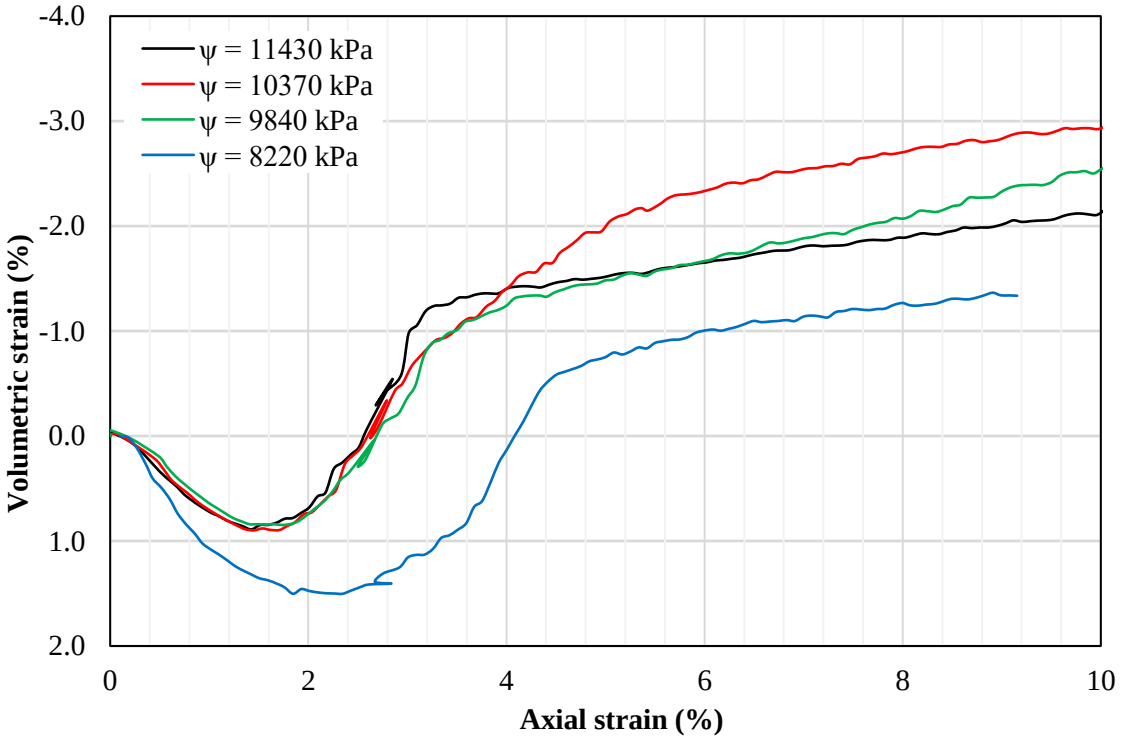

Figure C.161. Axial versus volumetric strain for CW tests with different suctions of soil 7R

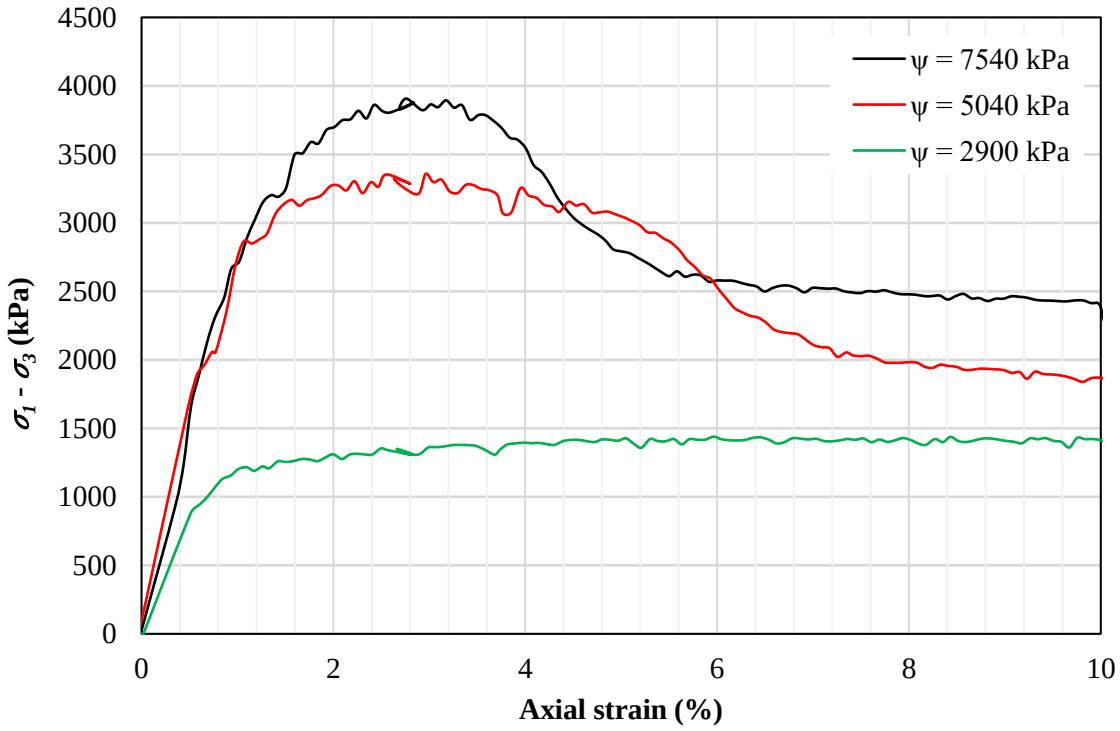

Figure C.162. Axial strain versus deviator stress for CW tests with different suctions of soil 7R

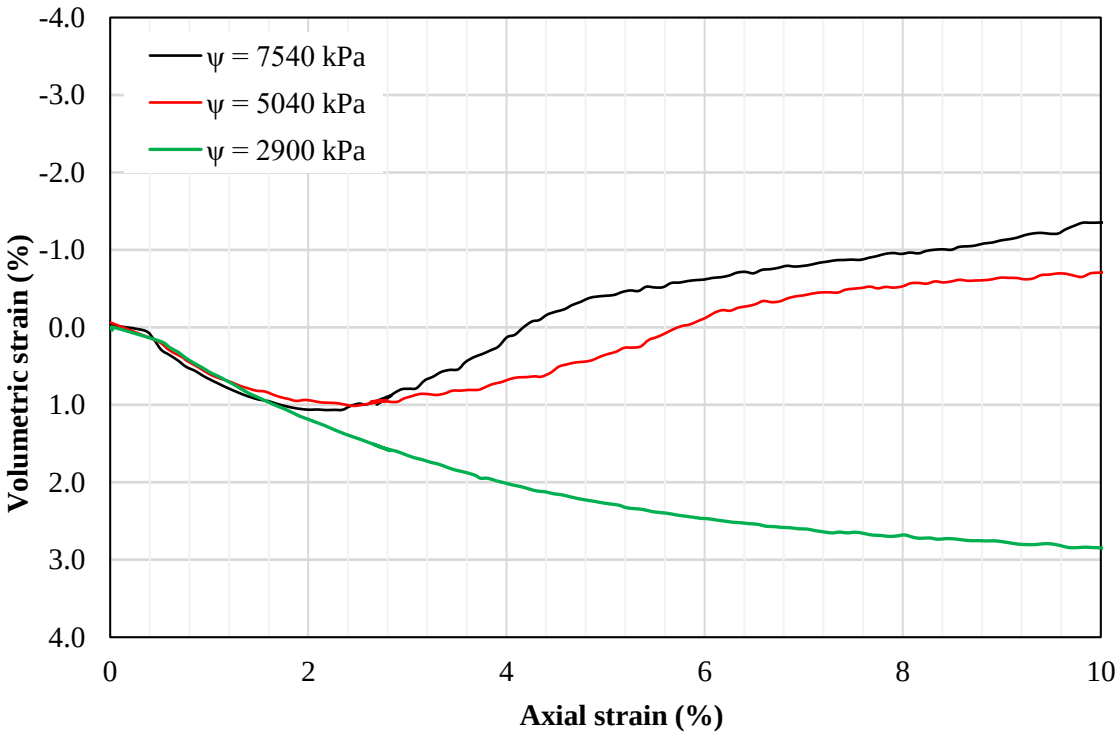

Figure C.163. Axial versus volumetric strain for CW tests with different suctions of soil 7R

- Failure criterion: maximum or peak shear stress

The data from the tests for maximum or peak shear stress as failure criterion are presented in Table C.27.

Table C.27. Shear strength data from soil 7R for peak failure criterion

Test	$\sigma_1 - \sigma_3$ (kPa)	$\sigma_3 - u_a$ (kPa)	$r = u_a - u_w$ (kPa)	t (kPa)	s* (kPa)
CD	59.24	0	0	29.62	29.62
	325.48	79	0	162.74	241.74
	449.65	134	0	224.83	359.18
	823.80	316	0	411.90	727.63
	370.78	20	100	185.39	205.39
	676.89	150	100	338.45	488.45
	901.20	290	100	450.60	740.60
	531.18	20	200	265.59	285.59
	807.28	150	200	403.64	553.64
	1010.74	230	200	505.37	735.37
CW	--	20	41900	1541	1561
		20	36980	1447	1467
		20	20220	1424	1444
		20	17450	1512	1532
		20	15130	1613	1633
		20	13860	1579	1599
		20	5260	1617	1637
		20	11670	1831	1851
		20	10570	1736	1756
		20	5090	1626	1646
		20	8780	1886	1906
		20	5840	1900	1920
		20	1400	1002	1022
		20	1790	1202	1222
		20	920	933	953
		300	53140	2162	2462
		300	12000	2314	2614
		300	20410	2028	2328
		300	15070	2252	2552
		300	16440	2270	2570

Test	$\sigma_1 - \sigma_3$ (kPa)	$\sigma_3 - u_a$ (kPa)	$r = u_a - u_w$ (kPa)	t (kPa)	s* (kPa)
		300	11930	2314	2614
		300	12960	2298	2598
		300	11680	2354	2654
		300	10580	2403	2703
		300	10370	2353	2653
		300	9350	2507	2807
		300	7870	2374	2674
		300	5350	2062	2362
		300	3600	1752	2052
		300	960	763	1063
			310	238	119
			540	370	185
			1090	657	329
			4130	805	403
			8150	907	454
			1810	943	472
			5360	1052	526
			39510	790	395
			17020	778	389
			11020	837	418
			61180	642	321
BT	--	--	12030	673	337
			10800	902	451
			14420	708	354
			70	162	81
			520	326	163
			470	570	285
			870	819	410
			1990	1004	502
			20830	754	377
			29220	704	352
			36880	809	404
			47360	409	204
			52210	589	295

Firstly, it was performed a fitting considering only the CD tests (i.e., matric suctions under 200 kPa). The graph in terms of *s** and *t* (Fig. C.164) points out to a linear relationship between these variables meaning that the angle ψ' has a unique value for each matric

suction. Fig. C.165 also presents the fitting equations from which the intercepts (*d*) can be obtained. The values of ψ^b were obtained using a fitting procedure based on the minimization of the squared errors of *t* by changing the values of ψ^b. The shear strength parameters obtained from this process are presented in Table C.28.

Table C.28. Shear strength data after fitting for soil 7R at maximum or peak failure criterion and matric suctions under 200 kPa

$\sigma_1 - \sigma_3$ (kPa)	$\sigma_3 - u_a$ (kPa)	$u_a - u_w$ (kPa)	t (kPa)	s* (kPa)	d (kPa)	ψ'	ϕ' (sec)	c_{app} (kPa)	ψ^b	ϕ^b (sec)
59.2	0	0	29.6	29.6	23.5	28.5	32.8	27.9	0.0	
325.5	79	0	162.7	241.7	23.5	28.5	32.8	27.9	0.0	
449.7	134	0	224.8	359.2	23.5	28.5	32.8	27.9	0.0	
823.8	316	0	411.9	727.6	23.5	28.5	32.8	27.9	0.0	
370.8	20	100	185.4	205.4	87.4	26.4	29.8	100.7	30.9	35.6
676.9	150	100	338.4	488.4	87.4	26.4	29.8	100.7	35.9	41.4
901.2	290	100	450.6	740.6	87.4	26.4	29.8	100.7	30.7	35.4
531.2	20	200	265.6	285.6	112.4	28.0	32.1	132.8	24.3	28.7
807.3	150	200	403.6	553.6	112.4	28.0	32.1	132.8	23.2	27.4
1010.7	230	200	505.4	735.4	112.4	28.0	32.1	132.8	24.4	28.9

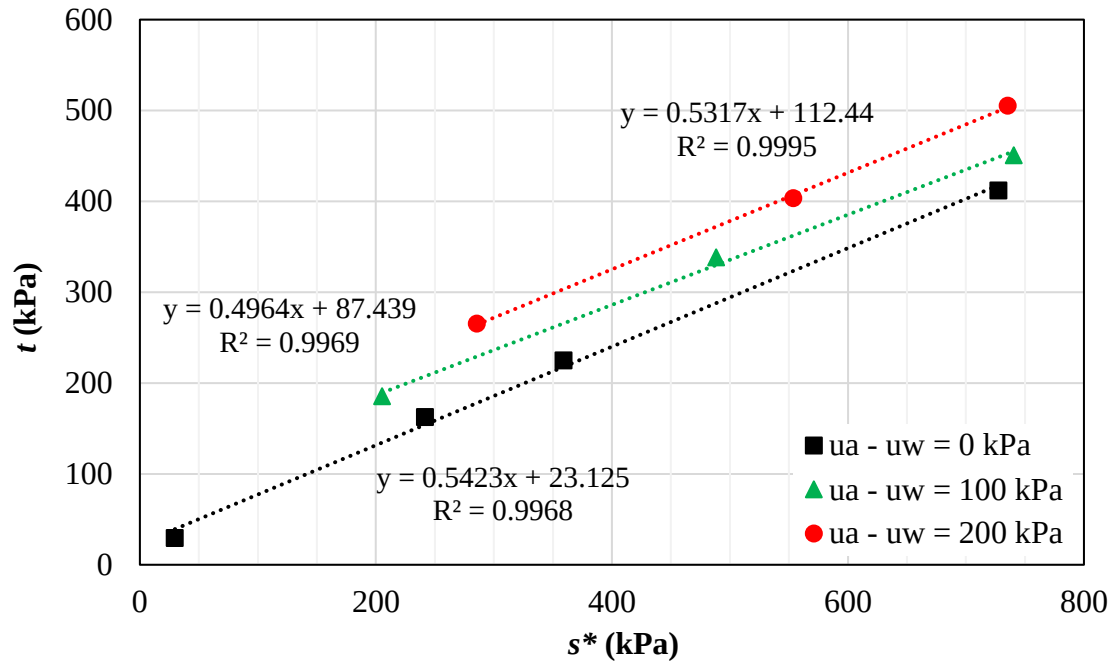

Figure C.164. Failure envelope in terms of *s and *t* for soil 7R at maximum or peak failure and low suctions (i.e. ≤ 200 kPa)**

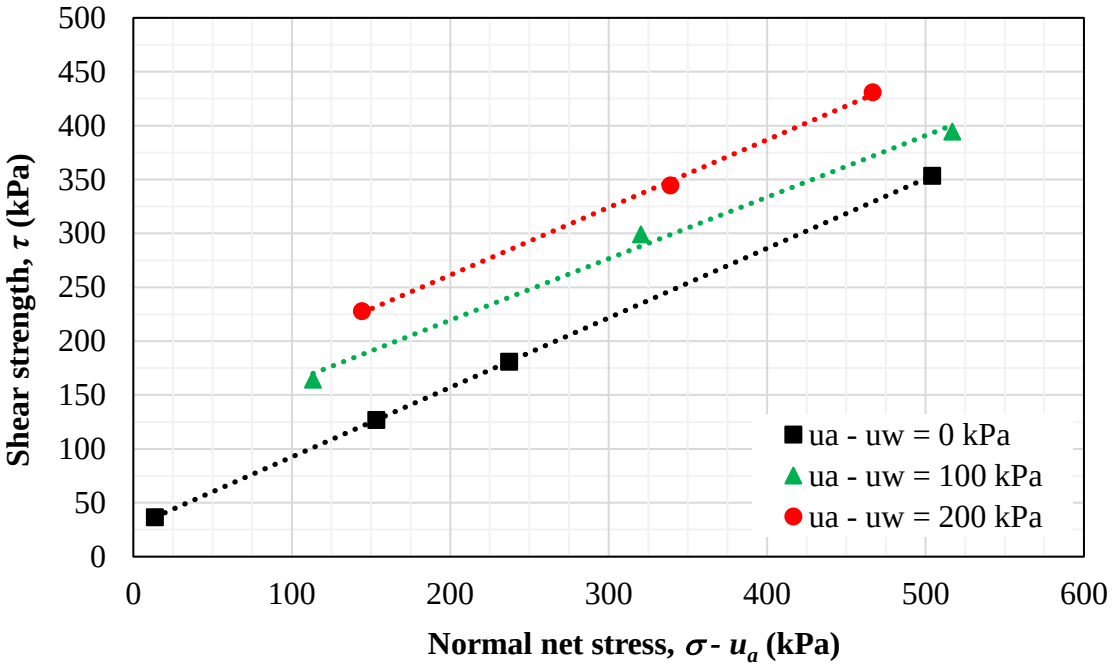

Figure C.165. Failure envelope in terms of (σ - u_a) and τ for soil 7R at maximum or peak failure and low suctions (i.e. ≤ 200 kPa)

The data from Table C.28 were fitted using the Modified Bi-Hyperbolic model. The fitting parameters are presented in Table C.29. The goodness-of-fit obtained are R^2 = 0.997 and RMSE = 7.1, demonstrating that the Modified Bi-Hyperbolic model is quite suitable to represent the measured data. The extended Mohr-Coulomb failure surface is depicted in Fig. C.166.

Table C.29. Parameters obtained for the Modified Bi-Hyperbolic model for soil 7R at maximum or peak failure and low suctions (i.e. ≤ 200 kPa)

c' (kPa)	27.9	s_b	50.0
ϕ' (degrees)	32.8	n	1.0
ϕ^b (degrees)	32.5	a_1	1.552
τ_{ult1} (kPa)	1.13×10^4	b_1	8.84×10^{-5}
τ_{ult2} (kPa)	6.92×10^2	a_2	1.570
τ_{peak} (kPa)	1796.9	b_2	1.50×10^{-3}
τ_{ult} (kPa)	1796.9		

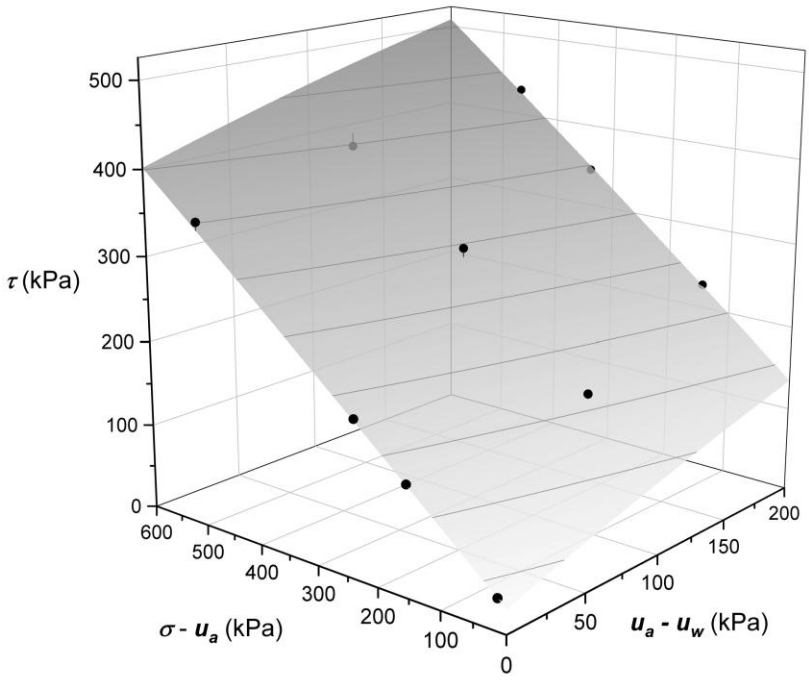

Figure C.166. Extended Mohr-Coulomb failure surface fitted using the Modified Bi-Hyperbolic model of soil 7R at maximum or peak failure for low matric suctions (≤ 200 kPa)

For the triaxial CW data presented by other authors, the shear strength parameters were obtained by arranging tests with similar suctions. This procedure has not proved adequate for the data presented in Table C.27 because the suctions are dispersed along a wide range. Therefore, the failure envelope in terms of stress points for all suctions was obtained by fitting *r*, *s** and *t* into the Modified Bi-Hyperbolic model. Figures C.167 and C.168 illustrates the fitted stress-point and extended Mohr-Coulomb failure envelopes.

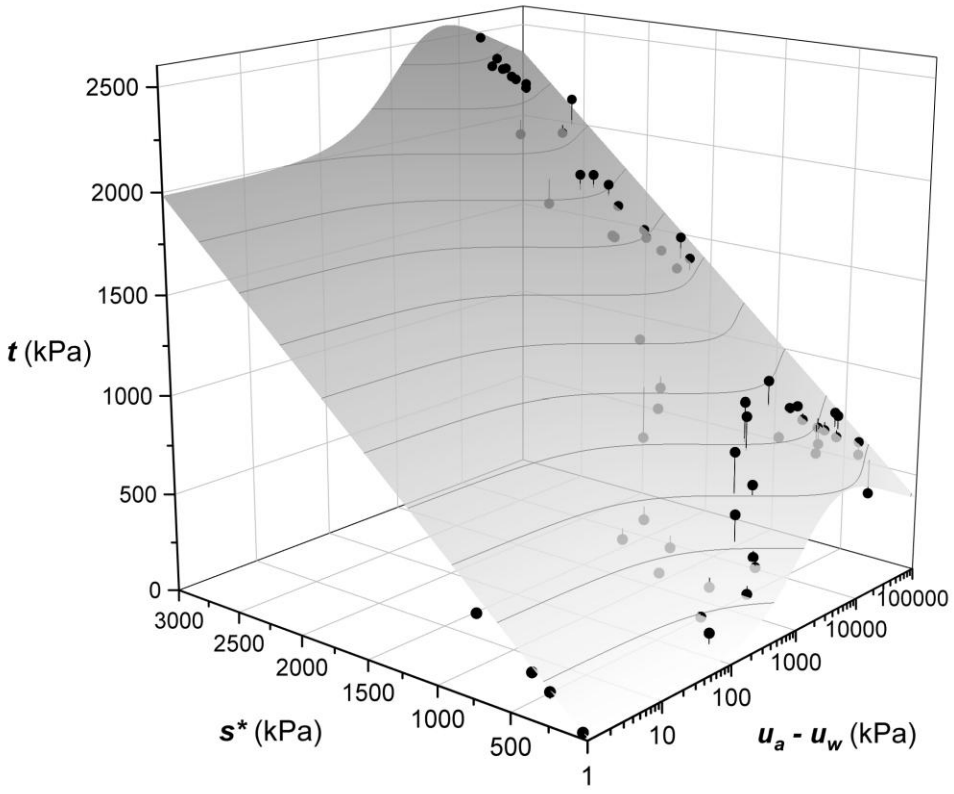

Figure C.167. Stress-point failure surface fitted using the Modified Bi-Hyperbolic model of soil 7R at maximum or peak failure for all suctions

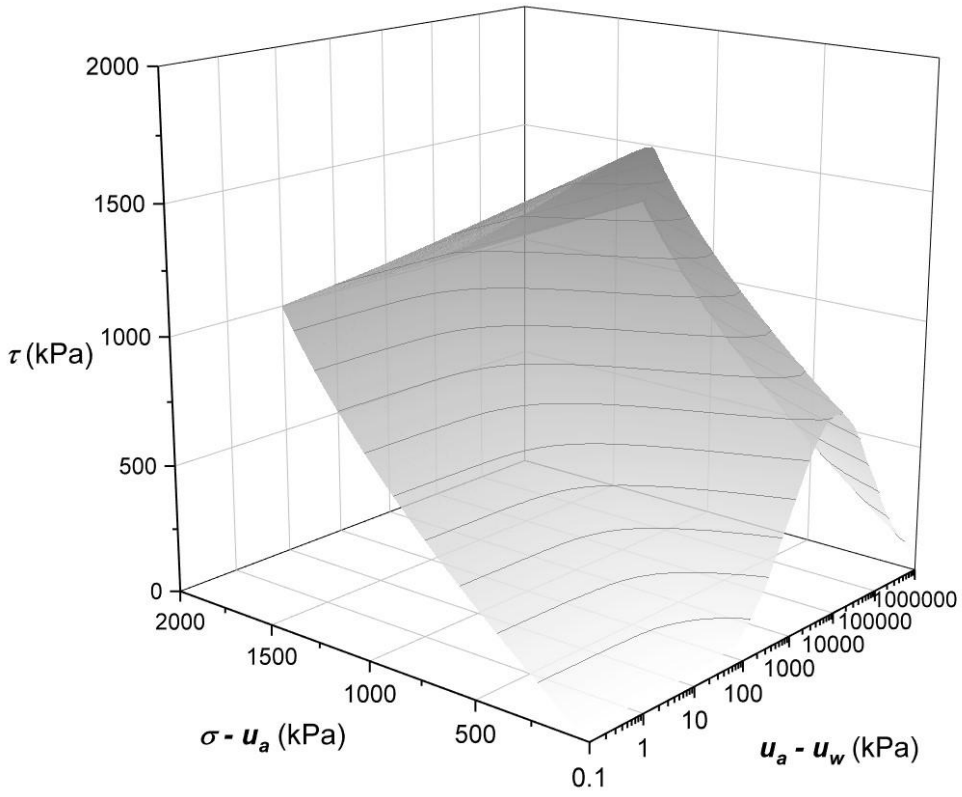

Figure C.168. Extended Mohr-Coulomb failure surface fitted using the Modified Bi-Hyperbolic model of soil #7R at maximum or peak failure for all suctions

- General comments

The graphs showing axial strain versus deviator stress indicate strain-hardening behavior for higher net normal stresses and low suctions (Figs. C.142, C.144, and C.146). For high suctions (> 200 kPa), the soil exhibited a clear peak (Figs. C.148, C.150, C.152, C.154, C.156, C.158, C.160, and C.162). In summary, the shear strength parameters considering maximum shear strength as failure criterion indicate:

- For low suctions (≤ 200 kPa):
  - The angle ϕ' is constant to approximately 31.7° (Table C.28);
  - The angle ϕ^b is greater than ϕ' at matric suctions of 100 kPa, which is between the first air-entry value (72 kPa) and the first residual

suction (230 kPa), as shown in Table C.28. Also, ϕ^b decreases with the matric suction only.

- For all suctions:
  - The angle ϕ^b starts of approximately $0.82\phi'$. When the matric suction approaches 300 kPa (the first residual suction is 230 kPa), ϕ^b begins do decrease abruptly;
  - The angle ϕ' is always constant and equal to 41.1°;
  - Depending on how the fitting procedure is done, very similar performance in terms of goodness-of-fit is obtained. However, fitting using different equations may result in $\phi^b > \phi'$;
  - The extended failure envelope exhibits a peak around suction of 6000 kPa that is independent of the net normal stress;
  - The BT tests may not be suitable for analyzing the behavior of in ϕ^b and ϕ' because applying compression stress on the specimens lead to emergence of perpendicular tensile stresses. The failure occurs when the maximum tensile strength is surpassed. Thus, the specimen fails but does not shear and the aggregations are submitted to a different combination of stresses of those from triaxial and direct shear tests.

C.8 Fernandes (2016) – 2U

- Soil basic information and characteristics
    - Void ratio (e_0) = 0.77
    - Density of solids (ρ_s) = 2.68
    - Dry density (ρ_d) = 1.52
    - Liquid limit (w_L) = 19.5%
    - Plastic limit (w_P) = NP
    - USCS = SC (disaggregated) / SC (aggregated)

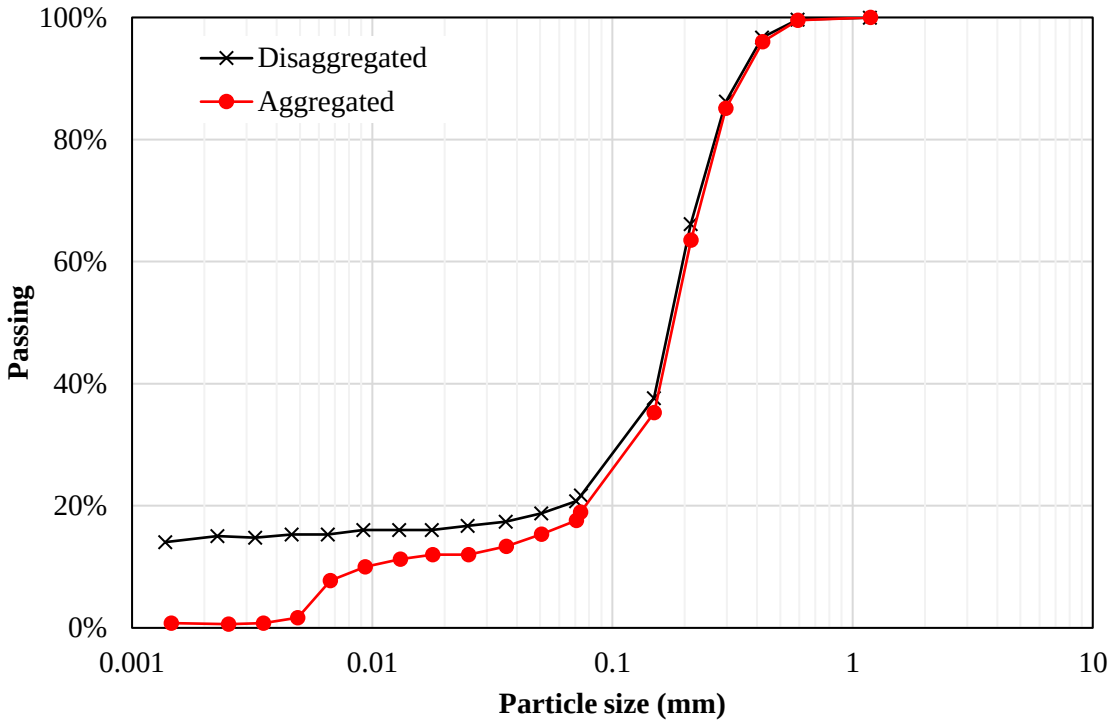

Figure C.168. Grain-size distribution curve of soil 2U

- SWCC

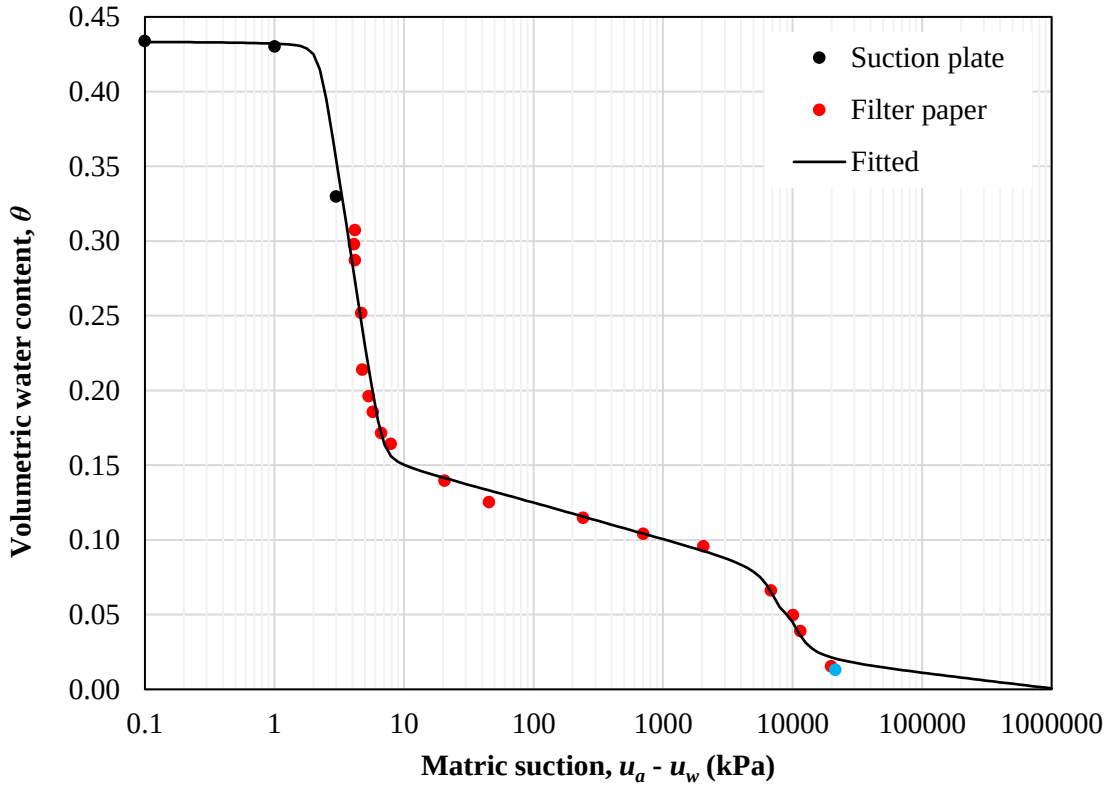

Figure C.169. Soil-water characteristic curves of soil 2U

- Shear strength data:
  - Initial void ratio (e_0) = 0.77
  - Type: modified triaxial CD
  - Volume measurement: double walled cell
  - Shear velocity: 0.05 mm/min

i) $u_a - u_w = 0$ kPa

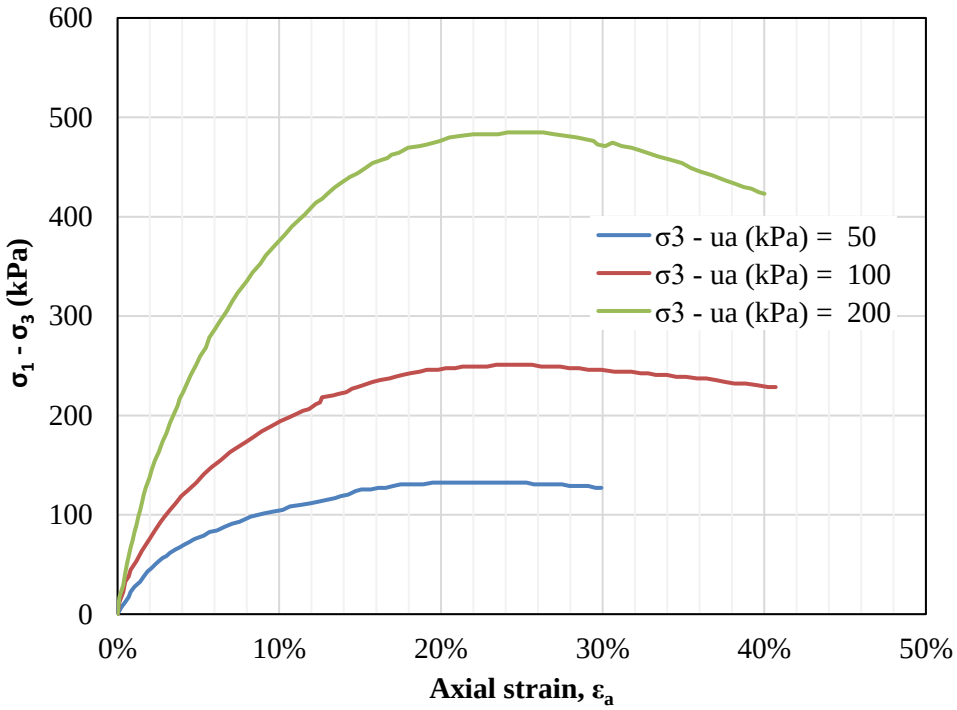

Figure C.170. Axial strain versus deviator stress of saturated tests of soil 2U

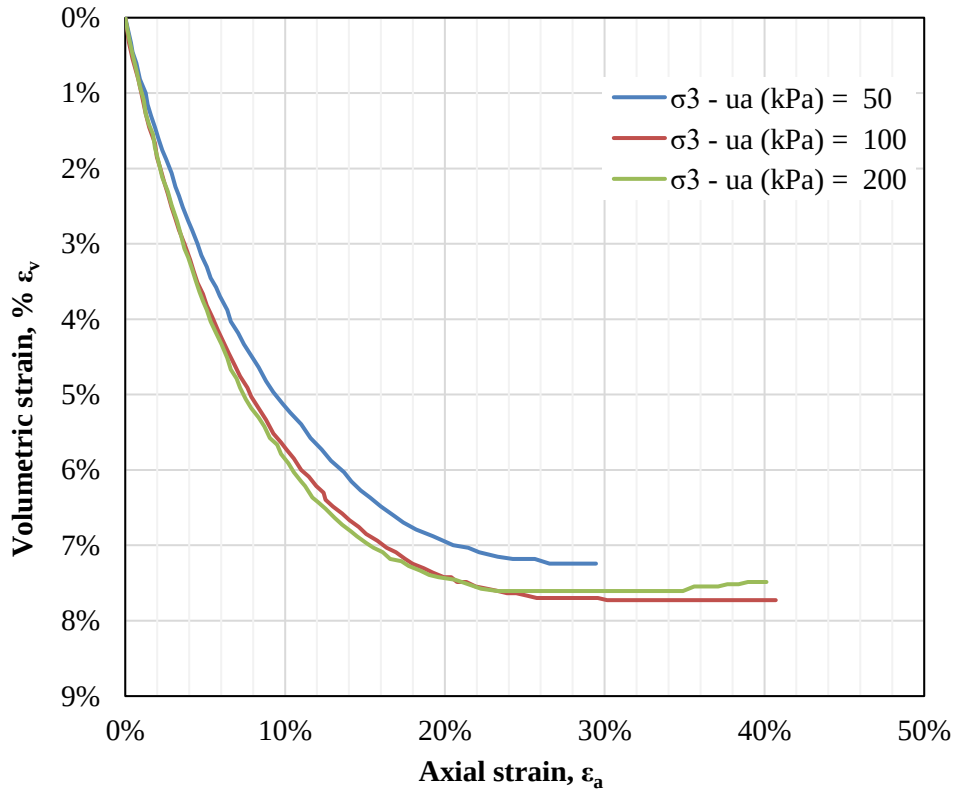

Figure C.171. Axial strain versus volumetric strain of saturated tests of soil 2U

ii) $u_a - u_w$ = 50 kPa

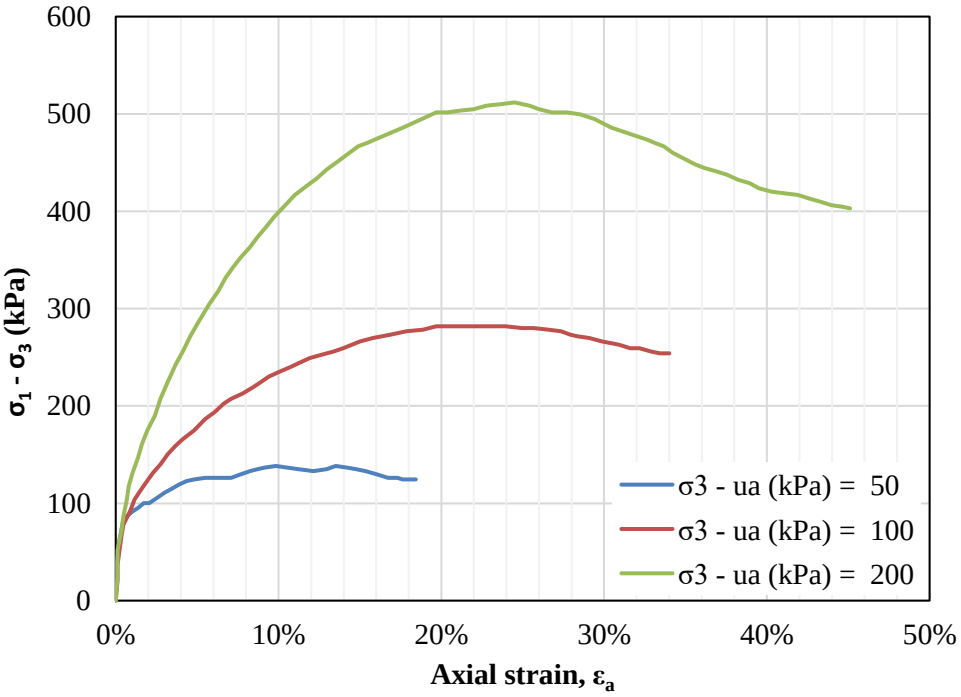

Figure C.172. Axial strain versus deviator stress of unsaturated triaxial tests with (u_a - u_w) = 50 kPa of soil 2U

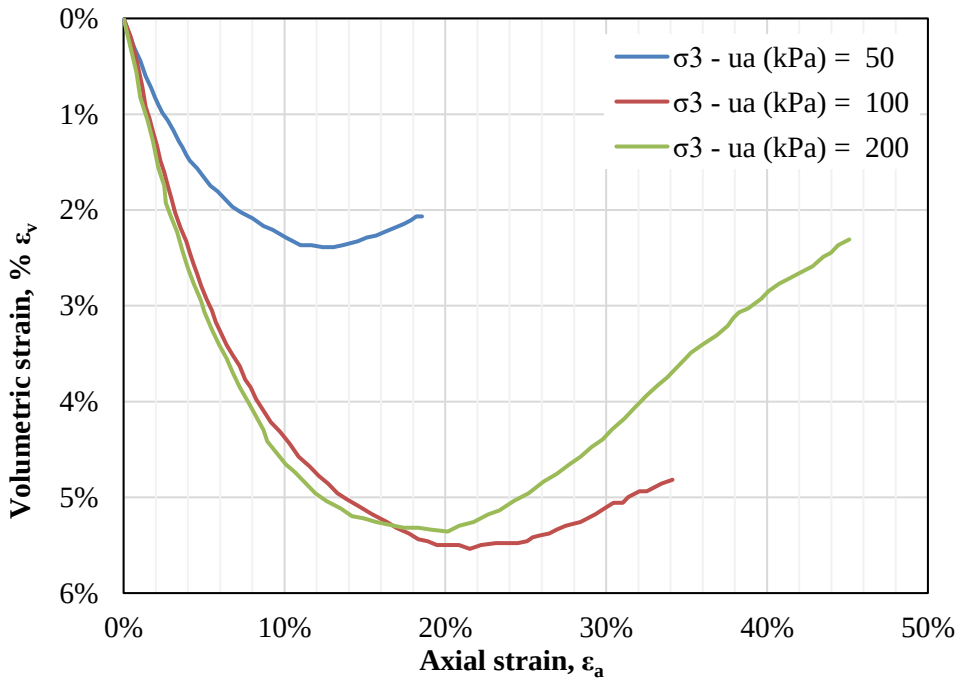

Figure C.173. Axial strain versus volumetric strain of unsaturated triaxial tests with (u_a - u_w) = 50 kPa of soil 2U

iii) $u_a - u_w$ = 200 kPa

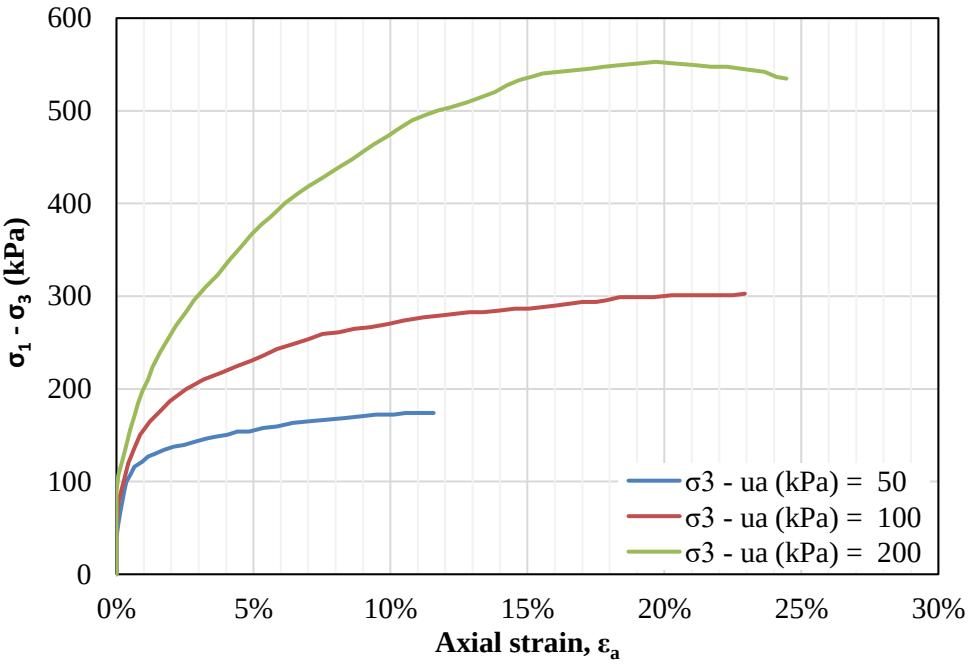

Figure C.174. Axial strain versus deviator stress of unsaturated triaxial tests with (u_a - u_w) = 200 kPa of soil 2U

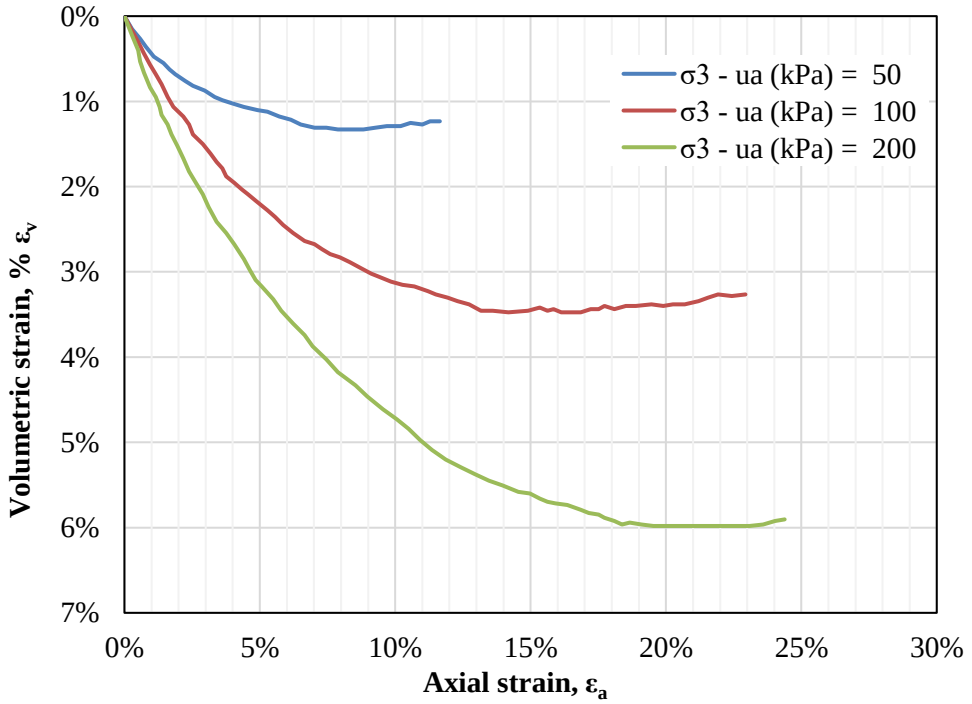

Figure C.175. Axial strain versus volumetric strain of unsaturated triaxial tests with (u_a - u_w) = 200 kPa of soil 2U

iv) $u_a - u_w$ = 400 kPa

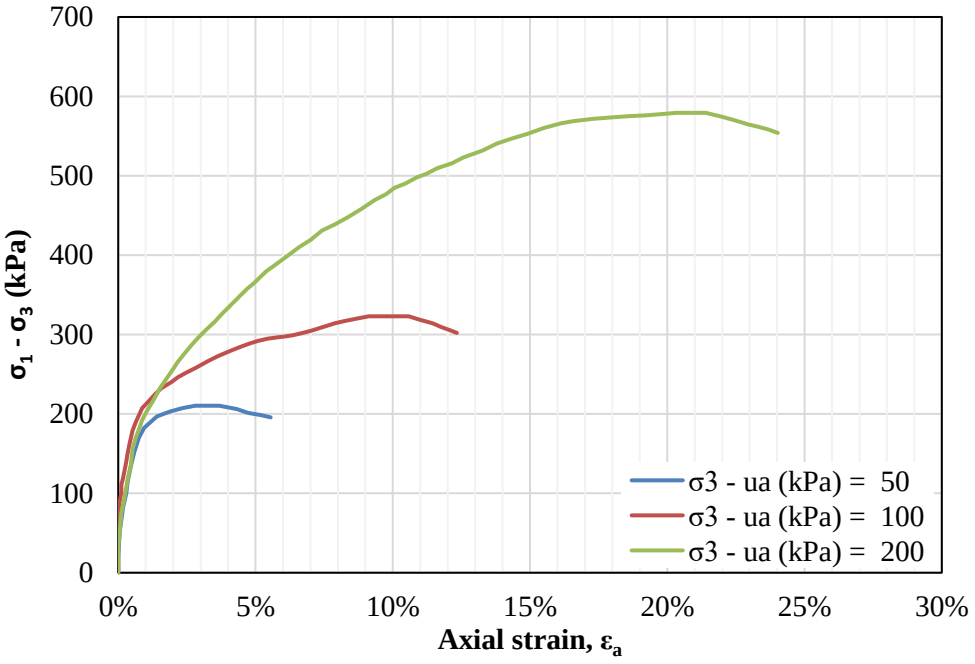

Figure C.176. Axial strain versus deviator stress of unsaturated triaxial tests with (u_a - u_w) = 400 kPa of soil 2U

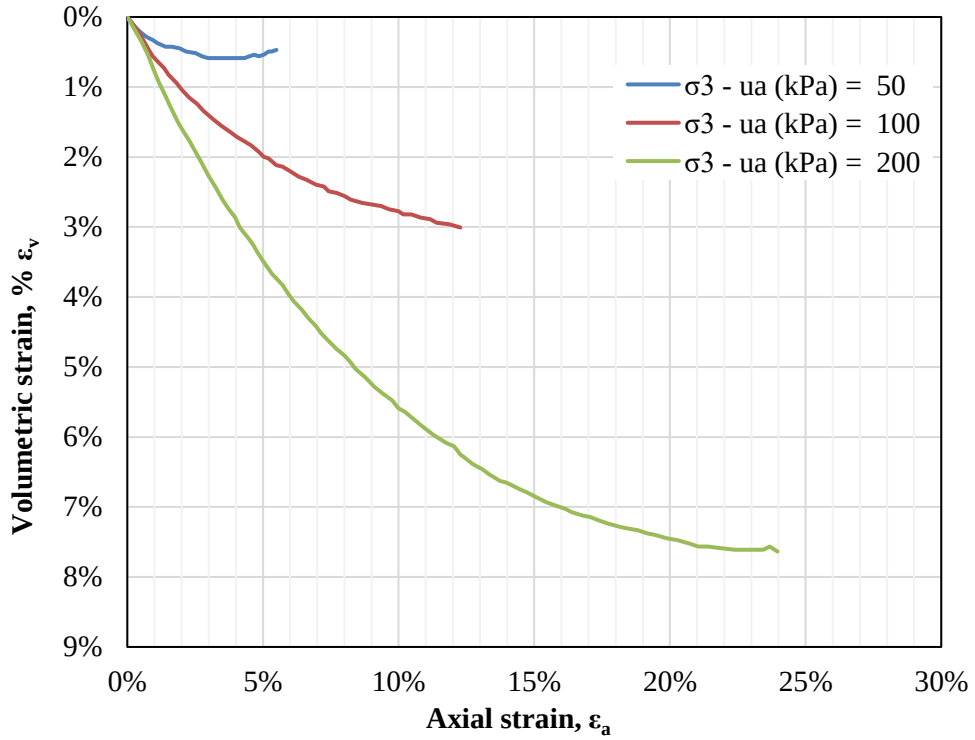

Figure C.177. Axial strain versus volumetric strain of unsaturated triaxial tests with (u_a - u_w) = 400 kPa of soil 2U

- Failure criterion: peak

The data from the shear strength tests for peak failure criterion is presented in Table C.30.

Table C.30. Shear strength parameters from soil 2U for peak failure criterion

$\sigma_1 - \sigma_3$ (kPa)	$\sigma_3 - u_a$ (kPa)	$r = u_a - u_w$ (kPa)	t (kPa)	s (kPa)	d (kPa)	ψ'	ϕ'	c_{app} (kPa)	ψ^b	ϕ^b	t fitted	Error²	σ_f (kPa)	τ_f (kPa)
132.4	50		66.2	116.2							66.3	0.01	80.4	55.8
251.0	100	0	125.5	225.5	3.6	28.4	32.7	4.2			125.3	0.03	157.7	105.4
484.8	200		242.4	442.4							242.5	0.00	311.5	204.1
138.3	50		69.2	119.2					0.0	0.0	69.4	0.04	81.0	57.9
281.8	100	50	140.9	240.9	5.1	28.9	33.5	6.1	4.9	5.9	140.9	0.00	163.1	117.4
511.8	200		255.9	455.9					0.6	0.8	255.9	0.00	314.6	213.3
174.0	50		87.0	137.0					2.0	2.4	87.0	0.00	88.5	72.2
302.7	100	200	151.4	251.4	10.8	29.2	33.9	13.0	2.2	2.6	151.4	0.00	166.9	125.6
552.9	200		276.4	476.4					2.0	2.5	276.4	0.00	322.3	229.4
210.4	50		105.2	155.2					2.3	2.7	105.2	0.00	97.0	87.6
323.0	100	400	161.5	261.5	18.3	28.9	33.6	22.0	1.9	2.3	161.5	0.00	172.2	134.5
579.3	200		289.6	489.6					2.2	2.6	289.6	0.00	329.4	241.3

SSE	8.77E-02
R^2	1.000
RMSE	0.085

The failure envelope in terms of *s** and *t* shown in Fig. C.178 indicates a constant value of ψ' for each matric suction. To obtain the values of ψ^b, it was performed a fitting procedure based on the minimization of the squared errors of *t* by changing the values of ψ^b.

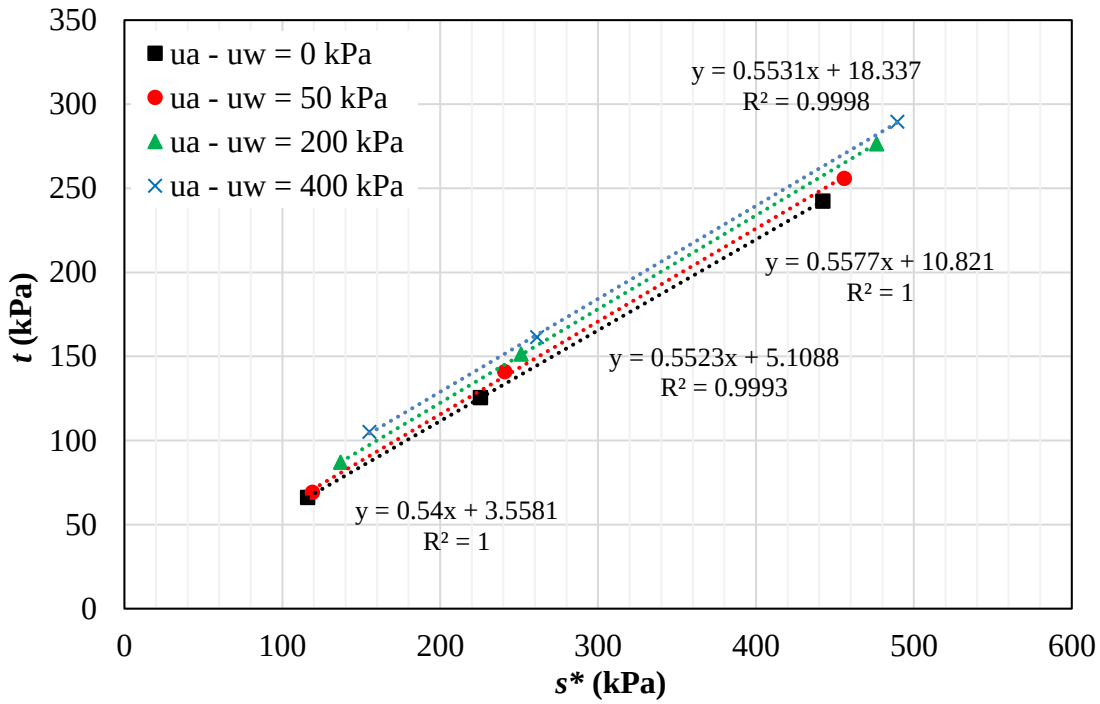

Figure C.178. Failure envelope in terms of *s and *t* for soil 2U**

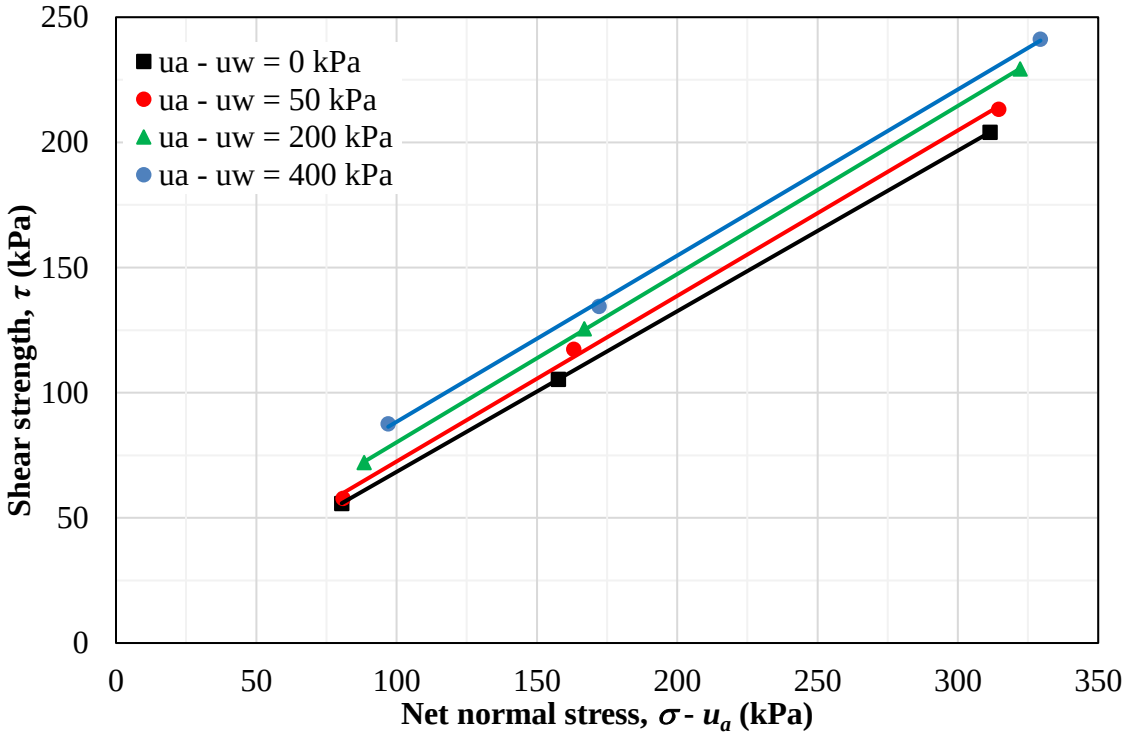

Figure C.179. Failure envelope in terms of (σ - u_a) and τ for soil 2U

The values presented in Table C.30 indicate that ϕ^b does not change with the net confining stress. For matric suctions of 50 kPa, ϕ^b is can be assumed as 5.9º. For matric suctions of 200 and 400 kPa, ϕ^b is 2.5º. Table C.30 also shows that the effective friction angle ϕ' is on average 33.4º, and it is not affected by changes in the confining stress or the matric suction. Fitting the data from Table C.30 using the Modified Bi-Hyperbolic model resulted in the extended Mohr-Coulomb failure surface depicted in Fig. C.180. The goodness-of-fit for this fitting (R^2 = 0.999 and RMSE = 2.1) points out to a great adherence of the model to the data. The fitting parameters are presented in Table C.31.

Table C.31. Parameters obtained for the Modified Bi-Hyperbolic model

c' (kPa)	4.2	s_b	1.0
ϕ' (degrees)	33.1	n	0.8
ϕ^b (degrees)	5.7	a_1	1.535
τ_{ult1} (kPa)	6.02×10^5	b_1	1.66×10^{-6}
τ_{ult2} (kPa)	6.17×10^1	a_2	9.985
τ_{peak} (kPa)	16.5	b_2	1.74×10^{-2}
τ_{ult} (kPa)	14.2		

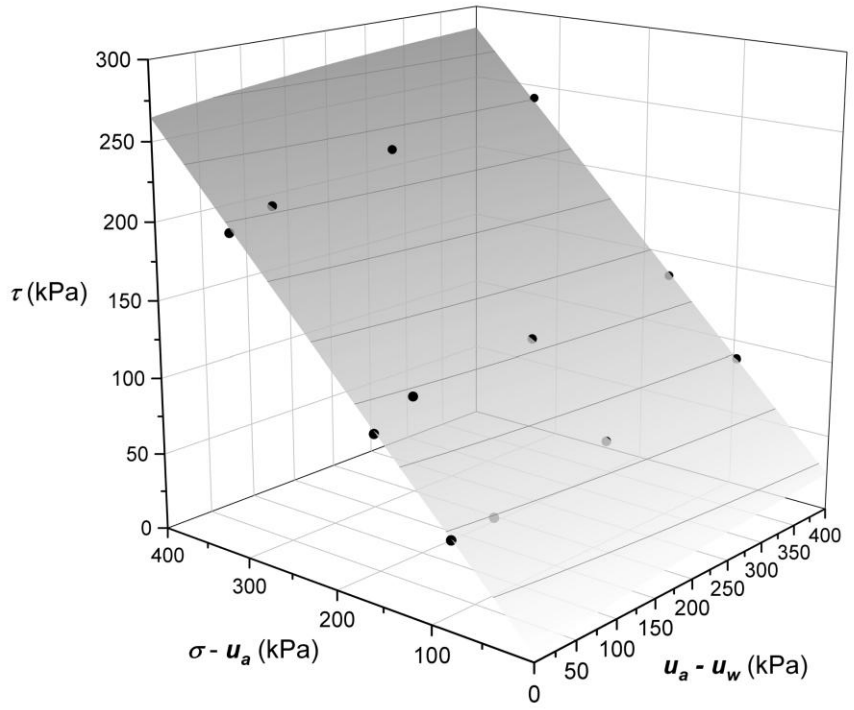

Figure C.180. Extended Mohr-Coulomb failure surface fitted using the Modified Bi-Hyperbolic model of soil 2U

- General comments

The graphs showing axial strain versus deviator stress indicate that most of the curves presented strain-hardening behavior with a slight peak (Figs. C.170, C.172, C.174, and C.176). Some tests were performed until significative axial strains surpassing 40%. In summary, the shear strength parameters considering peak shear strength as failure criterion points out:

ix. The angle ϕ^b is lower than ϕ', however, the maximum ϕ^b obtained is equivalent to 0.18ϕ' for matric suction of 50 kPa, which is superior than the first residual suction (7 kPa), as shown in Table C.30 and Fig. C.169;

x. The angle ϕ' can be considered constant and equal to 33.4° (Table C.30);

xi. The magnitude of the axial strains indicate that the specimens presented ductile behavior.

C.9 Fernandes (2016) – 3U

- Soil basic information and characteristics
  - Void ratio (e_0) = 0.68
  - Density of solids (ρ_s) = 2.69
  - Dry density (ρ_d) = 1.60
  - Liquid limit (w_L) = 21.3%
  - Plastic limit (w_P) = NP
  - USCS = SC (disaggregated) / SC (aggregated)

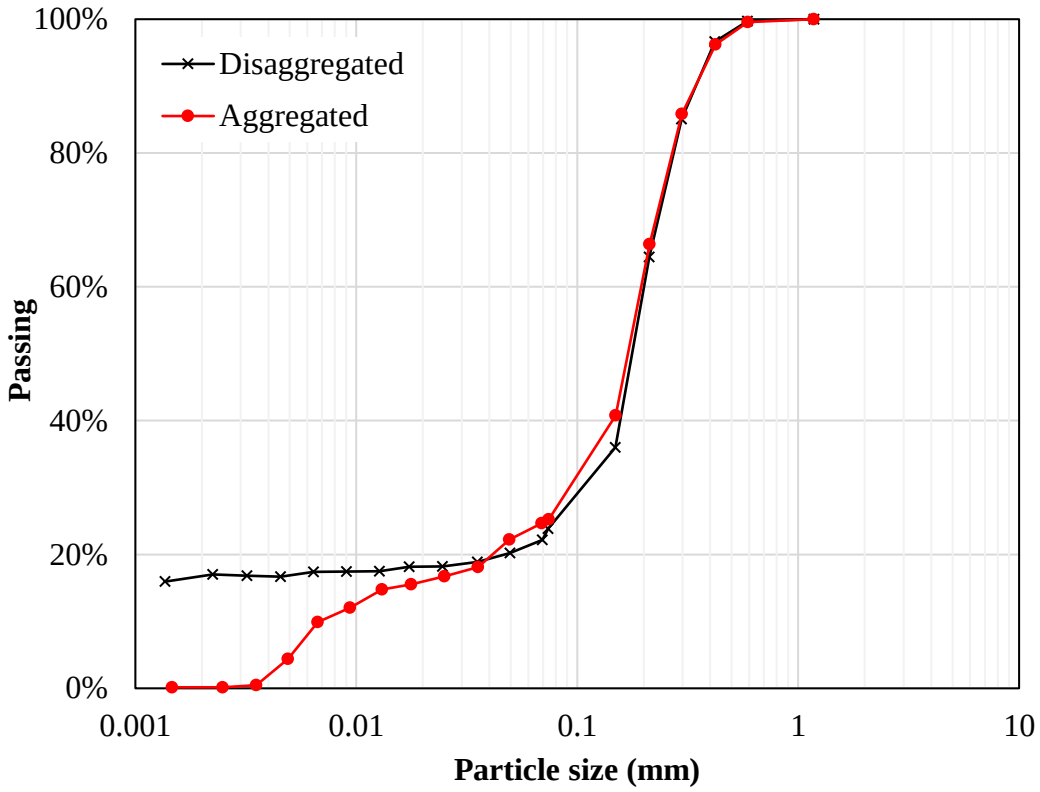

Figure C.181. Grain-size distribution curve of soil 3U

- SWCC

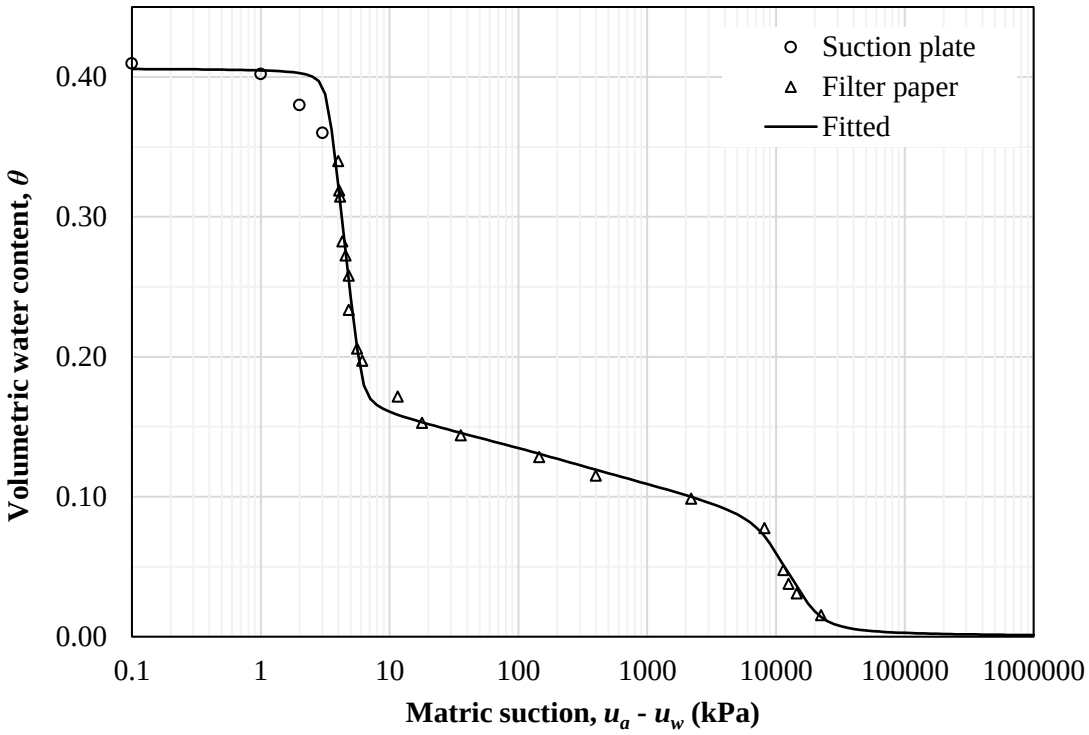

Figure C.182. Soil-water characteristic curves of soil 3U

- Shear strength data:
  - Initial void ratio (e_0) = 0.68
  - Type: modified triaxial CD
  - Volume measurement: double walled cell
  - Shear velocity: 0.05 mm/min

i) $u_a - u_w = 0$ kPa

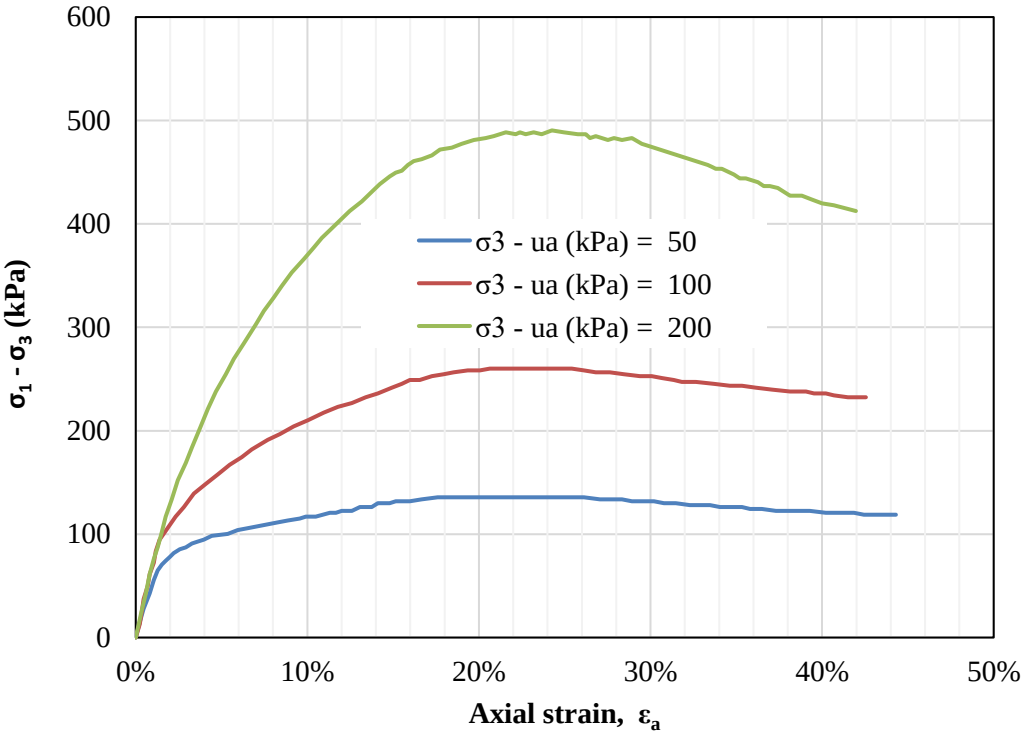

Figure C.183. Axial strain versus deviator stress of saturated tests of soil 3U

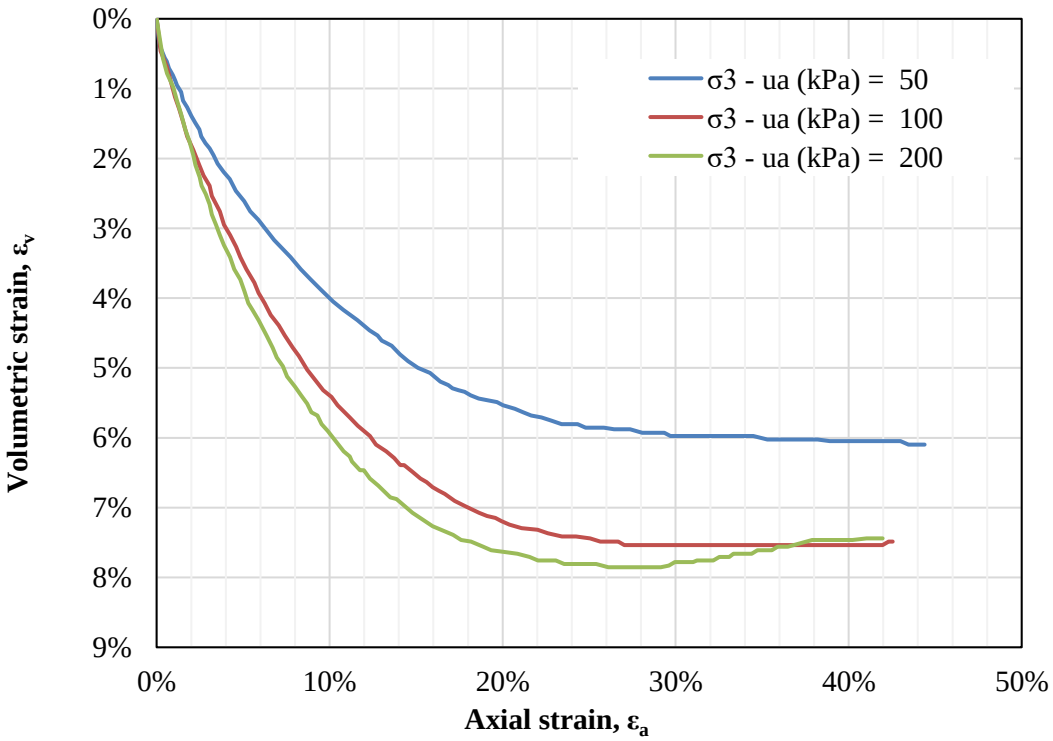

Figure C.184. Axial strain versus volumetric strain of saturated tests of soil 3U

ii) $u_a - u_w$ = 50 kPa

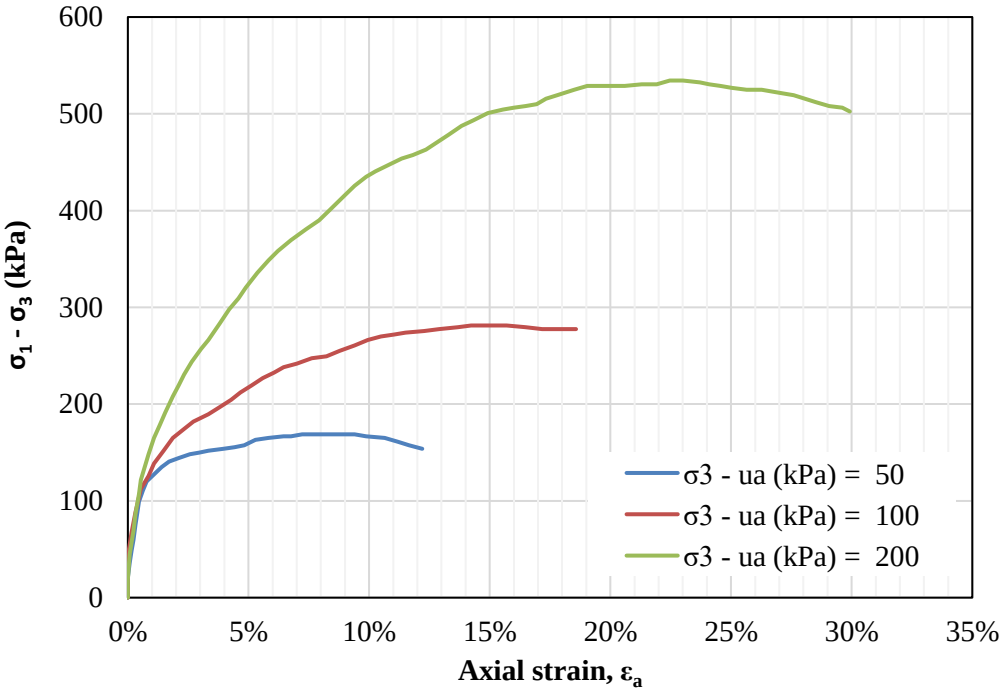

Figure C.185. Axial strain versus deviator stress of unsaturated triaxial tests with (u_a - u_w) = 50 kPa of soil 3U

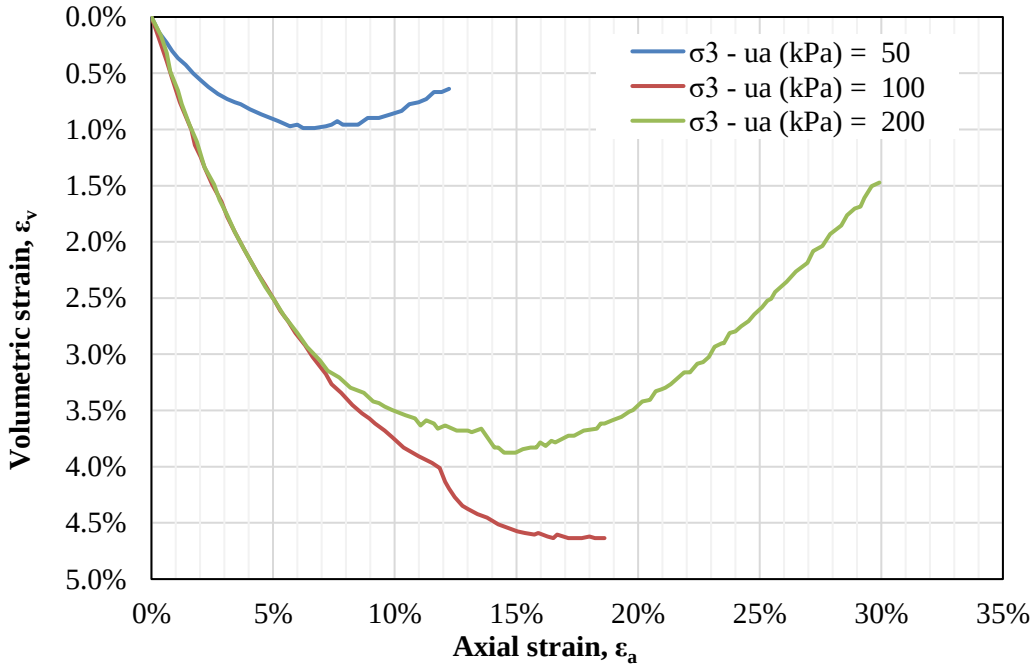

Figure C.186. Axial strain versus volumetric strain of unsaturated triaxial tests with (u_a - u_w) = 50 kPa of soil 3U

iii) $u_a - u_w$ = 200 kPa

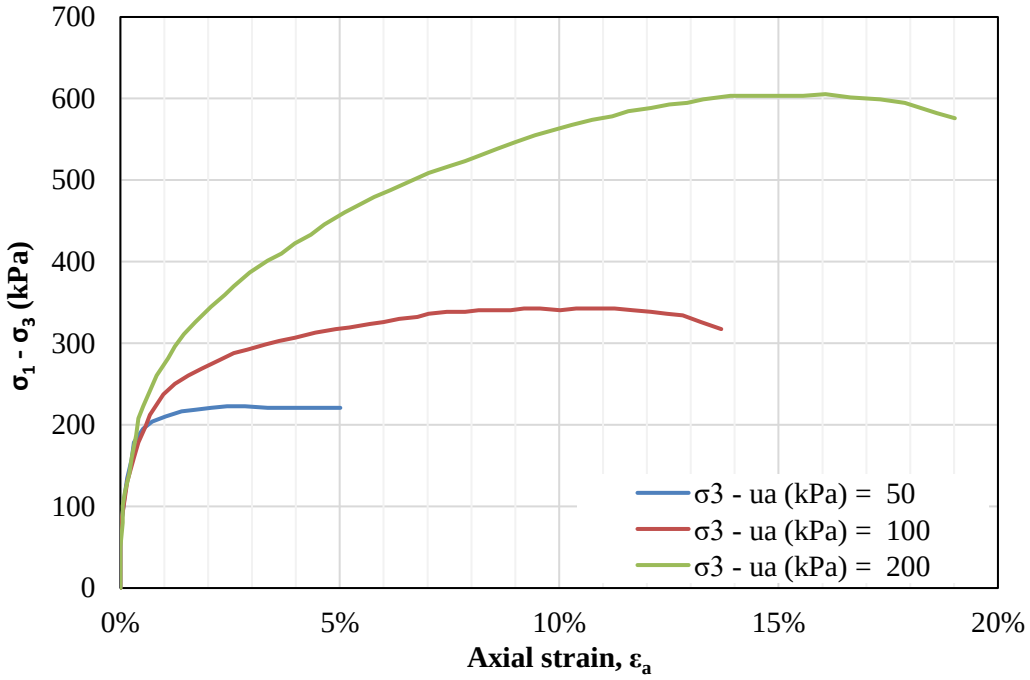

Figure C.187. Axial strain versus deviator stress of unsaturated triaxial tests with (u_a - u_w) = 200 kPa of soil 3U

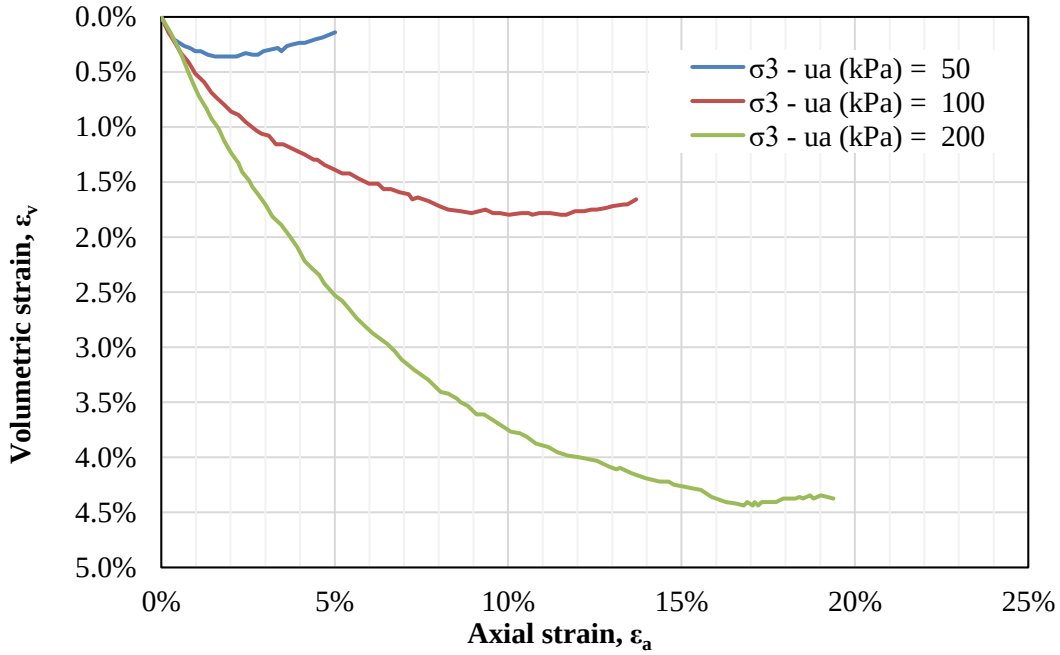

Figure C.188. Axial strain versus volumetric strain of unsaturated triaxial tests with (u_a - u_w) = 200 kPa of soil 3U

iv) $u_a - u_w$ = 400 kPa

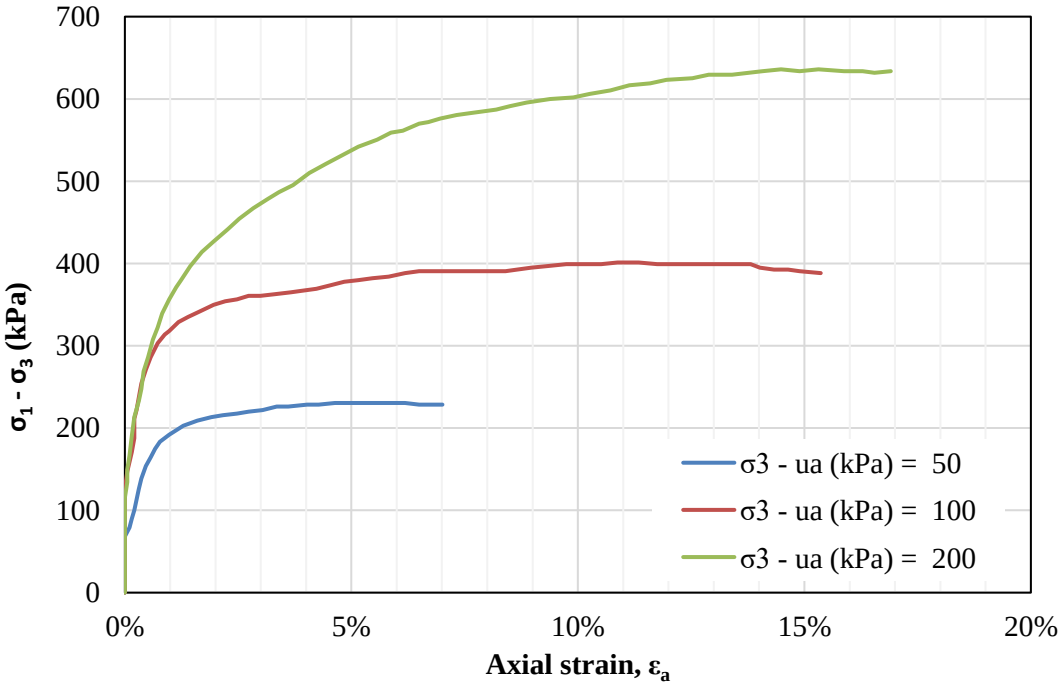

Figure C.189. Axial strain versus deviator stress of unsaturated triaxial tests with (u_a - u_w) = 400 kPa of soil 3U

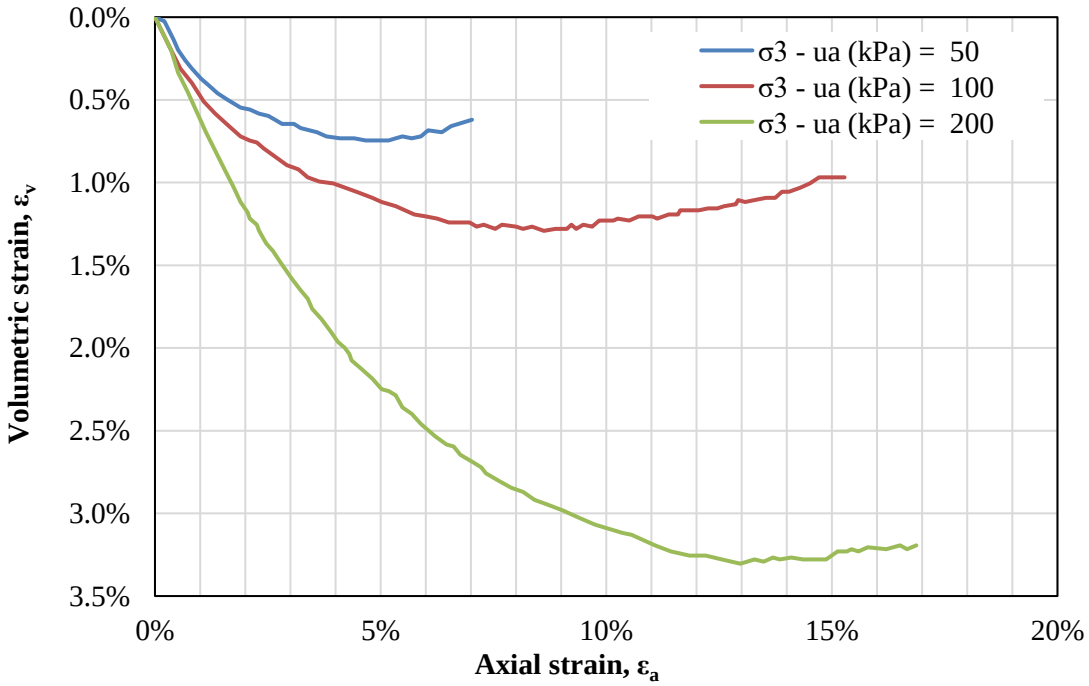

Figure C.190. Axial strain versus volumetric strain of unsaturated triaxial tests with (u_a - u_w) = 400 kPa of soil 3U

- Failure criterion: peak

The data from the shear strength tests for peak failure criterion is presented in Table C.32.

Table C.32. Shear strength parameters from soil 3U for peak failure criterion

$\sigma_1 - \sigma_3$ (kPa)	$\sigma_3 - u_a$ (kPa)	$r = u_a - u_w$ (kPa)	t (kPa)	s* (kPa)	d (kPa)	ψ'	ϕ'	c_{app} (kPa)	ψ^b	ϕ^b	t fitted	Error²	σ_f (kPa)	τ_f (kPa)
135.6	50		67.8	117.8							68.4	0.36	81.1	57.7
260.1	100	0	130.0	230.0	4.7	28.4	32.7	5.6			129.1	0.84	159.7	108.3
490.4	200		245.2	445.2							245.5	0.10	312.6	206.6
168.8	50		84.4	134.4					6.5	7.8	84.4	0.00	87.9	70.4
281.3	100	50	140.6	240.6	9.4	28.8	33.4	11.3	3.9	4.7	140.6	0.00	163.2	117.3
534.4	200		267.2	467.2					5.9	7.1	267.2	0.00	320.0	223.0
222.8	50		111.4	161.4					4.6	5.6	111.4	0.00	98.8	92.1
342.6	100	200	171.3	271.3	20.0	29.3	34.2	24.2	4.1	4.9	171.3	0.00	175.1	141.7
605.4	200		302.7	502.7					4.5	5.4	302.7	0.00	332.7	250.4
230.5	50		115.2	165.2					2.3	2.8	115.2	0.00	99.4	94.4
401.2	100	400	200.6	300.6	23.9	29.7	34.9	29.1	3.5	4.2	200.6	0.00	186.0	164.5
636.0	200		318.0	518.0					2.5	3.0	318.0	0.00	336.3	260.8

SSE	1.3E+0
R^2	1.00
RMSE	0.33

The failure envelope in terms of *s** and *t* shown in Fig. C.191 indicates that ψ' increases slightly with the matric suction. To obtain the values of ψ^b, it was performed a fitting procedure based on the minimization of the squared errors of *t* by changing the values of ψ^b.

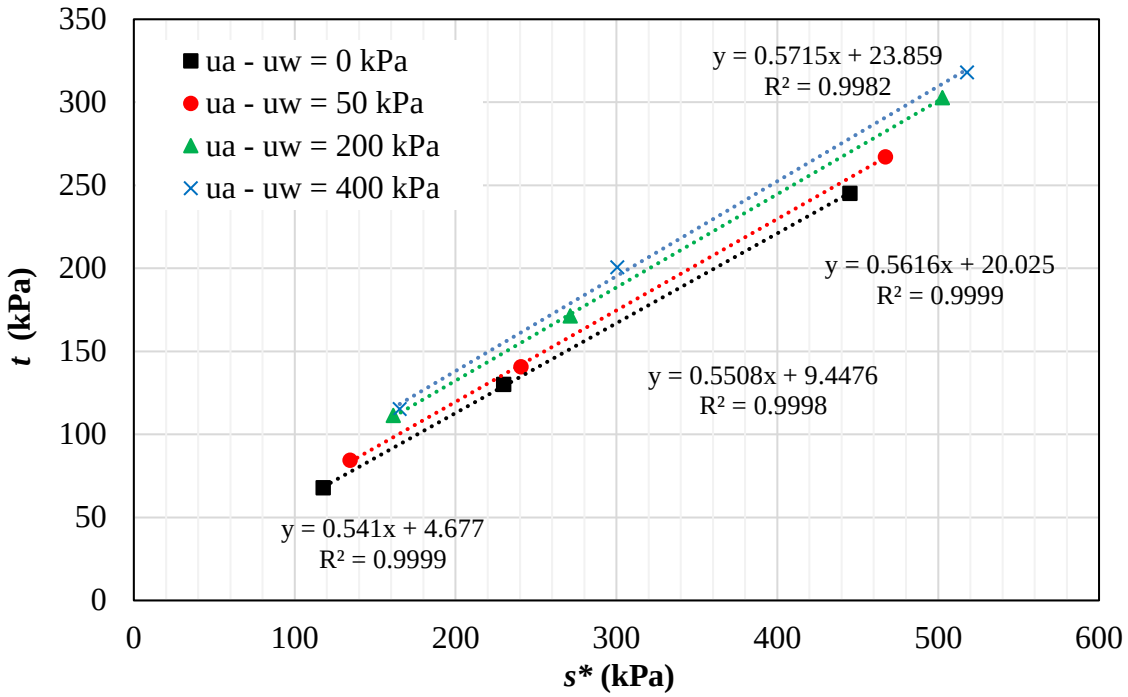

Figure C.191. Failure envelope in terms of *s and *t* for soil 3U**

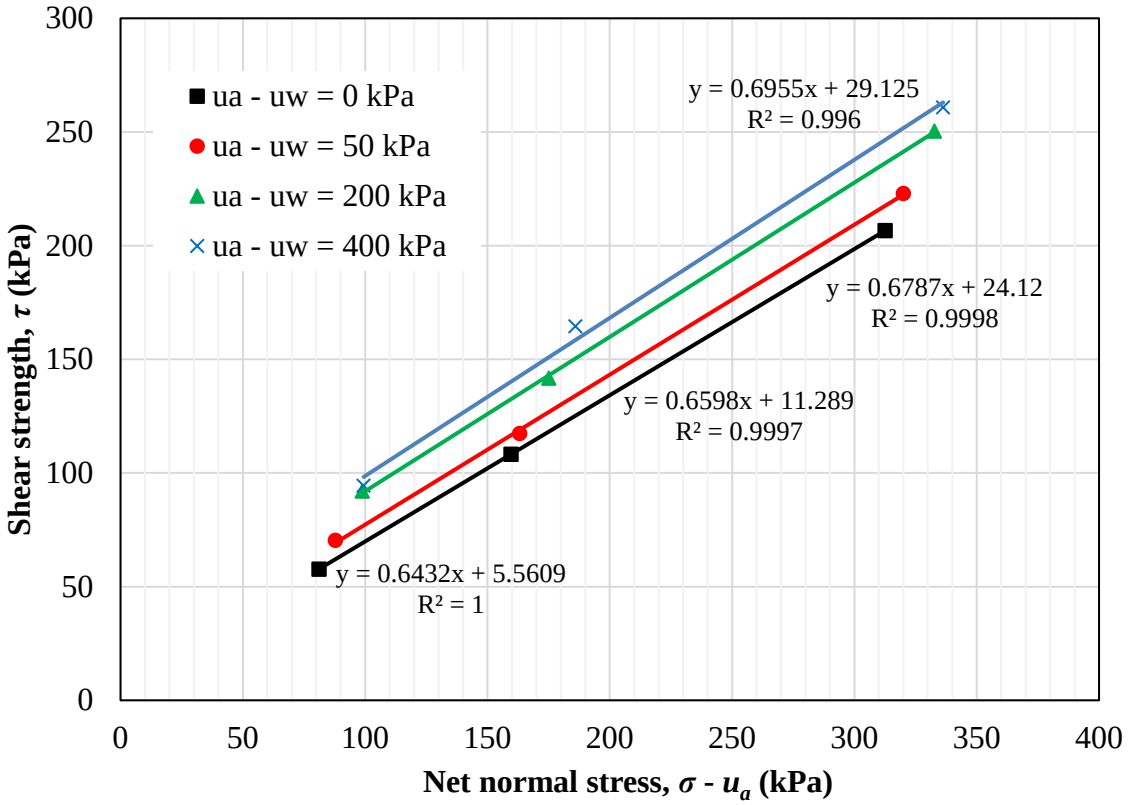

Figure C.192. Failure envelope in terms of (σ - u_a) and τ for soil 3U

The values presented in Table C.32 indicate that ϕ^b reduces as long as the matric suction increases. The values of ϕ^b are on average 6.5º, 5.3º and 3.3º for matric suctions of 50, 200 and 400 kPa, respectively. Table C.32 also shows that the effective friction angle ϕ' increases slightly as matric suction is increased.

Fitting the data from Table C.32 using the Modified Bi-Hyperbolic model resulted in the extended Mohr-Coulomb failure surface depicted in Fig. C.193. The goodness-of-fit obtained (R^2 = 0.998 and RMSE = 3.0) indicate a great data adherence. The fitting parameters are presented in Table C.33.

Table C.33. Parameters obtained for the Modified Bi-Hyperbolic model

c' (kPa)	0.0	s_b	2.4
ϕ' (degrees)	34.1	n	0.4
ϕ^b (degrees)	12.9	a_1	1.479
τ_{ult1} (kPa)	2.81×10^4	b_1	3.55×10^{-5}
τ_{ult2} (kPa)	5.47×10^1	a_2	4.382
τ_{peak} (kPa)	1.0	b_2	1.83×10^{-2}
τ_{ult} (kPa)	1.0		

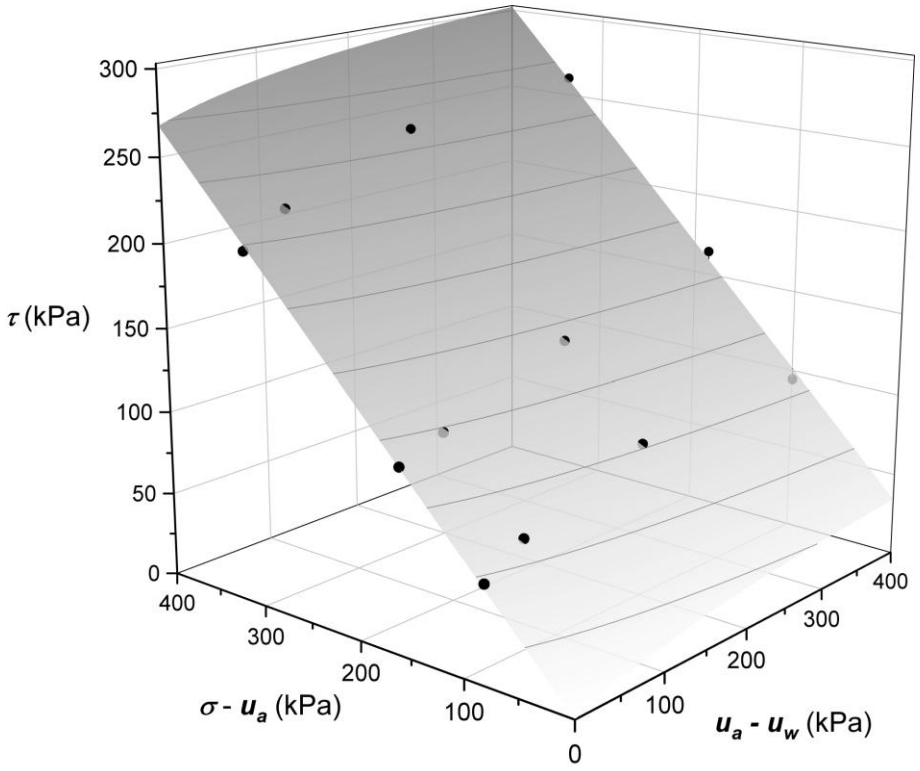

Figure C.193. Extended Mohr-Coulomb failure surface fitted using the Modified Bi-Hyperbolic model of soil 3U

- General comments

The graphs showing axial strain versus deviator stress indicate that most of the curves presented strain-hardening behavior with a slightly peak (Figs. C.183, C.185, C.187, and C.189). Some tests were performed until significative axial strains surpassing 40%. In summary, the shear strength parameters considering peak shear strength as failure criterion points out:

xii. The angle ϕ^b is lower than ϕ', however, the maximum ϕ^b obtained is equivalent to $0.19\phi'$ for matric suction of 50 kPa, which is superior than the first residual suction (6 kPa), as shown in Table C.32 and Fig. C.182;

xiii. The angle ϕ' seems to increase slightly with the matric suction;

xiv. The magnitude of the axial strains as well the images taken after the tests indicate that the specimens presented ductile behavior.